

Development of a new temperature-controlled oedometer

Andrew Kirkham

A thesis submitted in partial fulfilment of the requirements for the degree of
Doctor of Philosophy

Department of Civil and Environmental Engineering
Imperial College London

2020

Declaration

The work presented in this thesis was carried out in the Department of Civil and Environmental Engineering at Imperial College London. This thesis is the result of my own work and any quotation from, or description of the work of others is acknowledged herein by reference to the sources, whether published or unpublished. This thesis is not the same as any that I have submitted for any degree, diploma or other qualification at any other university. No part of this thesis has been or is being concurrently submitted for any such degree, diploma or other qualification.

The copyright of this thesis rests with the author. Unless otherwise indicated, its contents are licensed under a Creative Commons Attribution-Non Commercial-No Derivatives 4.0 International Licence (CC BY-NC-ND).

Under this licence, you may copy and redistribute the material in any medium or format on the condition that; you credit the author, do not use it for commercial purposes and do not distribute modified versions of the work.

When reusing or sharing this work, ensure you make the licence terms clear to others by naming the licence and linking to the licence text.

Please seek permission from the copyright holder for uses of this work that are not included in this licence or permitted under UK Copyright Law.

Andrew Kirkham
London, July 2020

images/declaration/by-nc-nd-eps-converted-to.pdf

Acknowledgements

Here is where I get to say thank you. I've re-written this a few times, partly because it's fun to finally write first-person, partly because I'm procrastinating, but mostly because I can't find the right words. It's not nearly enough, I know, but I mean it - thank you.

To my supervisors, Dr Katerina Tsiamposi and Professor David Potts, for your guidance, good advice, and for generally getting me through to the end.

To Dr Jamie Standing and Dr David Taborda, for your help, interest, and enthusiasm along the way.

To Steve Ackerley, laboratory legend, genius, and MVP, without whom, I guarantee, more than half of these tests wouldn't have worked half as well. And to Stef Karapanagiotidis, future laboratory legend. It almost goes without saying that it's the laboratory staff who make an experimental PhD possible, but I'll say it anyway.

To Dr Emil Ushev, for the vegan sushi, being my Bulgarian tour-guide, and for keeping me somewhat sane, some of the time.

To my mum and dad, for your love, support and biscuits.

To Jolly Boat, the Beatles, the Beat Generation, Brian Wilson and all the other Beach Boys. To Pink Floyd, Janelle Monáe and Electric Wizard. To Weval. To Ash, Misty, Brock, Professor Oak, and PikachuTM. To Mouse-rat and Chewie.

But most of all, to you, Pip.

Abstract

A new temperature-controlled oedometer has been designed at Imperial College London and commissioned to investigate the thermo-hydro-mechanical (THM) behaviour of soils. The proposed application of the research is the design of underground structures which heat or cool the surrounding soil, such as ground source heating/cooling systems, and geological disposal facilities for nuclear waste. High-quality laboratory test data, which are currently lacking, are required for understanding thermal effects on soil, and for calibrating THM constitutive models, used for modelling soil-structure interactions.

In the new equipment, the temperature of the tested specimen is controlled between 5 °C and 70 °C with a temperature-controlled water bath. For heating above ambient temperature, the water bath is heated directly using three 150 W heaters. For cooling below ambient temperature, an external chiller unit is used, in combination with a heat exchanger. Water is continuously circulated through a hollow plate, directly below the specimen, which minimises the temperature gradient across the specimen.

A full, thermal and mechanical calibration of the equipment has been carried out. Vertical thermal and mechanical compliance is determined by repeating the full heating/loading path for the proposed test, with no soil specimen in place. The thermal and mechanical corrections are applied separately, not in combination, because of the much larger magnitude of mechanical strains (and associated error). The instrumentation (load cell and displacement transducers) is raised above the lid of the water bath to isolate it from temperature changes. The differential, thermal, lateral expansion of the confining ring and soil has been considered in the calculation of the soil volume, as too has the thermal expansion of the solid phase of the soil in the calculation of the void ratio. The effect of friction, tilting, and compressible components of the equipment (filter papers and porous stones), has been investigated. Based on these tests, the use of filter papers is discouraged for testing in general, and for thermal testing in particular.

New methodologies for performing thermal tests using the new equipment have been developed and are presented here. These cover calibration, testing, and data-processing, and make explicit exactly how all measured and calculated values are obtained, including how the calibration is determined and applied. Soil tests have been performed to develop and validate the calibration, testing, and data-processing methodologies, using bentonite clay, Leighton Buzzard sand, and KSS clay (a mixture of kaolin, silt and sand). The results from the final series of thermal tests, on KSS, constitute a high-quality data-set, which could be used to calibrate a constitutive model, such as the IC Thermal model used in the Imperial College Finite Element Program (ICFEP). The effect of repeated thermal cycling on normally-consolidated and over-consolidated soil, and the effect of temperature and temperature history on soil behaviour has been tested.

The new temperature-controlled oedometer, together with the new calibration, testing, and data-processing methodologies, can now be used to obtain high-quality data on the one-dimensional thermo-hydro-mechanical properties of other soils.

Contents

List of Figures	9
List of Tables	23
List of Symbols	25
1 Introduction	27
1.1 Research background	27
1.2 Research objectives	28
1.3 Thesis layout	29
2 Development of temperature-controlled oedometers	31
2.1 Overview	31
2.2 Historical advances	31
2.2.1 Introduction and definitions	31
2.2.2 Gray (1936)	41
2.2.3 Finn (1952)	42
2.2.4 Paaswell (1967)	43
2.2.5 Plum and Esrig (1969)	43
2.2.6 Eriksson (1989)	44
2.2.7 Tidfors and Sällfors (1989)	44
2.2.8 Towhata et al. (1993)	47
2.2.9 Moritz (1995)	48
2.2.10 Romero (1999)	50
2.2.11 Villar and Lloret (2004)	52
2.2.12 Abuel-Naga et al. (2005)	54
2.2.13 François et al. (2007)	55
2.2.14 Shariatmadari and Saeidijam (2011)	58
2.2.15 Ye et al. (2012)	59

2.2.16	Mon et al. (2013)	61
2.2.17	Di Donna and Laloui (2015)	63
2.2.18	Vega and McCartney (2015)	65
2.2.19	Favero et al. (2016)	68
2.2.20	Ng et al. (2017)	69
2.2.21	Sittidumrong et al. (2019)	70
2.2.22	Summary of historical advances	71
2.3	Temperature calibration	72
2.3.1	Introduction	72
2.3.2	Literature review of temperature calibration	73
2.3.3	Summary	82
2.4	Soil behaviour	83
2.4.1	Introduction	83
2.4.2	Volume change	85
2.4.3	Pre-consolidation pressure	109
2.4.4	Compression characteristics	122
2.4.5	Consolidation characteristics	132
2.4.6	Permeability	141
2.4.7	Water retention and swelling capacity	147
2.4.8	Pore water pressure	152
2.4.9	Summary of soil behaviour	153
3	Development of a new temperature-controlled oedometer	155
3.1	Introduction	155
3.2	Design overview	155
3.3	Design evolution	161
3.4	Design details	168
3.4.1	Lower section	169
3.4.2	Upper section	171
3.4.3	Water bath	176
3.4.4	Base-plates	181
3.4.5	Chiller and heat exchanger	185
3.4.6	PC and data acquisition	188
3.5	Equipment specification	190
3.5.1	Load frame	190

3.5.2	Load cell	192
3.5.3	Displacement transducers	192
3.5.4	Temperature sensors	194
3.5.5	Heaters	195
3.5.6	Chiller	196
3.6	Ambient temperature oedometer	196
3.7	Summary	197
4	Calibration	199
4.1	Introduction	199
4.2	Friction	200
4.3	Tilting	206
4.4	Vertical thermal and mechanical deformation	214
4.4.1	Calibration - motivation and methodology	215
4.4.2	Calibration - tests 1A and 1B	217
4.4.3	Determining a combined thermal and mechanical calibration	228
4.4.4	Calibration - tests 2 and 3	242
4.5	Filter papers and porous stones	248
4.6	Lateral thermal and mechanical deformation	268
4.6.1	Strain	269
4.6.2	Calculation: thermal deformation of confining ring	271
4.7	Void ratio	281
4.8	Summary	284
5	Thermal tests on bentonite	286
5.1	Introduction	286
5.2	Material description	288
5.3	Overview	290
5.4	Methodology	292
5.5	Results and discussion	292
5.6	Summary	309
6	Thermal tests on sand	311
6.1	Introduction	311
6.2	Material description	311
6.3	Overview	314
6.4	Methodology	319
6.5	Results and discussion	319
6.6	Summary	344

7	Thermal tests on KSS - methodology	346
7.1	Data processing	346
7.1.1	Introduction	346
7.1.2	Measured values	346
7.1.3	Calculated values	347
7.2	Testing	356
7.2.1	Introduction	356
7.2.2	Pre-test	356
7.2.3	Test methodology	357
7.2.4	Setting up the test	358
7.2.5	Running the test	373
7.2.6	Finishing the test	374
7.2.7	Calibration tests	375
7.2.8	Summary	376
8	Thermal tests on KSS - results and discussion	377
8.1	Introduction	377
8.2	Material description	377
8.3	Test overview	378
8.4	Calibration	383
8.5	Results and discussion	392
8.5.1	Effect of current temperature on reloading behaviour	395
8.5.2	Thermal over-consolidation	405
8.5.3	Thermal volume change at different OCR and pressure values	415
8.5.4	Effect of pressure level on thermal volume change	425
8.5.5	Effect of over-consolidation ratio on thermal volume change	427
8.5.6	Compression characteristics	430
8.5.7	Consolidation characteristics	436
8.5.8	Coefficient of permeability	437
8.6	Summary	438
9	Conclusions	440
9.1	Introduction	440
9.2	Research objectives	440
9.3	Recommendations	443
9.3.1	Equipment modifications	443
9.3.2	Testing methodology	445
9.3.3	Further testing	446

A Calibration: load cell	449
B Calibration: LVDTs	455
C Calculation: perpendicular and total thermal expansion coefficients	464
D Calculation: linear and volumetric thermal expansion coefficients	467
E Definitions: compression parameters	470
F Equipment dimensions	473
G Calculation: specimen height using three displacement transducers	476
H Calculation: deformation of dummy specimen	480
I Calculation: void ratio at ambient temperature	482
J Methodology: tests on sand	491
K Methodology: writing TRIAX stages in plain text	495
Bibliography	498

List of Figures

2.1	Schematic - isobaric heating test	37
2.2	Schematic - isothermal loading test	38
2.3	Schematic - conventional oedometer	39
2.4	Equipment photograph (Finn, 1952)	42
2.5	Equipment schematic (Paaswell, 1967)	43
2.6	Equipment schematic - incremental load tests (Tidfors and Sällfors, 1989) . . .	46
2.7	Equipment schematic - constant-rate-of-strain tests (Tidfors and Sällfors, 1989)	46
2.8	Equipment schematic (Towhata et al., 1993)	47
2.9	Equipment schematic (Moritz, 1995)	48
2.10	Equipment photograph (Moritz, 1995)	49
2.11	Equipment schematic (Romero, 1999)	51
2.12	Equipment photographs (Romero, 1999)	51
2.13	Equipment schematic (Villar and Lloret, 2004)	53
2.14	Equipment schematic (Abuel-Naga et al., 2005)	54
2.15	Equipment photograph (François and Laloui, 2010)	56
2.16	Equipment schematics (Salager et al., 2008; François and Laloui, 2010)	57
2.17	Equipment schematic (Shariatmadari and Saeidijam, 2011)	58
2.18	Equipment schematic - overview (Ye et al., 2012)	60
2.19	Equipment schematic - detail (Ye et al., 2012)	60
2.20	Equipment schematic - overview (Mon et al., 2013)	62
2.21	Equipment detail and photograph (Mon et al., 2013)	62
2.22	Equipment photograph (Di Donna and Laloui, 2015)	64
2.23	Equipment schematics (El Tawati, 2010)	66
2.24	Equipment photographs (El Tawati, 2010)	67
2.25	Equipment schematic (Favero et al., 2016)	68
2.26	Equipment schematic (Ng et al., 2017)	70
2.27	Equipment schematic (Sittidumrong et al., 2019)	71
2.28	Components of equipment compliance for Conbel consolidometer (Fredlund, 1969)	74

2.29	Time-dependent compression of filter papers (Fredlund, 1969)	75
2.30	Compressibility of filter papers (Fredlund, 1969)	75
2.31	Temperature calibration of oedometer cell for non-isothermal paths (Romero, 1999)	77
2.32	Vertical thermal expansion of oedometer apparatus (Abuel-Naga et al., 2006) .	78
2.33	Diametrical thermal expansion of confining ring (Abuel-Naga et al., 2006) . . .	78
2.34	Vertical thermal displacement of oedometer apparatus (François and Laloui, 2010)	79
2.35	Diametrical thermal expansion of confining ring (François and Laloui, 2010) . .	79
2.36	Vertical thermal deformation of oedometer apparatus (Shariatmadari and Saeidijam, 2011)	80
2.37	Vertical thermal deformation of oedometer apparatus (Ye et al., 2012)	81
2.38	Thermal axial displacement of oedometer apparatus (Vega and McCartney, 2015)	82
2.39	Thermal strain of NC Penn soil (Paaswell, 1967)	89
2.40	Thermal strain of NC illite (Plum and Esrig, 1969)	89
2.41	Effect of OCR on thermal strain of illite (Plum and Esrig, 1969)	90
2.42	Thermal void ratio change of normally-consolidated MC clay	91
2.43	Thermal void ratio change of normally-consolidated bentonite	92
2.44	Effect of stress level on thermal void ratio change of normally-consolidated MC clay (Towhata et al., 1993)	93
2.45	Effect of OCR on thermal void ratio change of MC clay, for heating following unloading path (Towhata et al., 1993)	94
2.46	Effect of OCR on thermal void ratio change of MC clay, for heating following reloading path (Towhata et al., 1993)	94
2.47	Effect of thermal cycling on normally-consolidated MC clay (Towhata et al., 1993)	94
2.48	Isobaric heating of NC soil - load path for test 1 (Abuel-Naga et al., 2005) . . .	95
2.49	Isobaric heating of OC soil - load path for test 2 (Abuel-Naga et al., 2005) . . .	95
2.50	Isothermal loading of OC soil - load path for test 3 (Abuel-Naga et al., 2005) .	96
2.51	Effect of OCR on thermal strain of soft Bangkok clay (Abuel-Naga et al., 2005)	96
2.52	Effect of OCR on thermal strain of soft Bangkok clay - heating path (Abuel-Naga et al., 2005)	97
2.53	Effect of pre-consolidation pressure on thermal void ratio change of soft Bangkok clay at different OCR (Abuel-Naga et al., 2005)	98
2.54	Thermal void ratio change of OC Sion silt - heating path (François and Laloui, 2010)	98
2.55	Thermal volume change of NC and OC Geneva clay (Di Donna and Laloui, 2015)	99
2.56	Effect of number of thermal cycles on incremental thermal strain of NC Geneva clay (Di Donna and Laloui, 2015)	100

2.57	Effect of plasticity on thermal volume change of NC Geneva clay (Di Donna and Laloui, 2015)	100
2.58	Isobaric thermal cycling of Bonny silt at different OCR - test path (Vega and McCartney, 2015)	101
2.59	Thermal strain of Bonny silt at OCR = 1.00 (NC) (Vega and McCartney, 2015)	102
2.60	Thermal strain of Bonny silt at OCR = 30.29 (highly OC) (Vega and McCartney, 2015)	102
2.61	Effect of OCR on permanent thermal strain of Bonny silt due to temperature cycling (Vega and McCartney, 2015)	103
2.62	Effect of OCR on thermal strain of Opalinus clay (Favero et al., 2016)	104
2.63	Axial strain of NC low-plasticity clay due to thermal cycling (Ng et al., 2017) .	105
2.64	Axial strain of NC Toyoura sand due to thermal cycling (Ng et al., 2017) . . .	105
2.65	Thermal strain of NC Bangkok sand over five thermal cycles (Sittidumrong et al., 2019)	106
2.66	Effect of stress level and relative density on strain induced in NC Bangkok sand by thermal cycling (Sittidumrong et al., 2019)	107
2.67	Schematic - pre-consolidation pressure, p_c	109
2.68	Isothermal loading test path - test 1 (Gray, 1936)	111
2.69	Effect of temperature increase on compression behaviour of fine-grained soil - test 1 (Gray, 1936)	111
2.70	Isothermal loading test path - test 2 (Gray, 1936)	112
2.71	Effect of temperature decrease on compression behaviour of fine-grained soil - test 2 (Gray, 1936)	112
2.72	Effect of thermal cycling on compression behaviour of illite (Plum and Esrig, 1969)	113
2.73	Effect of temperature on pre-consolidation pressure of silty clay (Eriksson, 1989)	114
2.74	Effect of temperature on compression behaviour and pre-consolidation pressure of Bäckebol clay (Tidfors and Sällfors, 1989)	114
2.75	Effect of temperature on pre-consolidation pressure of Linköping clay (Moritz, 1995)	115
2.76	Effect of temperature on pre-consolidation pressure of soft Bangkok clay at different stress levels (Abuel-Naga et al., 2005)	116
2.77	Effect of maximum cyclic temperature on pre-consolidation pressure of soft Bangkok clay at different stress levels (Abuel-Naga et al., 2005)	116
2.78	Effect of maximum cyclic temperature on thermally-induced OCR of soft Bangkok clay at different stress levels (Abuel-Naga et al., 2005)	117
2.79	Effect of temperature on pre-consolidation pressure of Sion silt at different suction levels (François et al., 2007)	118
2.80	Reloading at 23 °C of Opalinus clay - test 1 (Favero et al., 2016)	118
2.81	Reloading at 80 °C of Opalinus clay - test 2 (Favero et al., 2016)	119

2.82	Reloading at 80 °C of Opalinus clay - test 3 (Favero et al., 2016)	119
2.83	Isothermal loading - test paths (Finn, 1952)	122
2.84	Effect of temperature on NCL of highly-compressible clay (Finn, 1952)	123
2.85	Effect of temperature on NCL of illite (Plum and Esrig, 1969)	124
2.86	Comparison of compression behaviour of Bäckebol clay, heated at different stress levels (Tidfors and Sällfors, 1989)	125
2.87	Effect of heating on NCL of MC clay (Towhata et al., 1993)	126
2.88	Effect of a thermal cycle on NCL of MC clay (Towhata et al., 1993)	126
2.89	Effect of temperature on compressibility indices λ and κ of Sion silt (François et al., 2007)	127
2.90	Effect of temperature on compressibility indices λ and κ of GMZ01 bentonite (Ye et al., 2012)	127
2.91	Effect of temperature on coefficient of volume compressibility m_v of kaolin clay (Mon et al., 2013)	128
2.92	Effect of temperature on shear wave velocity v_s of kaolin clay (Mon et al., 2013)	128
2.93	Effect of temperature on oedometric modulus of Geneva clay (Di Donna and Laloui, 2015)	129
2.94	Effect of temperature on oedometric modulus of Opalinus clay (Favero et al., 2016)	129
2.95	Schematic - coefficient of secondary consolidation, C_a	133
2.96	Schematic - comparison of coefficients of secondary consolidation, C_a and C_{ae} .	133
2.97	Effect of temperature on coefficient of consolidation of highly-compressible clay (Finn, 1952)	134
2.98	Effect of temperature on rate of consolidation of bentonite (Towhata et al., 1993)	135
2.99	Effect of temperature on rate of consolidation of soft Bangkok clay (Abuel-Naga et al., 2005)	135
2.100	Effect of temperature on coefficient of consolidation c_v of kaolin clay (Mon et al., 2013)	136
2.101	Effect of temperature on coefficient of consolidation c_v of Geneva clay (Di Donna and Laloui, 2015)	137
2.102	Effect of temperature on coefficient of consolidation of Opalinus clay (Favero et al., 2016)	137
2.103	Effect of heating on secondary consolidation of illite (Plum and Esrig, 1969) . .	138
2.104	Effect of heating on secondary consolidation of MC clay (Towhata et al., 1993)	139
2.105	Effect of temperature on secondary consolidation of Opalinus clay (Favero et al., 2016)	139
2.106	Effect of temperature on coefficient of permeability of NC bentonite (Towhata et al., 1993)	142
2.107	Effect of temperature on coefficient of permeability of Linköping clay (Moritz, 1995)	143

2.108	Effect of temperature on coefficient of permeability of Boom clay (Romero et al., 2001)	144
2.109	Effect of temperature on hydraulic conductivity of FEBEX bentonite (Villar and Lloret, 2004)	145
2.110	Effect of temperature on coefficient of permeability of soft Bangkok clay (Abuel-Naga et al., 2005)	145
2.111	Effect of temperature on hydraulic conductivity of NC Geneva clay (Di Donna and Laloui, 2015)	146
2.112	Effect of temperature on water content of Boom clay at constant suction (ψ) (Romero et al., 2001)	148
2.113	Effect of temperature on suction (ψ) of Boom clay at constant water content (Romero et al., 2001)	148
2.114	Effect of temperature on water retention capacity of FEBEX bentonite (Villar and Lloret, 2004)	149
2.115	Effect of temperature on swelling pressure of FEBEX bentonite (Villar and Lloret, 2004)	149
2.116	Effect of temperature on swelling strain of FEBEX bentonite (Villar and Lloret, 2004)	150
2.117	Effect of temperature on swelling strain of a sand-bentonite mix (Shariatmadari and Saeidijam, 2011)	150
2.118	Effect of temperature on pore water pressure, for first heating-cooling cycle on Bonny silt (Vega and McCartney, 2015)	152
2.119	Effect of temperature on pore water pressure, for all heating-cooling cycles on Bonny silt (Vega and McCartney, 2015)	153
3.1	Schematic of the temperature-controlled oedometer	157
3.2	Photograph of the temperature-controlled oedometer	158
3.3	Schematic of the temperature-controlled oedometer system	159
3.4	Photograph of the temperature-controlled oedometer system	160
3.5	Development schematic 1 of 4	162
3.6	Development schematic 2 of 4	163
3.7	Development schematic 3 of 4	164
3.8	Development schematic 4 of 4	165
3.9	Thermal camera photograph - side view of cell	166
3.10	Thermal camera photograph - top view of cell	167
3.11	Thermal camera photograph - instrumentation plate detail	167
3.12	Effect of water circulation on temperature variation in oedometer cell	168
3.13	Schematic of the temperature-controlled oedometer - lower section	169
3.14	Photograph of the top-cap and confining ring	170

3.15	Photograph of an aluminium oxide (alumina) porous stone	171
3.16	Schematic of the temperature-controlled oedometer - upper section	172
3.17	Photograph of the load cell and instrumentation plate, with lid in place	173
3.18	Photograph of the instrumentation plate, central lid section and water bath	174
3.19	Photograph of the instrumentation plate, showing LVDT adjustment detail	175
3.20	Photograph of the three-part lid with front part removed	178
3.21	Schematic showing connection of oedometer components	179
3.22	Photograph of the heaters and temperature sensor	180
3.23	Photograph of the base drainage and hydrostatic back-pressure	182
3.24	Photograph of the hollow base-plate	183
3.25	Photograph of the pump used for water circulation	184
3.26	Schematic of the cooling system	185
3.27	Photograph of the heat exchanger	186
3.28	Photograph of the chiller unit	187
3.29	Photograph of the 16 channel data acquisition device, within enclosure	189
3.30	Photograph of the load frame	191
3.31	Photograph of an LVDT, with extension piece and heat dissipator	193
3.32	Photograph of an LVDT core piece and extension assembly	193
3.33	Photograph of the LDS	193
3.34	Photograph of a temperature sensor	194
3.35	Photograph of a 150 W cartridge heater	195
3.36	Photograph of limescale build-up on the heaters	196
4.1	Friction effects during consolidation and swelling tests	200
4.2	Schematic of the confining ring showing o-ring seal	201
4.3	Friction test 1 - effect of displacement rate	203
4.4	Friction tests 1 & 2 - effect of applying grease	204
4.5	Hypothetical test with friction (equivalent pressure) of 10 kPa	205
4.6	Photographs of the two inclinometers used to investigate tilting of the loading ram	207
4.7	Schematic of an inclinometer (tilt-sensor)	208
4.8	Schematic plan view of the instrumentation plate showing inclinometer set-up for first set of tilting tests	208
4.9	Tilting tests - set-up and results	210
4.10	Photograph of the two horizontally aligned displacement transducers	211
4.11	Schematic plan view of the instrumentation plate showing inclinometer and horizontal LVDT set-up for second set of tilting tests	212

4.12	Tilting tests - vertical displacement	212
4.13	Tilting tests - inclinometer results	213
4.14	Tilting tests - schematic of top-cap movement based on inclinometer and horizontally aligned displacement transducer data	213
4.15	Tilting tests - horizontal displacement	214
4.16	Schematic showing the effect of heating and loading on measured vertical displacement	216
4.17	Calibration test 1A: simplified flowchart	218
4.18	Calibration test 1B: simplified flowchart	219
4.19	Tests 1A and 1B: specimen set-up for calibration tests	219
4.20	Test 1A: (a) 3D plot (b) displacement vs temperature	221
4.21	Test 1B: (a) 3D plot (b) displacement vs temperature	223
4.22	Tests 1A and 1B: combined 3D plot (a) logarithmic pressure axis (b) linear pressure axis	224
4.23	Tests 1A and 1B: displacement vs pressure	225
4.24	Tests 1A and 1B: displacement vs temperature	226
4.25	Test 1A: inferred thermal response (a) 3D plot (a) displacement vs temperature	227
4.26	Tests 1A and 1B: pressure vs temperature	228
4.27	Semi-log fitting methodology - one-part logarithmic fit	230
4.28	Sigmoid fitting methodology - showing parameters L and x_0	230
4.29	Semi-log fitting methodology - single logarithmic fit	231
4.30	Semi-log fitting methodology - showing discontinuity between fit 1 and fit 2	232
4.31	Semi-log fitting methodology - showing continuous two-part fit	232
4.32	Semi-log fitting methodology - effect of temperature on parameter m_1	234
4.33	Semi-log fitting methodology - effect of temperature on parameter c_1	234
4.34	Semi-log fitting methodology - effect of temperature on parameter c_2	235
4.35	Parameters for semi-log fit	236
4.36	Semi-log fitting methodology - two-part logarithmic fit	237
4.37	Sigmoid fitting methodology - effect of temperature on parameters L , k & x_0	237
4.38	Parameters for sigmoid (logistic) fit	238
4.39	Sigmoid fitting methodology - single fit through 22.5 °C data	239
4.40	Sigmoid fit - comparison of displacement-pressure response at different temperature values	240
4.41	Sigmoid fit - comparison of displacement-temperature response at different pressure values	240
4.42	Absolute error in displacement-pressure response for both fits at 22.5 °C	241

4.43	Absolute error in displacement-temperature response for both fits at 2.5 kPa . . .	241
4.44	Calibration tests 2 and 3: simplified flowchart	243
4.45	Tests 2 and 3: specimen set-up	243
4.46	Test 2: displacement response for pre-loading stage	244
4.47	Test 2: thermally-induced equipment displacement at pressure values of 2.5 kPa, 300 kPa and 1500 kPa	245
4.48	Test 2: thermally-induced equipment displacement at 2.5 kPa pressure	245
4.49	Tests 2 and 3: thermally-induced equipment displacement at 2.5 kPa pressure .	246
4.50	Test 3: thermally-induced equipment displacement at pressure values of 2.5 kPa, 300 kPa and 1500 kPa	247
4.51	Schematic displacement response showing residual displacement (d_{res}) and max- imum displacement (d_{max})	250
4.52	Schematic test set-up for first set of filter paper compliance tests (CO:1-4) . . .	251
4.53	Filter paper compliance tests: displacement vs pressure for first two load/unload cycles (CO:1-4)	252
4.54	Maximum, residual, and range for displacements for filter paper compliance tests (CO:1-4)	252
4.55	Comparison between measured response CO:4, and composite response based on CO:2 and CO:3	253
4.56	Schematic test set-up for filter paper compliance tests in ambient-temperature oedometer (ML:1-7)	255
4.57	Maximum, residual, and range for displacements for filter paper compliance tests in ambient-temperature oedometer (ML:1-7)	256
4.58	Comparison between measured response ML:2, and composite response based on ML:3 and ML:4	256
4.59	Schematic test set-up for filter paper compliance tests in temperature-controlled oedometer (TC:1-9)	258
4.60	Maximum, residual, and range for displacements for filter paper compliance tests in TC oedometer (TC:1-4)	259
4.61	Maximum, residual, and range for displacements for filter paper compliance tests in TC oedometer (TC:5-9)	259
4.62	Schematic showing load/unload response for test TC:2	262
4.63	Test TC:2 - loading cycles 1 - 3	263
4.64	Test TC:2 - loading cycle 9	263
4.65	Test TC:2 - comparison of previous fit based on test TC 1A (semi-log), and new fit based on TC:2 (poly6)	264
4.66	Schematic test set-up for filter paper variability tests (VAR:1-5)	264
4.67	Maximum, residual, and range for displacements for filter papers from same box (VAR:1-5)	265

4.68	Schematic test set-up for tests TC:5,6,7	266
4.69	Tests TC:5,6,7 - displacement vs pressure for first two load/unload cycles . . .	266
4.70	Schematic test set-up for test ML:5	267
4.71	Test ML:5 - displacement vs pressure for first three load/unload cycles	268
4.72	Schematic showing thermal expansion of a hollow cylinder	272
4.73	Schematic showing effect of heating on dimensions of confining ring and soil . .	273
4.74	Schematic showing differential lateral expansion of confining ring and soil . . .	274
4.75	Schematic: calculation of change in specimen height	275
4.76	Schematic: alternative calculation of change in specimen height	276
4.77	Extreme cases for confining ring height correction (a) $\nu = 0.5$ (b) $\nu = 0$	278
4.78	Example phase relationship diagrams at ambient and elevated temperature . .	282
5.1	Schematic - engineered barrier concept showing bentonite buffer	287
5.2	Schematic - thermo-hydro-mechanical actions on the bentonite buffer	287
5.3	Specimen set-up for bentonite tests	291
5.4	Test path for bentonite test 6	295
5.5	Bentonite test 6 - pressure vs time	295
5.6	Bentonite test 6 - displacement vs pressure	296
5.7	Bentonite test 6 - incremental response for 300 kPa loading stage	297
5.8	Bentonite test 6 - comparison of ambient-temperature void ratio calculation methods	298
5.9	Test path for bentonite test 7	299
5.10	Bentonite test 7 - Void ratio vs pressure	299
5.11	Calculation of yield point for bentonite tests - schematic	300
5.12	Calculation of yield point for bentonite test 7, showing reloading path only . .	301
5.13	Comparison between potential reloading paths	302
5.14	Test path for bentonite test 9	303
5.15	Bentonite test 9 - pressure (Y1) and temperature (Y2) vs time in days	303
5.16	Bentonite test 9 - full test - strain vs pressure	304
5.17	Bentonite test 9 - full test - strain vs temperature	305
5.18	Bentonite test 9 - heating only - effect of vertical compliance correction	305
5.19	Bentonite test 9 - heating only - effect of confining ring expansion correction . .	306
5.20	Bentonite test 9 - heating only - void ratio	306
5.21	Bentonite test 9 - cooling only - incremental and sub-incremental strain	307
5.22	Test path for bentonite test 11	308
5.23	Bentonite test 11 - incremental response for 300 kPa reloading stage	309

6.1	Schematic test path for sand tests 1, 2 and 4	316
6.2	Schematic test path for sand test 3 and 5	316
6.3	Schematic test path for sand tests 6 and 7	317
6.4	Schematic test path for sand test 8	317
6.5	Schematic test path for sand tests 9, 10, 11 and 12	318
6.6	Specimen set-up for sand tests	318
6.7	Full test path for sand test 1	320
6.8	Sand test 1 - vertical compliance correction for sigmoid and semi-log fits	321
6.9	Sand test 1 - vertical compliance correction for polynomial fit	322
6.10	Combined test path for sand tests 3, 5, 6, 7 and 8	324
6.11	Full test path for sand test 3	325
6.12	Sand test 3 - pressure and temperature vs time (cycle 1 of 3)	326
6.13	Sand test 3 - strain vs pressure	327
6.14	Sand test 3 - strain vs temperature	327
6.15	Sand test 3 - void ratio vs temperature	328
6.16	Comparison of sand test 3 (saturated) and 5 (dry) - initial heating path at 50 kPa	329
6.17	Full test path for sand test 6	330
6.18	Sand test 6 - strain vs pressure	330
6.19	Comparison of sand test 6 (no grease) and 7 (grease) - full test	331
6.20	Full test path for sand test 8	332
6.21	Sand test 8 - strain vs pressure (full test)	332
6.22	Sand test 8 - strain vs temperature (full test)	333
6.23	Sand test 8 - strain vs temperature (thermal cycles)	334
6.24	Comparison of sand test 3 (heating at 50 kPa) and 8 (heating at 1200 kPa) - initial heating path	335
6.25	Sand test 8 - void ratio vs temperature	335
6.26	Sand test 8 - comparison of specimen strain (Y1) and solids strain (Y2)	336
6.27	Full test path for sand test 9	338
6.28	Sand test 9 - part 1/3 (determine calibration and pre-load filter papers) - displacement response for load cycles 1 to 3	338
6.29	Sand test 9 - part 1/3 (determine calibration and pre-load filter papers) - displacement response for load cycles 2 and 3	339
6.30	Sand test 9 - part 2/3 (main soil test) - displacement vs pressure (log scale) . .	340
6.31	Sand test 9 - part 2/3 (main soil test) - displacement vs pressure (linear scale)	340
6.32	Sand test 9 - comparison between part 1/3 and part 3/3 - load cycles 1 to 3 . .	341
6.33	Sand test 12 - part 1/3 (determine calibration) - load cycles 1 to 3	342

6.34	Sand test 12 - part 1/3 (determine calibration) - load cycles 2 and 3	342
6.35	Sand test 12 - part 2/3 (main soil test) - displacement vs pressure	343
6.36	Sand test 12 - comparison between part 1/3 and part 3/3 - load cycles 1 to 3	343
7.1	Schematic showing calculation of total and incremental values	350
7.2	Schematic showing calibration process	352
7.3	Density of water as a function of temperature	355
7.4	Dynamic viscosity of water as a function of temperature	355
7.5	Equipment required for setting up, running, and finishing the test	359
7.6	Installing the specimen into the confining ring - part 1/2	361
7.7	Installing the specimen into the confining ring - part 2/2	362
7.8	Installing the specimen into the confining ring - schematic sequence	363
7.9	Equipment required for measuring the specimen height	364
7.10	Measuring the specimen height	365
7.11	Equipment required for setting the test initial condition	367
7.12	Setting the test initial condition - photographs	368
7.13	Setting the test initial condition - schematics	369
7.14	Instrumentation installation - part 1/2	371
7.15	Instrumentation installation - part 2/2	372
8.1	Test path for KSS tests A1, A2 & A3	380
8.2	Test path for KSS tests B1, B2 & B3	380
8.3	Test path for KSS tests C1, C2 & C3	381
8.4	Specimen set-up for KSS tests	382
8.5	Compliance data for test series A	384
8.6	Compliance data for calibration test 3	385
8.7	Compliance fits for test series A	386
8.8	Vertical thermal compliance for tests A1, B1 and B2 - initial heating path	388
8.9	Vertical thermal compliance for tests A1, B1 and B2 - first thermal cycle	388
8.10	Vertical thermal compliance for tests A2, B1 and B2 - initial heating path	389
8.11	Vertical thermal compliance for tests A2, B1 and B2 - first thermal cycle	389
8.12	Vertical thermal compliance for tests A3, C1 and C2	390
8.13	Compliance data for test series C	390
8.14	Compliance for test A3, compared with confining ring correction for Poisson's ratio of 0.5 and 0.4	391
8.15	Schematic showing application of vertical compliance correction and confining ring correction	392

8.16	Effect of temperature on shape and position of NCL and swelling lines, based on the IC Thermal constitutive model	393
8.17	Primary isotropic yield surface in $p - J - T$ space (Gawecka, 2017)	394
8.18	Primary and secondary isotropic yield surfaces in the $p - T$ plane (Gawecka, 2017)	394
8.19	Effect of current temperature on reloading behaviour - example test paths in the isotropic $p - T$ plane	395
8.20	Pressure and temperature vs time for test C1 - full test	396
8.21	Pressure and temperature vs time for test C2 - full test	396
8.22	Pressure and temperature vs time for test C3 - full test	397
8.23	Void ratio vs pressure for test C3 - full test	398
8.24	Void ratio vs pressure for test C3 - comparison of sampling techniques	398
8.25	Incremental response for 300 kPa reloading stage for test C3	399
8.26	Comparison of measured and corrected data for test C1	400
8.27	Normalised void ratio vs pressure for tests C1-3 - reloading only	401
8.28	Normalised void ratio vs pressure for tests C1-3 - yield point	401
8.29	Calculation of yield point for test C1, showing reloading path only	402
8.30	Calculation of yield point for test C2, showing reloading path only	403
8.31	Calculation of yield point for test C3, showing reloading path only	404
8.32	Yield point for tests C1, C2, C3	405
8.33	Effect of temperature history on reloading behaviour - example test paths in the isotropic $p - T$ plane	406
8.34	Pressure and temperature vs time for test B1 - full test	407
8.35	Pressure and temperature vs time for test B2 - full test	407
8.36	Pressure and temperature vs time for test B3 - full test	408
8.37	Normalised void ratio vs pressure for tests B1-3 - reloading only	409
8.38	Normalised void ratio vs pressure for tests B1-3 - yield point	409
8.39	Calculation of yield point for test B1, showing reloading path only	410
8.40	Calculation of yield point for test B2, showing reloading path only	411
8.41	Calculation of yield point for test B3, showing reloading path only	412
8.42	Yield point for tests B1, B2, B3 - showing assumed yield surface from test series C	413
8.43	Yield point for tests B1, B2, B3 - showing inferred yield surface from test series B	414
8.44	Effect of isobaric heating on the isotropic yield surface	414
8.45	Effect of OCR on thermal volume change - example test paths in the isotropic $p - T$ plane	415
8.46	Yield surface in the $q - p$ plane - NC loading	417
8.47	Yield surface in the $q - p$ plane - NC loading followed by unloading to OC . . .	417

8.48	Behaviour predicted by IC Thermal model for tests A1-3	418
8.49	Pressure and temperature vs time for test A1 - full test	419
8.50	Pressure and temperature vs time for test A2 - full test	419
8.51	Pressure and temperature vs time for test A3 - full test	420
8.52	Sub-incremental strain for thermal cycles in tests A1-3	420
8.53	Components of thermally-induced strain for test A1	422
8.54	Components of thermally-induced strain for test A2	423
8.55	Components of thermally-induced strain for test A3	423
8.56	Normalised void ratio for thermal cycles in tests A1-3	424
8.57	Comparison of measured and corrected data for test A3	425
8.58	Effect of pressure level on thermal strain for OCR 1	426
8.59	Schematic showing effect of initial loading and unloading on void ratio	427
8.60	Effect of OCR on thermal strain for $P = 300$ kPa	428
8.61	Effect of OCR on thermal strain for $P = 50$ kPa	429
8.62	Void ratio vs pressure for tests B1-3 - NCL	430
8.63	Void ratio vs pressure for tests C1-3 - NCL	431
8.64	Compression index C_c for test series B and C	431
8.65	Schematic showing (a) void ratio and (b) normalised void ratio for two hypothetical normal consolidation lines	432
8.66	Effect of temperature on position of NCL	433
8.67	Effect of temperature history on position of NCL	434
8.68	Coefficient of volume compressibility m_v for tests C1, C2, C3 (reloading path)	435
8.69	Coefficient of consolidation c_v for tests C1, C2, C3 (reloading path)	436
8.70	Coefficient of permeability k for tests C1, C2, C3 (reloading path)	437
8.71	Intrinsic permeability K_{int} for tests C1, C2, C3 (reloading path)	438
9.1	Schematic showing proposed back-pressure system	445
9.2	Proposed test path for additional test C4	447
9.3	Proposed test path for additional tests A4, A5, and A6	447
A.1	Schematic - Budenberg dead-weight calibrator	450
A.2	Linear regression for load cell	454
A.3	Regression error for load cell	454
B.1	Photograph of micrometer set up for LVDT calibration	456
B.2	Photograph of micrometer set up for LVDT calibration - detail	457
B.3	Photograph of LVDT components and brass housings for micrometer calibration	457

B.4	Linear regression for LVDT 1	461
B.5	Regression error for LVDT 1	461
B.6	Linear regression for LVDT 2	462
B.7	Regression error for LVDT 2	462
B.8	Linear regression for LVDT 3	463
B.9	Regression error for LVDT 3	463
C.1	Montmorillonite lattice, showing perpendicular and parallel measurement directions	465
C.2	Strain directions, with perpendicular and parallel measurement directions . . .	465
D.1	Dimensions of rectangular cuboid at initial temperature T_i	468
E.1	Schematic - compression index, C_c and swelling index, C_s	471
E.2	Schematic - plastic compressibility, λ and elastic compressibility, κ	471
E.3	Schematic - coefficient of volume compressibility, m_v	472
E.4	Schematic - oedometric modulus, E_{oed}	472
F.1	Equipment dimensions - confining ring	473
F.2	Equipment dimensions - LVDT assembly and top-cap	474
F.3	Instrumentation plate dimensions - side view	475
F.4	Instrumentation plate dimensions - plan view	475
G.1	Calculation of specimen height - plan view and 3D sketch	477
I.1	Calculation of void ratio - method 1	483
I.2	Calculation of void ratio - method 2	485
I.3	Calculation of void ratio - method 3	487
I.4	Calculation of void ratio - comparing method 1 and method 3	489
J.1	Photograph of the levelling tool used for sand tests	493
J.2	Schematic showing set-up of initial condition for sand tests	494

List of Tables

2.1	Summary of soil types and index properties for literature sources dated 1936 to 1999	33
2.2	Summary of soil types and index properties for literature sources dated 2000 to 2019	34
2.3	Summary of tested temperature and pressure ranges for literature sources dated 1936 to 1999	35
2.4	Summary of tested temperature and pressure ranges for literature sources dated 2000 to 2019	36
2.5	Summary of key aspects of soil thermal behaviour and relevant references	84
2.6	Volume change: summary of observed results from TC oedometer tests	108
2.7	Pre-consolidation pressure: summary of observed results from TC oedometer tests	121
2.8	Compression characteristics: summary of observed results from TC oedometer tests	131
2.9	Consolidation characteristics: summary of observed results from TC oedometer tests	140
2.10	Permeability: summary of observed results from TC oedometer tests	146
2.11	Water retention capacity and swelling capacity: summary of observed results from TC oedometer tests	151
3.1	Summary of oedometer components	190
4.1	Summary of combined thermal and mechanical compliance tests	217
4.2	Calibration test series CO - summary	251
4.3	Calibration test series ML - summary	255
4.4	Calibration test series TC - summary	258
5.1	Summary of physical properties of Bentosund A100 bentonite	288
5.2	Overview of bentonite tests 1 to 11	290
5.3	Summary of initial height H_0 , diameter d_0 , and void ratio e_0 for bentonite tests LA and 3 to 11	292
5.4	Test duration for bentonite tests LA and 3 to 11	293

5.5	Comparison of bentonite tests 3, 4 and 5	294
6.1	Summary of physical properties of Leighton Buzzard sand	312
6.2	Summary of volumetric thermal expansion coefficient (α_v) values for sand	313
6.3	Overview of sand tests 1 to 12	315
6.4	Comparison of sand tests 1, 2 and 4	320
6.5	Summary of calibrations used for selected sand tests	323
6.6	Comparison of sand tests 3, 5, 6, 7 and 8	324
6.7	Comparison of sand tests 9 to 12	337
7.1	Initial/final specimen measurements	347
7.2	Equipment instrumentation measurements	347
7.3	Calculated values	348
7.4	Equipment measurements	360
7.5	Initial specimen measurements	366
7.6	Final specimen measurements	375
8.1	Summary of physical properties of KSS clay	378
8.2	Overview of KSS tests	379
8.3	Summary of initial height H_0 , initial mass m_0 , initial void ratio e_0 , and void ratio following consolidation to 300 kPa e_1 , for KSS tests	382
8.4	Summary of test durations for KSS tests	383
8.5	Test series C - reloading temperature and yield point	405
8.6	Test series B - maximum temperature of thermal cycle and yield point	413
8.7	Test series A - pressure and OCR at which thermal cycles applied	415
8.8	Test summary: effect of pressure level on thermal volume change for OCR = 1	425
8.9	Test summary: effect of OCR on thermal volume change for P = 300 kPa	428
8.10	Test summary: effect of OCR on thermal volume change for P = 50 kPa	428
A.1	Calibration data for 10 kN load cell	453
B.1	Calibration data for LVDT 1	460
B.2	Calibration data for LVDT 2	460
B.3	Calibration data for LVDT 3	460
H.1	Brass dummy specimen deformation	481
I.1	Obtained values from each void ratio calculation method	482
I.2	Required measurements for each void ratio calculation method	490

List of Symbols

Abbreviations and acronyms

CRS	constant rate of strain
CSL	critical state line
GSHP	ground source heat pump
ICFEP	Imperial College Finite Element Program
IP	plasticity index
KSS	kaolin-silt-sand
LL	liquid limit
LVDT	linear variable displacement transformer
NC	normally-consolidated
NCL	normal consolidation line
OC	over-consolidated
OCR	over-consolidation ratio
OED	oedometer
PL	plastic limit
RO	reverse-osmosis
SWRC	soil water retention curve
TC	temperature-controlled
THM	thermo-hydro-mechanical
WRC	water retention capacity

Greek alphabet

α_L	coefficient of linear thermal expansion
α_v	coefficient of volumetric thermal expansion

ϵ_v	volumetric strain
$\epsilon_{mechanical}$	mechanical strain
$\epsilon_{thermal}$	thermal strain
$\epsilon_{v,inc}$	incremental strain
$\epsilon_{v,sub-inc}$	sub-incremental strain
$\epsilon_{v,total}$	total strain
κ	elastic compressibility
λ	plastic compressibility
μ_w	dynamic viscosity of water
ρ_w	density of water
σ_v	vertical stress

Latin alphabet

C_a, C_{ae}	coefficient of secondary consolidation
C_c	compression index
C_s	swelling index
c_v	coefficient of primary consolidation
e	void ratio
E_{oed}	oedometric modulus
G_s	specific gravity
k	coefficient of permeability
K_{int}	intrinsic permeability
m_v	coefficient of volume compressibility
P	pressure
p_c	pre-consolidation pressure
t_{50}	time for 50 % consolidation
w	water content
w_L	water content at liquid limit
w_P	water content at plastic limit

Subscripts

0	initial value
f	final value

Chapter 1

Introduction

1.1 Research background

Human activity is affecting the environment, causing climate change, environmental degradation, mass extinction and biodiversity loss, ecological crises and ecological collapse. This is a fact, undisputed in mainstream science, and this is the background against which all current research is carried out.

Currently, in the United Kingdom, and other countries, high-level (heat-emitting) radioactive waste is stored at surface level, in large water tanks. This is expensive, and unsustainable in the long term. To ensure the security of the waste into the distant future, permanent solutions have been proposed. One of these potential solutions is deep geological disposal of the waste within an underground repository. In such a scheme, natural and engineered barriers will prevent radionuclides reaching the biosphere until they have decayed to a safe level. One of the engineered barriers will be a buffer of low-permeability swelling clay, such as compacted bentonite, which will be affected by the heat emitted from the radioactive waste. A better understanding of how this heat affects the properties of the buffer is required in order to prove the safety of repository design. The data collected need to be relevant to the development of constitutive models. No laboratory experiment can run for the timescale required for deep geological disposal of nuclear waste. However, the results obtained in the laboratory can be used to develop and validate constitutive models, which can simulate the full design life of the repository. Only through a combination of laboratory testing and numerical analysis can the questions relating to repository safety be satisfactorily answered.

Ground source energy systems, such as geothermal piles, can reduce the demand for energy which is currently generated in an unsustainable way, using fossil fuels. Knowledge of how heating and cooling affects the properties of the soil surrounding these systems could lead to more efficient design, and expose non-conservative design.

This research improves our understanding of the thermal behaviour of soil, through the development of laboratory equipment that enables thermal tests to be carried out accurately and repeatably. Temperature-controlled (TC) oedometer tests can be used to investigate the effect of temperature on soil under one-dimensional conditions. However, previous TC oedometer schemes from the literature have limitations, either in apparatus design, calibration and testing procedure, or data interpretation methodology, which have negatively affected the accuracy, reliability, and clarity of the results. In particular, the importance of accurate calibration has been underestimated in previous schemes. As a result, there is a lack of high-quality experimental

data from temperature-controlled oedometer schemes. Existing data are either incomplete, or in some cases, contradictory. This in turn affects the accuracy of constitutive models, which are developed and calibrated with laboratory test data.

In this thesis, the design and development of a new temperature-controlled oedometer, which has some advantages over previous schemes, is described. In addition, calibration, testing, and data-processing methodologies have been developed, which enable accurate thermal tests to be performed in a repeatable way, with a clear understanding of how measured and calculated values are obtained.

1.2 Research objectives

The primary aim of this research is to develop a new piece of laboratory equipment, the temperature-controlled oedometer. This oedometer can then be used for thermal testing of various soils, which has applications to ground source heat pumps (GSHPs) and energy foundations, and deep geological disposal of nuclear waste. The objectives of the research, to achieve the primary aim, are listed below. Additionally, each objective is broken down into the smaller steps taken to achieve that objective.

1. *Develop a new temperature-controlled (TC) oedometer for thermal testing*
 - Control temperature above and below ambient temperature
 - Ensure isotropic heating of the soil specimen
 - Avoid the direct effect of temperature on instrumentation
2. *Calibrate the TC oedometer for thermal testing*
 - Quantify tilting and friction effects
 - Measure the equipment vertical thermal and mechanical compliance
 - Assess the accuracy of a combined thermal and mechanical vertical compliance calibration
 - Quantify the effect of filter papers on vertical compliance, and assess the accuracy of a mechanical compliance with/without filter papers
 - Determine the effect of thermal lateral expansion of the oedometer confining ring, and develop a correction for the volumetric strain to account for this
 - Determine the effect of differential thermal expansion of the solid and water phases of a saturated soil, and develop a correction for the void ratio to account for this
3. *Develop clear, comprehensive methodologies for calibration, testing, and data processing, for the TC oedometer*
 - Develop a calibration methodology that accurately accounts for thermal and mechanical effects
 - Develop a clear, repeatable, testing methodology for performing thermal tests with the TC oedometer
 - Develop a data-processing methodology which can be used for calculating corrected volumetric strains, void ratio, and various other parameters of interest including: yield point, compression and consolidation parameters

4. *Validate these methodologies through tests on soil*

- Perform thermal tests on bentonite clay, Leighton Buzzard sand, and KSS clay
- Modify and improve the methodologies as issues arise during testing
- Assess the accuracy of the methodologies based on the expected soil behaviour, from the literature, and from a constitutive model

1.3 Thesis layout

The thesis comprises nine chapters. **Chapter 1** introduces the research, giving the research background and objectives, and explaining the layout of the thesis.

Chapter 2 provides a comprehensive review of the published literature relating to temperature-controlled oedometer testing. The literature review is split into three sections: historical advances, calibration, and soil behaviour. In the first section, the key features of each scheme are outlined: soil used, equipment used, and types of test performed. In the second section, the calibration process for each scheme is described (where available). In the final section, key soil behaviour results from each scheme are given. Historical advances and calibration are ordered chronologically, while soil behaviour is split into separate sections, each of which considers a certain aspect of the thermal response.

Chapter 3 covers the design and development of the new temperature-controlled oedometer. The final equipment design is described in a series of different scales: system overview, oedometer, and oedometer components. The equipment specification is given for all the electronic components. The chronological development of the equipment, modifications made and the motivation for doing so, is also explained.

Chapter 4 describes the development of the calibration methodology for the temperature-controlled oedometer. This includes tests to quantify the effect of friction and tilting. A combined vertical thermal and mechanical calibration is discussed. The effect of compressible components such as filter papers and porous stones is evaluated through a series of mechanical compliance tests. The effect of lateral thermal expansion of the oedometer confining ring is considered, and corrections are proposed for the measured volumetric strain and void ratio to account for this.

Chapter 5 describes a series of thermal tests carried out on bentonite clay, using the TC oedometer. The primary aim of these tests was development of the testing, calibration, and data-processing methodology. A method is explained for calculating the yield point for an over-consolidated soil reloaded at elevated temperature.

Chapter 6 describes a series of thermal tests carried out on Leighton Buzzard sand, using the TC oedometer. The primary aim of these tests was to assess the accuracy of the calibrations developed in Chapter 4. The limitations of these calibrations are discussed, and an improved calibration methodology is tested.

Chapter 7 describes the final testing and data-processing methodology, used for tests on KSS clay, developed from previous calibration tests (Chapter 4), and tests on bentonite (Chapter 5) and sand (Chapter 6). In the data-processing methodology, full details are given on what measured data are required, and how the calculated values, such as volumetric strain and void ratio are obtained from these data, including how the vertical and lateral thermal corrections are applied. In the testing methodology, a step-by-step explanation is given of exactly how to perform a thermal test with the TC oedometer: setting up, running, and finishing a test.

Chapter 8 describes a series of thermal tests carried out on KSS clay, using the TC oedometer. The primary aim of these tests was to validate the final testing and data-processing methodology, given in Chapter 7. The secondary aim of these test was to understand the effect of temperature on KSS. The results are compared qualitatively with results from the literature, and with predicted results from a constitutive model.

Chapter 9 concludes to what extent the research objectives outlined in Section 1.2 have been met, and gives recommendations for future research.

Chapter 2

Development of temperature-controlled oedometers

2.1 Overview

In this chapter the published literature on temperature-controlled oedometers is reviewed. This research builds upon a number of high-quality PhD theses published at Imperial College London. Martínez Calonge (2017) gives a comprehensive review of temperature-controlled triaxial and isotropic schemes. Gawecka (2017) gives an excellent, extensive review of thermo-hydro-mechanical behaviour of soils. This review focuses on temperature-controlled oedometer schemes and therefore supplements the existing body of knowledge, rather than duplicates it.

It is split into three sections. Section 2.2 gives an overview of each scheme. Section 2.3 reviews the methods for calibration of temperature-controlled oedometers. Section 2.4 reviews soil behaviour, using results obtained from temperature-controlled oedometer schemes. Each section can be read independently.

2.2 Historical advances

2.2.1 Introduction and definitions

The pioneering research involving TC oedometers was done in the USA. Starting with Gray (1936), these early schemes (Finn, 1952; Paaswell, 1967; Plum and Esrig, 1969) focused on the issue of difference in temperature between the laboratory test conditions, and the in-situ conditions. Oedometer tests were performed in order to determine the effect of temperature on the one-dimensional consolidation characteristics of the soil, which can be used to determine the rate and magnitude of settlement under load.

Beginning in the late 1980s, the potential use of saturated clay deposits for heat energy storage became a subject of academic research. Early research in this topic was performed in Sweden, by Eriksson (1989), Tidfors and Sällfors (1989), and Moritz (1995). Again, oedometer tests were performed, this time to understand what effect temperature changes would have on settlement.

Around this time also, the use of swelling clays as buffer materials in geological disposal facilities was first investigated. Towhata et al. (1993) were the first to perform thermal tests on bentonite,

and many subsequent schemes have focused on this application (Romero, 1999; Villar and Lloret, 2004; Abuel-Naga et al., 2005; François et al., 2007; Shariatmadari and Saeidijam, 2011; Ye et al., 2012; Favero et al., 2016).

More recently, to reduce energy costs and environmental impact, understanding the effect of ground source heat pumps (GSHPs) and energy foundations has been of interest. A variety of soils have been tested for this application, including kaolin clay (Mon et al., 2013), Geneva clay (Di Donna and Laloui, 2015), Bonny silt (Vega and McCartney, 2015) and Bangkok sand (Sittidumrong et al., 2019).

It should be noted that the development of TC oedometer testing did not occur in isolation from the development of other temperature-controlled soil-testing equipment. In particular, the pioneering work involving temperature-controlled triaxial apparatus, by Mitchell and Campanella (1964), and their subsequent collaboration (Campanella and Mitchell, 1968), are frequently cited as important milestones in the development of temperature-controlled laboratory testing. However, as discussed above, this review will focus on TC oedometer schemes.

A summary of the soil types and index properties for literature sources is given in Table 2.1 (1936 to 1999), and Table 2.2 (2000 to 2019). Tested temperature and pressure ranges are summarised in Tables 2.3 and 2.4.

Table 2.1: Summary of soil types and index properties for literature sources dated 1936 to 1999

Reference	Soil type	Soil index properties: LL, PL, IP, w [all %], G_s [-]
Gray (1936)	“Fine grained soil”	none given
Finn (1952)	“Slightly organic silt or clay with high compressibility”	LL = 64, PL = 38, IP = 26
Paaswell (1967)	Clay (Penn Soil)	IP = 8.9, G_s = 2.76
Plum and Esrig (1969)	Clay (Illite, Newfield)	Illite (LL = 112, PL = 28, IP = 84, G_s = 2.76, w = 180), Newfield (LL = 25, PL = 14, IP = 11, G_s = 2.74, w = 44)
McGinley (1983)	Clay (Georgia kaolin, smectite)	Georgia kaolin (IP = 19), smectite (IP = 89)
Eriksson (1989)	“Sulphite-rich silty clay”	Luleå (LL = 110, PL = 50, IP = 60, w = 110), Kalix (LL = 103, PL = 37, IP = 66, w = 105)
Tidfors and Sällfors (1989)	Clay (five different Swedish clays)	Bäckebo (LL = 78 to 85, w = 76 to 82)
Towhata et al. (1993)	MC clay, bentonite	MC clay (LL = 70, PL = 41, IP = 29, G_s = 2.751, w = 160), bentonite (LL = 450, PL = 29, IP = 421, G_s = 2.785, w = 700)
Moritz (1995)	Linköping clay	none given
Romero (1999)	Boom clay	LL = 56, PL = 29, IP = 27, G_s = 2.70, w varies

Table 2.2: Summary of soil types and index properties for literature sources dated 2000 to 2019

Reference	Soil type	Soil index properties: LL, PL, IP, w [all %], G_s [-]
Villar and Lloret (2004)	Bentonite clay (FEBEX)	LL = 102, PL = 55, IP = 47, w = 14
Abuel-Naga et al. (2005)	Soft Bangkok clay	LL = 103, PL = 43, IP = 60, G_s = 2.68, w = 90 to 95
François et al. (2007)	Sandy silt (from Sion region, Switzerland)	LL = 25.4, PL = 16.7, IP = 8.7, G_s = 2.74, w = 38
Shariatmadari and Saeidijam (2011)	Sand-Bentonite clay mixture (silica, sodium bentonite from Iran Barite group)	Bentonite (LL = 321, PL = 36, IP = 285, G_s = 2.78), Bentonite/sand mix (LL = 290, PL = 35, IP = 255, G_s = 2.72)
Ye et al. (2012)	Bentonite clay (GMZ)	LL = 313, PL = 38, IP = 38, G_s = 2.66
Mon et al. (2013)	Kaolin clay	LL = 69, PL = 30, IP = 39, G_s = 2.658
Di Donna and Laloui (2015)	Geneva clay	LL = 31.4 to 42.6, PL = 20.1 to 24.2, IP = 11.1 to 18.4, G_s = 2.71 to 2.78, w = 22.3 to 27.9
Vega and McCartney (2015)	Bonny silt	LL = 25, PL = 21, IP = 4, G_s = 2.63
Favero et al. (2016)	Opalinus clay	LL = 38, PL = 23, IP = 15, G_s = 2.75
Ng et al. (2017)	“Low plasticity clay”, Toyoura sand	Clay (LL = 36, PL = 19, IP = 17, G_s = 2.69), Toyoura sand (G_s = 2.65)
Sittidumrong et al. (2019)	Bangkok sand	G_s = 2.68

Table 2.3: Summary of tested temperature and pressure ranges for literature sources dated 1936 to 1999

Reference	Temperature range [°C]	Maximum pressure [MPa]	Additional controlled variables
Gray (1936)	10 to 22	2.0	-
Finn (1952)	4.4 to 26.7	0.8	-
Paaswell (1967)	20 to 75	0.3	-
Plum and Esrig (1969)	24 to 50	1.4	-
McGinley (1983)	26.7 to 85	0.0	Pore water pressure measured
Eriksson (1989)	5 to 55	0.3	-
Tidfors and Sällfors (1989)	7 to 40	2.0	-
Towhata et al. (1993)	20 to 90	2.2	-
Moritz (1995)	20 to 70	0.1	-
Romero (1999)	Ambient to 80	1.2	Suction up to 32 MPa

Table 2.4: Summary of tested temperature and pressure ranges for literature sources dated 2000 to 2019

Reference	Temperature range [°C]	Maximum pressure [MPa]	Additional controlled variables
Villar and Lloret (2004)	30 to 80	5.5	-
Abuel-Naga et al. (2005)	20 to 95	0.3	-
François et al. (2007)	22 to 80	1.0	Suction up to 0.5 MPa
Shariatmadari and Saeidijam (2011)	25 to 90	1.0	-
Ye et al. (2012)	20 to 80	80.0	Suction up to 120 MPa
Mon et al. (2013)	5 to 40	1.3	-
Di Donna and Laloui (2015)	5 to 60	1.0	-
Vega and McCartney (2015)	18 to 91	1.3	Pore water pressure measured
Favero et al. (2016)	23 to 80	100.0	-
Ng et al. (2017)	15 to 70	0.05	-
Sittidumrong et al. (2019)	28 to 50	4.0	-

Definitions

Accuracy and precision

For a set of measurements, accuracy refers to closeness of the measurements to the true value, while precision refers to the closeness of the measurements to each other. In the literature, instrumentation accuracy and precision is often preceded by the \pm sign.

Displacement transducer

A device which converts displacement into an electrical signal. A linear variable displacement/differential transformer (LVDT) is a type of displacement transducer, which works by inducing voltage in a coil by moving a metal core through it. Alternatively, a strain-gauge displacement sensor, also known as a linear position/displacement sensor/transducer (LDS/LDT) may be used. This works by converting axial displacement into lateral deflection of a pair of cantilevered arms, using a tapered wedge. Strain gauges attached to the arms convert this displacement into an electrical signal. In the literature, strain-gauge displacement sensors are sometimes incorrectly referred to as LVDTs.

Isobaric heating test

An isobaric heating test involves heating or cooling the soil at constant pressure. In Figure 2.1, three isobaric heating paths are shown in the temperature - pressure plane, at pressure values P_1, P_2 and P_3 . Only the heating path is shown, but isobaric heating tests may involve both heating and cooling paths, and sometimes multiple cycles of heating and cooling.

These tests can be performed at a number of different, constant pressure values, and the results compared. They are used to determine the effect of stress level, and stress history, on thermal volume change.



Figure 2.1: Schematic - isobaric heating test

Isothermal loading test

An isothermal loading test involves loading a soil at constant temperature. This test can be performed at a number of different, constant temperature values, and the results compared. In Figure 2.2, three isothermal loading paths are shown in the temperature - pressure plane, at temperature values T_1 , T_2 and T_3 . Only the loading path is shown, but isothermal loading tests may involve both loading and unloading paths.

This test is used to determine the effect of temperature on the compression and consolidation characteristics. These include: compression and swelling indices, coefficient of volume compressibility, coefficients of primary and secondary consolidation and coefficient of permeability (indirectly). The effect of temperature on pre-consolidation pressure can also be determined with this test.

The terminology used to refer to this type of test is not consistent in the literature. In Abuel-Naga et al. (2005), isothermal loading is referred to as “isothermal mechanical loading”, to differentiate it from isobaric heating (see below), which is referred to as “thermal loading”. These terms are somewhat ambiguous, which is why isothermal loading and isobaric heating are preferred in this thesis.



Figure 2.2: Schematic - isothermal loading test

Load cell

A force transducer - converts force into an electrical signal. In geotechnical laboratories, the most common type of load cell uses strain gauges, often set in a specific circuit called a Wheatstone bridge.

Oedometer

An oedometer is a standard piece of geotechnical laboratory equipment, used to determine the consolidation characteristics of soils. This is done by applying loads to a soil specimen and measuring the deformation response. No lateral deformation is allowed, so it is a one-dimensional test.

A schematic of an oedometer cell is shown in Figure 2.3. The soil specimen sits within a confining ring, usually made of stainless-steel. Above and below the specimen are

porous stones, which allow movement of water between the soil and the water bath which surrounds the confining ring. The vertical load is applied through the top-cap. The static force can be generated either using hanging weights, or with air- or water-pressure computer-controlled rams. Force is measured using a load cell, from which pressure is calculated based on the cross-sectional area of the specimen. Displacement is measured using one or more displacement gauges. These may be linear variable displacement transformer (LVDTs) or strain-gauge linear displacement transducers (LDTs). Manually-read dial gauges have nowadays mostly been replaced with automated recording.

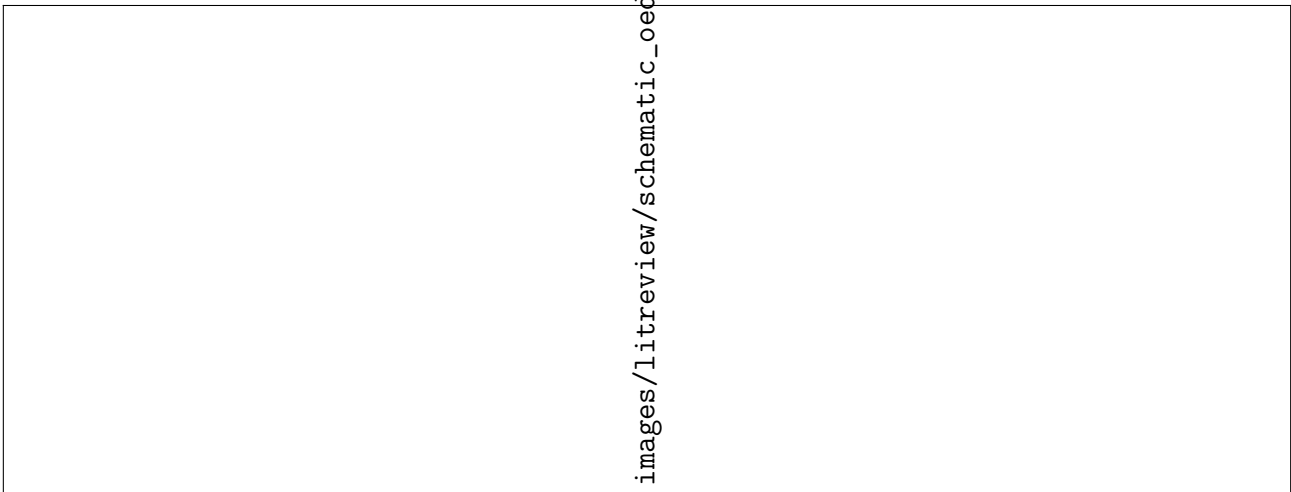


Figure 2.3: Schematic - conventional oedometer

Pressure

The terms *pressure* and *stress* are used interchangeably in the literature on this subject. Both are forces acting upon an area, and have units of N m^{-2} , but they are not the same. Stress occurs when a force is applied to an object in any direction. It can be positive (compressive) or negative (tensile). It can be perpendicular to a surface (normal stress), parallel (shear stress), or at any other angle. Pressure is a special type of stress. It is always positive (compressive), and always perpendicular (normal) to the surface on which it acts. When describing the applied force, divided by the specimen cross-sectional area, in an oedometer test, the terms *applied vertical pressure*, or *applied vertical stress* are slightly less ambiguous alternatives.

Effective stress is the total stress minus the pore water pressure. Both mechanical and thermal loading can result in changes in pore water pressure. Because pore water pressure is not generally measured in oedometer schemes (with some exceptions, e.g. Vega and McCartney (2015)), its value has to be assumed. For mechanical or thermal paths, excess pore water pressure is assumed to reduce to zero once enough time has passed for the excess pore water pressure to dissipate. For this reason, the distinction between total and effective stress is not so rigorously maintained in the TC oedometer literature.

Reconstituted soil

Soil consolidated from a slurry mixed at water content equal to or greater than its liquid limit.

Remoulded soil

Soil mixed without changing the water content, to destroy its structure.

Suction

Suction is another word for negative pore water pressure. Suction either causes air to enter the soil pores, or form within them. *Matrix* suction can be defined as the difference between pore air and water pressure.

$$s = u_a - u_w \quad (2.1)$$

where:

- s = matrix suction
- u_a = pore-air pressure
- u_w = pore-water pressure

Total suction ψ , is the sum of the *matrix* suction s , and *osmotic* suction π . Matrix suction relates to the combination of particle type and structural arrangement, whereas osmotic suction relates to the concentration of salts in the soil water.

$$\psi = s + \pi \quad (2.2)$$

Matrix suction can be controlled in oedometer tests using the axis-translation method (also known as the air-overpressure method). In the axis-translation method, negative pore water pressure is avoided by applying elevated air pressure, so that the appropriate matrix suction is maintained. This method of suction control was used by Romero (1999) and François et al. (2007).

Total suction can be controlled using the vapour-equilibrium method, which makes use of the direct relationship between relative humidity and total suction, as defined by the psychrometric law (or Kelvin's law). Air of a controlled relative humidity is circulated past the soil, until the soil pores come into equilibrium with the air. Relative humidity can be controlled using saturated salt solutions, as in Ye et al. (2012), or mixing dry and wet air in controlled ratios, as in Mantikos (2018), which is a suction-controlled oedometer without temperature control.

Temperature-controlled oedometer

A temperature-controlled (TC) oedometer is an oedometer which can also control temperature. TC oedometers may be modified conventional oedometers, or purpose-built novel designs. With a temperature-controlled oedometer, two main tests can be performed: isothermal consolidation and isobaric heating. With more advanced TC oedometers, complex paths can be followed in the temperature - pressure plane.

In addition to the conventional oedometer components, a TC oedometer will have some form of temperature control system. This generally comprises a heater, a thermocouple, and a thermostat. The heater may be used to directly heat the oedometer water bath, in which case, ring or radial heaters are often used. It may also be used to heat a separate thermal bath, which is connected to the oedometer water bath. In this case, a pump is used to circulate the heated water from the thermal bath to the oedometer

water bath. Sometimes, the heating fluid and the water in the oedometer bath do not mix, and instead the heating fluid is in a closed loop and heating is done through heat exchange. One or more temperature sensors are used to measure temperature. These can be thermocouples or thermistors. Lastly, some form of feedback and control is required, to determine whether to heat or cool based on the temperature measurement. This control device is known as a thermostat (or cryostat). In more recent papers, this role is often performed by a computer program which interacts with the thermocouples and heaters.

Temperature transducer

A device which converts temperature into an electrical signal. Several types of temperature transducer are available: thermocouples, resistance temperature detectors (RTDs), thermistors, and integrated circuit (IC) temperature sensors. There are different types of thermocouples, differentiated by designated letters, which are made from different materials, allowing for different temperature ranges. The most common are Type K (Nickel-Chromium / Nickel-Alumel) and Type T (Copper / Constantan). There are advantages and disadvantages to each transducer type, relating to output stability, sensitivity, accuracy, measurement repeatability, and linearity. Other factors affecting choice of temperature transducer type are temperature range, simplicity, durability, size, and cost. An overview of the advantages and disadvantages of each type is given by Gums (2018). Details on thermocouple types are given by REOTEMP Instruments (2011). Further details on the advantages and disadvantages of all sensors, but particularly IC sensors (the type of sensor used in this project), are given by Omega Engineering (2020).

Transducer

A device that converts variations in a physical quantity, such as force (load cell), displacement (LVDT), or temperature (thermocouple), into an electrical signal.

2.2.2 Gray (1936)

Gray (1936) at Harvard University, USA, performed isothermal consolidation tests at two different temperatures, 10 °C and 22 °C. The aim of the research was to investigate the effect of temperature on the consolidation of a fine-grained soil.

An outline of the research was published as a progress report in the proceedings of the 1st International Conference of Soil Mechanics and Foundation Engineering. Unfortunately, almost no details of the equipment or soil type are given. It is likely that a conventional oedometer was used in a temperature-controlled environment, which was the method used later by Finn (1952). The tested soil is described as “fine-grained”.

Although only a small number of tests were performed, they provide information on the effect of temperature on the pre-consolidation pressure (Section 2.4.3), the slope of the normal consolidation line (Section 2.4.4), and the coefficient of secondary consolidation (Section 2.4.5).

2.2.3 Finn (1952)

Finn (1952) at the University of California, Berkeley, USA, performed isothermal consolidation tests at a range of temperatures, from 4.4 °C to 26.7 °C. Their aim was to study the effect of temperature on the compressive characteristics of “remoulded” clay.

A small, portable lever-arm oedometer was used, housed in a temperature controlled room. A photograph of the equipment is given in Figure 2.4. Based on the photograph, the equipment appears to operate like a conventional lever-arm oedometer. Load is applied by adding free-weights to the hanger at the end of the lever-arm, which then multiplies and transmits the load to the soil specimen. Displacement is measured with a dial gauge. No further details are given about temperature measurement and control.

The tested soil is described as “slightly organic silt or clay with high compressibility” (LL = 64 %, PL = 38 %, IP = 26 %). The loading device was capable of applying a maximum pressure of 766 kPa, for a specimen with a diameter of 50.8 mm, and an initial height of 12.7 mm.

The soil was first air-dried and pulverised, then reconstituted (rather than remoulded, as implied by the title of the paper) by adding enough water to bring the water content to just below the liquid limit. It was then stored, until required for testing, in a room which was kept at a constant temperature of 21.1 °C and 100 % relative humidity. Before testing, the equipment and sample material were either heated or cooled, presumably by placing both in the same temperature-controlled room.

The test results provide information on the slope of the compression curve (Section 2.4.4), and the coefficient of consolidation (Section 2.4.5).



Figure 2.4: Equipment photograph (Finn, 1952)

2.2.4 Paaswell (1967)

Paaswell (1967) at the State University of New York, Buffalo, USA, performed isobaric heating tests, at a range of temperatures, from 20 °C to 75 °C. The tested soil was Penn Soil (IP = 8.9 %, $G_s = 2.76$), which is described as being a derivative of the Brunswick Shale formation.

They developed a temperature-controlled oedometer, shown schematically in Figure 2.5, to evaluate the effect of temperature on a consolidating soil. Direct heating was used, meaning that a higher temperature could be reached. This was an improvement on previous schemes using standard oedometers in temperature-controlled rooms, such as Finn (1952).

The heating element was a flexible tubular unit within the water bath surrounding the specimen. Eight type T thermocouples were used to measure temperature. Four were positioned above and four below the specimen, at the centre, outside and third points of the drainage faces, to check that temperature was uniform across the specimen. They were positioned at the specimen surfaces, rather than within the soil, to avoid affecting the consolidation process. A potentiometer was used to measure the output voltage from the thermocouples.

The soil was remoulded at a water content of 18 %, then saturated in distilled water prior to mechanical loading. The maximum applied pressure was 306 kPa.

This was the first oedometer scheme to use isobaric heating. The effect of heating on volume change of normally-consolidated soil was one of the key results, discussed further in Section 2.4.2. The author proposed that when heated, the soil might behave in a manner something like mechanical loading, and so the phenomena observed could be explained in terms of primary and secondary consolidation.

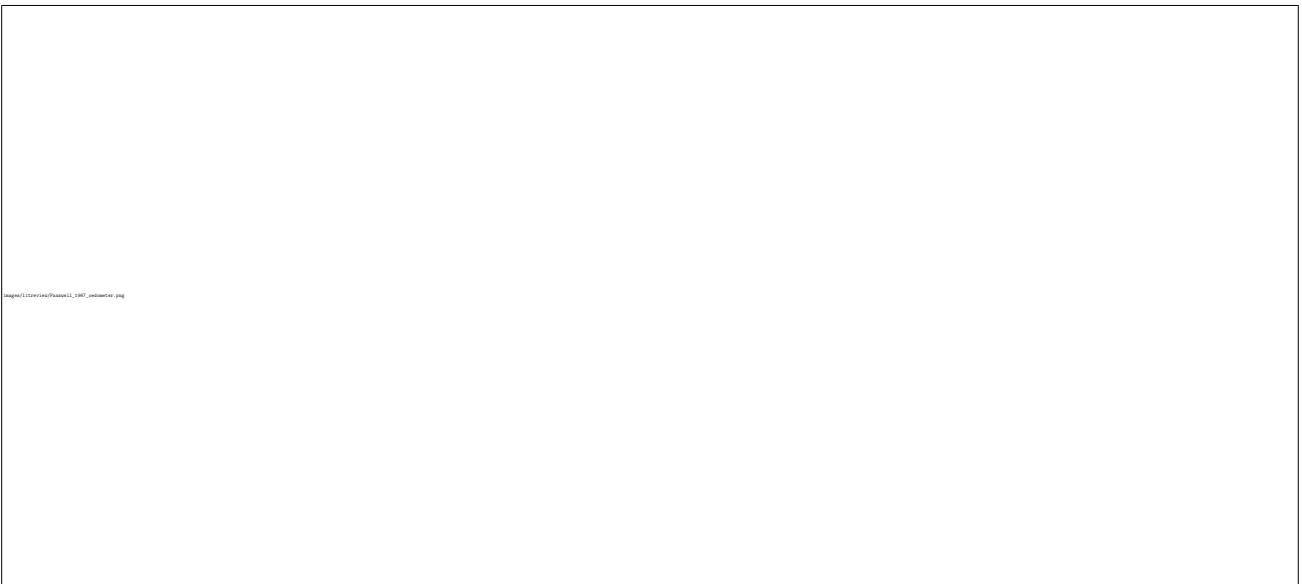


Figure 2.5: Equipment schematic (Paaswell, 1967)

2.2.5 Plum and Esrig (1969)

Plum and Esrig (1969) at Cornell University, USA, used a temperature-controlled oedometer to determine the effect of temperature on soil compressibility and pore water pressure. Tests were performed at temperatures from 24 °C to 50 °C. Two soils were used. One was illite clay

(LL = 112 %, PL = 28 %, IP = 84 % WC = 180 %, $G_s = 2.76$), the other was a glacial lake clay from Newfield, New York (LL = 25 %, PL = 14 %, IP = 11 %, WC = 44 %, $G_s = 2.74$).

The equipment is described as an oedometer within which water can be circulated at a constant temperature around the submerged specimen. Unfortunately, no further details are given. Although the soil is at one point described as “remoulded”, it was actually reconstituted as a slurry, so that it would be normally-consolidated at very low pressure. When maintaining a fixed temperature, the maximum temperature variation was less than 2 °C from the target value. These temperature variations were found to have “virtually no effect on the readings”. The initial specimen height was 19.05 mm. The maximum applied pressure was 1379 kPa.

The types of test performed were quite varied, depending on the property of interest, and are discussed together with the results in Section 2.4. This was the first oedometer study to investigate the effect of over-consolidation ratio on thermal volume change (Section 2.4.2). The authors also presented data on the effect of temperature on pre-consolidation pressure (Section 2.4.3), slope of the compression curve (Section 2.4.4), and secondary consolidation coefficient (Section 2.4.5).

2.2.6 Eriksson (1989)

Eriksson (1989) at the University of Luleå, Sweden, used a temperature-controlled oedometer to investigate temperature effects on consolidation properties of sulphide clays. The research application was heat energy storage in clays with naturally high water content, such as the sulphite-rich clays of northern Sweden. Water has a higher heat capacity than the solid phase of the soil, which makes these clays suitable for heat storage. The storage process involves heating and cooling the clays, so the effect of temperature on consolidation properties is important to understand.

No details are given on the equipment used, or the method of temperature control. The range of temperatures used was 5 °C to 55 °C. The soil tested was “black sulphite-rich silty clay with some organic content” from two locations in northern Sweden, Luleå (LL = 110 %, PL = 50 %, IP = 60 % WC = 110 %) and Kalix (LL = 103 %, PL = 37 %, IP = 66 % WC = 105 %).

The maximum applied pressure was 320 kPa. The method of specimen preparation is not given, but based on the water content values, both soils were initially at, or above, their liquid limit.

Two sets of tests were performed with the temperature-controlled oedometer. The first were standard incremental oedometer tests at different temperatures from 5 °C to 55 °C, with 24 h load increments. The aim of these tests was to determine the effect of temperature on pre-consolidation pressure (Section 2.4.3) and the compression curve (Section 2.4.4). The second were creep tests, at temperatures from 5 °C to 45 °C, with 16 day load increments. The aim of these tests was to determine the effect of temperature on secondary consolidation (Section 2.4.5).

2.2.7 Tidfors and Sällfors (1989)

Tidfors and Sällfors (1989) at Chalmers University, Gothenburg, Sweden, developed two new temperature-controlled oedometers to investigate the effect of temperature on pre-consolidation pressure.

Like Eriksson (1989), they were interested in heat storage in deep, soft clay deposits, using heat exchangers. They wanted to check that the geotechnical properties of the clay would not be

altered to the point that excessive settlements occur, or stability or bearing capacity become too low.

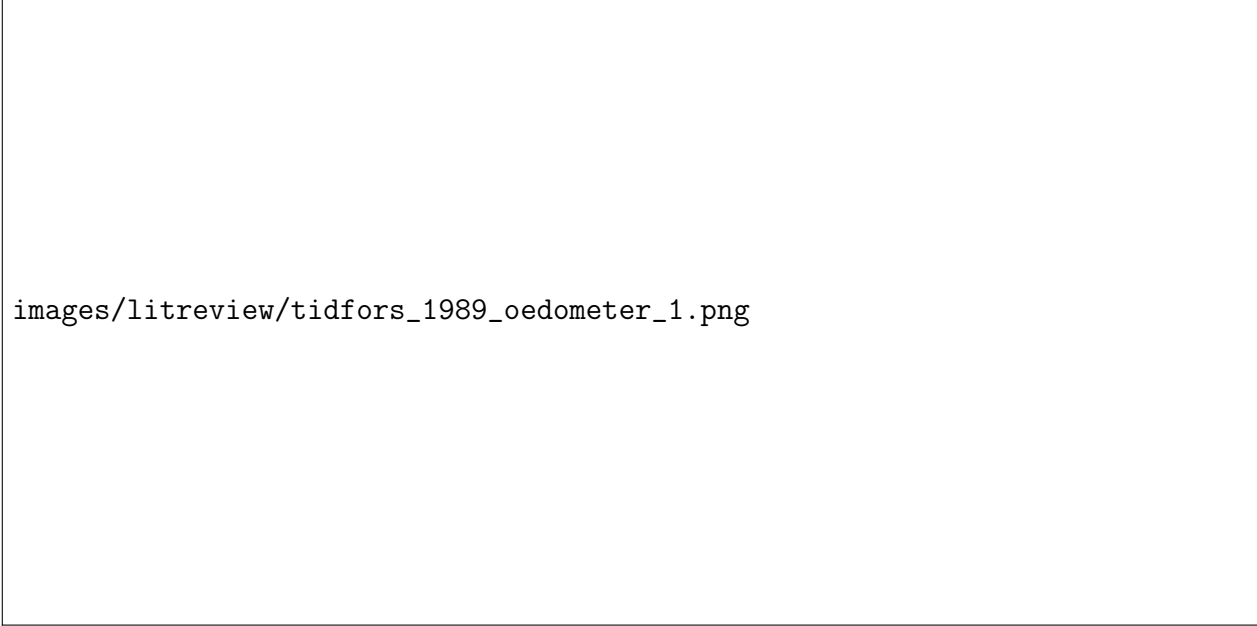
Two pieces of equipment were developed, for performing standard, and constant-rate-of-strain (CRS) oedometer tests. The motivation for using two different types of test is not explained, but the CRS tests may have been used to investigate rate-effects in the soft clay soils tested. Multiple tests could be performed simultaneously using the standard oedometers, as shown in Figure 2.6. This reduces test duration considerably. The choice of equipment might therefore have been determined by time constraints. In both cases, “conventional” oedometers were used, which were modified for temperature control. For the standard incremental load tests, warm water was circulated through the oedometer cell, as shown in Figure 2.6. For the CRS tests, the whole oedometer was submerged in a water bath, as shown in Figure 2.7.

No further details on the equipment are given, but some inferences can be made based on the figures provided. In both tests, no details on displacement measurement are provided, nor are displacement transducers labelled on the oedometer schematics. It is safe to assume that displacement was measured in some way, but the effect of temperature on displacement transducers, or any other instrumentation, is unknown. For the standard incremental load tests, shown in Figure 2.6, it appears that four oedometers were connected in series, to which water from the heated bath was circulated. A v-shaped overflow notch allowed water to flow back into a second, unheated container. This water was then pumped back into the heated bath. The temperature of this heated bath was controlled using a thermostat. According to the authors, “the temperature variation during a test was less than $0.5\text{ }^{\circ}\text{C}$ ”. However, since there appears to be no local measurement of temperature within the oedometer cells, this figure may not be conservative. This system is similar to that used by Sittidumrong et al. (2019), albeit in a simpler form.

For the CRS tests, shown in Figure 2.7, there is a pore-pressure transducer labelled at the base of the oedometer. This suggests that drainage was one-way, with pore-pressure measured at the base of the specimen, in a similar way to Moritz (1995) and Vega and McCartney (2015). An o-ring is labelled at the base of the confining ring, which supports this idea. In fact, the CRS oedometer is remarkably similar to the one used later by Moritz (1995). A thermostat was used to keep the water temperature constant, and a force transducer was used to measure vertical force. The temperature range used in the research was $7\text{ }^{\circ}\text{C}$ to $40\text{ }^{\circ}\text{C}$. The maximum applied vertical stress was 2000 kPa , although most tests were performed up to a maximum of $\approx 170\text{ kPa}$.


Five different clays were tested, with different geological history and composition. All the results given in this review are for Bäckebol clay, a very sensitive marine clay ($\text{LL} = 78\%$ to 85% , $\text{WC} = 76\%$ to 82%). However, it is important to note that temperature effects are dependent on a soil’s clay content, water content, and depositional environment. The material preparation method is not given, although it seems likely, based on the research aims, that the specimens were taken from undisturbed samples and tested at their natural water content, which for the Bäckebol clay was close to the liquid limit.

The effect of temperature on pre-consolidation pressure is given in Section 2.4.3, and the effect on the slope of the normal compression line is given in Section 2.4.4.



images/litreview/tidfors_1989_oedometer_1.png

Figure 2.6: Equipment schematic - incremental load tests (Tidfors and Sällfors, 1989)



images/litreview/tidfors_1989_oedometer_2.png

Figure 2.7: Equipment schematic - constant-rate-of-strain tests (Tidfors and Sällfors, 1989)

2.2.8 Towhata et al. (1993)

Towhata et al. (1993) at the University of Tokyo, Japan, investigated thermally induced volume change in clays. They performed consolidation tests at temperatures from 20 °C to 90 °C. Two soils were used. The first was “MC clay” (LL = 70 %, PL = 41 %, IP = 29 %, $G_s = 2.751$, WC = 160 %), which is described as having a similar mineral content to kaolin clay. The second was bentonite (LL = 450 %, PL = 29 %, IP = 421 %, $G_s = 2.785$, WC = 700 %). For the tests, a slurry was made by mixing the MC clay at a water content of 160 % ($2.3\times$ liquid limit), and the bentonite at 700 % ($1.5\times$ liquid limit). Before testing, a vacuum was applied to remove air from the slurry, to ensure full saturation. The tested specimens had an initial height of 20 mm and a diameter of 60 mm.

The apparatus used was a modified conventional oedometer, equipped with a heater and a thermostat. A schematic of the equipment is given in Figure 2.8. Temperature was controlled by heating the water in the bath. A thermostat was used to measure temperature, and an electric motor with a propeller was used to continuously stir the water, to make the temperature homogeneous in the bath. The temperature in the bath was kept constant within ± 2 °C. The “insulation sheet”, a glass plate, reduces heat-loss through the base of the apparatus, which reduces the temperature gradient across the specimen, although this temperature gradient was not measured. A water tank was connected to the oedometer bath with a siphon, and used to maintain the water level in the bath. Vertical pressure was applied through a loading beam, probably using hanging weights since the equipment is described as “conventional”. The maximum vertical stress applied in the tests was 2230 kPa. Vertical displacement was measured with a dial gauge directly above the top-cap. A calibration was made of the thermal deformation of the apparatus, which is discussed in Section 2.3.

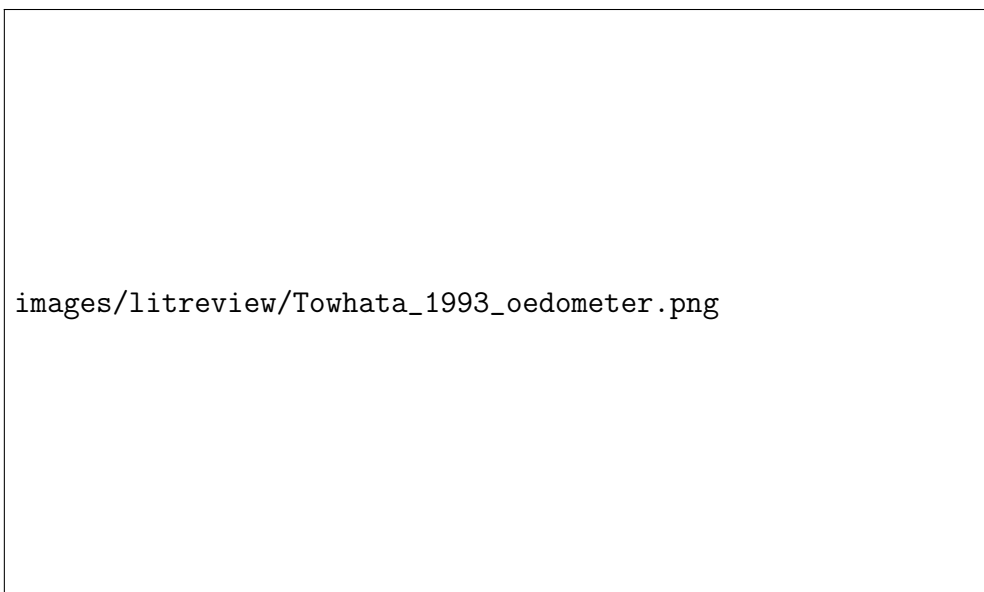


Figure 2.8: Equipment schematic (Towhata et al., 1993)


A comprehensive range of tests was performed, investigating most effects of temperature on consolidation. Volume change was considered in far greater detail than previous schemes, including the effect of stress level, OCR, thermal cycles, and plasticity (Section 2.4.2). Compression characteristics are covered in Section 2.4.4. Consolidation characteristics, both primary and secondary consolidation, are covered in Section 2.4.5. Finally, the effect of temperature on permeability is covered in Section 2.4.6.

2.2.9 Moritz (1995)

Moritz (1995) at the Swedish Geotechnical Institute, performed isothermal consolidation tests using a modified constant-rate-of-strain (CRS) oedometer. They tested intact piston-sampled clay from the Linköping region of Sweden. The results discussed in this review are for specimens taken at 6 m depth (LL = 66 %, WC = 71 %).

The equipment used was a CRS oedometer, capable of temperature control in the range 20 °C to 70 °C. The maximum applied vertical pressure was 140 kPa. This was possibly a modified version of the oedometer used by Tidfors and Sällfors (1989), using a different method of temperature control, but similar measurement of pore-pressure. A schematic is shown in Figure 2.9 and a photograph is shown in Figure 2.10.

The specimen was mounted in a confining ring, labelled “Teflon ring” of diameter 50 mm and height 20 mm, which was placed on a “filter stone”. The internal surface of the ring was coated with Teflon (PTFE), to reduce friction between the soil and the ring. The confining ring was held in position with a guide and clamp ring. This also helped guide the loading arm and maintain verticality. The top-cap had a filter stone which could fit within the confining ring. During the test, one-way drainage conditions were imposed. At the top there was free drainage, while at the base, there was no drainage. Instead, pore-pressure was measured using a transducer. A “deformation transducer” mounted on the clamp ring, measured the displacement of the top-cap.



images/litreview/Moritz_1995_oedometer_1.png

Figure 2.9: Equipment schematic (Moritz, 1995)

Strips of heat foil, which can be seen in Figure 2.10, were used to apply the heat. A thermostat connected to the foil was used to control the temperature to within $\pm 0.1^\circ\text{C}$. To minimise thermal deformation of the confining ring, it was made from Invar (64% steel, 36% nickel), chosen for its low coefficient of thermal expansion ($a_L = 1.5 \times 10^{-6} \text{ }^\circ\text{C}^{-1}$). For comparison, the (linear) thermal expansion coefficient of steel is approximately $11.5 \times 10^{-6} \text{ }^\circ\text{C}^{-1}$. Note that both of these values are from Moritz (1995).

Results from this research relating to the effect of temperature on oedometer modulus (stiffness) are given in Section 2.4.4. The effect of temperature on pre-consolidation pressure is given in Section 2.4.3. The effect of temperature on the coefficient of permeability is given in Section 2.4.6.



Figure 2.10: Equipment photograph (Moritz, 1995)

2.2.10 Romero (1999)

Romero (1999) at the Universitat Politècnica de Catalunya (UPC), Barcelona, Spain, designed, developed and calibrated a temperature- and suction-controlled oedometer as part of their PhD thesis. The aim of the research was to analyse the effects of temperature and hydration on clay volume change behaviour, permeability and water retention characteristics. The temperature range used in the tests was from 22 °C to 80 °C.

The material tested was unsaturated Boom clay (LL = 56 %, PL = 29 %, IP = 27 %, $G_s = 2.70$). As the author points out, information on the thermal behaviour of unsaturated soil is relatively limited, compared to saturated soil. Specimens were prepared by statically compacting powder at the hygroscopic water content to the target dry density of 1.7 Mg m⁻³. Water was then added until the water content reached 15 %.

This research is published as a PhD (Romero, 1999), and several journal papers: Romero et al. (2001) focus on temperature effects on hydraulic behaviour of Boom clay, while Romero et al. (2005) compare the thermo-hydro-mechanical behaviour of Boom clay and FEBEX bentonite (LL = 102 %, PL = 55 %, IP = 47 %).

A schematic of the equipment is shown in Figure 2.11, and photographs are shown in Figure 2.12. A full description of each component of the equipment is given in Romero (1999), and it is well worth reading the relevant section, as it goes in to much more detail than is possible with journal papers.

Suction was controlled using the axis translation technique (see definitions at the start of this section). This requires separate air pressure and water pressure to be applied to the specimen. Air pressure was applied at the top of the specimen, and water pressure at the base, through stainless-steel coarse porous stones of 15 µm pore size and 19 kPa air-entry value.

Axial strain was measured using a dial gauge, positioned directly above the specimen, which registered the displacement of the top platen. This can be seen most clearly in Figure 2.12. Vertical stress was applied using air pressure, which acted on the loading platen, separated by a rubber membrane from the pore-air pressure chamber. According to the author, the design of the loading system means that the loading platen did not tilt during stress path testing, although it is not clear how that was ensured in practice, or whether this was checked.

Temperature control was achieved using a 500 W helical electric heater in a silicone oil bath which surrounded the specimen. Silicone oil was used rather than water as the heating fluid, presumably because of its higher boiling point, which means temperatures close to 100 °C could be reached without phase change of the fluid. However, the thermal conductivity of silicone oil is approximately 25 % of the thermal conductivity of water (Shin Etsu Silicone, 2019). This makes it more likely that heat gradients would be induced in the fluid. The surface of the cell was covered with a 6 mm thick cork insulating layer. At 80 °C, the measured temperature variations were less than ±0.5 °C. A type K thermocouple was positioned close to the soil specimen, to measure soil temperature. A thermostat was used to control the heater, based on the measured soil temperature. The initial specimen dimensions were: height 10 mm, diameter 50 mm.

Calibration of this equipment is covered in Section 2.3. Results relating to the effect of temperature on the coefficient of permeability are given in Section 2.4.6, and the effect of temperature on water-retention capacity is given in Section 2.4.7.

images/litreview/Romero_1999_oedometer_1.png

Figure 2.11: Equipment schematic (Romero, 1999)

images/litreview/Romero_1999_oedometer_2.png

Figure 2.12: Equipment photographs (Romero, 1999)

2.2.11 Villar and Lloret (2004)

Villar and Lloret (2004) at CIEMAT, Madrid, Spain, and UPC, Barcelona, Spain, performed tests to determine swelling pressure and hydraulic conductivity as a function of temperature. The application of the research was the design of geological disposal facilities for nuclear waste. Bentonite clay is proposed as a sealing material. As such, it is important to understand its behaviour when subjected to hydraulic and thermal changes.

The soil used was FEBEX bentonite (LL = 102 %, PL = 55 %, IP = 47 %, WC = 14 %), which is the buffer material proposed by the Spanish agency for radioactive waste management, ENRESA. This bentonite has a montmorillonite content greater than 90 %.

They used a high-pressure oedometer, shown in Figure 2.13. The oedometer was placed in a bath of silicone oil, which was kept at a constant temperature. Silicone oil was also used as the heating fluid by Romero (1999) and is discussed in Section 2.2.10. Displacement was measured using two LVDTs mounted on the projecting sides of the clamping ring, which held the oedometer confining ring in place. Although using two LVDTs allowed volume change to be accurately calculated, three are required to fully understand the effect of tilting. The amount of water going in and out of the specimen was also measured, as an alternative way to calculate volume change. The vertical load was measured using a load cell installed on the loading frame.

The specimens were prepared by compacting granulated clay at room temperature, at the hygroscopic water content ($\approx 14\%$), to a nominal dry density of 1.6 g cm^{-3} , under a vertical stress of $15 \pm 1 \text{ MPa}$. They were then heated to the target temperature, and saturated by injecting water through the inlet at the base of the specimens at 0.6 MPa , while keeping the outlet at the top of the specimens open. This process formed part of the swelling capacity test. The initial specimens had diameter 50 mm and height 12 mm.

Using this equipment, the authors investigated the effect of temperature on the swelling capacity of clay. This was done in two ways. To measure swelling capacity in terms of pressure, the soil was soaked under constant volume conditions, at fixed temperatures, ranging from 30°C to 80°C , and the resulting swelling pressures measured with the load cell. Swelling pressures up to 5.5 MPa were measured, but the capacity of the oedometer was at least 15 MPa . To measure swelling capacity in terms of strain, the soil was soaked under constant pressure conditions, at fixed temperatures, and the resulting swelling strains measured with the LVDTs. Results from these tests are discussed in Section 2.4.7.

They also investigated the effect of temperature on hydraulic conductivity. At a range of temperatures from 22°C to 80°C , they applied a pressure gradient across the specimen, measuring the outflow, and used Darcy's law to calculate the hydraulic conductivity. Results from these tests are discussed in Section 2.4.6.



Figure 2.13: Equipment schematic (Villar and Lloret, 2004)

2.2.12 Abuel-Naga et al. (2005)

Abuel-Naga et al. (2005) at the Asian Institute of Technology, Thailand, carried out extensive thermal testing on Soft Bangkok clay ($LL = 103\%$, $PL = 43\%$, $IP = 60\%$, $G_s = 2.68$, $WC = 90$ to 95). The material preparation method was not specified but can be inferred from the description of the testing method: “The specimens . . . were consolidated under different stress levels greater than their natural pre-consolidation pressure. Based on the results . . . the natural pre-consolidation pressure was found to be 70 kPa ”. The reference to *natural* pre-consolidation pressure, and its measured value, suggests that the specimens were undisturbed, rather than remoulded or reconstituted. The natural water content was just below the liquid limit for this soil. The initial specimen diameter was 65 mm . The initial specimen height is not specified.

A modified oedometer was used, shown schematically in Figure 2.14. As in a conventional oedometer, load was applied through a loading beam, and displacement measured with a dial gauge positioned centrally above the specimen. The maximum applied vertical pressure in the tests was 300 kPa . A 600 W ring heater was attached to the outer ring of the oedometer. The soil was heated indirectly, by heating the water in the bath which surrounds the soil specimen. A ring heater was used to try and heat the soil specimen evenly, although the homogeneity of the soil temperature was not independently measured. A hot water supply, at the same temperature as the water in the bath, was used to replenish water lost due to evaporation. Temperature in the bath was measured using a type K thermocouple, placed in the bath, rather than within the specimen, to avoid disturbing the specimen. Temperature was controlled using a thermo-controller unit with an accuracy of $0.1\text{ }^\circ\text{C}$. With this system, temperature was kept constant within the range $\pm 0.1\text{ }^\circ\text{C}$. The tested temperature range was $20\text{ }^\circ\text{C}$ to $90\text{ }^\circ\text{C}$.



Figure 2.14: Equipment schematic (Abuel-Naga et al., 2005)

An extensive range of tests was performed, which makes this a particularly useful reference. Various factors which can affect thermal volume change were considered, including the effect of over-consolidation ratio, stress level and soil plasticity. These results, as well as the effects of thermal cycling, and the phenomenon of thermally-induced over-consolidation are presented in Section 2.4.2. The effect of temperature on pre-consolidation pressure, including the effect of stress level, is presented in Section 2.4.3. The effect of temperature on the coefficient of

consolidation is given in Section 2.4.5. Finally, the effect of temperature on the coefficient of permeability is given in Section 2.4.6. Calibration of the equipment is given in Section 2.3.

2.2.13 François et al. (2007)

François et al. (2007) at the École polytechnique fédérale de Lausanne (EPFL), Switzerland developed an oedometer with combined temperature and suction control. This research was published in several journal papers, including Salager et al. (2008) and François and Laloui (2010). In particular, François and Laloui (2010) go into great detail on the equipment design and calibration, of which the latter is discussed further in Section 2.3.

The soil used is described as “sandy silt” from the Sion region of Switzerland, referred to as Sion silt (LL = 25.4 %, PL = 16.7 %, IP = 8.7 %, $G_s = 2.74$, WC = 38 %). It was re-constituted at a water content of $1.5 \times$ liquid limit to form a saturated slurry. Before testing, the slurry was vibrated to remove any trapped air bubbles.

A photograph of the cell is shown in Figure 2.15, and schematics are given in Figure 2.16. The initial specimen dimensions were: height 23 mm and diameter 80 mm. Temperature, applied vertical pressure, pore air pressure, and pore water pressure, could all be controlled independently.

Suction was controlled using the axis-translation method (also known as the air-overpressure method). For more details on this method, see the definitions at the start of this section. Pore-air pressure was applied through a loading piston fixed to a perforated disc, which during testing was in contact with the top of the specimen. Pore-water pressure was applied through a 500 kPa air-entry-value ceramic plate at the base of the specimen.

Vertical pressure was applied by increasing water pressure within the loading chamber, above a Monothane (a type of polyurethane resin) membrane. The membrane, shown in Figure 2.16c, had an “annular groove”, within which deformation was concentrated. This meant that friction due to the membrane was not affected by the overall displacement. Vertical displacement was measured using a dial gauge fixed to the external frame, in contact with the air pressure loading piston. The volume of water exchanged was also measured, and could be used to calculate volume change.

Heating was applied by heating water with a cryostat (a thermostat which can also maintain below-ambient temperatures), then circulating the water through the ring-shaped temperature chamber. Details on the material type used for the oedometer structure were not given, but from the photograph in Figure 2.15, it appears to be made primarily of stainless-steel. The entire oedometer was placed in an insulated box to reduce the influence of the laboratory temperature. The temperature of the air and water used to control suction and vertical pressure was controlled using a 20 °C cooling chamber, shown in Figure 2.16b. For this equipment, the maximum applied vertical stress was 1 MPa, the maximum applied suction was 500 kPa, and the temperature range is 20 °C to 80 °C.

Results from this research are given in the following sections: thermal volume change - Section 2.4.2, effect of temperature on pre-consolidation pressure - Section 2.4.3, effect of temperature on compressibility parameters - Section 2.4.4.



Figure 2.15: Equipment photograph (François and Laloui, 2010)

images/litreview/Salager_2008_oedometer_1.png

(a)

images/litreview/Salager_2008_oedometer_2.png

(b)

images/litreview/Francois_2010_oedometer_3.png

(c)

Figure 2.16: Equipment schematics (a) oedometer cell (b) auxiliary devices (c) membrane detail (Salager et al., 2008; François and Laloui, 2010)

2.2.14 Shariatmadari and Saeidijam (2011)

Shariatmadari and Saeidijam (2011) at the Iran University of Science and Technology modified a conventional oedometer to perform swelling and compression tests at high temperatures.

The tested material was a 1:1 mixture by weight of bentonite and sand (LL = 290 %, PL = 35 %, IP = 255 %, $G_s = 2.72$). The bentonite was a sodium bentonite from the Iran Barite Group. The sand was a natural silica sand, called Firuzkuh 161, with a specific gravity of 2.66. This material was chosen because bentonite-sand mixtures are considered to be suitable as buffer materials for geological disposal facilities. Adding sand to bentonite is expected to reduce creep, while increasing thermal conductivity and strength.

The soil was mixed at the target water content then statically compacted. After installing the compacted soil in the oedometer, it was saturated. The method used to saturate the specimen was not given. The initial specimen dimensions were 60 mm diameter and 15 mm height.

The apparatus consisted of a conventional oedometer, surrounded by a water bath, which was connected via insulated pipes to a thermal bath. This is shown schematically in Figure 2.17. Water from the thermal bath was circulated, using a pump, around the specimen, and so heated the water in the oedometer. Temperature within the thermal bath was measured and controlled using a thermostat, although the temperature was recorded using a thermocouple. This was described as a “PT100 thermocouple” with an accuracy of ± 0.1 °C. A PT100 is actually a type of resistance temperature detector (RTD), rather than a thermocouple, but both devices measure temperature. Within the oedometer water bath there were two more PT100 RTDs for recording temperature close to the specimen. The tested temperature range was 22 °C to 90 °C. Load was applied through a loading beam, and vertical displacement was measured using an LVDT, positioned centrally above the specimen. The maximum load reached during testing was 1 MPa. A water supply was used to maintain the water level in the oedometer water bath. An insulation plate minimised heat loss through the base of the oedometer.

Results relating to the effect of temperature on swelling capacity are given in Section 2.4.7.



Figure 2.17: Equipment schematic (Shariatmadari and Saeidijam, 2011)

2.2.15 Ye et al. (2012)

Ye et al. (2012) at Tongji University, Shanghai, China, developed an oedometer with combined temperature and suction control. The material tested was Gaomiaozhi (GMZ) bentonite, referred to as GMZ01 (LL = 313 %, PL = 38 %, IP = 275 %, $G_s = 2.66$).

The research was split into two papers. Ye et al. (2012) focus on the effect of temperature and suction on the compression behaviour of bentonite. Ye et al. (2013) focus on the effect of vertical stress and suction on the thermal volumetric behaviour of bentonite. Both papers describe the development and calibration of the new equipment, and the experimental procedures.

The soil was prepared by compacting bentonite powder at a water content of 8.6 % to a target dry density of 1.7 Mg m^{-3} . It was then saturated by injecting water through the inlets at the top and base of the cell. The soil was allowed to swell under constant vertical pressure of 0.1 MPa until equilibrium was reached, defined here as a volumetric strain rate less than $0.025 \% \text{ d}^{-1}$.

The tested temperature range was 20°C to 80°C . The tested suction range was 0 MPa to 120 MPa. The tested range of applied vertical pressures was 0.1 MPa to 80 MPa.

The equipment is shown schematically in Figures 2.18 and 2.19. Almost the entire oedometer cell sat within a temperature-controlled water bath. A thermostat was used to control and measure temperature. This thermostat consisted of a heater, a thermocouple (to measure temperature) and a temperature control unit with a precision of $\pm 0.1^\circ\text{C}$.

Load was applied with a piston, and vertical displacement was measured with a strain gauge of precision 0.001 mm, fixed to the loading piston. Since the strain gauge was not positioned centrally above the specimen, it is possible that tilting of the loading piston affected the measured displacements. Although the strain gauge was not within the water bath, it is reasonable to assume that heat would be conducted through the top part of the oedometer, which may have affected the measured displacement at elevated temperature, although this issue was not considered in the paper. The initial specimen dimensions were: height 10 mm, diameter 50 mm.

Suction was controlled using the vapour-equilibrium method with saturated salt solutions. The humidity-controlled air was circulated past the specimen using a pneumatic pump, and tubing connected to inlets and outlets at the top and bottom of the oedometer cell. Stainless-steel porous plates allowed this air to reach the specimen. O-rings prevented water from the bath reaching the specimen and affecting the suction.

The effect of temperature on the compression characteristics (plastic compressibility λ and elastic compressibility, κ) is discussed in further detail in Section 2.4.4.

images/litreview/Ye_2012_oedometer_1.png

Figure 2.18: Equipment schematic - overview (Ye et al., 2012)

images/litreview/Ye_2012_oedometer_2.png

Figure 2.19: Equipment schematic - detail (Ye et al., 2012)

2.2.16 Mon et al. (2013)

Mon et al. (2013) at Saitama University, Tokyo, Japan, developed an oedometer to investigate the effect of temperature on the geotechnical properties of clay. The material used was ASP 100 kaolin (LL = 69 %, PL = 30 %, IP = 39 %, WC = 200 %, $G_s = 2.658$). The soil was mixed as a slurry at $2.9\times$ the liquid limit. It was then placed in a vacuum for 1 h to remove air bubbles. Two specimen heights were used, 20 mm and 100 mm. In both cases, the diameter was 60 mm.

A schematic overview of the equipment is given in Figure 2.20. A detail schematic and photograph of the sample cell is given in Figure 2.21. The equipment was a modified hanging-weight oedometer. Details of load application and displacement measurement were not given, but from the photograph in Figure 2.21b, it appears that load was applied directly by adding dead-weights below the specimen, and displacement was measured with a dial-gauge directly above the specimen top-cap. Silicone grease was spread on the inner sides of the specimen ring to reduce side friction. The range of vertical pressures tested was 9.8 kPa to 1255.7 kPa.

Temperature was controlled by circulating water from the thermostatic water bath, through high-conductivity copper coils which surround the specimen. This allowed heat to transfer to or from the water-filled cell, which indirectly heated the soil. Water temperature within the cell was measured using a temperature sensor. This measured temperature value was used to determine whether to increase or decrease the temperature in the water bath. Tests were performed at three temperatures, 5 °C, 15 °C and 40 °C.

An innovative aspect of this equipment was the use of bender elements to measure soil stiffness at small strains, by measuring elastic shear wave propagation. A pair of 3 mm long bender elements were installed at each end of the specimen, in the top cap and base of the cell. A wave generator and digital oscilloscope were used to produce the waves and measure their travel time between the transmitter (at the top of the specimen) and receiver (at the base).

The technique for measurement of coefficient of permeability was also quite innovative. Rather than indirect calculation, the coefficient of permeability was measured directly, using the falling head method. After each consolidation increment, the system was sealed by closing off the drainage valves, then water from the burette was allowed to flow through the system, under pressure, from the base to the top.

Results relating to the effect of temperature on the coefficient of volume compressibility and shear-wave velocity (stiffness) are given in Section 2.4.4. Effects of temperature on the coefficient of consolidation are given in Section 2.4.5



Figure 2.20: Equipment schematic - overview (Mon et al., 2013)



(a)



(b)

Figure 2.21: Sample cell (a) detail (b) photograph (Mon et al., 2013)

2.2.17 Di Donna and Laloui (2015)

Di Donna and Laloui (2015) at the École polytechnique fédérale de Lausanne (EPFL), Switzerland, adapted four oedometric cells to include temperature control. They used this new equipment to experimentally investigate the response of a natural silty clay to cyclic heating. The tested soil was a saturated, medium-plasticity clay, referred to as Geneva clay (LL = 31.4 % to 42.6 %, PL = 20.1 % to 24.2 %, IP = 11.1 % to 18.4 %, $G_s = 2.71$ to 2.78, WC = 22.3 % to 27.9 %). Four undisturbed, natural samples were tested. Before testing, the samples were kept in a humid chamber to maintain their natural, saturated condition. The initial dimensions of the tested specimens were: height 20 mm, diameter 60 mm.

The oedometer equipment is shown in Figure 2.22. The oedometers were lever-arm style, modified for temperature control. Vertical stress was applied using calibrated dead-weights. The maximum applied vertical stress tested was 1000 kPa. Vertical displacement was measured using an LVDT, positioned centrally above the top-cap. Heating was applied by circulating pre-heated water through spiral tubes around the specimen. A thermostat was used to heat water within a bath to the target temperature. Each bath supplied water for two oedometers. A pump was used to circulate this water from the bath around the oedometer. A supply of demineralised water was used to replenish water losses due to evaporation during heating, and keep the specimen saturated at all times. The tested temperature range was 5 °C to 60 °C. Temperature was measured inside the oedometer cell using a type K thermocouple, with an accuracy of 0.1 °C. The cells were insulated using polystyrene to minimise thermal losses, although from the available photographs it appears they are not insulated at the base. The confining ring was made of Invar, which has a very low thermal expansion coefficient. This material was chosen by Moritz (1995) for the confining ring, for the same reasons - to minimise thermal radial deformations and ensure oedometric conditions during temperature changes.

The testing programme consisted of two parts. In the first part, the material was characterised from a thermal point of view. This part consisted of isothermal tests in which the soil was consolidated at 20 °C, 40 °C and 60 °C. Results from these tests provide information on the effect of temperature on the soil's compression characteristics (Section 2.4.4), consolidation characteristics (Section 2.4.5), hydraulic conductivity (Section 2.4.6) and pre-consolidation pressure (Section 2.4.3).

In the second part, the effects of thermal cycles were investigated. This part consisted of isobaric tests. Results from these test provide information on the effect of over-consolidation ratio on the thermal volume change of the soil (Section 2.4.2), as well as the effects of plasticity and repeated thermal cycling, within the same section.

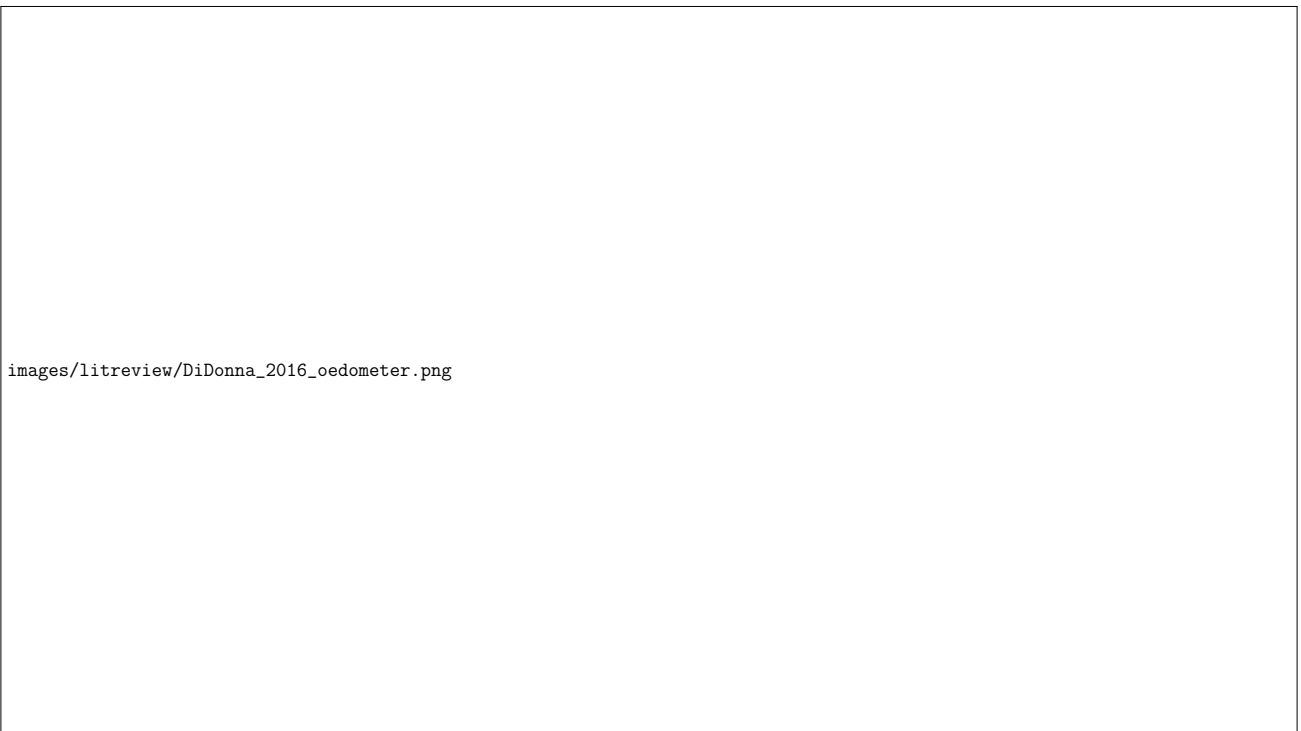


Figure 2.22: Equipment photograph (a) global view (b) detail - 1: tubes with circulating water at the desired temperature, 2: LVDTs, 3: thermocouples, 4: water supply, 5: insulation, 6: acquisition system, 7: heaters (Di Donna and Laloui, 2015)

2.2.18 Vega and McCartney (2015)

Vega and McCartney (2015) at the University of Colorado, USA, used a temperature-controlled oedometer, to test the effect of over-consolidation ratio and thermal cycling on the volume change response of Bonny silt (LL = 25 %, PL = 21 %, IP = 4 %, $G_s = 2.63$).

This oedometer was previously developed by McGinley (1983), as a PhD project, to test the effects of temperature on the consolidation process of saturated fine-grained soils. The soils tested were clays - Georgia kaolin (IP = 19 %) and a smectite (IP = 89 %). Later, it was renovated and improved by El Tawati (2010), as an MSc project, who tested the same Bonny silt as Vega and McCartney (2015). The soil was statically compacted, de-aired by applying a vacuum, and then saturated by applying a back-pressure of 210 kPa.

A comprehensive description of the oedometer design is given by El Tawati (2010). The equipment comprised a pressure cell, a mechanical loading system, and a heating system. A schematic of the whole system is given in Figure 2.23a, with a detailed schematic of the pressure cell in Figure 2.23b.


The main components of the pressure cell were made of type 316 stainless-steel. Using components of the same material minimises the differential displacement during temperature changes. The pressure cell was held together with steel rods. An innovative aspect of this oedometer was the ability to apply back pressure to saturate the specimen. Cell fluid pressure was controlled using the back-pressure reservoir. A photograph of the pressure cell exterior is given in Figure 2.24a.

The static axial load was generated with a pneumatic air cylinder, and monitored with an S-type load cell. Mechanical load was applied through a loading shaft, which passed through the upper plate of the pressure cell, and was sealed by a Bellofram rolling diaphragm. The maximum axial stress tested was ≈ 1300 kPa. Displacement was measured using a strain-gauge linear displacement transducer (LDT) (incorrectly described as an “LVDT”), which is mounted on the loading piston outside the pressure cell. The LDT armature can be seen in Figure 2.24a. Using a single displacement transducer, which is not mounted centrally above the specimen, could introduce tilting effects to the measured displacement. Verticality of the loading rod was maintained using a linear ball bushing, although tilting was not measured.

Another innovation with this oedometer was the ability to measure pore-pressure. Unlike a conventional oedometer which has two-way drainage, this one had one-way drainage. There was free drainage at the top of the specimen, but no drainage at the base. This allowed pore-pressure to be measured at the base with a differential pressure transducer.


The heating system comprised a heater, a temperature control unit, and a circulation pump. A 4500 W tubular coiled heater surrounded the specimen. Temperature was measured using a type J thermocouple, and controlled using a Watlow temperature regulator. A circulation pump was used to homogenise the cell fluid temperature. The accuracy of temperature control was approximately ± 0.5 °C. A photograph of the pressure cell interior is given in Figure 2.24b, which shows the coiled heater surrounding the confining ring. The tested temperature range was 18 °C to 91 °C. Initial specimen dimensions were: height 25.4 mm, diameter 83 mm.

Results from McGinley (1983) relating to the effect of temperature on the coefficient of consolidation are given in Section 2.4.5. Results from El Tawati (2010) are not given, since this thesis focused mostly on the renovation of the oedometer, and a more systematic testing programme is presented by Vega and McCartney (2015). The effect of temperature on the volume change of silt, as observed by Vega and McCartney (2015) is discussed in Section 2.4.2.



images/litreview/ElTawati_2010_oedometer_1.png

(a)



images/litreview/ElTawati_2010_oedometer_2.png

(b)

Figure 2.23: Equipment schematics (a) overview (b) pressure cell detail (El Tawati, 2010)



(a)



(b)

Figure 2.24: Equipment photographs (a) pressure cell exterior (b) pressure cell interior, showing heating coil and confining ring (El Tawati, 2010)

2.2.19 Favero et al. (2016)

Favero et al. (2016) at the École polytechnique fédérale de Lausanne (EPFL), Switzerland, used a high-pressure oedometer cell, equipped with a temperature-control system, to investigate the effects of temperature on the yield stress and mechanical properties of Opalinus clay (LL = 38 %, PL = 23 %, IP = 15 %, $G_s = 2.75$). Opalinus clay, which is actually a shale, was considered to be a possible host-material for a deep geological repository for radioactive waste in Switzerland. The tested specimen was undisturbed, with initial height 12.5 mm and diameter 35 mm. Before applying any thermal cycles, the specimen was saturated at ambient temperature by applying a pore water pressure at the base and top of the specimen.

The oedometer is shown schematically in Figure 2.25. Vertical load was applied using a hydraulic jack, connected to a loading ram, which pushed against a high-rigidity loading frame. Vertical stresses up to 100 MPa were tested. Vertical displacement was measured using “a system of LVDTs”, although how many was not stated.

Temperature was controlled by directly heating the oedometer cell with a 3 mm thick heating mat which wrapped around the cell and was fixed in place with steel rings. Three thermocouples with a resolution of 0.1 °C were used to measure the temperature. Two were positioned at the interface between the heating mat and the cell, while the third was positioned in contact with the specimen. This third thermocouple was inserted through the drainage line, and was only used during the calibration stage. The tested temperature range was 23 °C to 80 °C. Drainage conditions could be manipulated using valves connected to the drainage lines at the top and base of the specimen. Pore pressure at the base and top of the specimen could be controlled.

images/litreview/Favero_2016_oedometer.png

Figure 2.25: Equipment schematic (Favero et al., 2016)

Three tests were carried out, which were all complex combinations of isobaric heating and isothermal loading. The effect of over-consolidation ratio on thermal volume change is covered in Section 2.4.2, the effect of temperature on the pre-consolidation pressure is covered in Section 2.4.3, compression characteristics in Section 2.4.4, and consolidation characteristics in Section 2.4.5. Thermal calibration of the equipment is covered in Section 2.3.

2.2.20 Ng et al. (2017)


Ng et al. (2017) at the Hong Kong University of Science and Technology, Hong Kong, investigated the effect of oedometer-soil interaction, by performing thermal tests, and comparing results for two confining ring materials: steel and Invar.

Two soils were tested, a clay and a sand. The clay was an unnamed “clay of low plasticity” (LL = 36 %, PL = 19 %, IP = 17 %, $G_s = 2.69$). It was statically compacted at a water content of 9.2 % and an initial dry density of 1.18 g cm^{-3} . Then, water was added to the cell to submerge and saturate the specimen. To ensure full saturation, a vacuum of 80 kPa was applied and maintained in the cell. The sand was Toyoura sand, a uniform fine sand, with sub-rounded to sub-angular particles, as characterised by Verdugo and Ishihara (1996) ($C_u = 1.7$, $e_{min} = 0.597$, $e_{max} = 0.977$, $G_s = 2.65$). It was prepared using air pluviation, giving an initial relative density of 21 %.

The apparatus, shown in Figure 2.26, was a modified conventional oedometer, incorporating a heating and cooling system. A heating-cooling unit was used to heat or cool water in a bath. This water was circulated with a pump through the spiral tube which surrounded the soil specimen. The water in the oedometer cell was heated or cooled through heat exchange with the circulating water. A thermocouple within the oedometer cell measured the temperature. The variation in temperature, at the thermal equilibrium state, was $<0.1^\circ\text{C}$. Based on the apparatus schematic, it appears that displacement was measured with an LVDT mounted on the loading rod. There are two potential issues with the method of displacement measurement shown. The first issue is that displacement was measured from the cell lid, not the top-cap, which may not necessarily represent the specimen displacement. The second issue is that a single displacement transducer is sufficient only if positioned centrally above the specimen. For non-centrally positioned displacement transducers, at least two are required for accurate height (and volume) measurement, and at least three are required to ensure that tilting effects are either negligible, or at least accounted for. Neither issue is mentioned in the paper. The first can be (and presumably was) solved through careful calibration. The second may or may not have affected the results, depending on whether tilting was significant for this equipment.

Two confining rings were used: one made of steel and another made of Invar. The results from both were then compared. Invar confining rings were previously used by Moritz (1995) and Di Donna and Laloui (2015). Invar was chosen because of its low thermal expansion coefficient ($a_L = 0.5 \times 10^{-6} \text{ }^\circ\text{C}^{-1}$) compared to steel ($a_L = 15 \times 10^{-6} \text{ }^\circ\text{C}^{-1}$). Note that these are the values given by the author.

Multiple heating and cooling cycles were applied to the clay or sand specimens, under an effective vertical stress of 50 kPa, and the thermally-induced axial strain was compared for the Invar and steel confining rings. Results from this scheme are important in the discussion on equipment calibration, which is covered in Section 2.3. Results relating to the effect of multiple thermal cycles on mechanically normally-consolidated soil are discussed in Section 2.6.



images/litreview/Ng_2017_oedometer.png

Figure 2.26: Equipment schematic (Ng et al., 2017)

2.2.21 Sittidumrong et al. (2019)

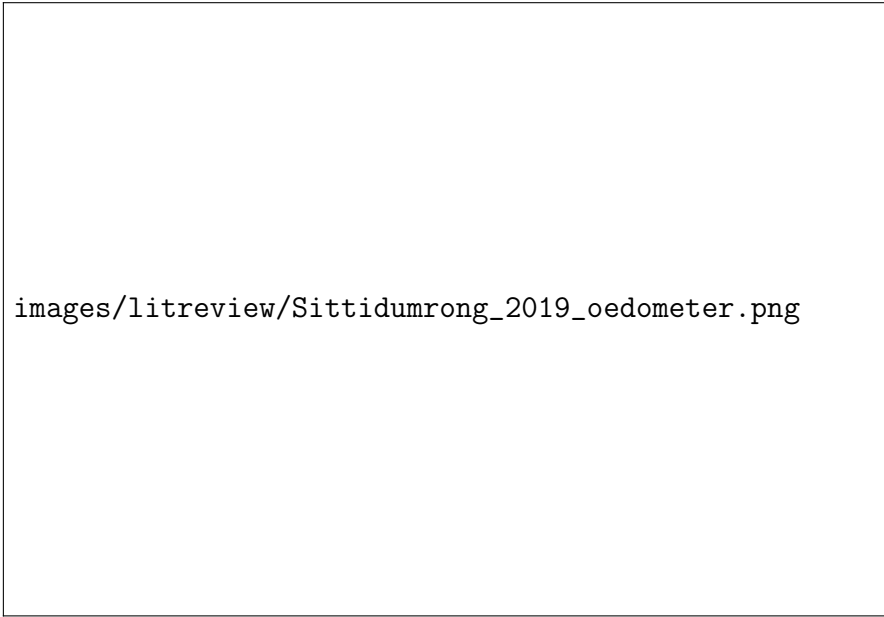
Sittidumrong et al. (2019) at Kasetart University, Bangkok, Thailand, investigated the effect of repeated thermal cycling on the volumetric behaviour of saturated Bangkok sand.

The application of the research was in the design of ground source heat pumps (GSHPs) and energy piles in tropical countries. Shallow geothermal energy can be used for cooling buildings, which improves their energy efficiency, and reduces the “heat island” phenomena (where urban areas have higher temperatures than surrounding rural areas).

They carried out 100 thermal cycles, $28 \rightarrow 50 \rightarrow 28$ °C, at three different vertical stresses, 2.0 MPa, 3.2 MPa and 4.0 MPa. The frequency was 1 cycle/hour (60 Hz).

Tests were performed on both reconstituted and undisturbed sand ($WC = 15.2\%$, $G_s = 2.68$) from a block sample. The soil was classified as a poorly graded sand. It comprised mainly quartz, with small traces of mica, feldspar and kaolinite. The reconstituted samples were prepared by compacting dry sand to four different dry unit weights, corresponding to very-dense, dense, medium-dense, and loose states. The equipment was a conventional oedometer, modified for temperature control. A schematic is given in Figure 2.27. The load was applied through the

top cap, using hanging dead weights, and displacement was measured using an LVDT above the loading frame, mounted centrally above the specimen. The initial specimen dimensions were: height 20 mm, diameter 50 mm. The specimen sat within a greased 2 mm thick confining ring, and between saturated top and base porous steel plates, allowing two-way drainage.



images/litreview/Sittidumrong_2019_oedometer.png

Figure 2.27: Equipment schematic (Sittidumrong et al., 2019)

Temperature control was achieved by circulating hot or cold water to the inlet using a peristaltic pump. The water flowed around the specimen to the outlet. A thermistor within the water bath measured temperature. An Arduino microprocessor was used to control the opening and closing of two pairs of solenoid valves, which regulated the flow of hot or cold water, depending on the current temperature. The hot water came from a constant temperature bath, heated to 50 °C. The cold water came from underground storage, at a constant temperature of 28 °C. The hot and cold water was not mixed before it reached the oedometer water bath. The oedometer was covered with expanded polystyrene (EPS) foam insulation to prevent fluctuations in room temperature affecting the results. No further details were given on the accuracy and stability of the temperature control system.

Results from this research relating to strains generated from thermal cycling are discussed in Section 2.4.2. Calibration of the equipment is discussed in Section 2.3.

2.2.22 Summary of historical advances

Temperature-controlled oedometer testing is not new, but instead has been a process of continual innovation and improvement. Not only has the equipment itself improved over time, but the scope of the testing programmes has expanded. Improvements to instrumentation have allowed more accurate and precise measurements of load, displacement, temperature, pore-air and pore-water pressure. Monitoring and control of these variables is now mostly automated. Calibration procedures have become more thorough.

The first temperature-controlled oedometer was arguably that of Paaswell (1967). Previous schemes used conventional oedometers in temperature-controlled rooms. Using built-in heaters

enabled testing at much higher temperatures. The first temperature-controlled oedometer which measured pore-pressure was that of McGinley (1983). The research of Towhata et al. (1993), although not notable in terms of equipment design or calibration procedure, was a clear advancement on previous schemes in terms of the broad scope of the testing programme. This was the first scheme to measure the effect of temperature on the equipment itself. The first oedometer to control both suction and temperature was that of Romero (1999). The oedometer design for François and Laloui (2010) is notable for a number of innovations, particularly the use of a pressurised membrane for load application. Although this idea is not new, its application in this context clearly is. Most recently, Mon et al. (2013) was the first to use bender elements within a temperature-controlled oedometer to measure stiffness.

The issues with previous schemes have been considered in the design and development of the new oedometer, which is discussed in Chapter 3. The growing understanding of importance of calibration, discussed in the following section, becomes apparent when reading these references in chronological order. Calibration of the new equipment forms the major part of this thesis. The issue of measuring displacement with transducers not mounted centrally above the specimen, is not covered in the literature, but became apparent during the current development process. Temperature uniformity across the tested specimen has been addressed by previous schemes by insulating the base of the oedometer. The new oedometer described in this thesis solves this issue by circulating temperature-controlled water underneath the base of the specimen. The direct effect of temperature on instrumentation is also not well addressed in the literature. This lack of information was one of the reasons for the decision to isolate the instrumentation from any temperature changes in the new oedometer. The ability to control temperatures above and below ambient temperature means the new oedometer can perform tests relevant to ground source heat pumps and energy foundations, as well as buffer materials for deep geological repositories.

2.3 Temperature calibration

2.3.1 Introduction

In the development and commissioning of a new piece of laboratory equipment, calibration is one of the most important steps. It is also arguably the most complex and time-consuming. François and Laloui (2010), described calibration as “the most critical issue” in the development of their combined temperature- and suction-controlled oedometer. Vega and McCartney (2015) wrote that calibration is “critical to evaluate the machine deflection of the thermal oedometer during both mechanical loading and subsequent temperature changes”.

Calibration is the act of comparing measured values with known values. Ambient-temperature calibration is a well-understood process, and is not discussed further in this section. The ambient-temperature calibration of the instrumentation used in this project is covered in Appendix A (load cell) and Appendix B (LVDTs). The measured responses of the transducers are compared with known values. For example, the load cell is calibrated using dead-weights, and the displacement transducers are calibrated using a micrometer.

Temperature (or thermal) calibration is different and more challenging. The “known” values are not yet known, and must first be measured as part of the calibration procedure. Then, they can be used to correct the values measured during a test on soil. Temperature affects not only the soil, but also the apparatus.

Temperature has four measurable effects on the apparatus. These are (i) the vertical deformation of the apparatus (ii) the radial deformation of the confining ring (iii) the change in the isothermal mechanical response due to loading at different temperatures (iv) the direct effect of temperature on instrumentation.

The vertical deformation of the apparatus can be measured by applying a thermal cycle under constant pressure, either with a dummy specimen in place of the soil specimen, whose thermal expansion coefficient is known, or no specimen at all. If a dummy specimen is used, the theoretical vertical deformation of the specimen can be calculated, and subtracted from the total measured vertical deformation, to give the apparatus vertical deformation. To determine the effect of pressure, this test can be repeated at a number of different, constant pressure values. This is equivalent to a series of isobaric heating tests, shown schematically in Figure 2.1.

The radial deformation of the confining ring can be measured in a similar way to the vertical deformation, although it is more difficult in practice since local instrumentation is required within the confining ring.

The effect of temperature on the isothermal mechanical response due to loading can be measured by carrying out loading cycles under constant temperature. For ambient-temperature oedometer testing, apart from calibration of the instrumentation, this is generally the only calibration test carried out, and the response is referred to as the equipment compliance. For temperature-controlled oedometer testing, the equipment compliance must be determined over the full temperature range, to establish what effect, if any, temperature has on it. This is equivalent to a series of isothermal loading tests, shown schematically in Figure 2.2.

Finally, there is the direct effect of temperature on the instrumentation. In practice, this is almost impossible to quantify. Any instrumentation that is made of materials with non-zero thermal expansion coefficients (that is, all instrumentation), will be affected to some extent by temperature. This fact was the main driver in the decision to isolate the instrumentation from the heat source, in the oedometer described in this thesis, which is discussed fully in Chapter 3. Manufacturers give specifications on the temperature range that their instrumentation should be used in, and within that range, the expected effect of temperature. Some instrumentation is pre-calibrated for temperature change within the specified range of working temperatures, and temperature effects are negligible. This is common for temperature transducers.

In the following section, a review of the methods of temperature calibration is given, in chronological order.

2.3.2 Literature review of temperature calibration

Finn (1952) was perhaps the first to consider not only the effect of temperature on the tested soil, but on the oedometer apparatus as well. For tests at non-ambient temperature, all equipment and sample material was pre-cooled or pre-heated. Since the tests performed were isothermal loading, this meant that during the test, there would be no further thermal deformation of the apparatus. However, the effect of temperature on the instrumentation (dial gauge for displacement measurement) is not addressed.

Fredlund (1969) tested the compliance of five different types of ambient-temperature oedometers, including the effect of porous stones and filter papers.

Figure 2.28 shows the factors contributing to the compressibility (compliance) of an oedometer, in this case a Conbel consolidometer. The compressibility of the porous disks is a significant

part of the total compressibility. The porous disks are the main contributors to the hysteresis effect, and the residual deformation following unloading. Calculations of deflection based on the elastic moduli of the material involved show that many times as much deflection occurs when loading as would theoretically be expected.



images/litreview/Fre69_fig6.png

Figure 2.28: Components of total equipment compliance for Conbel consolidometer (0.01 inch = 0.254 mm) (Fredlund, 1969)

Test on filter paper found that it compresses instantaneously when load is applied, and compresses further with time, as shown in Figure 2.29. The compressibility of filter paper is significant. In Figure 2.30, deformation of two types of filter papers are shown for a load/unload cycle to a maximum pressure of approximately 100 kg cm^{-2} (9800 kPa). At 1 kg cm^{-2} (98 kPa), the compression of the filter papers is approximately 5 times apparatus compression, and 2.5 times apparatus compression at 10 kg cm^{-2} (980 kPa). Various types of filter paper were tested, each giving different results, but showing the same general behaviour.

The author made a series of conclusions, several of which are particularly relevant to this research. They found that friction in the pressure measuring device (i.e. load cell) to be significant only under small pressures, and recommended not placing special significance on the shape of rebound curves at low pressures, unless those pressures can be determined precisely. Regarding porous stones, they found that a high proportion of the total equipment compressibility is produced by the porous stones, and that the seating of the porous stones and soil specimen is hard to evaluate, and is significant primarily at low pressures. Finally, they found that filter paper undergoes compression several times higher than the oedometer itself upon loading, and recommended not using filter papers for tests on the swelling properties of soil.

Towhata et al. (1993) directly addressed the issue of thermal deformation of the apparatus. The distortion of the apparatus was measured after a long time elapsed in hot water. What, exactly, was measured, and after how long, and for what temperature change, is not specified.



Figure 2.29: Time-dependent compression of filter papers (0.001 inch = 0.0254 mm) (Fredlund, 1969)



Figure 2.30: Compressibility of filter papers (0.016 inch = 0.406 mm)(Fredlund, 1969)

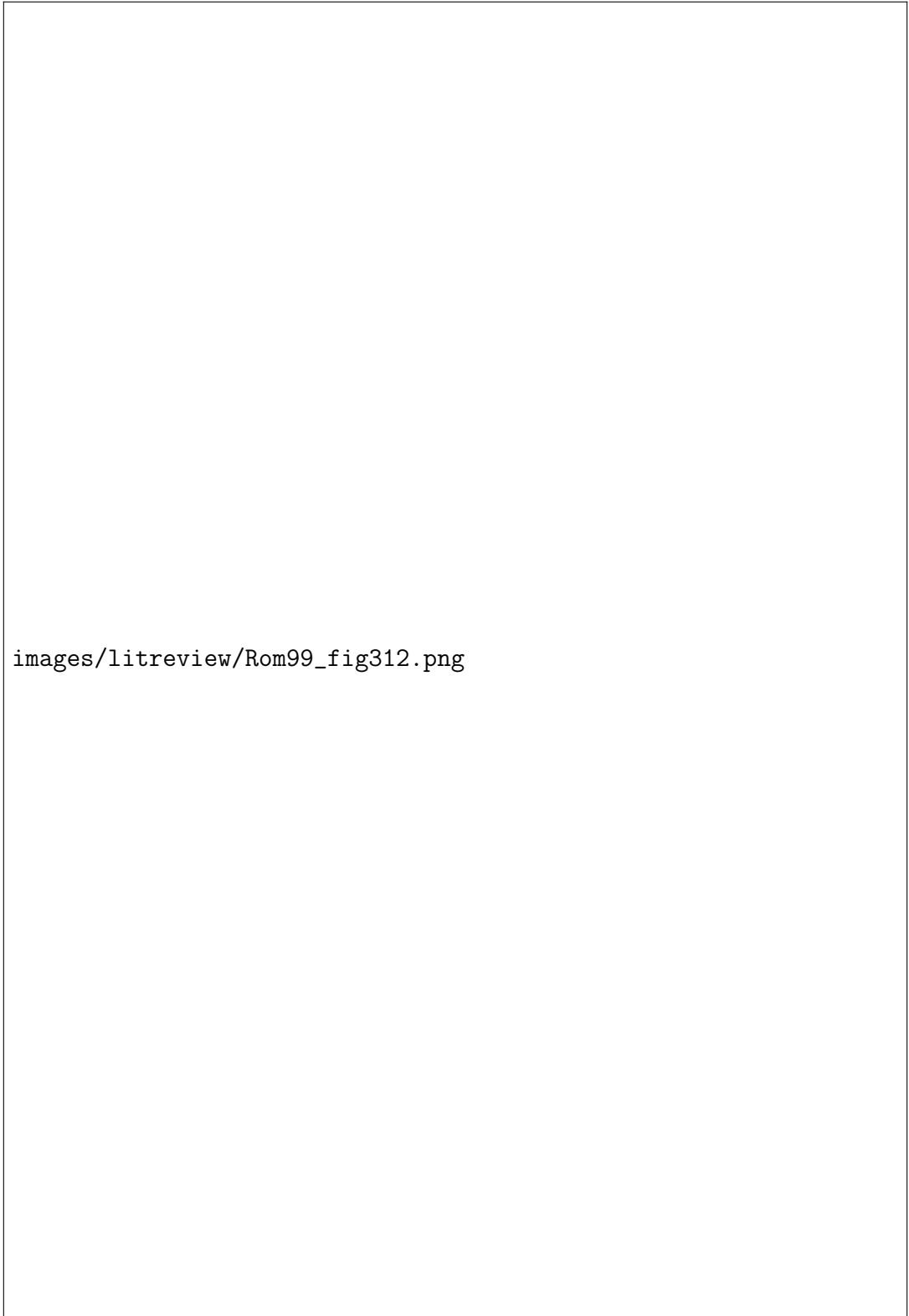
How these measurements were used as a calibration is also not specified. Only the ultimate distortion was measured, not the transient distortion during heating. They noted that the radial distortion of the apparatus (presumably, the change in diameter of the confining ring), was too small to affect the evaluation of the radial strain.

Romero (1999) provides, in their PhD thesis, a thorough analysis of thermal calibration. Mechanical calibration was carried out at temperatures of 22 °C and 80 °C. Temperature calibration was carried out at net vertical stresses of 0.026 MPa and 0.085 MPa. As in Towhata et al. (1993), transient thermal deformations during heating or cooling could not be calibrated precisely. Thermal deformations affecting vertical measurements were associated with the following elements (with reference to Figure 2.11): ceramic disc and porous stone, loading head, measurement frame, and dial gauge. The results are given in Figure 2.31a. A quadratic expression was developed for the change in height of the cell Δh_c over the reference specimen height h_0 (10 mm), as a function of temperature change *above ambient* ΔT , also given in this figure.

Radial deformation of the confining ring was also investigated. The internal diameter of the confining ring was measured using a bore gauge, at a range of temperatures. The results are given in Figure 2.31b. A linear expression was developed for the change in diameter Δd over the reference specimen diameter d_0 (50 mm), as a function of temperature change above ambient, which is also given in this figure. The horizontal line on this figure shows the maximum recommended change in diameter in order not to lose oedometer conditions. This value is given as 0.03 %, although Section 6.2.4 of ASTM Standard D2435/D2435M-11 (ASTM International, 2011) suggests a value of 0.04 % is acceptable. For a temperature increase of >20 °C above ambient, oedometer conditions are no-longer maintained. The change in diameter can be related to an equivalent vertical displacement to obtain an overall correction. The overall correction, the sum of the correction due to vertical dilation of the oedometer elements, and equivalent vertical contraction due to radial dilation of the confining ring, is given in Figure 2.31c, graphically and as a quadratic equation. The author concluded that thermal deformation of the confining ring does not significantly affect the volume change response of the soil.


Abuel-Naga et al. (2005) also calibrated the thermal deformation of the apparatus. This calibration is discussed further in Abuel-Naga et al. (2006). Vertical deformation of the apparatus was determined by running tests at temperatures from 25 °C to 90 °C and stress levels of 100 kPa, 200 kPa and 300 kPa, without the soil specimen in place. The results of this calibration are given in Figure 2.32. Radial deformation of the confining ring was determined by direct measurement, after heating it for a long time in an oven at temperatures from 25 °C to 60 °C. Figure 2.33 shows the change in confining ring diameter Δd over initial diameter d_0 (i.e. diametrical strain), for the change in temperature above 25 °C ΔT . Using a constant-volume assumption, this radial deformation can be converted into an equivalent vertical deformation. They concluded, in agreement with Towhata et al. (1993), that the effect of radial deformation is not significant and can be neglected.

Temperature calibration of the equipment described by **François et al. (2007)** is discussed in much more detail by Salager et al. (2008) and François and Laloui (2010). As in previous calibration schemes, two thermal effects are considered. These are: thermal vertical deformation of the apparatus, and thermal deformation of the confining ring. Thermal vertical deformation of the apparatus was determined by running a thermal cycle from 20 °C to 80 °C at 20 °C increments, using an inox (stainless-steel) dummy sample in place of the soil specimen. The thermal expansion coefficient of stainless-steel is known, so the theoretical change in height of the dummy sample can be calculated, and subtracted from the total measured change in height, giving the change in height of the apparatus. The results of this test are given in Figure 2.34, on



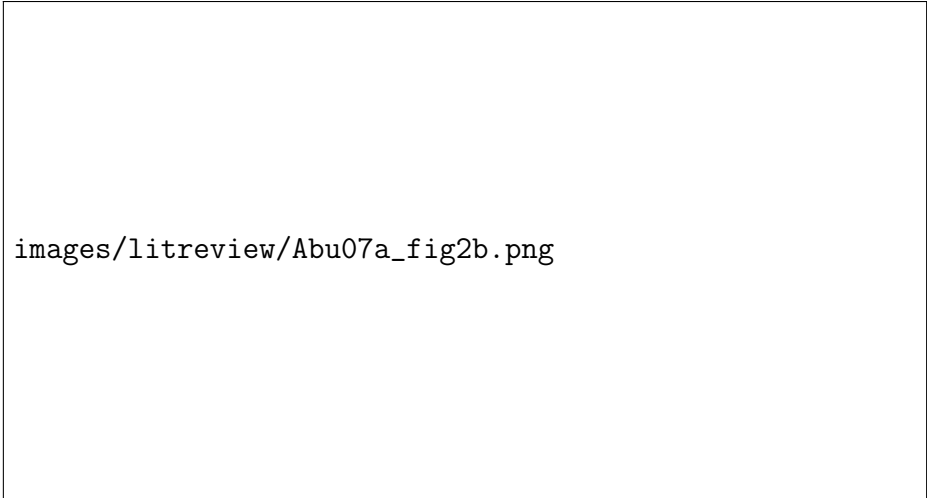
images/litreview/Rom99_fig312.png

Figure 2.31: Temperature calibration of oedometer cell for non-isothermal paths (a) vertical thermal expansion (b) thermal expansion of confining ring (c) overall correction. Negative strain = expansion (Romero, 1999)



images/litreview/Abu07a_fig2a.png

Figure 2.32: Vertical thermal expansion of oedometer apparatus. Negative Δh = expansion (Abuel-Naga et al., 2006)



images/litreview/Abu07a_fig2b.png

Figure 2.33: Diametrical thermal expansion of confining ring. Negative Δd = expansion (Abuel-Naga et al., 2006)

which the measured displacement, theoretical displacement of the dummy sample, and corrected displacement are plotted. Note that there is some hysteresis in the response, resulting in a small residual displacement following heating and cooling, although this issue is not commented upon by the authors. A linear calibration is suggested, as a function of change in temperature.

The thermal deformation of the confining ring was measured using strain gauges, in the circumferential, axial and radial directions. Two thermal cycles from 22 °C to 80 °C were performed. The results are given in Figure 2.35. The expansion corresponds to the known thermal expansion coefficient of steel. In agreement with previous authors, they concluded that thermal deformation of the confining ring does not significantly affect the oedometric conditions.

Shariatmadari and Saeidijam (2011) performed mechanical calibration tests at three different temperatures, 22 °C, 55 °C and 85 °C. A 15 mm thick steel dummy sample was used, in place of the soil specimen. The results are given in Figure 2.36, where measured displacement (Δ) is plotted against applied vertical stress ($\log \Delta p$). As with François et al. (2007), there is hysteresis in the measured displacement due to heating and cooling. However, in this case, the resulting



Figure 2.34: Vertical thermal displacement of oedometer apparatus. Negative displacement = expansion (François and Laloui, 2010)



Figure 2.35: Diametrical thermal expansion of confining ring. Negative strain = expansion (François and Laloui, 2010)

residual displacement appears to be significant. It is not explained how this hysteresis is accounted for in the calibration. The effect of temperature on the confining ring diameter is not considered.

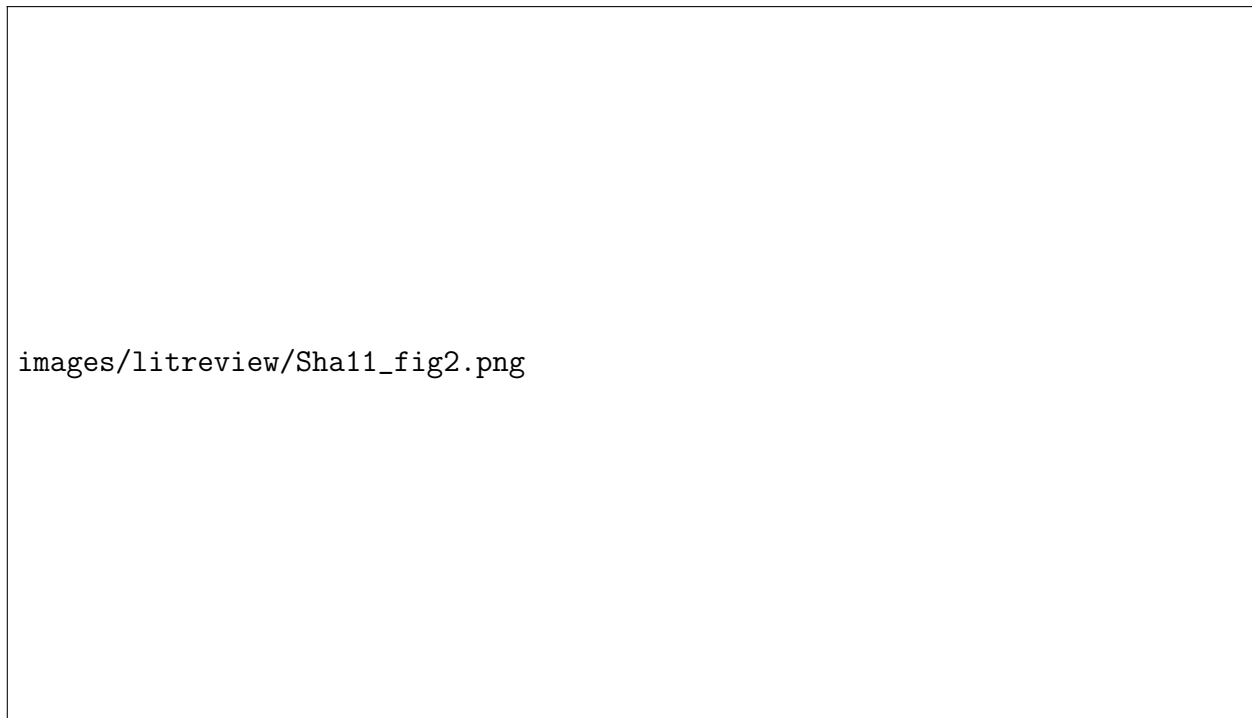



Figure 2.36: Vertical thermal deformation of oedometer apparatus (Shariatmadari and Saeidijam, 2011)

Ye et al. (2012) calibrated for the vertical deformation of the oedometer apparatus by carrying out loading/unloading cycles at temperatures of 20 °C, 40 °C and 80 °C. The results of these tests are given in Figure 2.37. There is some hysteresis between the loading and unloading paths, with the unloading paths (hollow markers) plotting above the loading paths (filled markers), although this is not commented upon by the authors. This hysteresis is more noticeable at vertical pressures above 1 MPa.

In **Di Donna and Laloui (2015)** it is mentioned that the apparatus was calibrated for temperature, but no further details are given.

The subject of calibration is considered in detail in **Vega and McCartney (2015)**. Thermal axial displacement of the equipment was measured during a heating/cooling cycle, using a steel dummy sample. The displacement of the steel dummy sample, calculated from its known thermal expansion coefficient, was subtracted from the total displacement to give the machine displacement. This is shown in Figure 2.38. The theoretical displacement of the steel dummy sample, and the corrected machine deflection are plotted together. The theoretical steel displacement response is linear, with respect to temperature, and is a function of the thermal expansion coefficient of the material. The machine deflection is non-linear, and expansive, during heating. During cooling, the machine deflection is more linear, and contractive. There is clear hysteresis, and residual contraction following the heating/cooling cycle. This residual displacement was attributed to interaction between the components of the pressure cell, particularly the holding-down rods, and the o-rings. How this calibration was implemented is not explained.

The authors also noted the issue of thermal radial displacement of the confining ring. Unlike previous studies, such as Abuel-Naga et al. (2005), they concluded that the effects of thermal



images/litreview/Ye12_fig3.png


Figure 2.37: Vertical thermal deformation of oedometer apparatus (Ye et al., 2012)

expansion of the oedometer ring may be significant. They suggested that radial contraction of the ring during cooling, which increases contact between the ring and the soil, may have a greater effect on the volume change of the soil than radial expansion of the ring during heating. This is because steel has a higher thermal expansion coefficient than the tested soil. However, they noted that the thermal expansion coefficient of over-consolidated soils is not very different from steel. Depending on the boundary conditions though, the confining ring and soil may heat up at different rates, so transient effects during heating are still important. They did not directly measure the thermal deformation of the confining ring, but used the theoretical deformation, based on the material properties, in their analysis of the test results.

Favero et al. (2016) calibrated vertical displacements under load at temperatures from 20 °C to 80 °C, using a steel dummy sample. They found that apparatus deformations were higher at higher temperatures, although there was no significant difference between the deformations generated under 60 °C and 80 °C conditions. Radial displacement of the confining ring was measured using four strain gauges. This measured radial displacement was used to correct the measured thermal volume change for non-isothermal soil tests.

Ng et al. (2017) considered the effect of confining ring material on the response of normally-consolidated clay and sand specimens to thermal cycling. They performed identical tests using a confining ring made of steel, and Invar. The linear thermal expansion coefficient of Invar ($a_L = 0.5 \times 10^{-6} \text{ }^\circ\text{C}^{-1}$) is much lower than steel ($a_L = 15 \times 10^{-6} \text{ }^\circ\text{C}^{-1}$). The thermal expansion coefficient of steel is on the high end of the range of thermal expansion coefficient values for soil mineral solids, whereas the value for Invar is much lower. This means that expansion and contraction of the Invar confining ring is negligible compared to the soil, and the test conditions can be considered truly one-dimensional.

For both clay and sand, they observed that the accumulated plastic (contractive) strains due to thermal cycling were higher for the steel confining ring than for the Invar one. This result is discussed further in Section 2.6, but it is also relevant to the discussion of equipment calibration.



images/litreview/Veg15_fig5b.png

Figure 2.38: Thermal axial displacement of oedometer apparatus. Negative displacement = expansion (Vega and McCartney, 2015)

Expansion and contraction of the steel ring itself resulted in additional soil deformation during thermal cycles. Previous researchers such as Romero (1999) and Abuel-Naga et al. (2005) tried to account for this by correcting the vertical compliance for the change in diameter of the confining ring, assuming no change in soil volume. However Ng et al. found that such corrections overestimate the influence of boundary conditions on axial strains by more than threefold (i.e. they overestimate the additional axial strain of the soil specimen due to expansion and contraction of the confining ring).

Sittidumrong et al. (2019) accounted for the vertical deflection of the oedometer components (cell, top-cap, loading frame) due to temperature change by measuring the displacement during a number of thermal cycles, without the soil specimen in place. They observed an elastic response, with no residual displacement due to heating and cooling. Radial strain of the confining ring was not measured, but was assumed to be negligible. The mechanical compliance was also measured, although whether this was carried out at a range of temperatures is not specified.

2.3.3 Summary

The literature shows a series of improvements in calibration procedure, although no scheme seems to have addressed the issue in its entirety. In some schemes, only the thermal vertical deformation is measured, and at only one pressure value. This means that the effect of pressure level on the thermal vertical deformation is unknown, as is the effect of temperature on mechanical compliance. Several studies have observed a hysteretic response for the equipment due to heating and cooling (François et al., 2007; Shariatmadari and Saeidijam, 2011; Vega and McCartney, 2015) although only Vega and McCartney (2015) comment on this issue directly, and no author suggests a solution.

Thermal deformation of the confining ring has been recognised as an issue as early as Towhata et al. (1993), but there is no consensus on how to apply a correction for this effect. Some schemes

have concluded that the change in the confining ring diameter does not significantly affect the volume change response (Towhata et al., 1993; Romero, 1999; Abuel-Naga et al., 2005; François et al., 2007), whereas others have suggested that it is important (Di Donna and Laloui, 2015; Vega and McCartney, 2015). Where a calibration has been given for this effect, it generally relies on the assumption that the soil volume remains constant, so that the radial expansion of the confining ring can be converted into an equivalent change in height of the soil specimen. This assumption is used by Romero (1999) and Abuel-Naga et al. (2005).

Finally, it is worth noting that despite the importance of calibration to the accuracy of subsequent results, in all cases, few details (if any) are given on how the measured calibration was used to correct the test data.

2.4 Soil behaviour

2.4.1 Introduction

In this section, the effect of temperature on soil behaviour is presented. All of the graphs are from the temperature-controlled oedometer schemes introduced chronologically in Section 2.2. Some results from other non-oedometer schemes (isotropic or triaxial) are discussed for comparison.

Each sub-section relates to a specific behaviour. Section 2.4.2 covers volume change, including the effect of soil stress history (over-consolidation ratio, loading/unloading paths), temperature history (thermal cycling), and plasticity. Section 2.4.3 covers pre-consolidation pressure. Section 2.4.4 covers compressibility characteristics, including compression and swelling indices (C_c and C_s), compressibility indices (λ and κ), coefficient of volume compressibility (m_v) and its reciprocal, oedometric modulus (E_{oed}). Section 2.4.5 covers consolidation characteristics, including coefficient of (primary) consolidation (c_v), and coefficient of secondary consolidation (C_a or C_{ae}). Section 2.4.6 covers coefficient of permeability (k). Section 2.4.7 covers water retention capacity, including swelling capacity. Finally, Section 2.4.8 covers pore water pressure.

Table 2.5 gives a summary of the main aspects of soil thermal behaviour that have been considered in the literature, with the relevant references. Soil index properties are summarised in Tables 2.1 and 2.2. Tested temperature and pressure ranges are summarised in Tables 2.3 and 2.4.

Table 2.5: Summary of key aspects of soil thermal behaviour and relevant references

Aspect of soil thermal behaviour	References
Volume change	Paaswell (1967), Plum and Esrig (1969), Towhata et al. (1993), Abuel-Naga et al. (2005), François et al. (2007), Di Donna and Laloui (2015), Vega and McCartney (2015), Favero et al. (2016), Ng et al. (2017), and Sittidumrong et al. (2019)
Pre-consolidation pressure	Gray (1936), Plum and Esrig (1969), Eriksson (1989), Tidfors and Sällfors (1989), Moritz (1995), Abuel-Naga et al. (2005), François et al. (2007), and Favero et al. (2016)
Compression characteristics	Gray (1936), Finn (1952), Plum and Esrig (1969), Eriksson (1989), Tidfors and Sällfors (1989), Towhata et al. (1993), François et al. (2007), Ye et al. (2012), Mon et al. (2013), Di Donna and Laloui (2015), and Favero et al. (2016)
Consolidation characteristics	Finn (1952), Plum and Esrig (1969), McGinley (1983), Towhata et al. (1993), Abuel-Naga et al. (2005), Mon et al. (2013), Di Donna and Laloui (2015), and Favero et al. (2016)
Permeability	Towhata et al. (1993), Romero et al. (2001), Villar and Lloret (2004), Abuel-Naga et al. (2005), and Di Donna and Laloui (2015)
Water retention and swelling capacity	Romero et al. (2001), Villar and Lloret (2004), and Shariatmadari and Saeidijam (2011)
Pore pressure	Moritz (1995) and Vega and McCartney (2015)

2.4.2 Volume change

Changing the temperature of a soil can result in volume change. Various terminology is used in the literature - thermal or thermally-induced volume change, strain, contraction, and expansion. These terms are used to define the change in volume of the soil, which is the direct or indirect result of temperature change. Strain describes a relative change, and can be linear (relative change in length) or volumetric (relative change in volume). Linear and volumetric strains are not equal in an oedometer test unless one-dimension conditions are maintained (zero lateral strain).

In some cases the effect of temperature on void ratio is reported, which provides information on the relationship between the different soil phases, which is not given by the strain value. Soil is a multi-phase material, comprising solid and liquid phases if fully saturated, plus a gas phase if unsaturated. The thermal expansion coefficient of solid minerals and water is different, which means that a change in temperature can result in a change in void ratio, without a similar change in total volume. More importantly, temperature affects the properties of each phase differently. In any case, a vital piece of information is the thermal expansion coefficients of the solid and water phases. The latter is well understood and can be found in materials handbooks. However, the thermal expansion coefficient of the solid phase is often missing from literature sources.

Thermal volume change is defined as the change in volume ΔV of the soil due to a change in temperature ΔT . The change in volume can be normalised by the initial volume V_0 , which gives thermal strain, ϵ_v :

$$\epsilon_v = \frac{\Delta V}{V_0} \quad (2.3)$$

For true one-dimensional conditions, the cross-sectional area of the specimen remains constant, so height ($H_0, \Delta H$) can be used interchangeably with volume ($V_0, \Delta V$), to calculate one-dimensional volumetric strain ($\epsilon_{v,1D}$). The one-dimensional volumetric strain is equal to the linear strain.

$$\epsilon_{v,1D} = \frac{\Delta H}{H_0} \quad (2.4)$$

For thermal tests, this is often not the case, because the diameter of the oedometer confining ring changes with temperature. When a temperature change is applied to the soil, the total volume change or total strain ϵ_v^{total} , is the sum of two components. These are the strain due to the thermal expansion of the solid phase of the soil, $\epsilon_v^{thermal}$, which depends on the volumetric thermal expansion coefficient of the solid phase, α_v , and the strain due to mechanical actions, $\epsilon_v^{mechanical}$, which can affect the volume, such as effective stress change.

$$\epsilon_v^{total} = \epsilon_v^{thermal} + \epsilon_v^{mechanical} \quad (2.5)$$

Total strain is the measured value, either calculated from the measured change in height, accounting for the change in diameter of the oedometer confining ring, or calculated from the measured flow of water in or out of the specimen, accounting for the change in density of the water. $\epsilon_v^{thermal}$ is calculated by multiplying the thermal expansion coefficient of the solid phase, α_v , by the change in temperature, ΔT .

$$\epsilon_v^{thermal} = \alpha_v \cdot \Delta T \quad (2.6)$$

The mechanical component, $\epsilon_v^{mechanical}$ cannot be measured, but is calculated from the other two components.

$$\epsilon_v^{mechanical} = \epsilon_v^{total} - \epsilon_v^{thermal} \quad (2.7)$$

A more thorough discussion on the components of strain is given in Section 4.6.1.

Note that in the literature, the term “thermal strain” is sometimes used when referring to the total strain due to temperature change, which is a combination of purely thermal and mechanical strains.

In thermal testing, a key property of the soil is its thermal expansion coefficient. The thermal expansion coefficient of a material is the relative thermal expansion (i.e. strain) of the material for a given change in temperature. It can be volumetric, area or linear. This distinction is important. The term *thermal expansion coefficient*, as commonly used in soil mechanics papers, is ambiguous. It could refer to the linear or volumetric thermal expansion coefficient (area thermal expansion coefficient is rarely used). Therefore, for clarity, it is important to specify which type of thermal expansion coefficient is being referred to.

The linear thermal expansion coefficient is the change in length over the original length (linear strain) of an object due to a change in temperature.

$$\alpha_L = \frac{\Delta L}{L_i} \cdot \frac{1}{\Delta T} \quad (2.8)$$

where:

α_L = linear thermal expansion coefficient
 ΔL = change in length
 L_i = initial length
 ΔT = change in temperature

The volumetric thermal expansion coefficient is the change in volume over the original volume (volumetric strain) of an object due to a change in temperature.

$$\alpha_v = \frac{\Delta V}{V_i} \cdot \frac{1}{\Delta T} \quad (2.9)$$

where:

α_v = volumetric thermal expansion coefficient
 ΔV = change in volume
 V_i = initial volume
 ΔT = change in temperature

For anisotropic materials, the volumetric thermal expansion coefficient can be calculated from the linear thermal expansion coefficients perpendicular and parallel to a reference axis. For clay, linear coefficients are measured perpendicular and parallel to the orientation of the clay layers. For sand, linear coefficients are measured perpendicular and parallel to the crystallographic axis of the sand.

$$\alpha_v = \alpha_{L\perp} + 2 \cdot \alpha_{L\parallel} \quad (2.10)$$

where:

α_v = volumetric thermal expansion coefficient

$\alpha_{L\perp}$ = linear thermal expansion coefficient perpendicular to reference axis

$\alpha_{L\parallel}$ = linear thermal expansion coefficient parallel to reference axis

The derivation of this result is given in Appendix C.

For isotropic materials, the volumetric thermal expansion coefficient can be calculated from the linear thermal expansion coefficient, and vice-versa, as follows:

$$\alpha_v = 3 \times \alpha_L \quad (2.11)$$

$$\alpha_L = \frac{1}{3} \times \alpha_v \quad (2.12)$$

where:

α_v = volumetric thermal expansion coefficient

α_L = linear thermal expansion coefficient

The derivation of this result is given in Appendix D.

In the results from the literature that follow, thermal effects are presented in terms of axial and volumetric strain, and void ratio. For ambient-temperature oedometer conditions, these can be used interchangeably. However, as discussed above, this is not the case for thermal oedometer tests. The issues involved with calculation of strain and void ratio in thermal oedometer tests are discussed in detail in Chapter 4 of this thesis, but it is important here to call attention to them briefly. These issues relate to the corrections applied to the measured displacement values. First, the correction to the axial displacement, to account for vertical thermal equipment compliance. Second, the correction to axial displacement, and volumetric strain, to account for lateral thermal expansion of the confining ring. Third, the correction to the void ratio, to account for the differential thermal expansion of the solid and water phases of the soil. The measurement and application of these corrections in the literature is discussed in Section 2.3.

Paaswell (1967) gives results as strain, presumably axial strain since no details are given on thermal calibration. Plum and Esrig (1969) gives results as strain, defined as follows:

$$\epsilon = \frac{\Delta e}{1 + e} \quad (2.13)$$

where:

ϵ = strain

Δe = change in void ratio

e = initial void ratio

This approach is based on the assumption that the volume of solids remains constant, which is not the case for thermal tests. Towhata et al. (1993) give results as void ratio, but without

explaining how the void ratio was calculated. Abuel-Naga et al. (2005) give results as both volumetric strain and void ratio. The volumetric strain is calculated accounting for the lateral thermal expansion of the confining ring, and the void ratio is calculated based on an assumed thermal expansion coefficient for the solid phase of the soil. In François et al. (2007), results are given as void ratios. In this case, the water flow in and out of the specimen was measured, enabling void ratio to be measured, without requiring a correction to account for the thermal expansion of the solid phase of the soil. Di Donna and Laloui (2015) give results as volumetric strain, but do not provide any details on how these values are calculated. Vega and McCartney (2015) give results as axial strain, which has been corrected for vertical thermal equipment compliance, but not for lateral thermal expansion of the confining ring. Favero et al. (2016) give results as measured axial strain, corrected for vertical thermal equipment compliance, and volumetric strain, accounting for lateral thermal expansion of the confining ring. Where results are given for void ratio change (Section 2.4.3), the thermal expansion of the solid phase of the soil has been accounted for. In Ng et al. (2017) results are given as axial strain, without accounting for the lateral thermal expansion of the confining ring. Sittidumrong et al. (2019) also give results as axial strain, without accounting for the lateral thermal expansion of the confining ring.

As can be seen, previous volume change results have been calculated and presented in different ways. The corrections to account for vertical thermal equipment deformation, lateral thermal confining ring deformation, and thermal change in volume of soil solids, have not been consistently applied. Furthermore, the application of these corrections has not always been clearly documented. One of the aims with this research therefore, has been to develop a clear data-processing methodology which clarifies exactly how each value has been calculated, including which corrections have been applied, and in which order.

Volume change: results

Paaswell (1967) performed isobaric heating tests on normally-consolidated Penn soil, varying the heating rate, duration, and the total change in temperature.

They found that following completion of primary consolidation, at ambient temperature, subsequent heating of a normally-consolidated soil results in contraction, as shown in Figure 2.39, for a “long time (i.e. slow heating rate), high temperature rise” test ($\Delta T = 30^\circ\text{C}$, 5°C/h). The labels 1 and 8 refer to two numbered temperature sensors.

They also investigated the effect of pressure on thermal strain, by carrying out heating tests at different pressures, but found no clear relationship between pressure and thermal strain for normally-consolidated soil.

To investigate the effect of heating on normally-consolidated clay, **Plum and Esrig (1969)** carried out an isobaric heating test on illite. The results are given in Figure 2.40. When the soil was heated from 24°C to 50°C at constant applied vertical pressure, they observed a reduction in void ratio, which agrees with the result of Paaswell (1967).


They were the first researchers to present data on the effect of over-consolidation ratio (OCR) on thermal volume change. In the test shown in Figure 2.41, they applied the same temperature change (heating from 24°C to 50°C), to remoulded illite, at OCR values between 1.0 (normally-consolidated) and 1.7 (over-consolidated). They found that thermal contraction reduces with increasing OCR. At an OCR of 1.7, the thermal contraction was essentially zero.



Figure 2.39: Thermal strain of NC Penn soil - heating path. Positive strain = contraction (Paaswell, 1967)



Figure 2.40: Thermal strain of NC illite - heating path. Positive strain = contraction (Plum and Esrig, 1969)



images/litreview/Plu69_fig4b.png


Figure 2.41: Effect of OCR on thermal strain of illite. Positive strain = contraction (Plum and Esrig, 1969)

Towhata et al. (1993) carried out thermal tests on MC clay and bentonite clay. To investigate thermal volume change of normally-consolidated soil, they performed isobaric heating tests. Figure 2.42a shows the effect of heating following completion of primary consolidation of MC clay under a vertical stress of 2230 kPa. Figure 2.42b is an enlargement of the same data. The temperature was increased incrementally from 22 °C to 40 °C, 60 °C and 90 °C. They observed that heating causes further reduction in void ratio, in agreement with previous research.

The same tests performed on MC clay (Figures 2.42a and 2.42b) were repeated using bentonite (Figures 2.43a and 2.43b). At the same stress level (2230 kPa) and for the same temperature increase (22 °C to 90 °C), the associated reduction in void ratio was higher for bentonite ($\Delta e = 0.075$) than MC clay ($\Delta e = 0.0275$). Since bentonite has much higher plasticity than MC clay, the authors suggest that the magnitude of thermal volume change increases with plasticity.

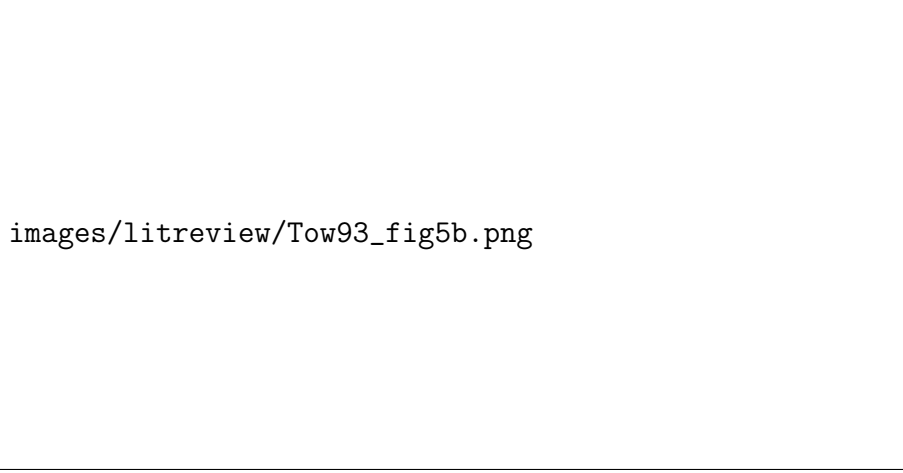
They were then able to determine the effect of stress level on thermal volume change by applying the same heating path at different stress levels. Based on a series of such tests, at stress levels from 40 kPa to 2230 kPa, they found the amount of volume contraction due to heating to be independent of stress level. This is shown for MC clay in Figure 2.44. They concluded that the result for 40 kPa was an anomaly, due to the soil being in a slurry state at such a low stress level.

The effect of OCR was also assessed. Six soil specimens were consolidated to 2230 kPa then unloaded to OCR values from 1.7 to 56, and heated from 22 °C to 90 °C. These tests are summarised in Figure 2.45 for MC clay. At the lowest OCR value of 1.7, the void ratio increases slightly (expansive response) for heating between 22 °C, and 60 °C, then decreases sharply (contractive response) between 60 °C, and 90 °C, so that overall the heating results in a reduction in void ratio. Note that this reduction in void ratio ($\Delta e = 0.0025$) is an order of magnitude smaller than the reduction in void ratio for the normally-consolidated MC clay ($\Delta e = 0.0275$),



images/litreview/Tow93_fig5a.png

(a)




images/litreview/Tow93_fig5b.png

(b)

Figure 2.42: Thermal void ratio change of normally-consolidated MC clay (a) full increment (b) heating detail (Towhata et al., 1993)


as shown in Figures 2.42a and 2.42b. For all the other OCR values, the void ratio increases over the whole temperature range, with higher OCR values resulting in the greatest increases.

By increasing the range of temperature and OCR values considered, they were able to build on the conclusions of Plum and Esrig (1969), who observed that thermal contraction reduces with increasing OCR. Towhata et al. found for normally-consolidated soil, heating results in a reduction in the void ratio, or contraction. At intermediate OCR, heating initially results in an increase in the void ratio, followed by a reduction at higher temperature. At higher OCR values, heating results in an increase in the void ratio, or swelling. Since all specimens were loaded to the same maximum stress before unloading to their target OCR, they were heated at different stress levels. Highly over-consolidated specimens were heated at relatively low stresses compared to specimens unloaded to lower OCR values. Without considering the effect of OCR, this would imply that the thermal volume change was not independent of stress level, which contradicts the result in Figure 2.44. From this test alone, it is not possible to say definitively whether thermal volume change is independent of stress level.



images/litreview/Tow93_fig8a.png

(a)




images/litreview/Tow93_fig8b.png

(b)

Figure 2.43: Thermal void ratio change of normally-consolidated bentonite (a) full increment (b) heating detail (Towhata et al., 1993)

Another series of tests was carried out on over-consolidated soil. This time, soils were consolidated to 2230 kPa, unloaded to 20 kPa, then reloaded to the target OCR. Compared to the tests shown in Figure 2.45, both OCR and stress level is the same, but the stress history has changed. In the previous series of tests, heating follows an unloading path, but in these tests, heating follows a reloading path. Figure 2.46 shows the results for these tests. For all OCR values, heating causes a reduction in void ratio, which is independent of OCR. This contrasts with the results for heating following unloading, discussed above, which shows a dependence on OCR, with increased thermal volume expansion with increasing OCR. In this case, all specimens experienced thermal volume contraction, regardless of OCR.

Finally, Towhata et al. investigated the effect of a thermal cycle by applying a $20 \rightarrow 90 \rightarrow 20$ °C cycle to a normally-consolidated soil. Figure 2.47 shows the effect of a thermal cycle on MC clay following a consolidation increment from 80 kPa to 160 kPa. Heating to 90 °C causes volume contraction, which is not recovered by subsequent cooling to 20 °C. This suggests that heating effects on normally-consolidated clay are not reversible.



images/litreview/Tow93_fig6.png


Figure 2.44: Effect of stress level on thermal void ratio change of normally-consolidated MC clay (Towhata et al., 1993)

Abuel-Naga et al. (2005) carried out a range of thermal tests on soft Bangkok clay. They carried out isobaric heating tests on NC soil (test 1), isobaric heating tests on OC soil (test 2), and isothermal loading tests (test 3). Load paths for these tests, on temperature - effective stress axes, with the expected behaviour on void ratio - effective stress axes, are given in Figures 2.48 (test 1), 2.49 (test 2) and 2.50 (test 3).

Figure 2.51 shows the thermal volume change resulting from one heating cycle ($22 \rightarrow 90 \rightarrow 22^\circ\text{C}$) at various OCR values. These data are from tests 1 and 2. The normally-consolidated specimen ($\text{OCR} = 1$) contracts during heating, but this volume change is not reversed upon subsequent cooling. The specimen at $\text{OCR} = 2$ shows a small expansion when heated to 50°C , followed by contraction at higher temperature. Again, this contraction appears to be irreversible. At higher OCR values, heating causes expansion. The authors suggest that this expansion is reversible, but based on the figure, it appears that the expansion resulting from heating at $\text{OCR} = 8$ is not recovered during subsequent cooling. In other words, for the first cycle of heating and cooling, the resulting thermally-induced volume change may be irreversible, at any OCR.


Figure 2.52 shows the same data in a different way: volumetric strain ϵ_v as a function of the OCR for heating to three temperatures, 50°C , 70°C and 90°C . It is seen that at a certain OCR, the volumetric strain may be positive (contractive) or negative (expansive). For normally-consolidated soil ($\text{OCR} = 1$), the response is contractive across the full temperature range. For lightly over-consolidated soil ($\text{OCR} = 2$), the response is expansive for 50°C and 70°C , but contractive at 90°C . At OCR values of 4 or 8, the response is expansive for all three temperatures. This behaviour is consistent with the observations of Towhata et al. (1993) using MC clay.

The results from the isothermal loading test (test 3) are shown in Figure 2.53. Specimens were loaded to a certain pre-consolidation pressure, followed by unloading to various OCR values, before heating from 25°C to 90°C , and finally reloaded at elevated temperature. In total, twelve test were performed, at OCR values of 1, 2, 4 and 8, for pre-consolidation pressures of 100 kPa, 200 kPa and 300 kPa. The final reloading path is the isothermal loading part of the



images/litreview/Tow93_fig16.png

Figure 2.45: Effect of OCR on thermal void ratio change of MC clay, for heating following unloading path. Positive Δe = expansion (Towhata et al., 1993)




images/litreview/Tow93_fig19.png

Figure 2.46: Effect of OCR on thermal void ratio change of MC clay, for heating following reloading path. Negative Δe = contraction (Towhata et al., 1993)




images/litreview/Tow93_fig4.png

Figure 2.47: Effect of thermal cycling on normally-consolidated MC clay (Towhata et al., 1993)



images/litreview/Abu05_fig2a.png

Figure 2.48: Isobaric heating of NC soil - load path for test 1 (Abuel-Naga et al., 2005)



images/litreview/Abu05_fig2b.png

Figure 2.49: Isobaric heating of OC soil - load path for test 2 (Abuel-Naga et al., 2005)



Figure 2.50: Isothermal loading of OC soil - load path for test 3 (Abuel-Naga et al., 2005)



Figure 2.51: Effect of OCR on thermal strain of soft Bangkok clay. Positive ϵ_v = contraction (Abuel-Naga et al., 2005)



Figure 2.52: Effect of OCR on thermal strain of soft Bangkok clay - heating path. Positive ϵ_v = contraction (Abuel-Naga et al., 2005)

test, but it is useful at this point to consider the heating path before reloading ($c \rightarrow d$ in Figure 2.50). By carrying out heating tests on specimens which were at the same OCR, but different pre-consolidation pressures (or in other words, at different stress levels), they were able to separate the effects of OCR and stress level, an issue Towhata et al. (1993) raised. There is a clear relationship between thermally induced change in void ratio Δe and OCR. This can be seen by comparing the results for the four tested OCR values for each pre-consolidation pressure value. There is no clear relationship between the pre-consolidation pressure and void ratio change, which can be seen by comparing the results for the three pre-consolidation pressure values for each OCR value. This suggests that thermal volume change is independent of the pre-consolidation pressure, i.e. independent of stress level.

François et al. (2007) carried out controlled temperature and suction tests on Sion silt, mixed as slurry at $1.5 \times$ liquid limit. Results from François and Laloui (2010), using the same equipment, are given in Figure 2.54, consisting of three plots (a) void ratio vs vertical stress (b) void ratio vs suction and (c) void ratio vs temperature. The specimen was normally consolidated, then unloaded to $\text{OCR} = 10$ (highly over-consolidated). Following unloading, the specimen was heated (path $C \rightarrow D$ on the figure), at constant vertical stress and suction. This causes the void ratio to increase, which is most clearly seen in Figure 2.54c. This result agrees with previous studies which also found that highly over-consolidated soils expand when heated.

Di Donna and Laloui (2015) carried out thermal cyclic loading tests on four intact samples of silty clay from Geneva, Switzerland. Figure 2.55 shows the results of six isobaric heating tests on the four samples: S1, S3, S4, and S4b. Each sample was taken at a different depth, and so had a different in-situ state. The over-consolidated specimens (open markers, labelled OC) were unloaded to $\text{OCR} = 16.7$ before applying the thermal cycles. The normally-consolidated specimens (filled markers, labelled NC) contract during the first heating phase, whereas over-consolidated specimens either expand or show minimal volume change. During subsequent cooling, NC specimens contract further, but the magnitude of volume change is less than the initial contraction due to heating. OC specimens show minimal volume change during cooling.



Figure 2.53: Effect of pre-consolidation pressure on thermal void ratio change of soft Bangkok clay at different OCR. Positive Δe = contraction. (Abuel-Naga et al., 2005)

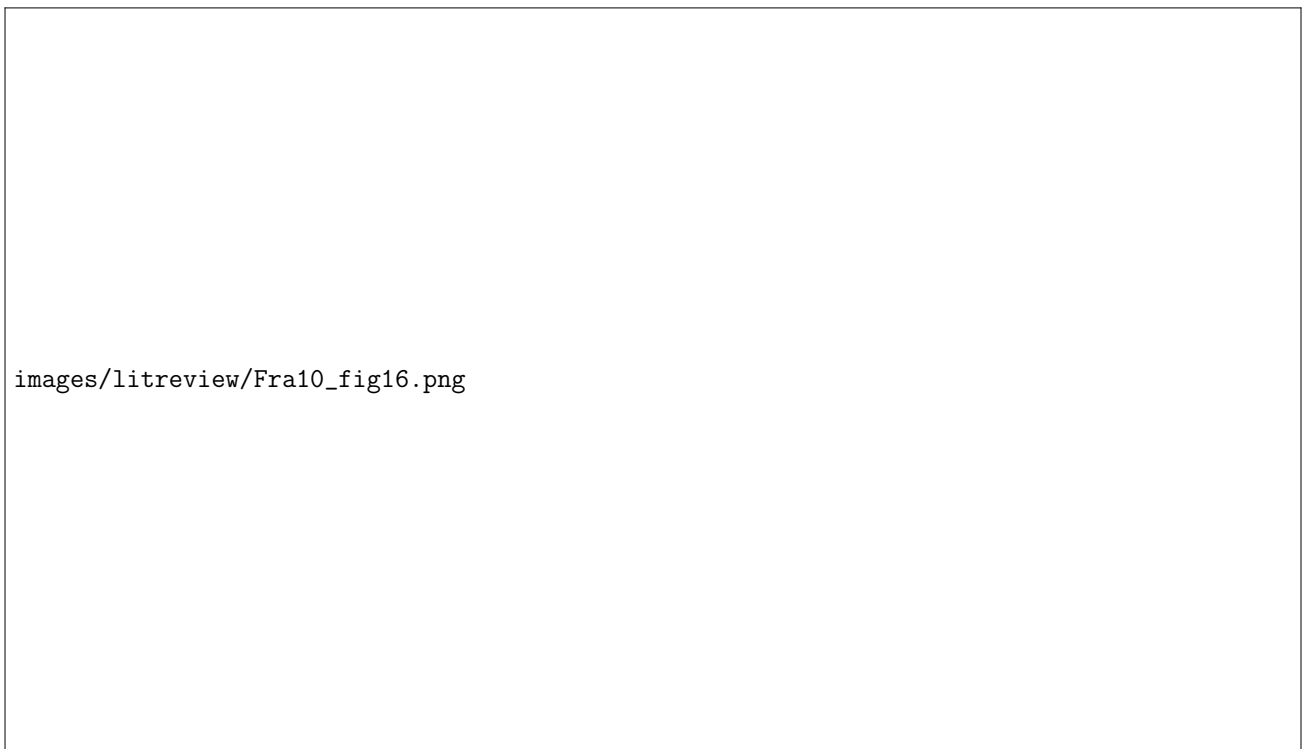


Figure 2.54: Thermal void ratio change of OC Sion silt - heating path. Positive Δe = expansion (François and Laloui, 2010)

images/litreview/DiD15_fig7.png

Figure 2.55: Thermal volume change of NC and OC Geneva clay. Positive ϵ_v = contraction (Di Donna and Laloui, 2015)

For the NC specimens, most of the thermal volume change occurs during the first thermal cycle, and the accumulation of strain reduces with each cycle. This is shown in Figure 2.56, for up to four thermal cycles, where the increment of volumetric deformation $\Delta\epsilon_v$ refers to the volumetric strain following the cooling path of each heat/cool cycle. The difference in magnitude of volume change between normally-consolidated specimens is linked to their plasticity index. Figure 2.57 shows that thermal volume change increases with increasing plasticity, which agrees with the results of Towhata et al. (1993).



Figure 2.56: Effect of number of thermal cycles on incremental thermal strain of NC Geneva clay. Positive $\Delta\epsilon_v$ = contraction (Di Donna and Laloui, 2015)



Figure 2.57: Effect of plasticity on thermal volume change of NC Geneva clay. Positive ϵ_v = contraction (Di Donna and Laloui, 2015)

Vega and McCartney (2015) carried out thermal tests on compacted, saturated Bonny silt. They performed four thermal cycles ($18 \rightarrow 91 \rightarrow 18^\circ\text{C}$) at OCR values between 1 (NC), and 30.29 (highly OC). A schematic of the testing sequence is given in Figure 2.58.

Figures 2.59 and 2.60 show the development of thermally-induced strain for the NC and highly OC cases respectively. As expected, the NC specimen contracts during heating, whereas the OC specimen expands. With subsequent cycles, the NC specimen continues to contract, but the OC specimen experiences no further strain after the first cycle, in agreement with Favero et al. (2016). This result is also shown in Figure 2.61, where for $\text{OCR} = 1$ (NC) there is an increase in thermally-induced contractive strain with each cycle, and a similar response for $\text{OCR} = 1.28$ and 1.80, but with lower magnitude of strain at increasing OCR. For $\text{OCR} = 7.36$ and 30.29, the thermally-induced strain is expansive, and increase in strain with repeated cycles is minimal.




Figure 2.58: Isobaric thermal cycling of Bonny silt at different OCR - test path (Vega and McCartney, 2015)



Figure 2.59: Thermal strain of Bonny silt at $OCR = 1.00$ (NC). Positive axial strain = contraction (Vega and McCartney, 2015)



Figure 2.60: Thermal strain of Bonny silt at $OCR = 30.29$ (highly OC). Positive axial strain = contraction (Vega and McCartney, 2015)



images/litreview/Veg15_fig10.png


Figure 2.61: Effect of OCR on permanent thermal strain of Bonny silt due to temperature cycling. Positive axial strain = contraction (Vega and McCartney, 2015)

Favero et al. (2016) carried out tests on Opalinus clay. Figure 2.62 shows the thermally induced strain for temperature cycles of $23.5 \rightarrow 80 \rightarrow 23.5$ °C, at OCR values of 4 and 12.

Note that Opalinus clay is actually a shale, i.e. a sedimentary rock, with a yield stress that is affected not only by overburden, but also by other physical and chemical changes that occur during the conversion of sediment to sedimentary rock. The authors define OCR as the ratio of the maximum vertical effective stress to the current vertical effective stress.

Measured axial strain refers to the axial strain directly measured by the LVDTs. Computed volumetric strain refers to the volumetric strain, corrected for the thermal expansion or contraction of the confining ring. This is why the values at 23.5 °C are the same in both cases, whereas the values at elevated temperature are shifted towards the expansive side. Heating causes radial expansion of the confining ring, resulting in a reduction in height of the specimen, which can be corrected by assuming constant soil volume. At $OCR = 4$, heating induces contraction, whereas at $OCR = 12$, heating induces expansion. In both cases, this volume change appears to be irreversible.

Cooling of both specimens results in contraction. Further thermal cycles carried out on the high OCR specimen result in reversible expansion during heating, but the expansion resulting from the first cycle is not recovered.



images/litreview/Fav16_fig11.png

Figure 2.62: Effect of OCR on thermal strain of Opalinus clay. Positive strain = contraction (Favero et al., 2016)

Ng et al. (2017) performed multiple heating/cooling cycles, in the temperature range 15 °C to 70 °C, on mechanically normally-consolidated low-plasticity clay and Toyoura sand. The results, in terms of thermally-induced axial strain, for steel and Invar confining rings were compared.

The results for the two tests on clay are presented in Figure 2.63. The result for a steel confining ring is shown in Figure 2.63a, and for Invar in Figure 2.63b. For the steel confining ring, the first heating path induces an axial strain of 0.43 %. A negligible amount of axial strain is recovered during subsequent cooling. Further thermal cycling leads to accumulation of irreversible axial strain. This accumulation decreases with each cycle, until a stable state is reached after four cycles. For the Invar confining ring, the behaviour is qualitatively similar, but the irreversible axial strain measured with the Invar ring is lower than for the steel ring. The reason given by the authors for this difference is the higher thermal expansion coefficient of steel. During heating, the steel ring expands more than the soil, inducing additional settlement of the soil specimen.

The results for the two tests on Toyoura sand are presented in Figures 2.64a (steel confining ring) and 2.64b (Invar confining ring). The results for the steel confining ring show that thermal cycling causes an accumulation of contractive plastic axial strain, which decreases with each cycle. A stable state is reached after several cycles, where heating causes contraction and cooling causes expansion. For the Invar confining ring, not only are the measured strains lower than for the steel confining ring (as was the case for clay, in Figure 2.63), but at the stable state, heating causes expansion, and cooling causes contraction. The authors suggest that with the steel confining ring, the actual soil contraction during cooling is offset by the greater contraction of the steel confining ring, resulting in overall measured expansion.



(a)



(b)

Figure 2.63: Axial strain of NC low-plasticity clay due to thermal cycling, for confining ring made of (a) steel (b) Invar. Positive strain = contraction (Ng et al., 2017)




(a)



(b)

Figure 2.64: Axial strain of NC Toyoura sand due to thermal cycling, for confining ring made of (a) steel (b) Invar. Positive strain = contraction (Ng et al., 2017)

Sittidumrong et al. (2019) carried out thermal tests on Bangkok sand. They applied multiple thermal cycles at constant pressure. Figure 2.65 compares the behaviour of two specimens at different relative densities. Both heating and cooling cause contractive strains. The first thermal cycle induces the largest strain, and subsequent cycles result in progressively smaller *additional* strain. The initial relative density does not affect the first cycle, but leads to larger strains for the looser sample during subsequent cycles.



images/litreview/Sit19_fig9.png

Figure 2.65: Thermal strain of NC Bangkok sand over five thermal cycles. Positive vertical strain = contraction (Sittidumrong et al., 2019)

The effects of relative density and stress level are compared in Figure 2.66. Each group of three bars represents three tests on sand at a given relative density, four reconstituted (R) samples from 98 % to 30 % relative density, and one undisturbed sample (UD) at 44 % relative density. Each bar represents a test at 2.0 MPa, 3.2 MPa or 4 MPa (from left to right in the figure). The hatched sections of each bar represent the vertical strain after 1, 20 and 100 cycles. First, by comparing the groups of bars (effect of relative density), it can be seen that lower relative density specimens experience higher thermal volume change. By comparing the bars within each group (effect of stress level), it can be seen that thermal volume change generally increases with stress level, although this is not true for all relative density values. Finally, by comparing the height of the hatched areas within each bar (effect of number of cycles), it can be seen that although the first cycle results in the greatest strain for any one cycle, there is still significant strain generated from further cycles, and the response is clearly not elastic.

images/litreview/Sit19_fig15.png

Figure 2.66: Effect of stress level and relative density on strain induced in NC Bangkok sand by thermal cycling. Positive vertical strain = contraction (Sittidumrong et al., 2019)

Volume change: summary

Stress history has an important influence on the behaviour of soil when heated or cooled. For normally-consolidated and lightly over-consolidated soil, heating causes contraction following completion of primary consolidation. At high over-consolidation ratios (OCRs), heating causes thermal expansion. However, even at the same OCR, the response may depend on whether the preceding stage was loading or unloading (Towhata et al., 1993). There is not a consensus on whether the amount of thermal volume change is affected by stress level. Some studies have found it to be independent of stress level (Paaswell, 1967; Towhata et al., 1993; Abuel-Naga et al., 2005), while others have found a dependence (Sittidumrong et al., 2019).

The effect of thermal cycling has been examined by many studies. Of particular interest is whether thermal volume change resulting from the first heating stage is reversed during subsequent cooling. For normally-consolidated and lightly over-consolidated soil, contraction due to heating is not reversed by cooling. For highly over-consolidated soil, expansion due to heating may be reversible (Abuel-Naga et al., 2005), but some studies have found otherwise (Di Donna and Laloui, 2015; Favero et al., 2016).

The effect of multiple cycles is also of interest. For both normally-consolidated and over-consolidated soils, most thermal volume change occurs during the first heating-cooling cycle. For normally-consolidated and lightly over-consolidated soil, subsequent cycles result in accumulation of volume change, the amount reducing with each cycle. For highly over-consolidated soils, subsequent cycles do not cause any further volume change (Vega and McCartney, 2015).

Finally, it is important to note the importance of soil type. Results are presented for a range of different soils - high plasticity swelling clays such as bentonite (Towhata et al., 1993), medium plasticity silty clays (Di Donna and Laloui, 2015), silty sands (François et al., 2007), sand-bentonite mixtures (Shariatmadari and Saeidijam, 2011) and sand (Sittidumrong et al., 2019). Thermal volume change increases with increasing plasticity (Towhata et al., 1993; Di Donna and Laloui, 2015).

The key results for thermal volume change behaviour from TC oedometer schemes are summarised in Table 2.6.

Table 2.6: Volume change: summary of observed results from TC oedometer tests

Tested effect	Observed result	References
Effect of heating	Heating NC soil causes contraction following completion of primary consolidation	Paaswell (1967), Plum and Esrig (1969), Towhata et al. (1993), Abuel-Naga et al. (2005), Ng et al. (2017), and Sittidumrong et al. (2019)
	Magnitude of contraction reduces with increasing OCR	Plum and Esrig (1969)
	Heating causes contraction for NC and lightly OC soil, and expansion for highly OC soil	Towhata et al. (1993), Abuel-Naga et al. (2005), François et al. (2007), Di Donna and Laloui (2015), Vega and McCartney (2015), and Favero et al. (2016)
	Magnitude of contraction is independent of stress level	Paaswell (1967), Towhata et al. (1993), and Abuel-Naga et al. (2005)
	Magnitude of contraction depends on stress level	Sittidumrong et al. (2019)
Effect of thermal cycling on NC and lightly OC soil	Magnitude of contraction increases with increasing plasticity	Towhata et al. (1993) and Di Donna and Laloui (2015)
	Initial thermal contraction is not reversed upon cooling	Towhata et al. (1993) and Abuel-Naga et al. (2005)
Thermal cycles on OC soil	Most strain occurs during first thermal cycle, and accumulation of strain reduces with each cycle	Di Donna and Laloui (2015), Vega and McCartney (2015), Ng et al. (2017), and Sittidumrong et al. (2019)
	Initial thermal expansion is irreversible	Vega and McCartney (2015) and Favero et al. (2016)
	Initial thermal expansion is reversible	Abuel-Naga et al. (2005)

2.4.3 Pre-consolidation pressure

Pre-consolidation pressure is the stress at which consolidation behaviour changes from that of an over-consolidated soil to that of a normally-consolidated soil. Temperature is one of several environmental factors, including changes in pH, salt concentration, and ground-water table elevation that can affect pre-consolidation pressure. Pre-consolidation pressure is an important property of the soil to know since it directly relates to settlement. According to Moritz (1995), it “corresponds empirically to the effective pressure to which the soil may be subjected under normal conditions without major consolidation settlement occurring.”

Laboratory tests to determine the effect of temperature on pre-consolidation pressure involve heating then reloading over-consolidated specimens at constant temperature. These tests are referred to as isothermal loading.

For ambient temperature testing, a soil is described as normally-consolidated (NC) if it has never experienced an effective vertical stress greater than the current one. A soil is described as over-consolidated (OC) if it has experienced an effective vertical stress greater than the current one. However, these definitions are not appropriate for thermal testing, where soil can behave as though over-consolidated, despite never having experienced higher stresses in the past. This inadequate definition has led to the profusion of confusing terms such as “apparent over-consolidation”.

A soil is normally-consolidated if it plots on the normal consolidation line (NCL), as shown schematically in Figure 2.67. If it plots below the NCL, it is over-consolidated. This may seem like a circular definition, but this is not the case. The first step is to identify the NCL, which is not always a straight line, then on this basis, the soil can be defined as OC or NC based on its behaviour (i.e. whether it plots on, or below, the NCL).

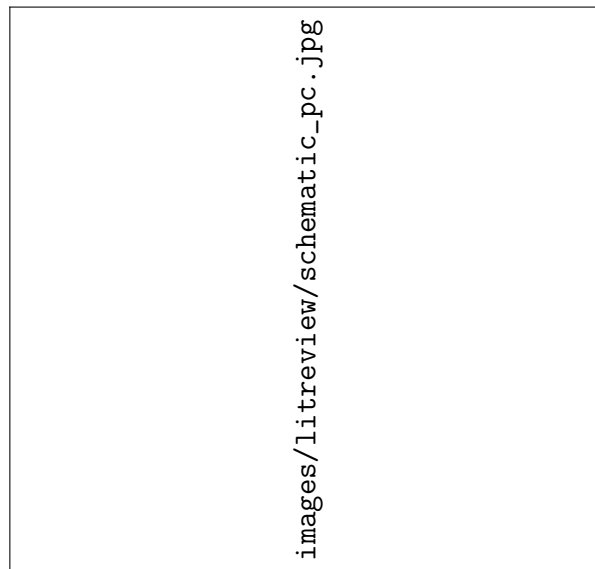


Figure 2.67: Schematic - pre-consolidation pressure, p_c

For ambient temperature testing, the over-consolidation ratio (OCR) is defined as the ratio between the maximum vertical stress a soil has experienced in the past, and the current vertical stress. However, for thermal testing, a better definition is the ratio between the pre-consolidation

pressure p_c , and the current vertical stress σ'_v .

$$OCR = \frac{p_c}{\sigma'_v} \quad (2.14)$$

Pre-consolidation pressure is often defined as the maximum pressure that has acted on a soil, some time in the past. This definition is satisfactory for isothermal oedometric conditions, where the pre-consolidation pressure equals to the maximum applied vertical stress. However, change in temperature can affect the pre-consolidation pressure, so that it no longer equals to the maximum applied vertical stress. In some publications, the term “apparent pre-consolidation pressure” is used to distinguish pre-consolidation pressure calculated at elevated temperature from the ambient temperature value.

It is preferable to define the pre-consolidation pressure in terms of the soil behaviour, rather than its history. Pre-consolidation pressure, p_c is the pressure where the swelling line intersects the normal compression line. In other words, it is the stress level that separates over-consolidated and normally-consolidated behaviour, as shown schematically in Figure 2.67.

Pre-consolidation pressure: results

Gray (1936) performed two isothermal loading tests. In test 1, Figure 2.68 (testing schematic) and Figure 2.69 (results), the soil was consolidated then unloaded to an over-consolidated state at 10 °C, heated to 22 °C, then reloaded at this higher temperature. In test 2, Figure 2.70 (testing schematic) and Figure 2.71 (results), the soil was loaded then unloaded to an over-consolidated state at 22 °C, cooled to 10 °C, then reloaded at this lower temperature. The *isothermal loading* stage refers to the final reloading stage at constant temperature.

From test 1, in Figure 2.69, it is seen that increasing temperature shifts the NCL down, although the gradient remains the same. If the pre-consolidation pressure were estimated based on the reloading line at 22 °C, it would be lower than the maximum pressure reached at 10 °C. This means that the pre-consolidation pressure has reduced as a result of the increase in temperature. Test 2 confirms that this relationship holds for cooling as well as heating. Figure 2.71 shows that reducing the temperature shifts the NCL up, so that the pre-consolidated pressure increases. Again, the gradient of the NCL remains the same. Note that the results are plotted in terms of void ratio, rather than specimen height, but no details are given on how the void ratio was calculated, or whether any correction was applied to account for the thermal volume change of the solid phase of the soil.

Plum and Esrig (1969) found that thermal cycling affects the pre-consolidation pressure but not the gradient of the NCL. Figure 2.72 shows the results from a test in which a normally-consolidated illite specimen was subjected to a thermal cycle (24 → 50 → 24 °C), before being consolidated further. The same thermal cycle was applied again at a higher pressure. This thermal cycling, and specifically the cooling path, causes the soil to behave as though over-consolidated, increasing the pre-consolidation pressure. It causes the NCL to shift up, but the gradient remains the same. The same effect, observed by Gray (1936) in Figure 2.71, for reloading following a cooling path, is observed here for a heating and cooling path, with no net temperature change. This contrasts with the later observations of Tidfors and Sällfors (1989) in Figure 2.74a, who found that the position of the NCL is uniquely determined by temperature. Instead, it appears, the position of the NCL depends on the temperature history of the soil (and can be considered analogous to the effect of stress level and OCR).

images/litreview/Gra36_fig1.pdf

Figure 2.68: Isothermal loading test path - test 1 (Gray, 1936)

images/litreview/Gra36_fig3.pdf

Figure 2.69: Effect of temperature increase on compression behaviour of fine-grained soil - test 1 (Gray, 1936)

images/litreview/Gra36_fig2.pdf

Figure 2.70: Isothermal loading test path - test 2 (Gray, 1936)

images/litreview/Gra36_fig4.pdf

Figure 2.71: Effect of temperature decrease on compression behaviour of fine-grained soil - test 2 (Gray, 1936)



Figure 2.72: Effect of thermal cycling on compression behaviour of illite (10 psi = 69 kPa, 50 psi = 345 kPa) (Plum and Esrig, 1969)

The result from Gray (1936), that pre-consolidation pressure reduces with increasing temperature, was repeated by later researchers (Eriksson, 1989; Tidfors and Sällfors, 1989; Moritz, 1995; Abuel-Naga et al., 2005; Favero et al., 2016) using a range of different soils.

Eriksson (1989) performed tests on silty clay, shown in Figure 2.73. Consolidation tests were performed at temperatures between 5 °C and 55 °C. It was found that the pre-consolidation pressure reduced non-linearly with increased temperature.

Tidfors and Sällfors (1989) performed tests using a constant-rate-of-strain (CRS) oedometer on five different Swedish clays. Figure 2.74a shows the result of a CRS test on Bäckebol clay in which the temperature was changed several times. Pre-consolidation pressure reduces with increasing temperature, shown by the NCL shifting to the left with increasing temperature. The gradient of the NCL is independent of temperature. There also appears to be a unique relationship between the temperature and the pre-consolidation pressure, as indicated by the dotted lines, which show that when the soil is cooled from 40 °C to 25 °C, it re-joins the (assumed) 25 °C NCL upon reloading, and similarly for cooling from 25 °C to 7 °C.

The effect of temperature on pre-consolidation pressure is shown in Figure 2.74b. A linear relationship is suggested by the authors, in contrast to the non-linear relationship suggested by Eriksson (1989), but there is quite wide scatter in the data.

Moritz (1995) observed a non-linear reduction in pre-consolidation pressure with increasing temperature for Linköping clay, shown in Figure 2.75. This non-linear reduction was previously observed by Eriksson (1989). They proposed a power-law relationship, given in the figure, for the pre-consolidation pressure which is a function of the current temperature T , room temperature T_0 , and pre-consolidation pressure at room temperature σ'_{cT_0} .



(a)



(b)

Figure 2.73: Effect of temperature on pre-consolidation pressure of silty clay (Eriksson, 1989)




(a)



(b)

Figure 2.74: Effect of temperature on (a) compression behaviour (b) pre-consolidation pressure, of Bäckebol clay (Tidfors and Sällfors, 1989)



images/litreview/Mor95_fig72.png

Figure 2.75: Effect of temperature on pre-consolidation pressure of Linköping clay (Moritz, 1995)

Abuel-Naga et al. (2005) observed a reduction in pre-consolidation pressure with temperature for soft Bangkok clay. They carried out isothermal loading tests at two stress levels. This is shown in Figure 2.76. The eight data points are from eight tests, in which an over-consolidated specimen was either kept at ambient temperature or heated to 50 °C, 70 °C or 90 °C. In four tests, the maximum pressure before unloading was 100 kPa and in the other four, it was 200 kPa. After heating, the specimens were reloaded to a pressure above this value, and the pre-consolidation pressure was recalculated. In agreement with previous studies, they found that pre-consolidation pressure reduces with increased temperature. They were able to go further too, and conclude that the change in pre-consolidation pressure due to heating is independent of the stress level. For the 100 kPa case, the pre-consolidation pressure at 90 °C was 24 % lower than at room temperature, compared to a reduction of 22 % for the 200 kPa case. This difference is small, showing that stress level has a negligible effect on the change in pre-consolidation pressure.

The effect of temperature on pre-consolidation pressure was also determined from another series of tests, in which a heating-cooling cycle was carried out on a normally consolidated specimen, which was subsequently loaded further at ambient temperature. This is shown in Figure 2.77 which compares the maximum cyclic temperature (i.e. the maximum temperature reached during the cycle) to the pre-consolidation pressure calculated from the subsequent consolidation response. Nine tests were performed, heating to 50 °C, 70 °C and 90 °C at pressures of 100 kPa, 200 kPa and 300 kPa. They found that the pre-consolidation pressure increases with maximum cyclic temperature value. Note that this does not contradict the result from the previously discussed tests which showed that pre-consolidation pressure reduces with increasing temperature. In this test, all loading was done at ambient temperature. The change in pre-consolidation pressure is higher for higher initial pre-consolidation pressure values (higher stress levels). These data are shown in Figure 2.78, this time in terms of OCR, instead of pre-consolidation pressure. The increase in OCR due to thermal cycling is referred to as “thermally-induced OCR”. From this figure, it can be seen that thermally-induced OCR is independent of stress level.



Figure 2.76: Effect of temperature on pre-consolidation pressure of soft Bangkok clay at different stress levels (Abuel-Naga et al., 2005)



Figure 2.77: Effect of maximum cyclic temperature on pre-consolidation pressure of soft Bangkok clay at different stress levels (Abuel-Naga et al., 2005)



Figure 2.78: Effect of maximum cyclic temperature on thermally-induced OCR of soft Bangkok clay at different stress levels (Abuel-Naga et al., 2005)

François et al. (2007) carried out isothermal loading tests on over-consolidated Sion silt. At ambient temperature, they consolidated the specimens to 100 kPa, before unloading to 10 kPa. Next, they applied the desired temperature and suction conditions. Finally, they reloaded the specimen under constant temperature and suction conditions. Results from this test are shown in Figure 2.79. The axes are normalised by the initial values - pre-consolidation pressure, σ'_c (initial σ'_{c0}), temperature, T (initial T_0). The solid line shows the result for zero suction, and the dashed line shows the result for 300 kPa suction. As in previous research, they found that the pre-consolidation pressure reduces with temperature, although the non-linear shape of the curve is an assumption. The change in pre-consolidation pressure is the same at both suction levels, which suggests that it is independent of suction level.

Favero et al. (2016), testing Opalinus clay, observed a reduction in pre-consolidation pressure with increasing temperature. Figure 2.80 shows the schematic test path and results for test 1. This is a complex testing path, combining isothermal loading and isobaric heating. The reloading path (red line) at 23 °C plots above the expected compression line at 80 °C, which implies an increase in pre-consolidation pressure with reducing temperature. This test is comparable to test 2 of Gray (1936), shown in Figures 2.70 and 2.71.

Figure 2.81 shows the schematic test path and results for test 2. This time, the reloading path at 80 °C plots below the expected compression line at 23 °C, which implies a reduction in pre-consolidation pressure with increasing temperature. This test is comparable to test 1 of Gray (1936), shown in Figures 2.68 and 2.69.

Figure 2.82 shows the schematic test path and results for test 3. As in test 2, the reloading path at 80 °C plots below the expected compression line at 23 °C, confirming the result from test 2, that pre-consolidation pressure reduces with increasing temperature.



Figure 2.79: Effect of temperature on pre-consolidation pressure of Sion silt at different suction levels (François et al., 2007)



(a)



(b)

Figure 2.80: Reloading at 23°C of Opalinus clay - test 1 (a) schematic (b) results (Favero et al., 2016)



(a)



(b)

Figure 2.81: Reloading at 80 °C of Opalinus clay - test 2 (a) schematic (b) results (Favero et al., 2016)



(a)



(b)

Figure 2.82: Reloading at 80 °C of Opalinus clay - test 3 (a) schematic (b) results (Favero et al., 2016)

Pre-consolidation pressure: Summary

There is generally good agreement in the literature on the effect of temperature on the pre-consolidation pressure. If an over-consolidated soil is heated, then reloaded, its pre-consolidation pressure will be lower than at ambient temperature. If instead it is cooled, then reloaded, its pre-consolidation pressure will be higher than at ambient temperature (Gray, 1936; Plum and Esrig, 1969; Eriksson, 1989; Tidfors and Sällfors, 1989; Moritz, 1995; Abuel-Naga et al., 2005; Favero et al., 2016).

The position of the normal consolidation line (NCL) is also discussed in this section, since pre-consolidation pressure is calculated based on the reloading line and the NCL. Some researchers found that the position of the NCL is uniquely determined by the current temperature (Tidfors and Sällfors, 1989). However, others found that its position depends not just on the current temperature, but on the temperature history (Plum and Esrig, 1969).

The change in pre-consolidation pressure due to temperature change is independent of the stress level (Abuel-Naga et al., 2005), and suction level (François et al., 2007), although both aspects have received little attention in the literature.

The key results from TC oedometer schemes, relating to the effect of temperature on pre-consolidation pressure, are summarised in Table 2.7.

Table 2.7: Pre-consolidation pressure: summary of observed results from TC oedometer tests

Tested effect	Observed result	References
Effect of temperature on pre-consolidation pressure, p_c	Pre-consolidation pressure reduces with increasing temperature	Gray (1936), Plum and Esrig (1969), Eriksson (1989), Tidfors and Sällfors (1989), Moritz (1995), Abuel-Naga et al. (2005), François et al. (2007), and Favero et al. (2016)
	Reduction in p_c due to temperature increase is independent of stress level	Abuel-Naga et al. (2005)
	Reduction in p_c due to temperature increase is independent of suction level	François et al. (2007)
Effect of maximum cyclic temperature on pre-consolidation pressure	Pre-consolidation pressure increases with increasing maximum cyclic temperature	Abuel-Naga et al. (2005)
Effect of temperature and temperature history on position of NCL	Position of NCL depends on temperature history	Plum and Esrig (1969)
	Position of NCL is uniquely determined by temperature	Tidfors and Sällfors (1989)


2.4.4 Compression characteristics

In this section results from the literature relating to the effect of temperature on the compression characteristics of soil are discussed. These include compression and swelling indices (C_c and C_s), compressibility indices (λ and κ), coefficient of volume compressibility (m_v) and oedometric modulus (E_{oed}). These parameters are defined in Appendix E. Consolidation characteristics (time-dependent compression characteristics) are discussed in Section 2.4.5.

Compression characteristics - Results

Gray (1936) found that gradient of the normal compression line (NCL) is independent of temperature, for a “fine grained soil”. By performing the two tests described in Section 2.4.3, they found that temperature affects the position of the normal compression line, but not the gradient. This result is shown in Figure 2.69 for a temperature increase, and Figure 2.71 for a temperature decrease. Heating causes the NCL to shift down, and cooling causes the NCL to shift up, resulting in a change in the pre-consolidation pressure, as discussed in Section 2.4.3. However, since the gradient of the NCL does not change, these results suggest that the compression index, C_c , is independent of temperature.

Finn (1952), in agreement with the work of Gray (1936), found that the gradient of the NCL is independent of temperature, for a highly-compressible clay. Nine isothermal loading tests were performed in total. Two each at 4.4°C, 10.0°C and 26.7°C, and three at 21.1°C, as shown schematically in Figure 2.83. The specimens were heated or cooled to the target temperature, then consolidated incrementally, allowing 24 h per increment.



images/litreview/fin52_fig_schematic.pdf

Figure 2.83: Isothermal loading - test paths (Finn, 1952)

The results for these isothermal loading tests on normally-consolidated soil are plotted in Figure 2.84. The normal compression lines at different temperatures between 40 °F (4.4 °C) and 80 °F (26.7 °C) plot parallel to each other, meaning C_c is independent of temperature.



images/litreview/Fin52_fig6.png


Figure 2.84: Effect of temperature on NCL of highly-compressible clay (40 °F = 4.4 °C, 80 °F = 26.7 °C, 1 ton/ft² = 95.8 kPa) (Finn, 1952)

In contrast to previous research, **Plum and Esrig (1969)** found that temperature does affect compressibility. Figure 2.85 shows the results for three consolidation tests on illite. Below 40 psi (275 kPa) the NCL is steeper for the 50 °C test than the two 24 °C tests (although it is worth noting that there is some variation between these tests too). Above 40 psi (275 kPa) the gradient of the NCL is parallel for all three tests.

Eriksson (1989) found no change in the gradient of the NCL with temperature, as shown in Figure 2.73a. A series of isothermal loading tests were performed on sulphide-rich silty clay, at temperatures from 5 °C to 45 °C. The temperature affects the pre-consolidation pressure, as discussed in Section 2.4.3, but the normal consolidation lines are parallel, so C_c is independent of temperature.

Tidfors and Sällfors (1989) found no change in the gradient of the NCL with temperature, as shown in Figure 2.86. They carried out tests in which a normally-consolidated specimen of Bäckebol clay was heated from room temperature to 55 °C incrementally, through 25 °C, 35 °C and 45 °C. This heating was done at stress levels of 40 kPa, 50 kPa, 60 kPa and 80 kPa. After heating, each specimen was loaded to 120 kPa. They found that after reloading all specimens eventually reach the same NCL at 55 °C. The faint dashed lines on the figure link points of the same temperature. These lines are approximately parallel above 60 kPa, from which it is inferred by the authors that C_c is independent of temperature. In fact, between 40 kPa and 60 kPa these lines are not parallel, so this conclusion does not necessarily follow from the data.

Towhata et al. (1993) consolidated a specimen of MC clay to 160 kPa at room temperature, before heating to 90 °C, holding this temperature for 2 months, 2 weeks or 1 day, then continuing consolidation. This is shown in Figure 2.87. Following heating, the soil behaves as though over-consolidated, crossing the room temperature NCL (dashed line). At higher pressure, the



images/litreview/Plu69_fig2.png

Figure 2.85: Effect of temperature on NCL of illite (Plum and Esrig, 1969)

data approaches the room temperature NCL asymptotically, from above. Figure 2.88 shows a similar test, also on MC clay, but this time, following heating to 90 °C, the soil was cooled to room temperature before continuing consolidation. The results are similar to the first test, but this time the data re-join the NCL at lower pressure. The authors suggest that these tests show that the gradient of the NCL is independent of temperature. However, it could also be inferred from these data that the gradient of the NCL increases with increasing temperature.

François et al. (2007) found temperature to have an almost negligible effect on the compressibility indices. They performed isothermal loading tests at 22 °C and 80 °C, to get the results shown in Figure 2.89. Results are given in terms of λ and κ , rather than C_c and C_s . The plastic compressibility λ is independent of temperature. The elastic compressibility κ may increase slightly with temperature, although more data points are required to justify this conclusion.

Ye et al. (2012), testing GMZ01 bentonite clay, suggested that the compressibility parameter λ , which is linked to the compressibility index, decreases with increasing temperature. They performed consolidation tests at constant temperature and suction. This result, shown in Figure 2.90, contrasts with François et al. (2007) who observed no change in λ with temperature. However, based on the figure, this conclusion is not clearly supported by the limited data. They found that the compressibility parameter κ to be independent of temperature.

Mon et al. (2013), testing kaolin clay, suggested that the coefficient of volume compressibility, m_v reduces with increasing temperature for over-consolidated soil, but is independent of temperature for normally-consolidated soil. This is shown in Figure 2.91, with results plotted against mean pressure \bar{p} . Although a plot of m_v vs OCR is not given in the paper, it can be seen that for OC soil, below the pre-consolidation pressure of 150 kPa, m_v reduces with increasing temperature. Above this value, for NC soil, m_v is independent of temperature.



Figure 2.86: Comparison of compression behaviour of Bäckebol clay, heated at different stress levels (Tidfors and Sällfors, 1989)



Figure 2.87: Effect of heating on NCL of MC clay (Towhata et al., 1993)



Figure 2.88: Effect of a thermal cycle on NCL of MC clay (Towhata et al., 1993)



Figure 2.89: Effect of temperature on compressibility indices λ and κ of Sion silt (François et al., 2007)



Figure 2.90: Effect of temperature on compressibility indices λ and κ of GMZ01 bentonite (Ye et al., 2012)

Uniquely, in this paper, Mon et al. also measured the shear wave velocity of the soil, v_s , using bender elements. Shear wave velocity can be used to calculate the small-strain shear modulus, G . They measured the shear wave velocity during a consolidation test at 5 °C and 40 °C, and found higher shear wave velocity at higher temperature, corresponding to higher stiffness, as shown in Figure 2.92.



Figure 2.91: Effect of temperature on coefficient of volume compressibility m_v of kaolin clay (Mon et al., 2013)



Figure 2.92: Effect of temperature on shear wave velocity v_s of kaolin clay (Mon et al., 2013)

Di Donna and Laloui (2015), testing Geneva silty clay, found the oedometric modulus E_{oed} to be independent of temperature, as shown in Figure 2.93. Results are given for isothermal loading at temperatures of 20 °C, 40 °C and 60 °C, showing no effect of temperature on the oedometric modulus. The specimens tested were from undisturbed, natural samples, with an in-situ stress of ≈ 150 kPa, and the final stress reached in the test was 1000 kPa.



Figure 2.93: Effect of temperature on oedometric modulus of Geneva clay (Di Donna and Laloui, 2015)

Favero et al. (2016), testing Opalinus clay, found that the oedometric modulus reduces with increasing temperature, as shown in Figure 2.94, for temperatures of 23 °C and 80 °C. However, the effect becomes less significant at higher stress levels.



Figure 2.94: Effect of temperature on oedometric modulus of Opalinus clay (Favero et al., 2016)

Compression characteristics: Summary

The general consensus seems to be that temperature has a negligible effect on compressibility. Most researchers concluded that C_c is independent of temperature (Gray, 1936; Finn, 1952; Eriksson, 1989; Tidfors and Sällfors, 1989; Towhata et al., 1993). Some observed a small effect. Plum and Esrig (1969) found that C_c increases with temperature. François et al. (2007) found that λ increases with temperature, whereas Ye et al. (2012) on the other hand, found that it decreases. In all three cases, the effect is based on limited data, and should be treated with a degree of suspicion. Both François et al. (2007) and Ye et al. (2012) found that κ is independent of temperature.

The effect of temperature on m_v and its inverse E_{oed} has been considered in the literature. The terminology used appears to have changed over time, and is not clear in some cases. Results from Moritz (1995) have been excluded because the terms compressibility modulus, oedometer modulus and compression modulus are used, but never clearly defined. Mon et al. (2013) found that m_v reduces with increasing temperature, but only for over-consolidated soil. For normally consolidated soil, there is no measurable effect. Di Donna and Laloui (2015) found no effect on E_{oed} , for either OC or NC soil. Favero et al. (2016) found that E_{oed} reduces with increasing temperature, which contradicts the result of Mon et al. (2013) (since E_{oed} is the inverse of m_v). However, Mon et al. (2013) tested kaolin up to a pressure of 1250 kPa while Favero et al. (2016) tested Opalinus clay at a much higher range of pressures, between 1 MPa and 100 MPa. With two quite different materials, tested at different pressures, it is unsurprising to see a discrepancy in the results. Mon et al. (2013) also measured small-strain stiffness using bender elements, and found that the shear stiffness G is larger at higher temperatures.

The key results relating to compression characteristics observed in TC oedometer schemes are summarised in Table 2.8.

Table 2.8: Compression characteristics: summary of observed results from TC oedometer tests

Tested effect	Observed result	References
Effect of temperature on coefficient of consolidation C_c (gradient of NCL), and λ (gradient of isotropic NCL)	C_c independent of temperature	Gray (1936), Finn (1952), Eriksson (1989), Tidfors and Sällfors (1989), and Towhata et al. (1993)
	C_c increases with temperature	Plum and Esrig (1969)
	λ independent of temperature	François et al. (2007)
	λ reduces with temperature	Ye et al. (2012)
Effect of temperature on coefficient of volume compressibility m_v	m_v independent of temperature	Di Donna and Laloui (2015)
	m_v increases with temperature	Favero et al. (2016)
	m_v reduces with temperature (OC soil), independent of temperature (NC soil)	Mon et al. (2013)

2.4.5 Consolidation characteristics

In this section, the effect of temperature on time related consolidation parameters is discussed. For the primary phase of consolidation, the relevant parameter is the coefficient of consolidation, c_v . For the secondary phase, it is the coefficient of secondary consolidation, C_a . Secondary consolidation, either rate or amount, is sometimes referred to as *creep*. Coefficient of consolidation c_v is a function of the coefficient of permeability, k , the coefficient of volume compressibility, m_v and the bulk unit weight of water, γ_w :

$$c_v = \frac{k}{m_v \gamma_w} \quad (2.15)$$

Since c_v and m_v can be calculated from oedometer data, and γ_w is well known, this equation is commonly re-arranged and used to calculate the coefficient of permeability, k . Note that the density of water, ρ_w , from which γ_w is derived, changes with temperature. The coefficient of permeability is dependent on the fluid (in this case water) dynamic viscosity μ_w , which also changes with temperature. For more details, see Section 2.4.6. Clearly these parameters are not independent of each other, but for clarity, the effect of temperature on each is discussed separately, and this section focuses on c_v only (and C_a for secondary consolidation).

The coefficient of secondary consolidation is the change in volumetric strain per \log_{10} cycle of time following completion of primary consolidation. This is shown schematically in Figure 2.95. It can be defined in terms of change in void ratio Δe (denoted C_a), or change in volumetric strain $\Delta \epsilon$ (denoted $C_{a\epsilon}$). These are compared in Figure 2.96.

$$C_a = \frac{\Delta e}{\Delta \log_{10} t} \quad (2.16)$$

$$C_{a\epsilon} = \frac{\Delta e}{1 + e_0} \cdot \frac{1}{\Delta \log_{10} t} \quad (2.17)$$

where:

$$\frac{\Delta e}{1 + e_0} = \Delta \epsilon \quad (2.18)$$

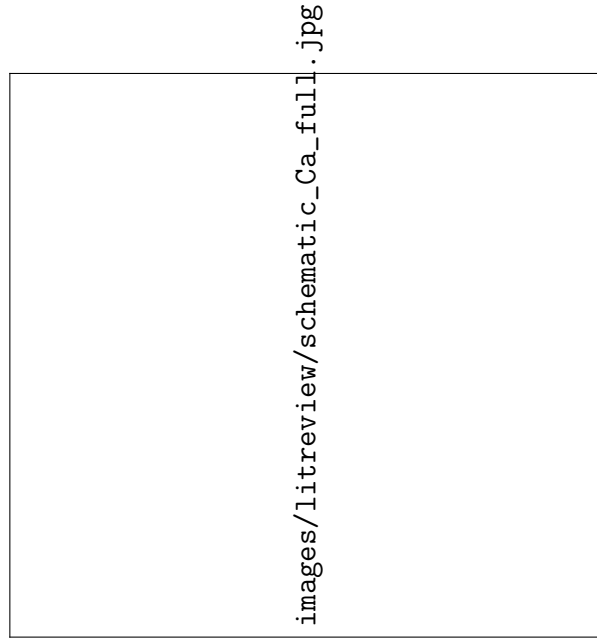
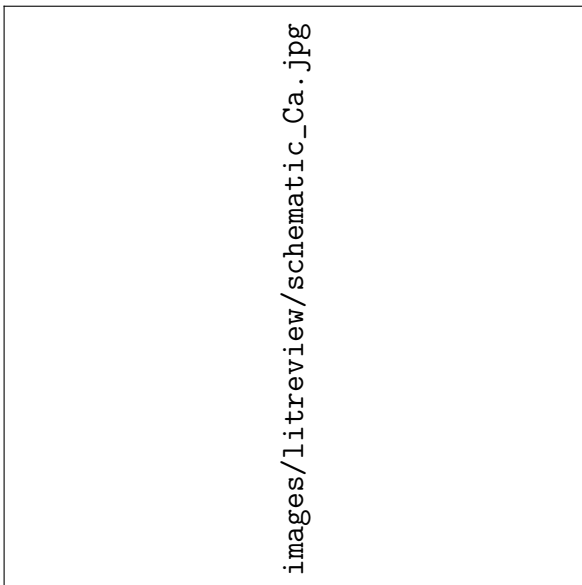
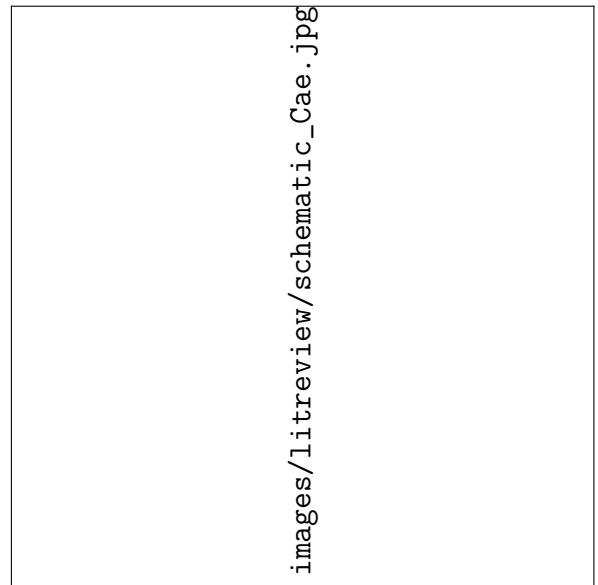


Figure 2.95: Schematic - coefficient of secondary consolidation, C_a



(a)



(b)

Figure 2.96: Schematic - coefficient of secondary consolidation (a) in terms of void ratio, C_a
(b) in terms of strain, C_{ae}

Primary consolidation: results

Finn (1952) performed nine isothermal consolidation tests on highly-compressible clay, at temperatures between 40 °F (4.4 °C) and 80 °F (26.7 °C). These tests are shown schematically in Figure 2.83, and the results are given in Figure 2.97. The coefficient of consolidation, c_v was calculated using the log-time method. For temperatures between 40 °F (4.4 °C) and 70 °F (21.1 °C), c_v varies considerably, increasing with increasing temperature. However, for temperatures between 70 °F (21.1 °C) and 80 °F (26.7 °C), c_v does not vary.

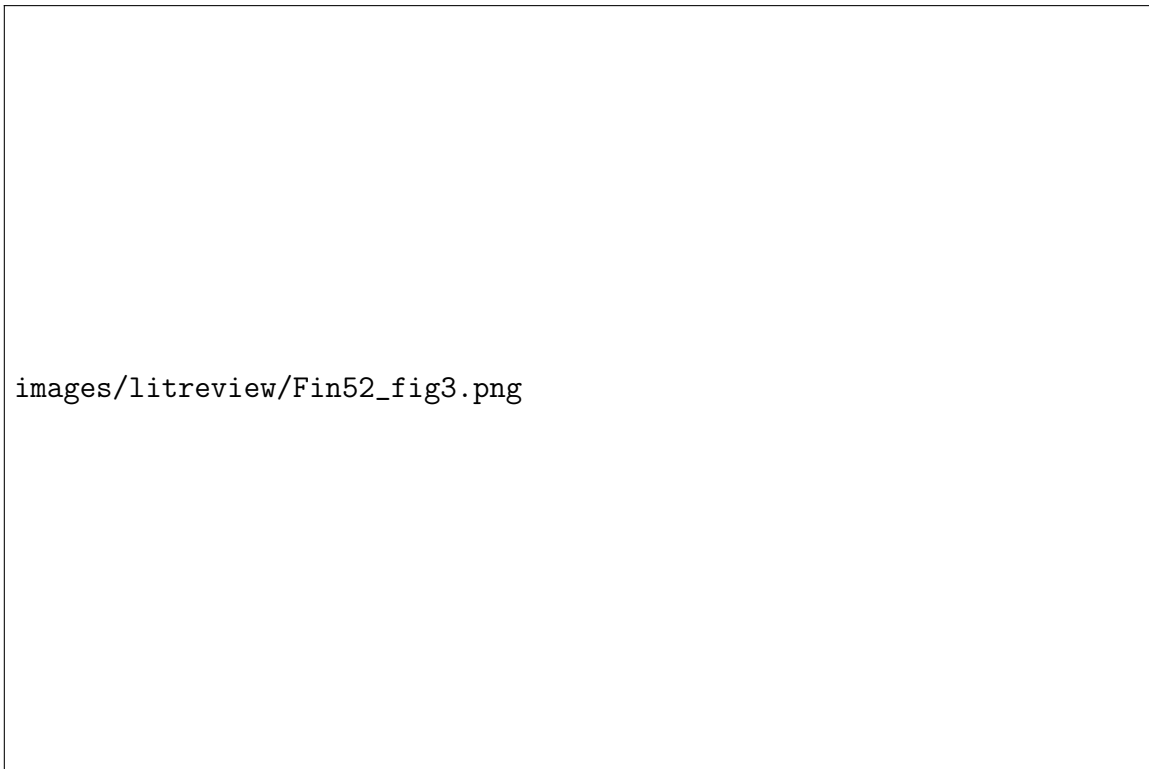



Figure 2.97: Effect of temperature on coefficient of consolidation of highly-compressible clay (Finn, 1952)

McGinley (1983) found that for the two soils tested, Georgia kaolin, and smectite, c_v increases with temperature, in the temperature range 26.7 °C to 85 °C. These results are not plotted, but described as reported in El Tawati (2010).


Towhata et al. (1993) observed that primary consolidation develops more rapidly when the temperature is higher. Figure 2.98 shows void ratio against time for a single stress increment, from 380 kPa to 500 kPa, using bentonite clay. The response at 90 °C plots below the one for 20 °C. That means, at any time, the void ratio has reduced more when consolidating at high temperature, compared to low temperature. After enough time though, both specimens reach the same void ratio. This suggests that temperature affects *rate* of consolidation, but not total *amount*. Similar behaviour was observed for MC clay.

Abuel-Naga et al. (2005) repeated the results of Towhata et al. (1993), using soft Bangkok clay. Figure 2.99 shows results for an increment of consolidation, from 160 kPa to 320 kPa at three temperatures, 25 °C, 70 °C and 90 °C. At higher temperature, the consolidation rate increases, but the total consolidation is the same at the end of the increment.



images/litreview/Tow93_fig21.png

Figure 2.98: Effect of temperature on rate of consolidation of bentonite (Towhata et al., 1993)



images/litreview/Abu05_fig16.png

Figure 2.99: Effect of temperature on rate of consolidation of soft Bangkok clay (Abuel-Naga et al., 2005)

Mon et al. (2013) also found that c_v increases with increasing temperature, for kaolin. This effect is most noticeable at higher OCR values although there is wide scatter in the results given in Figure 2.100. The pre-consolidation pressure for the over-consolidated specimens was 150 kPa.



Figure 2.100: Effect of temperature on coefficient of consolidation c_v of kaolin clay (Mon et al., 2013)

Di Donna and Laloui (2015) isothermally consolidated Geneva clay specimens at temperatures of 20 °C, 40 °C and 60 °C. The results are given in Figure 2.101. They found that c_v increases with temperature.

Favero et al. (2016) isothermally consolidated Opalinus clay specimens at two temperatures, 23 °C and 80 °C. The results are given in Figure 2.102. In agreement with previous studies, they found that c_v was higher at elevated temperature.



Figure 2.101: Effect of temperature on coefficient of consolidation c_v of Geneva clay (Di Donna and Laloui, 2015)

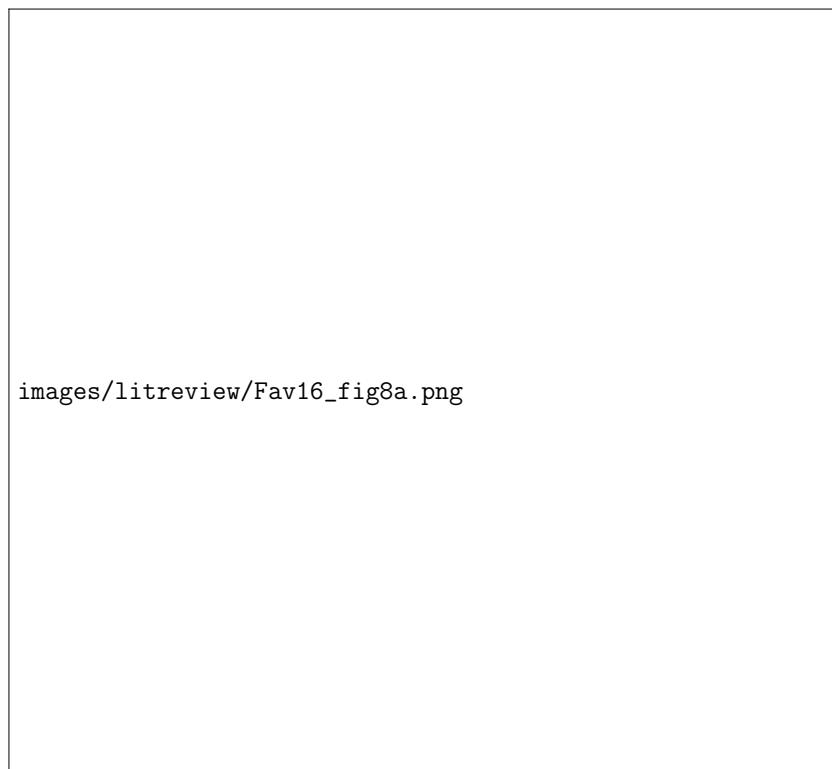


Figure 2.102: Effect of temperature on coefficient of consolidation of Opalinus clay (Favero et al., 2016)

Secondary consolidation: results

The effect of temperature on rate, and amount of secondary consolidation is less well understood. This could be due to the difficulty of separating the effects of temperature change and secondary consolidation, an issue discussed by Plum and Esrig (1969). The long testing duration required to observe temperature effects on secondary consolidation, especially in clays, may also explain the scarcity of studies investigating this behaviour.

Plum and Esrig (1969) investigated the effect of temperature on secondary consolidation of illite. A loading increment, from 180 psi to 209 psi (1241 kPa to 1441 kPa) was held for long enough to determine the secondary consolidation coefficient, C_{ae} at 24 °C. The specimen was then heated to 50 °C, and allowed to change in volume, until C_{ae} could be determined again. The results are shown in Figure 2.103. They found that C_{ae} increases only slightly with increasing temperature, from 0.0048 at 24 °C to 0.0053 at 50 °C. The authors make a good point that it is easy to misinterpret volumetric strains associated with heating as increases in the coefficient of secondary consolidation. A relatively long time is required to separate these two effects (note how the results are plotted on a logarithmic time scale).



Figure 2.103: Effect of heating on secondary consolidation of illite (Plum and Esrig, 1969)

Towhata et al. (1993) observed a similar response for MC clay, shown in Figure 2.104. The specimen was heated during the secondary consolidation phase, following primary consolidation at 160 kPa, from room temperature (open markers) to 90 °C (filled markers). Heating results in a substantial initial contraction, followed by further contraction at a much slower rate. As noted by Plum and Esrig (1969), it is important to allow enough time to separate the two effects - the initial thermally induced contraction, and the subsequent secondary consolidation. They suggest that this volume change would have occurred anyway, but heating re-activates the primary type of consolidation. This is not entirely supported by the data. Although the data for the specimen heated after approximately 20 minutes seems to approach the data for the

room temperature specimen, after ≈ 5000 minutes, the lines are parallel, no longer converging. This suggests that (i) heating induces further volume change than would have occurred anyway, at ambient temperature, (ii) secondary consolidation is accelerated by heating and (iii) the coefficient of secondary consolidation is independent of temperature.



Figure 2.104: Effect of heating on secondary consolidation of MC clay (Towhata et al., 1993)

Favero et al. (2016) observed a slight increase in the coefficient of secondary consolidation of Opalinus clay with temperature, as shown in Figure 2.105. They consolidated specimens at 23 °C and 80 °C at vertical stress levels up to 100 MPa. Although there is some evidence to suggest that the coefficient of secondary consolidation (here “compression”) increases with temperature, they concluded that the effect of temperature on C_a is not significant, particularly at higher stress levels.



Figure 2.105: Effect of temperature on secondary consolidation of Opalinus clay (Favero et al., 2016)

Consolidation characteristics: summary

Temperature has a clear and measurable effect on the *rate* of primary consolidation. c_v increases with increasing temperature (Finn, 1952; McGinley, 1983; Towhata et al., 1993; Abuel-Naga et al., 2005; Mon et al., 2013; Di Donna and Laloui, 2015; Favero et al., 2016). This is in contrast to the *amount* of primary consolidation, which is independent of temperature (Towhata et al., 1993; Abuel-Naga et al., 2006).

Heating a soil during the secondary phase of consolidation results in an initial increase in the rate of consolidation (Plum and Esrig, 1969; Towhata et al., 1993). This is not an increase in the coefficient of secondary consolidation, but rather a reactivating of the primary phase of consolidation. Towhata et al. (1993) suggests that this consolidation would have occurred anyway, given enough time, and that heating just speeds the process up. Once this initial thermally-induced volume change has stabilised, as can be seen by the data (void ratio or strain) forming a straight line against logarithmic time, the new coefficient of secondary consolidation can be determined.

Temperature has been found to have an insignificant effect on the rate of secondary consolidation, C_a or $C_{a\epsilon}$. Some studies observed a slight increase in C_a or $C_{a\epsilon}$ with temperature (Plum and Esrig, 1969; Favero et al., 2016). Others found no clear relationship between rate of secondary consolidation and temperature (Towhata et al., 1993).

The key results from TC oedometer schemes, relating the effect of temperature on consolidation characteristics, are summarised in Table 2.9.

Table 2.9: Consolidation characteristics: summary of observed results from TC oedometer tests

Tested effect	Observed result	References
Effect of temperature on coefficient of primary consolidation, c_v	c_v increases with temperature	Finn (1952), McGinley (1983), Towhata et al. (1993), Abuel-Naga et al. (2005), Mon et al. (2013), Di Donna and Laloui (2015), and Favero et al. (2016)
Effect of temperature on coefficient of secondary consolidation, C_a	C_a independent of temperature	Plum and Esrig (1969) and Towhata et al. (1993)
	C_a increases with temperature	Favero et al. (2016)

2.4.6 Permeability

The coefficient of permeability, also known as hydraulic conductivity, k , can be measured directly in the laboratory using constant- or falling-head permeameter tests, or indirectly, from oedometer tests. Since k is a property of the soil and the fluid, the effect of temperature can be complex. It affects the solid phase of the soil, changing its fabric and structure, as well as the fluid, changing its dynamic viscosity and density. The coefficient of permeability is commonly referred to as “permeability” in the literature. However, this term is potentially ambiguous, so in this thesis, the terms coefficient of permeability and intrinsic permeability are used instead.

Coefficient of permeability k is also known as hydraulic conductivity. It quantifies how easily a given fluid can move through a soil, and is a property of the soil *and* the fluid. It can be calculated from the following equation:

$$k = m_v c_v \gamma_w \quad (2.19)$$

where:

- k = coefficient of permeability
- m_v = coefficient of volume compressibility
- c_v = coefficient of consolidation
- γ_w = bulk unit weight of fluid (water)

The coefficient of volume compressibility m_v , and the coefficient of consolidation c_v , can both be obtained from oedometer consolidation tests. The bulk unit weight of water γ_w depends on the density of water ρ_w , which changes with temperature. The coefficient of permeability k depends on the dynamic viscosity of the water μ_w , which also changes with temperature.

Intrinsic permeability K_{int} is a property of the soil only, not the fluid, and can be calculated from this equation:

$$K_{int} = k \cdot \frac{\mu_w}{\gamma_w} \quad (2.20)$$

where:

- K_{int} = intrinsic permeability
- k = coefficient of permeability
- c_v = coefficient of consolidation
- μ_w = dynamic viscosity of water
- γ_w = bulk unit weight of water

For water at 20 °C, $\mu_w \approx 1 \times 10^{-6}$ kPa s, and $\gamma_w \approx 10$ kN m⁻³, which gives the following (rough) estimate of K_{int} in m², for a value of k in m s⁻¹:

$$K_{int} \approx k \times 10^{-7} \quad (2.21)$$

Permeability: results

Towhata et al. (1993) found that the coefficient of permeability increases with increasing temperature. Figure 2.106 compares the permeability calculated from the parameters m_v and c_v at two temperatures, 20 °C and 90 °C, for normally-consolidated bentonite clay. Similar behaviour was observed for MC clay.




Figure 2.106: Effect of temperature on coefficient of permeability of NC bentonite (Towhata et al., 1993)

On the other hand, **Moritz (1995)** observed a reduction in the coefficient of permeability with increasing temperature, for Linköping clay, as shown in Figure 2.107. However, they attributed this observation to microscopic bubbles, which at room temperature are dissolved in the pore water, being released and filling out individual larger pores at elevated temperatures. Note that the thermal expansion coefficient of air is much greater than water. They suggested that applying back pressure to ensure full water saturation of the specimen could eliminate this effect.

Romero et al. (2001) found that the effect of temperature on the coefficient of permeability of Boom clay is not significant. They used direct measurement, by applying a suction and measuring the flow of water out of the specimen, rather than indirect calculation based on m_v and c_v . At low suction values (high degree of saturation), k increases with increasing temperature, but at high suction values (low degree of saturation), there is no measurable effect. This result is shown in Figure 2.108, in which k is shown for temperatures of 22 °C and 80 °C. Two fitted curves are shown, for void ratios of 0.93 and 0.60.

Villar and Lloret (2004) found that the coefficient of permeability of bentonite clay increases with increasing temperature. In Figure 2.109, the experimental values (calculated from consolidation tests) are compared with the theoretical values. This theoretical increase is based on the reduction of dynamic viscosity of the pore water with increasing temperature. They found that the increase in coefficient of permeability is lower than predicted based on this parameter only.



images/litreview/Mor95_fig75.png

Figure 2.107: Effect of temperature on coefficient of permeability of Linköping clay (Moritz, 1995)

Abuel-Naga et al. (2005) also observed an increase in the coefficient of permeability with temperature, testing soft Bangkok clay. This result is shown in Figure 2.110, where the “measured” value (actually calculated from oedometer data) is compared with the “calculated” value, which is an estimate based on the known thermal variation of pore water viscosity. Note that the coefficient of permeability has been normalised by the value at 25 °C. Compared to Villar and Lloret (2004), they found a better agreement between the measured and theoretical coefficient of permeability.

Di Donna and Laloui (2015) observed an increase in the coefficient of permeability of Geneva clay with increasing temperature, as shown in Figure 2.111. Hydraulic conductivity (coefficient of permeability) is plotted against stress for three temperatures, 20 °C, 40 °C and 60 °C. The effect of temperature is found to be significant.



Figure 2.108: Effect of temperature on coefficient of permeability of Boom clay (Romero et al., 2001)



Figure 2.109: Effect of temperature on hydraulic conductivity of FEBEX bentonite (Villar and Lloret, 2004)

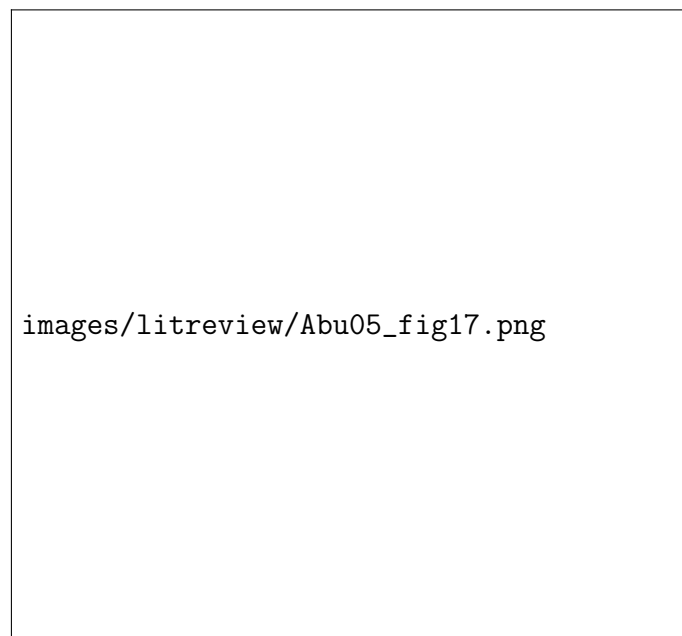


Figure 2.110: Effect of temperature on coefficient of permeability of soft Bangkok clay (normalised by value at 25 °C) (Abuel-Naga et al., 2005)



Figure 2.111: Effect of temperature on hydraulic conductivity of NC Geneva clay (Di Donna and Laloui, 2015)

Permeability: summary

The coefficient of permeability increases with increasing temperature (Towhata et al., 1993; Romero et al., 2001; Villar and Lloret, 2004; Abuel-Naga et al., 2005; Di Donna and Laloui, 2015). One scheme did observe the opposite effect, but attributed this to limitations in the testing method (Moritz, 1995). Most schemes used results from consolidation tests (c_v and m_v) to indirectly calculate k (Towhata et al., 1993; Villar and Lloret, 2004; Abuel-Naga et al., 2005; Di Donna and Laloui, 2015). However, Romero et al. (2001) directly measured k and found that at high suction values, k is independent of temperature.

The key results from TC oedometer schemes investigating the effect of temperature on permeability are given in Table 2.10.

Table 2.10: Permeability: summary of observed results from TC oedometer tests

Tested effect	Observed result	References
Effect of temperature on coefficient of permeability, k	k increases with temperature	Towhata et al. (1993), Romero et al. (2001), Villar and Lloret (2004), Abuel-Naga et al. (2005), and Di Donna and Laloui (2015)
	k reduces with temperature	Moritz (1995)

2.4.7 Water retention and swelling capacity

Swelling capacity is a measure of the swelling response of soil upon wetting. For constant-volume swelling tests, it is the pressure required to prevent volume change of a soil upon wetting, and is measured in units of pressure. For constant-pressure swelling tests, it is the volume change under constant pressure of a soil upon wetting, and is measured in units of strain.

Water retention capacity is a measure of the ability of a soil to retain water at a given suction. The water retention curve (or soil water characteristic curve) gives the relationship between water content w and total suction ψ for a soil.

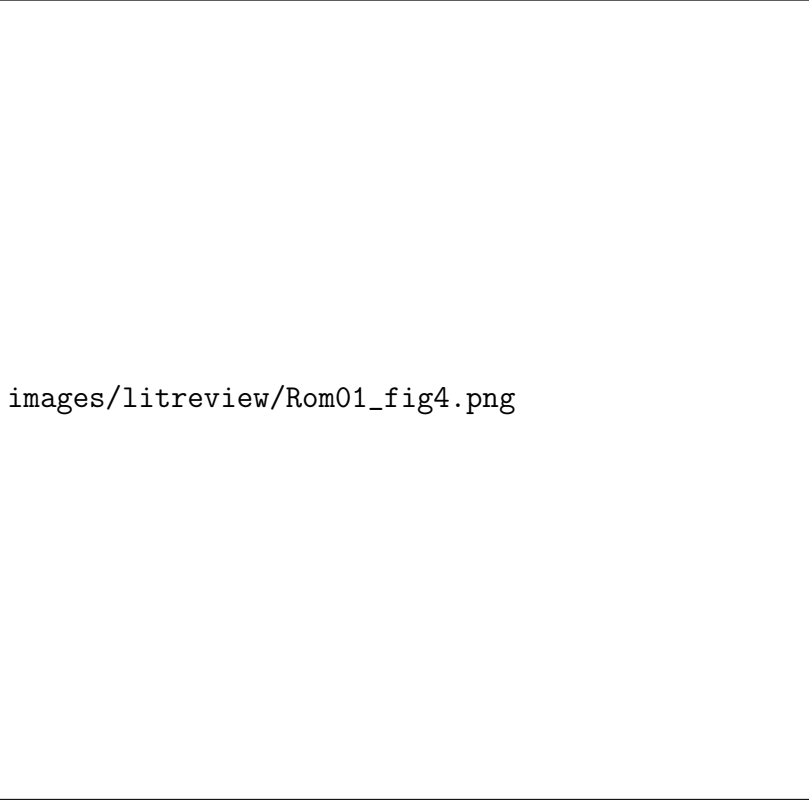
Water retention and swelling capacity - Results

Romero et al. (2001) tested a moderately-swelling soil, Boom clay, using the vapour-equilibrium method, which enables control of total suction. Note that these tests were separate from the tests performed using the combined suction- and temperature-controlled oedometer, discussed in Section 2.2.10. At fixed suction values of 6 MPa, 8 MPa, 10 MPa and 32 MPa, temperature was increased from ambient to 80 °C, and the water content of the soil was measured every 20 °C. In Figure 2.112, it is seen that at constant suction, ψ , water content decreases with increasing temperature. On a soil water retention curve (SWRC), with axes of suction against water content, this corresponds to a shift to the left. Figure 2.113 confirms this behaviour. At constant water content from 6 % to 11 %, suction decreases with increasing temperature. On an SWRC with axes of suction against water content, this corresponds to a shift down. In both cases, increasing temperature leads to a reduction in the water retention capacity. The decrease in suction with temperature is larger for higher initial suction values (lower water contents) than for lower initial suction values.

Villar and Lloret (2004) confirmed the result of Romero et al. (2001), this time using a highly-swelling soil, FEBEX bentonite clay. Water retention curves were obtained at 20 °C, 40 °C and 60 °C, shown in Figure 2.114. At higher temperature, the curves shift to the left (or down), which implies a reduction in water retention capacity.


Additionally, Villar and Lloret tested the effect of temperature on the swelling capacity, both in terms of swelling pressure and swelling strain. They measured the swelling pressure resulting from wetting the soil at constant volume, at a range of temperatures. This is shown in Figure 2.115. They found that swelling pressure reduces with increasing temperature. They also measured the swelling strain resulting from wetting the soil under constant pressure, at a range of temperatures. This is shown in Figure 2.116 for pressure values of 0.5 MPa, 1.5 MPa and 3 MPa. They found that the swelling strain reduces with increasing temperature.

Finally, **Shariatmadari and Saeidijam (2011)** performed a similar test on a sand-bentonite mix. In this case, they measured the swelling strain generated by wetting the soil under constant pressure. They found that the swelling strain reduces with increasing temperature, as shown in Figure 2.117, confirming the result from Villar and Lloret (2004).



images/litreview/Rom01_fig4.png

Figure 2.112: Effect of temperature on water content of Boom clay at constant suction (ψ) (Romero et al., 2001)



images/litreview/Rom01_fig5.png

Figure 2.113: Effect of temperature on suction (ψ) of Boom clay at constant water content (Romero et al., 2001)



Figure 2.114: Effect of temperature on water retention capacity of FEBEX bentonite (Villar and Lloret, 2004)



Figure 2.115: Effect of temperature on swelling pressure of FEBEX bentonite (Villar and Lloret, 2004)



Figure 2.116: Effect of temperature on swelling strain of FEBEX bentonite (Villar and Lloret, 2004)



Figure 2.117: Effect of temperature on swelling strain of a sand-bentonite mix (Shariatmadari and Saeidijam, 2011)

Water retention and swelling capacity: summary

The effect of temperature on water retention and swelling capacity has not been extensively studied using oedometers. However, the few available sources are in agreement on the effect. Water retention capacity reduces with increasing temperature (Romero et al., 2001; Villar and Lloret, 2004). That is, at higher temperature, for a given suction, the water content will be lower. Swelling capacity also reduces with increasing temperature, either when measured in terms of swelling pressure at constant volume (Villar and Lloret, 2004), or swelling strain at constant pressure (Villar and Lloret, 2004; Shariatmadari and Saeidijam, 2011).

The key results from TC oedometer schemes, for the effect of temperature on water retention capacity or swelling capacity, are summarised in Table 2.11.

Table 2.11: Water retention capacity and swelling capacity: summary of observed results from TC oedometer tests

Tested effect	Observed result	References
Effect of temperature on water retention capacity	Water retention capacity reduces with temperature	Romero et al. (2001) and Villar and Lloret (2004)
Effect of temperature on swelling capacity	Swelling pressure reduces with temperature	Villar and Lloret (2004)
	Swelling strain reduces with temperature	Villar and Lloret (2004) and Shariatmadari and Saeidijam (2011)

2.4.8 Pore water pressure

Undrained heating of a soil causes an increase in pore water pressure, due to the higher thermal expansion coefficient of the pore water relative to the solid mineral phase. Excess pore water pressures will develop even when the test is “drained” if the permeability of the soil is low, but this pore water pressure dissipates over time. Examples from the literature of oedometer schemes in which pore water pressure is measured are scarce, probably because the drainage conditions required for consolidation tests make measurement of pore water pressure difficult. Some studies have used isotropic or triaxial cells to measure thermally induced pore water pressure changes, such as Plum and Esrig (1969) (triaxial) and Abuel-Naga et al. (2007) (isotropic). These are discussed in detail in Gawecka (2017), so only the key results are included here.

Pore water pressure: results

Moritz (1995) measured pore water pressure during the heating phase of their tests on Linköping clay. Pore pressure was measured at 20 minute intervals, and a maximum value of 1.1 kPa was measured at 70 °C, although this result was not plotted. The excess pore water pressure generated during heating was allowed to dissipate before starting the subsequent consolidation stage, which meant that a certain amount of consolidation had already taken place by the start of the elevated-temperature consolidation stage. They concluded that the heating rate should be slow to keep excess pore water pressure low.

Vega and McCartney (2015) measured pore water pressures during consolidation tests on Bonny silt by imposing one-way drainage conditions. Drainage was through the top of the specimen, allowing pore water pressures to be measured at the base. Figure 2.118 shows the pore water pressure that develops during a single heating-cooling cycle, with a total change in temperature of 75 °C. Figure 2.118a shows change in temperature and axial stress over time, while Figure 2.118b shows change in height and pore water pressure over time. Excess pore water pressure is generated while the temperature is increasing at the maximum rate ($\approx 1.5\text{ }^{\circ}\text{C h}^{-1}$), reaching a maximum value of $\approx 9.5\text{ kPa}$. It begins to reduce even while heating continues at a slower rate, and reduces to $\approx 3\text{ kPa}$ by the time the maximum temperature is reached.



(a)



(b)

Figure 2.118: Effect of temperature on pore water pressure, for first heating-cooling cycle on Bonny silt (a) temperature and axial stress (b) change in height ΔH and pore water pressure, over time (Vega and McCartney, 2015)

Figure 2.119 shows the same results but for four temperature cycles. Figure 2.119a shows change in temperature and axial stress over time, while Figure 2.119b shows change in height and pore water pressure over time. The pore water pressure peaks during heating and then quickly dissipates. The maximum pore water pressure decreases slightly with each cycle.



Figure 2.119: Effect of temperature on pore water pressure, for all heating-cooling cycles on Bonny silt (a) temperature and axial stress (b) change in height ΔH and pore water pressure, over time (Vega and McCartney, 2015)

Pore water pressure: summary

As discussed above, the drainage conditions required for consolidation tests make measurement of pore water pressure difficult, and as a result, not many schemes have investigated the effect of temperature on pore water pressure. Moritz (1995) and Vega and McCartney (2015) both observed excess pore water pressure generation during heating. Using a triaxial cell, Plum and Esrig (1969) found that repeated temperature cycling of Newfield clay causes a reduction in residual pore water pressure with each cycle. With an isotropic cell Abuel-Naga et al. (2007) observed that the amount of thermally-induced excess pore water pressure of soft Bangkok clay decreases with increasing OCR (for the same pressure level), and increases with pressure level (for normally-consolidated soil).

2.4.9 Summary of soil behaviour

In this section, results from temperature-controlled oedometer schemes in the literature have been presented. Key aspects of soil behaviour were considered: volume change, pre-consolidation pressure, compression and consolidation behaviour, permeability, water retention and swelling capacity, and pore water pressure. Some of these aspects have been studied extensively while others have received little attention so far. This discrepancy can in some cases be attributed to the intended application of the research. For example, earlier schemes, considering the issue of the difference in temperature between in-situ conditions and laboratory test conditions, focused on the effect of temperature on the one-dimensional consolidation characteristics of soil. In some cases, this is due to the relative advantages and limitations of the oedometer compared to other available laboratory equipment, such as isotropic or triaxial cells. As discussed in the chapter overview, Gawecka (2017) gives a full review of thermo-hydro-mechanical behaviour of soils,

which is why in this section results have been presented from temperature-controlled oedometer schemes only.

A summary of the relevant papers for each aspect of soil behaviour is given in Table 2.5. At the end of each sub-section, following the discussion of results, a short written summary is given, together with a summary table. The relevant sections and summary tables are as follows:

- Volume change (Section 2.4.2, Table 2.6),
- Pre-consolidation pressure (Section 2.4.3, Table 2.7)
- Compression behaviour (Section 2.4.4, Table 2.8)
- Consolidation behaviour (Section 2.4.5, Table 2.9)
- Permeability (Section 2.4.6, Table 2.10)
- Water retention and swelling capacity (Section 2.4.7, Table 2.11)
- Pore water pressure (Section 2.4.8)

Chapter 3

Development of a new temperature-controlled oedometer

3.1 Introduction

In this chapter, the design and development of the temperature-controlled oedometer is covered. An overview of the final design is given in Section 3.2. The design evolution in Section 3.3 covers how, and why, the design has changed over the course of this research project. A full description of the oedometer in its current form is given in Section 3.4. Where appropriate, details of the equipment specification are given in Section 3.5. The ambient temperature oedometer, which was used for some comparative tests, is briefly described in Section 3.6. In Section 3.7, the advantages and limitations of the design are summarised.

3.2 Design overview

Certain capabilities are fundamental to all oedometers: the ability to apply a controlled vertical load, the ability to restrict displacement of the specimen to the vertical direction only, and the ability to measure this vertical displacement. In addition to these basic requirements, the TC oedometer must be able to maintain a controlled temperature. Therefore, it should not be surprising that many of the components of the TC oedometer are familiar, even if the full assembly looks quite different to the conventional oedometer.

A schematic of the temperature-controlled oedometer cell is shown in Figure 3.1, and a photograph is shown in Figure 3.2. The numbered labels in Figure 3.1 are as follows:

- (1) Loading ram (upper section)
- (2) Load cell
- (3) Loading ram (lower section)
- (4) Top-cap
- (5) Soil specimen, between porous stones
- (6) Confining ring (including collar and holding-down bolts)
- (7) Instrumentation plate (including LVDTs)
- (8) LVDT assembly (core, connection piece, heat dissipator, extension piece)
- (9) PVC lid

- (10) PVC water bath
- (11) Upper steel plate
- (12) Lower (hollow) steel plate
- (13) PVC base
- (14) Heater (in brass housing)
- (15) Temperature sensors in upper plate
- (16) Temperature sensor in water bath (in brass housing)
- (17) Specimen base drainage
- (18) Water circulation system (including pump and chiller)

With reference to Figure 3.1, components (1) to (4) can be found in any modern electronic oedometer. Load is applied using a computer-controlled stepper-motor within the load frame, via the loading ram. The loading ram is divided into an upper (1) and lower (3) section. Between these is the load cell (2) which is used to measure the current load. This value is fed back to the computer. The computer then determines whether any change is required, based on the current and target load. The lower section of the loading ram is much longer than the upper section. This is to allow space for the instrumentation plate (7) above the water-bath lid (9), but below the load cell. The upper section of the loading ram is as short as possible, to minimise the total length of the loading ram. The top-cap (4) is screwed into the lower section of the loading ram.

The tested specimen (5) sits between two porous stones, allowing two-way drainage. There are drainage paths through the top-cap (4) and the upper steel plate (11) for the same purpose. The base drainage (17) is connected to a water reservoir at hydrostatic pressure. The confining ring (6) prevents lateral displacement of the specimen. It comprises a ring, a collar, and six holding-down bolts.

Displacement is measured with three linear variable displacement transducers (LVDTs) mounted on the instrumentation plate (7). The LVDT core connects to an extension piece (8), which passes through a small hole in the central lid section (9) to reach the confining ring collar. Heat dissipators are attached to the extension pieces, just above the lid. The PVC lid (9) and base (13) prevent excessive heat-loss, as well as insulating the instrumentation above the water bath.

The water bath is formed from a PVC cylinder (10), which sits above two stainless-steel plates (11) and (12). A novel feature of this oedometer is the lower plate (12), which has a hollow section directly below the specimen. Water drains down from the water bath, through the upper plate (11), and then spreads out in the hollow section of the lower plate. A water circulation system (18) is used to pump the water out of the lower plate, and back into the water bath. By circulating water below the specimen, it is heated from below as well as from the sides and above. This isotropic heating minimises the temperature gradient across the specimen, which is a potential issue with previous schemes. Temperature is controlled using the water bath surrounding the specimen. The water is heated by three 150 W electrical heaters (14) within the bath, spaced at equal distance radially and circumferentially around the specimen. Using this system, temperature can be controlled between 22.5 °C and 70 °C. Heating and cooling can also be applied using an external heating/cooling unit, in combination with a custom-built heat exchanger, which is part of the circulation system (18). With this combined system, temperature can be controlled in the range 5 °C to 70 °C.

Temperature is measured at three points - two beneath the specimen and confining ring (15) and one within the water bath (16). The measuring instrumentation and the heaters are connected to TRIAX, software that can be used to control variables such as temperature, force and displacement.

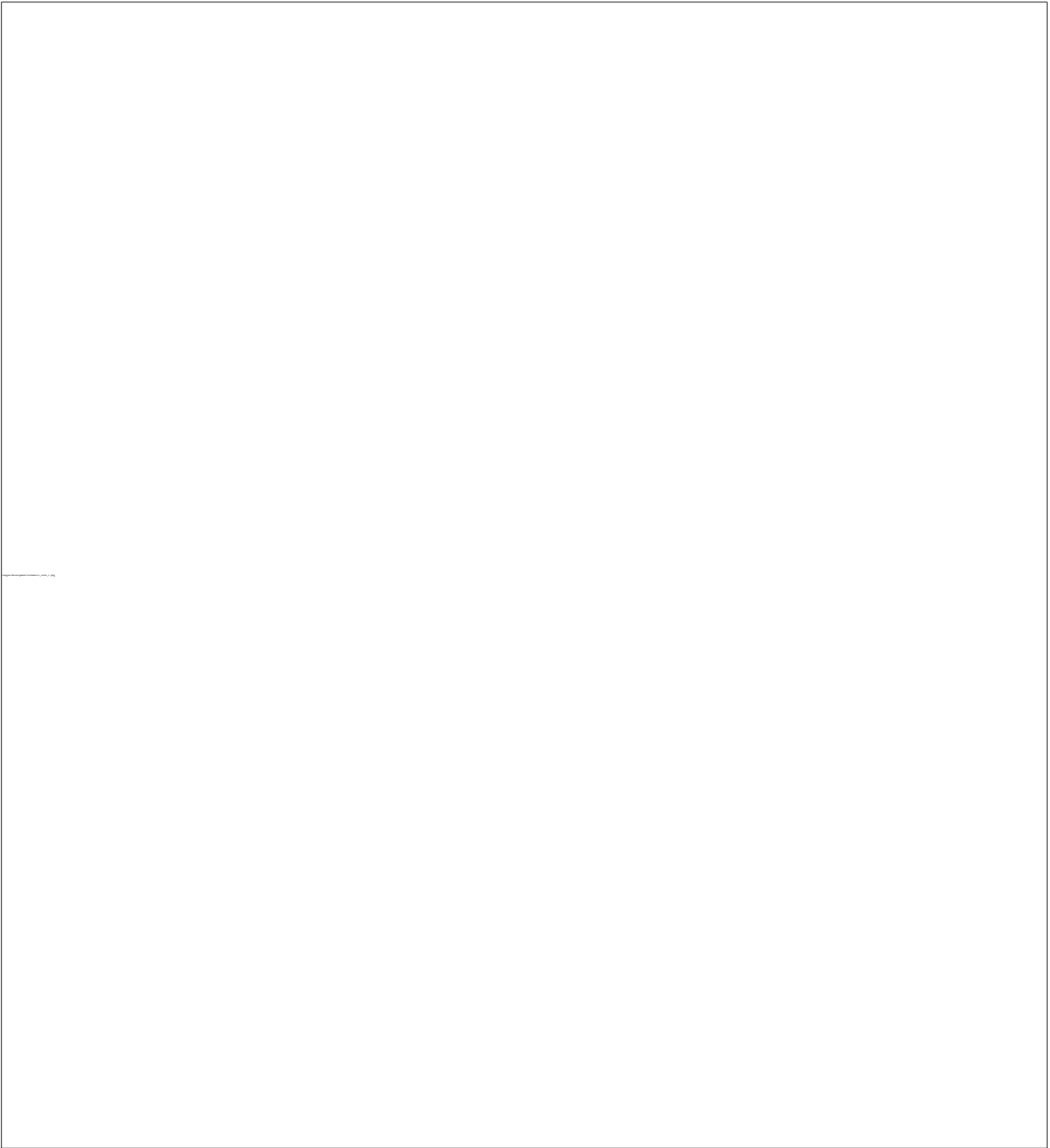


Figure 3.1: Schematic of the temperature-controlled oedometer, numbered as follows:

- | | |
|----------------------------------|--|
| 1) Loading ram (upper section) | 10) PVC water bath |
| 2) Load cell | 11) Upper steel plate |
| 3) Loading ram (lower section) | 12) Lower (hollow) steel plate |
| 4) Top-cap | 13) PVC base |
| 5) Soil specimen | 14) Heater (in brass housing) |
| 6) Confining ring | 15) Temperature sensors in upper plate |
| 7) Instrumentation plate & LVDTs | 16) Temperature sensor in water bath |
| 8) LVDT extension piece assembly | 17) Specimen base drainage |
| 9) PVC lid | 18) Water circulation system |

images/development/photo_cell_1.JPG

Figure 3.2: Photograph of the temperature-controlled oedometer

A system schematic is shown in Figure 3.3. The system can be split by function into Measurement and Control. The measurement part of the system consists of sensors that determine the current state of the system (temperature, displacement, load). Temperature is measured with integrated-circuit type temperature sensors, displacement is measured with LVDTs, and load is measured with a load cell.

Data acquisition hardware acts as the interface between the sensors and the PC. In this system, a 16 channel measurement processor provides this interface, digitising the incoming signals from the sensors. On the PC, TRIAX software is used to record the measured values, calculate what changes to the current state are required, and feed-back these required changes to the control part of the system.

The control part of the system consists of instruments that can change the state of the system (temperature, displacement, load). Temperature is controlled using heaters (above ambient temperature), or the chiller unit (below ambient temperature). The heaters are controlled by TRIAX, so above-ambient temperature control is automated. However, the chiller has to be manually programmed, so sub-ambient temperature control is not automated. Displacement or load is controlled using an actuator within the load frame, and is automated.

A photograph of the system is shown in Figure 3.4. On the left is the load frame and the oedometer. The enclosure at the centre of the photograph houses the data acquisition system, which is connected to a PC stored under the bench. The PC is connected to a monitor (output) and keyboard (input). Not visible on the photograph is the chiller unit, and the heat exchanger, although the insulated tubing to the pump can be seen (the two large, grey tubes coming down from either side of the water bath).

In the following section, the development of the oedometer is explained. Further details of the current equipment set-up are given in Section 3.4.

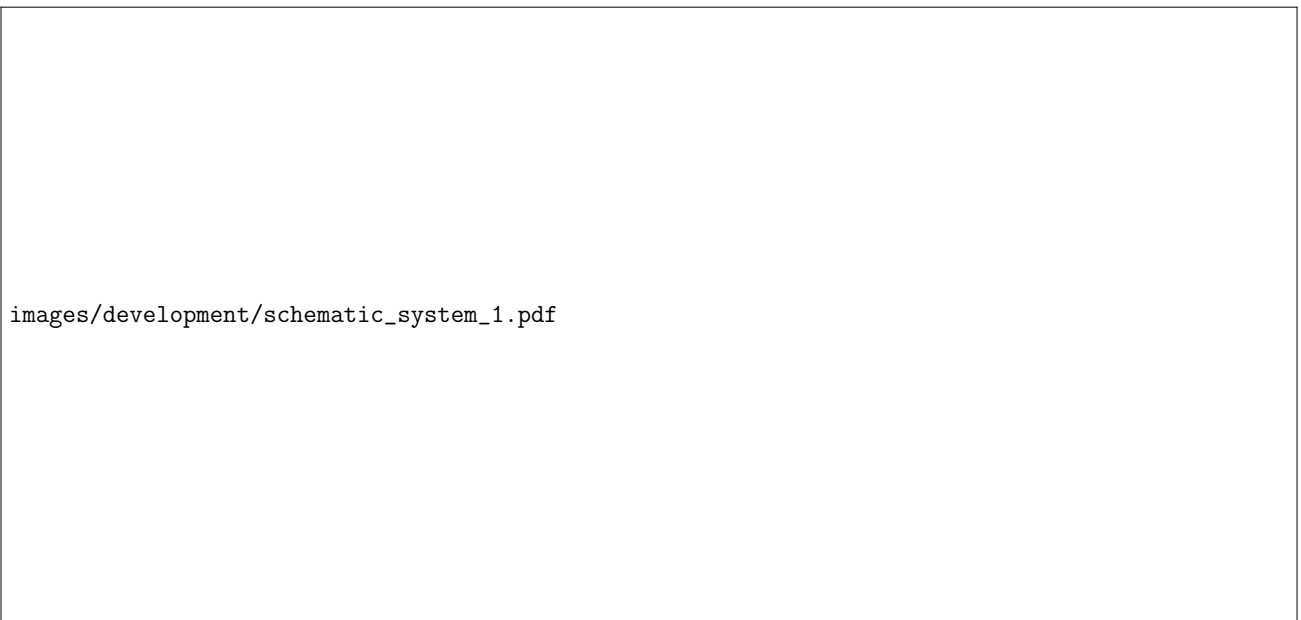


Figure 3.3: Schematic of the temperature-controlled oedometer system



Figure 3.4: Photograph of the temperature-controlled oedometer system

3.3 Design evolution

The starting point for the design is the “conventional” or “standard” oedometer. That is not to say that this oedometer is a modified version of an existing conventional oedometer, but rather that there are some basic attributes of the conventional oedometer that enable one-dimensional loading of soils, and these attributes form the first iteration of the temperature-controlled oedometer design. These are: a confining ring to prevent lateral deformation of the specimen, provision for drainage of water from the soil, a method of load application and measurement, and a method of displacement measurement. Such a scheme is shown in Figure 3.5. Load is applied through the top-cap and loading ram, connected to a load frame. A load cell is used to measure the load. Three LVDTs, mounted on an instrumentation plate, and equally spaced, radially and circumferentially, are used to measure displacement. The specimen is laterally restrained within a confining ring, and two-way drainage is facilitated by having porous stones at the top and base of the specimen.

Next, a method of temperature control is required. Indirect heating, using a water bath, was chosen, as shown in Figure 3.6. The water bath is made of PVC. Three 150 W cartridge heaters, within waterproof brass housings are used to heat the water bath. Brass was chosen for its high thermal conductivity. Three temperature sensors are used to measure the temperature at different locations within the equipment - within the water bath, directly below the specimen, and below the wall of the confining ring.

The issue now is the effect of temperature on the instrumentation. The LVDTs (Section 3.5.3) have an operational temperature range of $-20\text{ }^{\circ}\text{C}$ to $125\text{ }^{\circ}\text{C}$. However, the load cell (Section 3.5.2) only has an operational temperature range of $5\text{ }^{\circ}\text{C}$ to $50\text{ }^{\circ}\text{C}$. The ability to perform tests at temperatures above $50\text{ }^{\circ}\text{C}$ is desirable, since high-temperature tests are relevant to the design of buffers in geological disposal facilities. To avoid temperature effects on the instrumentation, the lower section of the loading ram is extended, giving space for a PVC lid between the water bath and the instrumentation. This is shown in Figure 3.7. Extension pieces allow the LVDTs to reach the confining ring. The lid minimises heat transfer through convection, but there is still the issue of conduction through the loading ram and the LVDT extension pieces. On the LVDT extension pieces are heat dissipators, which are small brass collars, with a relatively large surface area due to their shape. These conduct heat away from the stainless-steel extension pieces, and allow it to dissipate into the air. The same principle applies to the instrumentation plate itself, which allows heat from the loading ram to dissipate from its large flat surface. A cooling fan is used to aid this process.

The next issue to solve is the development of temperature gradients across the specimen. The heat from the water bath conducts through the wall of the confining ring, and the top-cap, to heat the specimen from the sides and the top. However, unless the specimen is also heated from the base, a temperature gradient will develop across the specimen, with higher temperatures at the top and sides, and lower temperatures at the base. For this reason, a hollow steel base-plate is used, which allows water to circulate directly below the specimen. This is shown in Figure 3.8. Circulation of the water with a pump also prevents build up of higher temperatures around the heaters, and ensures the water temperature is homogeneous within the bath.

To assess whether isolation of the instrumentation from the heat source was effective, a thermal camera was used to measure the surface temperature of the oedometer during a thermal test. These images were obtained before the installation of the cooling fan. Figure 3.9 shows a photograph of the cell taken with the thermal camera. The sides and lid of the water bath show up clearly against the ambient-temperature background. However, the temperature of the

images/development/schematic_dev_1.png

Figure 3.5: Development schematic 1 of 4

images/development/schematic_dev_2.png

Figure 3.6: Development schematic 2 of 4


images/development/schematic_dev_3.png

Figure 3.7: Development schematic 3 of 4

images/development/schematic_dev_4.png

Figure 3.8: Development schematic 4 of 4

instrumentation plate is not significantly higher than ambient-temperature. Figure 3.10 shows a view from the top of the cell. The temperature of the instrumentation plate and load cell is much lower than the cell lid below. Finally, Figure 3.11 shows the instrumentation plate from the side. It appears that some heat is conducted up through the loading ram. The previous figure shows that the temperature of the load cell is not affected. The heat dissipators on the LVDT extension pieces are seen to be effective, as the temperature of the extension piece is significantly lower above the heat dissipator. Although these images alone are perhaps not conclusive, further experience has shown that the temperature of the instrumentation remains constant during testing. During thermal tests at the maximum cell temperature of 70 °C, the instrumentation plate remains cool to the touch.



images/development/thermal_camera_1.jpg

Figure 3.9: Thermal camera photograph - side view of cell

To assess the effect of water circulation, two heating tests were performed, with and without water circulation. Both tests were performed without any soil specimen in place. The water bath was heated up to a temperature of 70 °C, and the temperature was measured at two locations, directly below the specimen (T_{middle}) and within the water bath (T_{cell}), corresponding to numbers (15) and (16) in Figure 3.1. The results from the two tests are compared in Figure 3.12. The difference between the measured temperature values increases with cell temperature. A large temperature difference results in a steeper temperature gradient across the specimen. With the circulator off, the temperature difference is up to 17 °C for a cell temperature of 70 °C. With the circulator on, the maximum temperature difference is less than 0.5 °C. This suggests the unique circulation design of this oedometer is an improvement on previous designs.

images/development/thermal_camera_2.jpg

Figure 3.10: Thermal camera photograph - top view of cell

images/development/thermal_camera_3.jpg

Figure 3.11: Thermal camera photograph - instrumentation plate detail

images/development/circulation_T_variation.pdf

Figure 3.12: Effect of water circulation on temperature variation in oedometer cell

3.4 Design details

In this section, the current equipment set-up is described in detail, and is split as follows:

- Lower section - confining ring, porous stones and top-cap.
- Upper section - loading ram, load cell, instrumentation plate, LVDTs and fan.
- Water bath - water bath and lid, insulation, heaters and temperature sensors.
- Base-plates - base-plates, water circulation system and drainage.
- Chiller - chiller and heat exchanger.
- PC and data acquisition - hardware and software for data acquisition and system control.

Note that numbers in brackets refer to the numbered components on the equipment schematic given in Figure 3.1. Key dimensions are given in the text. Additionally, dimensioned figures of some important components (confining ring, top-cap, LVDT assembly, and instrumentation plate) are given in Appendix F.

3.4.1 Lower section

In this section, the following are discussed in detail:

- Top-cap, including o-ring (4)
- Porous stones (5)
- Confining ring, including collar and holding-down bolts (6)

A schematic showing detail of the confining ring is shown in Figure 3.13, and a photograph is shown in Figure 3.14. The stainless-steel confining ring has an internal diameter of 70 mm, and a height of 70 mm (not including collar). It sits in a shallow recess in the upper base-plate, which prevents lateral movement and ensures it remains centrally below the top-cap. For most tests, 6 mm thick aluminium oxide (alumina) porous stones, shown in Figure 3.15, are placed above and below the specimen. Initially, filter papers were placed between the porous stones and the specimen, to prevent clogging of the pores of the porous stones. However, the use of filter papers was found to be inappropriate for all tests, and particularly so for thermal tests. This is discussed further in Chapter 4. The maximum possible specimen height is ≈ 50 mm. The ring and collar are made of stainless-steel, as is the top-cap. The top-cap has diameter ≈ 0.4 mm smaller than the ring, which allows it to move freely in the vertical direction. It is screwed into the base of the loading ram. A fixed connection was chosen rather than, for example, a half-ball connection. This decision was made to minimise the possibility of tilting of the top-cap, which could cause it to jam against the confining ring. A nitrile rubber (NBR) o-ring sits in a small groove in the side-wall of the top-cap, which helps keep the loading ram vertical, preventing sticking of the top-cap and the ring due to tilting effects. It also allows the specimen to be isolated from the water within the bath, so that a controlled back-pressure can be applied. However, friction between the o-ring and the inner surface of the confining ring is a source of error, which is discussed further in Section 4.2.

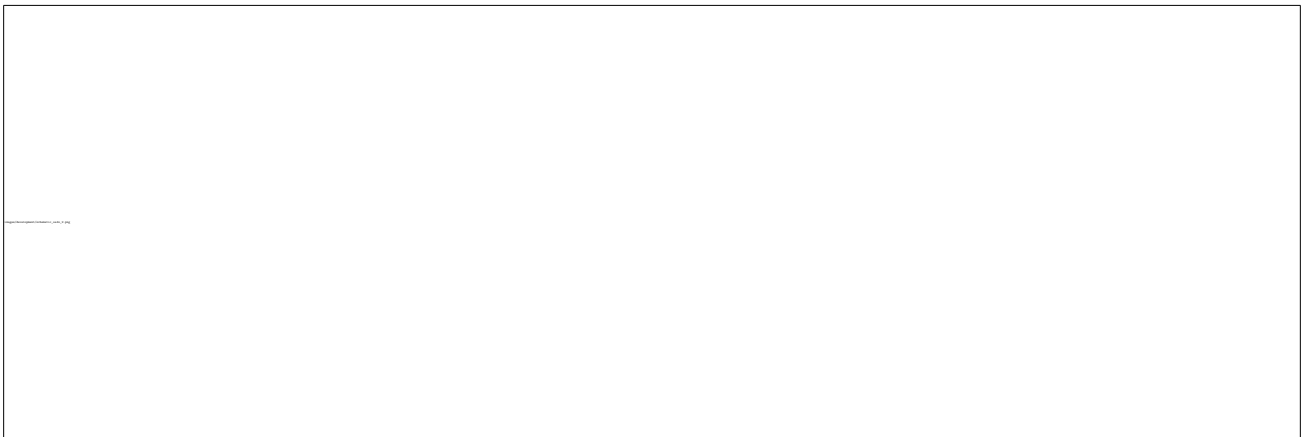


Figure 3.13: Schematic of the temperature-controlled oedometer - lower section

images/development/photo_CR_1.JPG

Figure 3.14: Photograph of the top-cap and confining ring

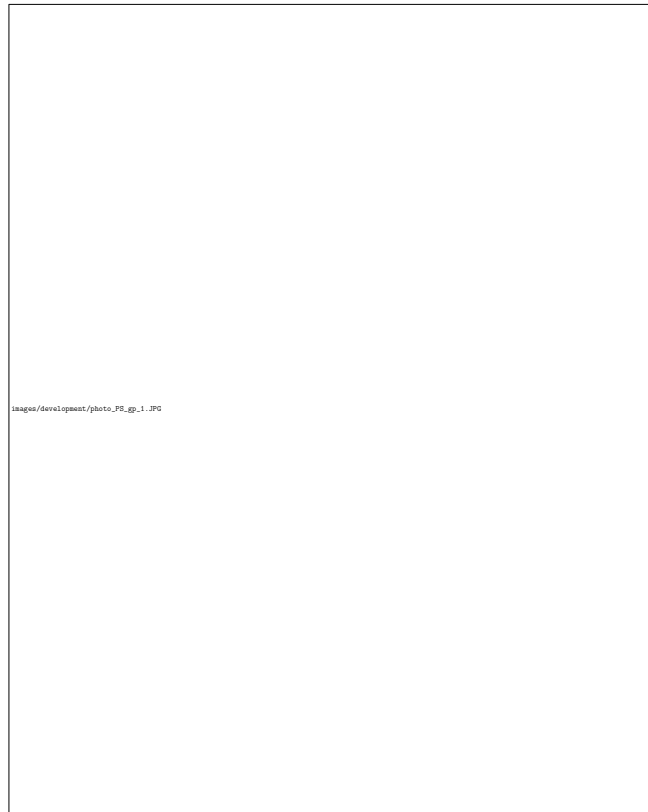


Figure 3.15: Photograph of an aluminium oxide (alumina) porous stone

3.4.2 Upper section

In this section, the following are discussed in detail:

- Loading ram (1) and (3)
- Load cell (2)
- Instrumentation plate (7)
- LVDTs, including extension pieces and heat dissipators (8)

The upper section of the apparatus is shown schematically in Figure 3.16, with photographs in Figure 3.17 and 3.18. At the top, the loading ram connects to the load frame with three bolts, which can be adjusted to ensure the loading ram is vertical and centrally positioned. The upper section of the loading ram is required because it houses the cable which emerges from the top of the load cell. The upper section of the loading ram, including the connection to load frame, can be seen in Figure 3.2. The load cell is screwed into the upper section of the loading ram above, and the lower section below. The lower section of the loading ram is longer than the upper section, because it has to extend from the load cell, above the cell lid, to the specimen, within the water bath. Below the load cell, the instrumentation plate is fixed to the lower section of the loading ram with a bolt that tightens against the loading ram itself. The instrumentation plate, shown in Figure 3.17, is a 6 mm thick, 125 mm diameter stainless-steel plate, with six equally-spaced holes for holding displacement transducers. The holes are like cup-holders for the LVDTs, which slot into a brass housing, secured with a bolt which tightens against the LVDT itself, as shown in Figure 3.19. Since the LVDTs have only 10 mm travel, they need re-setting during tests, especially when consolidating clay slurry. Coarse adjustment can be done by raising

the instrumentation plate. Fine adjustment can be done by raising each LVDT individually. Specifications are given below for the load frame (Section 3.5.1), load cell (Section 3.5.2), and LVDTs (Section 3.5.3).

The LVDTs consist of a body, core, connection piece and extension piece. The body is fixed with a small screw to the instrumentation plate, which is in turn fixed to the lower section of the loading ram. The core is connected to an extension piece using a brass connection piece. The brass heat dissipator is fixed to the extension piece below the connection piece. This assembly (core, connection piece, extension piece) rests on the collar of the confining ring, and is unaffected by specimen displacement. However, since the extension piece is directly exposed to temperature changes, thermal expansion/contraction of the extension piece has to be accounted for. The same is true for the lower section of the loading ram, the confining ring, and even the base-plates - in fact any part of the equipment that is exposed to temperature changes. This calibration is covered in Section 4.4. Vertical displacement of the specimen results in displacement of the LVDT body relative to the core, which gives the raw displacement, recorded by the equipment, before applying any corrections in post-processing.

A fan is fixed to the load frame, and directed at the instrumentation plate and load cell. The air-flow from the fan convects heat away from the instrumentation and ensures that the instrumentation remains at ambient temperature during thermal testing. The fan is a 12 V DC axial fan, manufactured by RS Components. This type of fan is commonly used for cooling in PCs. It has dimensions $80\text{ mm} \times 80\text{ mm} \times 25\text{ mm}$, and provides an air-flow of $68\text{ m}^3\text{ h}^{-1}$ (40 cfm).

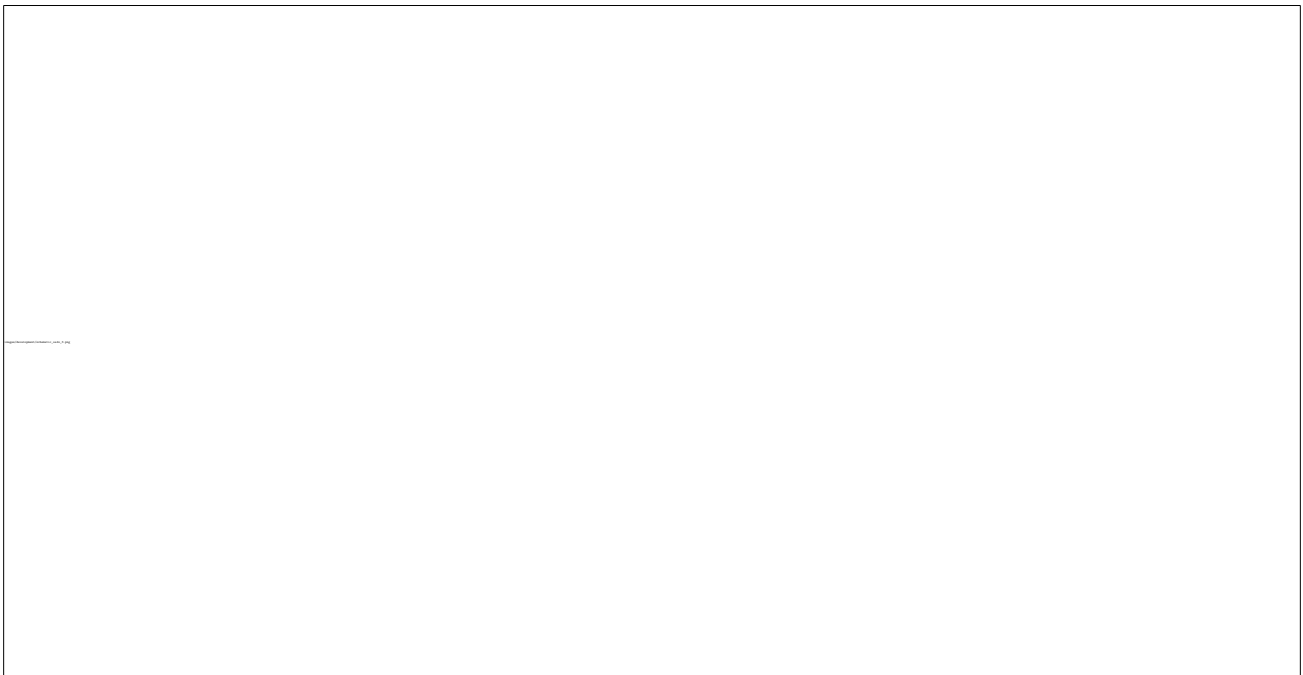
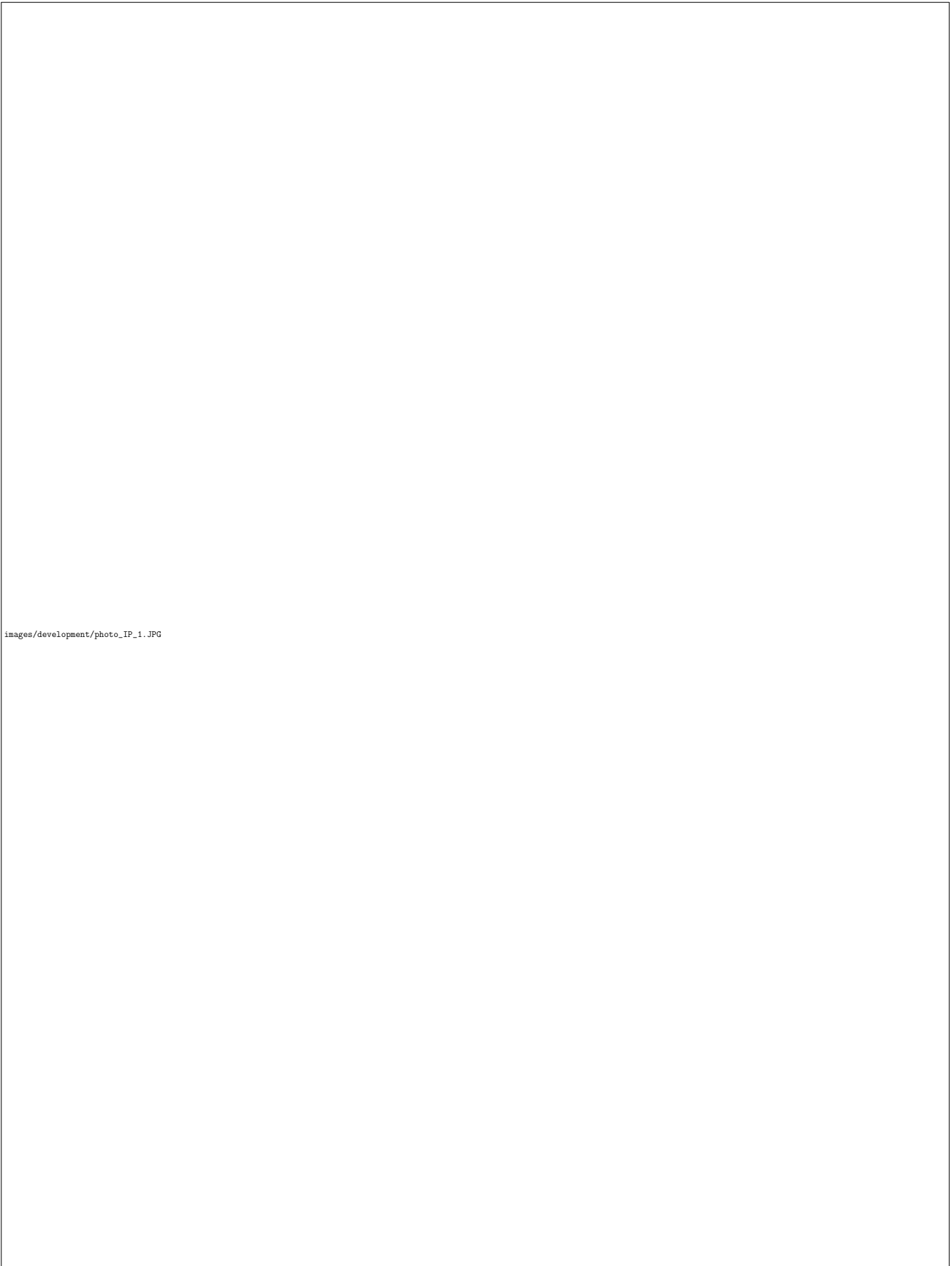


Figure 3.16: Schematic of the temperature-controlled oedometer - upper section



images/development/photo_IP_1.JPG

Figure 3.17: Photograph of the load cell and instrumentation plate, with lid in place

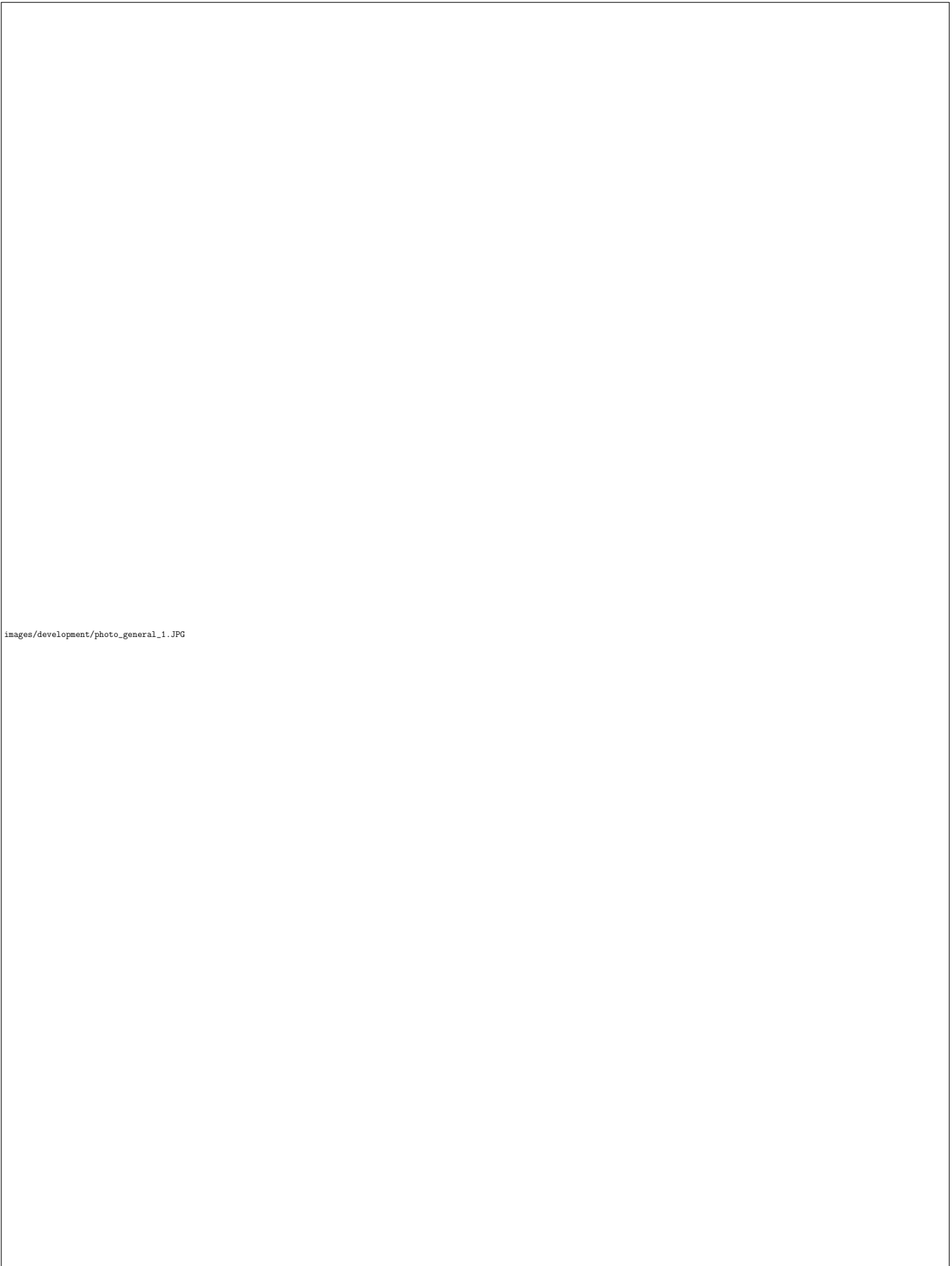
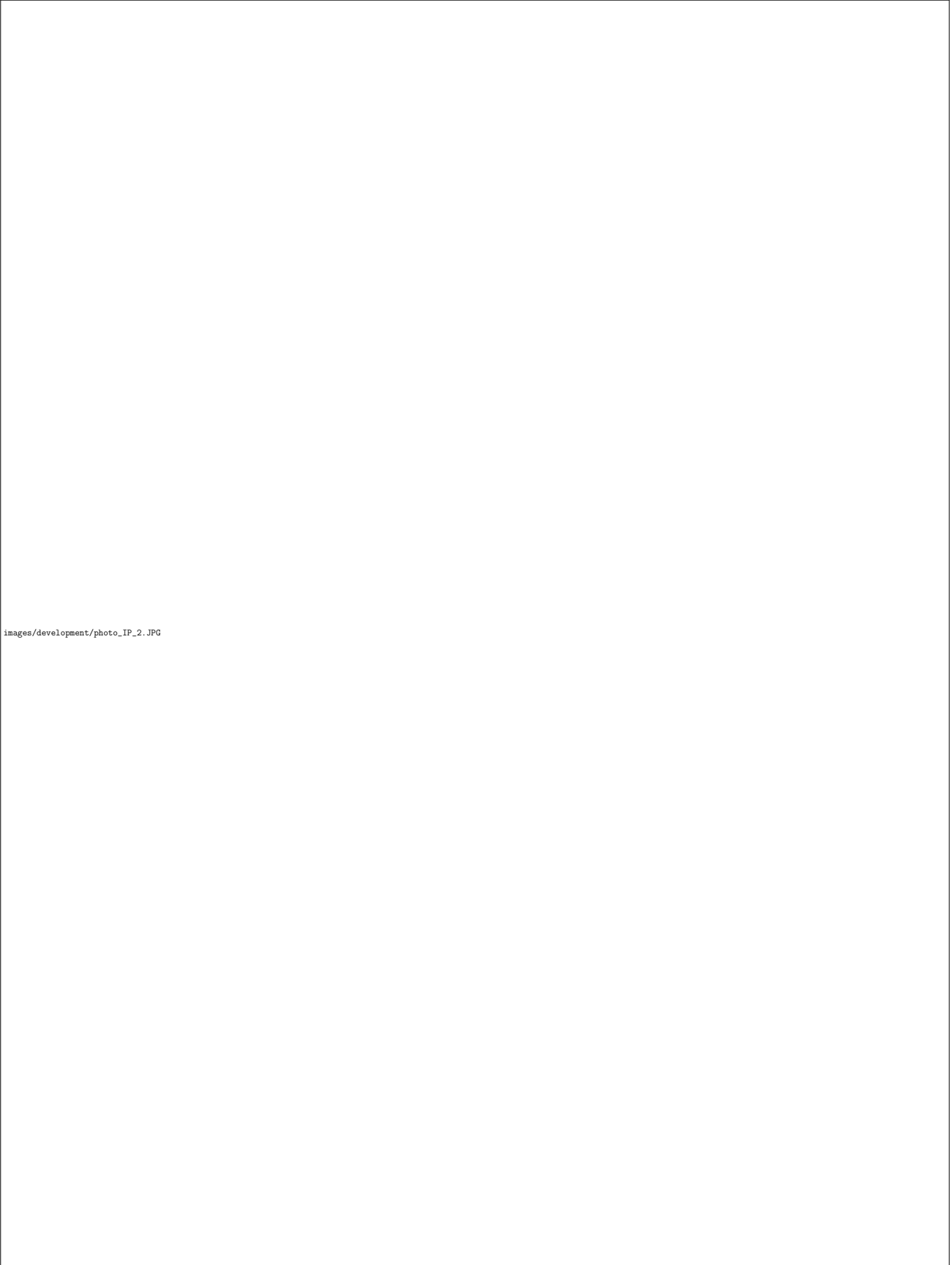


Figure 3.18: Photograph of the instrumentation plate, central lid section and water bath



images/development/photo_IP_2.JPG

Figure 3.19: Photograph of the instrumentation plate, showing LVDT adjustment detail

3.4.3 Water bath

In this section, the following are discussed in detail:

- PVC water bath, including three-piece lid (9) and (10)
- Water bath insulation
- Heaters (14)
- Temperature sensor within water bath (16)

A water bath is used to heat or cool the specimen. The bath is made from unplasticised polyvinyl chloride (PVC-U or UPVC) which is suitable for temperatures up to 70 °C. PVC-U has a Vicat softening point of 75 °C, above which, it begins to soften (Smiths Metal Centres, 2018). Therefore, with the current set-up, the upper temperature limit for the equipment is determined by the properties of the PVC-U. An alternative would be to use post-chlorinated polyvinyl chloride (PVC-C or CPVC), which has a Vicat softening point of 105 °C (Smiths Metal Centres, 2018). With PVC-C, the upper temperature limit of the equipment would instead be determined by the properties of the circulating fluid, which is water. To avoid the effects of phase-change of the water, an upper limit of 85 °C to 90 °C is recommended. This temperature could be reached without any changes to the installed heating capacity.

The capacity of the bath is 10 L. The water bath is insulated using two layers of 10 mm thick EPF30 polyethylene closed-cell foam sheet. This insulation improves the efficiency of the heating system. EPF30 polyethylene has a working temperature range of -60°C to 90°C . It has low thermal conductivity ($0.0410\text{ W m}^{-1}\text{ K}^{-1}$). Also, it is flexible, waterproof, chemically resistant, and impervious to bacteria, mildew and rot (Simply Foam Products, 2010).

The water bath is covered with a three-part lid, also made of PVC-U, shown (with the front part removed) in Figure 3.20. The front and back parts each have the shape of a semi-circular annulus, which allows the LVDT extension pieces to pass through the centre. At the outer edge is a step which rests on the top lip of the water bath wall. The central part is circular, with small holes for the LVDT extension pieces. It can be fixed to the lower section of the loading ram using a bolt on a central collar, which tightens directly onto the loading ram. This is used when setting up a test. However, when a test is running, this bolt is fully loosened, so that the central lid part can move freely up and down, relative to the loading ram and the LVDT extension pieces. Figure 3.21 shows how the components of the oedometer are connected. Components connected to the top of the load frame are shown as shaded blue. These include: the upper and lower sections of the loading ram, the load cell, the instrumentation plate and the LVDT bodies. All other components, which are shown as unshaded, are connected to the base of the load frame, and therefore move relative to the blue-shaded components. Two components require further clarification: the three-part lid is not fixed, but rests on the top lip of the water bath wall, and the other parts of the LVDTs (core, connection piece, extension piece, and heat dissipator), which are also not fixed, but rest on the confining ring collar. These two components can in fact move relative to each other. Displacement is measured from the confining ring collar, rather than from the top of the lid, because measurements so remote from the soil would be unreliable. It is for this reason that local measurement of displacement is preferred to external measurement. For example, Martínez Calonge (2017) used local instrumentation as part of a temperature-controlled triaxial scheme.

The water bath is heated using three 150 W heaters. The heaters are equally spaced, at 120° intervals. Between two of the heaters is a temperature sensor, within a brass housing.

A photograph of two heaters and the sensor are shown in Figure 3.22. The sensor housing is the central one in the figure, slightly thinner than the heaters. There is potential to install up to 11 heaters in total (or 12 if the temperature sensor is removed) using the spare holes through the base-plates, which are currently sealed by stainless-steel plugs and o-rings. However, three heaters are sufficient to heat the bath to at least 70 °C. The maximum temperature is limited by the PVC lid, which begins to deform at temperatures above this value, and the heating rate is limited not by the equipment capability, but by the soil permeability, especially for low permeability clays. If the heating rate is too fast, excess pore-water pressure is generated in the soil, and drained conditions can no-longer be assumed. Specifications are given below for the temperature sensors (Section 3.5.4), and heaters (Section 3.5.5).

images/development/photo_lid_1.JPG

Figure 3.20: Photograph of the three-part lid with front part removed

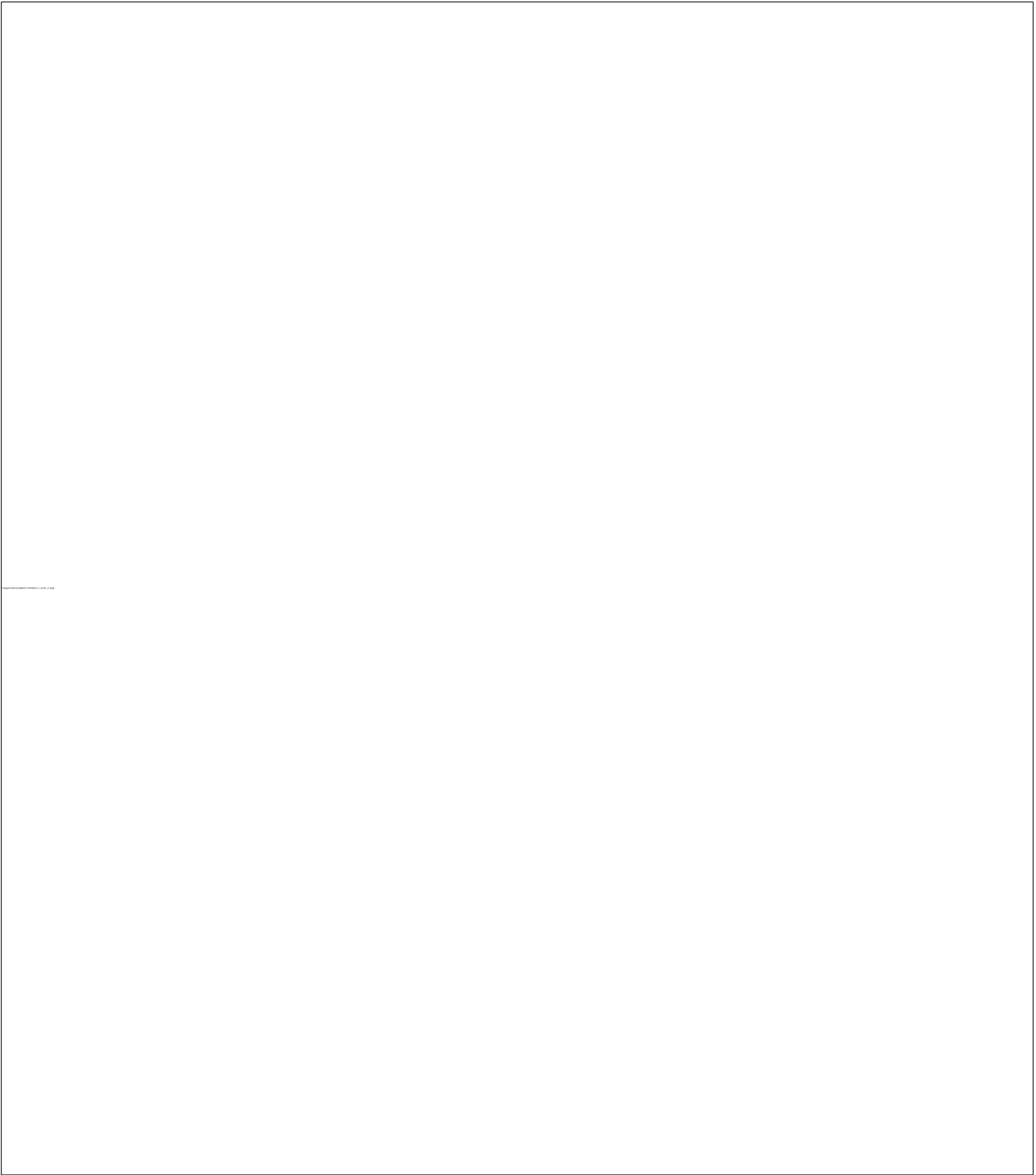


Figure 3.21: Schematic showing connection of oedometer components



Figure 3.22: Photograph of the heaters and temperature sensor

3.4.4 Base-plates

In this section, the following are discussed in detail:

- Base-plates (11), (12) and (13)
- Temperature sensors within upper base-plate (15)
- Specimen drainage: top (4) and base (17)
- Water circulation, including pump (18)

The confining ring is secured to the upper base-plate with six bolts, which screw directly into threaded holes in the base-plate. The confining ring is shown in Figure 3.18, and the threaded holes in the base-plate can be seen in Figure 3.22. The two small holes in the centre of the base-plate are for specimen base drainage. These drains turn at 90° within the upper base-plate and can be controlled using valves at the side of the upper base-plate. One of these valves is shown in Figure 3.23, with base drainage connected to a water-filled syringe that provides hydrostatic back-pressure to the base of the specimen. Within this plate, but not visible, are two temperature sensors, which are positioned 2 mm below the surface - one, below the centre of the specimen, and the other below the confining ring wall. This can be seen more clearly in Figure 3.24, and is discussed further below. The black ring, in Figure 3.22, is an o-ring which sits in a shallow groove, and seals the base of the confining ring. The confining ring itself sits in a shallow recess in the upper base-plate, which secures it in place laterally, while the bolts secure it vertically. The threaded bolt holes are those closest to the lip marking the edge of the confining ring.

Further out than the threaded bolt holes, are six slightly larger holes, also shown in Figure 3.22, which provide drainage from the water bath into the lower base-plate. This component is one of the innovative aspects of this oedometer design. It allows heated (or cooled) water to circulate directly below the specimen, preventing a temperature gradient developing in the specimen due to heat-loss at the base of the specimen. Other schemes in the literature have insulated the base of the oedometer, to reduce heat-loss, but this is the first scheme to heat the soil sample from the base. A photograph of the lower base-plate is given in Figure 3.24. This plate sits directly below the upper base-plate. Near the centre, two small holes can be seen, sealed with o-rings. These are for the two temperature sensors which terminate just below the surface of the upper base-plate. The hollow section is formed of two concentric rings, connected by six drainage paths. Water drains from the bath, through the six drains shown in Figure 3.22, into the outer ring. It then passes through the six drainage paths to the inner ring, and then drains out through the single drain which can be seen partially in Figure 3.24, in line with the two specimen drains. Water is continuously circulated from the water bath, through the hollow base-plate, and back into the bath, through flexible silicone tubing, using an electronic pump. A photograph of the pump is given in Figure 3.25. It is a simple, inexpensive, 12 V DC hot-water circulation pump, suitable for circulating water temperatures up to 100 °C.

The circulated water also passes through a heat exchanger, which is described in the next section. In combination with a chiller unit, this allows control over sub-ambient temperatures, as low as 5 °C. Surrounding the hollow section is another o-ring, then the twelve large-diameter holes for the heaters or temperature sensors, shown in Figure 3.24. Near the outside of the plate are twelve holes used to bolt the base-plates together. The hollow plate sits on a PVC base-plate, which insulates the base, preventing excessive heat-loss that would otherwise occur through the stainless-steel hollow plate.

images/development/photo_drainage_1.JPG

Figure 3.23: Photograph of the base drainage and hydrostatic back-pressure

images/development/photo_waffle_1.jpg

Figure 3.24: Photograph of the hollow base-plate



Figure 3.25: Photograph of the pump used for water circulation

3.4.5 Chiller and heat exchanger

In this section, the following are discussed in detail:

- Chiller unit
- Heat exchanger
- Pipe insulation

One of the advantages of this equipment is the ability to control temperature across a range of above- and sub-ambient values. Temperatures of 22.5 °C and above are controlled automatically, using TRIAX software, with the three heaters in the water bath. Temperatures below 22.5 °C are controlled manually, using the chiller unit. The system used for control of sub-ambient temperatures is shown schematically in Figure 3.26. It comprises four components: the cell, which here refers to the oedometer water bath, the heat exchanger, the chiller, and the pump. Water from the cell is continuously circulated through the heat exchanger by the pump, even when the chiller is not in operation. Continuous circulation is required to prevent build up of high temperatures around the heaters, and to heat the specimen evenly, by circulating water through the hollow base-plate, as described above.

A photograph of the heat exchanger is given in Figure 3.27. It is a bespoke shell-and-tube type heat exchanger, designed and built in-house. It comprises a ≈ 70 mm diameter PVC outer tube, which contains two highly-conductive copper pipes. These copper pipes are connected using a short length of silicone tubing at one end, so that they form a single path, which passes twice through the inside of the larger PVC tube. When the chiller is operating in cooling mode, the cold water from the chiller circulates through the PVC tube. The hot water from the cell circulates through the copper pipes. The high conductivity of the copper pipes, and the large surface area from doubling back, efficiently transfers the heat. The heat exchanger is insulated using three layers of closed-cell foam, the same used to insulate the water bath. The silicone tubes leading to and from the heat exchanger, via the pump, are insulated with Climaflex polyethylene pipe insulation. A photograph of the chiller is given in Figure 3.28, and specifications are given in Section 3.5.6.

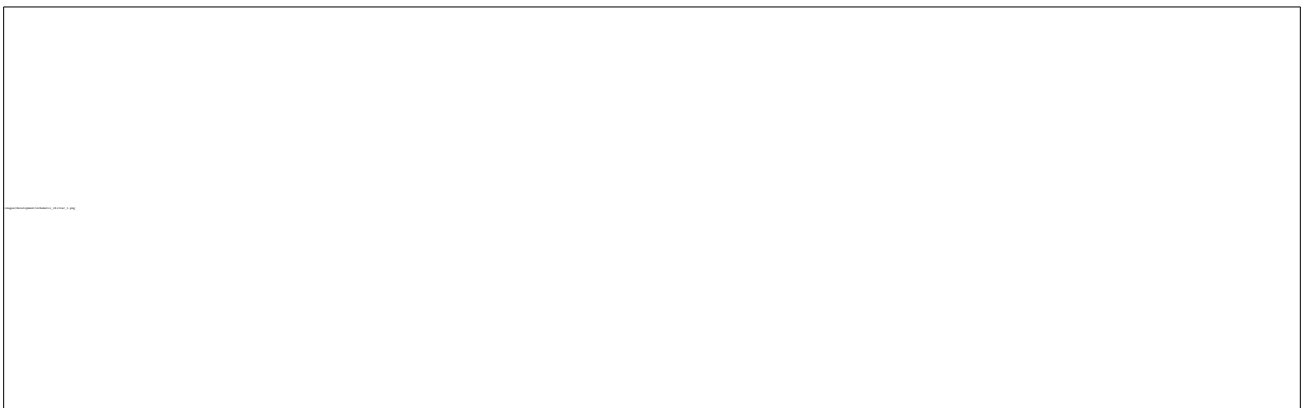


Figure 3.26: Schematic of the cooling system

images/development/photo_HE_1.JPG

Figure 3.27: Photograph of the heat exchanger

images/development/photo_chiller_1.JPG

Figure 3.28: Photograph of the chiller unit

3.4.6 PC and data acquisition

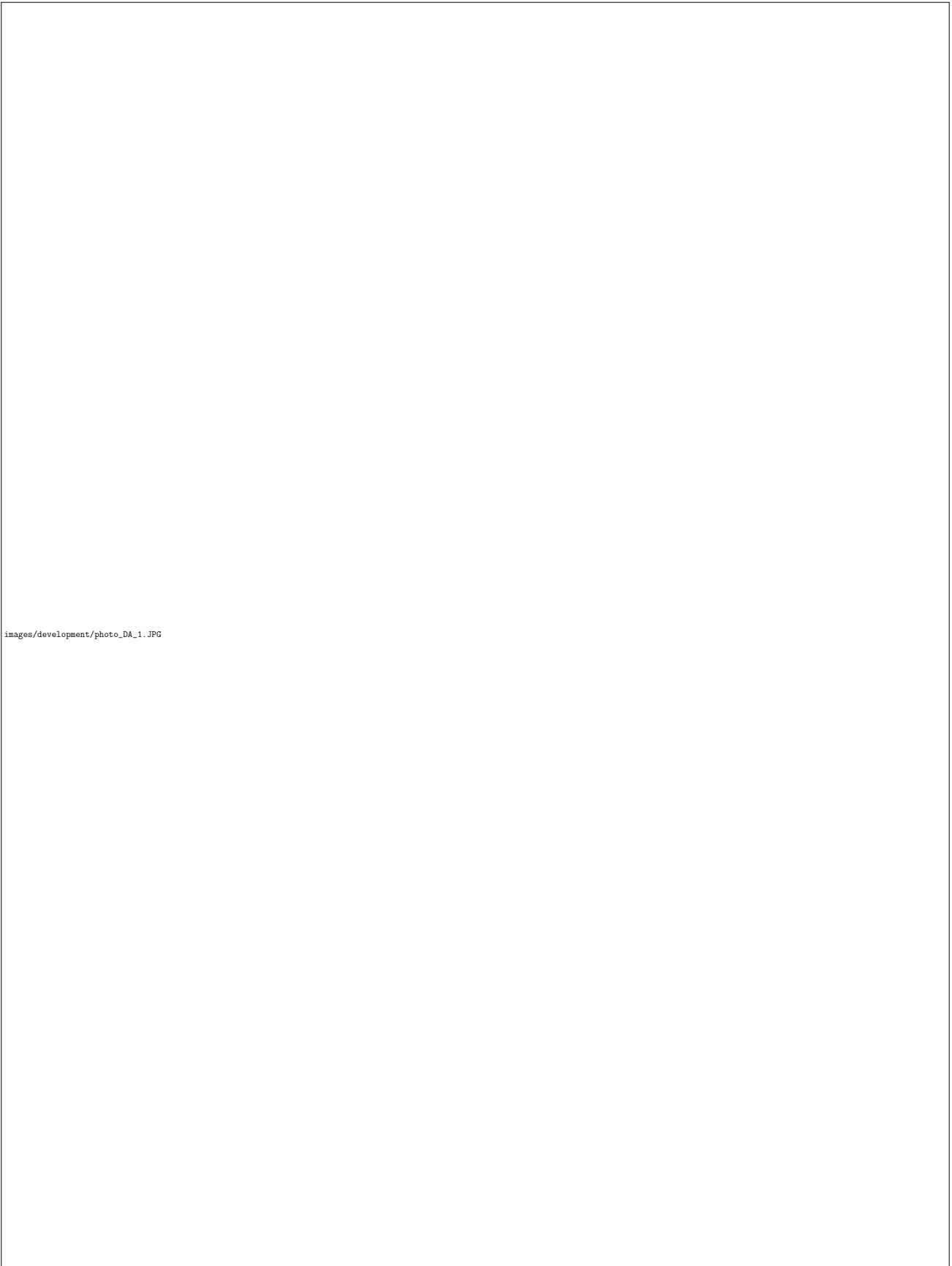
In this section, the following are discussed in detail:

- TRIAX software
- Data acquisition device
- Uninterruptible power supply

A PC with TRIAX software (Toll, 1999) is used to control the tests. This enables automated, independent control of temperature and displacement, or load. Target values, or target rates of change, can be specified. Alarms can be set so that control moves to the next stage once a certain value is reached (of load, displacement, temperature, or time). This software is also used for recording the values measured by the instrumentation. In most tests, two variables are controlled - load (force measured by the load cell) and water bath temperature. One is kept constant while the other changes. Stages are either load/unload (at constant temperature), heat/cool (at constant load), or hold (maintain current conditions).

The data acquisition device is a 16 channel measurement processor, model Datascan 7220, manufactured by Measurement Systems Ltd (MSL), shown in Figure 3.29 (within an enclosure). It acts as the interface between the PC and the equipment.

To prevent interruption of long-term tests in the event of a power cut, an uninterruptible power supply (UPS) is used. The UPS used is model NPW 1000, manufactured by Riello UPS, which has a rated apparent power of 1000 VA.



images/development/photo_DA_1.JPG

Figure 3.29: Photograph of the 16 channel data acquisition device, within enclosure

3.5 Equipment specification

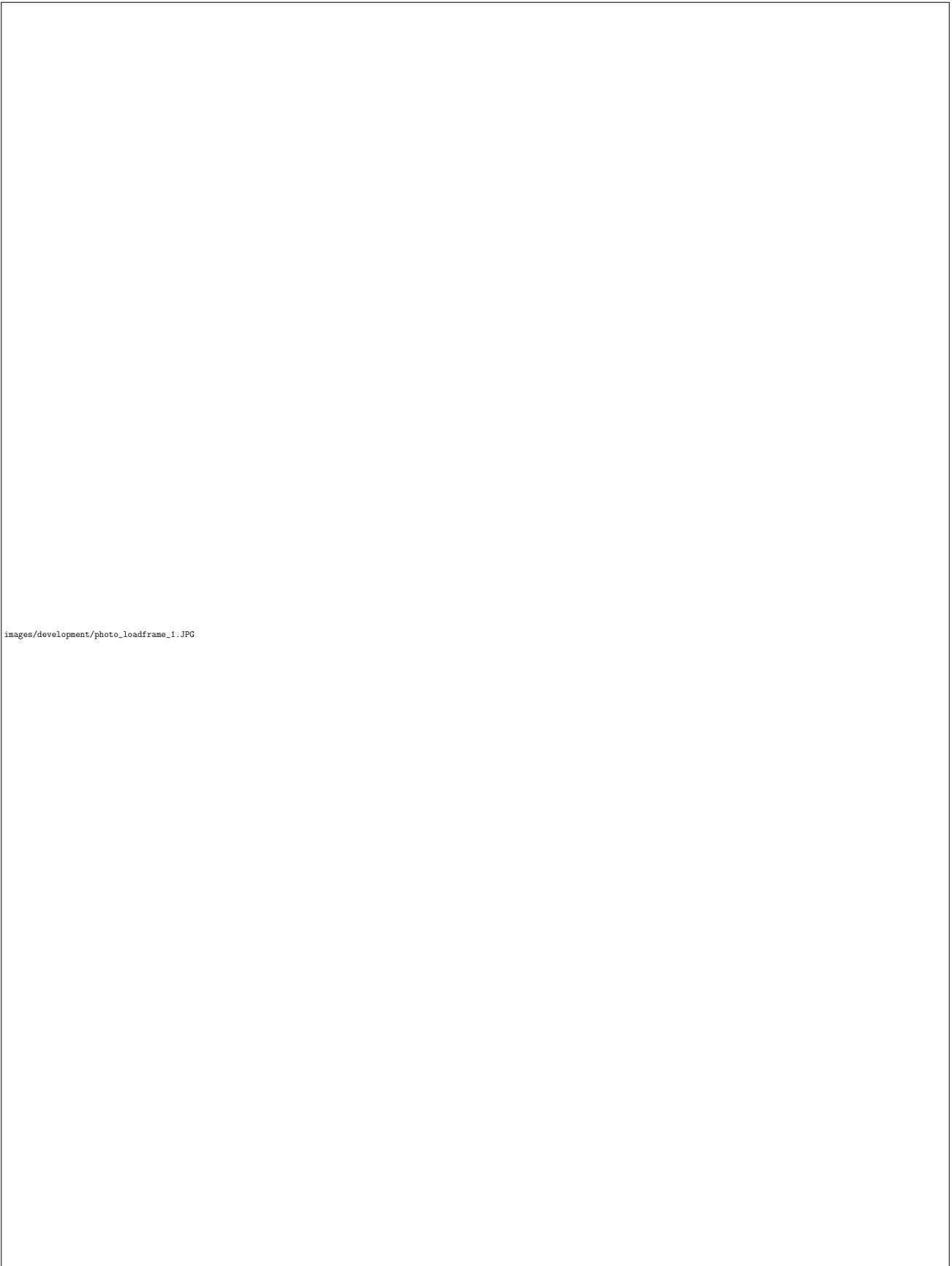
A summary of the components used in the oedometer is given in Table 3.1. Bespoke components are not listed, only those that have been sourced from an external supplier. Where possible, the model and product number are given, for reference. The pump and fan are not listed as these are both generic components and many suitable alternatives are available. Specification details of these components are given below.

Table 3.1: Summary of oedometer components (not including bespoke components)

Component	Quantity	Model	Product number	Manufacturer
Load frame	1	TriSCAN 100 Standard	VJT5100	VJ Tech
Load cell	1	STALC-3 (10 kN)	41170	Applied Measurements
LVDT	3	D5/200W	-	RDP
LDS	1	LDS-50	12780	LD Sensors
Temperature sensor	3	LM35 CAZ/NOPB	533-5878	Texas Instruments
Heater	3	10 mm × 50 mm (150 W)	724-2068	RS Pro
Chiller	1	K1	-	ATC
Data acquisition device	1	Datascan 7220	-	MSL

3.5.1 Load frame

Load is applied using a load frame with stepper motor control, manufactured by VJ Tech, model TriSCAN 100 Standard. A photograph of the load frame is given in Figure 3.30. It can apply a maximum vertical load of 100 kN. Displacement rate is controlled using TRIAX software.



images/development/photo_loadframe_1.JPG

Figure 3.30: Photograph of the load frame

3.5.2 Load cell

The load cell is a submersible load cell, model STALC-3, manufactured by Applied Measurements, and shown in Figure 3.17. It has a rated capacity of 10 kN, which translates to a maximum vertical pressure of 2.6 MPa for a 70 mm diameter specimen. The STALC-3 load cell comes in capacities up to 100 kN, so capacity could be increased to 26 MPa if necessary. No other changes to the equipment set-up would be required. Mantikos (2018) used a 70 kN STALC-3 load cell in a relative humidity-controlled oedometer with similar geometry to the TC oedometer.

The operating temperature range of the load cell is 5 °C to 50 °C. The thermal performance of an identical load cell was tested by Martínez Calonge (2017). They performed heating and cooling tests under zero-load conditions, and analysed the readings. Based on these tests, they concluded that this type of load cell is unsuitable for use at temperatures above 50 °C. This is not an issue with the temperature-controlled oedometer because the load cell is isolated from any temperature changes.

3.5.3 Displacement transducers

LVDTs are used to measure displacement. These are model D5/200W submersible LVDT displacement transducers, manufactured by RDP. They have a range of ± 5 mm (travel of 10 mm). They have an operating temperature range of -20 °C to 125 °C, which makes them suitable for the tested temperature range. Three LVDTs are used, since displacement cannot be measured directly above the centre of the specimen. The average of the three displacements gives the displacement at the centre of the specimen. A calculation confirming the accuracy of this method is included in Appendix G.

A photograph of one of the LVDTs is given in Figure 3.31, which shows the LVDT body, along with the core (or armature), brass connection piece, brass heat dissipator, and stainless-steel extension piece. The core piece and extension assembly is shown in Figure 3.32.

In addition to the three LVDTs, a strain-gauge displacement sensor, or linear displacement transducer/sensor (LDT/LDS) is used. This is a model LDS-50, manufactured by LD Sensors. A photograph of this sensor is given in Figure 3.33. An extension piece, identical to the one shown in Figure 3.31 is used with the LDS. At the start of this research, this was the only displacement transducer used, but was replaced by the three LVDTs once it became apparent that tilting effects were important. However, it was kept in addition to the other transducers due to its 50 mm travel, which is useful when setting up specimens. Values from this transducer are not used to calculate specimen displacement during tests.

images/development/photo_LVDT_gp_1.pdf

Figure 3.31: Photograph of an LVDT, with extension piece and heat dissipator

images/development/photo_LVDT_gp_2.JPG

Figure 3.32: Photograph of an LVDT core piece and extension assembly

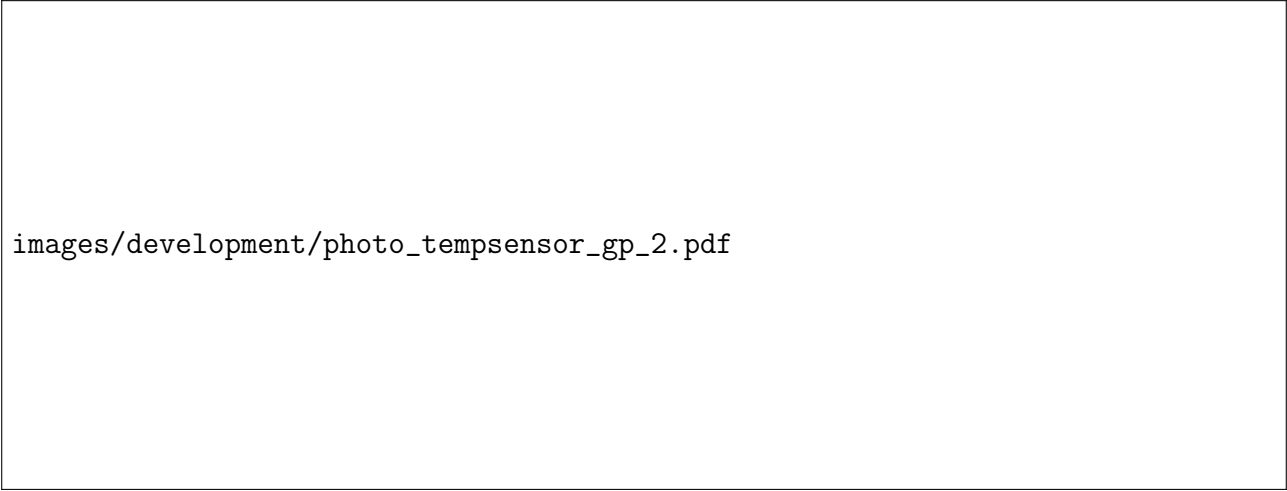
images/development/photo_LVDT_gp_4.JPG

Figure 3.33: Photograph of the LDS

3.5.4 Temperature sensors

Three integrated-circuit type temperature sensors, model LM35, manufactured by Texas Instruments, are used. A photograph of one of the temperature sensors is given in Figure 3.34. Temperature is measured at the tip of the sensor. The brass housing which waterproofs the sensor is also shown, and is shown in position in the equipment in Figure 3.22. The sensors have an operating temperature range of -40°C to 110°C which makes them suitable for use in tests at both elevated and sub-ambient temperatures. They have an accuracy of $\pm 0.2^{\circ}\text{C}$. One is positioned inside the water bath, within a brass housing. The other two are positioned within the upper plate, 2 mm below the surface. Of these two sensors, one is below the centre of the specimen, and the other is below the wall of the confining ring.

Integrated-circuit type temperature sensors have some advantages over other types of temperature sensors (thermocouples, resistance temperature detectors, thermistors). They produce an output current linearly proportional to absolute temperature, which makes calibration simple, and accurate. They are also inexpensive, and compact. Due to their small size, it was possible to position two sensors within the upper base-plate, only 2 mm from the surface of the plate, and thus get an accurate measurement of temperature at the base of the specimen.



images/development/photo_tempsensor_gp_2.pdf

Figure 3.34: Photograph of a temperature sensor

3.5.5 Heaters

Three 150 W cartridge heaters, manufactured by RS Pro, are used to heat the water within the bath. A photograph of one of the heaters is given in Figure 3.35, together with the brass housing used to waterproof the heater. The heater is shown in position in the equipment in Figure 3.22. The heater dimensions are: length 50 mm, diameter 10 mm. They are equally spaced within the water bath, centred 55 mm from the outer face of the confining ring. The water is continuously circulated to prevent any build-up of temperature around the heaters. Heater operation is fully automated, and controlled through TRIAX. The power output is fixed, not variable, i.e. the heaters are either on, or off. If the target temperature is higher than the current temperature (e.g. during a heating stage), the heaters are switched on for a portion of each cycle (which is set in TRIAX, and lasts a few seconds). The proportion of each cycle that the heater is on depends on how far the current temperature is below the target temperature. This method avoids overshooting the target temperature. If the target temperature is below the current temperature, the heaters are switched off for the whole cycle. At the end of each cycle, the current temperature is fed back to TRIAX, which adjusts the subsequent cycle accordingly.

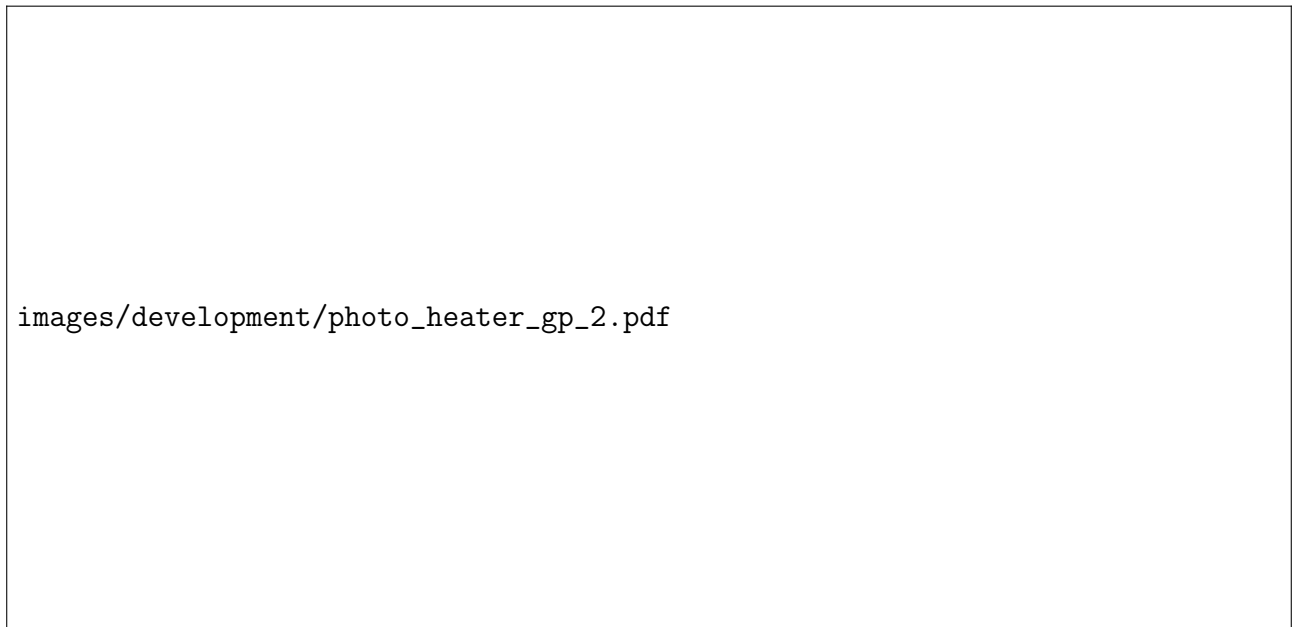


Figure 3.35: Photograph of a 150 W cartridge heater

An issue that was noted during initial testing was the build-up of limescale on the heaters, as shown in Figure 3.36. This level of limescale build-up resulted from several weeks of thermal testing, using filtered tap-water as the cell fluid. For thermal testing of low-permeability clays such as bentonite, test durations of several months are required, and further limescale build-up could reduce the capacity and service life of the heaters. For all subsequent thermal tests, purified reverse-osmosis (RO) water was used. For thermal testing in hard-water areas such as London, the use of RO water is recommended, rather than filtered tap-water.

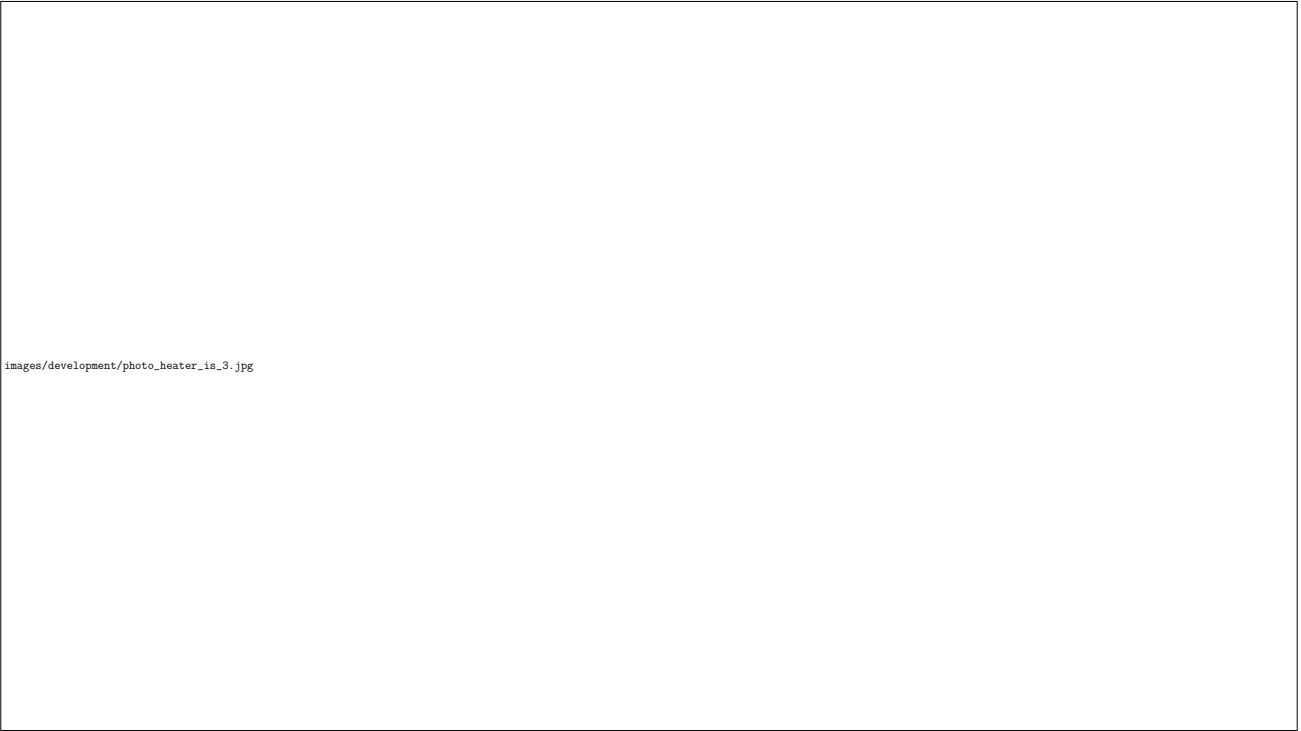


Figure 3.36: Photograph of limescale build-up on the heaters

3.5.6 Chiller

The chiller is a K1 type, manufactured by Applied Thermal Control (ATC), and shown in Figure 3.28. It has a 1750 W cooling capacity. It can control temperature in the range 4 °C to 35 °C, although in the current set-up it is used to control temperatures between 5 °C and 22.5 °C. The temperature stability is ± 0.1 °C. The target temperature is input manually, using a keypad on the chiller unit. The chiller fluid is in a closed-loop - it does not circulate through the oedometer. Heat is transferred using a purpose-built heat exchanger.

The chiller fluid has to be circulated at relatively high pressure. However, high pressure circulation of water through the oedometer is not desirable, since it may affect the measurement of displacement by moving the LVDT extension pieces. Instead, two closed-loop systems interact via a heat exchanger. One system includes the oedometer cell, and is heated by the three 150 W cartridge heaters. The other system includes the chiller. In both systems, the water is continuously circulated.

3.6 Ambient temperature oedometer

A second oedometer has been set up to perform ambient temperature tests, to obtain data that can be compared with that obtained from the temperature-controlled oedometer.

A brief description of this oedometer is given here, for completeness. The confining ring, and top-cap, are identical to those used in the TC oedometer. There is no water bath, and no method of temperature control. However, the laboratory temperature is controlled. Displacement is measured using three spring-return strain-gauge displacement sensors, with 25 mm travel, calibrated using a micrometer. These are mounted on a PVC plate below the load cell, which

is similar to the instrumentation plate in the TC oedometer. The load cell is an Imperial College type load cell, calibrated using a dead weight calibrator. Load is applied using a Type D double-acting diaphragm air cylinder, manufactured by Bellofram. The ram pressure is controlled using TRIAX software. Displacement cannot be directly controlled, as in the TC oedometer. In this manner, it functions more like a conventional dead-weight oedometer. However, displacement can be indirectly controlled by reactive, automated adjustment of the ram pressure, through TRIAX.

3.7 Summary

A new temperature-controlled oedometer has been designed and built. A water bath is used to indirectly heat the soil specimen. This method was chosen, rather than direct heating, as it enables sub-ambient temperature tests to be performed, which are relevant to the design of ground source heat pumps (GSHPs) and energy foundations. With indirect heating, temperature changes are slower, which improves temperature stability, and results in smaller temperature gradients across the specimen. The specimen can be isolated from the water in the bath, which means that tests can be carried out under dry or unsaturated conditions, or with controlled back-pressure.

The water in the bath is circulated, using a pump, through a hollow plate directly below the specimen. This ensures that the specimen is heated isotropically. This is the first oedometer to heat the specimen from all directions, and is an advantage over previous schemes which have instead used base-insulation to reduce temperature gradients across the soil specimen. The temperature gradient across the cell has been measured with temperature sensors positioned within the water bath, and directly below the specimen, and found to be $<0.5\text{ }^{\circ}\text{C}$ for a water bath temperature of $70\text{ }^{\circ}\text{C}$.

Three cartridge heaters, within brass housings, are used to heat the water bath. For sub-ambient temperatures, a chiller unit and custom-built heat exchanger are used to cool the continuously circulating water. Temperature is measured with three temperature sensors.

Load is applied using an electronic load frame, and measured with a load cell. Displacement is measured using three LVDTs mounted on an instrumentation plate below the load cell. For accurate height (and volume) measurement, and to understand tilting effects, at least three LVDTs are required, unless mounted directly above the centre of the specimen. This three-LVDT system is therefore a potential improvement over previous schemes which have used less than three non-centrally mounted displacement transducers.

To avoid temperature effects on the displacement transducers and load cell, all instrumentation (except the temperature sensors) is fully isolated from the water bath, and remains at ambient temperature during thermal testing. This improves the accuracy of the measured values, and avoids the complex hysteretic responses associated with direct temperature effects on instrumentation. Extension pieces, which incorporate heat dissipators, are connected to the LVDT cores so that displacement can be measured from the confining ring, which is more reliable than measuring displacement far away from the specimen. The vertical thermal compliance must be measured to account for the change in length of components subjected to temperature change, such as the LVDT extension pieces, and the lower section of the loading ram.

The maximum vertical pressure that can be applied using the oedometer in its current set-up is 2.6 MPa . This is limited by the 10 kN load cell. If additional capacity is required, the STALC-3

load cell (Section 3.5.2) comes in capacities up to 100 kN (26 MPa), which is the limit of the load frame (Section 3.5.1). The temperature range is 5 °C to 70 °C. The lower limit is determined by the capacity of the chiller unit (Section 3.5.6), and to avoid the additional complication of freezing of the pore-water. The upper limit is determined by the softening of the PVC-U water bath and lid at temperatures above 70 °C. If higher temperature is required, the PVC-U can be replaced with a material less susceptible to thermal softening, such as PVC-C. This change would not affect the equipment calibration. Heating power can be increased by replacing the 150 W cartridge heaters with higher power equivalents, or increasing the number of heaters, although it is possible to reach temperatures of at least 85 °C with the three heaters currently in place. Up to 12 heaters can be installed, if required. The specimen dimensions are 70 mm diameter, and up to 50 mm height.

Chapter 4

Calibration

4.1 Introduction

This thesis relates primarily to the development of a new piece of equipment. Calibration of this equipment has been the most complex part of the development process. As discussed in the literature review, Section 2.3, accurate calibration is an integral component of equipment development. In a scheme using standard equipment, perhaps even used in a novel way, the focus is generally on soil behaviour, rather than equipment development. For such a scheme, it would be possible to divide the thesis into independent, roughly chronological sections: calibration, testing, results, discussion. However, that is not possible in this case. A chronological treatment of the calibration and testing process would perhaps have been the easiest story to write, but certainly the hardest to read. The narrative of equipment development does not divide nearly so neatly as the standard story of testing soil behaviour.

In fact, the development process is iterative, rather than linear. Good ideas and bad ideas (unfortunately, for the researcher) do not come with a label. They have to be tested. The calibration tests discussed in this chapter were carried out in some cases before the soil tests discussed in subsequent chapters, in some cases concurrently. For example, a combined thermal and mechanical compliance was developed (Section 4.4), which was initially applied to data from tests on bentonite (Chapter 5) and later to tests on sand (Chapter 6). Based on the results of the sand tests, a new calibration was developed, which was also applied to the sand test data, and compared with the first calibration. More calibration tests were performed, and more soil tests. The limitation of the chronological treatment is that describing the development process in order would require that sections skip back and forth, between calibration and soil testing.

Within this chapter, the effect of filter papers and porous stones (Section 4.5) is presented in a separate section to thermal and mechanical deformation (Section 4.4). However, that is not to say that the tests discussed in Section 4.4 take no account of the effect of filter papers and porous stones. Similarly, the tests on bentonite and sand, discussed in Chapters 5 and 6, led to modifications and improvements in the calibration procedure and test methodology, which are discussed in this chapter. The standard distinction of calibration, testing, results and discussion is not appropriate here. Both chapters, together with this one, can be considered as a combination of all of these components of the development process.

In this chapter, the key issues relating to calibration of the new equipment are discussed. These are: friction, tilting, vertical thermal and mechanical deformation, effect of filter papers and porous stones, lateral thermal and mechanical deformation, and finally, void ratio. Soil

testing, conducted in large part concurrently to the calibration process, is discussed in Chapter 5 (bentonite) and Chapter 6 (sand).

4.2 Friction

There are several issues relating to friction in oedometer testing, as also discussed in Mantikos (2018). For consolidation tests, where the top-cap is moving down (Figure 4.1a), friction shifts the normal-consolidation line (NCL) to the right (higher pressure is required to reach the same void ratio). For swelling (wetting) tests, where the top-cap is moving up, or is being pushed up (Figure 4.1b), friction reduces the measured vertical strain (under constant pressure conditions), or reduces the measured vertical pressure (under constant volume conditions). Finally, load values lower than the frictional resistance may not get applied to the soil. This is most important at the start of the test. These are all sources of error.

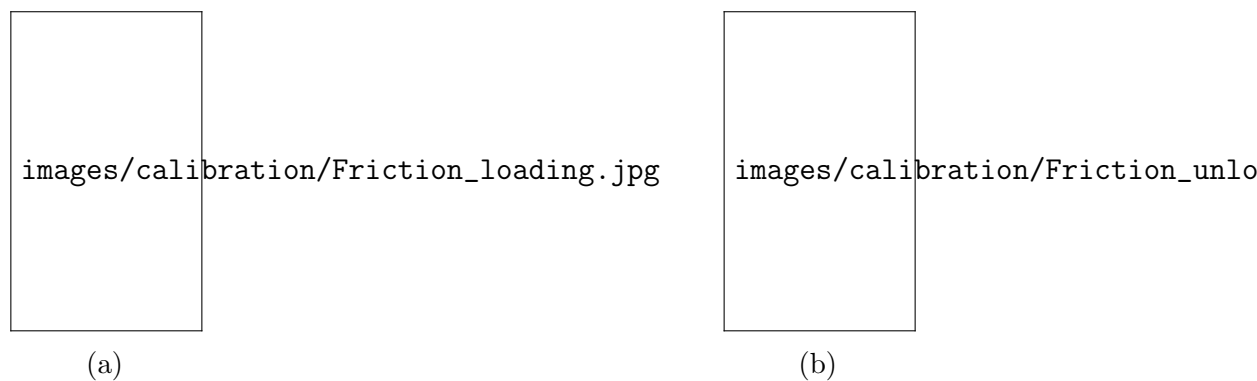


Figure 4.1: Friction effects during (a) consolidation tests - top-cap moving down (b) swelling (wetting) or unloading tests - top-cap moving up

In the temperature-controlled (TC) oedometer, there are two sources of friction. The first is friction between the o-ring on the top-cap, and the inner surface of the confining ring. This has been measured using the tests described below. Friction between the top-cap o-ring and confining ring does not affect the soil directly, but does affect the measurement of its behaviour and properties. The second is friction between the side of the soil specimen and the inner surface of the confining ring. This component is difficult to measure. Its value changes during the test, as the soil condition and properties, such as height and water content, change. The relatively large diameter (70 mm) of the confining ring was chosen to minimise, as far as practicable, this component of friction, relative to the total resistance. The total resistance is a function of the specimen area ($f(d^2)$), whereas the side friction is a function of the specimen circumference only ($f(d)$), so increasing the confining ring diameter reduces the relative contribution of side-friction to the total resistance. For this reason too, the inner surface of the confining ring is lubricated with high-vacuum grease before installing the soil specimen.

In this section, two series of tests are discussed, which were used to quantify the friction between the o-ring on the top-cap, and the inner surface of the confining ring. When discussing these tests, some terms are used that could imply the presence of a soil specimen - loading, unloading, and equivalent pressure. However, in these tests, there is no specimen in position. Downward displacement of the top-cap relative to the confining ring (Figure 4.1a) is referred to as *loading*. Upward displacement of the top-cap relative to the confining ring (Figure 4.1b) is referred to as

unloading. The term *equivalent pressure*, given in units of kPa, is used to quantify the frictional resistance. This is the force (in N) divided by the specimen cross-sectional area. Equivalent pressure, rather than force, is used so that the frictional resistance can be more easily compared to applied pressures from soil tests, which are also given in kPa.

A schematic showing the top-cap with o-ring is given in Figure 4.2. There is a small gap (slightly exaggerated, for clarity, in the figure) between the top-cap and the confining ring, which allows the top-cap to move freely up and down, without sticking. The confining ring internal diameter is ≈ 0.4 mm larger than the top-cap diameter, which means there is a gap of ≈ 0.2 mm between the two. To prevent direct contact between the top-cap and confining ring, a small, straight-sided groove has been cut into the top-cap, near the base, in which sits an o-ring. The o-ring has two purposes. The first, is to provide a seal, allowing the specimen to be isolated from the water bath. This is important when performing relative-humidity controlled suction tests, as in Mantikos (2018), or when applying a back-pressure to the specimen. The addition of relative-humidity control, and back-pressure control, are proposed future modifications to the equipment. The seal also prevents soil slurry from squeezing into the cap between the top-cap and confining ring during consolidation tests. The second purpose is to guide the top-cap through the confining ring, maintaining verticality and avoiding sticking due to metal-on-metal contact. The o-ring protrudes slightly more than 0.2 mm, enough to maintain a hydraulic seal, whilst minimising friction.

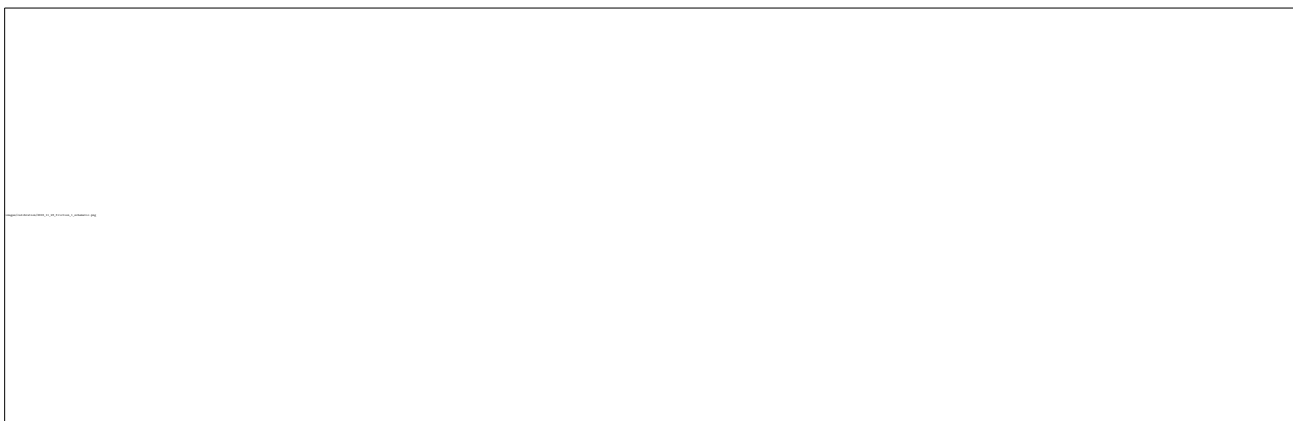


Figure 4.2: Schematic of the confining ring showing o-ring seal

In the first series of tests performed to measure friction between the o-ring and the confining ring, fixed-rate relative displacements were applied, with no specimen in position. Three displacement rates, of 2 mm min^{-1} , 1 mm min^{-1} and 0.05 mm min^{-1} , were tested, for movement in either direction (i.e. up or down). Two tests were performed, one with clean, dry equipment, and a second where the inner surface of the confining ring, and the o-ring itself were lightly coated with high vacuum grease for lubrication. For the first case (no grease) a frictional resistance of 110 N (29 kPa equivalent pressure) was measured, which was not strongly dependent on the displacement rate. For the second case (lightly greased), the frictional resistance was a maximum of 40 N (10 kPa equivalent pressure) for a displacement rate of 0.05 mm min^{-1} . Applying grease reduced the frictional resistance by approximately a factor of three.

A second series of tests was performed, following modification of the equipment to reduce friction. The o-ring groove was made slightly deeper, with the aim of reducing the friction, while still maintaining a hydraulic seal. The methodology followed in these tests was similar to the first series, with one un-greased case, and one greased case, although different displacement rates were

used: 5 mm min^{-1} , 0.1 mm min^{-1} , 0.05 mm min^{-1} and 0.01 mm min^{-1} . The 5 mm min^{-1} rate was chosen for convenience. At the start of the test the top-cap has to displace $\approx 20 \text{ mm}$ to pass the confining ring collar, fully into the confining ring (see Figure 4.2). This is the case for all tests in the temperature-controlled oedometer, so the initial fast rate accurately simulates test conditions. Except for setting up the initial condition, this fast rate is not used during soil consolidation tests. The 0.1 mm min^{-1} and 0.05 mm min^{-1} rates were chosen to enable comparison with the previous series of friction tests. The 0.01 mm min^{-1} rate corresponds to the maximum displacement rate used in the consolidation tests. Results for the second series of tests are discussed in more detail below.

Results for test 1 (no grease) are shown in Figure 4.3. These two figures show the total displacement (Y1 axis), and displacement rate (Y2 axis), over time. Each rate was maintained for five minutes in each direction, and the direction of loading was reversed when changing to a new rate. The full test is shown in Figure 4.3a, with the slow rates only in Figure 4.3b.

Combined results for tests 1 and 2 are shown in Figure 4.4. The friction is given in terms of equivalent pressure, against displacement rate. Positive displacement rates correspond to loading (top-cap moving down relative to the confining ring), and negative rates to unloading. Only the slow rates (0.1 mm min^{-1} , 0.05 mm min^{-1} and 0.01 mm min^{-1}) are shown in this figure. For loading at 0.1 mm min^{-1} , the friction is $\approx 15 \text{ kPa}$ for test 1 (no grease), and $\approx 5 \text{ kPa}$ for test 2 (greased). As with the first series of tests, it seems that applying grease reduces the friction by about a factor of three. For unloading, at the same rate, the friction reduces to $\approx 1 \text{ kPa}$ for both cases. The relatively high friction for the first loading case may be because this loading immediately followed the fast rate of 5 mm min^{-1} . It seems that the friction due to displacement at the fast rate is locked in, and affects the subsequent stage. There is a slight drift in the results, which is upwards (towards positive friction values) for loading, and downwards (towards negative friction values) for unloading. The friction for loading and unloading at 0.05 mm min^{-1} is not significantly lower than for the unloading stage at 0.1 mm min^{-1} ($2\times$ slower). However, the friction for loading and unloading at 0.01 mm min^{-1} ($10\times$ slower) is noticeably lower, less than 1 kPa . This rate corresponds to the maximum used in consolidation tests. From this test, it appears that friction reduces with reduced displacement rate. This friction value therefore can be considered as the upper-bound value for consolidation tests. The modification to the top-cap o-ring groove appears to have reduced the friction by an order of magnitude, from $\approx 10 \text{ kPa}$ (in the first series of tests) to $< 1 \text{ kPa}$. At such a low value, the friction can be considered negligible, except at the start of a test.

Based on the second series of tests, it can be concluded that the magnitude of the frictional resistance reduces at lower displacement rates. This was not clearly observed in the first series of tests because the direction of loading was not reversed when changing rates. At a displacement rate corresponding to the maximum rate used in consolidation tests, 0.01 mm min^{-1} , the friction, as an equivalent pressure, is $< 1 \text{ kPa}$. However, this does not agree with the behaviour observed during subsequent tests, for example, the tests on sand (Chapter 6). These tests showed that the effect of friction is not negligible, that it is complex, and cannot be accounted for with a single correction. Since any correction would be, at best, an educated guess, no correction has been applied, and the potential effect of friction on results is considered for all tests.

An example of this complexity is given in Figure 4.5. This shows a hypothetical test in which the friction is 10 kPa for the loading and unloading rate applied. The pressure is increased from 0 kPa to 50 kPa , reduced to 10 kPa , then -10 kPa , and finally increased again to 50 kPa . Three results are plotted: the measured (or controlled) pressure, the friction (in terms of equivalent pressure), and the pressure that is actually applied to, or felt by, the soil. The measured pressure

images/calibration/2018_11_26_friction_test_1_full.pdf

(a)

images/calibration/2018_11_26_friction_test_1_slow.pdf

(b)

Figure 4.3: Friction test 1 - effect of displacement rate - displacement (Y1) & rate of displacement (Y2) vs time for (i) full test and (ii) slow rates only

images/calibration/2018_11_26_friction_combined.pdf

Figure 4.4: Friction tests 1 & 2 - effect of applying grease

would be the pressure calculated from the load measured by the oedometer load cell. The soil will undergo compression only when the pressure felt by the soil increases (or extension, when the applied pressure reduces).

At the start of the first loading stage, as the measured pressure increases from 0 kPa to 10 kPa, the pressure felt by the soil remains at zero. The magnitude of friction increases (in the opposite direction to the measured pressure) until it reaches its maximum (negative) value of -10 kPa. Measured pressure and friction are balanced. Compression of the soil only begins when the measured pressure is greater than the maximum friction value.

As the measured pressure increases from 10 kPa to 50 kPa, the pressure felt by the soil increases from 0 kPa to 40 kPa, while the friction stays constant at -10 kPa, resulting in compression of the soil.

At the start of the unloading stage, as the measured pressure reduces from 50 kPa to 30 kPa, the direction of friction reverses, going from -10 kPa (acting upwards, as in Figure 4.1a) to 10 kPa (acting downwards, as in Figure 4.1b). The pressure felt by the soil remains constant until the friction has reached its maximum value in the opposite direction. Then, as the measured pressure reduces from 30 kPa to 10 kPa, the pressure felt by the soil reduces from 40 kPa to 20 kPa.

As the measured pressure reduces from 10 kPa to 0 kPa, the pressure felt by the soil reduces from 20 kPa to 10 kPa. So the soil still feels a positive pressure, under zero measured pressure. The soil continues to feel a positive pressure until the measured pressure reduces to -10 kPa, at which point, the pressure felt by the soil is zero.

At the start of the reloading stage, as the measured pressure increases from -10 kPa to 10 kPa, the direction of friction reverses, going from 10 kPa (acting downwards, as in Figure 4.1b) to -10 kPa (acting upwards, as in Figure 4.1a). The pressure felt by the soil does not change

images/calibration/Friction_example_graph.pdf

Figure 4.5: Hypothetical test with friction (equivalent pressure) of 10 kPa

until the friction has reached its maximum (negative) value of -10 kPa. Then, as the measured pressure increases from 10 kPa to 50 kPa, the pressure felt by the soil increases from 0 kPa to 40 kPa.

Generally, during loading stages, the pressure felt by the soil is lower than the measured pressure. The direction of displacement is downwards (positive, compression), and friction acts in the opposite direction, upwards (negative). During unloading, the pressure felt by the soil is higher than the measured pressure. The direction of displacement is upwards (negative, extension), and friction acts in the opposite direction, downwards (positive). The exceptions to this general case are (i) initial loading, and (ii) following a change in the direction of loading (from loading to unloading, or vice-versa). For initial loading, there is no increase in the pressure felt by the soil until the measured pressure is greater than the maximum friction value. For a change from loading to unloading, or vice-versa, the friction direction reverses, and there is no change in the pressure felt by the soil until the friction again reaches a maximum.

For a measured pressure of 10 kPa, the pressure felt by the soil may be zero (initial loading) or 20 kPa (unloading). During initial loading, an increase in measured pressure of 10 kPa from 0 kPa to 10 kPa will not change the pressure felt by the soil, but an increase of the same magnitude, from 10 kPa to 20 kPa, will increase the pressure felt by the soil by 10 kPa. This means that for the same value of measured pressure, the applied pressure may be different. It is not as simple as adding or subtracting the friction value from the measured pressure - the loading history needs to be considered.

There are additional factors to be taken into account. The friction depends on the displacement rate, but only following a change in the direction of movement. For example, in the second series of tests, reducing the loading rate resulted in a clear reduction in friction. In this case,

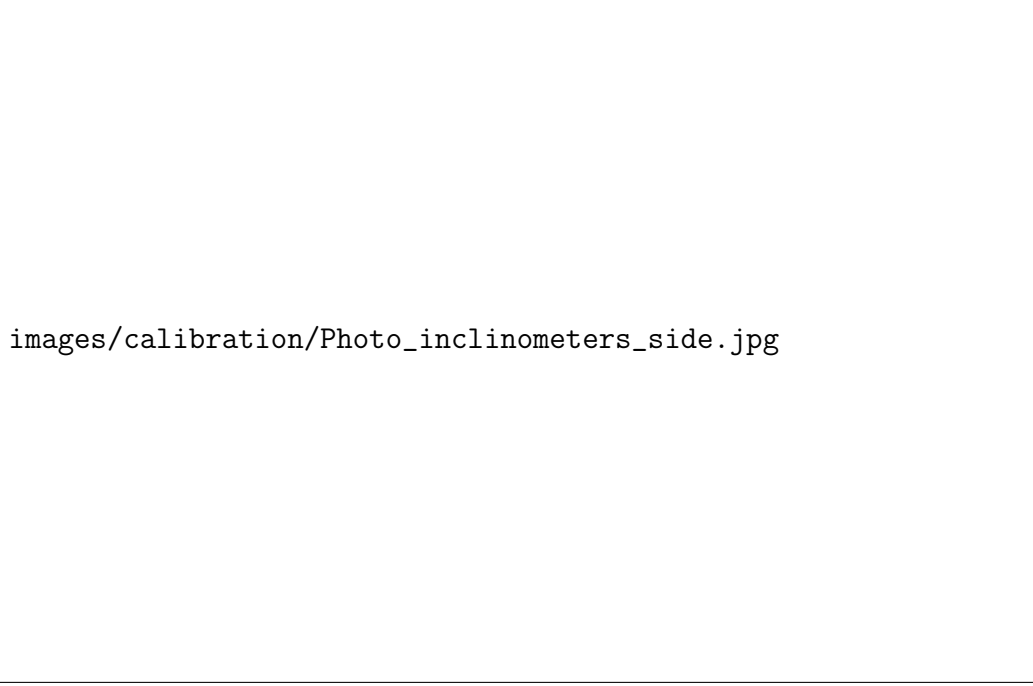
the new loading was applied in the opposite direction to the previous loading. However, in the first series of tests, reducing the loading rate did not result in a clear reduction in friction. In this case, the new loading was applied in the same direction to the previous loading. This is especially important when setting up and starting a new test. The loading ram is initially moved down at a fast rate ($>5 \text{ mm min}^{-1}$), to bring the top-cap (almost) into contact with the upper porous stone. This appears to *lock in* a certain amount of friction. Changing direction, then reloading is not possible because this would move the top-cap away from the specimen. This means that consolidation of the soil does not begin until a relatively high ($\approx 10 \text{ kPa}$) value of friction is overcome. The same issue is not encountered when unloading to low pressures since the pressure applied to the soil is higher than the measured pressure.

4.3 Tilting

Tilting of the loading ram, or top-cap (which is rigidly connected to the bottom of the loading ram) is an issue with this equipment (although by no means unique to this equipment) previously identified by Mantikos (2018). For conventional oedometers, this is not generally an issue, since displacement is measured directly above the centre of the top-cap. This means that even if the top-cap tilts, the volume measurement will still be accurate. However, with this oedometer, and several other temperature-controlled oedometers from the literature, displacement is measured at a point away from the centre of the top-cap. This could lead to an inaccurate calculation of specimen volume. Tilting can be reduced by minimising the length of the loading ram, or guiding it (for example, using a linear ball bushing, as in Vega and McCartney (2015)). However, even with these improvements, the amount of tilt (negligible or otherwise) cannot be known unless multiple displacement transducers are used in combination. A minimum of two displacement transducers, positioned equidistant and opposite sides of the specimen, is necessary for accurate volume calculation, and a minimum of three are required to measure tilting effects. In the temperature-controlled oedometer, three linear variable displacement transducers (LVDTs) are used. By positioning the LVDTs at 120° intervals (i.e. equally spaced), the correct displacement can be found simply by taking the average value. The calculation confirming this assertion is given in Appendix G. Building on the work of Mantikos (2018), further tests were performed. The aim of these tests was to understand the tilting behaviour more fully, and validate the results of tests carried out using this arrangement of displacement transducers.

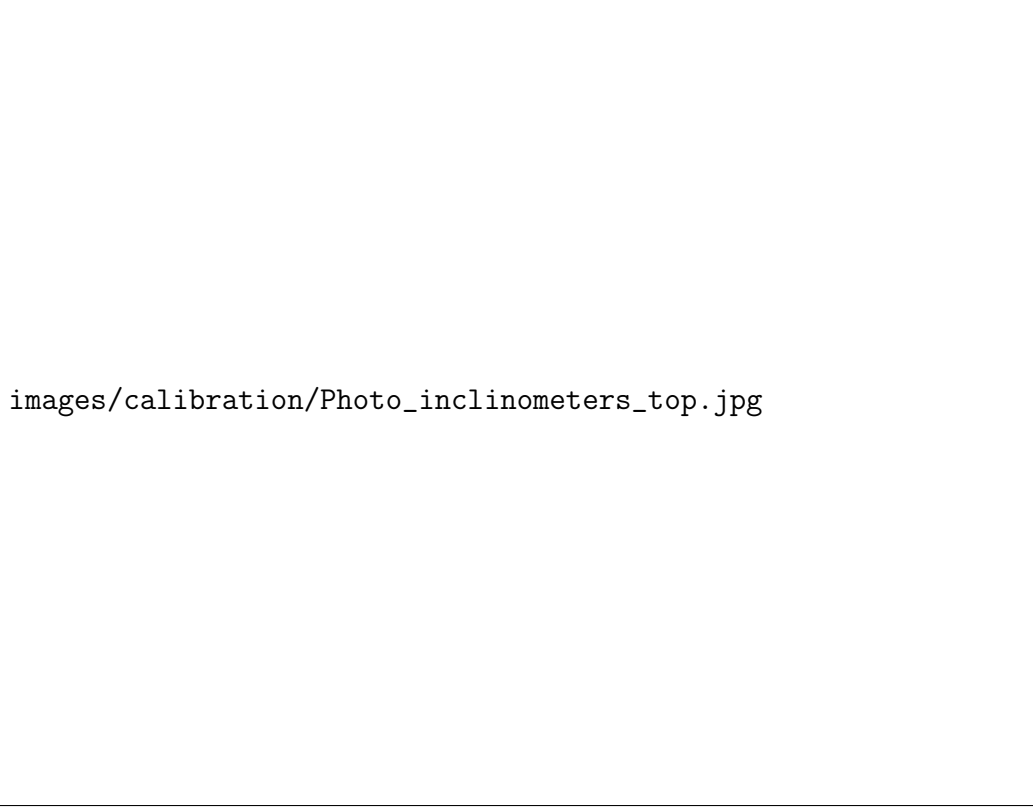
In the first set of tests, a pair of inclinometers, or tilt-sensors, was mounted on the instrumentation plate, below the load cell, as shown in the photographs given in Figure 4.6. The inclinometers used were three-pin electrolytic tilt-sensors (electrolevels), as shown schematically in Figure 4.7. They consist of a glass capsule, containing an electrolyte solution (iodine), which is able to conduct electricity. Three co-planar electrodes protrude into the capsule and are partially immersed in the electrolyte solution. An alternating current (AC) is applied, and the impedance (resistance) between the central and outer electrodes varies as the inclinometer tilts. The output is amplified and demodulated to produce a direct current (DC) output. The two inclinometers are mounted perpendicularly to each other, as shown in Figure 4.8. In this configuration, tilting forward corresponds to a positive output for the inclinometer labelled *Inc 1*, and tilting to the right corresponds to a positive output for the inclinometer labelled *Inc 2*.

In each test, a load cycle was applied at ambient temperature, increasing the load from a nominal value to a maximum of 9.62 kN (2500 kPa equivalent pressure), before unloading fully. The tests were performed with the instrumentation plate either in the high position (close to the load



images/calibration/Photo_inclinometers_side.jpg

(a)



images/calibration/Photo_inclinometers_top.jpg

(b)

Figure 4.6: Photographs of the two inclinometers used to investigate tilting of the loading ram
(a) view from side and (b) view from top



Figure 4.7: Schematic of an inclinometer (tilt-sensor)

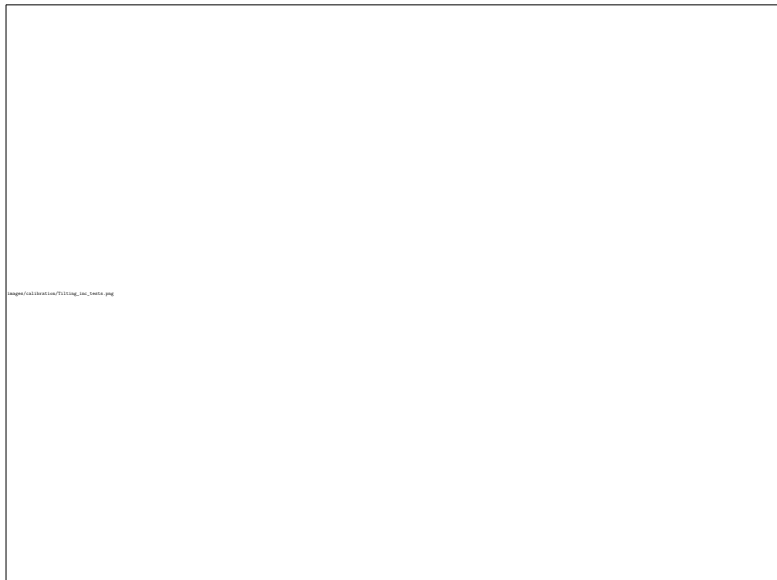


Figure 4.8: Schematic plan view of the instrumentation plate showing inclinometer set-up for first set of tilting tests

cell) or low position (close to the confining ring), as shown in Figure 4.9a. For the low position, the LVDT extension legs were not used. A dummy specimen comprising two vertically stacked, 15 mm thick, brass cylindrical discs was used for all tests. Eight tests were performed in total, comprising four pairs of tests - one for the high position and one for the low position. In the first pair of tests, the o-ring on the top-cap was removed. For all subsequent tests, the o-ring was kept in place on the top-cap. The second, third, and fourth pair of tests were similar, except for the orientation of the instrumentation plate. In the second pair of tests, it was orientated exactly as shown in Figure 4.8. For the third pair of tests, the instrumentation plate was rotated 60° to the left (anticlockwise). For the fourth pair of tests, the instrumentation plate was rotated 60° to the right (clockwise). This was to show that the results obtained were not dependent on the position of the instrumentation (inclinometers and LVDTs).

The results for all eight tests are summarised in Figure 4.9b. The position (high or low) of the instrumentation plate does seem to have an effect on the direction and magnitude of tilting. Results for the low position consistently show a higher degree of tilting than for the high position. This rules out the idea that the observed tilting is due to the LVDT extension legs. The direction of tilting too, is affected by the position of the instrumentation plate, with tests in the low position tilting more directly forwards. The tests performed with the instrumentation plate rotated left or right showed good agreement with the other tests, confirming that the observed tilt is not an error to do with calibration of the instrumentation. There was no significant difference between the results for the first pair of tests (without o-ring in place) and subsequent tests (with o-ring in place). This is not surprising, since the o-ring is made of rubber, and therefore highly compressible. The o-ring is not able to prevent tilting when loading a stiff specimen, where the load is high and the displacement is low. Instead, the o-ring can guide the top-cap through the confining ring, for conditions where the load is low, or zero, and displacement is high (for example, setting up the initial condition, or during the early consolidation stages for a slurry).

In the second set of tests, in addition to the two inclinometers, two horizontally-inclined LVDTs were used. These were mounted on boss-heads clamped to vertically-orientated, threaded rods, fixed rigidly to the oedometer base-plate. They were positioned to measure lateral displacement of the load cell, as shown in the photograph in Figure 4.10. The inclinometers and horizontal LVDTs were orientated as shown in the schematic in Figure 4.11. (Note, the instrumentation plate is shown, but the LVDTs were actually positioned to read horizontal displacement of the load cell.) In this configuration, tilting forward corresponds to a positive output for the inclinometer labelled *Inc 1*, and negative output for the horizontally-inclined LVDT labelled *D5*. Tilting to the right corresponds to a positive output for the inclinometer labelled *Inc 2*, and positive output for the horizontally-inclined LVDT labelled *D6*.

Three tests were performed. In the first test, a loading cycle of $0 \rightarrow 9.62 \rightarrow 0.1$ kN was applied. In the second test, a cycle of $0 \rightarrow 5 \rightarrow 0.1 \rightarrow 9.62 \rightarrow 0.1$ kN was applied. In the third test, a cycle of $0 \rightarrow 9.62 \rightarrow 2 \rightarrow 9.62 \rightarrow 2$ kN was applied.

Only the results for the third test are discussed, although the results for all three tests are in good agreement. The vertical displacements, measured with the three vertically-inclined LVDTs labelled D1, D2 and D3, are given in Figure 4.12. There is significant difference between the results for the three LVDTs. At the maximum load, there is a range of 0.23 mm between the results, with D2 highest (0.29 mm), then D3 (0.21 mm), and D1 lowest (0.06 mm). The magnitude of this range is not necessarily an issue, since the volume can be calculated accurately, given the three values. The aim of this test is to check that these displacements are accurate, despite their differences. Based on this result, with reference to the set-up of the instrumentation plate in Figure 4.11, it seems that the plate is tilting forwards (since D2 is the highest value),



(a)



(b)

Figure 4.9: Tilting tests (a) set-up, high and low instrumentation plate position (b) direction and relative magnitude of tilting for each test based on inclinometer data

and to the left (since D_3 is greater than D_1). The results for the inclinometers and horizontal LVDTs can be used to confirm the results for the vertical LVDTs. These results suggest that the instrumentation plate is tilting forwards and to the left (agreeing with the results from the first set of tests, shown in Figure 4.9b). For the inclinometer results, this suggests that Inc 1 should be positive, and Inc 2 should be negative.

The inclinometer results are given in Figure 4.13. As expected, Inc 1 is positive (tilting forwards) and Inc 2 is negative (tilting to the left). Note that only qualitative results are shown. For a positive Inc 1 value, it is expected that D_5 should be negative. Likewise, based on a negative Inc 2 value, it is expected that D_6 should also be negative. This is shown schematically in Figure 4.14. Since Inc 2 was more strongly negative than Inc 1 was positive, it is expected that D_6 will be more negative than D_5 . The measured horizontal displacements are given in Figure 4.15. Again, the results are as expected. Both horizontal LVDTs show negative displacements. Interestingly, the horizontal LVDTs show a hysteresis that is not observed for the vertical LVDTs or the inclinometers. All three methods of tilt measurement (comparison of vertical LVDT values, inclinometers, horizontal LVDTs) give the same qualitative result, which strongly suggests that the vertical LVDT results are correct.



images/calibration/Photo_horizontal_lvdtts.jpg

Figure 4.10: Photograph of the two horizontally aligned displacement transducers

Tilting of the loading ram is a potentially significant source of error in a novel oedometer. The key point is that if displacement is not measured directly above the centre of the specimen, a minimum of three equally-spaced LVDTs are necessary for accurate measurement of specimen height (and volume), and to measure tilting effects. In this case also, tilt has been minimised by reducing, as much as possible, the length of the loading ram (see Chapter 3), and by carefully checking the verticality of the loading ram prior to testing.



Figure 4.11: Schematic plan view of the instrumentation plate showing inclinometer and horizontal LVDT set-up for second set of tilting tests

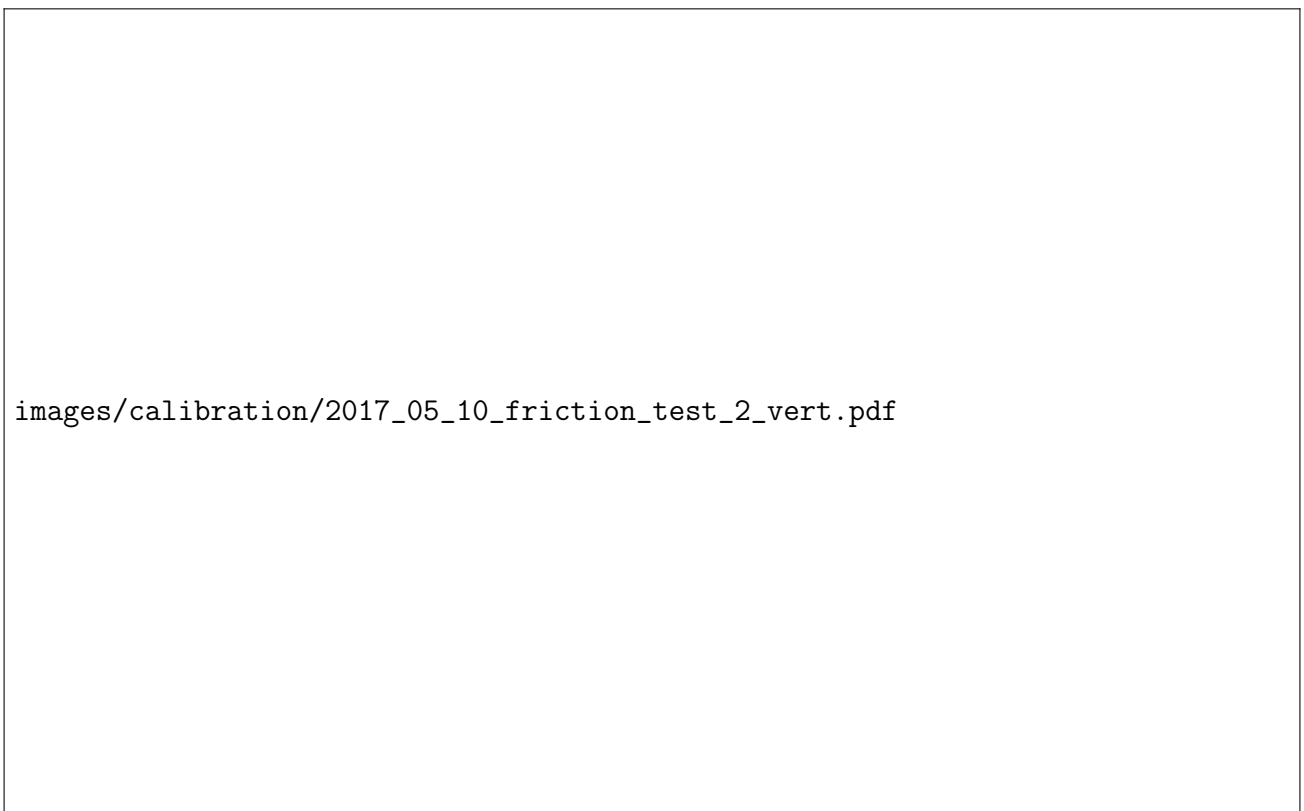


Figure 4.12: Tilting tests - vertical displacement

images/calibration/2017_05_10_friction_test_2_incl.pdf

Figure 4.13: Tilting tests - inclinometer results

images/calibration/tilt_d5.pdf

(a)

images/calibration/tilt_d6.pdf

(b)

Figure 4.14: Tilting tests - schematic of top-cap movement based on inclinometer and horizontally aligned displacement transducer data (a) Inc 1 and D5 (b) Inc 2 and D6

images/calibration/2017_05_10_friction_test_2_horiz.pdf

Figure 4.15: Tilting tests - horizontal displacement

4.4 Vertical thermal and mechanical deformation

In this section, calibration of the thermal and mechanical deformation of the equipment is covered. As discussed in the calibration section of the literature review (Section 2.3), temperature has four measurable effects on the apparatus. These are as follows:

1. Vertical (thermally-induced) deformation of the apparatus
2. Change in the isothermal mechanical response due to loading at different temperatures
3. Direct effect of temperature on instrumentation
4. Radial (thermally-induced) deformation of the confining ring

The vertical (thermally-induced) deformation of the apparatus refers to the vertical displacement of the apparatus due to temperature change at constant pressure. The term *apparatus* refers to the equipment itself, and any other components used during testing including porous stones and filter papers (if used), but not including the soil specimen. The use of filter papers causes a number of issues. Those directly relating to the tests below are discussed in this section. A range of tests focused specifically on the use of filter papers were performed - these are discussed in Section 4.5. The change in the isothermal mechanical response due to loading at different temperatures refers to the effect of temperature on the mechanical response. Both of these effects have been investigated and measured in the tests described below.

The direct effect of temperature on the instrumentation refers to the effect temperature has on the instrumentation itself. This is almost impossible to quantify, and was the primary motive behind the decision to isolate the instrumentation from the heat source, as discussed in

Section 3.3. Isolating the instrumentation in this way avoids the need for thermal calibration of the instrumentation - only standard, ambient-temperature, calibration of the load cell and displacement transducers is required.

The radial (thermally-induced) deformation of the confining ring was not measured directly, but calculated based on the material properties of the confining ring. This calculation is given in Section 4.6.

4.4.1 Calibration - motivation and methodology

This section focuses on calibration test motivation, methodology, and results. The details of the application of this calibration data, to correct test data, are given in Chapter 5 (bentonite) and Chapter 6 (sand). Development of new equipment is an iterative process, quite unlike a programme of conventional testing. In conventional testing, it is standard good-practice to obtain all the necessary calibration data before starting any soil tests. The method for obtaining the calibration, and applying the correction to the test data, is generally well-understood. When developing new equipment, there are no standards to follow. The calibration methodology must be developed from the ground up. Therefore, issues with the obtained calibration may only become apparent once the correction has been applied to the test data. If the corrected data are not as expected, according to theory or based on results from the literature, this suggests an issue with one or more of: the calibration methodology, the testing methodology, the equipment itself, or (finally, once the other options are exhausted) the theory or results from the literature. In the tests discussed below, some issues were identified, but it was not clear, until tests were performed with soil, whether these issues would significantly affect the final results. The calibration tests discussed below were not used to obtain the calibration used in the final set of tests, on KSS, described in Chapter 8. However, they form an integral part of the iterative process of development and improvement of the calibration methodology. This thesis aims to be not just a description of the temperature-controlled oedometer in its final, commissioned state, but a discussion of how, and why, the equipment, and testing methodology, developed as it did.

The calibration process has three distinct parts. First, the calibration test is performed. This stage involves carrying out a test that simulates a soil test, with a dummy specimen replacing the soil specimen. Next, the data from the calibration test are interpreted. This involves fitting lines to the data. A degree of judgement is required for the data interpretation, since the derived calibration will directly affect the final result. A number of choices have to be made at this point. The full set of data may be used, or alternatively, sampled at specific points. The data have to be divided into regions which will have individual calibration equations (to give some examples: heating/cooling, loading/unloading, loading below 18.75 kPa/loading above 18.75 kPa). Different fits may be used - linear, polynomial (of different orders), logistical (sigmoid), among others. The final stage is to apply the calibration to the data. This stage is the least subjective, although it is important to check that the final result is sensible, and that the calibration has been implemented correctly. In this section, the first two stages are discussed: carrying out the calibration tests, and deriving calibrations from the test data. Application of the calibrations to soil test data, and further appraisal of the calibration accuracy is covered in Chapters 5 and 6.

In these tests, the effect of pressure on the thermal deformation of the equipment, and the effect of temperature on the mechanical deformation of the equipment was investigated. A schematic showing the thermal and mechanical deformation of the core components of the equipment is given in Figure 4.16. Referring to the figure, loading causes compression of the loading ram, top-cap, porous stones, and filter papers. This would be measured by the displacement transducers as a

positive displacement (compression), because the instrumentation plate moves down (the body of the LVDT moves down, relative to the core). Heating causes expansion of the loading ram, top-cap, and porous stones (the effect of heating on the filter papers is less clear). This would be measured by the displacement transducers as a negative displacement (extension), because the instrumentation plate moves up (the body of the LVDT moves up, relative to the core). However, heating also causes extension of the confining ring, and the LVDT extension legs. This would be measured by the displacement transducers as a positive displacement (compression), because the LVDT core moves up, into the LVDT body (equivalent to the instrumentation plate moving down). So heating causes equipment deformation that may be measured as positive, or negative, depending on the relative expansion of different components.

The measured thermal deformation will be affected by the pressure value, because the thermal extension of the confining ring and the LVDT extension leg is independent of pressure, whereas the thermal extension of the loading ram, top-cap and porous stones, is not. These interactions are too complex to model to the required accuracy. Instead, a series of thermal and mechanical paths are tested, and the displacement is measured directly. If the displacement is measured directly, for a thermal path at a given pressure, or a loading path at a given temperature, then it does not matter exactly how (and how much) each component contributes to the final displacement. The displacement value is all that is required, as long as the conditions (and therefore the results, it is assumed) of the calibration test can be repeated for tests using soil.

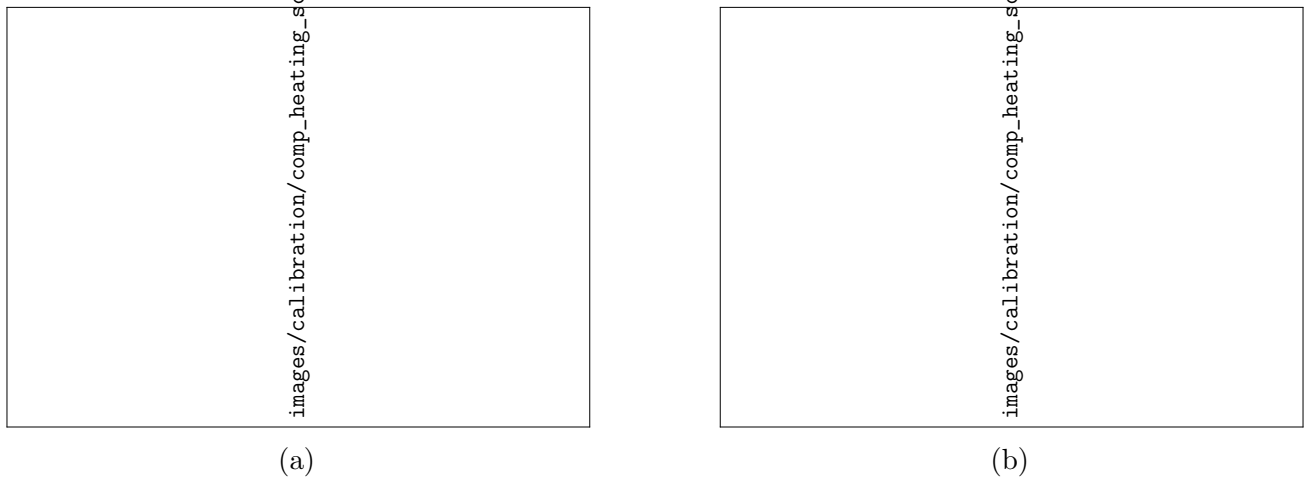


Figure 4.16: Schematic showing the effect of heating and loading on measured vertical displacement (a) thermal expansion and mechanical compression of equipment (b) measured response due to instrumentation plate moving up or down

The vertical thermal and mechanical deformation of the equipment can be measured by applying loading cycles at constant temperature (isothermal loading) or heating cycles at constant pressure (isobaric heating). When performing these calibration tests, without a soil specimen in place, the loading cycles can be performed quickly. However, the thermal cycles are time consuming. A single thermal cycle, comprising heating followed by cooling at the natural cooling rate, takes ≈ 48 h. For this reason, it would be useful to have a calibration that could be applied to any test using the same configuration of filter papers and porous stones (note, the issues with using filter papers are discussed in Section 4.5). This would substantially reduce total testing duration, and would simplify the application of the calibration, avoiding the need to fit a new series of calibration curves to each calibration test. The aim of the tests discussed in this section was to determine a single calibration that accounts for thermally-induced deformation (as a function of

pressure) and mechanical deformation (i.e. compliance, as a function of temperature), to give the total deformation as a function of pressure and temperature.

4.4.2 Calibration - tests 1A and 1B

Four tests were performed, using the temperature controlled oedometer. Tests 1A and 1B were a complementary pair of tests, performed to determine the combined calibration discussed above. Tests 2 and 3 were performed to determine thermally-induced deformation as a function of pressure. Test 2 used filter papers, whereas test 3 did not, following the conclusions of the filter paper tests discussed in Section 4.5, and sand tests discussed in Chapter 6.


Some key details of the four tests are summarised in Table 4.1. The *pre-load sequence* heading refers to a load/unload sequence performed before each test, or before each cycle, in order to mitigate the effects of filter paper compressibility. This is discussed in more detail below. In tests 1A, 1B, and 2, filter papers were used, but in test 3 they were not. In tests 1A and 1B, the o-ring was not installed on the top-cap, but in tests 2 and 3, it was. The rationale behind these decisions - when to apply the pre-load sequence, whether to use filter papers, or not, whether to use the top-cap o-ring, or not - is discussed in the sections that follow.

Table 4.1: Summary of combined thermal and mechanical compliance tests

Test	Description	Pre-load sequence	Filter papers?	Top-cap o-ring?
1A	Load/unload cycles at fixed temperatures (isothermal loading)	Before test	✓	✗
1B	Heat/cool cycles at fixed pressures (isobaric heating)	Before test	✓	✗
2	Isobaric heating	Before each cycle	✓	✓
3	Isobaric heating	Before each cycle	✗	✓

In test 1A, a series of load/unload cycles were performed at fixed temperatures. The test programme is shown in Figure 4.17 as a simplified flowchart. The load was applied at 30 min intervals, to the following target pressures: 2.5 kPa, 18.75 kPa, 37.5 kPa, 75 kPa, 150 kPa, 300 kPa, 600 kPa, 1200 kPa and 2400 kPa, and unloaded similarly from 2400 kPa to 2.5 kPa. Heating was applied at the maximum rate until the target temperature was reached, then held constant throughout the loading cycle. The target temperatures were 22.5 °C, 30 °C, 40 °C, 50 °C, 60 °C and 70 °C. Before testing, a pre-loading sequence was performed to pre-load the filter papers, to avoid the development of a large residual displacement in the first loading cycle. This pre-loading sequence comprised a series of load/unload cycles, between 2.5 kPa and 2400 kPa, at ambient temperature.

In test 1B, a series of heat/cool cycles were performed at fixed pressures. The test programme is shown in Figure 4.18 as a simplified flowchart. The heating was applied incrementally, to the




images/calibration/Flowchart_TC1.pdf

Figure 4.17: Calibration test 1A: simplified flowchart

following target temperatures: 22.5 °C, 30 °C, 40 °C, 50 °C, 60 °C and 70 °C, and cooled similarly from 70 °C to 22.5 °C. Following completion of the heat/cool cycle, pressure was increased until the target pressure was reached, then held constant throughout the next thermal cycle. The target pressures were 2.5 kPa, 37.5 kPa, 150 kPa, 600 kPa and 2400 kPa. The number of target pressure values in test 1B is less than the number of load/unload increments in test 1A. This was to save time, since each target pressure corresponds to a thermal cycle, and applying the thermal cycles is by far the most time consuming part of the test. As in test 1A, a filter-paper pre-loading sequence was performed before the main test.


The specimen set-up for tests 1A and 1B is shown in Figure 4.19. Two filter papers are placed between two porous stones. No dummy specimen is used. The o-ring on the top-cap has been removed, to minimise friction effects. Removing the o-ring means that the effect of friction is not included in the calibration obtained through this test, but has to be explicitly included as a correction to the measured data in a real test. The two calibrations (to the pressure value, due to friction, and to the displacement value, due to thermal and mechanical compliance) can be measured, and applied as corrections, separately. There is an issue with this approach though, which is that the calibration process is meant to determine known values, and compare them to measured values. In this case, it is known that when performing a real test with soil, the o-ring will be in place. It is also known that the friction due to the o-ring affects the obtained thermal and mechanical compliance. So whether or not to use the o-ring for the compliance test depends on the purpose of the test. If the purpose of the test is to determine the equipment compliance,



images/calibration/Flowchart_TC2.pdf

Figure 4.18: Calibration test 1B: simplified flowchart

independent from friction, then the o-ring should not be used. If the purpose of the test is to determine the equipment compliance, including frictional effects, then the o-ring should be used. Tests 1A and 1B were performed earlier in the research programme, when the individual and combined effects of different variables were relatively unknown, and obtaining the thermal and mechanical compliance independent of friction was valuable, so in these tests, the o-ring was removed. However, tests 2 and 3, performed later in the research programme, were performed with the direct and clear aim of obtaining the most accurate and applicable calibration, so in these tests, the o-ring was kept in place.



images/calibration/comp_FP_no_oring.jpg

Figure 4.19: Tests 1A and 1B: specimen set-up for calibration tests

The results for test 1A are given in Figure 4.20. Figure 4.20a is a 3D plot, and Figure 4.20b shows displacement against temperature. The effect of temperature is not so clear in Figure 4.20a, but some aspects of the response are worth discussing. The load/unload cycles at different temperatures result in a maximum displacement of approximately 0.25 mm. The loading and unloading paths show hysteresis, with the unloading path plotting above (i.e. at a higher displacement, for the same pressure) the loading path. The residual displacement following a load/unload cycle is not as high as might be expected for new, unused filter papers. This is because of the pre-loading sequence applied before the main test. There appears to be issues with the stability of pressure at low values, but this issue is exaggerated by the logarithmic pressure scale, and not considered to be significant.

Next, considering the response in Figure 4.20b, some potential temperature effects can be observed. The load/unload cycles at constant temperature are shown as vertical lines. The displacement at the maximum pressure, 2400 kPa, is independent of temperature. Note that in the first two cycles (at 22.5 °C and 30 °C), the target maximum pressure was not reached, so the maximum displacement is lower than for the other three cycles. However, for the four subsequent cycles, the maximum displacement is constant, and not varying either due to temperature or number of loading cycles.

The displacement, following heating, loading and unloading, increases with each cycle. This displacement can be split into components. Some of the displacement appears to be due to the direct effect of heating. Some of the displacement appears to be due to the residual displacement resulting from the load/unload cycles.

The residual displacement resulting from each load/unload cycle appears to increase with temperature. This increase in residual displacement appears to be a temperature effect, rather than the result of repeated load cycling, which results in only a slight increase in residual displacement that gets smaller with each cycle (see for example, the results from the pre-loading stage for test 2 below).

One issue with this testing procedure is splitting the effects of current temperature and temperature cycling. The temperature was reduced after each loading cycle, then increased to the target value. So it is unclear whether the increase in residual displacement is due to the increase in current temperature, or due to the increase in number of thermal cycles experienced.

As well as the hysteresis in the loading and unloading paths, there is hysteresis in the heating and cooling paths. The heating path plots below (i.e. at a lower displacement, for the same pressure) the cooling path. Interestingly, for the final cooling path, from 70 °C to 22.5 °C, the displacement reduces back to zero, cancelling out the residual displacement due to the load/unload cycles.

The results for test 1B are given in Figure 4.21. Figure 4.21a is a 3D plot, and Figure 4.21b shows displacement against temperature. As with test 1A, the effects of temperature are not so clear from the 3D plot.

The total residual displacement following unloading to 2.5 kPa increases significantly with each cycle (comprising a load, heat, cool, and unload path). The increase in residual displacement does not appear to reduce with cycle number, which could indicate that the thermal cycling has some effect on the residual displacement, as indicated in test 1A. However, the maximum pressure increases with each cycle, which may have contributed to this. Interestingly, in test 1A, the total residual displacement reduced almost to zero following unloading and cooling to the initial condition, whereas in test 1B, it continues to increase, despite returning to the initial condition at the end of each cycle. This suggests that the order of heating and cooling may affect the equipment response.

images/calibration/plot_3D_tc1-eps-converted-to.pdf

(a)

images/calibration/plot_d_t_tc1-eps-converted-to.pdf

(b)

Figure 4.20: Test 1A: (a) 3D plot (b) displacement vs temperature

Considering Figure 4.21b, the direct effect of temperature is clearly seen. First, the effect of temperature on the displacement, is much smaller than pressure, in the ranges tested. The thermally-induced displacement is approximately an order of magnitude less than the mechanical compliance. There is hysteresis between the heating and cooling paths, but the direction of this hysteresis is affected by the pressure value. At the lowest pressure of 2.5 kPa, the heating path plots above (i.e. at a higher displacement, for the same pressure) the subsequent cooling path, whereas for the other pressures, the heating path plots below the cooling path. This inversion could have several causes. It could be due to (i) the effect of the pressure value (ii) the effect of the number of cycles of loading, heating/cooling, and unloading, or (iii) the initial test condition. Any of these are plausible. The pressure value (i) can be expected to have an effect since at higher pressure, there is higher compressive stress in the system, particularly the loading ram, which would otherwise extend when heated. The effect of cycling of load and temperature (ii) is apparent from the increased residual displacement with each cycle, and may also have led to the different hysteresis response. Finally, the initial test condition (iii) may have had an effect. The result for the first thermal cycle is anomalous in more than one respect, not just the inverted hysteresis, but the fact that the full heating and cooling cycle results in overall negative displacement. This implies there was perhaps something about the initial condition of the equipment (including porous stones and filter papers) that led to this unusual response during the initial cycle.

For the thermal cycles at 2.5 kPa and 37.5 kPa heating causes positive (compressive) displacement, whilst cooling causes negative (expansive) displacement. This response is approximately linear from 22.5 °C to 50 °C, then flattens off. For the remaining thermal cycles at 150 kPa, 600 kPa and 2400 kPa, both heating and cooling cause positive (compressive) displacement, although the displacement due to cooling is smaller than for heating. Note that the final thermal cycle at 2400 kPa was cut short due to an issue with the equipment, and the final unloading path was not measured. At all pressures, there is still significant hysteresis between the heating and cooling paths.

The data from tests 1A and 1B are plotted together in Figure 4.22a (logarithmic pressure scale) and Figure 4.22b (linear pressure scale). The linear plot has been included to show that the agreement between the two tests is perhaps better than it first appears, based on the logarithmic plot. However, therein lies the issue. Thermally-induced displacement is approximately an order of magnitude lower than the mechanical compliance, for the temperature and pressure ranges tested. Above a certain pressure, therefore, mechanical compliance dominates the combined response. Although there may appear to be good agreement between the results from the two tests at higher pressures, the quality of agreement is relative. If the effect of pressure is of interest, the agreement is relatively good. If however, the effect of temperature is of interest, the agreement is relatively poor, since almost all of the total displacement is due to mechanical compliance.

Both tests show that at low pressures, heating causes compressive displacement, and cooling causes expansive displacement. Both tests show that cycling (of load and temperature), causes an increase in the total residual displacement. From test 1A, it appeared that this residual displacement increases with temperature. The loading/unloading responses for both tests are compared in Figure 4.23. In both cases, the residual displacement increases with increasing number of cycles (whether due to the increase in maximum cyclic temperature, or due to effects of repeated thermal cycling), although the maximum displacement in test 1A remains constant.


images/calibration/plot_3D_tc2-eps-converted-to.pdf

(a)

images/calibration/plot_d_t_tc2-eps-converted-to.pdf


(b)

Figure 4.21: Test 1B: (a) 3D plot (b) displacement vs temperature



images/calibration/plot_3D_log-eps-converted-to.pdf

(a)



images/calibration/plot_3D_linear-eps-converted-to.pdf

(b)

Figure 4.22: Tests 1A and 1B: combined 3D plot (a) logarithmic pressure axis (b) linear pressure axis

images/calibration/plot_d_p-eps-converted-to.pdf


Figure 4.23: Tests 1A and 1B: displacement vs pressure

The thermal responses for both tests are shown in Figure 4.24. From test 1A, only the thermal response at 2.5 kPa is clear, although the thermal response for the other pressure values can be inferred by connecting points at constant pressure for the different temperature values.

The inferred thermal response from the test 1A data is shown in Figure 4.25. For each loading/unloading path, at each pressure increment, the average displacement of the loading and unloading path is taken. Points at the same pressure are connected, giving the inferred thermal response at that pressure value. In Figure 4.25a, the inferred thermal response is shown, for pressure increments of 2.5 kPa, 18.75 kPa, 37.5 kPa, 75 kPa, 150 kPa, 300 kPa, 600 kPa and 1200 kPa. The 2400 kPa thermal path is not shown because the first two thermal cycles did not reach this pressure. In Figure 4.25b, the inferred thermal response is shown, for pressure increments of 2.5 kPa, 37.5 kPa, 150 kPa and 600 kPa (i.e. the target pressures from test 1B).

The inferred thermal responses from the test 1A data are qualitatively similar to the directly measured thermal responses from test 1B, shown in Figure 4.24. However, there is clear hysteresis in the heating/cooling paths in Figure 4.24, that is not reflected in the inferred response (which gives a single thermal response, rather than separate heating and cooling responses). Similarly, there is clear hysteresis in the loading/unloading paths in Figure 4.25a, which is not reflected in the inferred response. Even for 2.5 kPa heating and cooling, for which there is a continuous, comparable measured response available from test 1A, the inferred response either over- or under-estimates the measured response.

Determining a calibration based on these data is not easy. This is particularly true of the type of calibration originally envisioned, and the reason for performing these tests in this manner - a combined temperature and mechanical calibration, giving the equipment response as a function



images/calibration/plot_d_t-eps-converted-to.pdf

Figure 4.24: Tests 1A and 1B: displacement vs temperature

of both temperature and pressure. To obtain such a calibration, only the data from one of test 1A or 1B are required, since both give a network of points in 3D space. Performing two tests though, improves the reliability of the data. There are two main steps in determining the calibration. First, converting the quasi-continuous data into a smaller number of discrete points. Second, fitting a series of calibration curves, or a 3D surface, to these points. The first step requires a number of subjective decisions to be made. Initially, the mesh of data points is taken as the intersections of the two testing paths in pressure - temperature space. This is essentially the intersections of the two data sets seen in Figure 4.26. At each point, a displacement value is chosen. There are four displacement values to choose from, two from test 1A, and two from test 1B. Both tests show clear hysteresis between the load/unload paths, and the heat/cool paths.

Consider for example the point at 30°C , 150 kPa . Test 1A is following a load/unload path at 30°C , whereas test 1B is following a heat/cool path at 150 kPa . If only one value is required, then the average of the four values can be taken. This can be repeated for all the data points on the grid. Consider though, two other points on the grid - one at the same temperature (30°C), but at the next highest pressure value (600 kPa), and another at the same pressure value (150 kPa), but at the next highest temperature value (40°C). The average displacement calculated for the first case (same temperature, higher pressure), will certainly increase, compared to the initial value. However, the average displacement calculated for the second case (same pressure, higher temperature), will not necessarily follow the response expected based on the heating path at 150 kPa in test 1B. This is because the thermally-induced displacement is relatively small compared to the mechanical compliance. The mechanical effects, including hysteresis, dominate and obscure the thermal effects.

images/calibration/plot_3D_tc1_inferred_temp_response-eps-converted-to.pdf

(a)

images/calibration/plot_d_T_tc1_inferred_temp_response-eps-converted-to.pdf

(b)

Figure 4.25: Test 1A: inferred thermal response (a) 3D plot (a) displacement vs temperature

images/calibration/plot_p_t-eps-converted-to.pdf

Figure 4.26: Tests 1A and 1B: pressure vs temperature

Test 1B (thermal cycles at constant pressures) avoids the issues discussed above, to some extent. For each pressure value, a temperature response can be obtained. There were a number of issues with this test though, that raise questions about the reliability of the data, particularly for the 2.5 kPa thermal cycle. Despite these issues, at the time these calibration tests provided the best available data-set, and a calibration was determined based on the test 1A data, which is discussed in the next section. However, aware of the limitations of tests 1A and 1B, further tests were proposed, tests 2 and 3, which are discussed below.

4.4.3 Determining a combined thermal and mechanical calibration

In this section, the methodology used for determining the combined vertical thermal and mechanical calibration is described. This methodology was not used for the final set of tests on KSS. However, a description of the process is instructive because it makes explicit the steps involved in getting from the calibration test raw data to a set of calibration equations which can be used to correct soil test data. The raw data are the fullest, least biased data-set. Unfortunately, these are not directly useable as a calibration to correct test data. For example, when the load, or temperature, is being held constant, the measured value will actually fluctuate above and below the target value, as the computer control makes small corrections based on the current value. This means there will be more than one data point to choose from when trying to determine the compliance at a given load or temperature. Simplifications must be made to the raw data, which results in loss of information, and introduction of bias. As will be seen, the calibration process involves making a number of choices - which raw data to use (and, importantly, to be clear, which to not use), and what type of fit, or fits, to apply to this sub-set of the raw data.

The aim was to derive a set of equations, giving compliance (displacement) as a function of temperature and pressure. These equations can then be used to calculate the compliance for

any temperature and pressure combination. This compliance can be subtracted from the total measured displacement in a soil test, to give the isolated soil response.

For a standard, ambient-temperature oedometer test, using a hanging-weight lever-arm system, the compliance is determined by loading and unloading a dummy specimen, following the same sequence as in the proposed soil test. For each incremental load increase or decrease, the displacement is measured. This displacement can be subtracted from the total displacement in the soil test, to give the soil displacement only. With the temperature-controlled oedometer, the direct effect of thermal cycles (which is affected by the load), and the effect of mechanical cycles (which is affected by the temperature) must be considered. It would be possible to perform the calibration in a similar way to the standard, ambient-temperature method, but with the addition of thermal stages. In other words, to follow the proposed test sequence, using a dummy specimen. However, there are good reasons to consider alternative methods. Firstly, these calibration tests would be time-consuming. Cooling the equipment from 70°C to 22.5°C at the natural cooling rate takes ≈36 h. For any test involving multiple thermal cycles, the associated calibration test would take more than a week. Secondly, in the earlier stages of the research, it was not known exactly which tests would be performed. It would be an advantage to obtain a calibration that could be used flexibly, for any load or temperature condition, as this would allow any load and temperature path to be applied to a soil, and the calibration could be applied easily and repeatably.

The data from test 1A, described above, was used to determine the calibration. Test 1A involved a series of load/unload cycles at fixed temperatures. The basic approach was to first determine the displacement-pressure response, for each temperature value. Next, to establish how these responses vary with temperature. Two types of fit were used, a two-part semi-log fit, and a sigmoid (logistic) fit. The method for determining both was similar.

The semi-log fit was based on logarithmic expressions of the following form, which is also shown graphically in Figure 4.27. This expression appears to be linear, when plotted with logarithmic x axis. Note that $\ln 1 = 0$.

$$y = m \ln x + c \quad (4.1)$$

where:

- m = gradient of line (on logarithmic x axis)
- c = y axis intercept of line

The sigmoid fit was based on a logistic expression of the following form, which is also shown graphically in Figure 4.28.

$$y = \frac{L}{1 + e^{-k(x-x_0)}} \quad (4.2)$$

where:

- L = maximum y value of curve
- k = growth rate (steepness of curve)
- x_0 = x value of midpoint of curve (point of maximum gradient)

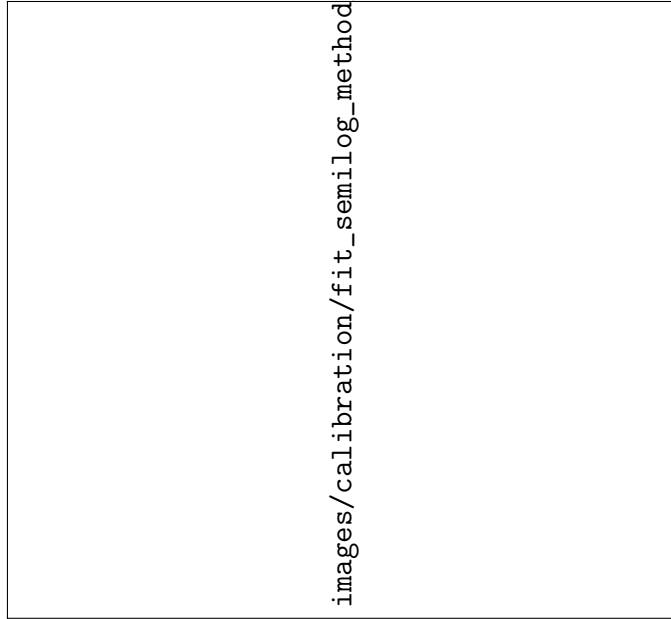


Figure 4.27: Semi-log fitting methodology - one-part logarithmic fit

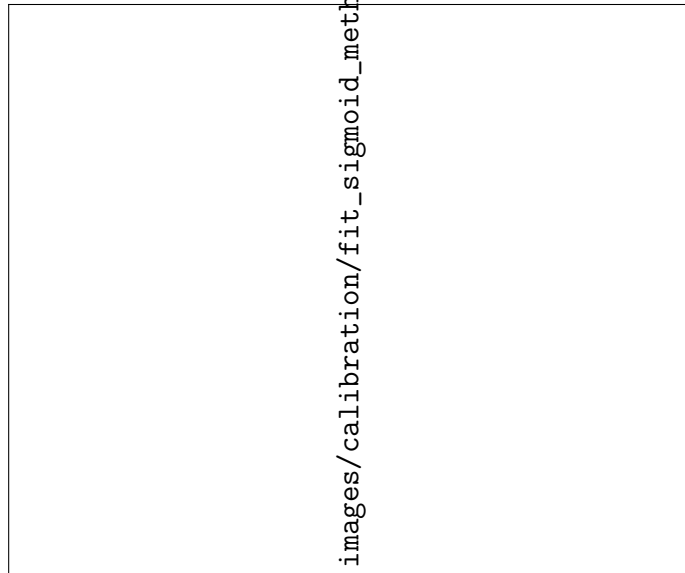


Figure 4.28: Sigmoid fitting methodology - showing parameters L and x_0

First, the displacement-pressure response was plotted separately for each temperature value. Rather than the full data set, the data were sampled at the end of each increment (end-of-increment data). The data for the load/unload cycle at 22.5 °C are shown in Figure 4.29. Note that there are two values for each pressure value (except the maximum pressure) - one for the loading path, and one for unloading. The logarithmic fit (linear on log pressure scale), is clearly inadequate. It implies negative compliance at 2.5 kPa, over-estimates the compliance for pressures below 150 kPa, and under-estimates the compliance for pressures above 150 kPa.

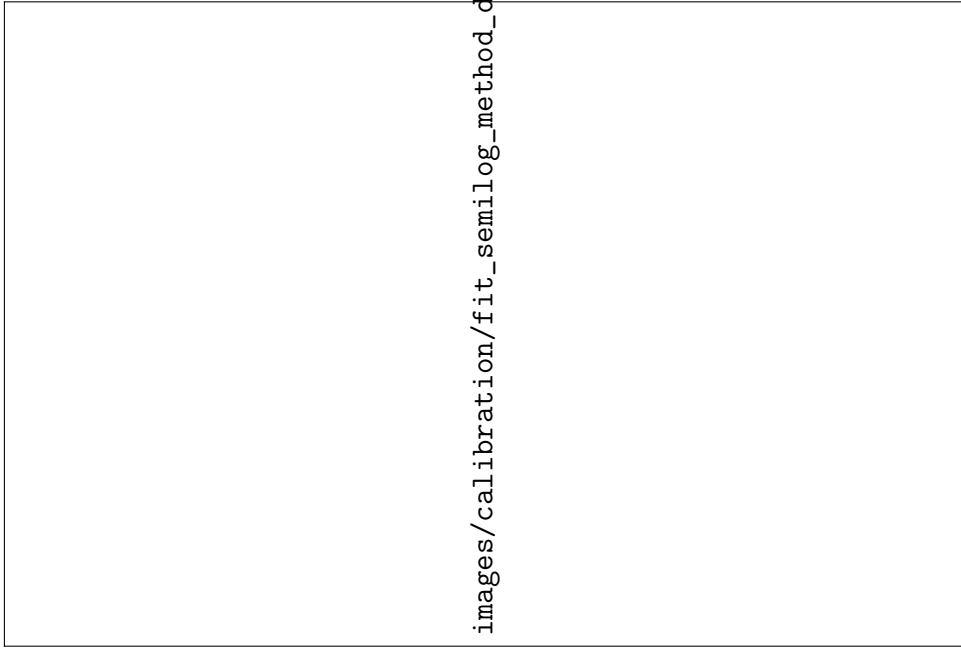
images/calibration/fit_semi-log_method_1.pdf

Figure 4.29: Semi-log fitting methodology - single logarithmic fit

For the semi-log fit, the sampled data for each temperature value were separated into two series. Series 1 for pressure ≥ 37.5 kPa, and Series 2 for pressure ≤ 37.5 kPa. Then, a logarithmic expression, of the form given in Equation 4.1 was fitted to both series (Series 1 \Rightarrow fit 1, Series 2 \Rightarrow fit 2).

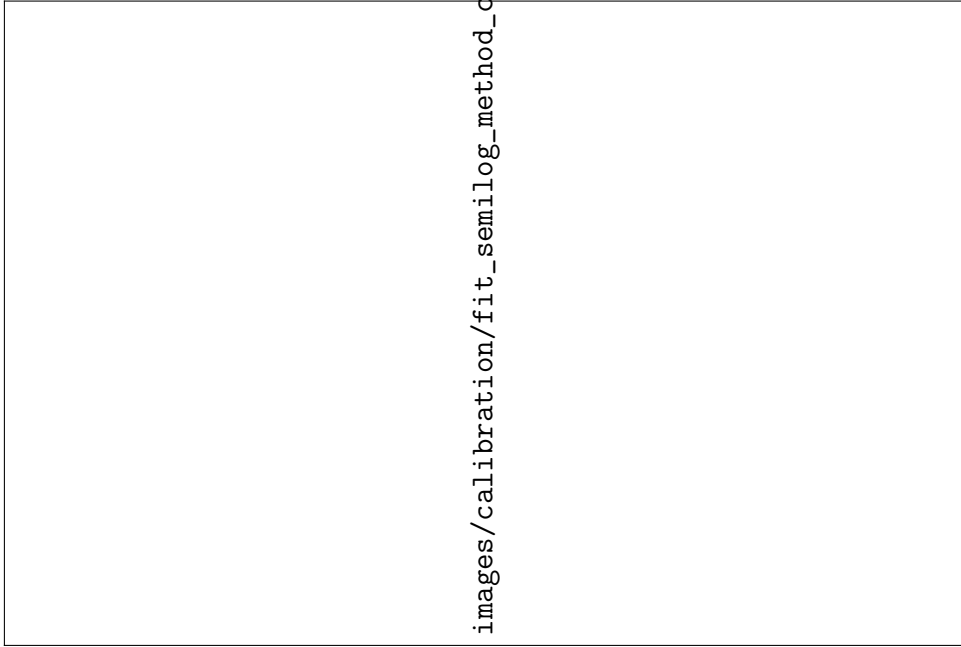
This is shown schematically in Figure 4.30. The gradient of fit 1 is m_1 (on a log pressure axis). The y axis intercepts (displacement, D , in Figure 4.30) of fit 1 and fit 2 are c_1 and c_2 respectively. The displacement at 37.5 kPa, given by fit 1, is $m_1 \ln 37.5 + c_1$. The data are discontinuous at 37.5 kPa, which is not ideal, because this discontinuity will then be erroneously inferred from the corrected soil response.

The solution is to derive a third fit (fit 3), which has the same y axis intercept as fit 2, but intercepts fit 1 at 37.5 kPa (where $D = m_1 \ln 37.5 + c_1$). This is shown schematically in Figure 4.31. This gives a compliance fit (fit 3, for $P \leq 37.5$ kPa, and fit 1, for $P \geq 37.5$ kPa) which is continuous over the full range of pressure values.



images/calibration/fit_semi_log_method_discontinuous.jpg

Figure 4.30: Semi-log fitting methodology - showing discontinuity between fit 1 and fit 2



images/calibration/fit_semi_log_method_continuous.jpg

Figure 4.31: Semi-log fitting methodology - showing continuous two-part fit

The equation of fit 3 can be found in the same way as calculating the equation of a straight line. The gradient, dD/dP , is calculated as follows.

$$dD = m_1 \ln 37.5 + c_1 - c_2 \quad (4.3)$$

$$dP = \ln 37.5 - \ln 1 \quad (4.4)$$

$$\frac{dD}{dP} = \frac{m_1 \ln 37.5 + c_1 - c_2}{\ln 37.5} \quad (4.5)$$

The y intercept of fit 3 is the same as fit 2, c_2 . The compliance therefore, is given by the following two equations.

$$D = \begin{cases} \left[(m_1 \ln 37.5 + c_1 - c_2) \cdot \frac{\ln P}{\ln 37.5} \right] + c_2 & \text{for } P \leq 37.5 \text{ kPa} \\ m_1 \ln P + c_1 & \text{for } P \geq 37.5 \text{ kPa} \end{cases} \quad (4.6)$$

where:

D = displacement (compliance) [mm]

P = pressure [kPa]

m_1 = gradient of fit 1

c_1 = y intercept of fit 1 (i.e. displacement for $P = 1$ kPa)

c_2 = y intercept of fit 2

This gives displacement as a function of pressure, and three parameters, m_1 , c_1 and c_2 . The next step is to determine how these parameters vary with temperature.

Figure 4.32a shows the typical displacement-pressure response for the extreme temperature values, for the high-pressure fit (fit 1). The gradient of fit 1 (m_1) reduces with temperature. This reduction takes the form of a quadratic, as shown schematically in Figure 4.32b. The value of m_1 is calculated for each temperature value, using the sampled end-of-increment data. The value of m_1 for each temperature increment, and equation of the derived quadratic fit (variation of m_1 with temperature) are shown in Figure 4.35a.

Figure 4.33a again shows the typical displacement-pressure response for the extreme temperature values, for the high-pressure fit (fit 1). The y intercept of fit 1 (c_1) increases with temperature. This increase takes the form of a quadratic, as shown schematically in Figure 4.33b. The value of c_1 for each temperature increment, and equation of the derived quadratic fit (variation of c_1 with temperature) are shown in Figure 4.35b.

Figure 4.34a shows the typical displacement-pressure response for the extreme temperature values, for the low-pressure fit (fit 2). The y intercept of fit 2 (c_2) increases with temperature. This increase takes the form of a quadratic, as shown schematically in Figure 4.34b. The value of c_2 for each temperature increment, and equation of the derived quadratic fit (variation of c_2 with temperature) are shown in Figure 4.35c.

The three parameters, m_1 , c_1 and c_2 , can therefore be expressed as quadratic functions of temperature. To calculate the compliance, all that is required is the temperature and pressure values. The parameters m_1 , c_1 and c_2 can be calculated based on the temperature value. These parameter values, and the pressure value, can be substituted into Equation 4.6 to give the displacement.

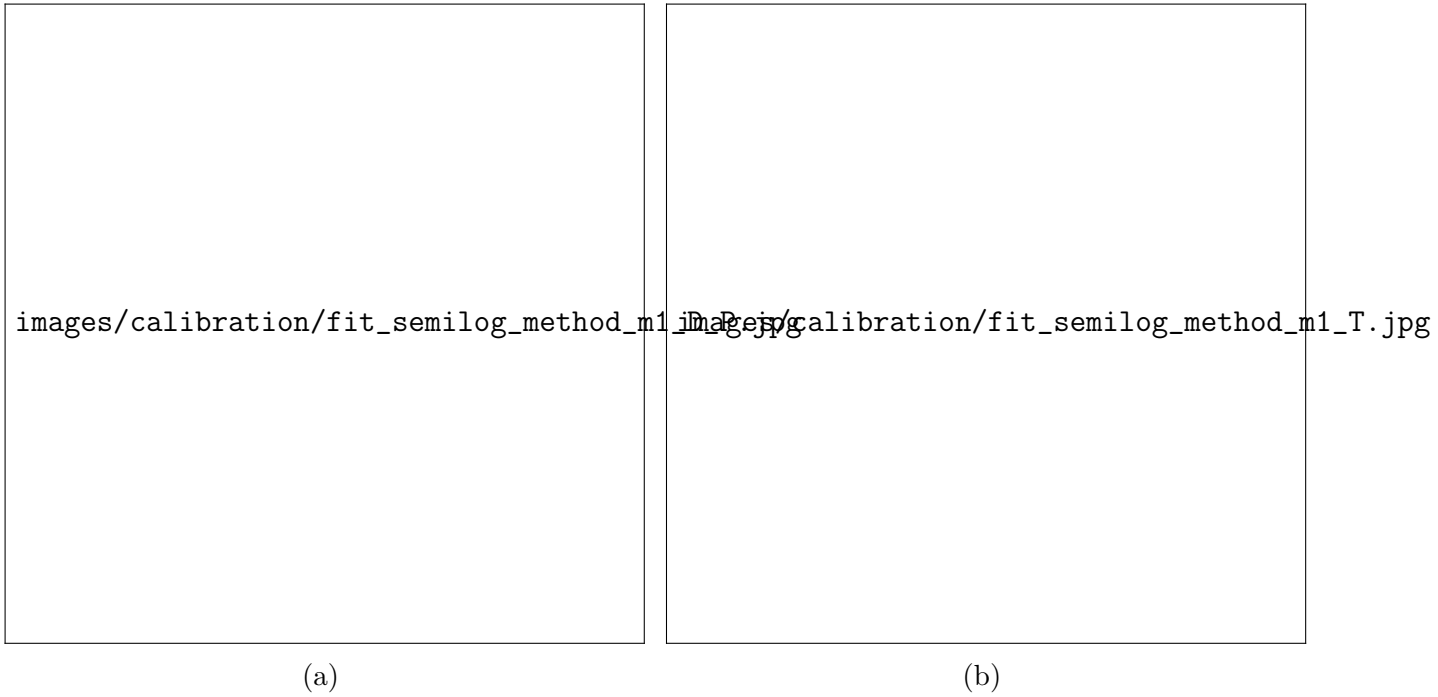


Figure 4.32: Semi-log fitting methodology - effect of temperature on parameter m_1 (a) displacement-pressure response (b) quadratic fit



Figure 4.33: Semi-log fitting methodology - effect of temperature on parameter c_1 (a) displacement-pressure response (b) quadratic fit

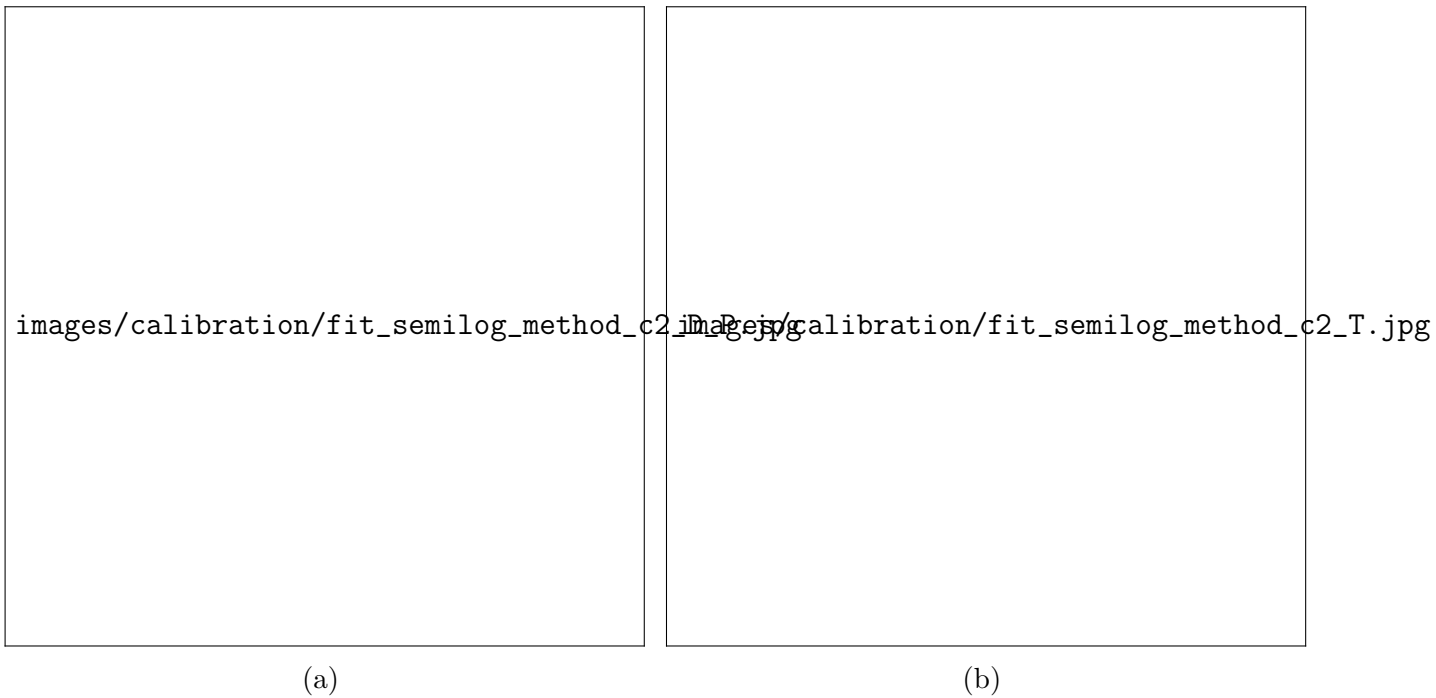


Figure 4.34: Semi-log fitting methodology - effect of temperature on parameter c_2 (a) displacement-pressure response (b) quadratic fit

The two-part semi-log fit for the load/unload curve at 22.5 °C is given in Figure 4.36. Compared to the single logarithmic fit shown in Figure 4.29, this fit is much better. However, there is actually a curved shape to the high-pressure (≥ 37.5 kPa) response, that is not reflected in the calibration. To account for this, the two-part fit could perhaps be split further, with separate equations for pressure from 37.5 kPa to 150 kPa and from 150 kPa to 2400 kPa. Instead, a second fit was developed which could account for the overall S-shaped response - the sigmoid fit.

For the sigmoid fit, a logistic function is fitted through the sampled data for each temperature value. The function takes the form given by Equation 4.2, and is given below in terms of displacement, D , and pressure, P .

$$D = \frac{L}{1 + e^{-k(\ln P - x_0)}} \quad (4.7)$$

The three parameters, L , k and x_0 can be expressed as functions of temperature. This can be done by comparing the parameter values for each temperature, and fitting a quadratic equation through these data. The parameter L increases with temperature, k reduces, while x_0 increases, as shown schematically in Figure 4.37.

The parameter values at each temperature increment, and calculated quadratic fits, are given in Figure 4.38a (L), 4.38b (k), and 4.38c (x_0).

As with the semi-log fit, for each test data point, L , k and x_0 can be calculated based on the temperature value. Then together with the pressure value, the displacement can be calculated using Equation 4.7.

images/calibration/fit_semi-log_m1.pdf

(a)

images/calibration/fit_semi-log_c1.pdf

(b)

images/calibration/fit_semi-log_c2.pdf

(c)

Figure 4.35: Parameters for semi-log fit (a) gradient of fit 1, m_1 , (b) y intercept of fit 1, c_1 , (c) y intercept of fit 2, c_2

images/calibration/fit_semi-log_method_2.pdf

Figure 4.36: Semi-log fitting methodology - two-part logarithmic fit

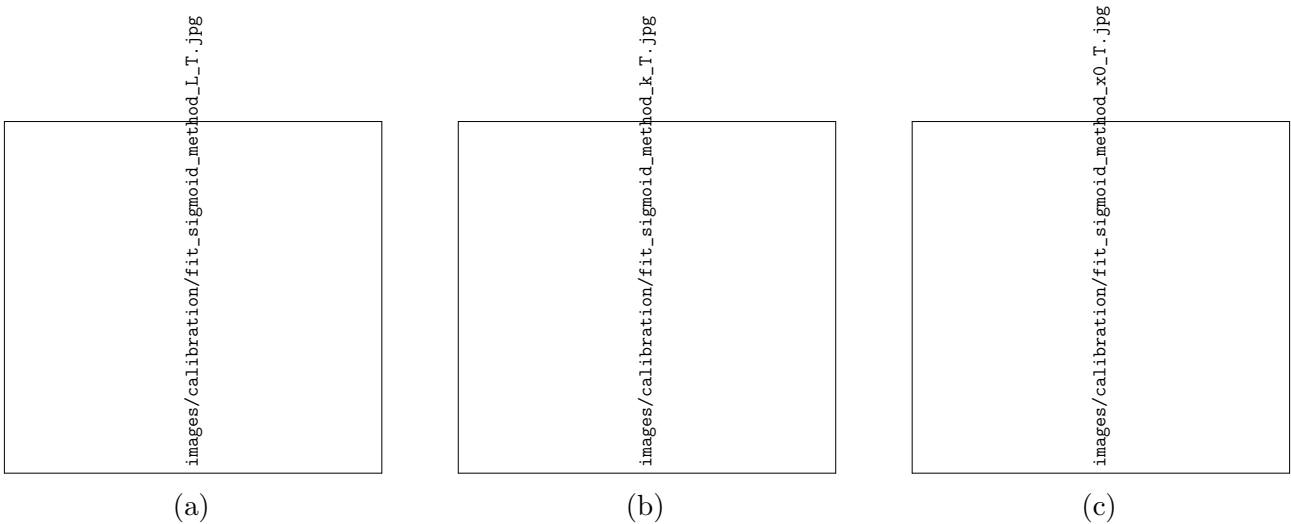


Figure 4.37: Sigmoid fitting methodology - effect of temperature on parameters (a) L (b) k (c) x_0

images/calibration/fig_sigmoid_L.pdf

(a)

images/calibration/fig_sigmoid_k.pdf

(b)

images/calibration/fig_sigmoid_x0.pdf

(c)

Figure 4.38: Parameters for sigmoid (logistic) fit (a) maximum y value, L , (b) growth rate (steepness of curve), k , (c) x value of sigmoid's midpoint, x_0

The sigmoid fit is shown in Figure 4.39, for the 22.5 °C data. Compared with the two-part logarithmic fit shown in Figure 4.36, the sigmoid fit is better at replicating the non-linearity of the response. The sigmoid fit is compared to the data in Figure 4.40 (displacement-pressure response) and Figure 4.41 (displacement-temperature response). The data, in this case, are the average of the two end-of-increment values for each pressure increment at different temperature values. In general, this calibration is able to capture the behaviour well, albeit imperfectly.

images/calibration/fit_sigmoid_D_P_22.pdf

Figure 4.39: Sigmoid fitting methodology - single fit through 22.5 °C data

The two fits are compared to the data in Figure 4.42 (displacement-pressure response at 22.5 °C) and Figure 4.43 (displacement-temperature response at 2.5 kPa). The displacement (measured, or calculated) is given on the Y1 axis, and the error (difference between measured and calculated displacement) is given on the Y2 axis. Comparing the error for the two fits in Figure 4.42, it can be seen that the sigmoid fit captures the true response better for pressure values from ≈ 100 kPa to 1000 kPa, whereas the semi-log fit performs better at the lowest and highest pressure values in the tested range. In both cases, the maximum error is less than 0.01 mm, which is acceptable given that the total mechanical displacement of a saturated clay slurry over this pressure range is likely to be >10 mm with this equipment (giving a relative error in the total displacement of 0.1 %).

Comparing the error for the two fits in Figure 4.43, it is seen that the semi-log fit performs slightly better over the full temperature range. Again, in both cases, the maximum error is less than 0.01 mm. The magnitude of the error is similar to the error in Figure 4.42. However, the total thermally-induced displacement of a soil is (very roughly, for this range of temperatures and pressures) up to two orders of magnitude lower than the mechanical displacement (giving a relative error in the total displacement of up to 10 %). This means that this error is no longer acceptable.

images/calibration/fit_sigmoid_D_P.pdf

Figure 4.40: Sigmoid fit - comparison of displacement-pressure response at different temperature values

images/calibration/fit_sigmoid_D_T.pdf

Figure 4.41: Sigmoid fit - comparison of displacement-temperature response at different pressure values

images/calibration/fit_comparison_D_P.pdf

Figure 4.42: Absolute error in displacement-pressure response for both fits at 22.5°C

images/calibration/fit_comparison_D_T.pdf

Figure 4.43: Absolute error in displacement-temperature response for both fits at 2.5 kPa

This source of error is one reason why the combined calibration method was not used in later tests. Even if the compliance data are representative of the test conditions, and repeatable (both of which are unlikely to be the case, to a greater or lesser extent, depending on the test details), the process of fitting compliance curves to account for both the pressure and temperature value, introduces some error.


4.4.4 Calibration - tests 2 and 3

In tests 2 and 3, the test programme, shown as a simplified flowchart in Figure 4.44, is similar to test 1B (thermal cycles at fixed pressures), with some improvements to the methodology. In tests 1A and 1B, a pre-loading sequence was performed before each test. In tests 2 and 3, a similar pre-load sequence was performed, this time before each cycle. As in previous tests, the first aim of this sequence is to pre-load the filter papers, so that subsequent loading sequences follow an elastic reloading path, rather than the plastic initial loading path, as described in more detail in Section 4.5. In test 2, this was important, since filter papers were used. However, in test 3, where filter papers were not used, this pre-load sequence was still performed because (i) it may help bed in the porous stones and (ii) the pre-load data can be compared to see the effect of removing the filter papers. The pre-load sequence is four load/unload cycles between 2.5 kPa and 1500 kPa, each of approximately 4 h duration. The second aim of the pre-load sequence is to try and remove the effects of the loading and temperature history of the previous load and temperature cycle.

Following the pre-load sequence, the pressure is increased to the target value of 2.5 kPa, 300 kPa or 1500 kPa. Under constant pressure, the thermal cycle is applied: heating from 22.5 °C to 70 °C, cooling from 70 °C to 5 °C, and finally heating from 5 °C to 22.5 °C. In some cases, multiple thermal cycles were performed. The heating rate between 22.5 °C and 70 °C is 2 °C h⁻¹, whereas the cooling rate between 70 °C and 22.5 °C is uncontrolled. Cooling from 22.5 °C to 5 °C, is controlled manually using the chiller unit and heat exchanger, and is applied in a single increment, as is heating from 5 °C to 22.5 °C.

The specimen set-up for tests 2 and 3 is shown in Figure 4.45. For test 2 (4.45a) two filter papers are placed between two porous stones. For test 3 (4.45b) only the porous stones are used. No dummy specimen is used.

The o-ring on the top-cap is kept in place, which simulates the real testing conditions more accurately than removing the o-ring. However, clearly the removal of the o-ring will affect the thermal and mechanical compliance. It is worth considering again the aim of these tests, which is to measure what happens to the equipment, when loaded and heated, in conditions resembling as closely as practicable, actual test conditions (but without the soil specimen in place). With this in mind, it seems sensible to perform the thermal and mechanical calibration tests with the o-ring in place, as it is in soil tests. A single correction can then be applied, rather than two separate ones (a correction to the load, accounting for friction, and a correction to the displacement, accounting for thermally-induced deformation and mechanical compliance), since the frictional component is already (implicitly) included in the thermal and mechanical calibration. The issue then simplifies to minimising the friction between the o-ring and confining ring. The magnitude of this friction, and attempts to reduce friction, are discussed in Section 4.2.



images/calibration/Flowchart_TCOMP.pdf

Figure 4.44: Calibration tests 2 and 3: simplified flowchart



images/calibration/comp_FP.jpg

(a) Test 2




images/calibration/comp_no_FP.j

(b) Test 3

Figure 4.45: Tests 2 and 3: specimen set-up for calibration tests

The displacement response for the pre-loading stage of test 2 is given in Figure 4.46. The first two load/unload cycles at ambient temperature are shown. Following the first cycle, there is a significant residual displacement, greater than 0.1 mm. Subsequent cycles re-trace the same reload/unload loop, with a slight increase in the residual displacement with further cycling, but negligible increase in the maximum displacement. The filter paper response is discussed in more detail in Section 4.5.



images/calibration/tcomp1_d_p.pdf

Figure 4.46: Test 2: displacement response for pre-loading stage

The thermally-induced displacement at pressure values of 2.5 kPa, 300 kPa and 1500 kPa are shown in Figure 4.47. At 2.5 kPa, initial heating causes negative displacement (extension). Cooling causes further negative displacement. Subsequent re-heating from 5 °C to 22.5 °C causes positive displacement (contraction), which reverses some of the extensive displacement due to cooling. This result is also shown in Figure 4.48, with the heating, cooling and re-heating paths identified. At 300 kPa and 1500 kPa, initial heating causes positive displacement (contraction). Subsequent cooling causes minimal displacement at 300 kPa, and a small positive displacement (contraction) at 1500 kPa. The re-heating path for both follows back along the cooling path. In all three cases, the initial heating and cooling results in residual displacement (contraction at 2.5 kPa and extension at 300 kPa and 1500 kPa), while the re-heating path follows the cooling path in reverse.

The initial heating and cooling paths from test 2 do not plot above one another. This makes determining a calibration difficult. Either two calibrations are required for each load value - one for the initial heating path, and one for subsequent cooling and reheating paths - or there needs to be a pre-heating sequence prior to testing, similar to the pre-loading sequence, to eliminate this effect. Neither of these options are ideal, so based on these data, and the results described in Section 4.5, the decision was made to not use filter papers at all.

images/calibration/tcomp1_d_t.pdf

Figure 4.47: Test 2: thermally-induced equipment displacement at pressure values of 2.5 kPa, 300 kPa and 1500 kPa

images/calibration/tcomp1_d_t_split.pdf

Figure 4.48: Test 2: thermally-induced equipment displacement at 2.5 kPa pressure

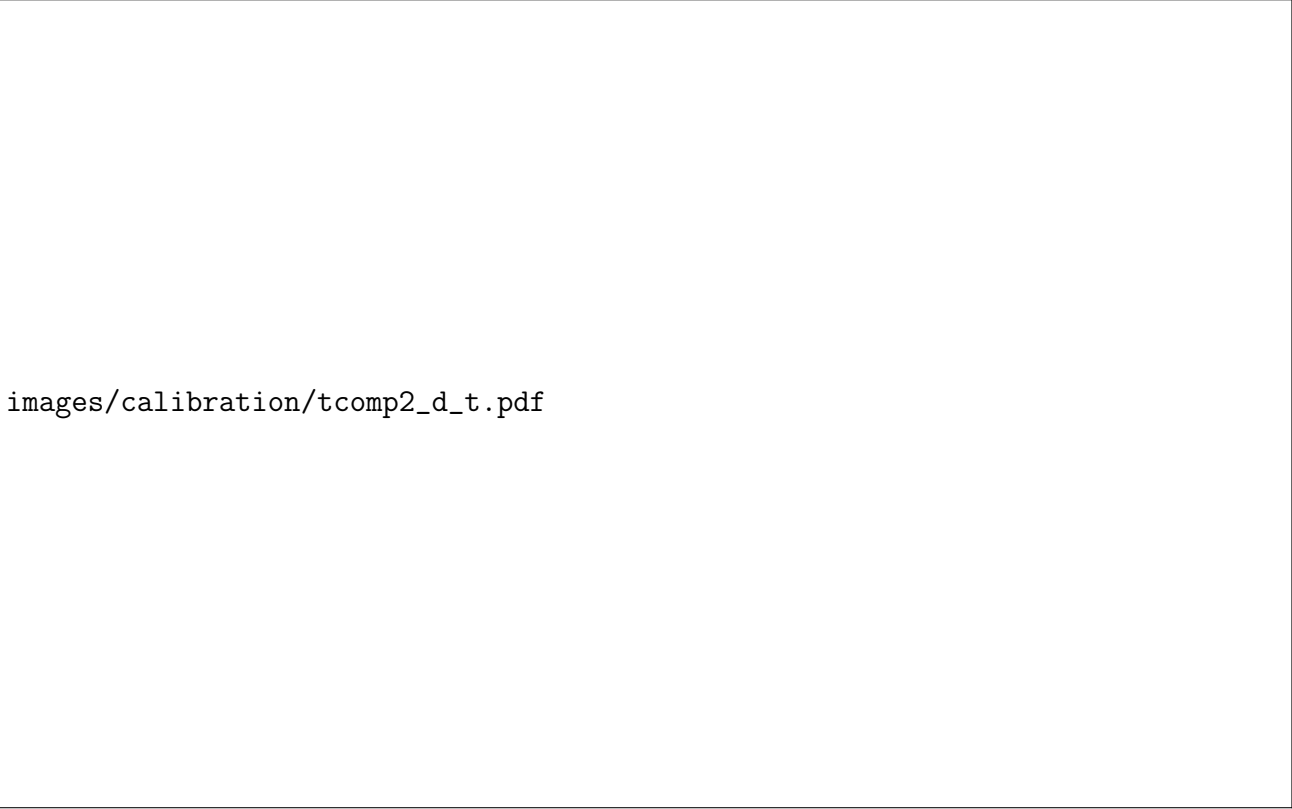
A repeat of test 2 was therefore performed, without using filter papers. The results for the 2.5 kPa thermal cycle for tests 2 (filter papers) and test 3 (no filter papers) are shown in Figure 4.49. The difference is stark. For test 3, initial heating causes positive displacement (contraction). The subsequent cooling path approximately reverses this contraction, resulting in overall expansion at the minimum temperature. Re-heating causes positive displacement (contraction). The full thermal cycle results in a small residual displacement (≈ 0.01 mm). Fitting a compliance curve to these data is much easier and less dependent on subjective assumptions than fitting to the data from test 2.



Figure 4.49: Tests 2 and 3: thermally-induced equipment displacement at 2.5 kPa pressure

The results from test 3 for the thermal cycles at 2.5 kPa, 300 kPa and 1500 kPa are shown in Figure 4.50. For all three cases, the response is approximately linear. The hysteresis between heating and cooling path reduces with increased pressure. The effect of increasing the pressure appears to pivot this linear response so that the displacement at higher temperature moves towards lower compression values, and displacement at lower temperature moves towards lower extension values. At 1500 kPa, the response pivots so far that heating causes slight expansion, and cooling causes slight contraction.

The magnitude of the compliance is significant. The thermal compliance over the tested temperature range for 2.5 kPa is ≈ 0.05 mm. For over-consolidated clays, thermally-induced displacement may be in this range (see for example, test A3 on KSS in Section 8.5.3). The compliance is particularly important when considering the effect of multiple thermal cycles on over-consolidated clay. In this case the measured displacements may be smaller than the compliance, and the compliance will play a major role in the analysis of the results.



images/calibration/tcomp2_d_t.pdf

Figure 4.50: Test 3: thermally-induced equipment displacement at pressure values of 2.5 kPa, 300 kPa and 1500 kPa

To conclude this section, it is worth summarising the key points and results. Calibration tests were performed to measure the vertical deformation of the equipment. Initially, the aim was to obtain a calibration in three dimensions, that would give the equipment deformation at any temperature and pressure value. To obtain this calibration, two tests were performed: load/unload cycles at different temperatures, and heat/cool cycles at different pressures. In general, the displacement due to loading was approximately an order of magnitude higher than the thermally-induced displacement. This meant a combined calibration could not accurately model the thermally-induced deformations. Another test was performed, with some improvements to the testing methodology (pre-loading the filter papers, having the top-cap o-ring in place), this time only with heat/cool cycles, at three different pressures. However, again it was not possible to obtain an accurate calibration. This time, it was possible to identify the use of filter papers as the primary issue. Filter papers behave a bit like soil. They are highly compressible, undergo permanent residual displacement following the initial load/unload cycle, and show hysteresis along subsequent load/unload paths, as well as along heat/cool paths. A final test was performed, a repeat of the previous test, but without filter papers. The issues relating to filter papers were solved, or reduced to an acceptable level. This test was the basis on which the final calibration methodology, discussed in Chapter 7, was developed.

4.5 Filter papers and porous stones

Filter papers and porous stones are commonly used in conventional oedometer testing. Porous stones (sometimes referred to as *disks*) are placed at the top and base of the specimen to provide two-way drainage conditions. Filter papers may be used to prevent fine soil from clogging the pores of the porous stones.

The issue of clogging was considered by Baracos (1976), who examined a “fine porous filter disc”, previously used in an oedometer to consolidate a kaolin slurry, under optical and scanning electron magnification. They observed that clay particles entered the interior pores of the disc, making the path for water through the disc more tortuous. They concluded that clogging could affect measurement of rates of flow and consolidation, and warned that soil loss into the filter could affect volume and weight measurements. These conclusions were based on the magnified images only, not on any measured flow rates, or mass measurements. There is also no mention of whether filter papers are effective at preventing such clogging.

Fredlund (1969) described the issues relating to filter paper compressibility. Filter paper compresses instantaneously when the load is applied, and compresses further with time. Filter paper also exhibits hysteresis due to loading and unloading. They found that under a vertical pressure of 98 kPa the compression of the filter paper was approximately five times that of the apparatus. Under a vertical pressure of 980 kPa, the compression of the filter paper was approximately 2.5 times that of the apparatus. Based on these results, they advised against using filter paper when testing swelling soils in an oedometer. In this section, data are presented which suggest that filter papers should not be used when performing thermal oedometer tests on any soil type. The reasons for this conclusion are as follows: (i) filter papers are highly compressible, and their load-displacement or temperature-displacement response dominates the total displacement response; (ii) the load-displacement response of filter papers is time-dependent; (iii) any calibration obtained is only valid for the exact conditions tested - using, or not using, a dummy specimen to obtain the calibration both have limitations; (iv) filter papers have a hysteretic load-displacement and temperature-displacement response, which is particularly significant for the first cycle of loading/unloading or heating/cooling, so multiple calibration equations are required, even for simple tests.

A review of the literature finds that the advice of Fredlund (1969) has not been consistently applied. This is not surprising when even the advice from the technical testing standards is not clear. ASTM Standard D2435/D2435M-11 (ASTM International, 2011) suggests, in Section 6.4, that a filter screen may be placed between the porous disk, to prevent intrusion of material into the pores of the porous disk. In Section 8.1.2 of the same standard, when discussing calibration of the oedometer, they suggest that when using filter papers, a calibration must be performed using the exact loading and unloading schedule to be used in the test. However, no details are given on the interpretation of the calibration data, particularly how to account for the hysteresis effects caused by the filter papers.

British Standard 1377-5:1990 (British Standards Institution, 1990) notes, in Section 3.2.4.2.1, that “if a filter paper is to be placed against each face of the specimen during a test, similar filter papers should be placed either side of the steel disc for the calibration, either dry or moist depending on the condition for the test.” Again, the importance of calibration is noted, but without giving details on how to interpret and implement the calibration. The results shown below also indicate that there is variation in the responses of filter papers of the same type (and indeed, from the same box), so the advice to use similar filter papers does not ensure that their

responses will also be similar. New, unused, filter papers have significantly different responses to previously-loaded ones.

Head and Epps (2011), an authoritative text on soil mechanics laboratory testing, advised against the use of filter paper, because fine soil particles can become enmeshed in the fibres of filter paper, causing clogging of the pores and impairing the drainage. This explanation is interesting, because preventing clogging of the pores of the porous stones is often given as the reason for using filter papers, whereas in this case, clogging of the filter paper itself is given as the reason to avoid their use.

In any case, conscious or not of these issues, a number of schemes, from theses and journal papers, have used filter papers. PhD theses from Jefferson (1994), Cunningham (2000), and Mantikos (2018), and a journal paper from Marcial et al. (2002) all used filter papers to prevent loss of soil and clogging of the drainage paths. Of these, only Mantikos (2018) explicitly questions their use, noting that inclusion of filter papers results in an initial irreversible displacement, and reduced stiffness for vertical pressures <2 MPa. Nevertheless, they concluded that the use of filter papers was justifiable as part of their final testing methodology.

Porous stones too, are compressible, although less so than filter papers. They are used in almost all conventional and temperature-controlled oedometer schemes. Their effect on total compliance has been investigated, and is discussed below. Their use was determined to be justified in this scheme.

The effect of filter papers and porous stones on the load-displacement response (i.e. compliance) of the equipment was determined by carrying out a number of loading tests at ambient temperature. The terms *compliance*, *calibration* and *correction* are used when discussing these results. Compliance is the inverse of stiffness. Here, it refers to deformation of the equipment under a certain load. Compliance is what is measured in these tests. Calibration is the process of comparing measured and known values. The purpose of these tests is to establish a set of known values by measuring the response of the equipment (including filter papers and porous stones). These known values can then be compared with, i.e. used to calibrate, the measured displacements from a soil test. Correction is the process of applying the calibration, by adjusting the measured test data to account for the equipment compliance. The three terms are closely linked, and can in some cases be used interchangeably.

Four sets of tests were performed, each comprising a number of individual tests. The sets of tests are labelled (CO - *compliance*, TC - *temperature-controlled oedometer*, ML - *main lab oedometer*, VA - *variability*), and each test is numbered (e.g. TC:5 refers to test series TC, test 5). When describing the test set-up, the shorthand FP and PS is used to refer to filter papers and porous stones respectively. So a test performed with two filter papers and two porous stones would be given as 2FP + 2PS.

In all tests, the same type of filter papers and porous stones were used, and the equipment set-up was not changed, unless stated. The filter papers were Whatman grade 54 hardened, low-ash, cotton filter papers, 70 mm diameter, cut to 68 mm diameter. The specified pore-size for these filter papers is 22 μm . The porous stones were 6 mm thick aluminium oxide (alumina) discs, manufactured by VJ Tech. They have a diameter of 69.75 mm at ambient temperature. Cylindrical brass dummy specimens were also used. The same dummy specimen was not used for all tests, so dimensions for each are given along with the relevant set of tests.

Tests were performed in dry conditions, at ambient temperature, unless stated otherwise. The top-cap o-ring was removed during these tests. This was done so that there would be no need to account for frictional resistance when investigating the individual component of compliance

(equipment, porous stones, and filter papers). This reduced the level of error in the results, and made the analysis less complex. However, when determining the total compliance, to obtain calibration equations and apply a correction, the o-ring is used. For example, see the testing methodology for KSS, in Chapter 7.

The first set of four tests, denoted CO:1-4, were performed because the load and temperature calibration tests, described in Section 4.4, showed hysteresis and non-linearity of the load-displacement response. These effects could either be due to the equipment (load frame, loading arm, top-cap, base-plates, and the connections between them), the porous stones, the filter papers, or a combination of all three. The aim of these tests was to determine the load-displacement response of the individual elements (equipment, porous stones, filter papers) that make up the combined response.

The results for these, and subsequent tests, are given in terms of maximum displacement d_{max} and residual displacement d_{res} . The maximum displacement d_{max} is the maximum displacement reached at the maximum load, at the end of the first loading path. The residual displacement d_{res} is the minimum displacement reached at the minimum load, at the end of the first unloading path. A typical filter paper response is shown schematically in Figure 4.51, with d_{max} and d_{res} labelled. Displacement response is shown for the first two load/unload cycles, against pressure on a linear scale (4.51a) and a logarithmic scale (4.51b). As indicated on the figure, further cycling can cause d_{max} and d_{res} to increase, but this increase is small compared to the initial values. There may also be hysteresis between the reloading and unloading paths. Both of these issues are discussed below.



Figure 4.51: Schematic displacement response showing residual displacement (d_{res}) and maximum displacement (d_{max}) against (a) linear pressure and (b) logarithmic pressure

The loading path followed in this test series (CO:1-4) was repeated cycles of loading to 9500 N (2469 kPa equivalent pressure) and unloading to 10 N (2.6 kPa equivalent pressure). Four tests were performed. Schematic diagrams showing the specimen set-up for tests CO:1-4 are given in Figure 4.52. Test CO:1 is the dummy only. Test CO:2 is the dummy below two porous stones. Test CO:3 is the dummy below two filter papers. Test CO:4 is the dummy below two porous stones and two filter papers, with the filter papers between the porous stones.

For each test, a brass, cylindrical dummy specimen was used (height: 26.1 mm, diameter: 63.4 mm). For the maximum load of 9500 N, the theoretical deformation of the dummy specimen

is <0.001 mm (see Appendix H for an example calculation), which is negligible compared to the other components of compliance. The test set-up information for test series CO is summarised in Table 4.2.

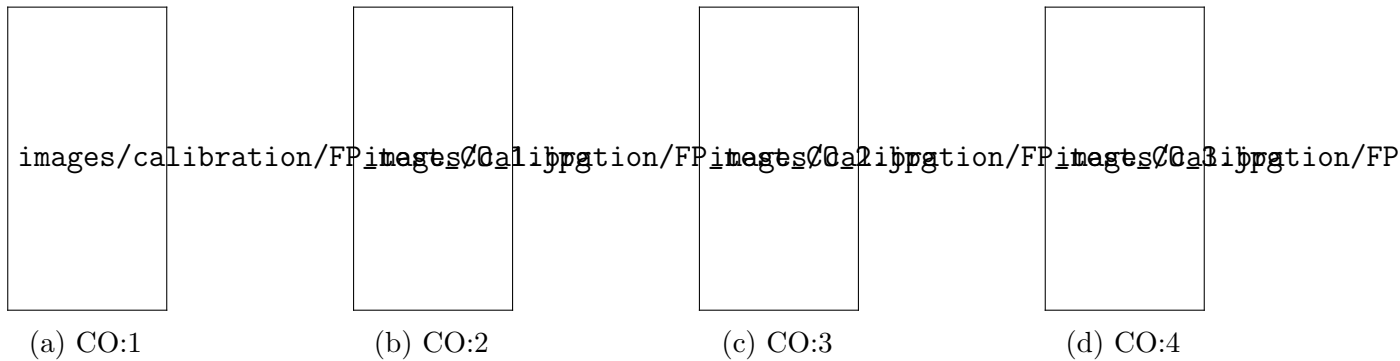


Figure 4.52: Schematic test set-up for first set of filter paper compliance tests (CO:1-4)

Table 4.2: Calibration test series CO - summary

Test	Equipment	Specimen (base \rightarrow top)	Brass dummy dimensions	
			Height [mm]	Diameter [mm]
CO:1	TC-OED	D	26.1	63.4
CO:2	TC-OED	D \cdot 2PS	26.1	63.4
CO:3	TC-OED	D \cdot 2FP	26.1	63.4
CO:4	TC-OED	D \cdot PS \cdot 2FP \cdot PS	26.1	63.4

The displacement response, against pressure, for tests CO:1-4 is shown in Figure 4.53, for the first two load/unload cycles of each test. These data are summarised, in terms of residual and maximum displacement, in Figure 4.54.

Figure 4.53 shows the uncorrected, measured displacement for the four tests. Note that the equipment compliance has not been subtracted, and is a component of each result.

The equipment (plus dummy specimen) response (CO:1) is non-linear, for displacement against log-pressure, with an observable increase in stiffness at ≈ 400 kPa. This may be due to the connections between the components closing up and tightening as the load is increased.

The response for the other three tests (CO:2,3,4) is quite different. After the first cycle of loading and unloading there is a residual compressive displacement. Further cycling causes both the maximum and residual displacements to increase slightly, but this increase is small compared to the initial values. Both porous stones and filter papers produce permanent compression during the first loading path. The magnitude of this residual displacement is similar for test CO:2 (2 PS) and CO:3 (2 FP). Subsequent load/unload paths result in a small amount of additional residual displacement.

For the final two tests (CO:3,4) with filter papers, in addition to the residual displacement resulting from the first cycle, there is hysteresis between the reloading and unloading response. The reloading path plots below the subsequent unloading path, meaning that displacement is lower during reloading, at a given pressure, than unloading. This hysteresis is present, but less significant for the two other tests, without filter papers. This suggests that the hysteresis is primarily due to the presence of filter papers.

images/calibration/FP_graph_CO_tests.pdf

Figure 4.53: Filter paper compliance tests: displacement vs pressure for first two load/unload cycles (CO:1-4)

images/calibration/FP_comp_CO_tests.pdf

Figure 4.54: Maximum, residual, and range for displacements for filter paper compliance tests (CO:1-4)

The estimated response for the final test (CO:4) can be calculated based on the previous three tests. The equipment (plus dummy specimen) response (CO:1) can be subtracted from the total response for CO:2 (2 PS), and CO:3 (2 FP), to isolate the response of these components. These isolated components can then be added together, with the equipment response, to estimate the response of porous stones and filter papers in combination. The response for CO:4, and the composite response based on the isolated components of CO:2, CO:3, and the equipment response, is shown in Figure 4.55. The estimated response was found to be a slight under-estimate for the measured residual displacement, and a significant under-estimate for the maximum displacement.



Figure 4.55: Comparison between measured response CO:4, and composite response based on CO:2 and CO:3

In CO:3 (2 FP), the filter papers were compacted between two flat, metal surfaces (the top-cap above, and the brass dummy specimen below). However, in test CO:4 (2PS + 2 FP), the filter papers were placed between the two porous stones, similar to the way they would be in a soil test, although with the caveat that in a soil test, the relatively highly-compressible soil specimen sits between the filter papers. The filter papers may deform into the pitted surface of the adjacent porous stones as the load increases. This would result in a greater compression value than predicted by the separate tests.

Following the first set of compliance tests (CO:1-4), tests with soil specimens were carried out, using filter papers and porous stones, on bentonite clay, and sand. These tests, discussed in Chapters 5 and 6, highlighted the need for a more thorough investigation of compliance.

Further compliance tests were carried out using the temperature-controlled oedometer, TC-OED (TC:1-9), as well as the ambient-temperature electronic oedometer, ML-OED (ML:1-7). Two oedometers were used in order to reduce the testing time, and to enable results to be compared. As discussed in Chapter 3, ML-OED is based on the same design of TC-OED, but without temperature control.

Seven tests were performed in the ambient temperature oedometer (ML:1-7). The loading path followed in these tests was repeated cycles of loading to 5390 N (1400 kPa pressure equivalent for a 70 mm diameter specimen) at 25 kPa min^{-1} and unloading to 5 N (1.3 kPa equivalent pressure) at the same rate. A constant load was held for 1 h at the end of each loading or unloading stage.

Schematic diagrams showing the specimen set-up for tests ML:1-7 are given in Figure 4.56. ML:1 is the dummy only. ML:2 is the dummy above two filter papers and one porous stone (one porous stone was used because these tests were initially performed to simulate the testing conditions used in the sand tests, described in Chapter 6). ML:3 is the dummy above one porous stone. ML:4 is the dummy below two filter papers. ML:5 is the dummy below two porous stones and two filter papers, with the filter papers between the porous stones. ML:6 is a repeat of ML:5, in saturated, rather than dry, conditions. ML:7 is the dummy sample between two porous stones.

For all tests, a brass, cylindrical dummy specimen was used. In tests ML:1-6 the dummy height was 26.1 mm, and diameter 63.4 mm. In test ML:7, the dummy height was 10.0 mm, and diameter 69.8 mm. For the maximum load of 5390 N the theoretical deformation of either dummy specimen is $<0.001 \text{ mm}$. The test set-up information for test series ML is summarised in Table 4.3.

Comparing the results for tests ML:1-7, in Figure 4.57, it is clear that using filter papers increases both the maximum and residual displacement. Residual displacement for tests 1, 3 and 7 (no FP) is negligible, whereas for tests 2, 4, 5 and 6 (with FP), it is not. For the purposes of calibration, the residual displacement is more of an issue than the maximum displacement. The problem is repeatability. When applying the calibration, the *known* values are assumed to remain constant. However, the loading response for the initial and subsequent cycles is different. Therefore, a calibration based on the initial cycle would not be valid for subsequent cycles. Potential solutions considered were to develop multiple calibrations (one for the initial loading, and one, or more, for subsequent unloading and reloading), or find a way to avoid the residual displacement, either by pre-loading the filter papers, or avoiding their use altogether.

The individual component response can be calculated by subtracting the response for ML:1 (equipment) from ML:3 (PS) or ML:4 (2FP). This allows the combined response to be calculated, and compared with ML:2 (PS + 2FP). The measured response (ML:2) is compared to the estimated response based on ML:3 and ML:4 in Figure 4.58. The estimated response underestimates both the measured residual displacement and the maximum displacement.

The same under-estimation of measured displacement, based on combined individual displacements, was observed in the previous set of tests (CO:1-4). Again, this shows that displacement components cannot just be added up, and that interaction between components is important. It seems that there is some interaction between the filter papers and the porous stones which results in increased residual and maximum displacement.

Test ML:5 was performed to assess the proposed calibration procedure (used for tests on sand, but superseded by a new procedure for tests on KSS), in which filter papers would be pre-loaded prior to testing. The data from the pre-loading test would be used to determine the calibration curve for the filter papers. This is discussed further below, and in Section 6.5.

The behaviour of dry and saturated filter papers was compared in tests ML:5 and ML:6, which had the same set-up (2PS + 2FP), but ML:5 was performed in dry conditions, and ML:6 in saturated conditions. The residual displacement is higher for ML:6, but the maximum displacement is lower. However, the response was qualitatively similar, and this variation may be due to inherent variability in the properties of the filter paper, rather than whether they are saturated or not. Inherent variability of filter papers was investigated with tests VAR:1-5, which are

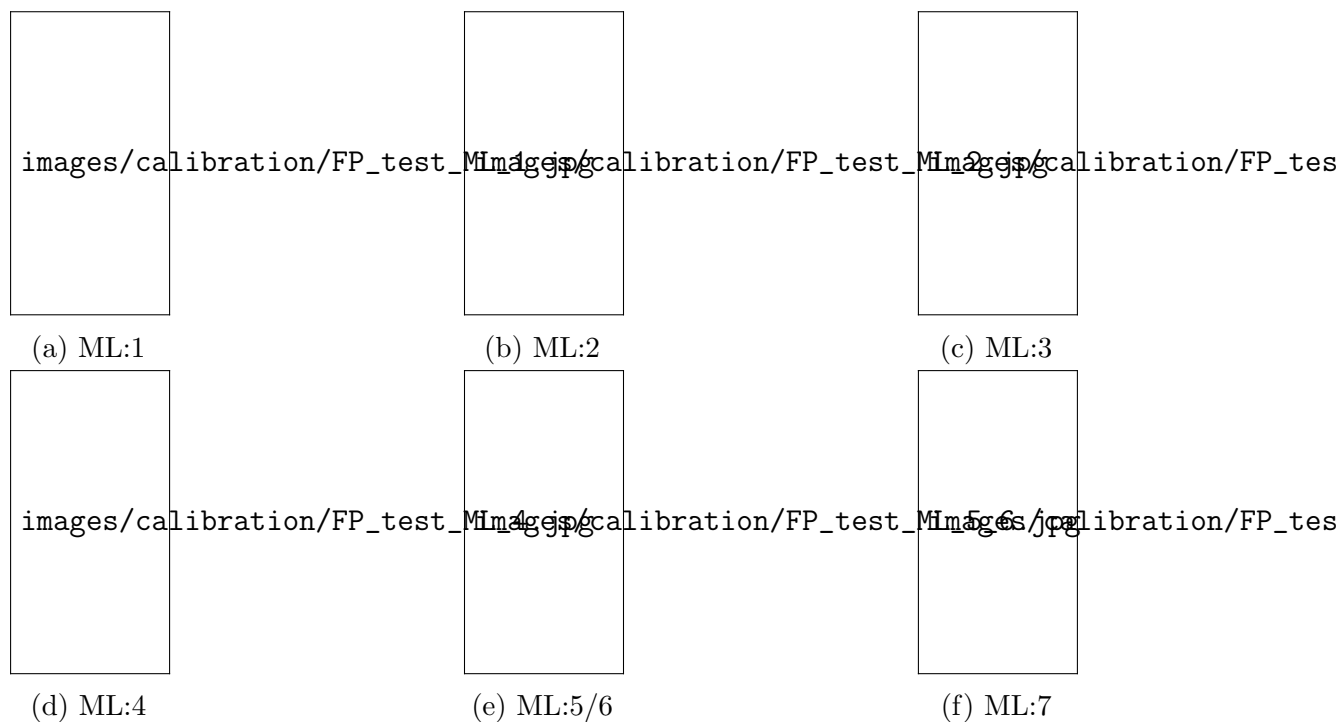


Figure 4.56: Schematic test set-up for filter paper compliance tests in ambient-temperature oedometer (ML:1-7)

Table 4.3: Calibration test series ML - summary

Test	Equipment	Specimen (base → top)	Brass dummy dimensions	
			Height [mm]	Diameter [mm]
ML:1	ML-OED	D	26.1	63.4
ML:2	ML-OED	PS · 2FP · D	26.1	63.4
ML:3	ML-OED	PS · D	26.1	63.4
ML:4	ML-OED	D · 2FP	26.1	63.4
ML:5	ML-OED	D · PS · 2FP · PS	26.1	63.4
ML:6	ML-OED	D · PS · 2FP · PS	26.1	63.4
ML:7	ML-OED	PS · D · PS	10.0	69.8

images/calibration/FP_comp_ML_1_7.pdf

Figure 4.57: Maximum, residual, and range for displacements for filter paper compliance tests in ambient-temperature oedometer (ML:1-7)

images/calibration/FP_comp_ML_composite.pdf

Figure 4.58: Comparison between measured response ML:2, and composite response based on ML:3 and ML:4

discussed below. It was concluded that results for tests using dry filter papers are valid, at least qualitatively, for both dry and saturated conditions.

Schematic diagrams showing the specimen set-up for the nine temperature-controlled oedometer (TC-OED) tests are given in Figure 4.59. Test TC:1 has the dummy above two filter papers and one porous stone. TC:2 has the dummy above three filter papers and one porous stone. TC:3 has the dummy above one porous stone. TC:4 has the dummy only. TC:5 has the dummy only (note: this is a different dummy to TC:4). TC:6 has the dummy below two porous stones. TC:7 has the dummy below two porous stones, which are either side of two filter papers. TC:8 has a similar set-up to TC:7, but with the dummy between the filter papers, rather than below the lower porous stone. TC:9 is a repeat of TC:8.

A brass, cylindrical dummy specimen was used for all tests. In tests TC:1-4, the dummy dimensions were: height = 15.3 mm, diameter = 50.8 mm. In tests TC:5-9, the dummy dimensions were: height = 10.0 mm, diameter = 69.8 mm. For the maximum load of 5770 N, in either case, the theoretical deformation of the dummy specimen is <0.001 mm. The test set-up information for test series TC is summarised in Table 4.4.

The loading path followed in these tests was repeated cycles of loading to 5770 N (1500 kPa pressure equivalent for a 70 mm diameter specimen) at 25 kPa min^{-1} and unloading to 5 N (1.3 kPa equivalent pressure) at the same rate, held for 1 h at the maximum and minimum load.

The results from tests TC:1-9 are summarised in Figure 4.60 (TC:1-4) and Figure 4.61 (TC:5-9). The results are split into two figures because a different dummy specimen was used for tests TC:1-4 and TC:5-9, so the results may not be directly comparable. Although the deformation of the dummy specimen is negligible in either case, the pressure applied to the compressible elements is affected by the dummy specimen cross-sectional area, and the resulting deformation may not be negligible.

Comparing the residual and maximum displacements in Figure 4.60 and Figure 4.61, again, the issue with filter papers is clear. Tests TC:3,4,5 (without FP) have negligible residual displacement, and lower maximum displacement, compared to tests TC:1,2,7,8,9 (with FP). One exception to this is TC:6 (2 PS), which has no filter papers, but two porous stones in direct contact, with the dummy specimen below. In this case, the residual displacement is not negligible, although it is lower than tests TC:2,7,8,9. This shows that there is interaction between the two porous stones. This result agrees with the result from test CO:2 (2 PS), which also found non-negligible residual displacement for two porous stones in direct contact. In test ML:7 (2 PS), which also used two porous stones, but with the dummy specimen between, rather than below them, the residual and maximum displacements were both low, and the result was similar to ML:1, for equipment (plus dummy specimen) only.

Comparing tests TC:1 (PS + 2FP) and TC:2 (PS + 3FP) shows that increasing the number of filter papers increases the residual and maximum displacement.

Comparing TC:3 (PS) and TC:4 (dummy only) again shows that summing the displacement values for separate components is not a valid way to estimate total displacement. Both tests have negligible residual displacement, as expected. However, the maximum displacement is higher for TC:4. It is not clear why this should be the case, but this result shows that any calibration obtained can only (at best) be valid for the same equipment configuration used to obtain the calibration. The fact that the calibration must necessarily be obtained without the soil specimen present means that no calibration procedure can be completely accurate. For this to be the case, the dummy specimen would have to have the same properties of the soil. Obtaining these properties is the purpose of the soil test, so clearly this ideal calibration is impractical.

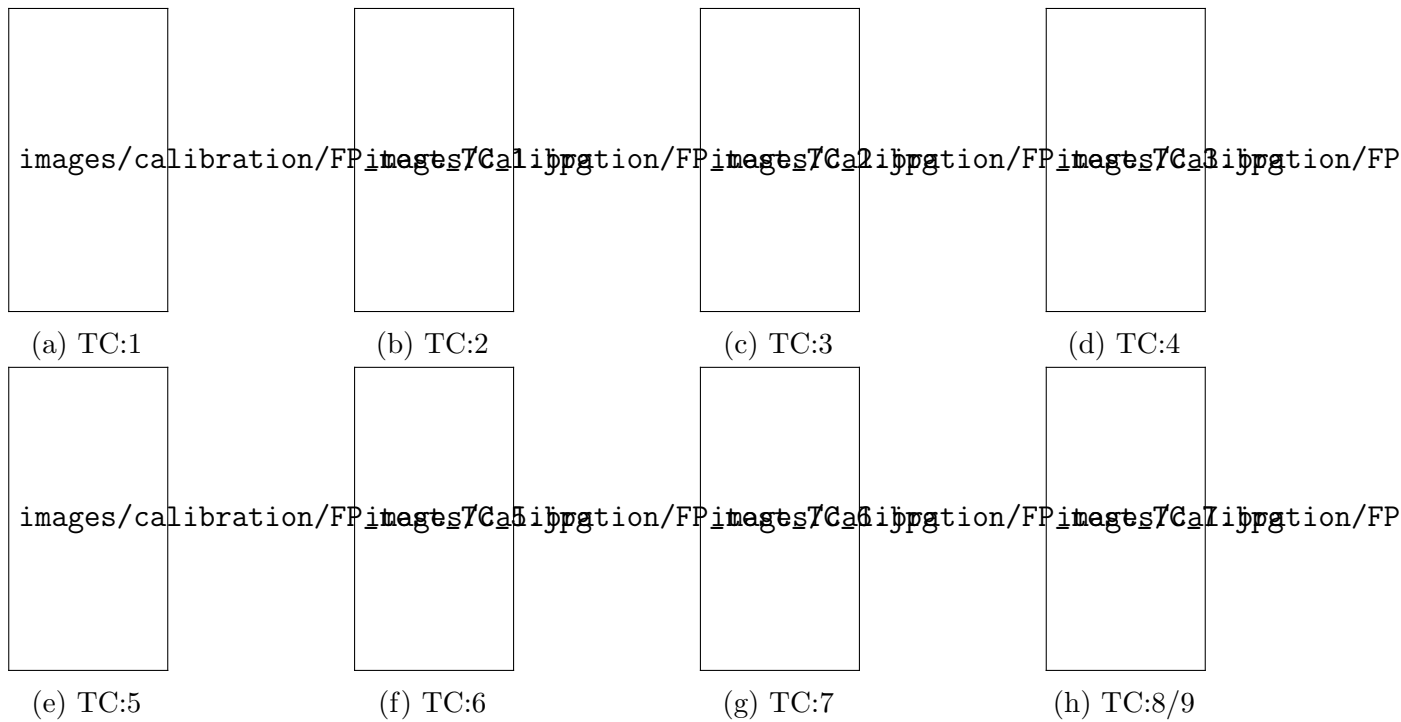


Figure 4.59: Schematic test set-up for filter paper compliance tests in temperature-controlled oedometer (TC:1-9)

Table 4.4: Calibration test series TC - summary

Test	Equipment	Specimen (base → top)	Brass dummy dimensions	
			Height [mm]	Diameter [mm]
TC:1	TC-OED	PS · 2FP · D	15.3	50.8
TC:2	TC-OED	PS · 3FP · D	15.3	50.8
TC:3	TC-OED	PS · D	15.3	50.8
TC:4	TC-OED	D	15.3	50.8
TC:5	TC-OED	D	10.0	69.8
TC:6	TC-OED	D · 2PS	10.0	69.8
TC:7	TC-OED	D · PS · 2FP · PS	10.0	69.8
TC:8	TC-OED	PS · FP · D · FP · PS	10.0	69.8
TC:9	TC-OED	PS · FP · D · FP · PS	10.0	69.8

images/calibration/FP_comp_TC_1_4.pdf

Figure 4.60: Maximum, residual, and range for displacements for filter paper compliance tests in TC oedometer (TC:1-4)

images/calibration/FP_comp_TC_5_9.pdf

Figure 4.61: Maximum, residual, and range for displacements for filter paper compliance tests in TC oedometer (TC:5-9)

Comparing TC:5 (dummy only) and TC:6 (2PS), it can be seen that the addition of two porous stones results in higher residual displacement, but slightly lower maximum displacement. This result is similar to the lower maximum displacement found for TC:4, compared to TC:3, suggesting that the first result, although unusual, is not erroneous.

The aim of tests TC:7 and TC:8 was to determine the effect the position of the dummy specimen had on the displacement. Both tests use two filter papers between two porous stones. In TC:7, the dummy specimen is below the lower porous stone, whereas in TC:8, the dummy specimen is between the filter papers. The residual and maximum displacements are significantly higher for TC:8. The maximum displacement was so high that TC:8 was repeated. This time, for TC:9, rather than using new, unused filter papers, the filter papers from TC:7 were reused. The results for TC:9 are similar to TC:7, with slightly lower residual and maximum displacements. It is possible that the high displacements measured in TC:8 are due to the inherent variability of the properties of the filter papers. Comparing tests TC:7 and TC:9 suggests that the position of the dummy specimen is not important in this case, although results from other tests suggest otherwise. For example, compare CO:2, or TC:6, to ML:7. All three tests have two porous stones, and no filter papers. Where the porous stones are adjacent, in CO:2 and TC:6, there is a significant residual displacement. However, in ML:7, where the dummy is placed between the porous stones, the displacement is negligible.

The combined thermal and mechanical calibration, using the data from test 1A in Section 4.4, was applied to the measured data for tests on sand, as discussed in Section 6.5. Based on these results, it was clear that even for ambient-temperature tests, this calibration was not accurate. A new calibration equation was therefore developed, based on the data from test TC:2. The specimen schematic for this test is given in Figure 4.59. In test TC:2, the brass dummy specimen (height: 15.3 mm, diameter: 50.8 mm) sits above three filter papers and one porous stone. This test path comprised nine load/unload cycles between 2.5 kPa and 1500 kPa.

This test was chosen because at the time it was the most relevant compliance test already completed, from which a calibration could be derived for the tests on sand. In the sand tests, discussed in Chapter 6, the sand specimen sits between two filter papers, with a porous stone below, but without one above (except for the final sand test). The set-up used for test TC:2 is similar. There are limitations though. First, the dummy specimen used in test TC:2 has a smaller diameter than the confining ring. This means that the pressure applied to the filter papers will be higher than assumed based on a 70 mm diameter specimen. Second, three filter papers were used in test TC:2, while only two were used for the tests with sand. Third, the load path followed in test TC:2 comprised a series of load/unload cycles between 2.5 kPa and 1500 kPa, whereas in the sand tests, more complex load paths were followed. These limitations are a necessary caveat for analysing this calibration, but it is also helpful to rephrase them in terms of guidelines for future compliance tests, for example, the tests on KSS. If a dummy specimen is used, it should be the same diameter as the tested soil specimen. The compliance test set-up should be the same as for the soil test (i.e. use the same number and configuration of filter papers and porous stones). The compliance test load path should be the same as in the soil test.

The method for determining the calibration is as follows, with reference to the schematic graphs in Figure 4.62. The displacement-pressure response for the first two load/unload cycles is shown in Figure 4.62a. The first cycle induces a residual displacement. Subsequent load/unload cycles induce a much smaller (additional) residual displacement, and a negligible increase in the maximum displacement. A compliance curve based on the initial loading path will not accurately reflect the response for subsequent unloading or reloading paths. A compliance curve based on

cycle 2 (for example), will reasonably accurately reflect the response for subsequent cycles, but not the initial cycle. Rather than using multiple calibration equations (initial loading, subsequent unloading/reloading), the initial response was avoided by pre-loading the filter papers. The assumption that pre-loaded filter papers would follow a path similar to cycle 2, not cycle 1, was checked with test ML:5, and discussed below. The displacement for cycle 2 (or a later cycle), is isolated and initialised (i.e. set to zero, for a pressure of 2.5 kPa), as shown schematically in Figure 4.62b. Determining the calibration fit is now easier, but still requires judgement. There is still a residual displacement following the load/unload cycle, although it is an order of magnitude less than for cycle 1. Also, there is hysteresis between the load and unload paths. A fit through the whole data set, as shown in Figure 4.62c, will over-estimate the compliance during loading stages, and under-estimate it during unloading.

The displacement-pressure response for the first three load/unload cycles of test TC:2 are shown in Figure 4.63. As expected, there is a significant residual displacement following cycle 1 (≈ 0.13 mm). For subsequent cycles, the increase in residual displacement is much less (≈ 0.016 mm for cycle 2), and reduces with increased cycle number. The maximum displacement likewise increases by a small amount with each cycle.

By cycle 9, the increase in residual displacement per cycle is < 0.001 mm, and the increase in maximum displacement is even lower. The data from cycle 9 was isolated and initialised, as shown in Figure 4.64. Then an equation was fitted through the data. A 6th order polynomial (Poly6) gave the best fit.

The new calibration and previous calibration are compared in Figure 4.65. The data from cycle 1 and 2 of test TC:2 is shown, together with the semi-log correction based on the combined thermal and mechanical calibration discussed in Section 4.4. The semi-log calibration does not capture the initial loading response particularly well, except for the displacement at maximum pressure. The initialised cycle 9 response can be considered indicative of the response for subsequent cycles. The semi-log correction significantly over-estimates the compliance. These corrections were both applied to sand test data, as discussed in Section 6.5, and the polynomial fit was found to be far more accurate than the semi-log fit.

This methodology was improved (based on the suggestions above) for deriving the compliance for sand tests 9 to 11. Following sand test 11, filter papers were no-longer used.

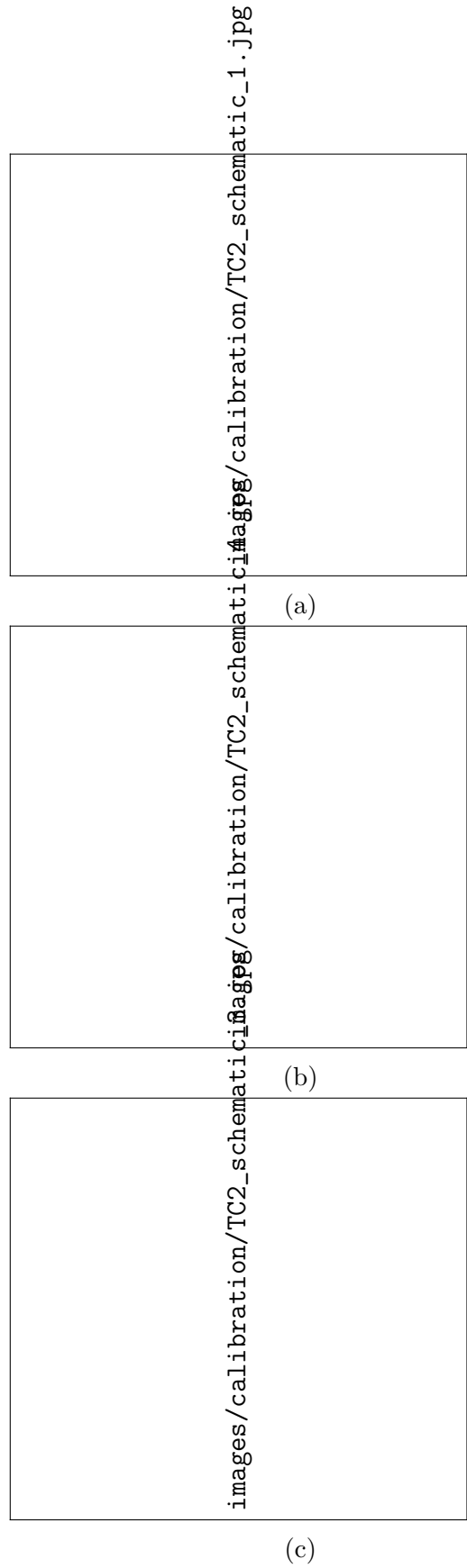



Figure 4.62: Schematic showing load/unload response for test TC:2 (a) first two cycles (b) cycle 2 response, initialised at start of cycle 2 (c) example fit through cycle 2 data

images/calibration/TC2_cycles_1_3.pdf

Figure 4.63: Test TC:2 - loading cycles 1 - 3

images/calibration/TC2_cycle_9.pdf

Figure 4.64: Test TC:2 - loading cycle 9




images/calibration/TC2_fit_comparison.pdf

Figure 4.65: Test TC:2 - comparison of previous fit based on test TC 1A (semi-log), and new fit based on TC:2 (poly6)

A final set of tests were performed, VAR:1-5, to investigate the inherent variability of filter papers. Five tests were performed, using the set-up shown in Figure 4.66. Tests VAR:1-3 were performed with filter papers that had previously been used in other compliance tests. Tests VAR:4-5 were performed with new, unused filter papers. All filter papers were the same type (Whatman 54), from the same box. The dummy dimensions were: height = 10 mm, diameter = 69.8 mm.

The results are shown in Figure 4.67. Tests VAR:1-3 (previously used filter papers) have higher maximum displacements, residual displacements, and range of displacements, than tests VAR:4-5 (new filter papers). This shows that the loading history of the filter papers does affect their properties, although as discussed in Section 4.4, this does not necessarily mean that their properties can be predicted. There was some variability between tests VAR:4-5, although this variability does not seem significant enough to have caused the anomalous result found for test TC:8.



images/calibration/FP_test_VAR.jpg

Figure 4.66: Schematic test set-up for filter paper variability tests (VAR:1-5)

images/calibration/FP_comp_VAR_1_5.pdf

Figure 4.67: Maximum, residual, and range for displacements for filter papers from same box (VAR:1-5)

The clear conclusion of these tests is to avoid the use of filter papers in any temperature-controlled oedometer tests. However, the initial aim of the tests was not to determine whether or not to use filter papers, but to find a repeatable, accurate method for correcting for their compressibility. For this reason, it is not considered necessary to go through the tests one-by-one, but instead to explain only the key results that led to this conclusion.

First, three test results from the filter paper compliance tests performed in the temperature-controlled oedometer (TC:5,6,7) are shown. These results are shown to emphasise how the choice of specimen affects not just the residual and maximum displacement, but the displacement response over the full range of tested pressures. The set-up for tests TC:5,6,7 is shown again in Figure 4.68, with the results in Figure 4.69. For each test, the first two load/unload cycles are plotted.

The equipment response, given by TC:5 (equipment plus dummy specimen), is non-linear, with a clear transition at ≈ 400 kPa. The residual displacement following the first cycle is negligible. In the second cycle, there is no significant hysteresis between the loading and unloading paths, and no increase in the residual or maximum displacement.

The porous stone response, given by TC:6 (2PS) shows a much clearer difference between the first loading path, and the subsequent response for unloading and second reload/unload cycle. The response for the second cycle is non-linear, with a smoother transition, at lower pressure (≈ 100 kPa), than for TC:5. The residual displacement is much higher than for TC:5 (dummy only), and is no-longer negligible. However, surprisingly, the maximum displacement for TC:6 is lower than for TC:5. As in TC:5, for the second cycle, there is no significant hysteresis between the loading and unloading paths. Displacements for the second cycle are higher than the first,

indicating that there is a slight ratcheting effect from repeated cycling, which is not observed for TC:5.

The combined porous stone and filter paper response is given by TC:7 (2PS + 2FP). The maximum and residual displacements are both high, compared to TC:5 and TC:6. The second cycle response is more linear than for TC:6, with a less distinct transition, at lower pressure (≈ 10 kPa). There is significant hysteresis between the reloading and unloading path for the second cycle, which is not observed for the other two tests. This hysteresis appears to be due to the presence of the filter papers. The ratcheting effect is more significant than for TC:6, although is still relatively small compared to the effects of the first loading path.

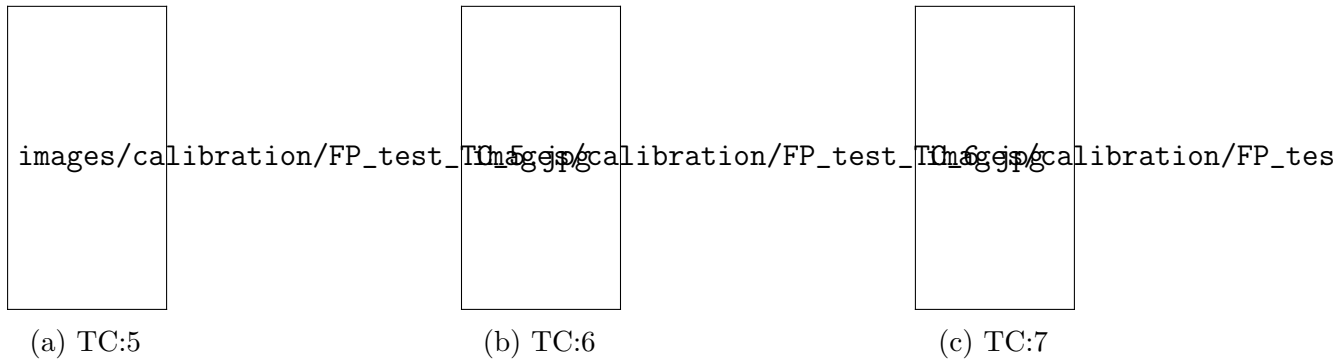


Figure 4.68: Schematic test set-up for tests TC:5,6,7

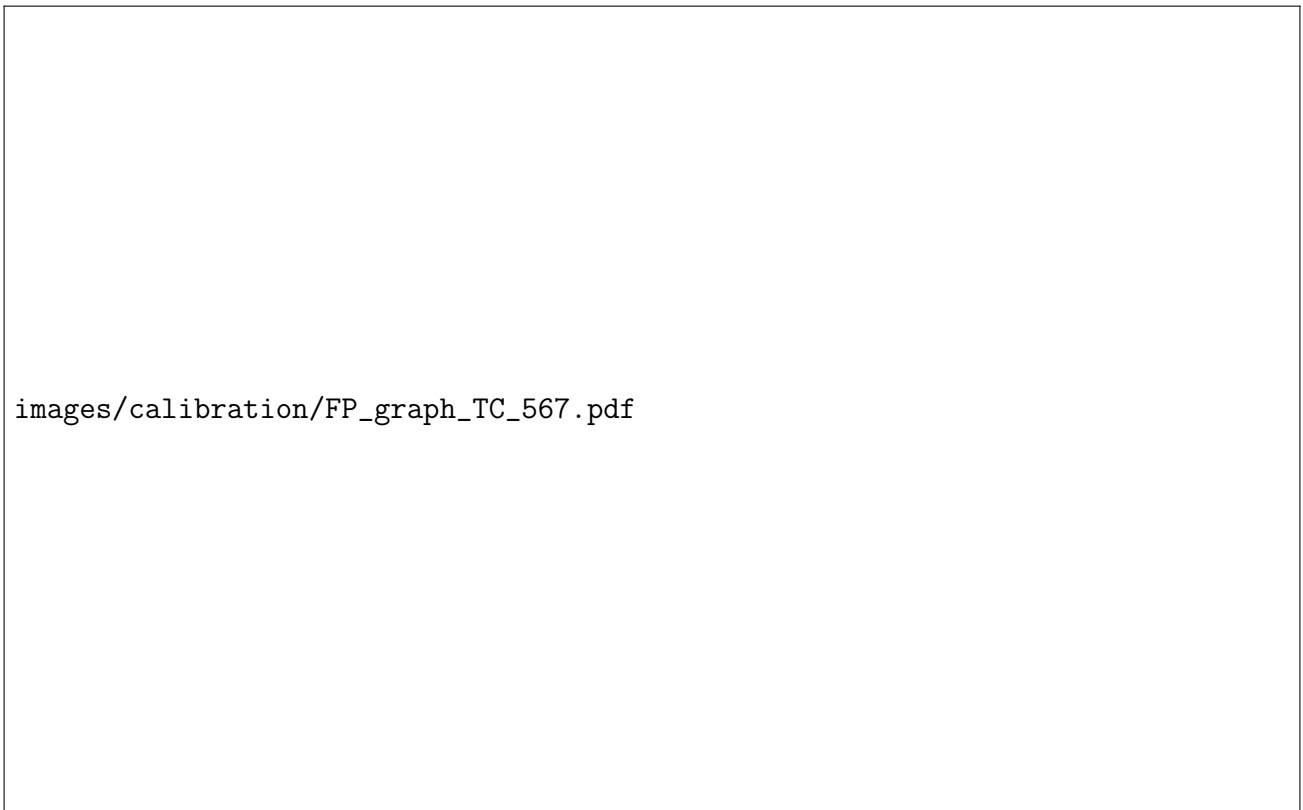


Figure 4.69: Tests TC:5,6,7 - displacement vs pressure for first two load/unload cycles

The next test to be discussed is test ML:5 from the series of calibration tests performed in the ambient temperature oedometer. The purpose of this test was to simulate a proposed calibration procedure, used for tests on sand, which involved pre-loading the filter papers before each test. This procedure is discussed further in Section 6.5. The set-up for test ML:5 is given in Figure 4.70, with the results, in terms of displacement against pressure, given in Figure 4.71.

Three load/unload cycles are plotted. Cycle 1 was the initial load/unload path, which was held for 24 h at the maximum load (1500 kPa equivalent pressure), and 16 h at the minimum load (2.5 kPa) following unloading. Cycle 2 was the second load/unload path, which was held for 1 h at the maximum and minimum loads. Cycle 3 was the third load/unload path, where the load was applied incrementally, with each increment of 24 h duration (seven loading increments in total). The incremental loading, and relatively long duration of this cycle was chosen to simulate actual test conditions on a soil, in which load increments would be held for at least 24 h.

There is a clear difference between cycle 1, and cycles 2 and 3. Cycle 1 results in a residual displacement, which does not increase significantly with further cycling. The unloading paths for all three cycles plot almost on top of each other, as do the reloading paths for cycles 2 and 3. This implies a response analogous to over-consolidation in soil. The loading path for cycle 1 causes permanent, irreversible displacement, which is not fully reversed during unloading, resulting in residual displacement. This is like the plastic response upon loading of a normally-consolidated soil. Subsequent reloading and unloading paths do not result in any further residual displacement. This is like the elastic response upon unloading and reloading of an over-consolidated soil.

This result seemed to support the proposed calibration methodology. In this case, a calibration based on cycle 2 would be valid for cycle 3. However, when applied to tests on sand, as described in Chapter 6, this methodology was found to be flawed. The filter paper response was found to only be repeatable under certain conditions. For example, the filter paper response before, and after, a test on soil, was found to not be repeatable. This is shown clearly in sand test 9, discussed in Section 6.5. The unsuitability of this methodology led to the decision to stop using filter papers completely, and only use porous stones, when carrying out tests on soil.

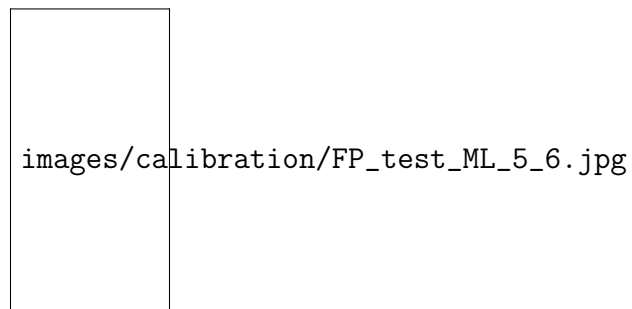


Figure 4.70: Schematic test set-up for test ML:5

The conclusion from all the tests described in this section is to avoid the use of filter papers. This is particularly important for thermal testing, since thermal effects are generally small compared to mechanical effects, and thus more sensitive to calibration errors. There are a number of issues associated with filter papers which make them unsuitable for these sorts of tests. Filter papers are highly compressible. They compress instantaneously upon loading, and compress further over time. Their compression response depends on their loading history, like a soil. The initial loading response is different from the subsequent unloading and reloading response. This results in significant residual displacement following the first load/unload path. Filter papers

images/calibration/FP_graph_ML_2e.pdf

Figure 4.71: Test ML:5 - displacement vs pressure for first three load/unload cycles

also show hysteresis, between the reloading and unloading responses, with higher displacements for unloading, compared to reloading, for the same pressure value.

Tests were performed to determine whether this residual displacement could be negated, by pre-loading the filter papers before each test, and using the pre-loading data to determine a calibration curve specific for each test. However, further tests on sand, described in Chapter 6, showed that this methodology would not work.

The use of porous stones is considered justifiable, although the effect of their interaction with the soil has not been quantified, and is a potential source of error. In isolation, porous stones show minimal residual displacement following load/unload cycles, and minimal hysteresis between the reloading and unloading path. However, when more than one porous stone is used adjacent to another, or in combination with other compressible elements (e.g. filter paper), they cause residual displacement to develop. This is not ideal, but porous stones are essential for allowing drainage of the specimen, and many of the uncertainties in their response can be mitigated through a well-designed calibration and testing methodology.

4.6 Lateral thermal and mechanical deformation

In this section, the radial (thermally-induced) deformation of the confining ring is discussed. This deformation was not measured, but calculated, based on the thermal expansion coefficient of the stainless-steel confining ring. The calculation of the radial deformation of the confining ring is simple. However, the effect of the differential thermal expansion (or contraction) of the confining ring and the soil specimen, is complex, and comprises the main part of this section.

4.6.1 Strain

In the discussion of the deformation of the confining ring, the term *strain* is used. Strain is a general term, but can have a number of more specific components, such as total strain, thermal strain, and mechanical strain. The definition of strain, its calculation, and components, are described in this section. The term strain is used in the literature when quantifying the relative magnitude of volume change. Volumetric strain ϵ_v is defined as the ratio of the change in volume to the initial volume:

$$\epsilon_v = \frac{\Delta V}{V_0} \quad (4.8)$$

where:

$$\begin{aligned} \Delta V &= \text{change in volume} \\ V_0 &= \text{initial volume} \end{aligned}$$

However, it is not strictly necessary to use the *initial* volume. The change in volume ΔV can be normalised by any reference volume. For example, consider a typical isobaric heating/cooling test, in which the specimen is normally-consolidated from slurry, then heated and cooled at constant pressure. Here, V_0 could be taken as the volume at the start of consolidation, or the volume at the start of heating. When comparing the thermally-induced volumetric strain for heating and cooling, V_0 could be taken as the volume at the start of heating in both cases, or V_0 at the start of heating or cooling could be used to calculate the heating and cooling strains respectively. These choices show that it is important to be clear about how strain is defined. In this research, three definitions of strain are given: total strain, incremental strain, and sub-incremental strain, defined below.

Strain definition and calculation

Total strain (relative to test initial condition) $\epsilon_{v,total}$ is defined as the total change in volume during the full test ΔV_{test} , relative to the volume at the start of the test $V_{0,test}$:

$$\epsilon_{v,total} = \frac{\Delta V_{test}}{V_{0,test}} \quad (4.9)$$

Incremental strain (relative to test initial condition) $\epsilon_{v,inc}$ is defined as the change in volume during the increment or stage ΔV_{inc} (e.g. during a heating stage, during a single heating/cooling cycle, or during multiple heating/cooling cycles), relative to the volume at the start of the test $V_{0,test}$:

$$\epsilon_{v,inc} = \frac{\Delta V_{inc}}{V_{0,test}} \quad (4.10)$$

Sub-incremental strain (relative to increment/stage initial condition) $\epsilon_{v,inc,stage}$ is defined as the change in volume during the increment or stage ΔV_{inc} , relative to the volume at the start of the increment or stage $V_{0,inc}$:

$$\epsilon_{v,sub-inc} = \frac{\Delta V_{inc}}{V_{0,inc}} \quad (4.11)$$

Which definition of strain is used, is a matter of preference. However, it is important to (i) be clear about which definition of strain is used, and (ii) only compare strains which have been defined in the same way.

Components of thermal strain

The change in volume, or strain, of a soil subjected to heating, is a result of thermal and mechanical actions.

The mechanical action cannot be measured directly. However, its effect can be inferred by considering the other strain components. The total strain, which is what is measured during the test, is the sum of the thermal and mechanical strains:

$$\epsilon_v^{total} = \epsilon_v^{thermal} + \epsilon_v^{mechanical} \quad (4.12)$$

where:

$$\begin{aligned} \epsilon_v^{total} &= \text{total strain} \\ \epsilon_v^{thermal} &= \text{thermal strain} \\ \epsilon_v^{mechanical} &= \text{mechanical strain} \end{aligned}$$

To clarify, all these terms (ϵ_v^{total} , $\epsilon_v^{thermal}$ and $\epsilon_v^{mechanical}$) refer to strains due to temperature change. ϵ_v^{total} is the total measured strain, resulting from a temperature change, under constant vertical pressure. $\epsilon_v^{thermal}$ is the strain directly due to thermal expansion of the soil, and is a function of the thermal expansion coefficient of the soil. For drained conditions, the thermal expansion coefficient of the soil skeleton is used, rather than the thermal expansion coefficient of the soil as a whole. $\epsilon_v^{mechanical}$ is the mechanical strain due to the differential thermal expansion of the soil and confining ring, and the differential thermal expansion of the solid and liquid phases of the soil. Note also that it is important to specify which reference volume has been used to calculate the total strain, as discussed above.

The thermal strain $\epsilon_v^{thermal}$ can be calculated, as shown below. The total strain ϵ_v^{total} can be measured in the oedometer. In fact, height, not volume, is measured. A correction for thermal expansion of the confining ring must first be made to the height value, from which the volume and volumetric strain can be calculated, as discussed below.

The thermal action is due to the thermal expansion of the soil skeleton, which is a function of the volumetric thermal expansion coefficient α_v of the solids, and the change in temperature ΔT . The thermal strain, $\epsilon_v^{thermal}$ is calculated as follows:

$$\epsilon_v^{thermal} = -\alpha_v \cdot \Delta T \quad (4.13)$$

The negative sign is required to conform to the sign convention used throughout this thesis, where positive strains correspond to compression. It means that for positive values of ΔT (i.e. for heating), thermal strain $\epsilon_v^{thermal}$ will be negative (i.e. expansive).

The mechanical action is more complex, and is due to changes in the lateral stress resulting from the specific confinement conditions of the oedometer. The first component of the mechanical action arises from the differential thermal expansion of the confining ring and the soil. The thermal expansion coefficient of the stainless-steel confining ring is typically greater than the thermal expansion coefficient of the soil skeleton. This means, during heating, the lateral

expansion of the confining ring is greater than that of the soil. However, due to the applied vertical load, the soil expands laterally to fill the available space, resulting in a reduction in soil height. The lateral expansion of the confining ring also results in a reduction in the lateral stress in the soil. During cooling, the lateral contraction of the confining ring is greater than that of the soil, and the soil is compressed laterally, resulting in an increase in the soil height, and an increase in the lateral stress in the soil. An increase in stress will cause an increase in pore-water pressure in low-permeability soil such as clay, which will result in a reduction in void ratio, once the excess pore-water pressure has dissipated. In effect, the increase in stress results in further consolidation of the soil. A correction is applied to account for the change in height, due to the interaction between the confining ring and the soil. The mechanical strain resulting from changes in the lateral stress in the soil due to this same interaction cannot be directly measured.

A second component of the mechanical action arises from the differential thermal expansion of the solid and liquid phases of the saturated soil. The thermal expansion coefficient liquid phase (water) is generally much higher than that of the solid phase of the soil. During heating, the pore-water expands more than the soil skeleton. If the soil is not free-draining (for example, if the soil is a low-permeability clay), this will result in an increase in the pore-water pressure, and a corresponding decrease in effective stress. Over time, this excess pore-water pressure dissipates, resulting in consolidation of the soil. The mechanical strain resulting from these stress changes cannot be directly measured.

Neither component of mechanical strain (due to differential thermal expansion of the confining ring and soil, and due to differential thermal expansion of the soil solid and liquid phases) is accounted for by $\epsilon_v^{thermal}$. Nevertheless, they will affect the measured total strain ϵ_v^{total} . Therefore, they are accounted for in the mechanical strain component $\epsilon_v^{mechanical}$ of the total strain.

The equation above can be rearranged to give the mechanical strain $\epsilon_v^{mechanical}$ in terms of the measured total strain ϵ_v^{total} and the calculated thermal strain $\epsilon_v^{thermal}$.

$$\epsilon_v^{mechanical} = \epsilon_v^{total} - \epsilon_v^{thermal} \quad (4.14)$$

4.6.2 Calculation: thermal deformation of confining ring

The calculations relating to the thermal deformation of the confining ring, its magnitude, effects, and corrections, are described in this section.

The thermally-induced lateral expansion of the soil specimen, and the confining ring, can be calculated based on their thermal expansion coefficients. The change in diameter of the soil, Δd_{soil} , is a function of the initial diameter d_0 , the *linear* thermal expansion coefficient of the soil $\alpha_{L,soil}$, and the change in temperature ΔT , where positive ΔT corresponds to an increase in temperature, and positive Δd corresponds to an increase in diameter:

$$\Delta d_{soil} = d_0 \cdot \alpha_{L,soil} \cdot \Delta T \quad (4.15)$$

The linear thermal expansion coefficient of the soil $\alpha_{L,soil}$, can be calculated from the volumetric thermal expansion coefficient, assuming the soil is isotropic, using the method described in Appendix D. Alternatively, for anisotropic soil, the linear coefficient of thermal expansion parallel to the lattice orientation of the soil can be used, if known. This is discussed further in relation to the tests on bentonite (Chapter 5) and sand (Chapter 6).

The change in the internal diameter of the confining ring can be calculated in the same way, although for the case of a hollow cylinder, this result is not intuitive. Holes in materials expand and contract as if they were made from the surrounding material (Duffy, 2012). An example of this theory is shown in Figure 4.72. Consider a solid disc with diameter equal to the outer diameter of the confining ring. A circle is drawn on this disc, so that the diameter of the circle matches the inner diameter of the confining ring. When the temperature is raised, the entire disc expands, including the circle that was drawn on the disc. Removing the material inside the circle leaves a ring. Doing this in reverse order - removing the inside of the circle and then raising the temperature - has the same result. The ring is the same size in both cases – a hole expands or contracts as if it were solid.

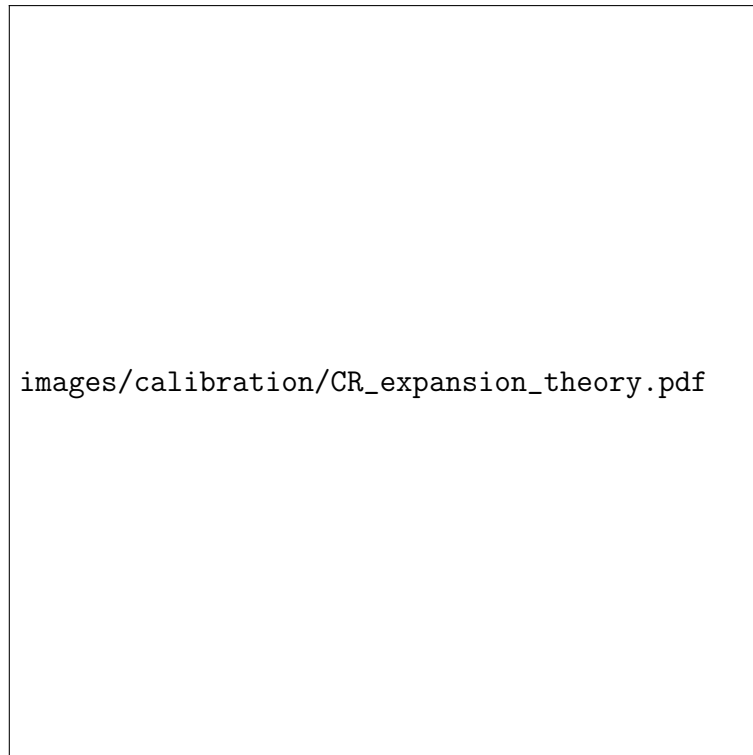


Figure 4.72: Schematic showing thermal expansion of a hollow cylinder

Therefore, the change in diameter of the confining ring can be calculated using the following equation.

$$\Delta d_{CR} = d_{CR,0} \cdot \alpha_{L,CR} \cdot \Delta T \quad (4.16)$$

where:

- Δd_{CR} = change in internal diameter of the confining ring
- $d_{CR,0}$ = initial internal diameter of the confining ring
- $\alpha_{L,CR}$ = linear thermal expansion coefficient of the confining ring (stainless-steel)
- ΔT = change in temperature

The aim of these calculations is to determine the effect of lateral thermal expansion/contraction of the confining ring on the specimen height. Heating causes expansion of the confining ring, and the soil specimen, in both the lateral and vertical direction, as shown in Figure 4.73. An increase in temperature ΔT , results in an increase in the internal diameter d_{CR} and height H_{CR} of the confining ring, and an increase in the diameter d_{soil} and height H_{soil} of the soil specimen.

For unconfined conditions, these changes ($\Delta d, \Delta H$) are a function of the thermal expansion coefficient of the confining ring, or soil specimen.

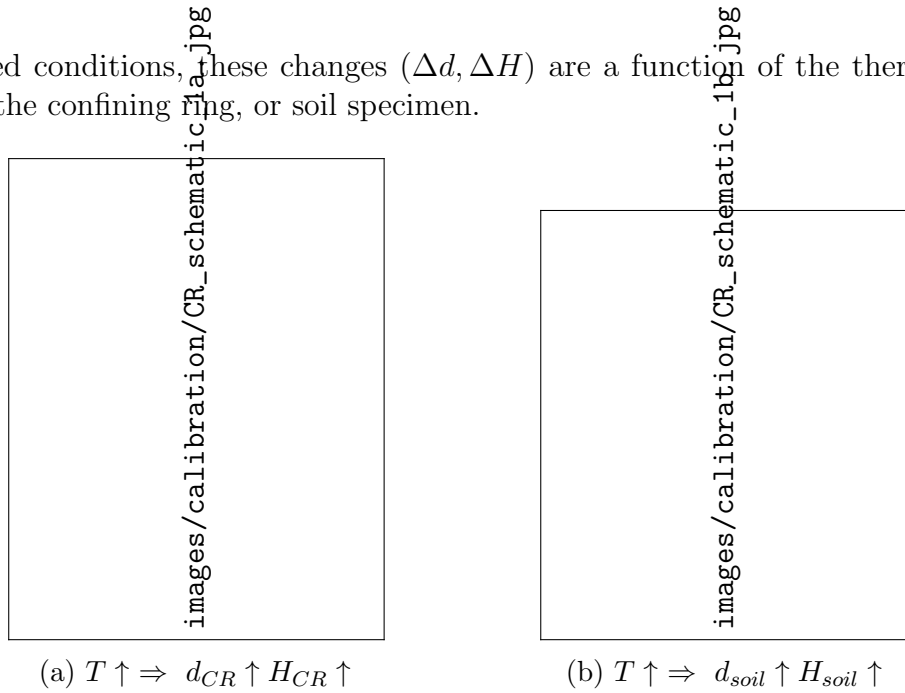


Figure 4.73: Schematic showing effect of heating on dimensions of (a) confining ring and (b) soil

However, for oedometric conditions, there is some interaction between the confining ring and the soil specimen that must be considered. The thermal expansion coefficient of the stainless-steel confining ring is typically higher than the tested soil. This means that when heated, the lateral, thermal expansion of the confining ring is higher than that of the soil.

Figure 4.74a shows the initial condition for a heating test under oedometric conditions. At ambient temperature, the soil diameter $d_{soil,0}$ is equal to the internal diameter of the confining ring $d_{CR,0}$.

Heating causes the diameter of the confining ring and the soil to increase, as shown in Figure 4.74b. The internal diameter of the confining ring $d_{CR,1}$ is greater than the soil diameter $d_{soil,1}$. Theoretically, a gap develops between the soil and the confining ring.

In practice, no gap develops, because of the vertical load applied to the soil. This causes the soil to expand laterally to fill the available space. This lateral expansion results in a reduction in the height of the soil ΔH_{soil} , as shown in Figure 4.74c. This reduction in height is not a direct thermal effect. It is a mechanical effect, resulting from the differential thermal expansion of the confining ring and the soil.

Consider a hypothetical case, with a specimen made of the same material as the confining ring. In this case, the confining ring can be ignored, since it expands laterally by the same amount as the specimen, and no lateral stresses due to differential expansion develop. The specimen still expands both vertically and laterally so true one-dimensional conditions are not maintained. However, this lateral expansion is a purely thermal effect. It has no effect on the specimen height, which increases as a result of heating, and therefore there would be no need to apply a correction to the height value. This example illustrates that it is not the thermal expansion coefficient of the soil alone that is important, but the difference between the thermal expansion coefficient of the confining ring and the soil. If this difference is zero, no correction is required.

Under hypothetical, true one-dimensional conditions, if the thermal expansion coefficient of the confining ring was zero, there would be no need to apply a correction to the height. There would still be a mechanical component to the thermal strain, because of the differential thermal

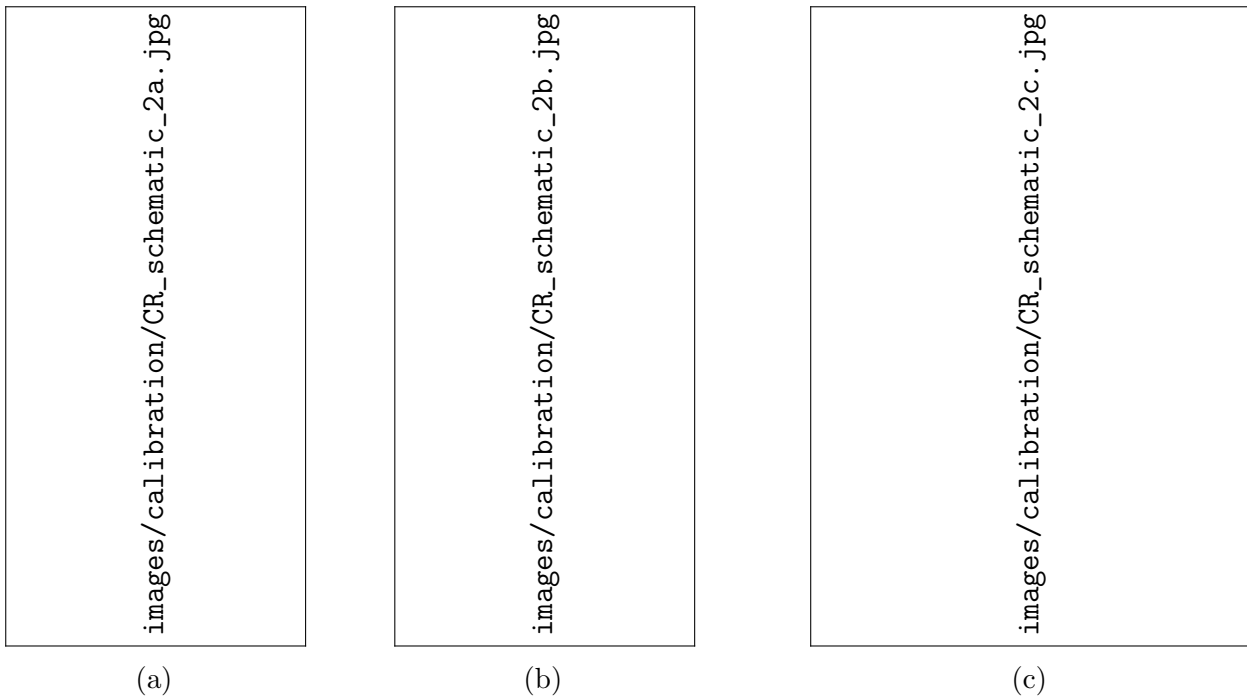


Figure 4.74: Differential lateral expansion of confining ring and soil (a) initial condition (b) following heating (isotropic conditions) (c) following heating (oedometric conditions)

expansion of the confining ring (in this case, zero), and the soil. In practice, confining rings made of Invar can be used, which has a coefficient of thermal expansion this is approximately $30\times$ smaller than stainless-steel. Moritz (1995) and Di Donna and Laloui (2015) are examples of temperature-controlled oedometer schemes which used Invar confining rings. Although the soil volume can be corrected by considering expansion of the confining ring, the effect of soil-equipment interaction on mechanical strain cannot. Ng et al. (2017) compared total thermally-induced strains for thermal cycles performed on normally-consolidated kaolin, using a steel or Invar confining ring, and found that thermally-induced contractive strains were lower for the Invar ring. Since the purely thermal strain was the same in each case (same material, same thermal path), the mechanical strain was lower for the Invar ring.

In the subsequent calculations, the change in height due to differential lateral expansion of the confining ring and the soil is quantified, so that a correction can be applied to the affected height value.

Theoretical change in specimen height

The theoretical change in specimen height can be calculated in two ways, as shown below. In both cases, an important assumption is made - that soil volume remains constant. That is, any lateral expansion/contraction of the soil, resulting from the thermal lateral expansion/contraction of the confining ring, results in a change in the *shape* of the soil, but no change in volume. This assumption is used by a number of other authors (Romero, 1999; Abuel-Naga et al., 2005) although its validity should be discussed. This assumption can also be considered in terms of Poisson's ratio. In effect, a Poisson's ratio of 0.5 is assumed. This assumption provides a limit value to the change in height. This is the maximum change in height that can theoretically occur. The other limit would be to assume a Poisson's ratio of zero, which gives the minimum change in height (i.e. zero, equivalent to not applying any correction). The true change in height

is between these two extremes. Additionally, this assumption does not consider the effects of changes in the lateral stress in the soil (which will decrease during heating, as the soil expands laterally, and will increase during cooling, as the soil is compressed laterally). However, the effect of lateral stress change can be calculated in terms of the mechanical strain component, as discussed in Section 4.6.1.

Consider the schematic shown in Figure 4.75. A two-dimensional cross-section is shown, through the centre of a soil specimen. The initial and final shape of the soil is shown for a heating stage. The initial volume, height and diameter are V_0, H_0 and d_0 . The final volume, height and diameter are V_1, H_1 and d_1 , and the change in height is ΔH . The diameter can be thought of either as the specimen diameter, or the internal diameter of the confining ring.

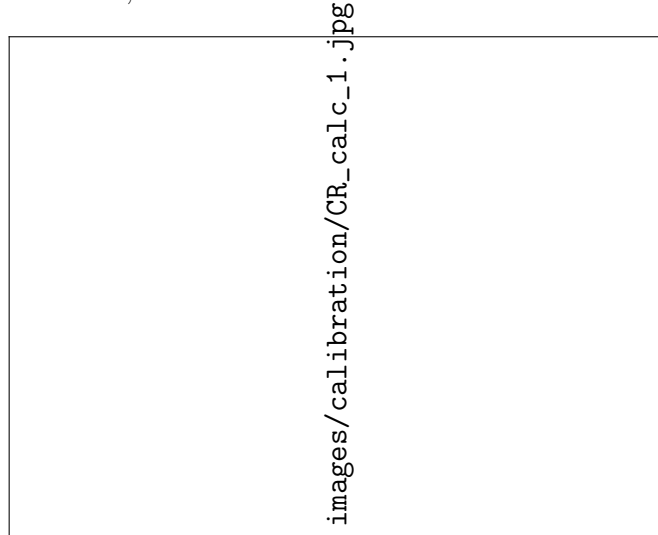


Figure 4.75: Schematic: calculation of change in specimen height

The initial volume V_0 and final volume V_1 can be calculated as the volume of a cylinder:

$$V_0 = \pi \cdot \frac{d_0^2}{4} \cdot H_0 \quad (4.17)$$

$$V_1 = \pi \cdot \frac{d_1^2}{4} \cdot H_1 \quad (4.18)$$

A constant-volume assumption is made. As discussed above, this is equivalent to assuming a Poisson's ratio of 0.5. This means that deformation of the soil does not cause any volume change, and that initial V_0 and final volume V_1 are equal:

$$V_0 = V_1 \quad (4.19)$$

which gives:

$$\pi \cdot \frac{d_0^2}{4} \cdot H_0 = \pi \cdot \frac{d_1^2}{4} \cdot H_1 \quad (4.20)$$

This can be rearranged as:

$$H_1 = H_0 \cdot \frac{d_0^2}{d_1^2} \quad (4.21)$$

The change in specimen height is given as:

$$\Delta H = H_0 - H_1 \quad (4.22)$$

$$= H_0 - H_0 \cdot \frac{d_0^2}{d_1^2} \quad (4.23)$$

$$= H_0 \left(1 - \frac{d_0^2}{d_1^2} \right) \quad (4.24)$$

Equation 4.21 can be rearranged as:

$$H_0 = H_1 \cdot \frac{d_1^2}{d_0^2} \quad (4.25)$$

which gives the change in specimen height as:

$$\Delta H = H_0 - H_1 \quad (4.26)$$

$$= H_1 \cdot \frac{d_1^2}{d_0^2} - H_1 \quad (4.27)$$

$$= H_1 \left(\frac{d_1^2}{d_0^2} - 1 \right) \quad (4.28)$$

An alternative method of calculating the change in specimen height is given below. Consider the schematic shown in Figure 4.76. As in the previous calculation, the initial and final shape of the soil is shown for a heating stage. This time though, instead of comparing the total volume of the soil, only the volume of soil that fills the theoretical void between specimen and confining ring during heating is considered.

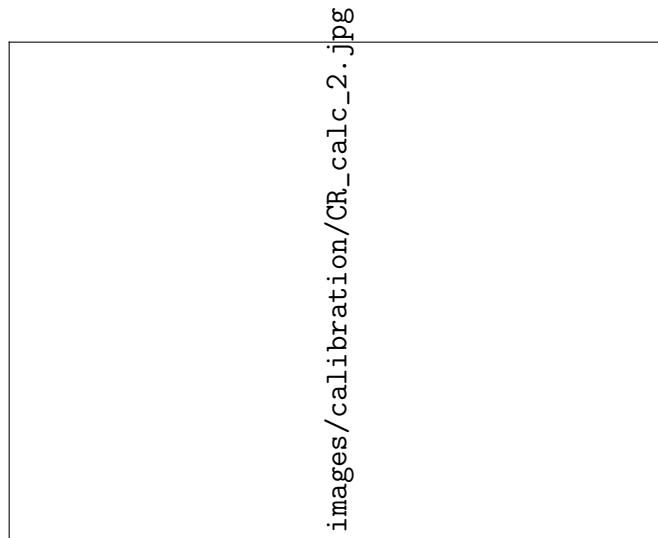


Figure 4.76: Schematic: alternative calculation of change in specimen height

The initial volume V_0 and final volume V_1 can be calculated as:

$$V_0 = \pi \cdot \frac{d_0^2}{4} \cdot (H_0 - H_1) \quad (4.29)$$

$$V_1 = \pi \cdot \frac{(d_1^2 - d_0^2)}{4} \cdot H_1 \quad (4.30)$$

Again, the constant-volume assumption is used:

$$V_0 = V_1 \quad (4.31)$$

which gives

$$\pi \cdot \frac{d_0^2}{4} \cdot (H_0 - H_1) = \pi \cdot \frac{(d_1^2 - d_0^2)}{4} \cdot H_1 \quad (4.32)$$

Expanding the brackets:

$$d_0^2 H_0 - d_0^2 H_1 = d_1^2 H_1 - d_0^2 H_1 \quad (4.33)$$

This can be rearranged as:

$$H_1 = H_0 \cdot \frac{d_0^2}{d_1^2} \quad (4.34)$$

The change in specimen height is given as:

$$\Delta H = H_0 - H_1 \quad (4.35)$$

$$= H_0 - H_0 \cdot \frac{d_0^2}{d_1^2} \quad (4.36)$$

$$= H_0 \left(1 - \frac{d_0^2}{d_1^2} \right) \quad (4.37)$$

which agrees with Equation 4.24.

The calculations above assume that soil volume remains constant, despite changing shape. This is equivalent to assuming a Poisson's ratio of 0.5. The Poisson's ratio of the soil can be considered, by adjusting the ΔH term.

Consider the two extreme cases, as shown in Figure 4.77. The initial values (diameter d_0 , height H_0 , and volume V_0) give the actual specimen dimensions. d_0 is the assumed specimen diameter, based on the thermal expansion coefficient of the confining ring. H_0 is the measured height, corrected for vertical equipment compliance. V_0 is the specimen volume, based on d_0 and H_0 . The final values (diameter d_1 , height H_1 , and volume V_1) give the specimen dimensions, after correcting for the differential expansion of the confining ring and the soil. d_1 is the assumed specimen diameter, based on the thermal expansion coefficient of the soil skeleton. H_1 is the measured height, corrected for vertical equipment compliance, and for differential expansion of

the confining ring and soil, using the method above. V_1 is the specimen volume, based on d_1 and H_1 .

The constant-volume case ($\nu = 0.5$) is shown in Figure 4.77a. In this case, $V_1 = V_0$. For temperature above ambient, $d_0 > d_1$, which means $H_1 > H_0$. This case gives the maximum theoretical change in height.

The constant-height case ($\nu = 0$) is shown in Figure 4.77b. In this case, $H_1 = H_0$. For temperature above ambient, $d_0 > d_1$, so $V_1 < V_0$. This is the baseline case, in which no correction is applied to the height term.

The change in height ΔH varies linearly with the Poisson's ratio ν . This is apparent from Figure 4.77. If the Poisson's ratio is reduced by half, the difference in height will reduce by half. The change in height can be corrected as follows:

$$\Delta H = \frac{\nu}{0.5} \cdot (\Delta H_{\nu=0.5}) \quad (4.38)$$

where:

- ΔH = correction to specimen height for Poisson's ratio between 0.5 and zero
- ν = Poisson's ratio
- $\Delta H_{\nu=0.5}$ = correction to specimen height for Poisson's ratio of 0.5

The correction to specimen height will vary between $\Delta H_{\nu=0.5}$ (for $\nu = 0.5$), and zero (for $\nu = 0$).

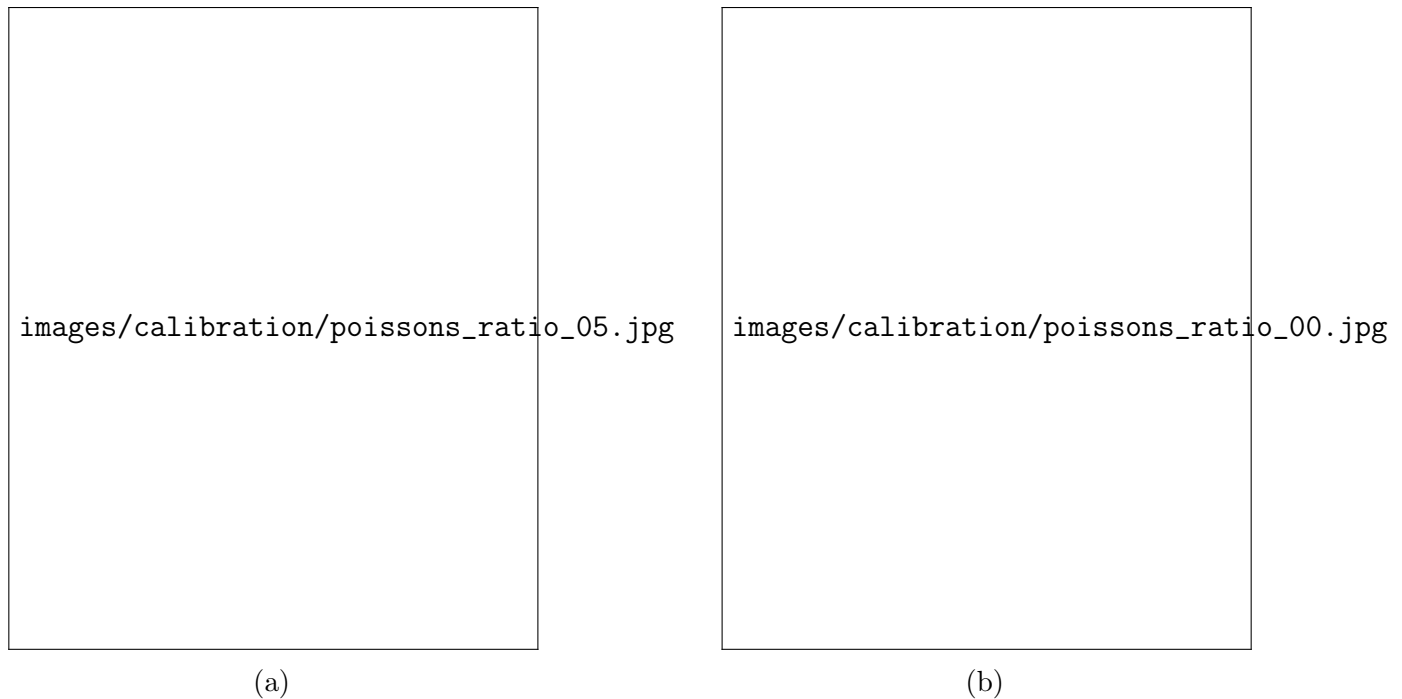


Figure 4.77: Extreme cases for confining ring height correction (a) $\nu = 0.5$ (b) $\nu = 0$

Applying the correction

The change in diameter of the soil specimen and the confining ring is calculated as (sign convention: positive $\Delta d =$ increase in diameter):

$$\Delta d_{soil} = d_{soil,0} \cdot \alpha_{L,soil} \cdot \Delta T \quad (4.39)$$

$$\Delta d_{CR} = d_{CR,0} \cdot \alpha_{L,CR} \cdot \Delta T \quad (4.40)$$

where:

Δd_{soil} = change in diameter of soil

Δd_{CR} = change in diameter of confining ring

$d_{soil,0}$ = initial diameter of soil

$d_{CR,0}$ = initial diameter of confining ring

$\alpha_{L,soil}$ = linear thermal expansion coefficient of soil

$\alpha_{L,CR}$ = linear thermal expansion coefficient of confining ring (stainless-steel)

ΔT = change in temperature

Note that, for the initial condition, $d_{soil,0} = d_{CR,0}$.

The resulting diameter of the soil specimen and confining ring is:

$$d_{soil,1} = d_{soil,0} + \Delta d_{soil} \quad (4.41)$$

$$d_{CR,1} = d_{CR,0} + \Delta d_{CR} \quad (4.42)$$

The change in height of the specimen can be expressed as a function of H_0 by substituting $d_{soil,1}$ and $d_{CR,1}$ into Equation 4.24, where $d_{soil,1}$ corresponds to d_0 , and $d_{CR,1}$ corresponds to d_1 .

$$\Delta H = H_0 \left(1 - \frac{d_{soil,1}^2}{d_{CR,1}^2} \right) \quad (4.43)$$

The change in height can alternatively be formulated in terms of H_1 , by substituting $d_{soil,1}$ and $d_{CR,1}$ into Equation 4.28:

$$\Delta H = H_1 \left(\frac{d_{CR,1}^2}{d_{soil,1}^2} - 1 \right) \quad (4.44)$$

This change in height can then be corrected for the Poisson's ratio of the soil ν :

$$\Delta H = \frac{\nu}{0.5} \cdot (\Delta H_{\nu=0.5}) \quad (4.45)$$

where:

$\Delta H_{\nu=0.5}$ = change in height calculated in the previous step

This can be applied as a correction to the measured height:

$$H_{corrected} = H_{measured} + \Delta H \quad (4.46)$$

The sign convention is positive ΔH = reduction in measured soil height (increase in corrected soil height). For a heating path (ΔT positive), ΔH will be positive, i.e. reduction in measured soil height. This is the reduction in height due to mechanical effects (lateral expansion of the soil to fill the available space). Therefore, to apply the correction, this calculated change in height is added to the measured value. This corrected value, $H_{corrected}$ is the theoretical soil height, for a case where the thermal expansion coefficients of the confining ring and the soil are the same (which is equivalent to unconfined conditions). In other words, the correction is applied by considering, for the same volume of soil, what the increase in height would be if the diameter of the soil (or cross-sectional area) was reduced back to the value for unconfined conditions.

Another way to think about these calculations is to consider the initial condition as the actual condition, and the final condition as the corrected condition. For example, in Figure 4.75, $V_1, H_1,$ and d_1 would correspond to the initial condition (i.e. what is actually measured), and $V_0, H_0,$ and d_0 would correspond to the final condition (i.e. the corrected shape). In this case, when substituting the values of $d_{soil,1}$ and $d_{CR,1}$ into Equation 4.24 or Equation 4.28, $d_{soil,1}$ corresponds to d_1 , and $d_{CR,1}$ corresponds to d_0 . The two methods are equivalent, and the final result, ΔH , is the same whichever method is used.

Summary and limitations

In this section, a method is described for determining the separate components of thermally-induced strain. This involves applying a correction to the measured specimen height, to account for the change in the cross-sectional area of the confining ring with temperature. The total strain can be split into two components: strain due to the thermal expansion of the soil skeleton, and strain due to mechanical effects. Two mechanical effects are identified: differential thermal expansion of the confining ring and soil, and differential thermal expansion of the solid and liquid phases of the soil.

The aim of oedometer testing is to determine soil behaviour under one-dimensional conditions, where strain is limited to one direction only - the direction of loading. However, in the case of the temperature-controlled oedometer, there is also strain perpendicular to the direction of loading, due to the lateral expansion and contraction of the confining ring with temperature. This is a limitation of the oedometer, common to most temperature-controlled oedometers in the literature.

The correction described above assumes that under hypothetical drained, unconfined conditions, the soil would expand laterally, by an amount determined by the thermal expansion coefficient of the soil skeleton.

The lateral expansion of the confining ring is calculated from the thermal expansion coefficient of stainless-steel. This gives the actual cross-sectional area of the soil, since under a vertical applied pressure the soil will expand laterally to fill all the available space. The actual cross-sectional area is compared to the hypothetical cross-sectional area of the soil, for unconfined conditions. The correction is applied to the height and cross-sectional area terms, by calculating the change in height that would occur if the cross-sectional area was changed from the actual value to the hypothetical value for unconfined conditions.

A further correction can be applied to this change in height, which accounts for the Poisson's ratio of the soil.

By correcting to the unconfined condition, rather the true oedometric condition of zero lateral strain, the thermal and mechanical strain components can be separated.

This correction has some limitations. The thermal strain is calculated from the thermal expansion coefficient of the soil solids. For soils generally, and for clays particularly, this value is not well understood.

Although this correction is able to show how much of the total strain is due to mechanical effects, it is not able to show what the strain would have been for true one-dimensional conditions of zero lateral strain. For example, if a confining ring made of a material with an extremely low thermal expansion coefficient, such as Invar, was used instead of stainless-steel. This issue has been investigated by Ng et al. (2017), who compared thermally-induced strains for identical tests using Invar and steel confining rings. If the cross-sectional area is corrected to the zero lateral strain condition, it becomes impossible to separate the thermal and mechanical strain components.

It would be interesting to compare the corrected results to those obtained using an Invar confining ring. This would enable a quantitative calculation of the accuracy of the correction described in this section.

4.7 Void ratio

The necessity of considering the thermal expansion of the solid phase of the soil at elevated temperature is explained in this section, together with the relevant calculations. The same methodology is applicable (and indeed, has been applied) for sub-ambient temperatures.

Three methods for calculating void ratio at ambient temperature are given in Appendix I. Although there are advantages and disadvantages to each method, the primary advantage of calculating void ratio in different ways is in the comparison of the results. Significant discrepancies between the void ratios calculated with each method suggest either a measurement error or calculation error. Of course, the calculations have been checked, then automated, then rechecked, so measurement error is far more likely.

Method 1 provides the most information, but requires the final total mass m_f and the mass of solids m_s , so void ratio can only be calculated following completion of the test.

Method 2 allows void ratio to be calculated during the test, by assuming that the water content of the specimen trimmings is approximately equal to the initial water content of the specimen.

Method 3 requires the final water content w_f , so can only be calculated following completion of the test. The final degree of saturation S_f must be assumed.

The void ratio, e , of a soil is defined as the ratio between the volume of voids V_v and volume of solids V_s :

$$e = \frac{V_v}{V_s} \quad (4.47)$$

or, in terms of total volume V and volume of solids V_s :

$$e = \frac{V - V_s}{V_s} \quad (4.48)$$

For true oedometric conditions (constant cross-sectional area), void ratio can be defined in terms of height.

$$e = \frac{H - H_s}{H_s} \quad (4.49)$$

where:

H = total height

H_s = height of solids

However, for the temperature-controlled oedometer, the void ratio must be defined in terms of volume, not height. This is because the cross-sectional area is affected by temperature. This, in turn, affects the correction to the specimen height, discussed in Section 4.6. The volume of solids is also affected by temperature, which needs to be considered in the calculation of void ratio at elevated and sub-ambient temperatures.

This is shown schematically in Figure 4.78. The phase diagram is shown for a saturated soil at ambient temperature T_0 and elevated temperature T_1 , following a change in temperature ΔT . The subscript 0 refers to the initial condition, at ambient temperature T_0 , while the subscript 1 refers to the final condition, at elevated temperature T_1 . The total volume V_t has increased, from $V_{t,0}$ to $V_{t,1}$, as has the volume of solids V_s , from $V_{s,0}$ to $V_{s,1}$. The void ratio at elevated temperature, e_1 can only be calculated correctly if the increase in total volume V and the increase in volume of solids V_s are considered together.

images/calibration/VR_schematic.jpg

Figure 4.78: Example phase relationship diagrams at ambient and elevated temperature

The void ratio at elevated temperature can be calculated by considering the ratio between volume of voids V_v and volume of solids V_s . First, the initial volume of solids $V_{s,0}$ is calculated as from the initial height of solids $H_{s,0}$ and initial cross-sectional area A_0 :

$$V_{s,0} = H_{s,0} \cdot A_0 \quad (4.50)$$

The initial height of solids $H_{s,0}$ is calculated from the initial mass and dimension measurements for the test, using one of the methods described in Appendix I.

The initial total volume $V_{t,0}$ can be calculated from the initial total height H_0 and initial cross-sectional area A_0 :

$$V_{t,0} = H_0 \cdot A_0 \quad (4.51)$$

The final diameter d_1 can be calculated from the initial diameter d_0 , the *linear* thermal expansion coefficient of the soil $\alpha_{L,soil}$, and the change in temperature ΔT :

$$d_1 = d_0 \cdot [1 + (\alpha_{L,soil} \cdot \Delta T)] \quad (4.52)$$

which can be used to calculate the final cross-sectional area A_1 :

$$A_1 = \pi \cdot \frac{d_1^2}{4} \quad (4.53)$$

Note that A_1 is the assumed cross-sectional area of the soil specimen for unconfined conditions. The effect of the differential lateral thermal expansion of the confining ring and soil is already accounted for in the corrected total height H_1 , as discussed in Section 4.6. If the uncorrected (i.e. directly measured) height was used, then A_1 would have to be calculated based on the assumed cross-sectional area of the confining ring instead.

The final total volume $V_{t,1}$ can be calculated from the final total height H_1 and final cross-sectional area A_1 :

$$V_{t,1} = H_1 \cdot A_1 \quad (4.54)$$

The change in volume ΔV can be calculated as follows (sign convention: positive $\Delta V =$ compression):

$$\Delta V = V_0 - V_1 \quad (4.55)$$

The final volume of solids is given by:

$$V_{s,1} = V_{s,0} \cdot [1 + (\alpha_v \cdot \Delta T)] \quad (4.56)$$

where:

$V_{s,1}$ = final volume of solids

$V_{s,0}$ = initial volume of solids

α_v = volumetric thermal expansion coefficient of solids

ΔT = change in temperature

The final volume of voids $V_{v,1}$ is then calculated from the final total volume $V_{t,1}$ and final volume of solids $V_{s,1}$:

$$V_{v,1} = V_{t,1} - V_{s,1} \quad (4.57)$$

The final void ratio e_1 is the ratio between final volume of voids $V_{v,1}$ and final volume of solids $V_{s,1}$:

$$e_1 = \frac{V_{v,1}}{V_{s,1}} \quad (4.58)$$

At elevated temperatures, the void ratio accounting for change in volume of solids with temperature will be lower than the void ratio calculated by assuming no change in V_s . Re-formulating the equation above:

$$\begin{aligned} e &= \frac{V_{t,1} - V_{s,1}}{V_{s,1}} \\ &= \frac{V_{t,1}}{V_{s,1}} - 1 \end{aligned}$$

The final total volume V_t is the same in either case. Volume of solids V_s increases with temperature. So if the change in volume of solids V_s is accounted for, the ratio V_t/V_s will be lower, and the calculated void ratio will be lower. By the same logic, at sub-ambient temperatures, the void ratio accounting for change in volume of solids with temperature will be higher than the void ratio calculated by assuming no change in V_s .

There is a further discussion on void ratio as part of the analysis of the sand test results, in particular sand test 8, in Section 6.5.

4.8 Summary

The effect of friction between the o-ring on the top-cap and the inner surface of the confining ring was measured. By applying a thin layer of grease to the o-ring and confining ring, the friction was reduced by a factor of three. Calibration tests suggest that the friction value is low enough to be considered negligible, except at low pressures. However, some results from soil tests in subsequent chapters suggest that this is perhaps not the case.

Tilting of the loading ram was investigated through a series of tests, using a combination of vertically-orientated LVDTs, inclinometers, and horizontally-orientated LVDTs. The magnitude of tilting was found to be significant, but can be accounted for by using three equally-spaced LVDTs to measure displacement, and taking the average displacement value.

Vertical thermal and mechanical deformation was measured first in two tests that combined repeated load/unload and heat/cool cycles (tests 1A and 1B). These tests provided useful information on the equipment behaviour, but the calibration equations derived from the data were not accurate enough, as seen from the calibration results in isolation, and from the corrected soil test data using the combined calibration in Chapters 5 and 6.

Further tests (2 and 3) focused on applying thermal cycles at fixed pressure values, which was found to provide a more accurate calibration. The magnitude of the thermal compliance is significant, compared to the thermally-induced displacement in soil tests, particularly for over-consolidated clays, for example OC bentonite, discussed in Chapter 5, and OC KSS, discussed in Chapter 8.

The issues relating to the use of filter papers and porous stones were investigated with a series of ambient-temperature compliance tests. To account for the large residual displacement resulting from the initial loading of filter papers, a new testing methodology was proposed, which involved pre-loading the filter papers. This testing methodology was used, and developed further, on the subsequent tests on sand (Chapter 6). Based on these ambient-temperature compliance tests, together with the combined vertical thermal and mechanical deformation tests, and the tests on sand, a decision was made to avoid using filter papers completely.

A correction for the soil height was derived, which accounts for the differential lateral thermal expansion of the confining ring and the soil. This correction determines what the soil height would be under unconfined conditions, so that the mechanical component of strain can be accurately calculated. Rather than assuming constant-volume conditions, as in previous schemes, the correction accounts for the Poisson's ratio of the soil, to adjust the height correction accordingly.

Finally, a method was developed for calculating the void ratio at elevated (or sub-ambient) temperatures, which accounts for the thermal expansion of the solid phase of the soil.

Chapter 5

Thermal tests on bentonite

5.1 Introduction

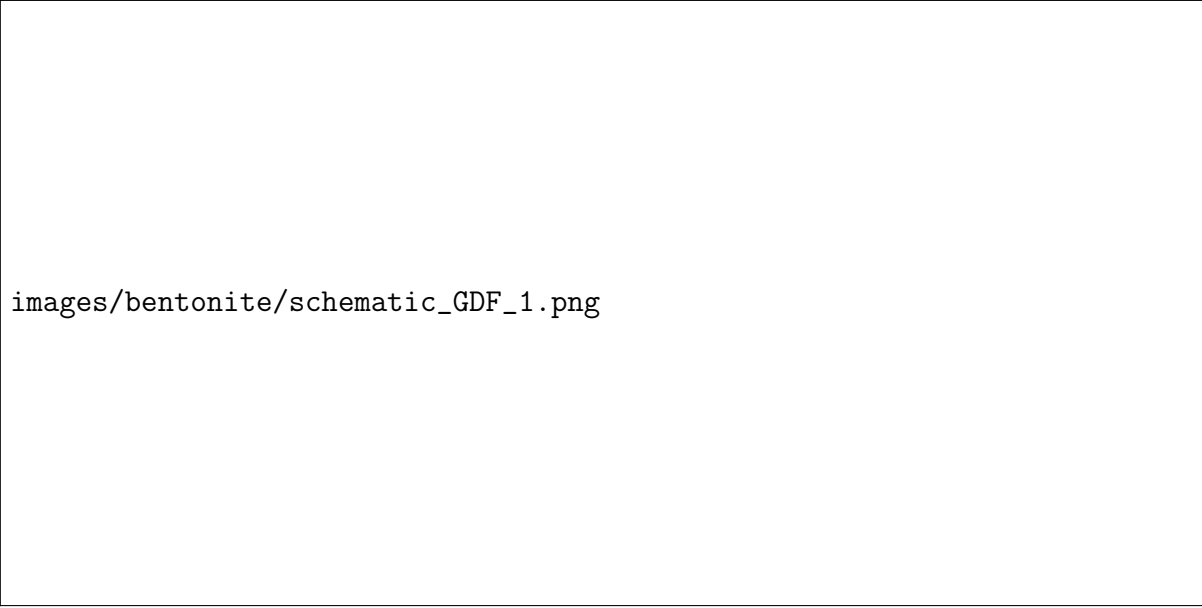
In this chapter, a series of tests performed on bentonite are discussed. The primary aim of these tests was the development of the equipment, the testing methodology, and the post-processing methodology, including calibration. Bentonite is a swelling clay, which has been proposed for use as a buffer material in the design of geological disposal facilities (GDF) for nuclear waste.

Deep geological disposal has been proposed as a solution for the disposal of high-level waste (HLW), of which there is a relatively small volume, but which is the most radioactive. In such a scheme, natural and engineered barriers prevent radionuclides reaching the biosphere until they have decayed to a safe level. One of the proposed engineered barriers is a buffer of low-permeability swelling clay, such as compacted bentonite, as shown in Figure 5.1.

The bentonite buffer is exposed to a series of thermo-hydro-mechanical actions, as shown in Figure 5.2. Heat is emitted by the waste canister, there is water infiltration through the host rock, and stresses are generated by swelling of the buffer in confined conditions. These actions do not act in isolation. Both the hydraulic and mechanical properties are affected by temperature. In turn, the mechanical properties are affected by degree of saturation, and the hydraulic properties are affected by stress level.


There were a number of challenges specific to the testing of bentonite. It has an extremely high liquid limit, and plasticity index, and extremely low hydraulic conductivity. The bentonite was tested as a slurry, mixed at $\approx 1.5 \times$ the liquid limit of the soil. The reason for this was to ensure fully-saturated conditions. A compromise had to be found for the initial specimen height. Reducing the initial height of the specimen reduces the time required for consolidation. Since bentonite has such low hydraulic conductivity, this can reduce the test duration from the order of months to weeks. However, if the initial height of the specimen is too low, the final specimen height following consolidation will be small. This is an issue when considering thermal volume changes. The volume change will be less for a smaller specimen, but the equipment compliance will stay the same, and therefore be relatively more important.

A description of the material is given in Section 5.2. There is a discussion on the thermal expansion coefficient value, which is relevant to thermal testing. An overview of the test programme is given in Section 5.3, explaining the motivation for each test. The testing methodology is described in Section 5.4. This focuses on the key differences between the methodology used for bentonite, and the one used for KSS. The full, final methodology for tests on clay, using the temperature-controlled oedometer is given in Chapter 7. This final methodology was developed from these



images/bentonite/schematic_GDF_1.png

Figure 5.1: Schematic - engineered barrier concept showing bentonite buffer



images/bentonite/schematic_GDF_2.png

Figure 5.2: Schematic - thermo-hydro-mechanical actions on the bentonite buffer

tests on bentonite, tests on sand (Chapter 6), and calibration tests (Chapter 4). These tests were vital for the development of the final testing methodology. The key results are presented and discussed in Section 5.5, followed by a brief summary.

5.2 Material description

The bentonite used in these tests was a Wyoming bentonite with the brand name *Bentosund A100*. A full characterisation of the Bentosund A100 bentonite is given by Mantikos (2018), who performed swelling tests on unsaturated, compacted specimens of this material, using the relative-humidity controlled oedometer at Imperial College London. They include a discussion on the structure of montmorillonite particles, double structure formation, optimum water content, and hydraulic properties.

Bentosund A100 bentonite is a natural sodium bentonite, with a montmorillonite content of $>80\%$. Montmorillonite swells with the addition of water. This property, as well as the extremely low hydraulic conductivity of montmorillonite means it has been considered for potential use as a buffer material in geological disposal facilities, as discussed above. A summary of the properties of the Bentosund A100 bentonite is given in Table 5.1. All values are from Mantikos (2018), except for the volumetric thermal expansion coefficient, which is from McKinstry (1965). The extremely high liquid limit of 392% and plasticity index of 341% produce particular challenges for soil testing.

Table 5.1: Summary of physical properties of Bentosund A100 bentonite

Property	Value
Montmorillonite content [%]	82
Specific gravity, G_s [-]	2.75
Plastic limit [%]	51
Liquid limit [%]	392
Plasticity index [%]	341
Volumetric thermal expansion coefficient α_v [$^{\circ}\text{C}^{-1}$]	39.3×10^{-6}

One issue with thermal testing of bentonite is the scarcity of data on the thermal expansion coefficient of the mineral solids. This value is required for accurate calculation of the thermal strain and void ratio.

The thermal expansion coefficient of a soil specimen can be calculated by heating or cooling the soil and measuring the resulting volumetric strain. If the volumetric strain is found to vary (approximately) linearly with temperature, the gradient of the response gives the volumetric thermal expansion coefficient. This is the thermal expansion coefficient for the whole soil specimen, not the mineral solids. This value is only relevant for similar soils, tested under the same conditions - same initial water content, void ratio, pressure, and temperature.

With this method, Tang et al. (2008) measured the volumetric thermal expansion coefficient $\alpha_{v,specimen}$ of MX-80 bentonite as $2 \times 10^{-4} \text{ }^{\circ}\text{C}^{-1}$, using a suction- and temperature-controlled isotropic cell. Cui et al. (2011) measured a value for $\alpha_{v,specimen}$ of $2 \times 10^{-4} \text{ }^{\circ}\text{C}^{-1}$, for Gaomiaozi (GMZ) bentonite, using the same equipment. Ye et al. (2012) measured a value for $\alpha_{v,specimen}$ of $1 \times 10^{-4} \text{ }^{\circ}\text{C}^{-1}$ for GMZ bentonite, using a suction- and temperature-controlled oedometer.

These values are only relevant to the specific conditions tested, as can be seen from the difference between the results of Cui et al. (2011) and Ye et al. (2012).

The thermal expansion coefficients for the mineral solids can be measured using x-ray diffraction techniques. Values for various clay minerals were measured in this way by McKinstry (1965). The results are given as linear thermal expansion coefficients, perpendicular ($\alpha_{L\perp}$) and parallel ($\alpha_{L\parallel}$) to the clay layers. The two linear coefficients can be converted into a single, volumetric thermal expansion coefficient, α_v using the following equation:

$$\alpha_V = \alpha_{L\perp} + 2(\alpha_{L\parallel}) \quad (5.1)$$

where:

α_V = volumetric thermal expansion coefficient [$^{\circ}\text{C}^{-1}$]

$\alpha_{L\perp}$ = linear thermal expansion coefficient perpendicular to clay layer [$^{\circ}\text{C}^{-1}$]

$\alpha_{L\parallel}$ = linear thermal expansion coefficient parallel to clay layer [$^{\circ}\text{C}^{-1}$]

The derivation of this result is given in Appendix C.

For isotropic materials, volumetric thermal expansion coefficient can be calculated from the linear thermal expansion coefficient, and vice-versa, as follows:

$$\alpha_v = 3 \times \alpha_L \quad (5.2)$$

$$\alpha_L = \frac{1}{3} \times \alpha_v \quad (5.3)$$

where:

α_v = volumetric thermal expansion coefficient [$^{\circ}\text{C}^{-1}$]

α_L = linear thermal expansion coefficient [$^{\circ}\text{C}^{-1}$]

The derivation of this result is given in Appendix D.

Of the minerals tested by McKinstry, pyrophyllite is the most similar to bentonite. A range of $36.1 \times 10^{-6} \text{ }^{\circ}\text{C}^{-1}$ to $42.5 \times 10^{-6} \text{ }^{\circ}\text{C}^{-1}$ is given for the volumetric thermal expansion coefficient for this material, with a mid-range estimate of $39.3 \times 10^{-6} \text{ }^{\circ}\text{C}^{-1}$. This value is calculated from the linear thermal expansion coefficients perpendicular and parallel to the clay layers, $\alpha_{L\perp} = (14.9 \pm 1.8) \times 10^{-6} \text{ }^{\circ}\text{C}^{-1}$, $\alpha_{L\parallel} = (12.2 \pm 0.7) \times 10^{-6} \text{ }^{\circ}\text{C}^{-1}$. As discussed in Section 6.2, it pays to investigate the primary sources for values cited in other literature sources. In this case, the result comes with the caveat that “these values are suspected of being too high”, due to the presence of a substantial amount of a second mineral component in the sample. Presumably this is the reason why Dixon et al. (1993) quotes this value as $<39 \times 10^{-6} \text{ }^{\circ}\text{C}^{-1}$, although by the time it is quoted by Laloui and Di Donna (2013), the value has become an unambiguous $39 \times 10^{-6} \text{ }^{\circ}\text{C}^{-1}$.

From the same table in McKinstry, the volumetric thermal expansion coefficient for kaolinite, $29 \times 10^{-6} \text{ }^{\circ}\text{C}^{-1}$, was used by Romero (1999), for Boom clay. Campanella and Mitchell (1968) used a representative value of $35 \times 10^{-6} \text{ }^{\circ}\text{C}^{-1}$, based on a range of measured thermal expansion coefficient values for other minerals of $15 \times 10^{-6} \text{ }^{\circ}\text{C}^{-1}$ to $52 \times 10^{-6} \text{ }^{\circ}\text{C}^{-1}$, from Hodgman et al. (1958). The same value was used by Abuel-Naga et al. (2006), for soft Bangkok clay.

Based on the available literature, a thermal expansion coefficient of $39.3 \times 10^{-6} \text{ }^\circ\text{C}^{-1}$ was used in this analysis. This is the widely recycled value from McKinstry (1965), which should be used with some caution. The availability in the literature of thermal expansion coefficient values for bentonite or similar materials, coupled with the difficulty of accurately measuring thermal volume change, as discussed below, was one of the motivations for performing tests on sand, discussed in Chapter 6.

5.3 Overview

Twelve oedometer tests in total were performed using bentonite. A summary of these tests is given in Table 5.2. *LA-OED* refers to the lever-arm oedometer, *ML-OED* (main-lab) refers to the electronic oedometer, while *TC-OED* refers to the temperature-controlled oedometer. The loading and heating path is given, together with the motivation for each test. To all of these could be added: development of understanding of equipment, development of understanding of bentonite behaviour, development of testing, calibration and data-processing methodology.

Table 5.2: Overview of bentonite tests 1 to 11

Test	Equipment	Loading and heating path	Motivation
1 & 2	ML-OED	Mechanical	Automated control using TRIAX
LA	LA-OED	Single mechanical cycle	Consolidation properties of bentonite
3	TC-OED	Single mechanical cycle	Consolidation properties of bentonite
4	ML-OED	Single mechanical cycle	Consolidation properties of bentonite
5	ML-OED	Repeat of test 4	Repeat results from test 4
6	TC-OED	2× mechanical cycles	Development of TC-OED testing methodology
7	ML-OED	1.5× mechanical cycles	Comparison of equipment. Observation of yield point
8	ML-OED	2× mechanical cycles	Baseline ambient-temperature response
9	TC-OED	Single combined thermal and mechanical cycle	Thermally-induced volume change. Consolidation at elevated temperature
10	ML-OED	3× mechanical cycles	Comparison of thinner specimens
11	TC-OED	2× mechanical cycles	Repeat results from test 10

The first tests, 1 and 2, were used to gain experience with setting up, running, and dismantling clay tests. The next four tests, LA, 3, 4 and 5, were ambient-temperature consolidation tests performed with three different oedometer cells. Test LA was performed using a traditional lever-arm oedometer (LA-OED), with specimen diameter of 45 mm. Test 3 was performed using the temperature-controlled oedometer (TC-OED), with specimen diameter of 70 mm. Tests 4 to 5 were performed using the air-pressure electronic oedometer (ML-OED), with specimen diameter of 50 mm.

The aim of these initial tests was to gain an understanding of the expected behaviour of the bentonite, and gain experience with the oedometer testing procedure. Following test 5, the ambient-temperature oedometer (ML-OED) was modified so that the confining ring and top-cap were the same as those used in the temperature-controlled oedometer.

Tests 6 to 8 were ambient-temperature consolidation tests performed with the TC oedometer and the ambient-temperature oedometer. The focus of these tests was the development of a testing and data-processing methodology that would enable the mechanical yield point to be found, to a high degree of accuracy. In test 6 (TC-OED) a continuous reloading path was applied to an over-consolidated soil. In test 7 (ML-OED) the reloading path was incremental, and a higher final pressure was reached than in test 6. Test 8 (ML-OED) was performed to obtain the virgin compression curve over the full tested pressure range, for comparison with other tests.

Test 9 was a thermal test, performed with the TC oedometer. Following consolidation at ambient temperature, a thermal and mechanical cycle was followed: heating to elevated temperature, loading and unloading at elevated temperature, and cooling back to ambient temperature. The direct thermally-induced volume change was calculated from the heating and cooling paths, and the effect of temperature on consolidation properties was observed from the load/unload path at elevated temperature.

The final two tests, tests 10 and 11 were ambient-temperature consolidation tests performed with the TC oedometer and the ambient-temperature oedometer. For these tests, the specimen initial height was much lower than for previous tests, ≈ 10 mm. The aim was to determine whether results from these tests were different from tests with thicker specimens. Using thinner specimens can potentially reduce testing duration significantly.

All tests were performed using the specimen set-up shown in Figure 5.3. Filter papers were placed above and below the specimen, between porous stones. The initial specimen height varied, from a maximum of 36.3 mm (test 4), to a minimum of 9.6 mm (test 11). The use of filter papers is discussed in detail in Section 4.5. The effect of specimen height is discussed further below.

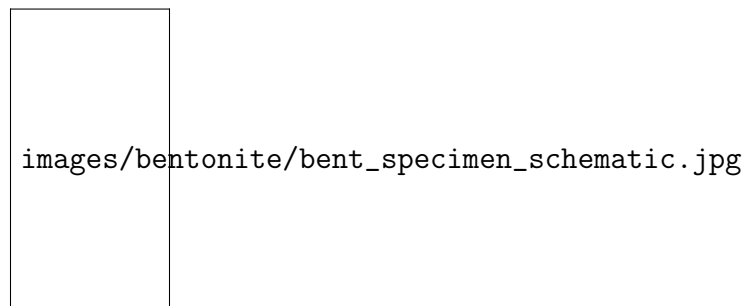


Figure 5.3: Specimen set-up for bentonite tests

5.4 Methodology

The development of the test methodology was an incremental process. With each test, particularly these early tests on bentonite, the methodology was refined. By the end of these tests, most of the equipment modifications had been carried out. One exception is the chiller system, which was first introduced for the KSS tests described in Chapter 7. The groove in the top-cap holding the o-ring in place was made deeper following test 8. This was done to reduce the friction between the top-cap o-ring and the confining ring, as discussed in Section 4.2. The calibration procedure is described in detail in Chapter 4.

The key difference between these tests, and the later tests on KSS, is the use of filter papers. For all tests on bentonite, filter papers were placed above and below the specimen. However, based on calibration tests discussed in Chapter 4, and following the tests on sand discussed in Chapter 6, a decision was made to avoid the use of filter papers entirely.

The top-cap o-ring was in position for all tests, lightly greased. Full details of the final calibration, testing, and data-processing methodology for tests on clay are given in Chapter 7.

The bentonite was prepared as a slurry by mixing air-dry powder with water, to a water content of $\approx 1.5 \times$ the liquid limit of the soil. For a liquid limit of 390%, this gives an initial water content of $\approx 585\%$. Before testing, the slurry was stored for several months in a sealed container. The soil was prepared as a slurry to ensure fully-saturated conditions. An alternative method to ensure full saturation would be to compress the soil at a water content close to its optimum water content, then saturate using back-pressure. This method was not used because it is not possible with the current equipment configuration to assess the variation of water content across the specimen, and thus ensure fully-saturated conditions.

5.5 Results and discussion

Initial specimen height, diameter and void ratio are given in Table 5.3 for tests LA and 3 to 11. Tests 1 and 2 are not discussed further in this section, as these tests were preliminary tests only, to check the TRIAX control software.

Table 5.3: Summary of initial height H_0 , diameter d_0 , and void ratio e_0 for bentonite tests LA and 3 to 11

Test	H_0 [mm]	d_0 [mm]	e_0 [-]
LA	20.1	45	17.6
3	36.3	70	15.8
4	19.0	50	14.9
5	19.0	50	14.9
6	21.5	70	17.8
7	30.3	70	17.1
8	23.7	70	16.7
9	27.7	70	17.6
10	12.0	70	18.5
11	9.6	70	16.0

Test duration is given in Table 5.4 for test LA and 3 to 11. Note that the test paths followed in these tests were quite simple, generally one or two mechanical cycles only. Even so, the test duration is significant. For tests with multiple cycles, following combined thermal and mechanical paths, such as sand test 3 (Section 6.5), or KSS test series A (Section 8.5.3), would take several months if bentonite was used. This is not necessarily an issue - after all, long-term tests on bentonite can continue for years. However, for the purpose of equipment development, such long-term tests are not ideal.

Table 5.4: Test duration for bentonite tests LA and 3 to 11

Test	Duration [Days]
LA	23
3	15
4	18
5	18
6	39
7	47
8	63
9	51
10	33
11	20

The results from tests LA, 3 to 5 are not shown graphically, but the key results are discussed. These tests were performed early in the research, and were valuable for gaining experience with the equipment and material, and identifying issues, but higher-quality results were obtained from subsequent tests, which are presented below.

In test LA, which was performed using the lever-arm oedometer, a single load/unload cycle was performed. The initial specimen height was 20.1 mm. At the maximum pressure of 1980 kPa, the specimen height was 2.1 mm. British Standard 1377-5:1990 (British Standards Institution, 1990), in Section 3.3.1, notes that “the mean diameter of the largest particle shall not exceed one-fifth of the height of the ring”. Clearly, for clay, this requirement is satisfied. However, no guidance is given on the minimum specimen height following consolidation. For thinner specimens, the relative contribution of the equipment compliance to the total measured displacement increases. For small, thermally-induced deformations, the potential error in the compliance calibration could be significant. ASTM Standard D2435/D2435M-11 (ASTM International, 2011) suggests, in Section 6.2.2, a minimum initial specimen height of 12 mm, and “not less than ten times the maximum particle diameter”. However, this 12 mm minimum may be not be sufficient for consolidation of bentonite slurry, given its extremely high water content.

In test 3, performed with the TC oedometer, a single load/unload cycle was performed. The initial specimen height was 36.3 mm. At the maximum pressure of 750 kPa, the specimen height was 12.0 mm. The total settlement of 24.3 mm exceeded the 10 mm travel of the LVDTs on the TC oedometer. It is possible to reset the LVDT position, either by adjusting the LVDT position relative to the instrumentation plate, or by adjusting the position of the instrumentation plate. For future tests, the initial loading increments were chosen to ensure that the LVDTs would not run out of travel during the increment (i.e. the displacement for each increment would be <10 mm). If, during the next increment, the LVDTs will run out of travel, they are reset near the end of the current increment. Further details on resetting the LVDTs are given in Section 7.2.

In tests 4 and 5, a single load/unload cycle was applied, with incremental loading from 4 kPa to 256 kPa, followed by a single unloading increment from 256 kPa to 128 kPa. These tests were carried out using the ambient temperature oedometer, but with a standard 50 mm diameter confining ring, and a top-cap with a tapered, integral, sintered-bronze porous stone. The loss of soil was estimated by comparing the dry mass of the soil in the specimen with that collected from the side of the top-cap and confining ring, for tests 3, 4 and 5. This is given in Table 5.5, as dry mass (m_s) relative to specimen dry mass. For test 3, for which the top-cap o-ring was in place, relative soil loss was much lower than for tests 4 and 5. This suggests that the o-ring seal effectively prevents slurry from squeezing between the top-cap and confining ring.

Table 5.5: Comparison of bentonite tests 3, 4 and 5

Test	Equipment	o-ring used?	m_s loss [%]
3	TC-OED	yes	1.5
4	ML-OED	no	10.5
5	ML-OED	no	15.6

Test 6 comprised two load/unload cycles at ambient temperature, using the TC oedometer. The full test path is shown in Figure 5.4. For the first load/unload cycle, pressure was increased from 2.5 kPa to 300 kPa (A \rightarrow B) in six increments (2.5 kPa, 10 kPa, 25 kPa, 50 kPa, 100 kPa, 200 kPa and 300 kPa), then reduced from 300 kPa to 25 kPa (B \rightarrow C) in two increments (300 kPa, 100 kPa and 25 kPa). Each increment duration was 48 h. For the second load/unload cycle, the pressure was increased at a continuous rate of 3 kPa h⁻¹ from 25 kPa to 200 kPa, held for 24 h, then increased at a slower rate of 1 kPa h⁻¹ from 200 kPa to 400 kPa, and held for another 24 h. Finally, pressure was reduced at a continuous rate of 8 kPa h⁻¹ from 400 kPa to 25 kPa.

The test pressure is shown against time in Figure 5.5. The first cycle of incremental loading and unloading covers the first 18 days. The second cycle of continuous loading and unloading covers the next 18 days.

The displacement response against pressure is given in Figure 5.6. The first point to note is that displacement remains negligible for the 2.5 kPa and 10 kPa pressure increments. Only at 25 kPa does the specimen begin to consolidate. It is reasonable to assume that the specimen should consolidate measurably, even under a low pressure of 2.5 kPa, and certainly under 10 kPa. It is possible that the specimen may have been slightly over-consolidated, but it seems more likely that this effect is due to friction. The measured friction for this equipment configuration was ≈ 10 kPa (See Section 4.2). No correction for friction has been applied to the data.

For pressure increments of 25 kPa and above, the response is stepped. As a new increment begins, the response is initially very stiff, with minimal displacement for increasing pressure. This transitions into a linear response as pressure increases. When the pressure reaches the target value, the displacement increases further. The displacement that takes place under constant load is time-dependent consolidation. The incremental displacement response is shown in Figure 5.7. The transition from primary to secondary consolidation is clearly visible, which shows that the 48 h increment duration was sufficient for this specimen. Note that with this equipment, a new target pressure cannot be applied instantaneously, as in a conventional hanging-weight oedometer. Instead, the displacement is increased until the target pressure is reached. This causes a delay between the start of the increment, and reaching the target pressure. The time taken to reach the target pressure of 300 kPa is indicated on Figure 5.7. The load application is fast compared to the increment duration. However, it is possible that this non-instantaneous

images/bentonite/bent_loadpath_6.pdf

Figure 5.4: Test path for bentonite test 6

images/bentonite/bent_6_P_time.pdf

Figure 5.5: Bentonite test 6 - pressure vs time

load application affects the shape of the incremental displacement response, from which the time for 50 % consolidation t_{50} is derived, which is used to calculate other consolidation properties such as the coefficient of consolidation c_v , and the coefficient of permeability k .

images/bentonite/bent_6_D_P.pdf

Figure 5.6: Bentonite test 6 - displacement vs pressure

The effect of applying the correction for vertical equipment compliance has been considered. For tests in the TC oedometer (TC-OED: tests 6, 9 and 11), the combined thermal and mechanical calibration, with sigmoid fit, derived from compliance test 1A was used to correct the measured data. This compliance test and the derivation of the sigmoid fit are discussed in Section 4.4. The equipment compliance is <0.3 mm at the maximum pressure used in any of the bentonite tests. Compared to the total displacement of ≈ 16 mm, the compliance is negligible. This conclusion applies to consolidation paths only. For tests in the ambient-temperature (ML-OED: tests 7, 8 and 10), no correction has been applied to the measured data. Since these are all ambient-temperature tests, and the mechanical compliance is negligible, this does not invalidate these results. For thermal paths, equipment compliance is relatively more important, as seen in test 9 below.

The second mechanical cycle for test 6 (continuous reloading and unloading) was performed to determine whether it was possible to observe yielding of the soil as it was reloaded above the pre-consolidation pressure. Initially, it was thought that the data obtained from incremental reloading would be too coarse for the yield point to be observed. A reloading rate of 3 kPa h^{-1} was applied from 25 kPa to 200 kPa. This pressure was held for 24 h, then a slower rate of 1 kPa h^{-1} was applied from 200 kPa to 400 kPa, and held again for 24 h. In Figure 5.6, the 24 h hold stage at 200 kPa can be seen, as a kink in the continuous reloading path, as the displacement increases under constant pressure. This suggests that the loading rate was too high to allow pore-pressures to fully dissipate, and that consolidation continued during the hold stage. There was no similar increase in displacement during the hold stage which followed the subsequent,

images/bentonite/bent_6_300kPa_inc.pdf

Figure 5.7: Bentonite test 6 - incremental response for 300 kPa loading stage

slower, loading stage. This suggest that for bentonite, a loading rate of 1 kPa h^{-1} is slow enough to allow full dissipation of pore-pressures.

In the final testing methodology, used for tests on KSS, incremental reloading was used, rather than continuous reloading. This decision was made for logistical reasons. Yielding of the specimen is determined based on the $e - \log P$ response of the soil. As a rough guideline, to observe the yielding, it is necessary to have data for approximately one order of magnitude above and below the yield point. So for test 6, with a pre-consolidation pressure of 300 kPa, a reloading path from 30 kPa to 3000 kPa would be required. For continuous reloading at a rate of 1 kPa h^{-1} , the test duration would be over 100 days. This duration could be reduced, by considering a narrower reloading path, and increasing the reloading rate at higher loads, but the test duration would still be much longer than for incremental reloading. Also, further tests (for example, test 7 below) showed that it was possible to accurately calculate the yield point from incremental data, so it was not necessary to make a compromise between test duration and accuracy (at least with respect to continuous/incremental loading).

Three methods for calculating ambient-temperature void ratio are given in Appendix I. In Figure 5.8, the void ratio response has been calculated using all three methods. The difference between the three results is negligible. This result is worth checking for two reasons: (i) the values are calculated independently, so this is a useful check for errors in the calculations (ii) a discrepancy between the void ratio calculated using method 1 and method 2 would indicate a measurement error.

One of the requirements of the equipment is the ability to determine the yield point of an over-consolidated soil which is reloaded beyond its pre-consolidation pressure. A methodology was developed for determining the yield point, which is discussed here using the data from test 7.

images/bentonite/bent_6_e_P.pdf

Figure 5.8: Bentonite test 6 - comparison of ambient-temperature void ratio calculation methods

In test 6, it was not possible to observe the yield point at 300 kPa by reloading from 200 kPa to 400 kPa. This test showed that it was necessary to reload to a significantly higher pressure than the pre-consolidation pressure in order to observe yielding. In test 7, the soil was loaded to 300 kPa, unloaded to 25 kPa, then reloaded to 1200 kPa. The test path is given in Figure 5.9.

The results for test 7 are given in Figure 5.10, which shows void ratio, normalised by the initial value, against pressure on a logarithmic scale. These values have not been corrected for equipment compliance, but as discussed above, the equipment compliance is negligible for ambient-temperature consolidation tests such as this. The initial load/unload response is shown in black, while the subsequent reload response is shown in blue, with markers at each increment. The response to the initial loading (2.5 kPa to 300 kPa) is non-linear, with the response becoming more steep below 25 kPa, then less steep at higher pressure. The reloading path is also non-linear, with the response becoming more steep below 300 kPa, and less steep at higher pressure.

The yield point is usually calculated as the intersection of the two linear sections of the reloading path in $e - \log P$ space. In other words, the yield point is defined as the point where there is a transition from high-stiffness (over-consolidated state) to lower stiffness (normally-consolidated state). However, the normal consolidation line (NCL) for this soil is non-linear in $e - \log P$ space. The yield point is thus defined as the point where there is a transition from a state of decreasing stiffness, to a state of increasing stiffness.

In mathematical terms, this transition from decreasing stiffness (increasing gradient) to increasing stiffness (decreasing gradient) is an inflection point. By fitting an equation through the data, this inflection point can be found. The inflection point corresponds to a turning point in the first derivative of the equation, and the x-axis intercept of the second derivative. This is shown schematically in Figure 5.11.

images/bentonite/bent_loadpath_7.pdf

Figure 5.9: Test path for bentonite test 7

images/bentonite/bent_7_e_P.pdf

Figure 5.10: Bentonite test 7 - Void ratio vs pressure

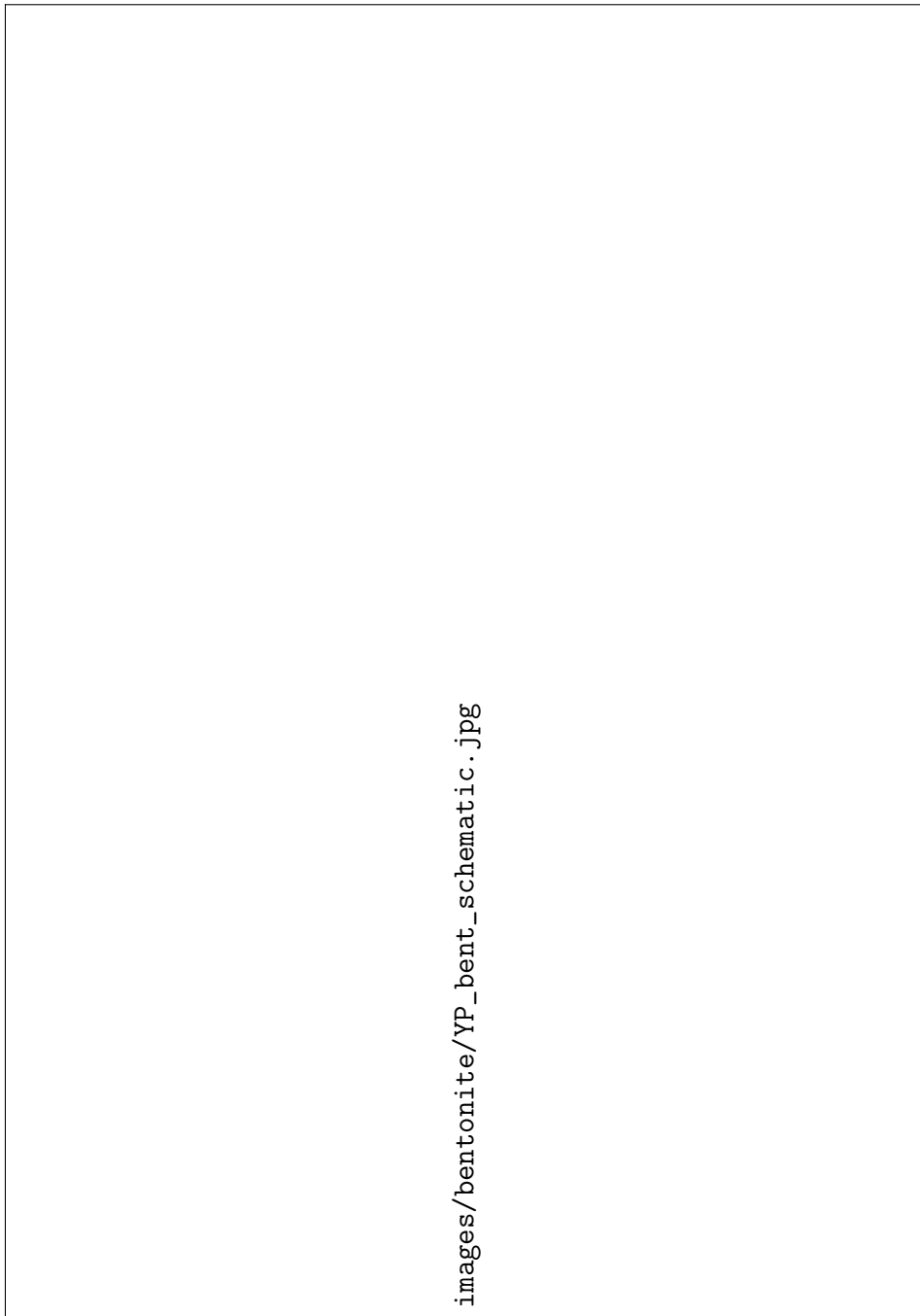


Figure 5.11: Calculation of yield point for bentonite tests - schematic

The yield point is indicated as the inflection point in the data (e), which is the point of maximum (negative) gradient. The first derivative ($de/d(\log_{10} \sigma_v)$) shows this gradient, and the turning point which corresponds to the yield point. The second derivative ($d^2e/d(\log_{10} \sigma_v)^2$) shows the gradient of the first derivative, which is zero at the turning point.

In Figure 5.12, the data from the reloading path is presented, with a 4th order polynomial fit through the data. A two-term Fourier fit was also tested, and found to calculate the yield point with similar accuracy to the polynomial fit. The yield point is given by the inflection point in this fit. This is where the first derivative of the polynomial, $de/d(\log_{10} \sigma_v)$ is at a minimum, and the second derivative, $d^2e/d(\log_{10} \sigma_v)^2$ is zero. Using this method, the yield point for the reloading path in test 7 was found to be 308 kPa. A yield point of 300 kPa was expected based on the test path.

The same method was used to calculate the yield point for test 11, discussed below, giving a value of 309 kPa.



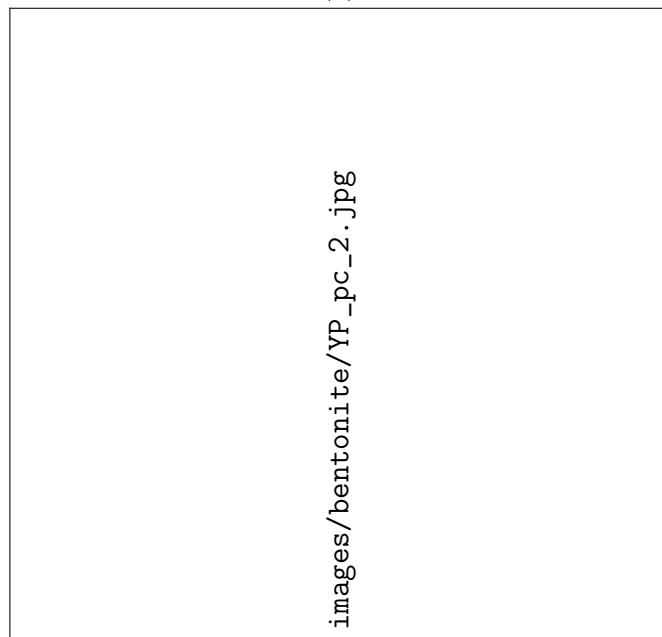
Figure 5.12: Calculation of yield point for bentonite test 7, showing reloading path only

It appears that the current method may over-estimate the yield point value. Alternatively, it is possible that these values are correct, based on the actual shape of the reloading path. The reloading path may not follow the same path that the virgin NCL would follow for pressure values above the pre-consolidation pressure. This is shown schematically in Figure 5.13. In Figure 5.13a, the conventional assumption is shown, in which the reloading path follows the same path that the virgin NCL would follow. The yield point is equal to the pre-consolidation pressure. In Figure 5.13b, the reloading path does not immediately rejoin the hypothetical virgin NCL. The yield point is greater than the pre-consolidation pressure. This shows that it is important, when considering the effect of temperature on the yield point, that an ambient-temperature baseline value is obtained, using the same method. The effect of temperature is the difference between the baseline value and the elevated-temperature value (not the difference between the assumed yield point and the elevated temperature value).

A slightly different method was used to calculate the yield point for the KSS tests. This was because the NCL was approximately linear for these tests, allowing the yield point to be calculated as the transition point from high to low stiffness (rather than decreasing to increasing stiffness).



(a)



(b)

Figure 5.13: Comparison between potential reloading paths (a) reloading path rejoins NCL at $\sigma_v = p_c$ (b) reloading path rejoins NCL at $\sigma_v > p_c$

Test 9 was the first thermal test performed in the temperature-controlled oedometer. The test path for test 9 is given in Figure 5.14. The specimen was first heated from 22.5 °C to 70 °C at 10 kPa (A → B). At 70 °C, the specimen was loaded incrementally to 1200 kPa, then unloaded to 10 kPa. Finally, the specimen was cooled from 70 °C to 22.5 °C at 10 kPa. The pressure and temperature values over the full test are shown in Figure 5.15.

images/bentonite/bent_loadpath_9.pdf

Figure 5.14: Test path for bentonite test 9

images/bentonite/bent_9_P_T_time_full.pdf

Figure 5.15: Bentonite test 9 - pressure (Y1) and temperature (Y2) vs time in days

The volumetric strain response with pressure is given in Figure 5.16. The strain resulting from heating and cooling is small compared to the mechanical strain. At the maximum pressure, the strain is $\approx 84\%$. As in test 6, there is negligible strain until the pressure increases above 25 kPa. The normal consolidation line is non-linear, with stiffness increasing with increased pressure. The unloading path is also non-linear, but the response is stiffer than for loading. Following the unloading cycle, the strain is $\approx 63\%$.

images/bentonite/bent_9_str_P_full.pdf

Figure 5.16: Bentonite test 9 - full test - strain vs pressure

The volumetric strain response with temperature is given in Figure 5.17. Both heating and cooling cause small expansive strains. The heating and cooling behaviour is discussed in more detail below.

The volumetric strain response with temperature for the heating path only is given in Figure 5.18. Heating causes expansion of the normally-consolidated bentonite. In the literature, heating of normally-consolidated clay causes contraction, so this result is unusual. The magnitude of the vertical correction is shown. This correction is the sigmoid combined thermal and mechanical calibration based on calibration test 1A, discussed in Section 4.4. In both cases, no correction for thermal lateral expansion of the confining ring has been applied.

The effect of applying the correction for thermal lateral expansion of the confining ring (see Section 4.6) is shown in Figure 5.19. In both cases, no correction for vertical compliance has been applied.

The void ratio (normalised by initial void ratio) is shown against temperature in Figure 5.20. The effect of applying either the vertical compliance correction, the confining ring correction, or both together, is compared to the raw data. Heating causes an increase in void ratio.

images/bentonite/bent_9_str_T_full.pdf

Figure 5.17: Bentonite test 9 - full test - strain vs temperature

images/bentonite/bent_9_str_T_heat_VC.pdf

Figure 5.18: Bentonite test 9 - heating only - effect of vertical compliance correction


images/bentonite/bent_9_str_T_heat_CR.pdf

Figure 5.19: Bentonite test 9 - heating only - effect of confining ring expansion correction

images/bentonite/bent_9_e_T_heat.pdf

Figure 5.20: Bentonite test 9 - heating only - void ratio

The volumetric strain response with temperature for the cooling path only is given in Figure 5.21. Cooling results in expansion (as did heating). The magnitude of the expansive strain due to cooling is approximately an order of magnitude greater than due to heating. When considering the cooling stage, either incremental or sub-incremental strain can be considered. Incremental strain is the increment volume change relative to the volume at the start of the test, whereas sub-incremental strain is the increment volume change relative to the volume at the start of the increment (i.e. at the start of cooling). The incremental strain is useful for comparing the absolute strain for two thermal paths. The sub-incremental strain is useful for determining the thermal expansion coefficient of a soil from a thermal path.



images/bentonite/bent_9_str_T_cool.pdf

Figure 5.21: Bentonite test 9 - cooling only - incremental and sub-incremental strain


The heating and cooling responses are both unusual. For heating of a normally-consolidated clay, contraction would be expected. For cooling of an over-consolidated clay, contraction would be expected, of smaller magnitude than the contraction due to NC heating. Instead, heating of the NC clay caused expansion, and cooling of the OC clay caused expansion, of larger magnitude than the expansion due to NC heating. There are a number of possible reasons why the observed response was not as expected. The presence of filter papers, which cannot be accurately accounted for in the calibration, may have affected the result. The calibration used (sigmoid, combined thermal and mechanical calibration based on calibration test 1A), was performed without the top-cap o-ring in place, so does not account for friction effects. This calibration is based on a series of loading/unloading paths at different temperatures, from which an inferred thermal response was derived for different pressures. As discussed in Section 4.4, this approach has limitations, which affect the accuracy of the inferred thermal response.

The pressure at which heating and cooling were performed was 10 kPa. Based on the consolidation response, and the friction tests discussed in Section 4.2, it is expected that friction may have an important effect on results at low pressures. For tests carried out after test 9, a minimum

pressure of 50 kPa was used for thermal paths. Finally, the cooling response may have been affected by the preceding unloading stage. If expansion due to unloading continued during the cooling stage, this expansion may have contributed to the unusually large expansion observed during cooling.

The final two tests, 10 and 11, were ambient temperature consolidation tests. The aim of these tests was to see the effect of using significantly thinner specimens. As can be seen in Table 5.3, the initial height of the specimens in tests 10 and 11 was approximately half that of the other tests. Test 10 was performed with the ambient-temperature oedometer (ML-OED), while test 11 was performed with the temperature-controlled oedometer (TC-OED). The test path for bentonite test 11 is given in Figure 5.22. The specimen was loaded incrementally from 2.5 kPa to 300 kPa (A → B), unloaded to 10 kPa (B → C), reloaded to 900 kPa (C → D), and unloaded to 10 kPa (D → C). Test 10 followed a similar path, with an additional third reload/unload cycle.

The increment duration for these tests was 24 h. The time required to reach a given degree of consolidation is a function of the square of the drainage path length. If the drainage path length is halved, the time required reduces by a factor of four. In previous tests, using specimens with >20 mm initial height, 48 h was found to be sufficient to observe the transition from primary to secondary consolidation. So for tests 10 and 11, it was assumed that 24 h would be sufficient. Figure 5.23 shows the incremental response for the 300 kPa reloading stage in test 11 (corrected using the combined thermal and mechanical calibration based on calibration test 1A - see Section 4.4). The transition from primary to secondary consolidation is clear, and occurs ≈6 h after the start of the increment. This is approximately 25 % of the time taken for the equivalent loading stage in test 6 (Figure 5.7), for a specimen thickness approximately double that used in test 11.



images/bentonite/bent_loadpath_11.pdf

Figure 5.22: Test path for bentonite test 11

images/bentonite/bent_11_300kPa_inc.pdf

Figure 5.23: Bentonite test 11 - incremental response for 300 kPa reloading stage

5.6 Summary

A series of oedometer tests were performed on bentonite, a swelling clay with extremely high plasticity and extremely low permeability. The bentonite was prepared as a slurry at $\approx 1.5\times$ liquid limit, to ensure fully-saturated conditions. Tests 1 to 5 were preliminary tests, to gain experience with the material, the equipment, and the data-processing methodology, including applying calibrations to the raw data. Tests 6 to 11 were ambient-temperature and thermal tests, performed in the ambient-temperature oedometer (ML-OED) and the temperature-controlled oedometer (TC-OED). The main aim of these tests was to develop and validate the testing methodology, by measuring the consolidation and thermal properties of bentonite.

A number of improvements were made to the testing methodology. A repeatable method for setting up, running, and dismantling clay tests in the TC oedometer was developed, which is discussed in Chapter 7. Friction between the top-cap o-ring and the confining ring was reduced by increasing the depth of the top-cap o-ring groove.

An accurate, repeatable method for determining the yield point of a reloaded, over-consolidated soil was developed. Continuous and incremental reloading paths were tested, but incremental reloading was chosen for future tests since it is quicker than continuous reloading, and just as accurate for determining the yield point. A numerical approach was used, which involved fitting a polynomial to the incremental reloading data. By differentiating this polynomial fit, the inflection point corresponding to the transition from reducing stiffness to increasing stiffness could be found. A key advantage of this method is that it is completely user-independent, equivalent to an algorithm.

The effect of applying corrections for vertical thermal and mechanical compliance, and differential thermal expansion of the confining ring and soil, were measured. The mechanical compliance was found to be negligible compared to consolidation of the soil. The vertical thermal compliance, and correction for differential thermal expansion of the confining ring and soil were found to be potentially significant. These tests made clear that an accurate thermal calibration was required, in order to accurately measure thermally-induced volume change.

Following these tests, a number of tests were performed using sand, discussed in the following chapter, before the final set of tests on KSS, discussed in Chapters 7 and 8. The decision to change material to sand was made for two reasons. First, to reduce the duration of each test, which allows more tests to be performed in the available time. Second, the thermal properties of sand are better understood than bentonite, which allows the soil behaviour to be predicted with more certainty, so that calibration errors can be picked up.

The decision to use KSS, rather than bentonite, for the final series of tests, is discussed in more detail in Chapter 8. The key reasons were the lower liquid limit (and plasticity) and higher hydraulic conductivity of KSS. The lower liquid limit of KSS means that it can be mixed as a slurry at much lower water content than bentonite. The higher hydraulic conductivity means that a thicker specimen can be used. The combined effect of lower water content and thicker specimen are that the KSS specimen height following consolidation is *much* greater than for bentonite. Thermal volume changes are therefore larger, in absolute terms, and importantly, relative to the equipment thermal compliance, which can be considered independent of specimen thickness.

It was not possible to accurately measure thermally-induced volume change in bentonite, because of the limitations of the calibration method used when performing these tests. However, these tests led to the development of a comprehensive calibration and testing methodology, used for the tests on KSS. This methodology, discussed in Section 7, is applicable for bentonite, although such tests could not be performed within the time-frame of the project, which involved development of the TC oedometer itself, and the technique for testing and calibration. In addition to deep geological disposal, the oedometer was designed with ground source energy applications in mind, which is why sub-ambient cooling capability was considered an important capability of the equipment. It is expected that future testing with the oedometer will be on various soil types, including sands, silts, and other clay types, such as London clay. The techniques developed through these tests on bentonite will enable accurate thermal testing of these other soil types.

Chapter 6

Thermal tests on sand

6.1 Introduction

A series of tests were carried out with the temperature-controlled oedometer, using sand. These tests on sand were carried out after the tests on bentonite, described in Chapter 5, to clarify the results already obtained.

The aim of these tests was to perform thermal tests on a soil with well-understood thermal properties. For this reason, sand was chosen as the test soil. The high permeability of sand allowed testing duration to be much lower than the tests on bentonite (days rather than months). The sand used was Leighton Buzzard sand, a standard laboratory silica sand.

The material properties are given in Section 6.2, followed by an overview of the tests performed in Section 6.3. The testing methodology is briefly discussed in Section 6.4, although further details are given in subsequent sections. The focus of this chapter is on the improvements made to the testing and calibration methodology based on these tests. These were used to develop the final methodology used for the tests on KSS, discussed in Chapter 7. The key results from the twelve sand tests performed are discussed in Section 6.5.

Note that care has been taken to avoid terms relating to consolidation, which are not appropriate for a free-draining soil such as this. Instead, test paths are described as being carried out *at the maximum applied pressure* (synonymous with normally-consolidated) or *below the maximum applied pressure* (synonymous with over-consolidated).

As with the tests on bentonite, some of these tests were performed at ambient temperature only, without any thermal stages. The reason for this is that to understand thermal effects (on the equipment, or on the soil), the ambient temperature behaviour must first be understood.

6.2 Material description

A standard laboratory silica sand was used for all tests. This sand, sourced from Leighton Buzzard, United Kingdom, is known as 16/30 sand. The 16/30 designation refers to standard US mesh sizes, which correspond to 1.19 mm and 0.595 mm sieve openings. A summary of the key properties of the Leighton Buzzard sand is given in Table 6.1. This is the same sand used by Martínez Calonge (2017) for isotropic loading and heating tests in the temperature-controlled triaxial cell at Imperial College London.

Table 6.1: Summary of physical properties of Leighton Buzzard sand

Property	Value
Size range [mm]	0.5 to 1
Coefficient of uniformity, C_u [-]	<1.4
Shape	rounded
Minimum void ratio, e_{min} [-]	0.5
Maximum void ratio e_{max} [-]	0.8
Specific gravity, G_s [-]	2.65
Volumetric thermal expansion coefficient α_v [$^{\circ}\text{C}^{-1}$]	27.0×10^{-6}

The minimum and maximum void ratio values are taken from Naughton and O’Kelly (2003), who also tested Leighton Buzzard sand. The maximum void ratio value was measured, and found to be the same as the literature value. The other properties are average values taken from a range of suppliers’ specifications, with the exception of the volumetric thermal expansion coefficient α_v , which was based on various literature values, discussed below.

Sand was chosen for its well-understood behaviour, and well-known properties. However, a literature review of thermal expansion coefficient values for sand found a large range of values. Literature values are often given in terms of linear thermal expansion coefficient parallel ($\alpha_{L\parallel}$) and perpendicular ($\alpha_{L\perp}$) to the crystallographic axis, from which the volumetric thermal expansion coefficient can be calculated using the following equation:

$$\alpha_v = \alpha_{L\perp} + 2 \cdot \alpha_{L\parallel} \quad (6.1)$$

where:

- α_v = volumetric thermal expansion coefficient [$^{\circ}\text{C}^{-1}$]
- $\alpha_{L\perp}$ = linear thermal expansion coefficient perpendicular to crystallographic axis [$^{\circ}\text{C}^{-1}$]
- $\alpha_{L\parallel}$ = linear thermal expansion coefficient parallel to crystallographic axis [$^{\circ}\text{C}^{-1}$]

The derivation of this result is given in Appendix C.

For isotropic materials, volumetric thermal expansion coefficient can be calculated from the linear thermal expansion coefficient, and vice-versa, as follows:

$$\alpha_v = 3 \times \alpha_L \quad (6.2)$$

$$\alpha_L = \frac{1}{3} \times \alpha_v \quad (6.3)$$

where:

- α_v = volumetric thermal expansion coefficient [$^{\circ}\text{C}^{-1}$]
- α_L = linear thermal expansion coefficient [$^{\circ}\text{C}^{-1}$]

The derivation of this result is given in Appendix D.

A summary of the volumetric thermal expansion coefficients for sand from the literature are given in Table 6.2. These data require some explanation. All the values are given as volumetric thermal expansion coefficients, but literature values for thermal expansion coefficient can be given in different forms. Commonly, the linear thermal expansion coefficient is given, rather than the volumetric thermal expansion coefficient. In this case, the volumetric thermal expansion coefficient has been calculated using Equation 6.2. Alternatively, the linear thermal expansion coefficient is given for two orientations - parallel and perpendicular to the crystallographic axis, giving two values, $\alpha_{L_{\parallel}}$ (parallel) and $\alpha_{L_{\perp}}$ (perpendicular). In this case, the volumetric thermal expansion coefficient has been calculated using Equation 6.1.

Table 6.2: Summary of volumetric thermal expansion coefficient (α_v) values for sand

Reference	α_v [$10^{-6} \text{ }^\circ\text{C}^{-1}$]
Kaye and Laby (1959)	28.7
Flügge (1962)	27.3
Skinner (1966)	34 to 57.6
Eshbach and Tapley (1990)	28.95
Engineering Toolbox (2003)	24 to 42
Granta Design Limited (2009)	24 to 60
Martínez Calonge (2017)	27.1
Sittidumrong et al. (2019)	24.3

Values can be given for a single temperature value (instantaneous coefficient), or for a range of values (mean coefficient). The instantaneous coefficient is derived by differentiating polynomial functions fitted to volume-temperature data. The mean coefficient is derived by considering the volumetric strain between two temperature values (usually between ambient temperature and an elevated temperature value). Further details are given in Skinner (1966). Where temperature ranges were specified in the literature source they have been given below.

Kaye and Laby (1959) reported values in terms of linear thermal expansion coefficient of *quartz*, parallel ($\alpha_{L_{\parallel}}$) and perpendicular ($\alpha_{L_{\perp}}$) to the crystallographic axis, from which the volumetric thermal expansion coefficient was calculated using Equation 6.1 ($\alpha_{L_{\parallel}} = 7.5 \times 10^{-6} \text{ }^\circ\text{C}^{-1}$, $\alpha_{L_{\perp}} = 13.7 \times 10^{-6} \text{ }^\circ\text{C}^{-1}$). Eshbach and Tapley (1990) similarly reported values for quartz in this way, for the temperature range $0 \text{ }^\circ\text{C}$ to $80 \text{ }^\circ\text{C}$ ($\alpha_{L_{\parallel}} = 7.97 \times 10^{-6} \text{ }^\circ\text{C}^{-1}$, $\alpha_{L_{\perp}} = 13.37 \times 10^{-6} \text{ }^\circ\text{C}^{-1}$).

Flügge (1962) reported a single linear thermal expansion coefficient for *sandstone*, noting that this value is valid up to a temperature of $204 \text{ }^\circ\text{C}$.

Skinner (1966), in Clark (1966), reported three values for quartz, given as volumetric thermal expansion coefficients, showing the importance of understanding how values were obtained. The lowest value of $34 \times 10^{-6} \text{ }^\circ\text{C}^{-1}$ was given for a temperature of $20 \text{ }^\circ\text{C}$. The intermediate value of $45 \times 10^{-6} \text{ }^\circ\text{C}^{-1}$ was given for a temperature range of $20 \text{ }^\circ\text{C}$ to $50 \text{ }^\circ\text{C}$. The highest value of $57.6 \times 10^{-6} \text{ }^\circ\text{C}^{-1}$ was given for a temperature range of $20 \text{ }^\circ\text{C}$ to $100 \text{ }^\circ\text{C}$. This is the value quoted by Dixon et al. (1993), without comment on the temperature range, or alternative values for other temperature ranges. Values from the same table in Dixon et al. (1993) are quoted by Laloui and Di Donna (2013), again without comment. This can give the impression that thermal expansion coefficients are well-established, with a narrow range of potential values, but this is not the case. Even within the same source, (Skinner, 1966), there is a significant degree of uncertainty.

Most of the more recent values found were from software and internet resources. CES EduPack software, a library of material properties (Granta Design Limited, 2009) gave a single linear thermal expansion coefficient for sandstone. The Engineering Toolbox website (Engineering Toolbox, 2003) gave the linear thermal expansion coefficient for mineral quartz, as a range.

The values given by Martínez Calonge (2017), for Leighton Buzzard sand, and Sittidumrong et al. (2019), for Bangkok sand, were not directly measured, but were given as the properties used in their analysis, and are included here for comparison. However, neither author comments on the importance and uncertainty relating to the values chosen.

The literature values for volumetric thermal expansion coefficient for sand vary significantly. Values range from $24 \times 10^{-6} \text{ }^\circ\text{C}^{-1}$ to $57.6 \times 10^{-6} \text{ }^\circ\text{C}^{-1}$ based on the sources discussed above. The volumetric thermal expansion coefficient of steel is $51 \times 10^{-6} \text{ }^\circ\text{C}^{-1}$. This means, for the lower limit of $\alpha_{v,sand}$, during heating, the thermally-induced lateral expansion of the confining ring will be greater than that of the soil, and the soil height will reduce as the soil expands laterally to fill the available space. At the upper limit of $\alpha_{v,sand}$, the thermally-induced lateral expansion of the confining ring will be lower than that of the soil, and the soil height will increase because of the increased lateral stress acting upon it. In this case, the correction discussed in Section 4.6 might not just be insufficient, but in the wrong direction. Not only that, but the void ratio correction discussed in Section 4.7 depends directly on the thermal expansion coefficient of the solid phase of the soil.

The value of α_v used in the analysis reported here was $27.0 \times 10^{-6} \text{ }^\circ\text{C}^{-1}$. This value is towards the lower end of the literature values. Similar values were used by Martínez Calonge (2017) ($27.1 \times 10^{-6} \text{ }^\circ\text{C}^{-1}$ for Leighton Buzzard sand), and Sittidumrong et al. (2019) ($24.3 \times 10^{-6} \text{ }^\circ\text{C}^{-1}$ for Bangkok sand).

6.3 Overview

In total, twelve tests were carried out using sand. The basic information about each test is summarised in Table 6.3. A brief description of the loading and thermal path (if applicable) for each test is given, as well as the primary motivation for performing the test. These are given for ease of reference, and discussed in more detail below.

To check whether results were repeatable using different equipment, some tests were performed using the temperature-controlled oedometer (TC-OED) and some using the ambient-temperature oedometer (ML-OED). All tests were performed under saturated conditions, except test 5, which was performed under dry conditions. Even when using the temperature-controlled oedometer, not all tests were thermal tests. As discussed above, it is important to understand the ambient temperature response of the equipment and material, in order to understand the additional complexities of the thermal response.

The schematic test path for tests 1, 2 and 4 is given in Figure 6.1. Two load/unload cycles were carried out at ambient temperature. Test 1 was performed using the temperature-controlled oedometer, whereas test 2 was performed using the ambient-temperature oedometer, enabling the effect of the equipment to be understood. Test 4 followed the same test path as tests 1 and 2, but with continuous loading and unloading (fixed rate of pressure change), rather than incremental loading and unloading (quasi-instantaneous pressure change), as in all other tests.

The schematic test path for tests 3 and 5 is given in Figure 6.2. Following loading at ambient temperature, three combined thermal and mechanical cycles were carried out. These combined

Table 6.3: Overview of sand tests 1 to 12

Test	Equipment	Loading and heating path	Motivation
1	TC-OED	2× mechanical cycles	Baseline ambient-temperature response
2	ML-OED	Repeat of test 1	Comparison of equipment
3	TC-OED	3× combined thermal and mechanical cycles	Thermal and mechanical response
4	ML-OED	Repeat of test 1 (continuous loading)	Comparison of continuous/incremental loading
5	TC-OED	Repeat of test 3 (dry conditions)	Comparison of dry/saturated conditions
6	TC-OED	3× mechanical cycles	Effect of repeated mechanical cycling at ambient temperature. Comparison with test 3 (elevated temperature)
7	TC-OED	Repeat of test 6 (greased confining ring)	Effect of greasing confining ring
8	TC-OED	3× thermal cycles	Response of sand to repeated thermal cycling. Comparison with test 3
9	ML-OED	3× mechanical cycles	Evaluation of new methodology (pre-load filter papers)
10	TC-OED	Repeat of test 9	Comparison of equipment
11	ML-OED	Repeat of test 9	Repeat results from tests 9 and 10
12	ML-OED	Repeat of test 9	Evaluation of new methodology (no filter papers)

cycles consisted of a heating stage, followed by a load/unload cycle at elevated temperature, then a cooling stage, back to ambient temperature. This path was chosen to enable comparison with the thermal test on bentonite (Bentonite test 9, see Section 5.5), which follows a similar path. By repeating the combined cycle three times, the thermal response of the material could be compared for pressure values at, or below, the maximum applied pressure. Test 5 was a repeat of test 3, but with dry, rather than saturated conditions.



Figure 6.1: Schematic test path for sand tests 1, 2 and 4



Figure 6.2: Schematic test path for sand test 3 and 5

The schematic test path for tests 6 and 7 is given in Figure 6.3. These tests were performed to obtain the baseline ambient-temperature response for the thermal tests (3 and 5). The test path was similar to test 3, but without the thermal stages. Following initial loading at ambient temperature, three further load/unload cycles were applied. In test 7, the top-cap o-ring and inner surface of the confining ring were greased, to see what effect this would have on the results. The schematic test path for test 8 is given in Figure 6.4. The test consisted of three thermal cycles performed at the maximum load reached during test 3.



Figure 6.3: Schematic test path for sand tests 6 and 7



Figure 6.4: Schematic test path for sand test 8

The schematic test path for tests 9, 10, 11 and 12 is given in Figure 6.5. Three load/unload cycles were performed, with the maximum pressure increasing with each cycle. These were ambient temperature tests, performed to validate a new testing methodology. In tests 9, 10 and 11, filter papers were placed either side of the specimen, as in previous tests, whereas in test 12 filter papers were not used.



Figure 6.5: Schematic test path for sand tests 9, 10, 11 and 12

The specimen set-ups for the sand tests are given in Figure 6.6. For tests 1 to 11 (Figure 6.6a), the sand specimen was installed between two filter papers, with a porous stone below, but no porous stone above. For test 12 (Figure 6.6b), filter papers were not used, and the sand specimen was installed between two porous stones - one above and one below. In all tests, the top-cap o-ring was in place, but grease was only used in test 7.

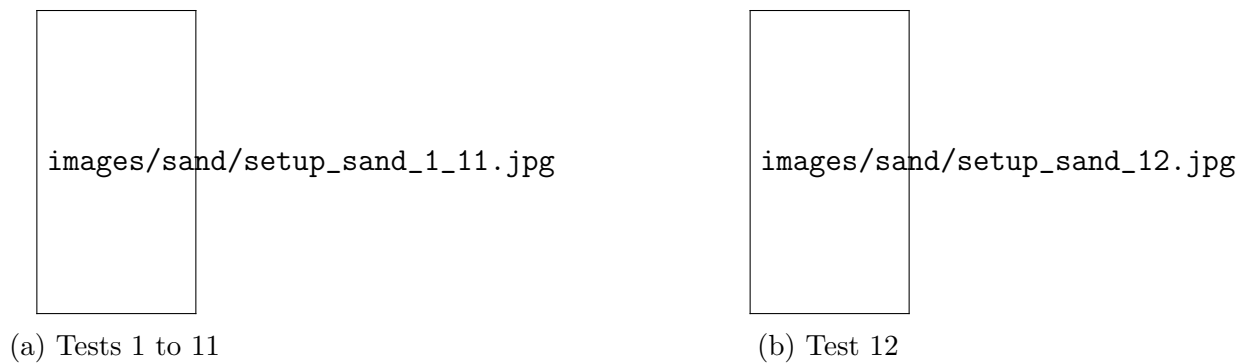


Figure 6.6: Specimen set-up for sand tests

6.4 Methodology

The full, final, testing and calibration methodology for the temperature-controlled oedometer, used for the tests on KSS, is given in Chapter 7. One of the key motivations for performing these tests on sand was to improve the methodology. This is an iterative process, which goes as follows:

1. A test is performed using the current methodology.
2. Potential improvements are considered, based on observations during, and after the test. These could relate to the procedure for setting up the test, for removing the specimen, for measuring the specimen mass and dimensions, for resetting the displacement transducers mid-test, for post-processing the results, among others. Improvements could be a change to test procedure, or physical modifications to the equipment itself.
3. These changes are then evaluated through further testing.

These tests on sand form part of the bigger picture - improving the general testing methodology. But in addition, there was an iterative process of improvement of the methodology specific for testing granular materials.

One difference between these tests, and the tests on bentonite (with the exception of sand test 12), is that there was no porous stone above the specimen (See Figure 6.6). This change was necessary because of the granular nature of the sand. There is a small gap between the edges of the porous stone (diameter: 69.75 mm) and the confining ring (inner diameter: 70.27 mm). This small gap enables the porous stone to move freely up and down within the confining ring. However, when testing sand, individual grains can become trapped in this gap, locking the porous stone in position. The porous stone can only be moved by applying a relatively high load and crushing these grains. This is a potential issue when setting up the specimen, and during testing. Without a porous stone above the specimen, a filter paper is required to prevent sand from being squeezed into the drainage holes in the top-cap. This consequently required a change to the methodology for setting the initial condition for the test, which is discussed in Appendix J, as part of a step-by-step procedure for setting up sand tests.

A similar methodology was followed for tests 1 and 8. For tests 9 and 12, a new multi-stage testing methodology was followed, which is discussed further below.

6.5 Results and discussion

In this section, the key results from the sand tests are presented and discussed.

In the first set of tests (1, 2 and 4), two cycles of mechanical loading and unloading were applied, at ambient temperature. The relevant test details are summarised and compared in Table 6.4. The effect of equipment is compared in test 1 and 2, and the effect of incremental or continuous reloading is compared in test 2 and 4.

The full test path for test 1 is given in Figure 6.7. It comprises incremental loading from 2.5 kPa to 300 kPa (A → B), unloading to 10 kPa (B → C), reloading to 900 kPa (C → D), and unloading to 10 kPa (D → C). Each increment was 30 min duration, and the total test duration was 13.5 h.

The displacement response with pressure is given in Figure 6.8. The raw data are compared with two corrected responses - semi-log and sigmoid. These are the two fits derived from the combined

Table 6.4: Comparison of sand tests 1, 2 and 4

Test	Equipment	Load application
1	TC-OED	Incremental
2	ML-OED	Incremental
4	ML-OED	Continuous

images/sand/full_loadpath_1.pdf

Figure 6.7: Full test path for sand test 1

load/temperature calibration test 1A described in Section 4.4. These data are corrected for the vertical mechanical compliance at 22.5 °C. Vertical thermal compliance is not relevant since this test was carried out at constant temperature.

The raw data show an initially stiff response, which becomes softer above 25 kPa. There are some kinks in the loading response, mostly evident at pressure values below 100 kPa, where a drop in pressure corresponds to a sudden increase in displacement. These may be caused by macro-scale reorientation of interconnected sand grains. However, the overall shape of the loading response is not affected. Unloading results in expansion, which is approximately linear against log-pressure. The reloading curve plots above the unloading curve (lower contractive displacement) until ≈ 100 kPa, then plots parallel to the loading curve, but shifted slightly down (higher contractive displacement). The second unloading curve plots parallel to the first.

The two corrections give similar results to each other, but both overestimate the compliance (i.e. how much of the total contractive displacement is due to contraction of the equipment), across the full range of pressures. This can be seen from the first unloading path, which is contractive, and the subsequent reloading path, which is extensive for pressures below 100 kPa. The second unloading curve is also contractive. This result shows the advantage of testing with

images/sand/sand_1_disp_p_semilog_sigmoid.pdf

Figure 6.8: Sand test 1 - vertical compliance correction for sigmoid and semi-log fits based on calibration test 1A


a well-understood soil such as sand. Clearly, during unloading (load reducing), expansion is expected, not contraction as implied by the corrected data. During reloading (load increasing), contraction is expected, not expansion as implied by the corrected data.

The limitations of the combined calibration were already known by this point, particularly the accuracy of the vertical thermal compliance. However, this result shows that the vertical mechanical compliance derived from this calibration is also inaccurate when applied to ambient-temperature loading data, and provides further evidence for rejecting the combined calibration.

A different correction was applied to the data, derived from the ambient-temperature calibration test TC:2, discussed in Section 4.5. The specimen used for calibration test TC:2, shown in Figure 4.59b, comprised a porous stone and *three* filter papers, rather than two, as in sand test 1. Another difference is that the top-cap o-ring was not in place for calibration test TC:2, so friction effects are not included in the calibration. This correction is based on a 6th order polynomial fit through a single load/unload cycle. Importantly through, the initial load/unload response was not used, avoiding the issue of the residual displacement resulting from the first cycle. These corrected data are shown in Figure 6.9, together with the raw data for comparison.

The new correction (labelled poly6 TC2) is a significant improvement on the previous corrections in Figure 6.8. Corrected unloading paths show expansion, and the reloading path shows contraction, as expected from the known properties of the sand.

Sand test 2 followed an identical test path to test 1. Sand test 4 also followed the same path, except that continuous loading/unloading at 30 kPa h^{-1} was applied, rather than incremental changes. Both tests were performed using the ambient-temperature oedometer. The results were found to be unreliable, since only one displacement transducer was used, positioned off-centre relative to



images/sand/sand_1_disp_p_poly6.pdf

Figure 6.9: Sand test 1 - vertical compliance correction for polynomial fit based on calibration test TC:2

the specimen. As discussed in Section 4.3 and Appendix G, multiple displacement transducers are necessary for accurate displacement (and volume) measurement, unless positioned directly above the centre of the specimen. These results are therefore not presented. The advantages and disadvantages of incremental and continuous loading are discussed in Section 5.5 (see for example, the discussion on bentonite tests 6 and 7). Following these tests, the ambient-temperature oedometer was modified to include an instrumentation plate with three displacement transducers, similar to the temperature-controlled oedometer.

The calibrations used to correct the test data for selected sand tests are summarised in Table 6.5. The *combined* calibration refers to the combined thermal/mechanical calibration derived from the calibration test 1A data (Section 4.4). From these data, two fits were derived: semi-log, and sigmoid. The *mechanical* calibration refers to the ambient-temperature mechanical calibration derived from the calibration test TC:2 data (Section 4.5). From these data, a 6th order polynomial fit (poly 6) was derived. As well as the vertical equipment compliance, all the thermal tests were corrected for the differential thermal expansion of the confining ring (CR) and soil (Section 4.6). Tests 9 to 12 used a different calibration methodology, discussed below, in which a unique calibration (power fit) was derived for each test, based on the first part of a three-part test sequence.

Table 6.5: Summary of calibrations used for selected sand tests

Test	Equipment	Calibration used	Calibration test reference
1	TC-OED	Combined (semi-log, sigmoid), Mechanical (poly 6)	1A, TC:2
3	TC-OED	Combined (semi-log), CR	1A
5	TC-OED	Combined (semi-log), CR	1A
6	TC-OED	Mechanical (poly 6)	TC:2
7	TC-OED	Mechanical (poly 6)	TC:2
8	TC-OED	Combined (semi-log), CR	1A
9	ML-OED	Mechanical (power)	Sand 9, part 1/3
12	ML-OED	Mechanical (power)	Sand 12, part 1/3

Tests 3, 6 and 8 were a series of thermal/mechanical and ambient-temperature tests performed using the temperature-controlled oedometer. The key differences between these tests are summarised in Table 6.6. In test 3, the mechanical path was performed at a temperature of 70 °C, and the thermal path at a pressure of 50 kPa. In test 6, the mechanical path was performed at ambient temperature (22.5 °C), and there was no thermal path. In test 8, there was no mechanical path, and the thermal path was performed at a pressure of 1200 kPa. Test 3 was repeated, under slightly different conditions, discussed below (test 5), as was test 6 (test 7). The calibrations used for each test are summarised in Table 6.5.

Table 6.6: Comparison of sand tests 3, 5, 6, 7 and 8

Test	Equipment	Mechanical path - temperature [°C]	Thermal path - pressure [kPa]
3, 5	TC-OED	70	50
6, 7	TC-OED	22.5	n/a
8	TC-OED	n/a	1200

The test paths are shown together in Figure 6.10. All tests began with loading at 22.5 °C to 50 kPa pressure (A → B). Test 3 comprised three combined thermal/mechanical cycles (B → C → D → C → B). Test 6 comprised three mechanical cycles at 22.5 °C (B → E → B). Test 8 comprised loading at 22.5 °C to 1200 kPa (B → E), followed by three thermal cycles at 1200 kPa (E → D → E).

images/sand/full_loadpath_368.pdf

Figure 6.10: Combined test path for sand tests 3, 5, 6, 7 and 8

The first test of the series, test 3, involved performing repeated thermal/mechanical cycles, as shown in the test path given in Figure 6.11. Following loading to 50 kPa at 22.5 °C (A → B), the thermal/mechanical cycle (B → C → D → C → B) was performed three times. This cycle comprised heating from 22.5 °C to 70 °C at 50 kPa (B → C), loading from 50 kPa to 1200 kPa at 70 °C (C → D), unloading to 50 kPa at 70 °C (D → C), and cooling from 70 °C to 22.5 °C at 50 kPa (C → B).

images/sand/full_loadpath_3.pdf

Figure 6.11: Full test path for sand test 3

The applied pressure and temperature is shown in Figure 6.12, for the first thermal/mechanical cycle. The duration of each cycle was ≈ 72 h. The heating rate was $2\text{ }^\circ\text{C h}^{-1}$. This heating rate was not limited by the soil properties (i.e. ability to dissipate excess pore-water pressure), or the heater capacity. In fact, for a granular, free-draining material such as Leighton Buzzard sand, much faster heating rates could be applied, without the development of excess pore-water pressure. Instead, this relatively slow heating rate was used to ensure that there were no transient thermal gradients across the equipment which may affect the measured displacement. The load was applied/removed incrementally, with each increment of 30 min duration. Compare this with the significantly longer 48 h duration required for consolidation increments on bentonite. The reduction in increment duration allows thermal tests on sand to be performed much more quickly than bentonite. For the purpose of equipment development, this is useful because it allows more tests, with more complex test paths, to be performed within the fixed time-scale of the research programme. The specimen was allowed to cool naturally over ≈ 36 h.

The strain-temperature response for the first three thermal/mechanical cycles is given in Figure 6.13. These results have been corrected for vertical mechanical compliance using the combined thermal and mechanical compliance (semi-log fit) derived from calibration test 1A in Section 4.4. As discussed in relation to sand test 1 above, this correction has some limitations. However, it was used here because the ambient-temperature fit (TC:2 poly 6) cannot account for vertical thermal

images/sand/sand_3_P_T_time.pdf

Figure 6.12: Sand test 3 - pressure and temperature vs time (cycle 1 of 3)

compliance. The results have also been corrected for the lateral expansion of the confining ring, using the correction discussed in Section 4.6. Here, sub-incremental strain is used (i.e. taking the initial condition as $P = 50 \text{ kPa}$, $T = 22.5^\circ\text{C}$) as opposed to total, or incremental strain - see the discussion in Section 4.6.1 for further details. The initial expansive strain under constant pressure corresponds to the first heating stage. The loading response at 70°C is non-linear below 100 kPa , then linear for higher pressure values. The unloading path is also linear. The reloading paths, following the heating/cooling cycle, plot above the unloading paths (lower contractive displacement), as in test 1, crossing the unloading path at $\approx 200 \text{ kPa}$ during cycle 2 reloading, and at $\approx 450 \text{ kPa}$ during cycle 3 reloading. There is ratcheting of the strain with each cycle, resulting in increasing residual contractive strain. Most of this contractive strain is due to the cycle 1 loading stage, and the additional contractive strain reduces with each subsequent cycle. The effect of the thermal cycles on the ratcheting behaviour is not clear from this graph.

The effect of temperature is seen more clearly in the strain-temperature response, shown in Figure 6.14. All heating paths cause expansion, and all cooling paths cause contraction. This, despite the fact that the initial heating path is applied to sand at the maximum applied pressure, whereas subsequent thermal paths are applied to sand at a pressure value below the maximum applied pressure. Where the heating path immediately follows the cooling path, as in cycle 2 and 3 heating, the contractive displacement due to cooling is fully reversed by the expansion due to heating. This suggests that the thermally-induced strain does not contribute to the ratcheting response observed in Figure 6.13. It is possible that the thermal cycling still has some effect on the subsequent reloading response, although this seems unlikely since thermal cycling does not result in any permanent strain or change in void ratio, discussed below.

images/sand/sand_3_Str_P.pdf

Figure 6.13: Sand test 3 - strain vs pressure

images/sand/sand_3_Str_T.pdf

Figure 6.14: Sand test 3 - strain vs temperature

The void ratio response is given in Figure 6.15. This is the temperature-corrected void ratio. There is no significant change in void ratio during the first heating stage. The cycle 1 cooling stage causes a reduction in void ratio. Subsequent heating stages cause an increase in void ratio, and cooling stages cause a reduction.

images/sand/sand_3_e_T.pdf

Figure 6.15: Sand test 3 - void ratio vs temperature

Sand test 5 was a repeat of test 3, but with dry, rather than saturated conditions. This was achieved by sealing the drainage paths through the top-cap to the water bath. The same calibration was used for both tests (combined thermal/mechanical, semi-log fit). The results, either in terms of displacement, strain, or void ratio, were qualitatively similar to those from test 3. However, the magnitude of thermal volume change was significantly lower than for test 3, as shown in Figure 6.16. The sudden drop in strain between 50 °C and 60 °C is probably due to the equipment being disturbed. If an LVDT slips down within its brass housing, this is registered as an increase in compressive displacement. The inferred response, based on the rest of the data for higher temperature, is shown as a dashed line. One possible explanation for the lower thermal volume change in test 5 is that the temperature within the specimen was lower than the temperature measured by the temperature transducer within the water bath. The base drainage, normally filled with water, was open to the air, albeit through a narrow drainage line through the upper base-plate. The temperature transducers below the specimen, within the upper base-plate, did not record significantly lower temperatures than the water bath temperature though. Two alternative explanations are that (i) the difference in the initial sand density caused this result, or (ii) the presence of water affected the thermal response of the sand, perhaps by lubricating the particle interfaces. The effect of initial density is important, and is discussed below, along with the other test limitations. The effect of dry/saturated conditions, suggested by this result, should not be ruled out, but further testing would be required before making any firm conclusions.

images/sand/sand_3_5_initial_heating.pdf

Figure 6.16: Comparison of sand test 3 (saturated) and 5 (dry) - initial heating path at 50 kPa

Sand test 6 involved three load/unload cycles at ambient temperature. The full test path is shown in Figure 6.17. This test was repeated, with minor variations, discussed below, as test 7. Following initial loading to 50 kPa (A → B), three load/unload cycles from 50 kPa to 1200 kPa, and back to 50 kPa (B → C → B) were carried out. This is similar to the elevated temperature load/unload cycle as in test 3 (C → D → C in Figure 6.11). However, in test 3, the mechanical cycles were part of a combined thermal and mechanical cycle. The results are therefore not directly comparable, apart from the initial loading path from 50 kPa to 1200 kPa. Note that a different calibration was used for test 3 (semi-log, based on calibration test 1A), and test 6 (polynomial, based on calibration test TC:2).

The results from test 6 are given in Figure 6.18, as strain vs pressure. This strain is the total strain, corrected for vertical mechanical compliance using the same polynomial fit (poly6 TC:2) as in test 1. The results are qualitatively similar to test 3 (see Figure 6.13), with an initially non-linear loading path, becoming linear at pressures above 50 kPa, and linear unloading paths. Again, the reloading paths plot above (lower contractive displacement) the immediately preceding unloading paths, crossing the unloading paths at ≈ 300 kPa for cycle 2 reloading, and 600 kPa for cycle 3 reloading. The additional permanent strain reduces with each cycle. It is expected that with enough cycles, the increase in permanent strain would become negligible, and the contractive strain due to reloading would be fully recovered during subsequent unloading.

Test 7 was performed to determine whether applying grease to the inside of the confining ring has a significant effect on the measured response of the soil to loading. The test path followed was identical to test 6, except for an additional unload/reload path at 300 kPa. The same calibration was used for both test (poly 6 TC:2). The results for test 6 and 7 are shown in Figure 6.19. Above 50 kPa, the loading response for test 7 is steeper than test 6. The response to subsequent unload/reload cycles is similar for both tests. This suggests that applying grease may affect the

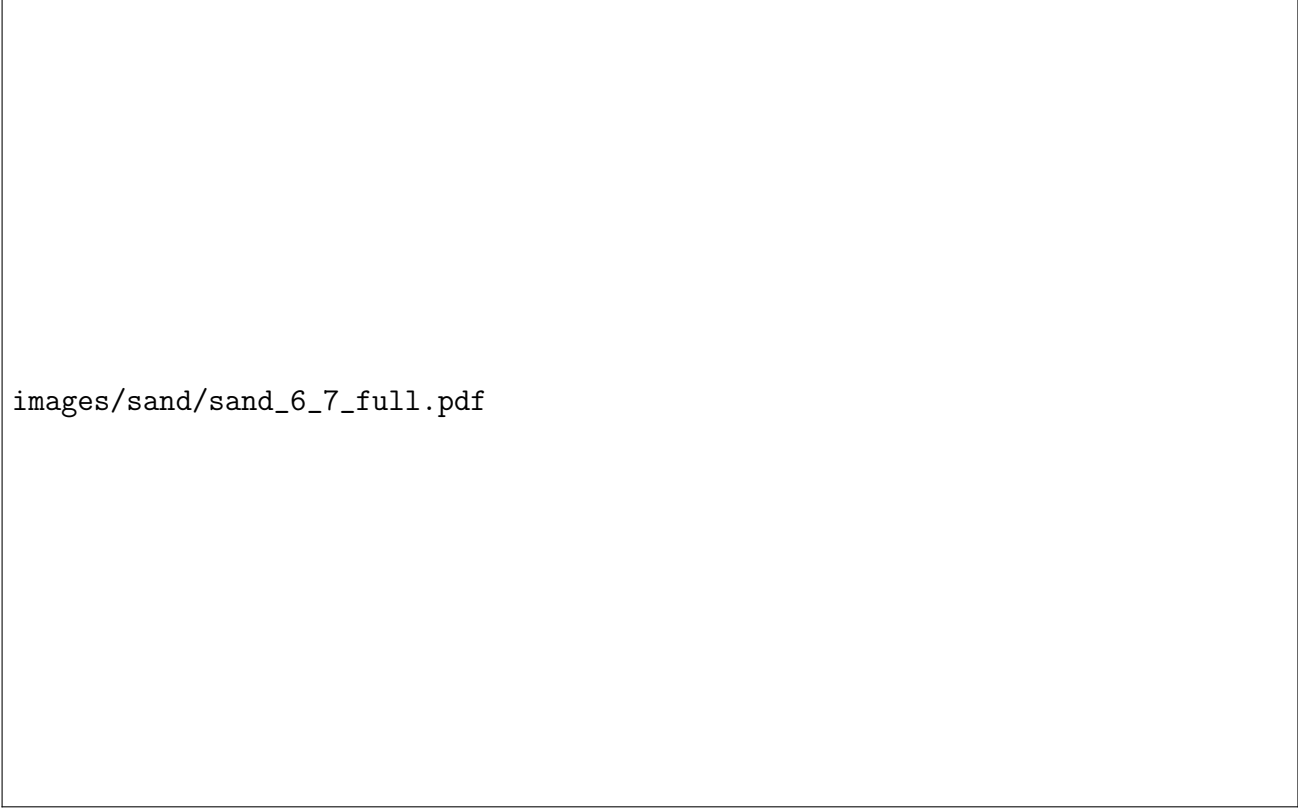
images/sand/full_loadpath_6.pdf

Figure 6.17: Full test path for sand test 6

images/sand/sand_6_Str_P.pdf

Figure 6.18: Sand test 6 - strain vs pressure

measured loading response. However, as discussed at the end of this section, the effect of relative density appears to be the major factor determining the response. The initial relative density for test 6 (13%) was higher than test 7 (6%), indicating a denser initial condition. The effect of applying grease could not be isolated from the effect of initial relative density. Based on the friction tests discussed in Section 4.2, applying grease seems to reduce friction, and was done for all tests using KSS. For tests on sand though, this may not actually reduce friction, because sand grains tend to stick to the grease on the side of the confining ring.



images/sand/sand_6_7_full.pdf

Figure 6.19: Comparison of sand test 6 (no grease) and 7 (grease) - full test

Test 8 was performed to compare the effect of temperature cycling on sand for pressure values at, or below, the maximum applied pressure. The full test path is shown in Figure 6.20. The specimen was loaded to 1200 kPa at 22.5 °C (A → B), then three thermal cycles were applied at constant pressure (B → C → B). The thermal cycles comprised heating from 22.5 °C to 70 °C at 2 °C h⁻¹ (B → C), then cooling back to 22.5 °C at the natural cooling rate of the equipment (C → B). As with the mechanical cycles in test 6, these thermal cycles are similar, but (apart from the initial heating path) not directly comparable with the thermal cycles in test 3, which are part of a combined thermal and mechanical cycle. The same combined thermal/mechanical calibration was used for test 3 and test 8 (semi-log, based on calibration test 1A).

The total strain vs pressure response is given in Figure 6.21. The strain has been corrected for vertical compliance using the combined thermal and mechanical semi-log fit based on calibration test 1A, as well as for the differential lateral expansion of the confining ring and soil. The loading response is initially non-linear, approaching a linear response for pressures above 200 kPa. The magnitude of strain due to thermal cycling is significantly lower than the strain due to mechanical loading. The thermal strains can be seen more clearly when plotted against temperature, as in Figure 6.22.

images/sand/full_loadpath_8.pdf

Figure 6.20: Full test path for sand test 8

images/sand/sand_8_Str_P.pdf

Figure 6.21: Sand test 8 - strain vs pressure (full test)

images/sand/sand_8_Str_T.pdf

Figure 6.22: Sand test 8 - strain vs temperature (full test)

The same data are plotted in Figure 6.23, focusing on the effect of thermal cycling on strain. All heating paths induce expansive strain, while all cooling paths induce contractive strain. The gradient of the initial heating path is lower than for subsequent heating paths. The cooling paths for all three cycles are approximately linear, and parallel. The heating paths for cycle 2 and 3 are linear, and expansive, for temperatures below $\approx 50^\circ\text{C}$, reversing the contraction due to the previous cooling path. Above 50°C , the amount of expansion with temperature reduces. The effect on this non-linearity is that each heat/cool cycle results in the accumulation of permanent strain. These results are in partial agreement with the results from other temperature-controlled oedometer schemes, testing sand. Sittidumrong et al. (2019), testing Bangkok sand, and Ng et al. (2017), testing Toyoura sand, observed similar ratcheting behaviour due to thermal cycling, resulting in a gradual increase in the permanent contractive strain. However, in both cases, initial heating of sand at the maximum applied pressure resulted in contraction, rather than expansion. Thermal ratcheting behaviour was also observed for normally-consolidated clay (KSS), discussed in Section 8.5.3.

The heating paths for cycle 2 and 3 can be compared with those from sand test 3, in Figure 6.14. In both cases, heating causes expansion, while cooling causes contraction. However, the expansive strain due to heating in test 3 fully reverses the contractive strain due to cooling, so that a cool/heat path (e.g. cycle 1 cooling \rightarrow cycle 2 heating) results in no additional permanent strain. A similar path in test 8 results in additional permanent strain, because the expansive strain due to heating is less than the contractive strain due to cooling. This may be explained by considering the loading history of the soil. In test 3, except for the first heating stage, all thermal stages are carried out on sand below the maximum applied pressure. Whereas in test 8, the thermal cycles were carried out on sand at the maximum applied pressure.

images/sand/sand_8_Str_T_thermal_cycles.pdf

Figure 6.23: Sand test 8 - strain vs temperature (thermal cycles)

The initial thermal response for test 3 and test 8 is compared in Figure 6.24. In both cases, a heating path is carried out on sand at the maximum applied pressure (see the load path in Figure 6.10). The thermal strain for test 3, at 50 kPa, is higher than for test 8, at 1200 kPa. This result is interesting, but it should be reiterated that it is based on the combined thermal/mechanical calibration, which is known to have limitations. By repeating these tests with the final calibration methodology used for the KSS tests, it would be possible to measure this behaviour more accurately and reliably.

The thermal response for test 8, in terms of void ratio, is given in Figure 6.25. This is the temperature-corrected void ratio, accounting for thermal expansion of the solid phase of the soil. The void ratio reduces during initial heating, and reduces further during subsequent cooling. For the next two cycles, heating causes an increase in void ratio, while cooling causes a reduction. The increase due to heating is non-linear, similar to the strain response, which results in a ratcheting effect, where void ratio reduces with each thermal cycle. This reduction gets smaller with each cycle.

To understand why the corrected void ratio gives this result, it may be helpful to compare the specimen strain and solids strain, as shown in Figure 6.26. Here, specimen strain refers to the sub-incremental strain for the whole specimen, which is the measured (and corrected) strain value. Solids strain refers to the sub-incremental strain for the solid phase, which is based on the initial volume of solids calculated from the initial specimen mass and the known solids density, and the change in volume of solids calculated from the (assumed) volumetric thermal expansion coefficient of the solid phase. Strains are compared, rather than absolute values (such as volume), to enable comparison, since strain is measure of a relative change. If the total volume and solid phase both change by the same relative amount (for example, both increase to twice their original volume), the void ratio will stay constant. However, if they both change by the same absolute

images/sand/sand_3_8_initial_heating.pdf

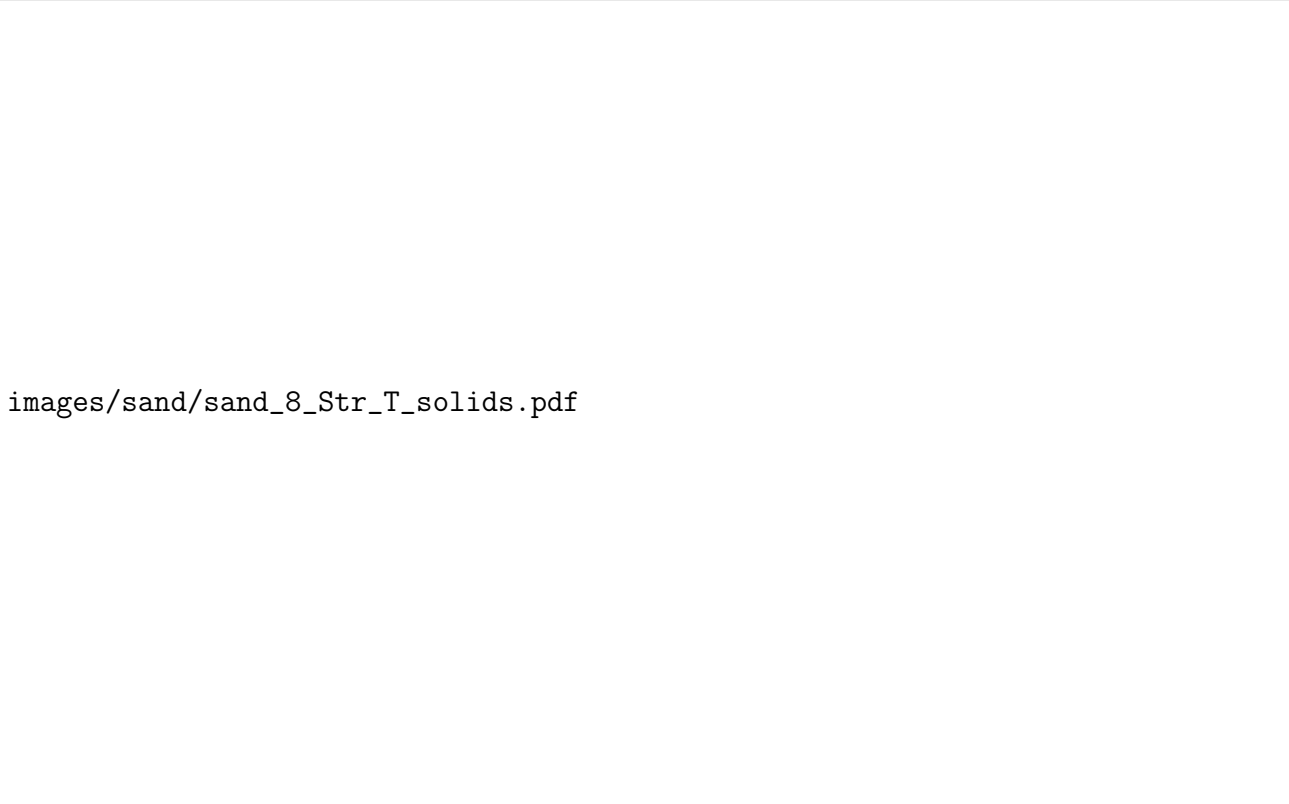
Figure 6.24: Comparison of sand test 3 (heating at 50 kPa) and 8 (heating at 1200 kPa) - initial heating path

images/sand/sand_8_e_T.pdf

Figure 6.25: Sand test 8 - void ratio vs temperature

amount (for example, both increase by 1 cm^3), the void ratio will not stay constant (unless the initial void ratio was 0.5). In Figure 6.26, the Y1 and Y2 axes have the same scale, so the data are directly comparable.

For the initial heating path, the expansive solids strain is higher (more expansive) than the expansive specimen strain. Both are expansive, but since the solids are expanding relatively more than the whole specimen, the void ratio reduces. For the cooling paths, the contractive solids strain is lower (less contractive) than the contractive specimen strain. The void ratio reduces, because the solids are contracting relatively less than the whole specimen. For the cycle 2 and 3 heating paths, the expansive solids strain is lower (less expansive) than the expansive specimen strain. Since the solids are expanding relatively less than the whole specimen, the void ratio increases. Note that at temperatures above $\approx 50^\circ\text{C}$, the gradient of both is approximately equal, which corresponds to the negligible change in void ratio at temperatures above 50°C observed for the heating paths.



images/sand/sand_8_Str_T_solids.pdf

Figure 6.26: Sand test 8 - comparison of specimen strain (Y1) and solids strain (Y2)

Tests 9, 10 and 11 followed a new methodology developed from a series of calibration tests, discussed in Section 4.5. The previous mechanical calibration used the data from calibration test TC:2. A 6th order polynomial was fitted through the TC:2 data, avoiding high residual displacement associated with the cycle 1 response. However, this calibration has a number of limitations: (i) a 50.8 mm brass dummy was used in TC:2, which affects the stress felt by the filter papers, (ii) three filter papers were used in TC:2, not two, as in the sand tests, (iii) the top-cap o-ring was not used in TC:2, and (iv) the test path in TC:2 was a series of load/unload cycles between 2.5 kPa and 1500 kPa, which is not the same as in the sand tests. The new calibration methodology aimed to address these limitations by (i) not using any brass dummy, (ii) using the same number of filter papers, and porous stones, as in the proposed soil test, (iii) performing the calibration with the o-ring in place, to account for friction. The final point (iv),

relating to the test path followed in the calibration test, was not addressed in this set of tests, but was addressed in the final calibration methodology used for KSS tests.

The aim of these tests was to assess the new testing and calibration methodology. Tests 9 and 11 were performed with the ambient-temperature oedometer (ML-OED), while test 10 was performed using the temperature-controlled oedometer (TC-OED). In test 12 (ML-OED) the same methodology was followed as in tests 9 to 11, but without using filter papers. This is summarised in Table 6.7.

Table 6.7: Comparison of sand tests 9 to 12

Test	Equipment	Filter papers used?
9	ML-OED	Yes
10	TC-OED	Yes
11	ML-OED	Yes
12	ML-OED	No

The new testing and calibration methodology had three distinct parts:

- Part 1:** Determine the calibration curve by applying a sequence of load/unload cycles, without a soil specimen present, up to the maximum load to be applied to the soil in part 2. The test set-up is exactly the same as for part 2, with the top-cap o-ring in place, and with the same number of filter papers and porous stones, except that no soil specimen is in place. If filter papers are used, this stage also acts as a pre-loading stage.
- Part 2:** Perform the main soil test, immediately following the end of part 1. The test data are corrected using a calibration curve derived from the part 1 data.
- Part 3:** Repeat the part 1 stage to determine the reliability of the part 1 data, and the derived calibration.

The full test path for part 2 of the three-part test, for sand test 9, is given in Figure 6.27. It comprises three load/unload cycles. Cycle 1 is loading from 2.5 kPa to 300 kPa, followed by unloading to 10 kPa (A → B → C). Cycle 2 is loading from 10 kPa to 900 kPa, followed by unloading to 10 kPa (C → D → C). Cycle 3 is loading from 10 kPa to 1500 kPa, followed by unloading to 2.5 kPa (C → E → A). All cycles were performed at ambient temperature.

The results for part 1 of the test (determine calibration and pre-load filter papers) are given in Figure 6.28. The first three load/unload cycles are shown. Note that these are not the same cycles as in part 2 of the test. The first cycle results in a residual displacement of ≈ 0.2 mm. Compare this to the next two cycles, which result in negligible further residual displacement, and have repeatable load and unload paths. However, there is still hysteresis between the load and unload paths. The isolated displacement for cycle 2 and 3 is shown in Figure 6.29. The part 1 data were used to determine the calibration curve to correct the part 2 data. When determining the calibration, the cycle 1 response is not used. This is similar to the way the mechanical calibration based on test TC:2 was determined (see Section 4.5).

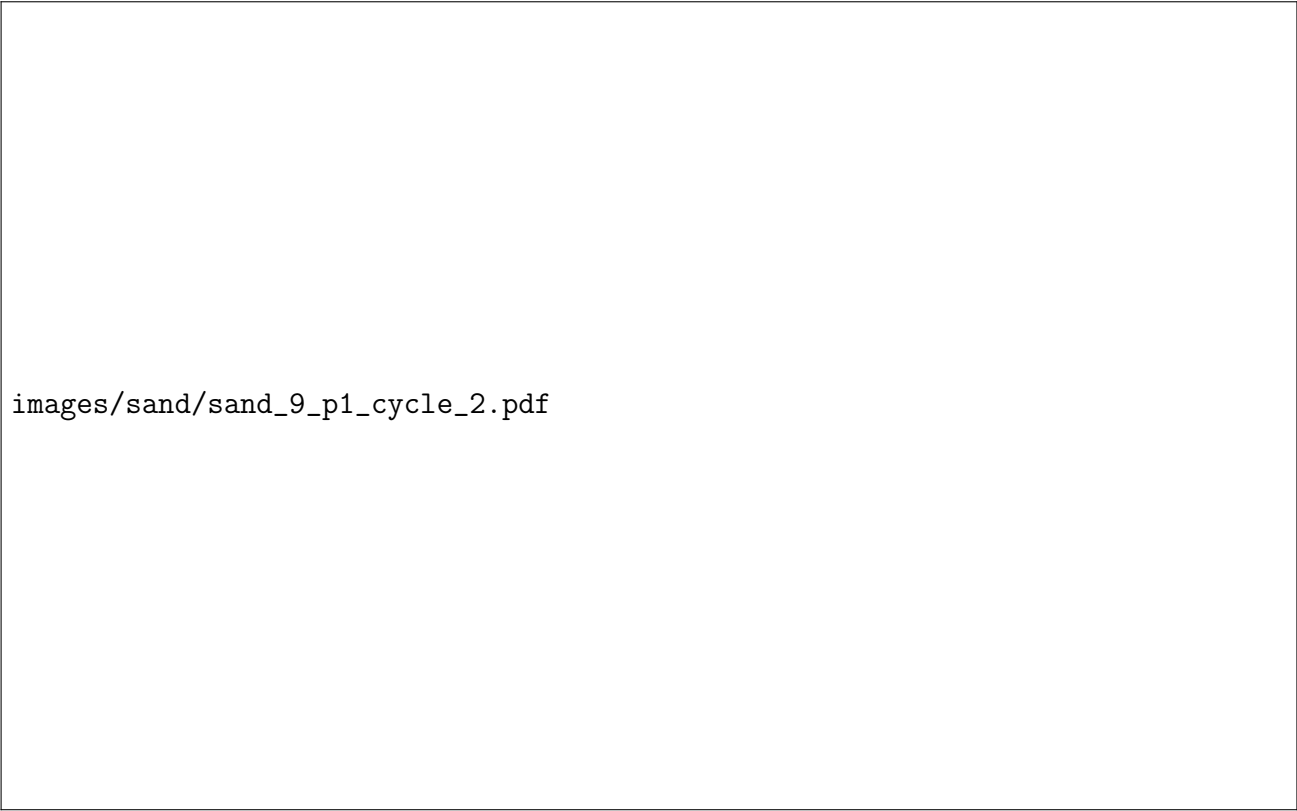
The results for the sand test (part 2/3) are given in Figure 6.30. The raw data are plotted, together with the corrected data. The corrected data have been adjusted for vertical compliance using a power fit through the part 1 data (not including the first load/unload cycle). There are some issues apparent in the corrected result. Following each loading stage, there is initially contraction during the subsequent unloading stage, where expansion would normally be expected.

images/sand/full_loadpath_9.pdf

Figure 6.27: Full test path for sand test 9

images/sand/sand_9_p1_full.pdf

Figure 6.28: Sand test 9 - part 1/3 (determine calibration and pre-load filter papers) - displacement response for load cycles 1 to 3



images/sand/sand_9_p1_cycle_2.pdf

Figure 6.29: Sand test 9 - part 1/3 (determine calibration and pre-load filter papers) - displacement response for load cycles 2 and 3

Following each unloading stage, there is initially expansion during the subsequent reloading stage, where contraction would normally be expected. This expansion can be seen more clearly when pressure is plotted on a linear scale, as in Figure 6.31. Note that the contraction upon unloading appears less pronounced when using a linear pressure scale.

Another example of the problem with this methodology can be found by comparing the part 1 and part 3 data. In part 1 of the test, repeated load/unload cycles were applied to the filter papers. Part 3 was a repeat of part 1, using the same filter papers that had been used in part 1 and part 2 (the sand test). The key assumption in this methodology is that recently pre-loaded filter papers, upon subsequent reloading (in a soil test), will show repeatable, predictable behaviour. This assumption is based on the calibration tests discussed in Section 4.5, particularly test ML:5. In other words, their response will be like that shown in Figure 6.29, and not like Figure 6.28. The data from part 3, shown in Figure 6.32, disproves this assumption. In fact, the residual displacement following the first load/unload cycle in part 3 was significantly higher than in part 1.

Tests 10 and 11 were performed to check these results, following the same methodology and test paths as in test 9. In both cases, the same issues were found. The calibrations derived from part 1 were inaccurate, as could be seen from the corrected part 2 data, which showed expansion where contraction would be expected, and vice-versa. As in test 9, the part 3 data showed significant residual displacement. Based on these three tests, and other calibration tests discussed in Chapter 4, a decision was made not to use filter papers in any other tests.

The final test in the series was test 12. As with tests 9 to 11, test 12 was performed to assess the new three-part testing methodology. Previous tests showed a number of issues relating to

images/sand/sand_9_D_P_log.pdf

Figure 6.30: Sand test 9 - part 2/3 (main soil test) - displacement vs pressure (log scale)

images/sand/sand_9_D_P_linear.pdf

Figure 6.31: Sand test 9 - part 2/3 (main soil test) - displacement vs pressure (linear scale)

images/sand/sand_9_p3.pdf

Figure 6.32: Sand test 9 - comparison between part 1/3 and part 3/3 - load cycles 1 to 3

calibration of the vertical compliance, which seemed to be primarily due to the use of filter papers. Accordingly, test 12 was performed without using filter papers. To prevent loss of soil through the top-cap drainage hole, a porous stone was used above the specimen, as shown in Figure 6.6b. Although no filter papers were used, the three-part methodology given above was still followed, although the purpose of part 1 was purely to determine the calibration curve, whereas in tests 9 to 11, part 1 served also as a pre-loading stage to change the subsequent mechanical response of the filter papers.

The results for part 1 (determine calibration) of sand test 12 are given in Figure 6.33. The residual displacement following cycle 1 is approximately an order of magnitude lower than the residual displacement following cycle 1 in test 9 part 1 (Figure 6.28). The isolated response for cycle 2 and 3 is shown in Figure 6.34.

The part 2 (main soil test) data are given in Figure 6.35. This time, the corrected data appear more reasonable. The reloading response is initially flat, rather than expansive as in test 9. The unloading response is still initially slightly contractive for the first two cycles, but the third cycle unloading is expansive only.

The part 1 and part 3 data are plotted together in Figure 6.36. The part 3 data look different because a number of intermediate loading and unloading cycles were performed (following the part 2 test path). However, overall the response is similar for both tests, in terms of the shape of the initial loading path, the total displacement, the shape of the unloading path, and the residual displacement. This suggests that the compliance response is repeatable, at least under the tested conditions, and that a calibration based on this response would be accurate.

It is worth repeating at this point that there were a number of limitations to these tests. These limitations do not mean these tests were not useful - far from it. These tests were valuable, and

images/sand/sand_12_p1_full.pdf

Figure 6.33: Sand test 12 - part 1/3 (determine calibration) - load cycles 1 to 3

images/sand/sand_12_p1_cycle_2.pdf

Figure 6.34: Sand test 12 - part 1/3 (determine calibration) - load cycles 2 and 3

images/sand/sand_12_D_P.pdf

Figure 6.35: Sand test 12 - part 2/3 (main soil test) - displacement vs pressure

images/sand/sand_12_p3.pdf

Figure 6.36: Sand test 12 - comparison between part 1/3 and part 3/3 - load cycles 1 to 3

vital to the development of the equipment, particularly the development of a repeatable, accurate calibration methodology. However, as observations of soil behaviour, they are lacking. The first issue was the difficulty of controlling the relative density of the sand. The relative density D_r affects the behaviour of the sand in response to loading or heating. The initial value of D_r varied between 6 (very loose), and 51 (medium dense). The method used for installing the sand into the confining ring was the same for all tests (except test 5, under dry conditions). It is possible that this discrepancy was due to measurement errors, rather than a true difference in the soil condition. Since it was quite easy to accurately measure the specimen mass, it is probable that the error was in measurement of the specimen height.

The second issue was in the application of the calibrations. The calibrations used for tests 1 to 8 - combined thermal and mechanical based on calibration test 1A, and ambient-temperature mechanical based on calibration test TC:2 - were based on similar specimen set-up and test paths. However, the accuracy of the calibration appears to depend on a calibration test that uses (as far as possible) the exact same specimen set-up and test path as used in the actual soil test.

Finally, with the exception of test 12, all tests were performed using filter papers. The inclusion of filter papers has a clear effect on the repeatability of calibration test results.

6.6 Summary

A series of twelve tests were carried out on sand, mainly using the temperature-controlled oedometer. The aim of these tests was to improve and validate the testing methodology, particularly the calibration procedure. Loading tests showed that the combined temperature and pressure calibration based on calibration test 1A, derived in Section 4.4 was not accurate, and overestimated the compliance at ambient temperature. The corrected data showed expansion initially upon reloading of sand below the maximum applied pressure, and contraction initially upon unloading of sand at the maximum applied pressure, which made clear that the calibration was not correct. The ambient-temperature mechanical calibration derived from calibration test TC:2 in Section 4.5 was found to be more accurate than the combined calibration, but cannot account for vertical thermal compliance.

The thermal and mechanical response of sand was investigated, and results were corrected by accounting for vertical thermal compliance as well as accounting for the lateral expansion of the confining ring during heating. Mechanical cycling and thermal cycling were both observed to cause ratcheting behaviour, where repeated cycling led to an increase in the permanent contractive strain. The magnitude of this strain was greater for mechanical cycling than thermal cycling, for the pressure and temperature ranges tested. Initial heating of sand at the maximum applied pressure was found to cause expansive strain, at both pressure values tested, which contrasts with the contractive strain observed in the literature. However, subsequent observed responses to thermal cycling agree with the literature.

A proposed three-part testing methodology was trialled. In part 1 of this methodology, a unique calibration for the test is obtained. When using filter papers, this part is also required for pre-loading the filter papers. The calibration derived from the part 1 data is used to correct the raw data from the main soil test (part 2). The third and final part is a repeat of part 1, performed to check the reliability of the part 1 data. These tests made clear that there was no way to avoid the issues stemming from the use of filter papers, which are highly compressible, undergo permanent residual displacement following the initial load/unload cycle, and show

hysteresis along subsequent load/unload paths, as well as along heat/cool paths. The three-part test was repeated, this time without any filter papers, and found to give satisfactory results. This methodology was developed further into the final methodology used for the tests on KSS, discussed in the next chapter.

Chapter 7

Thermal tests on KSS - methodology

7.1 Data processing

7.1.1 Introduction

In this section, the data processing methodology is explained.

Almost all of the data processing was done using Microsoft Visual Basic for Applications (VBA) version 7.1. The output from TRIAX is a generic data file (.dat) with delimiter-separated values (DSV) - either comma-separated values (CSV) or tab-separated values (TSV). Initially (i.e. at the start of the research), post-processing was done in Microsoft Excel, using worksheet functions. However, this was too time-consuming, both to set up the functions, and to run the analysis. Processing the data with Visual Basic (or an equivalent programming language such as MATLAB or Python) has a number of definite advantages. It is easier, faster (to set up, and to run), and less error-prone. It enables complex calculations to be checked more easily (by the original author of the code, or by others), corrections and additions can be applied to old data by re-running the updated code, and the format of the graphical output can be standardised for consistency.

Calculation of the yield point for reloading tests, and calculation of the t_{50} consolidation values, was done using MATLAB.

Values are split into two main groups, which can be split further. The first group is the measured values. These are single values that are measured before or after the test, and values recorded by the equipment instrumentation at each recording interval. Assumed values, based on others' measurements (i.e. literature review) are included in this group. The second group is the calculated values. These are the values calculated for every row of output data (or in some cases, for a subset of the output data), based on a combination of the measured values, and the output data.

7.1.2 Measured values

The measured values can be further split into two groups: initial/final specimen measurements, and equipment instrumentation measurements during testing. In addition, some values were previously measured, prior to testing, or assumed, based on the literature review. Assumed values are included here because they could be measured in the same way as the other measured values, although the process would be more involved and time-consuming.

The initial measured values were: specimen diameter d_0 , specimen height H_0 , total mass m_0 , and water content (from trimmings) w_0 . The final measured values were: total mass m_f , mass of solids m_s and water content w_f . This information is summarised in Table 7.1. Note that water content is technically a calculated value, but it makes sense to include it here.

Table 7.1: Initial/final specimen measurements

Measured values	Symbol	Units
Initial diameter	d_0	mm
Initial height	H_0	mm
Initial total mass	m_0	g
Initial water content from trimmings	w_0	[-] or %
Final total mass	m_f	g
Mass of solids	m_s	g
Final water content	w_f	[-] or %

The values measured by the equipment instrumentation during testing were: time t , load F , temperature T , and displacement D_1, D_2 and D_3 , as summarised in Table 7.2.

Table 7.2: Equipment instrumentation measurements

Measured values	Symbol	Units
Time	t	min
Load	F	N
Temperature	T	°C
Displacement $\times 3$	D_1, D_2, D_3	mm

The previously-measured/assumed values were: specific gravity of solids G_s , volumetric thermal expansion of solids α_v , and Poisson's ratio ν . The equations used to calculate temperature-dependent density of water ρ_w and dynamic viscosity of water μ_w were based on tabulated literature values for both, over the tested range of temperatures.

Details of how these measured values were obtained is given in Section 7.2. From these values, all the values calculated below were obtained.

7.1.3 Calculated values

The calculated values are based on the measured values from the previous section. In TRIAX, recording increments of 1 min were used. This results in 10 080 rows of data for a test duration of 1 week. The average duration of the KSS tests was 2 weeks, and the bentonite tests were considerably longer. This generates quite a lot of data, and the requirement for automation of the calculations should be clear.

A summary of the key calculated values is given in Table 7.3.

Table 7.3: Calculated values

Calculated values	Symbol	Units
Time (zeroed)	t_0	h or days
Pressure	P	kPa
Total displacement	D_0	mm
Incremental displacement	D_{inc}	mm
Height	H	mm
Volume	V	mm ³
Total strain	$\epsilon_{v,total}$	[-] or %
Incremental strain	$\epsilon_{v,inc}$	[-] or %
Sub-incremental strain	$\epsilon_{v,sub-inc}$	[-] or %
Thermal strain	$\epsilon_{thermal}$	[-] or %
Mechanical strain	$\epsilon_{mechanical}$	[-] or %
Vertical compliance amount	$D_{comp,vert}$	mm
Lateral compliance amount	$\Delta H_{comp,lat}$	mm
Rate of change of volume	dV/dt	mm ³ h ⁻¹
Rate of change of total strain	$d\epsilon_{v,total}/dt$	h ⁻¹
Void ratio	e	[-]
Normalised void ratio	e_{norm}	[-]
Coefficient of volume compressibility	m_v	m ² kN ⁻¹
Coefficient of consolidation	c_v	mm ² h ⁻¹
Density of water	ρ_w	kg m ⁻³
Dynamic viscosity of water	μ_w	kg m ⁻¹ s ⁻¹
Coefficient of permeability	k	m s ⁻¹
Intrinsic permeability	K_{int}	m ²
Time for 50% consolidation	t_{50}	h

Test meta-data

As well as the equipment instrumentation data (time t , load F , temperature T , displacement D_1 , D_2 and D_3), some test meta-data are required. Together with the measured values, this information is stored in an Excel workbook, which can be accessed via the VBA script.

The points at which the LVDTs were reset are defined. The LVDTs must be reset during testing because the total displacement exceeds the maximum travel of the LVDTs (10 mm). The end of each increment is also defined. These could be loading/unloading increments (e.g. loading from 10 kPa to 25 kPa), heating/cooling increments (e.g. heating from 60 °C to 70 °C), or hold stages, where current conditions are maintained.

The start of the testing increment of interest is defined. If the incremental, or sub-incremental, strain for a heating path is required, then the start of the increment is set to the start of the heating path.

The calibration type, and fitting parameters are defined. For example, for the KSS tests, a 2nd order polynomial fit was used for the calibration. In this case, the calibration type would be 2nd order polynomial (or Poly2), and three fitting parameters are required - the coefficients for the three terms in the polynomial equation. The calibration type is used as a label, so that several calibrations can be defined in the workbook. For the KSS tests, each test has a unique set of calibration equations, based on an individual calibration test, as discussed in Section 8.4.

Other information stored in the test meta-data includes the test date, name and type. The test date and name can be included in the title of the graphical output. The test type is used to differentiate between certain tests which require different calculation methods. For example, a slightly different calculation method is used for the tests carried out with the ambient-temperature oedometer (ML-OED) prior to installation of the three-LVDT instrumentation plate.

Time

The measured time value, in minutes, is initialised to zero at the start of the testing increment. Output is given in hours or days.

Pressure

The pressure, or vertical stress, is calculated based on the measured load (axial force) value from the load cell, and the initial specimen diameter:

$$P = \frac{F}{A} \cdot 1000 \quad (7.1)$$

where:

P = pressure [kPa]

F = axial force [N]

A = initial specimen cross-sectional area [mm²]

Note that when calculating pressure, the cross-sectional area is not adjusted for temperature, as it is in some later calculations. The specimen cross-sectional area will be minimum at the

minimum tested temperature, 5 °C and maximum at the maximum tested temperature, 70 °C. Over the full temperature range, the *change* in internal diameter of the stainless-steel confining ring is 0.08 mm (for $\alpha_{L,CR} = 17 \times 10^{-6} \text{ }^\circ\text{C}^{-1}$). This diameter increase corresponds to a reduction in pressure of 0.12 %, for heating under a constant axial force. At the maximum tested pressure of 2400 kPa, this gives a maximum error of <3 kPa, which is considered negligible.

Displacement

The measured displacement from the three LVDTs is used to calculate the average displacement. Two calculated displacement values are defined: total displacement, and incremental displacement. The total displacement is initialised to zero at the start of the test. The incremental displacement is initialised to zero at the start of the test increment. This is shown schematically in Figure 7.1. The total displacement, total strain, and void ratio are measured from the start of the test. The incremental displacement and sub-incremental strain are measured from the start of the increment. The normalised void ratio is normalised by the initial void ratio, which can either be the initial void ratio from the start of the test, or from the start of the increment. Whenever results are given in terms of normalised void ratio in Chapter 8, this has been indicated on the graph axis and in the discussion. The incremental strain is the incremental volume change relative to the initial volume at the start of the test.

First, the individual measured displacements are initialised to zero at the start of the test. The calculated value takes into account any resetting of the LVDTs during testing. The average of the three values is taken, giving the total displacement. The total displacement is corrected for equipment vertical compliance, as discussed below. Then the total displacement is initialised to zero at the start of the test increment, giving the incremental displacement.

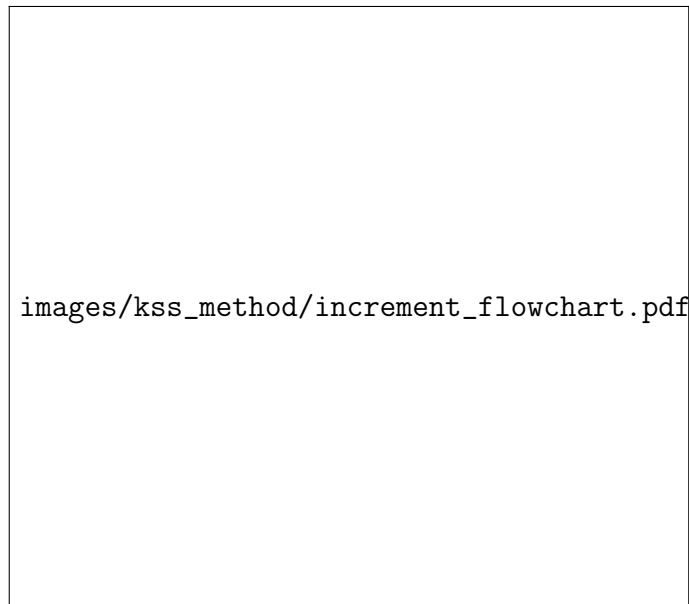


Figure 7.1: Schematic showing calculation of total and incremental values

Compliance & Height

The total displacement must be corrected for equipment vertical compliance.

The fitting parameters for the unique compliance equations for each test are defined together with the rest of the test meta-data. The correction amount is calculated by substituting the current temperature and pressure value into the compliance equation. Then the corrected total displacement is calculated by subtracting the equipment compliance from the total measured displacement.

$$D_{corrected} = D_{raw} - D_{compliance} \quad (7.2)$$

where:

$$\begin{aligned} D_{corrected} &= \text{displacement corrected for vertical compliance [mm]} \\ D_{raw} &= \text{total measured displacement [mm]} \\ D_{compliance} &= \text{displacement due to equipment compliance [mm]} \end{aligned}$$

The specimen height is then calculated from the initial measured specimen height and the corrected total displacement, as follows:

$$H = H_0 - D_{corrected} \quad (7.3)$$

where:

$$\begin{aligned} H &= \text{specimen height [mm]} \\ H_0 &= \text{initial specimen height [mm]} \\ D_{corrected} &= \text{displacement corrected for vertical compliance [mm]} \end{aligned}$$

Next, the specimen height must be corrected for the differential lateral expansion of the confining ring and soil. The effect of the Poisson's ratio of the soil is included in this correction. The full calculation for this correction is given in Section 4.6.

$$H_{corrected} = H + \Delta H \quad (7.4)$$

where:

$$\begin{aligned} H_{corrected} &= \text{specimen height, corrected for confining ring expansion [mm]} \\ H &= \text{specimen height [mm]} \\ \Delta H &= \text{change in height due to confining ring expansion [mm]} \end{aligned}$$

Note that $H_{corrected}$ is actually corrected for both vertical compliance and confining ring expansion, although the calculation can be performed for any combination of vertical compliance on/off and confining ring expansion on/off, for comparative purposes. The absolute magnitude of each correction, $D_{compliance}$ in Equation 7.2 and ΔH in Equation 7.4 are given as outputs from the VBA code.

The calibration process is shown schematically in Figure 7.2. The vertical compliance is applied first, to the displacement value, which is then used to calculate the specimen height. The lateral compliance is then applied to this height term, to get the specimen height corrected for both vertical and lateral compliance.

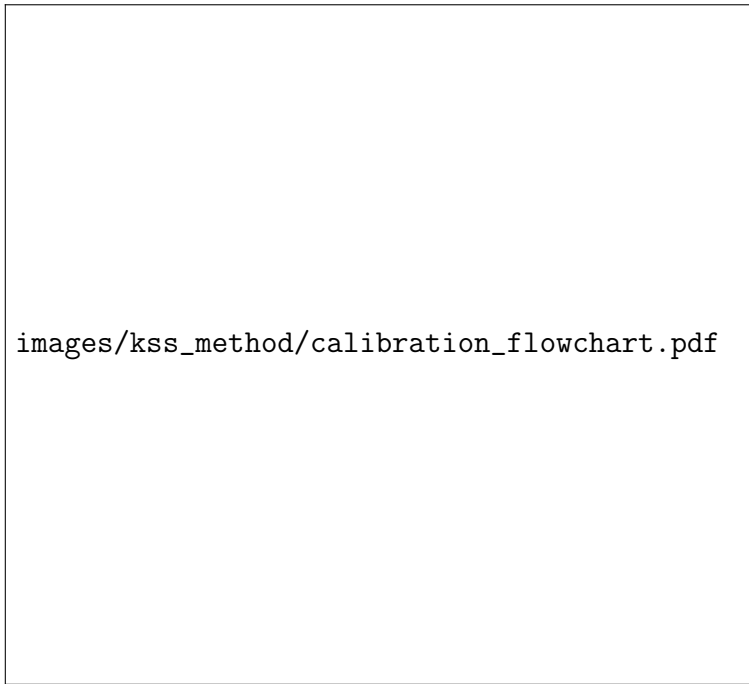


Figure 7.2: Schematic showing calibration process

Volume

The specimen volume is calculated from the corrected specimen height and the specimen cross-sectional area.

The cross-sectional area is calculated taking into account the theoretical lateral thermal expansion of the specimen under unconfined conditions. Although correcting the cross-sectional area for temperature has a negligible effect on the calculated pressure, as discussed above, this is not the case for the calculated volume. The lateral thermal expansion of the confining ring is not considered in this calculation because the effect of the differential expansion of the confining ring and soil is already accounted for in the corrected specimen height. The specimen diameter, accounting for change in temperature, is given by:

$$d = d_0 \cdot (1 + \alpha_{L,solids} \cdot \Delta T) \quad (7.5)$$

- d = specimen diameter, unconfined conditions [mm]
- d_0 = initial specimen diameter [mm]
- $\alpha_{L,solids}$ = linear thermal expansion coefficient of soil solids [$^{\circ}\text{C}^{-1}$]
- ΔT = change in temperature [$^{\circ}\text{C}$]

Note that the linear thermal expansion coefficient of the soil solids $\alpha_{L,solids}$, can be calculated from the volumetric thermal expansion coefficient of the soil solids $\alpha_{v,solids}$, assuming isotropic thermal properties. Alternatively, for a clay, if the linear thermal expansion coefficient parallel ($\alpha_{L\parallel}$) and perpendicular ($\alpha_{L\perp}$) to the clay layers is known, then $\alpha_{L\parallel}$ can be used to give $\alpha_{L,solids}$ in the radial direction. For the results presented in this thesis, isotropic thermal properties have been assumed, and $\alpha_{L,solids}$ is calculated using the equation below:

$$\alpha_L = \frac{1}{3} \times \alpha_v \quad (7.6)$$

The specimen cross-sectional area A is then calculated as follows:

$$A = \pi \cdot \frac{d^2}{4} \quad (7.7)$$

The specimen volume V can then be calculated, using the corrected specimen height:

$$V = H \cdot A \quad (7.8)$$

Strain

The total, incremental and sub-incremental strains are calculated from the specimen volume. The components of the thermally-induced strain - purely thermal, and mechanical - can also be calculated. Strain terminology, definitions and calculations are given in Section 4.6.1.

Rate of change of volume and total strain is calculated by using a 20 min sampling interval of the volume and strain values. Shorter intervals give output data that are too jagged.

Void ratio

The void ratio is calculated from the specimen volume, initial cross-sectional area and initial height of solids. This calculation is given in Section 4.7. As part of this calculation, the volume of voids V_v and volume of solids V_s are calculated.

Consolidation parameters

Calculation of the consolidation parameters: coefficient of volume compressibility m_v , and coefficient of consolidation c_v , is a multi-stage process. First, the raw data are analysed, and the calculations above are performed. The output data are then sampled at the end of each increment, based on the increments defined in the test meta-data.

The coefficient of volume compressibility m_v can be calculated from the sampled end-of-increment data.

$$m_v = \frac{\Delta V}{V_0} \cdot \frac{1}{\Delta P} \quad (7.9)$$

where:

m_v = coefficient of volume compressibility [$\text{m}^2 \text{kN}^{-1}$]

ΔV = change in volume over increment [mm^3]

V_0 = volume at start of increment [mm^3]

ΔP = change in pressure over increment [kPa]

To calculate the coefficient of consolidation c_v , the time to 50% degree of consolidation t_{50} must first be calculated for each increment. This can be done graphically, using the log-time method. This graphical method can be automated by fitting a polynomial to the sampled end-of-increment data, and differentiating to obtain the t_{100} point (and t_{50}), in the same way that the yield point

is calculated for the KSS tests (Section 8.5.1). The coefficient of consolidation can then be calculated as follows:

$$c_v = \frac{T_{50}}{t_{50}} \cdot l_{DP}^2 \quad (7.10)$$

where:

- c_v = coefficient of consolidation [$\text{mm}^2 \text{h}^{-1}$]
- T_{50} = time factor [-]
- t_{50} = time for 50 % consolidation [h]
- l_{DP} = length of drainage path [mm]

For a degree of consolidation of 50 %, the time factor $T_{50} = 0.197$. For two-way drainage, the drainage path length l_{DP} is half the average specimen height over the increment considered.

$$l_{DP} = \frac{H}{2} \quad (7.11)$$

Hydraulic properties

The hydraulic properties, coefficient of permeability (hydraulic conductivity) k , and intrinsic permeability K_{int} were calculated next.

The coefficient of permeability was calculated from the previously calculated consolidation parameters m_v and c_v , and the bulk unit weight of water:

$$k = m_v \cdot c_v \cdot \gamma_w \quad (7.12)$$

where:

- k = coefficient of permeability, aka hydraulic conductivity [m s^{-1}]
- m_v = coefficient of volume compressibility [$\text{m}^2 \text{kN}^{-1}$]
- c_v = coefficient of consolidation [$\text{m}^2 \text{s}^{-1}$]
- γ_w = bulk unit weight of the pore-water [kN m^{-3}]

Note that c_v is given here in units of $\text{m}^2 \text{s}^{-1}$ for consistency with the other parameters. Bulk unit weight of the pore-water is calculated as a function of temperature. The change in density of water (from which bulk unit weight is calculated) with temperature is shown in Figure 7.3, using data from Batchelor (2000) and Cengel et al. (2016).

The intrinsic permeability K_{int} , is calculated from the coefficient of permeability, taking into account the dynamic viscosity of the pore-water μ_w :

$$K_{int} = k \cdot \frac{\mu_w}{\gamma_w} \quad (7.13)$$

Both μ_w and γ_w are calculated as functions of temperature. The change in dynamic viscosity of water with temperature is shown in Figure 7.4, using data from Batchelor (2000) and Cengel et al. (2016).

images/kss_method/water_density.pdf

Figure 7.3: Density of water as a function of temperature (Batchelor, 2000; Cengel et al., 2016)

images/kss_method/water_dynamic_viscosity.pdf

Figure 7.4: Dynamic viscosity of water as a function of temperature (Batchelor, 2000; Cengel et al., 2016)

Since the γ_w terms cancel out, this equation reduces to:

$$K_{int} = m_v \cdot c_v \cdot \mu_w \quad (7.14)$$

where:

- K_{int} = intrinsic permeability [m^2]
- m_v = coefficient of volume compressibility [$\text{m}^2 \text{kN}^{-1}$]
- c_v = coefficient of consolidation [$\text{m}^2 \text{s}^{-1}$]
- μ_w = dynamic viscosity of pore-water [kPa s]

7.2 Testing

7.2.1 Introduction

The testing methodology given below has been developed based on the experience gained from the tests carried out on bentonite (Chapter 5) and sand (Chapter 6), and was used for the tests on KSS (Chapter 8). This methodology is for carrying out temperature-controlled tests with clay, using the temperature-controlled oedometer.

7.2.2 Pre-test

Several tasks should be carried out prior to testing. These are as follows:

- Mix and store the soil
- Calibrate the instrumentation at ambient temperature
- Write and check the test program in TRIAX

At least a week before testing, mix the soil and store in an air-tight container, away from sources of heat or light.

The instrumentation must be calibrated at ambient temperature. This calibration is separate from the calibration discussed in Section 8.4, which measures the equipment thermal and mechanical compliance. In this calibration, the output of the instrumentation in V (the measured value) is compared against known values (e.g. known forces, or known displacements).

The load cell was calibrated using a dead-weight load calibrator. A step-by-step calibration methodology is given in Appendix A. The load cell capacity is 10 kN which corresponds to a maximum pressure of 2600 kPa for a 70 mm diameter specimen.

The displacement transducers (LVDTs) were calibrated using a micrometer. A step-by-step calibration methodology is given in Appendix B. The LVDTs have a range of ± 5 mm (travel of 10 mm), and are orientated such that increasing displacement corresponds to compression of the specimen.

The temperature sensors were not independently calibrated. Instead, a two-point, linear calibration was used, based on the manufacturer's specifications. Between the two extreme values, 0 °C and 100 °C, the sensor output is assumed to increase linearly. This assumption is valid for the

integrated circuit (IC) type temperature sensors used in the temperature-controlled oedometer. Even if the sensors were independently calibrated, the regression type used would be linear. Since the assumed calibration is also linear, there may be a small error in the absolute temperature values, but relative values (temperature changes) will be as accurate as for an independent calibration.

The final important step prior to testing is to write the TRIAX program for the test. The program can be written in plain text, then loaded to the PC running TRIAX. For the same reasons given in Section 7.1 for using VBA rather than Excel worksheet functions (ease, speed, error-reduction, and error-checking), it is considered good practice to write the TRIAX stages in plain text, rather than use the TRIAX GUI (wizard), which is time-consuming and error-prone. Further details of how to write TRIAX stages are given in Appendix K.

7.2.3 Test methodology

A methodology was developed for setting up, running, and finishing tests with the TC oedometer (and similarly for the ambient-temperature oedometer, although not included here). A standard results sheet was developed, for recording the test details, initial and final measurements, and observations.

The testing methodology is split into the following sections:

- Setting up and starting the test:
 - Installing the specimen into the confining ring
 - Measuring the specimen height and mass
 - Installing the confining ring into the oedometer
 - Setting the test initial condition
 - Instrumentation installation and initialisation
- Running the test:
 - Resetting the LVDTs during the test
 - Checking the water level
 - Operating the chiller
- Finishing the test:
 - Removing the specimen and taking final measurements

There is also a section dealing with calibration tests (equipment thermal and mechanical compliance).

In each section, the equipment required is listed. Only tools are listed, not the removable components of the equipment, such as the porous stones, top-cap, LVDT components, confining ring, confining ring collar and holding-down bolts. Additionally, an electronic balance is required for taking mass measurements, and a drying oven for drying the specimen following completion of the test.

The key equipment required in most parts of the testing methodology is shown in Figure 7.5. The numbered items are listed in the box below.

Key equipment required (Figure 7.5):

1. Small plastic card for cleaning soil from the confining ring
2. 2× small plastic cards, used when installing the specimen
3. Bull’s-eye type spirit level
4. High-vacuum silicone grease
5. 5 mm ball-end hex key screwdriver
6. Large flat-blade screwdriver (≈ 8 mm tip)
7. Small flat-blade screwdriver (≈ 2 mm tip)
8. 150 mm steel ruler
9. 2× 80 mm diameter moisture-content tins with lids
10. 2× teaspoons

7.2.4 Setting up the test

Installing the specimen into the confining ring

Equipment required:

- small plastic cards
- 150 mm steel ruler
- 2× teaspoons
- high-vacuum silicone grease
- bull’s-eye type spirit level
- moisture content tin (for initial water content from trimmings)

1. Ensure all test equipment is thoroughly cleaned prior to testing.
2. Saturate the porous stones by placing them in a dish of purified water in a 20 mmHg vacuum for at least 20 min.
3. Lubricate the inner surface of the confining ring, confining ring collar, and the top-cap o-ring, by lightly coating with grease.
4. Measure the initial equipment masses and dimensions given in Table 7.4. Most of these values do not need to be re-measured for each test, and can be considered constants. The exception is the mass of the saturated porous stones, which is more variable. For the KSS tests, using the same two porous stones, the mass varied by 0.48 g between tests. Compared to the average initial specimen mass of 337 g, this error is small.
5. Place the 150 mm steel ruler on a clean, flat, work surface, with two plastic cards (or similar) of the same thickness as the ruler on either side (Figure 7.6a).

images/kss_method/photo_kss_equipment_all.pdf

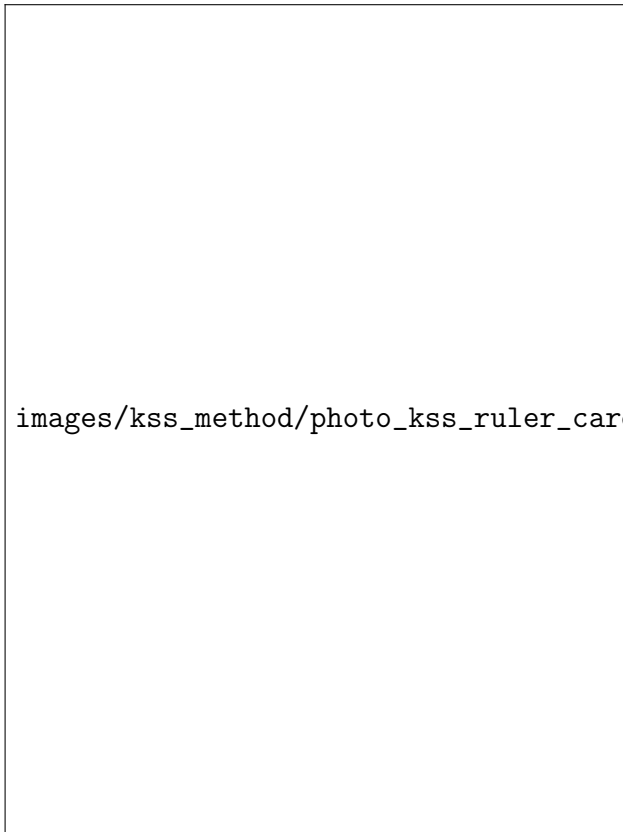
Figure 7.5: Equipment required for setting up, running, and finishing the test

Table 7.4: Equipment measurements

Measured values	Type	Units
Confining ring - internal diameter	dim	mm
Confining ring - height	dim	mm
Confining ring - mass	mass	g
Porous stones - combined thickness	dim	mm
Saturated porous stones - mass	mass	g
Steel ruler - mass	mass	g

The ruler is required for lifting the confining ring and installed specimen, for weighing, and installing into the confining ring. The plastic cards either side of the ruler are required to maintain a flat, stable, surface for the lower porous stone to rest upon. Without the cards in place, the lower porous stone tends to tilt to one side of the ruler.

6. Place the lower porous stone onto the centre of the ruler, so that it is supported on either side by the two cards (Figure 7.6b).
7. Push down the confining ring over the porous stone (Figure 7.6c).
8. Use the teaspoons to place the clay slurry into the confining ring. Start from the edges, going round with a circular motion, to push the slurry right into the bottom corner (Figure 7.7a). Do not mix, as this may introduce air bubbles into the slurry. Add the slurry one spoonful at a time. As the height approaches the target height, begin to level the surface using a small plastic card. Work from the centre outwards, applying as little pressure as possible (Figure 7.7b). This is shown schematically in Figure 7.8a and 7.8b.
9. Once the target height is reached, and the surface is flat, use the plastic card, then a tissue, to scrape the excess soil from the inner surface of the confining ring above the level surface of the soil. Avoid disturbing the surface of the soil while removing the excess. Re-check the soil height. Re-apply grease to the cleaned inner surface of the confining ring above the soil (Figure 7.7c). This is shown schematically in Figure 7.8c and 7.8d.
10. Position the upper porous stone above the top of the confining ring, then allow it to gently drop down onto the soil surface. By holding the upper porous stone with the fingernails of one hand, it is possible to position it almost completely within the confining ring before allowing it to drop.
11. Place a small bull's-eye type spirit level on the upper porous stone, and check that it is level. If adjustment is required, gently press down at the edge of the upper porous stone until it is level (Figure 7.7d).
12. Take an additional sample of the slurry, and measure the initial water content.



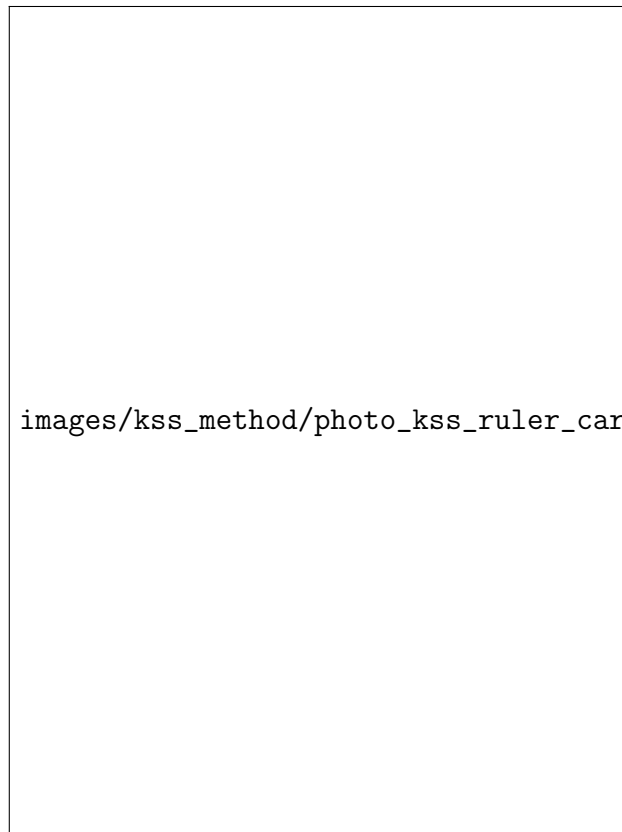
images/kss_method/photo_kss_ruler_card.JPG

(a)



images/kss_method/photo_kss_ruler_card_PS.JPG

(b)



images/kss_method/photo_kss_ruler_card_PS_CR.JPG

(c)

Figure 7.6: Installing the specimen into the confining ring: (a) stage 5 (b) stage 6 (c) stage 7

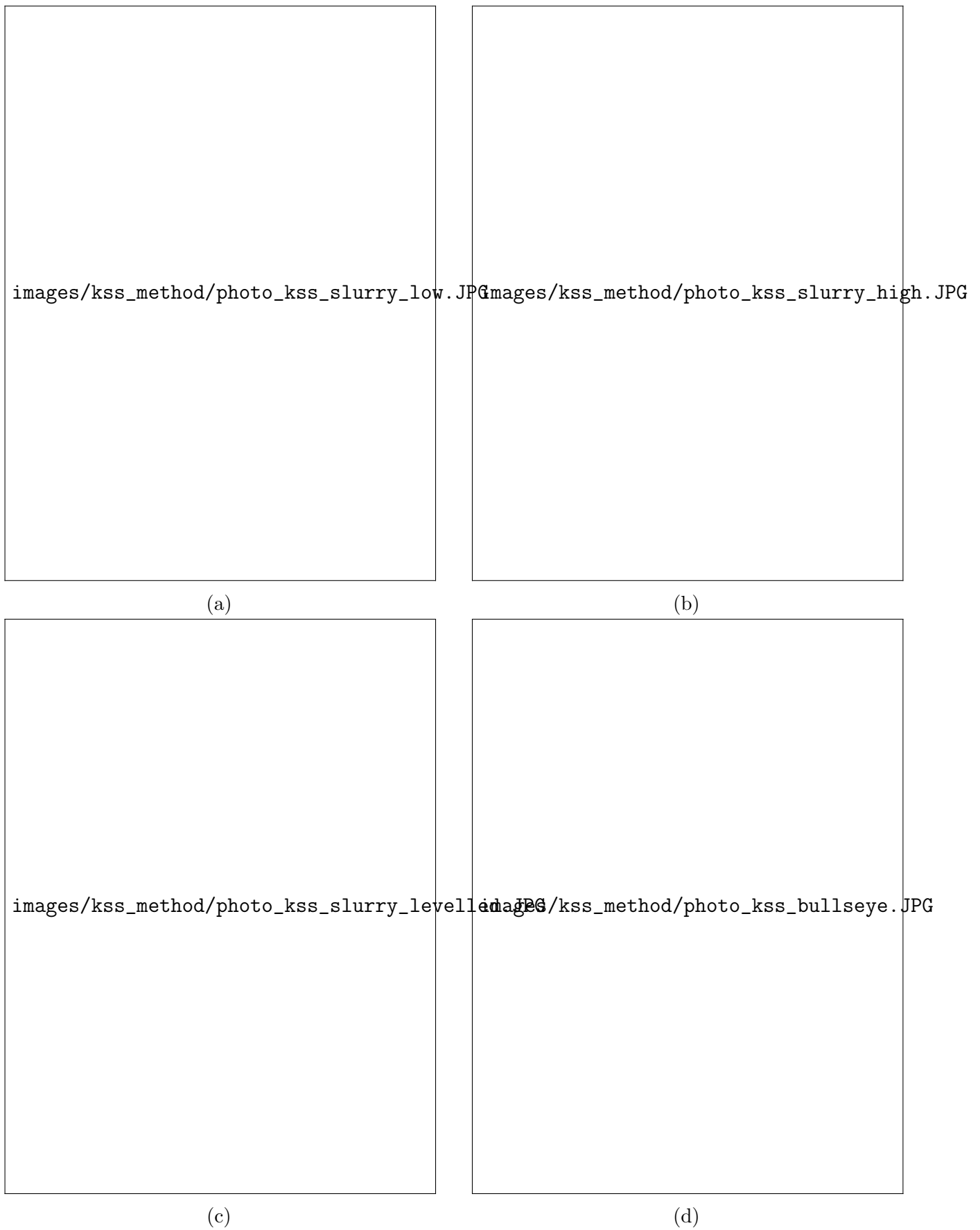


Figure 7.7: Installing the specimen into the confining ring: (a & b) installing the slurry - stage 8 (c) levelling the slurry - stage 9 (d) installing the upper porous stone - stages 10 & 11

images/kss_method/install_specimen_1.jpg

(a)

images/kss_method/install_specimen_2.jpg

(b)

images/kss_method/install_specimen_3.jpg

(c)

images/kss_method/install_specimen_4.jpg

(d)

Figure 7.8: Installing the specimen into the confining ring - schematic sequence for stages 8 & 9

Measuring the specimen height and mass

Equipment required (Figure 7.9):

- metal bar with square cross-section
- digital calipers

1. Measure the thickness of the metal bar.
2. To measure the depth to the upper porous stone, place the metal bar across the top of the confining ring, so that it crosses with one edge directly across the centre of the specimen. This can be done by marking two points on opposite side of the confining ring and aligning the edge of the bar with them. Measure down, from the top of the bar, to the top of the upper porous stone, using digital calipers. Avoid pushing down on the upper porous stone (Figure 7.10). Subtract the thickness of the bar to get the depth to the upper porous stone from the top of the confining ring.
3. Measure the total mass of the confining ring, ruler, and installed specimen between saturated porous stones, as summarised in Table 7.5. Use the ruler to carefully lift the confining ring, without allowing the lower porous stone to drop.

images/kss_method/photo_kss_equipment_height.pdf

Figure 7.9: Equipment required for measuring the specimen height

images/kss_method/photo_kss_height.JPG

Figure 7.10: Measuring the specimen height

Table 7.5: Initial specimen measurements

Measured values	Type	Units
Thickness of metal bar	dim	mm
Depth to upper porous stone	dim	mm
CR + ruler + saturated PS + installed specimen	mass	g

Installing the confining ring into the oedometer

Equipment required:

- 5 mm ball-end hex key screwdriver

1. After measuring the total mass, install the specimen into the oedometer. Place into the oedometer, with the ruler below, then carefully slide the ruler sideways, until the confining ring and lower porous stone rest on the upper base-plate. The ruler is rigid enough for lifting the confining ring and specimen, but flexible and thin enough to slide out from beneath them without disturbing the specimen.
2. Screw down the confining ring collar, using the six holding-down bolts.

Setting the test initial condition

Equipment required (Figure 7.11):

- Brass housing and core piece for LVDT

1. First, determine the contact value for the top-cap LVDT. This is the displacement value that the LVDT within the top-cap housing reads when the top-cap is on a flat surface. Any one of the three LVDTs can be used for this, but the same one must be used for obtaining the contact value, and for setting the initial position (see below), so it is good practice to use the same one all the time. Therefore, only LVDT 2 was used, for all tests. For LVDTs calibrated in the range -5 mm to 5 mm , the contact value will be approximately -1.85 mm .
2. Screw the brass housing into one of the drainage holes in the top-cap, then place the top-cap on the work surface. Drop the LVDT core into the drainage hole, then place the LVDT into the housing. Read the LVDT 2 displacement value from the TRIAX Monitor, and record on the test sheet (photograph: Figure 7.12a, schematic: Figure 7.13a).
3. Remove the LVDT from the housing.
4. Screw the top-cap onto the end of the loading ram (counter-clockwise to tighten). Use the load-frame controls to load at 10 mm min^{-1} until within 10 mm of the upper porous stone. It is not possible to check this visually, and must be calculated. A 50 mm travel displacement transducer can be used to measure how far the top-cap has moved into the confining ring.

images/development/photo_IPS_gp_3.pdf

Figure 7.11: Equipment required for setting the test initial condition

5. Drop the LVDT core through the top-cap drainage hole, and install LVDT 2 into the housing. To keep the LVDT in position, place a small weight on top of the LVDT (photograph: Figure 7.12b, schematic: Figure 7.13b). In TRIAX, set the update times for Graph and Monitor to 2 s. Using the Graph and Monitor output, load at 5 mm min^{-1} until the displacement is -3 mm . Readings will first decrease, then at approximately -8 mm will begin to increase non-linearly until -5 mm , then linearly from -5 mm to -3 mm . Load at 1 mm min^{-1} until the displacement is -2 mm , then at 0.5 mm min^{-1} until the contact value is reached. The displacement output in TRIAX for this loading sequence is shown schematically in Figure 7.13c, and the initial test condition, with the top-cap just in contact with the upper porous stone is shown in Figure 7.13d.
6. Remove the LVDT, unscrew the housing, and remove the LVDT core.



(a)

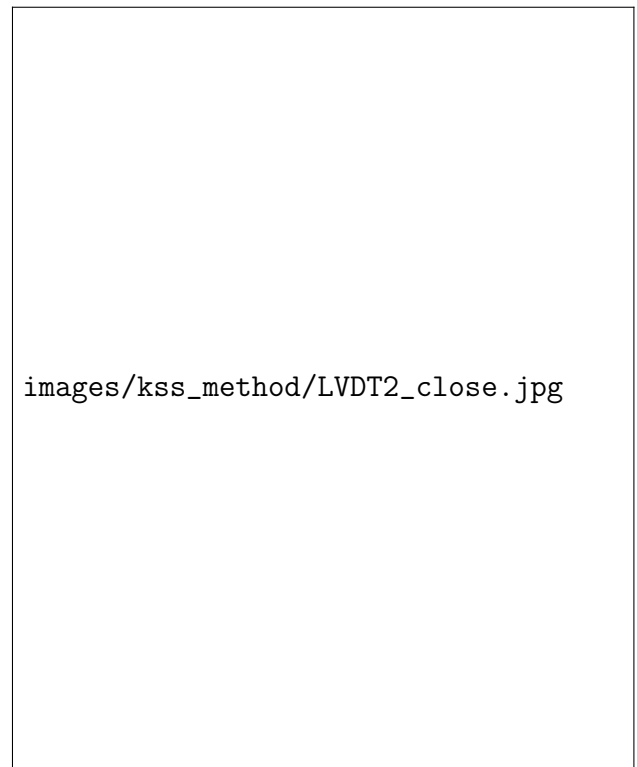


(b)

Figure 7.12: Setting the test initial condition: (a) determining LVDT contact value - stage 2
(b) loading until contact value reached - stage 5



(a)



(b)



(c)



(d)

Figure 7.13: Setting the test initial condition - schematics: (a) set-up (b) approaching contact with upper porous-stone (c) displacement response (d) initial test condition

Instrumentation installation and initialisation

Equipment required:

- large flat-blade screwdriver (≈ 8 mm tip)
- small flat-blade screwdriver (≈ 2 mm tip)

1. Install the LVDT extension pieces

- Drop the LVDT extension pieces through the holes in the instrumentation plate, through the heat dissipators and PVC lid. This needs to be done in this order because the heat dissipators will not fit through the holes in the instrumentation plate (Figure 7.14a).
- Fix the heat dissipators to the LVDT extension pieces, directly below the connection to the LVDT core, using the small screw on the side of the heat dissipator.

2. Install the LVDTs

- Sit the LVDTs in the brass housings on the instrumentation plate (Figure 7.14b).
- They can be fixed in place using the small screw on the side of the housing, but this is not necessary yet.

3. Fill the cell with purified reverse-osmosis (RO) water

- Check all base valves are closed, except specimen base drainage.
- Fill with a small amount of water, and visually check for any leaks.
- Fill to the marker on the inside of the cell (≈ 10 L).

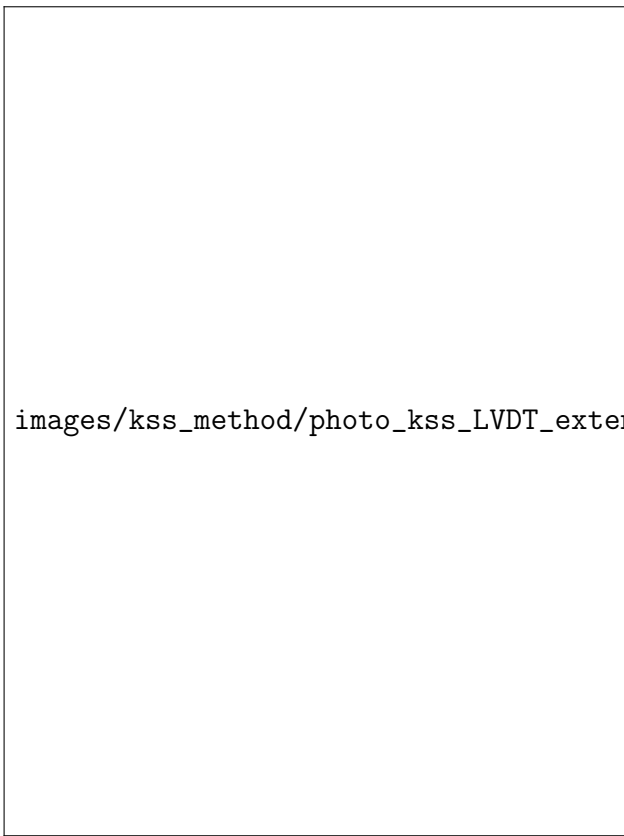
4. Cover the cell

- Install the two removable lid sections (Figure 7.14c).
- Loosen the screw holding up the central lid section so that it can move freely up and down along the loading ram (Figure 7.14d). The central lid section will remain free to move up and down throughout the test.

5. Set the initial LVDT values

- Adjust the position of the instrumentation plate so that the LVDTs values are close to the target value (coarse adjustment), then re-tighten the bolt holding the instrumentation plate to the loading ram (Figure 7.15a). For tests with initial consolidation stages, the target value will be -5 mm, which maximises the positive (contractive) travel.
- Adjust the individual position of the LVDTs by raising them within the LVDT housing, and tighten the small screw on the housing to fix this position (fine adjustment). Do not over-tighten the screw, as this may damage the LVDT (Figure 7.15b).
- Check that the LVDT extension pieces can still move freely through the central lid section

6. Check that the cooling fan is running



(a)



(b)



(c)



(d)

Figure 7.14: Instrumentation installation: (a) LVDT extension pieces and heat dissipators (b) LVDT in housing on instrumentation plate (c) removable outer lid sections in position (d) central lid section resting on outer lid sections and free to move relative to loading ram

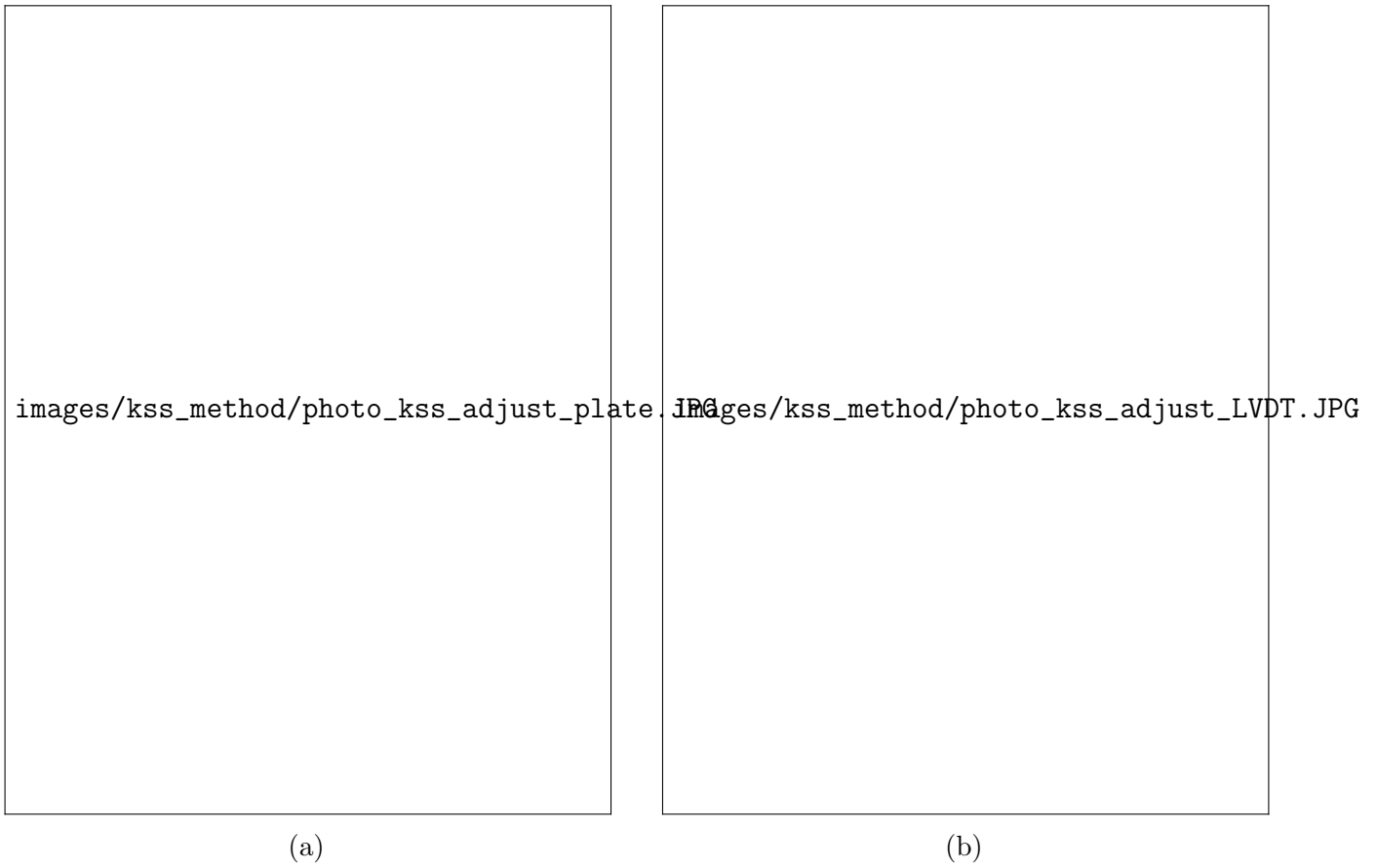


Figure 7.15: Instrumentation initialisation: (a) instrumentation plate - coarse adjustment
(b) LVDT housing - fine adjustment

7.2.5 Running the test

In TRIAX, begin Scanning and Control. Record the basic test information as comments in the output file. The first stage should always be the same initial condition: pressure to 2.5 kPa and temperature to 22.5 °C. Once pressure and temperature are stable at these values, reset the timer and begin the first consolidation stage.

Resetting the LVDTs during the test

Equipment required:

- large flat-blade screwdriver (≈ 8 mm tip)
- small flat-blade screwdriver (≈ 2 mm tip)

During the test, it may be necessary to reset the LVDT position. If the total displacement exceeds the travel of the LVDTs (10 mm), the displacement will be outside the linear, calibrated range of the LVDTs, and the results will be unreliable and potentially unusable. This is generally only an issue during consolidation of normally-consolidated soil, where displacements are much higher than for unloading, over-consolidated reloading, and thermal stages.

The best time to reset the LVDTs is near the end of an increment, after the displacement has stabilised. The displacement following the reset is assumed to be equal to the previous value, so any changes to the displacement that occur while the LVDTs are being reset will not be captured. If the displacement has already stabilised, any changes over the short time it takes to reset the LVDTs will be negligible. For this reason, the loading increments should be chosen such that the incremental displacement will be less than 10 mm, so the LVDTs do not need to be reset before the displacement has stabilised.

1. First, check that the LVDT displacement values are visible in the TRIAX Monitor window.
2. Record a comment in the TRIAX Scan window. This will make it much easier to find the reset point during post-processing. For example: “About to reset LVDTs. Stop Control. Stop Scanning.”
3. Stop TRIAX Control and Scanning. Control is stopped to prevent displacement changes while resetting the LVDTs. Scanning is stopped to prevent meaningless displacement values being written to the output while resetting the LVDTs.
4. Reset the LVDT positions by raising or lowering the instrumentation plate. Raising the plate will reduce the displacement, while lowering the plate will increase the displacement. Use the large screwdriver to adjust the position of the instrumentation plate (coarse adjustment), and then use the small screwdriver to adjust the individual position of the three LVDTs if necessary (fine adjustment). To maximise travel for further consolidation stages, set the LVDTs to almost their maximum negative value (-5 mm). Check the LVDT extension pieces can still move freely through the lid by lifting them and allowing them to drop.
5. Restart Control and Scanning, and record a comment, e.g. “LVDTs reset. Resume Control and Scanning.”

Checking the water level

The water level in the cell can be checked during the test by opening the upper base-plate drain, holding the silicone drainage tube above the cell lid, so that it fills to the same level as the cell. However, in long-term heating tests, such as KSS tests C1 and C2, there was no significant water loss, so it is not generally necessary to check the water level during testing, and probably best to avoid doing so because it may disturb the test.

Operating the chiller

General use of the chiller is covered in the manufacturer's user manual, but brief details are given here on how to use the chiller in the context of a temperature-controlled oedometer test. Currently, the chiller has to be manually controlled, rather than automatically through TRIAX.

To set a new temperature, first add a comment in TRIAX, so the start of the increment can be identified later during post-processing. Switch on the chiller, then set the target temperature manually on the chiller. Cooling with the chiller is much faster than natural cooling of the oedometer. If low permeability soil such as clay is being tested, thermal strains will exhibit a transient response, and the soil should be given time to reach equilibrium before applying further cooling. For the tests on KSS, cooling from 22.5 °C to 5 °C was performed in three increments, to temperatures of 15 °C, 10 °C and 5 °C, and the average displacement was allowed to stabilise before moving to the next increment. The final temperature of 5 °C was maintained overnight, before beginning the subsequent heating stage.

7.2.6 Finishing the test

To finish the test in TRIAX, first add a comment, e.g. "End test", then stop Scanning. This will make it clear when post-processing data that the file contains the full test data. Stop Control.

Removing the specimen and taking final measurements

Equipment required:

- 5 mm ball-end hex key screwdriver
- large flat-blade screwdriver (≈ 8 mm tip)
- small flat-blade screwdriver (≈ 2 mm tip)
- 2 × 80 mm diameter moisture-content tins with lids
- 10 L bucket

1. First, drain the water from the cell into a clean bucket, using the drainage valve in the upper base-plate. This water can be reused for future tests.
2. Use the load-frame controls to fully unload the load-frame.
3. Remove the top-cap by unscrewing in a clockwise direction. Then unscrew the six holding-down bolts and remove the confining ring collar.

4. Carefully lift the confining ring with the specimen inside, and measure the total mass. For tests with clay, the specimen and porous stones will not fall out during this process.
5. Place the confining ring over a cylinder with diameter greater than the internal diameter but less than the external diameter of the confining ring. An 80 mm diameter aluminium moisture-content tin was found to be suitable for this. Extrude the specimen by pushing down with both thumbs on the upper porous stone.
6. Lift off the upper porous stone from the extruded specimen. Then cover the specimen with another moisture-content tin, and carefully flip the tins, so that the specimen sits in the new tin, with the lower porous stone above. Lift off the lower porous stone, and store both porous stones in a moisture content tin with a lid. Weigh the extruded specimen, then the porous stones. The porous stones can be weighed together.
7. Dry the extruded specimen by heating in an oven at 105 °C for at least 24 h, then re-weigh.
8. Clean the porous stones by submerging in water and placing in a 20 mmHg vacuum for 20 min. This seems to draw out soil from the pores of the porous stone. Then use a small bristle brush (not a wire brush), under running water, to brush soil from the surface of the stone.

The measurements required for finishing the test are summarised in Table 7.6.

Table 7.6: Final specimen measurements

Measured values	Type	Units
CR + ruler + PS + specimen	mass	g
Porous stones	mass	g
Extruded specimen (immediately following test)	mass	g
Extruded specimen (following oven-drying)	mass	g

7.2.7 Calibration tests

It is recommended to perform an individual calibration test for each test (assuming each test has a different test path). Details of the calibration post-processing and application are given in Section 8.4.

The calibration test is performed using porous stones only, and no soil specimen. In general, the test methodology is the same as for a soil test, but much simpler. No initial or final measurements are required. The test initial position can be found by observing the load values in the TRIAX Monitor or Graph. There will be a much clearer increase in the load value once the top-cap is in contact with the upper porous stone than there is for a soil test.

The fundamental point is to set up and run the test in the same way as a soil test, except where this is not possible or practicable. The confining ring, collar, and top-cap o-ring should be greased, as in a soil test. The cell should be filled with water to the same level. The water should be circulated, as normal, and the fan should be running. There is no soil specimen present, which is the first, unavoidable, difference. The calibration tests for KSS were carried out with faster consolidation increments than the soil tests, which is considered an acceptable compromise, since any non-instantaneous load-induced deformation of the equipment (including the porous stones) is negligible. This speeds up the calibration tests considerably.

7.2.8 Summary

In this chapter, the methodology is presented for performing thermal and mechanical tests on clay, using the temperature-controlled oedometer. This is a new methodology, developed as part of the research. This includes both the testing methodology, and the methodology for processing the test data.

In the data processing methodology section, a list of measured and assumed values are given, followed by full details on how all calculated values are obtained from these values.

In the testing methodology section, a step-by-step explanation of how to set up, run, and finish a test is given, including when and exactly how to obtain all the required measurements.

This methodology was followed for the KSS tests discussed in the next chapter.

Chapter 8

Thermal tests on KSS - results and discussion

8.1 Introduction

In this chapter, thermal tests carried out on an artificial clay, KSS, are discussed. These tests were performed after the calibration tests described in Chapter 4, and the tests carried out on bentonite (Chapter 5) and sand (Chapter 6). They represent the highest-quality tests performed so far with the temperature-controlled oedometer.

The material description and preparation method is given in Section 8.2. An overview of the test programme is given in Section 8.3. The calibration methodology and results are given in Section 8.4. Soil test results are presented and discussed in Section 8.5, followed by a summary of the key results. The general testing and data-processing methodology is described in Chapter 7.

8.2 Material description

The soil used for the final series of tests was KSS, an artificial clay. KSS was one of the kaolin-based artificial soils developed at Imperial College London by Rossato et al. (1992), and used subsequently by Menkiti (1994) (hollow cylinder) and Martínez Calonge (2013) (temperature-controlled triaxial), among others.

The KSS was prepared as a slurry by mixing 50 % Speswhite kaolin clay, 25 % industrial quartz silt, and 25 % fine quartz sand (by dry weight) at a water content of $1.25 \times$ the liquid limit. The silt used was HPF-5, a fine, quartz silt. The sand used was Fuse sand, a fine, quartz sand, with a size range of 0.15 mm to 0.3 mm. A summary of the properties of KSS is given in Table 8.1. Values are from Rossato et al. (1992), except for the volumetric thermal expansion coefficient, which is discussed below.

The volumetric thermal expansion coefficient of the mineral solids was calculated from the thermal expansion coefficients of kaolin and quartz. For kaolin clay, α_v is given as $24.3 \times 10^{-6} \text{ }^\circ\text{C}^{-1}$ to $33.7 \times 10^{-6} \text{ }^\circ\text{C}^{-1}$ by McKinstry (1965), for a temperature range of 25 °C to 400 °C. This range is calculated from the linear thermal expansion coefficients: perpendicular to the clay layers, $\alpha_{L\perp} = (18.6 \pm 1.3) \times 10^{-6} \text{ }^\circ\text{C}^{-1}$; parallel to the clay layers, $\alpha_{L\parallel} = (5.2 \pm 1.7) \times 10^{-6} \text{ }^\circ\text{C}^{-1}$. A mid-range value of $29.0 \times 10^{-6} \text{ }^\circ\text{C}^{-1}$ was taken. For quartz, the primary component of the silt

and sand, α_v was taken as $27.0 \times 10^{-6} \text{ }^\circ\text{C}^{-1}$. This value is discussed in more detail in Section 6.2. The average thermal expansion coefficient for KSS, comprising 50 % kaolin clay, and 50 % quartz silt/sand is $28.0 \times 10^{-6} \text{ }^\circ\text{C}^{-1}$.

Table 8.1: Summary of physical properties of KSS clay

Property	Value
Clay content ($<2 \mu\text{m}$) [%]	43
Specific gravity, G_s [-]	2.63
Plastic limit [%]	17
Liquid limit [%]	35.5
Plasticity index [%]	18.5
Volumetric thermal expansion coefficient α_v [$^\circ\text{C}^{-1}$]	28.0×10^{-6}

8.3 Test overview

A total of eight tests were carried out on KSS. These tests are split into three test series: A, B and C. A summary of the tests is given in Table 8.2. All tests were performed using the temperature-controlled oedometer (TC-OED).

The aim of test series A was to investigate the effect of over-consolidation ratio on thermal volume change. In test A1, thermal cycles were applied to normally-consolidated KSS. In tests A2 and A3, thermal cycles were applied to over-consolidated KSS, at different OCR values.

The test path for tests A1-3 is given in Figure 8.1. All three tests begin with consolidation to 1500 kPa at $22.5 \text{ }^\circ\text{C}$ ($A \rightarrow B$). In test A1, this is followed by a thermal cycle at 1500 kPa, comprising heating from $22.5 \text{ }^\circ\text{C}$ to $70 \text{ }^\circ\text{C}$ ($B \rightarrow C$), cooling from $70 \text{ }^\circ\text{C}$ to $5 \text{ }^\circ\text{C}$ ($C \rightarrow D$), heating from $5 \text{ }^\circ\text{C}$ to $70 \text{ }^\circ\text{C}$ ($D \rightarrow C$), and finally cooling from $70 \text{ }^\circ\text{C}$ to $22.5 \text{ }^\circ\text{C}$ ($C \rightarrow B$). In test A2, following initial consolidation, the specimen is unloaded to 300 kPa, and an OCR of 5 ($B \rightarrow E$), at which pressure the same thermal cycle is applied ($E \rightarrow F \rightarrow G \rightarrow F \rightarrow E$). In test A3, following initial consolidation, the specimen is unloaded to 50 kPa, and an OCR of 30 ($B \rightarrow H$) at which pressure the same thermal cycle is applied ($H \rightarrow I \rightarrow J \rightarrow I \rightarrow H$).

The aim of test series B was to investigate the effect of thermal over-consolidation. In tests B1 and B2, a thermal cycle was applied to normally-consolidated KSS, which was then unloaded and reloaded beyond the initial pre-consolidation pressure, to measure the change in pre-consolidation pressure due to the thermal cycle. Test B3, in which no thermal cycle was applied, provided the baseline response, against which the results from tests B1 and B2 could be compared.

The test path for tests B1-3 is given in Figure 8.2. All three tests begin with consolidation to 300 kPa at $22.5 \text{ }^\circ\text{C}$ ($A \rightarrow B$). In test B1, this is followed by a thermal cycle at 300 kPa, comprising heating from $22.5 \text{ }^\circ\text{C}$ to $50 \text{ }^\circ\text{C}$ ($B \rightarrow C$), cooling from $50 \text{ }^\circ\text{C}$ to $5 \text{ }^\circ\text{C}$ ($C \rightarrow D$), and heating from $5 \text{ }^\circ\text{C}$ to $22.5 \text{ }^\circ\text{C}$ ($D \rightarrow B$). Then at $22.5 \text{ }^\circ\text{C}$, the specimen is unloaded to 50 kPa ($B \rightarrow E$), and reloaded from 50 kPa to 2400 kPa ($E \rightarrow F$). In test B2, the path is the same, except the maximum temperature reached during the thermal cycle is $70 \text{ }^\circ\text{C}$ ($B \rightarrow G \rightarrow D \rightarrow B$). In test B3 (baseline), no thermal cycle is applied.

The aim of test series C was to investigate the thermal evolution of pre-consolidation pressure. In tests C1 and C2, over-consolidated KSS was heated, then reloaded at elevated temperature

Table 8.2: Overview of KSS tests

Test	Equipment	Loading and heating path	Motivation
A1	TC-OED	Thermal cycles at 1500 kPa (NC)	NC thermal response
A2	TC-OED	Thermal cycles at 300 kPa (OCR 5)	OC thermal response
A3	TC-OED	Thermal cycles at 50 kPa (OCR 30)	OC thermal response
B1	TC-OED	Ambient-temperature reloading following thermal cycle (max. temperature 50 °C)	Thermal over-consolidation
B2	TC-OED	Ambient-temperature reloading following thermal cycle (max. temperature 70 °C)	Thermal over-consolidation
B3	TC-OED	Ambient-temperature reloading	Baseline response for tests B1 & B2
C1	TC-OED	Reloading at 50 °C	Effect of temperature on yield surface
C2	TC-OED	Reloading at 70 °C	Effect of temperature on yield surface
C3	TC-OED	Ambient-temperature reloading	Baseline response for tests C1 & C2

images/kss_method/loadpath_A.pdf


Figure 8.1: Test path for KSS tests A1, A2 & A3

images/kss_method/loadpath_B.pdf

Figure 8.2: Test path for KSS tests B1, B2 & B3

beyond the initial pre-consolidation pressure, to measure the change in pre-consolidation pressure with temperature. Test C3 is test B3, re-labelled. It is presented here as a separate test for clarity.

The test path for tests C1-3 is given in Figure 8.3. All three tests begin with consolidation to 300 kPa ($A \rightarrow B$), and unloading to 50 kPa ($B \rightarrow C$) at 22.5 °C. In test C1, this is followed by heating at 50 kPa, from 22.5 °C to 50 °C ($C \rightarrow D$). Then at 50 °C, the specimen is reloaded from 50 kPa to 2400 kPa ($D \rightarrow E$). In test C2, the specimen is heated to 70 °C ($C \rightarrow F$) before reloading ($F \rightarrow G$). In test C3 (which is the same test as B3), no heating is applied, and reloading is performed at 22.5 °C ($C \rightarrow H$).



images/kss_method/loadpath_C.pdf

Figure 8.3: Test path for KSS tests C1, C2 & C3

In all tests, loading and unloading was applied incrementally. Each loading or unloading increment duration was 24 h. The target pressures for the initial consolidation stage were 2.5 kPa, 25 kPa, 50 kPa and 300 kPa, with an additional loading stage to 1500 kPa for test series A only. In test series A, unloading from 1500 kPa to 300 kPa (A2) or 1500 kPa to 50 kPa (A3) was performed in two increments, over 48 h. In test series B and C, unloading from 300 kPa to 50 kPa was performed in a single 24 h increment. The reloading path in test series B and C, from 50 kPa to 2400 kPa, was applied with the following target pressures: 50 kPa, 100 kPa, 200 kPa, 300 kPa, 600 kPa, 1200 kPa and 2400 kPa.

For thermal paths, the heating rate was 2 °C h⁻¹. At the maximum target temperature of 50 °C or 70 °C, the temperature was held for 6 h before cooling. Cooling from 50 °C or 70 °C to 22.5 °C was at the natural cooling rate of the cell. Cooling from 22.5 °C to 5 °C was controlled using the chiller in three increments: 15 °C, 10 °C and 5 °C. The duration of each cooling increment was ≈2 h, and the final temperature of 5 °C was held for at least 6 h before re-heating. In test series A, the total duration of the two thermal cycles was 8 days. In test series B, a single thermal cycle

was applied, over 4 days. In test series C, the duration of the thermal stage was considerably shorter, approximately 1 day, because heating only was applied (no cooling, or re-heating). The pressure and temperature variation with time is shown graphically, for all tests, in the sections that follow.

All tests were performed using the specimen set-up shown in Figure 8.4. Porous stones were placed above and below the specimen. Filter papers were not used. The same set-up was used for the calibration tests, discussed in Section 8.4.

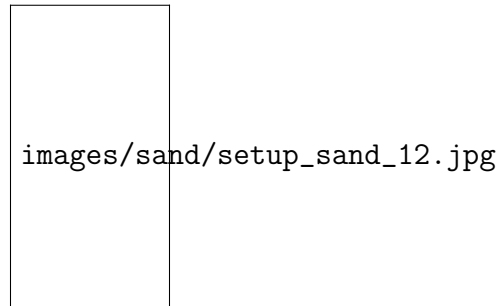


Figure 8.4: Specimen set-up for KSS tests

The initial height, total mass, and void ratio of the tested specimens are given in Table 8.3. The initial diameter of all specimens was 70 mm. The use of KSS, rather than bentonite, enabled specimen thickness to be increased. The maximum initial height is limited by the height of the confining ring. The difference in initial void ratio is because of the way the KSS slurry was stored, which led to the soil consolidating over time. However, all tests began with a consolidation stage to a minimum of 300 kPa, so this difference in initial void ratio does not have any significant effect on the subsequent responses. The void ratio for all tests is similar following consolidation to 300 kPa.

Table 8.3: Summary of initial height H_0 , initial mass m_0 , initial void ratio e_0 , and void ratio following consolidation to 300 kPa e_1 , for KSS tests

Test	H_0 [mm]	m_0 [g]	e_0 [-]	e_1 [-]
A1	48.1	316.6	1.28	0.65
A2	52.3	346.3	1.26	0.65
A3	51.1	341.9	1.24	0.65
B1	49.0	334.4	1.14	0.64
B2	52.4	358.6	1.13	0.63
B3	53.0	360.8	1.14	0.65
C1	47.4	314.6	1.24	0.64
C2	49.4	325.9	1.27	0.62
C3	53.0	360.8	1.14	0.65

A summary of the test durations is given in Table 8.4. Each test comprised a compliance test, and the main (soil) test. The compliance tests are discussed in Section 8.4. The average test duration is considerably less than for comparable tests on bentonite, such as bentonite test 9 (51 days), despite the specimen thickness for KSS tests being approximately double that of most of the bentonite tests, and the greater complexity of the KSS thermal paths. This was possible because of the higher coefficient of permeability of KSS. As a rough guide, the coefficient of

permeability of KSS ($\approx 1 \times 10^{-11} \text{ m s}^{-1}$) is approximately three orders of magnitude greater than bentonite ($\approx 1 \times 10^{-14} \text{ m s}^{-1}$), for equivalent conditions (temperature, pressure, and liquidity index).

Table 8.4: Summary of test durations for KSS tests

Test	Compliance [days]	Main [days]	Total [days]
A1	2	13	15
A2	2	13	15
A3	2	13	15
B1	2	15	17
B2	2	16	18
B3	1	11	12
C1	1	12	13
C2	1	12	13
C3	1	11	12

8.4 Calibration

For each test, a corresponding, individual calibration test was performed, to measure the thermal and mechanical compliance of the equipment. In each calibration test, the full test path was followed, although the duration of the loading and unloading stages was reduced significantly, and faster heating rates were used. Nevertheless, it was still important to apply these mechanical stages, because the thermal compliance may be affected by the preceding mechanical stage. Since the magnitude of mechanical compliance is greater than thermal compliance (for the range of pressures and temperatures tested), the preceding mechanical stage may have a significant effect on the subsequent measured thermal compliance.

The compliance data for each test were used to correct the main (soil) test data. Both sets of data were first split into thermal or mechanical sections. Each test section was then corrected with the relevant compliance test data. For example, test A1 was split into two sections: mechanical compliance from 2.5 kPa to 1500 kPa at 22.5 °C, and thermal cycling at 1500 kPa. The data from the A1 calibration test were split into the same two sections. Then the two sections of the test data were corrected using calibrations based on the relevant A1 calibration sections. This means that compliance equations for mechanical stages (consolidation, unloading, reloading) were functions of pressure only, while compliance equations for thermal stages (heating and cooling) were functions of temperature only. Although possible, it was not necessary to stitch the separate sections together, because the results can be analysed more effectively on a section-by-section basis.

The compliance data for the thermal stages of test series A are given in Figure 8.5. The measured vertical compliance is plotted against temperature. In all three tests, heating causes expansion (negative displacement) and cooling causes contraction (positive displacement). The compliance magnitude is greater for lower pressures (or higher OCR). Note that when discussing these results, the term OCR is used, although no soil specimen is present.

images/kss_results/kss_compliance_A_data.pdf

Figure 8.5: Compliance data for test series A

These results differ in important ways from the previous thermal calibration, which is discussed in Section 4.4 as calibration test 3, and plotted in Figure 8.6. Note that these same data are also shown in Figure 4.50, and are repeated here in modified form, for clarity. Calibration test 3 was a generic thermal calibration, not performed for a specific test, whereas the calibration tests A1-3 each followed a specific test path, corresponding to the relevant soil test.

In both cases, compliance magnitude reduces with increasing pressure. However, in calibration test 3, at lower pressures (2.5 kPa and 300 kPa), heating causes contraction (positive displacement), and cooling causes expansion (negative displacement). This is the opposite of the result obtained for calibration tests A1-3, for pressure values of 50 kPa and 300 kPa. The response for 1500 kPa is similar for both cases. This could suggest that the compliance tests are unreliable, so it is important to properly consider this result.

The result for calibration tests A1-3 makes more sense. Consider the schematic given in Figure 4.16, which shows the thermal and mechanical deformation of the core components of the equipment. Heating causes expansion of the loading ram, top-cap, and porous stones, which is measured by the displacement transducers as a negative displacement (extension), because the instrumentation plate moves up (the body of the LVDT moves up, relative to the core). However, heating also causes expansion of the confining ring, and the LVDT extension pieces, which is measured by the displacement transducers as a positive displacement (contraction), because the LVDT core moves up, into the LVDT body (equivalent to the instrumentation plate moving down). Mechanical contraction is not relevant in this case because the thermal cycles are carried out under constant pressure. The compliance will be affected by the pressure value, because the thermal extension of the confining ring and the LVDT extension leg is independent of pressure, whereas the thermal extension of the loading ram, top-cap and porous stones, is not. This is because the loading ram, top-cap and porous stones in combination have a non-linear stiffness, so

images/kss_results/tcomp2_d_t_kss_ch_edit.pdf

Figure 8.6: Compliance data for calibration test 3

that the same increase in stress due to temperature increase at a lower applied pressure results in a greater strain, than for higher applied pressure. For heating at low pressures, the loading ram will extend more than at high pressures. This means, at low pressures, thermal compliance is expected to be more expansive (or less contractive) than at high pressures. This is exactly what is observed for compliance tests A1-3.

There are several possible explanations for the conflicting result obtained from calibration test 3. First, the mechanical stage immediately preceding a thermal stage may affect the resulting thermal compliance. In calibration test A1, this mechanical stage was a loading path, whereas in calibration tests A2 and A3, it was an unloading path. In calibration test 3, all thermal stages were performed following loading paths. This would explain why there is reasonable agreement between the two tests for thermal cycles at 1500 kPa, which followed a loading path in both cases. Second, the lowest pressure value in calibration test 3, 2.5 kPa, is particularly unreliable, since this is in the same range as the friction value, and therefore may have been significantly affected by friction. In the KSS tests, thermal stages were performed at a minimum pressure of 50 kPa for this reason.

From the compliance test data shown in Figure 8.5, the compliance fits are derived. The main issue with deriving fits from these results is the residual displacement developed during the first heat/cool path (defined here as heating to 70 °C and cooling to 22.5 °C). In test A1 ($P = 1500$ kPa, OCR 1), the first heat/cool path causes an overall contractive displacement. In tests A2 ($P = 300$ kPa, OCR 5) and A3 ($P = 50$ kPa, OCR 30), the first heat/cool path causes an overall expansive displacement, which is smaller for test A2 than for A3.

One method tested was to regularly sample the compliance test data, and the soil test data, at 10 °C intervals, then apply the correction to the sampled soil test data. This correction accounts

for the difference between the first and second thermal cycle compliance. However, this solution suggests a high level of confidence in the repeatability of the compliance response. In fact, with the presence of the soil, the compliance response may be quite different (although this is an issue that affects almost all soil laboratory tests, not just these).

The method used for the final analysis was to fit a polynomial to the second heating path. This path was chosen because it appears to be a good approximation of the subsequent cooling path. This is clear when looking at the A1 compliance test data, where the second cooling path is almost identical to the preceding heating path. The displacement during the second thermal cycle in a soil test is generally lower than the first, so the accuracy of this compliance becomes relatively more important. Second order polynomial fits were used, with the intercept shifted so that the compliance is zero at 22.5°C. These fits are shown in Figure 8.7.

An advantage of the polynomial fit compared to sampling the data is that the correction can be applied to all measured data points. These data can then be subsequently sampled in a number of different ways, for example, at the end-of-increment points, for consolidation analysis, or at regular time intervals, to determine the rate of strain. If the data are sampled at regular temperature intervals in order to apply the compliance, then no further sampling is possible. A polynomial fit is also less sensitive to variations in individual measured values.



Figure 8.7: Compliance fits for test series A

The equipment compliance has a significant effect on the calculated thermal response (see Section 8.5.3). Ideally, a compliance test for a thermal test would be carried out both before and after the soil test, to gauge the reliability of the compliance data. Time constraints on the testing programme meant this was not possible. However, data from the calibration tests for test series B and C can be used instead.

In all tests, thermal paths were followed (except in baseline test B3/C3). In tests B1 and B2, a

thermal cycle was applied at 300 kPa at normally-consolidated conditions. In tests C1 and C2, a heating path was applied at 50 kPa at an OCR of 6.

First, in Figure 8.8, the compliance data for the first heating path in test A1 (1500 kPa) are compared with the first heating path in tests B1 and B2 (300 kPa), with all three tests at OCR 1. The expansion due to heating is lower for test A1 than tests B1 and B2. This suggests that expansion due to heating is higher at lower pressure. The responses for tests B1 and B2 are in good agreement, which suggest that the obtained compliance is reliable.

If the whole of the first thermal cycle is considered, as in Figure 8.9, the result is more complex. The gradient of the cooling path for tests B1 and B2 is similar, which means that in test B1, the overall response becomes contractive. Note that because of an issue with the chiller, the full cooling response for test B2 was not obtained. The gradient of the cooling path is lower for test A1 than tests B1 and B2, which suggests that contraction due to cooling is higher at lower pressure.

Next, in Figure 8.10, the compliance data for the first heating path in test A2 (300 kPa, OCR 5) is compared with the first heating path in tests B1 and B2 (300 kPa, OCR 1), to assess the effect of OCR. The expansion is slightly, but not significantly, higher for test A2, which is at a higher OCR. Together with Figure 8.8, this result suggests that pressure value is more important to the thermal compliance response than OCR.

The data for the full thermal cycle, in Figure 8.11, lead to the same conclusion. At first, the response for test B1 appears to be quite different to tests A2 and B2. The shape of the cooling path is similar for all three tests, but the overall compliance is contractive for test B1 because the maximum temperature reached (and resulting expansion) in the initial heating stage was lower.

Finally, in Figure 8.12, the compliance data for the first heating path in test A3 (50 kPa, OCR 30) are compared with the heating path in tests C1 and C2 (50 kPa, OCR 6). This time, the expansion is significantly higher for test A3, at higher OCR. This suggests that OCR may have a significant effect on the thermal compliance response at low pressure values.

As well as thermal compliance, mechanical compliance was measured. This compliance is relevant for the reloading paths in test series B and C, from which the pre-consolidation pressure was determined. The compliance data for the reloading path from 50 kPa to 2400 kPa for tests C1-3 are shown in Figure 8.13. The response is approximately linear (against logarithmic pressure), and appears to be independent of temperature. A logarithmic fit was derived, with zero displacement at 50 kPa. The same fit was used for all tests in series B and C. The significance of this fit is discussed in Section 8.5.1.

Following the application of the vertical compliance correction, the correction for differential lateral thermal expansion of the confining ring and soil is applied. Details on the derivation of this correction are given in Section 4.6, while its application is discussed in Section 7.1. The confining ring correction is shown in Figure 8.14, for test A3. The correction amount varies between tests, since it depends on the specimen height. The maximum theoretical correction, for a Poisson's ratio ν of 0.5, is shown, together with a low-range estimate of ν for saturated clay of 0.4. For the results presented in this chapter, a Poisson's ratio of 0.5 has been assumed. Note that the theoretical minimum correction, for a Poisson's ratio of zero, would be zero. The vertical thermal compliance for the first heating path in test A3 is shown for comparison.

images/kss_results/kss_compliance_OCR_1.pdf

Figure 8.8: Vertical thermal compliance for tests A1, B1 and B2 - initial heating path

images/kss_results/kss_compliance_OCR_1_full.pdf

Figure 8.9: Vertical thermal compliance for tests A1, B1 and B2 - first thermal cycle

images/kss_results/kss_compliance_P_300.pdf

Figure 8.10: Vertical thermal compliance for tests A2, B1 and B2 - initial heating path

images/kss_results/kss_compliance_P_300_full.pdf

Figure 8.11: Vertical thermal compliance for tests A2, B1 and B2 - first thermal cycle

images/kss_results/kss_compliance_P_50.pdf

Figure 8.12: Vertical thermal compliance for tests A3, C1 and C2

images/kss_results/kss_compliance_C_data.pdf

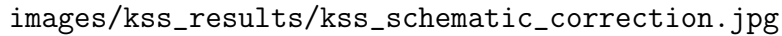
Figure 8.13: Compliance data for test series C

images/kss_results/kss_compliance_CR.pdf

Figure 8.14: Compliance for test A3, compared with confining ring correction for Poisson's ratio of 0.5 and 0.4

The compliance/corrections in this section are shown as positive or negative displacements, corresponding to contraction or expansion. To clarify, these are the displacements measured, or calculated, for the compliance/corrections. To account for these responses, these values are subtracted from the displacement measured in the soil test (or, in the case of the confining ring correction, added to the soil height, which is equivalent). This is shown schematically in Figure 8.15. The vertical compliance and confining ring (CR) corrections from Figure 8.14 are plotted on axes of temperature against displacement. This orientation is commonly used to display results for thermal cycling, because this gives more space (on a graph with landscape dimensions) for displacement/strain values, which tend to vary between tests, whereas the temperature range tends to remain constant.

The vertical compliance is expansive for temperatures above 22.5 °C. The displacement, corrected for vertical compliance, will be on the contractive (positive) side of the measured displacement (although it still may be expansive, just less so), as indicated by the arrow. The CR correction is contractive for temperatures above 22.5 °C. The displacement, corrected for CR/soil interaction, will be on the expansive (negative) side of the measured displacement.



images/kss_results/kss_schematic_correction.jpg

Figure 8.15: Schematic showing application of vertical compliance correction and confining ring correction

8.5 Results and discussion

In this section, some key results for the tests on KSS are discussed. The effect of current temperature on reloading behaviour is discussed in Section 8.5.1. Thermal over-consolidation is discussed in Section 8.5.2. Thermal volume change at different OCR and pressure values is discussed in Section 8.5.3. The effect of pressure level on thermal volume change is discussed in Section 8.5.4. The effect of over-consolidation ratio on thermal volume change is discussed in Section 8.5.5. Compression characteristics, consolidation characteristics, and coefficient of permeability are discussed in Sections 8.5.6, 8.5.7 and 8.5.8.

To avoid repetition, specific points relating to data analysis are generally only discussed once. These include: the pressure fluctuations observed during the initial low-pressure consolidation stages of each test, data sampling options, and yield point calculation method, which are all covered in Section 8.5.1.

The results are compared with the expected results based on the IC Thermal constitutive model (Gawecka, 2017) in the Imperial College Finite Element Program (ICFEP) (Potts and Zdravković, 1999; 2001). The first thermo-mechanical constitutive model was developed by Hueckel and Baldi (1990) and Hueckel and Borsetto (1990). Since this pioneering work, the availability and accuracy of experimental data have improved, which has enabled the development and improvement of the constitutive models formulated from these data. A chronological review of the development of these constitutive models is given by Gawecka (2017).

The IC Thermal model simulates the temperature dependence of a soil through an isotropic yield surface, which describes the variation of the pre-consolidation pressure with temperature. The formulation of this surface assumes the following:

1. Pre-consolidation pressure decreases with increasing temperature;
2. Behaviour within the yield surface is elastic until the yield surface is activated, then it becomes elasto-plastic;
3. The slopes of the NCL and swelling lines are independent of temperature (λ and κ are constant with temperature);

4. Heating under drained conditions within the yield surface does not induce changes in void ratio;
5. An increase in temperature causes the NCL to shift to lower void ratio values;
6. The position of the NCL is uniquely determined by temperature, and does not depend on temperature history.

The effect of temperature on the slope of the NCL and swelling lines, and the position of the NCL, is shown schematically in Figure 8.16, for two temperature values, T_0 and T_1 , where $T_1 > T_0$.

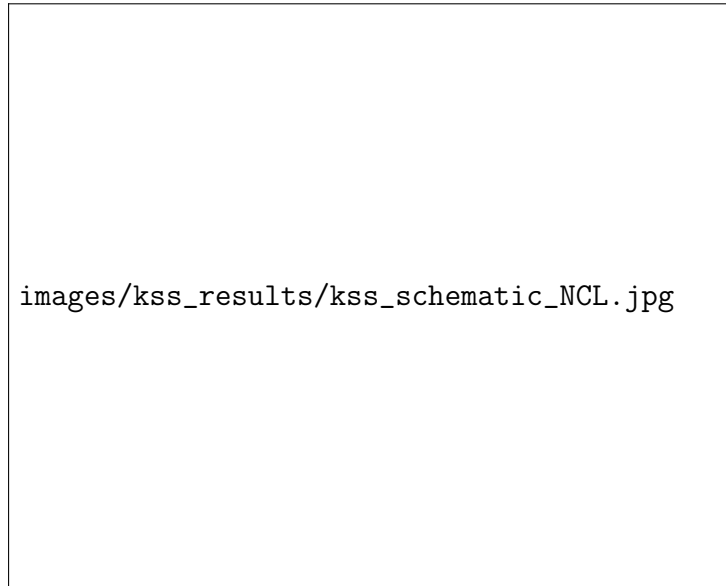
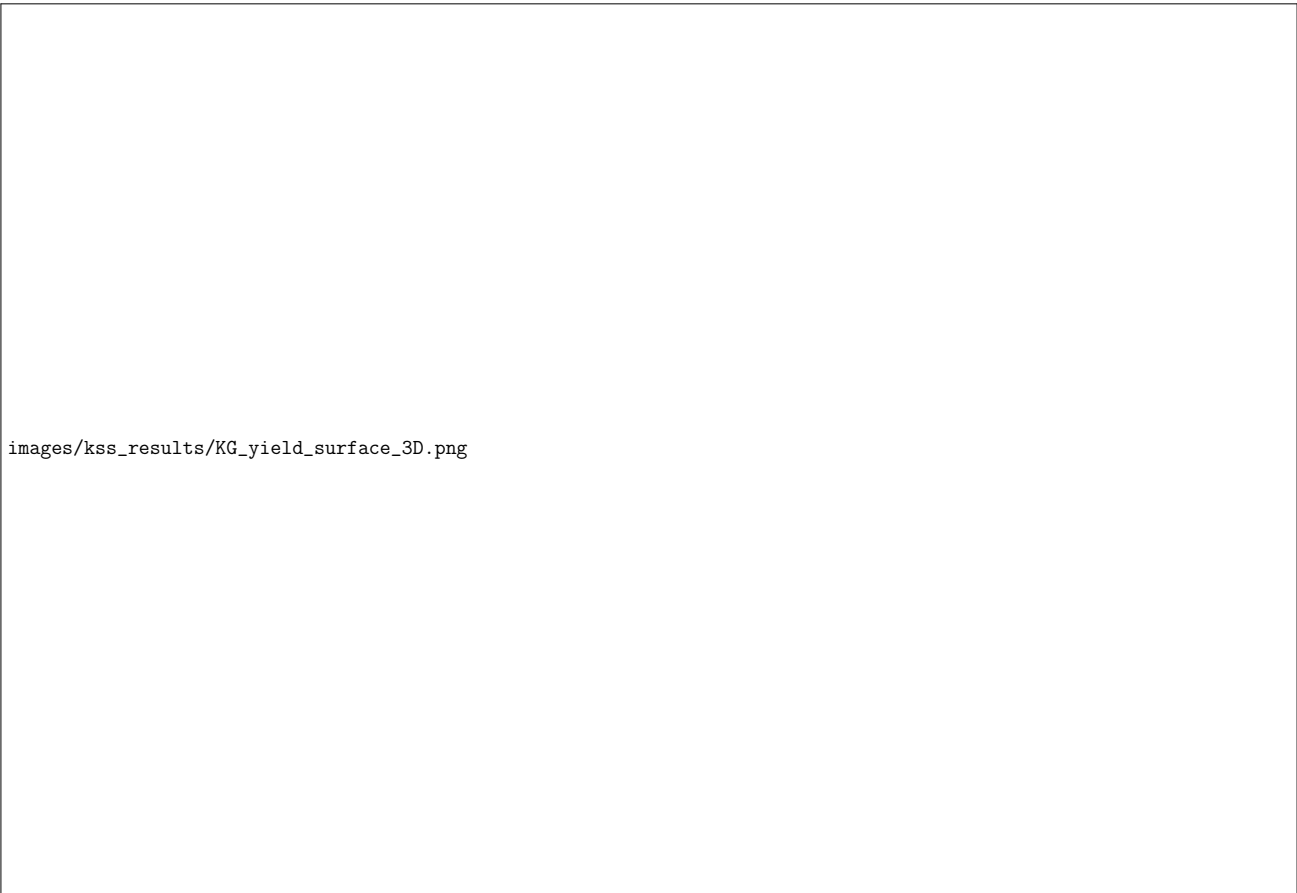


Figure 8.16: Effect of temperature on shape and position of NCL and swelling lines, based on the IC Thermal constitutive model

The primary isotropic yield surface is shown in shown in $p - J - T$ space in Figure 8.17.


This model also incorporates a secondary isotropic yield surface, which models the onset of plasticity observed during heating of moderately and highly over-consolidated soils. This surface, together with the primary isotropic yield surface, is shown in the $p - T$ plane in Figure 8.18. For the model predictions presented in this chapter, the secondary isotropic yield surface was not active.

These assumptions are discussed with the relevant test results in the subsequent sections. The tests on KSS, described in this chapter, constitute a set of results which can be used to fully calibrate the IC Thermal constitutive model for KSS. The only additional data required would be small-strain stiffness and strength parameters at ambient-temperature, which could be obtained from conventional triaxial tests.



images/kss_results/KG_yield_surface_3D.png

Figure 8.17: Primary isotropic yield surface in $p - J - T$ space (Gawecka, 2017)



images/kss_results/KG_yield_surface.PNG

Figure 8.18: Primary and secondary isotropic yield surfaces in the $p - T$ plane (Gawecka, 2017)

8.5.1 Effect of current temperature on reloading behaviour

The primary aim of test series C was to investigate the thermal evolution of pre-consolidation pressure. In other words, the effect of *current* temperature on reloading behaviour. Previous temperature-controlled oedometer schemes from the literature have found that pre-consolidation pressure reduces with increasing temperature (Gray, 1936; Plum and Esrig, 1969; Eriksson, 1989; Tidfors and Sällfors, 1989; Moritz, 1995; Abuel-Naga et al., 2005; François et al., 2007; Favero et al., 2016).

Three tests were performed: C1, C2 and C3. The full test path for these tests is given in Figure 8.3. The effect of current temperature on reloading behaviour was tested by heating an over-consolidated soil to a target temperature (50 °C for test C1, 70 °C for test C2), then reloading at this temperature, beyond the initial pre-consolidation pressure. The relationship between current temperature and measured pre-consolidation pressure upon reloading could then be assessed. Test C3 was performed without the heating stage, to obtain the baseline ambient-temperature pre-consolidation pressure, against which the values from tests C1 and C2 were compared.

In the IC thermal constitutive model, it is assumed that pre-consolidation pressure reduces with increasing temperature. This assumption defines the shape of the primary *isotropic* yield surface, shown schematically in Figure 8.19. Note that here p is the mean effective stress, but in the temperature-controlled oedometer, only the effective vertical stress σ'_v is measured. The initial pre-consolidation pressure, before unloading and heating, is denoted $p_{c,0}$. The primary yield surface, indicated with a dashed line, passes through $p_{c,0}$ at temperature T_0 . If the pre-consolidation pressure reduces with temperature, then at temperature T_1 , the pre-consolidation pressure (indicated by the hollow triangle) reduces to $p_{c,1}$, and at temperature T_2 , it reduces to $p_{c,2}$. Performing an intermediate temperature test T_1 , provides more information on the shape of the yield surface, otherwise it must be assumed to be linear in the isotropic $p - T$ plane.

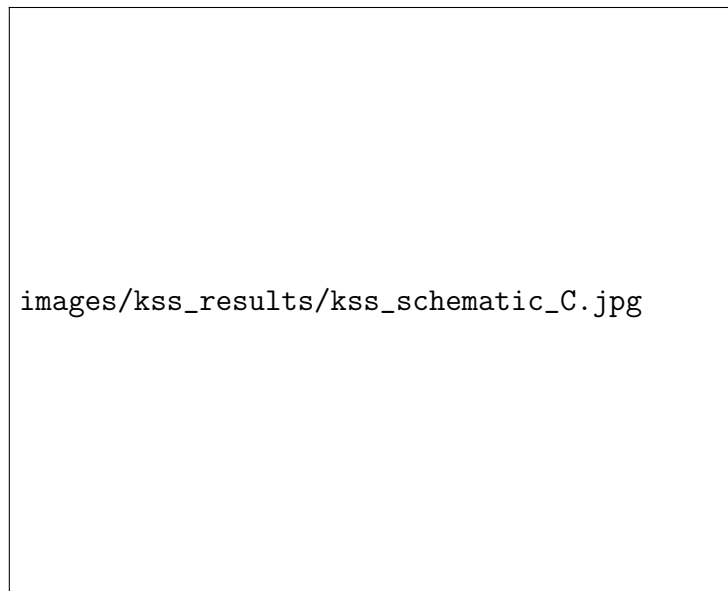


Figure 8.19: Effect of current temperature on reloading behaviour - example test paths in the isotropic $p - T$ plane

The pressure and temperature variation with time is shown in Figures 8.20, 8.21 and 8.22 for test C1, C2 and C3 respectively. The total duration for each test was approximately 12 days.

images/kss_results/kss_C1_P_T_time.pdf

Figure 8.20: Pressure and temperature vs time for test C1 - full test

images/kss_results/kss_C2_P_T_time.pdf

Figure 8.21: Pressure and temperature vs time for test C2 - full test

images/kss_results/kss_B3_P_T_time.pdf

Figure 8.22: Pressure and temperature vs time for test C3 - full test

In the second increment, from 1 to 2 days, the target pressure is 25 kPa. The measured pressure value fluctuates below this value, rising initially to almost 25 kPa, falling, then rising again until it reaches the increment target value. A similar response was observed for all tests, for this loading increment.

This initial pressure fluctuation can be seen in Figure 8.23, using data from test C3. However, the end-of-increment void ratio response (sampling the final data point before the start of the next increment), is linear against pressure on a logarithmic scale.

The choice of sampling technique is important, because sampled data, not the full data set, is used to calculate the yield point. Two potential techniques are compared in Figure 8.24. The full data show that once the pressure reaches the target value, there is additional strain (here, reduction in void ratio) under constant pressure. This additional strain comprises primary consolidation and secondary consolidation. The amount of secondary consolidation is relatively small compared to the primary consolidation, as shown in the incremental response for the 300 kPa reloading stage for test C3, in Figure 8.25. The amount of secondary consolidation is $\approx 10\%$ of the total consolidation for the increment. Note that the load is not instantaneously applied, but gradually increases to the target value. In this case, the target pressure is reached after 1 h. This may affect the shape of the incremental response, from which the coefficient of consolidation is determined, discussed further in Section 8.5.7. At the start of the next increment, there is initially an increase in pressure without a corresponding reduction in void ratio. As the pressure increases further, the void ratio reduces linearly against logarithmic pressure, until the target pressure is reached.

The result is an overall linear response, with notches at each target pressure value. One sampling option would be to sample the data before the target pressure is reached, and at some point after

images/kss_results/kss_C3_e_P.pdf

Figure 8.23: Void ratio vs pressure for test C3 - full test

images/kss_results/kss_C3_e_P_sampled.pdf

Figure 8.24: Void ratio vs pressure for test C3 - comparison of sampling techniques

images/kss_results/kss_C3_300kPa_inc.pdf

Figure 8.25: Incremental response for 300 kPa reloading stage for test C3

the start of the next increment, avoiding the notches. This is shown as the *mid-increment* sample in Figure 8.24. However, the mid-increment sample does not account for consolidation that occurs at the target pressure. The sampling technique used in this thesis is the *end-of-increment* sample, which accounts for this consolidation.

In Figure 8.26, the measured displacement is compared to the corrected displacement following subtraction of the vertical mechanical compliance. The compliance is small compared to the measured displacement. The same is true for all results for test series B and C. This result can be compared with test series A, for example test A3 in Figure 8.57, where the vertical thermal compliance is of a similar magnitude to the measured displacement. Clearly, compliance effects are particularly important for thermal stages.

The full reloading response for the three tests is shown in Figure 8.27, while Figure 8.28 shows the same data, but focusing on pressure values closer to the yield point. At this scale, the difference between the three test responses is more apparent. However, it is still difficult to determine the effect of the temperature conclusively. The void ratio has been normalised by the void ratio at 50 kPa. Care must be taken when using normalised void ratio values, as discussed in Section 8.5.6.

Rather than use a graphical method, the yield point for the reloading paths from 50 kPa to 2400 kPa was calculated using MATLAB, using a similar method to that used for the bentonite tests. The test data were sampled at the end of each reloading increment (plus the end of the previous unloading increment, to give the initial condition) giving seven data points at 50 kPa, 100 kPa, 200 kPa, 300 kPa, 600 kPa, 1200 kPa and 2400 kPa. The sampling method (mid-increment vs end-of-increment) affects the calculated yield point. However, excluding the first and last data points does not significantly affect the calculated yield point. From tests on

images/kss_results/kss_compliance_C1.pdf

Figure 8.26: Comparison of measured and corrected data for test C1

bentonite, it was suggested that three approximately equally-spaced (on logarithmic pressure scale) data points should be obtained either side of the estimated yield point. However, because the transition from over-consolidated to normally-consolidated behaviour is much more distinct for KSS than bentonite, it seems that two points either side is sufficient. Reducing the number of reloading increments could potentially reduce testing duration by several days. A polynomial was fitted through to the sampled end-of-increment data (6th order polynomial for 7 data points, 4th order polynomial for 5 data points), which could then be differentiated to find the yield point. The yield point calculation is shown for test C1 in Figure 8.29. The yield point is found at the inflection point of the first derivative, which corresponds to a turning point of the second derivative, and the x-axis intercept of the third derivative. The equivalent yield point calculation for tests C2 and C3 is shown in Figures 8.30 and 8.31 respectively.

The calculated yield point values are summarised in Figure 8.32 and Table 8.5. Note that results are given in terms of vertical stress σ_v . However, within the IC thermal model, mean stress p is used instead. With increasing temperature, the pre-consolidation pressure reduces, in agreement with the literature consensus. The increase is non-linear, although it is difficult to make a conclusion about the shape of the yield surface based on the limited number of data points. The dashed line in Figure 8.32 indicates the inferred shape of the yield surface. Using the data from tests C1 and C3 only (22.5 °C to 50 °C), the reduction in pre-consolidation pressure is 0.22 kPa °C⁻¹ (or 0.1 % °C⁻¹, as a percentage of p_c at 22.5 °C). Using the data from tests C1 and C2 only (50 °C to 70 °C), the reduction in pre-consolidation pressure is 1.25 kPa °C⁻¹ (or 0.4 % °C⁻¹, as a percentage of p_c at 22.5 °C). A literature review of the effect of temperature on pre-consolidation pressure, for oedometer and isotropic tests, conducted by Gawecka (2017), found a range of values from 0.1 % °C⁻¹ to 0.8 % °C⁻¹, noting that the magnitude of change in p_c may depend on soil type. Based on the literature values, the measured values seem reasonable.

images/kss_results/kss_C_e_P_full.pdf

Figure 8.27: Normalised void ratio vs pressure for tests C1-3 - reloading only

images/kss_results/kss_C_e_P.pdf

Figure 8.28: Normalised void ratio vs pressure for tests C1-3 - yield point

images/kss_results/kss4_YP-eps-converted-to.pdf

Figure 8.29: Calculation of yield point for test C1, showing reloading path only

images/kss_results/kss5_YP-eps-converted-to.pdf

Figure 8.30: Calculation of yield point for test C2, showing reloading path only

images/kss_results/kss11_YP-eps-converted-to.pdf

Figure 8.31: Calculation of yield point for test C3, showing reloading path only

images/kss_results/kss_C_pc.pdf

Figure 8.32: Yield point for tests C1, C2, C3

Table 8.5: Test series C - reloading temperature and yield point

Test	T [°C]	Yield point [kPa]
C3	22.5	319
C1	50	313
C2	70	288

8.5.2 Thermal over-consolidation

The primary aim of test series B was to investigate thermally-induced over-consolidation behaviour. The hypothesis is that the thermal history of the soil can affect its behaviour. In a similar way to mechanically normally-consolidated and over-consolidated soils, thermally over-consolidated soils may behave differently upon reloading (or reheating). Thermal over-consolidation ratio OCR_T , introduced by Gawecka (2017), is defined as the ratio between the maximum temperature reached by the soil T_{max} and the current temperature T :

$$OCR_T = \frac{T_{max}}{T} \quad (8.1)$$

The relevant parameter for over-consolidation is pre-consolidation pressure p_c . In test series B, the pre-consolidation pressure was measured for specimens with different thermal over-consolidation ratios OCR_T , giving the relationship between thermal history (in this case, the maximum temperature applied to the soil during a thermal cycle), and the measured pre-consolidation pressure. According to the available literature, pre-consolidation pressure increases with maximum cyclic temperature (Abuel-Naga et al., 2005).

Three tests were performed: B1, B2 and B3. The full test path for these three tests is given in Figure 8.2. In tests B1 and B2, a thermal cycle was applied to a normally-consolidated specimen. The thermal cycle comprised a single cycle of heating to the target maximum temperature T_{max} (50 °C for test B1, 70 °C for test B2), cooling to 5 °C, then heating to 22.5 °C.

The pre-consolidation pressure following this thermal cycle was measured by unloading the specimen, then reloading beyond the initial pre-consolidation pressure. Previous tests, for example bentonite test 7 (Section 5.5), showed that the calculated yield point for a reloading path is not necessarily exactly equal to the initial pre-consolidation pressure, even for ambient temperature. So rather than compare the yield point for tests B1 and B2 to an assumed value, a baseline test, B3, was performed, to obtain the yield point for ambient temperature.

As discussed in relation to test series C, in the IC thermal constitutive model, pre-consolidation pressure is assumed to decrease with temperature, which defines the shape of the primary isotropic yield surface. The expected behaviour for test series B, in the isotropic $p - T$ plane, according to the model, is shown schematically in Figure 8.33. The initial, ambient temperature, pre-consolidation pressure, before the thermal cycle is denoted $p_{c,0}$. The maximum temperature reached during the thermal cycle, T_{max} is denoted T_1 or T_2 . The primary yield surface is indicated with a dashed line. When the temperature is increased from T_0 to T_1 (as in test B1), the yield surface expands so that it passes through the current pressure and temperature value. Upon reloading at ambient temperature, the yield point, denoted by a hollow triangle, is reached at p_{c1} . This is the point at which the soil behaviour changes from over-consolidated to normally-consolidated. When the temperature is increased from T_0 to T_2 (as in test B2), the yield surface expands so that it passes through the current pressure and temperature value. Upon reloading at ambient temperature, the yield surface is reached at p_{c2} . This means that the pre-consolidation pressure increases with increasing thermal over-consolidation ratio OCR_T (i.e. with increasing T_{max}).

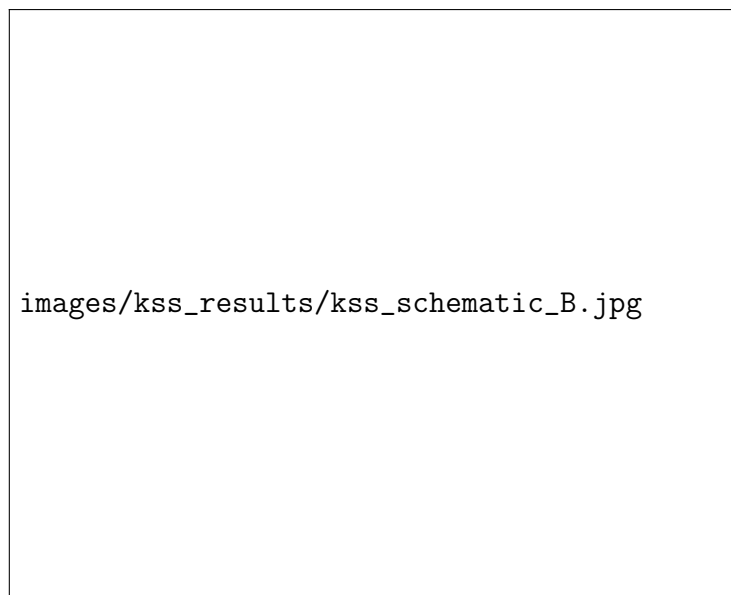


Figure 8.33: Effect of temperature history on reloading behaviour - example test paths in the isotropic $p - T$ plane

The pressure and temperature variation with time is shown in Figures 8.34, 8.35 and 8.36 for test B1, B2 and B3 respectively. The total test duration was approximately 16 days for tests B1 and B2, and 12 days for B3.

images/kss_results/kss_B1_P_T_time.pdf

Figure 8.34: Pressure and temperature vs time for test B1 - full test

images/kss_results/kss_B2_P_T_time.pdf

Figure 8.35: Pressure and temperature vs time for test B2 - full test

images/kss_results/kss_B3_P_T_time.pdf

Figure 8.36: Pressure and temperature vs time for test B3 - full test

The reloading response for tests B1-3 is shown in Figure 8.37. The void ratio has been normalised by the void ratio at 50 kPa to enable better comparison of the shape of the three test results. From this graph, the general shape of the reloading response is clear, but the variation between tests is less so. The reloading curve can be split into two clear sections. For pressures below 300 kPa, the response is non-linear, becoming steeper with increasing pressure. For pressures above 300 kPa, the response is distinctly steeper, and linear. The same data are shown in Figure 8.38, focusing on pressure values closer to the yield point.

The yield point was calculated in MATLAB, by fitting a 4th order polynomial to the sampled end-of-increment data. Further details on the data-sampling method and yield point calculation are given in Section 8.5.1. The yield point calculation for tests B1 (50 °C), B2 (70 °C) and B3 (baseline: 22.5 °C) is shown in Figures 8.39, 8.40, and 8.41 respectively.

The calculated yield point for tests B1-3 is summarised in Figure 8.42 and Table 8.6. The yield surface, based on the results from test series C (Figure 8.32) is shown as a dashed line passing through the yield point for each test. The baseline ambient-temperature value, for test B3, is 319 kPa. For test B2 ($T_{max} = 50$ °C), the yield point is 325 kPa. For test B3 ($T_{max} = 70$ °C), the yield point is 328 kPa. The yield point value increases with maximum cyclic temperature, in agreement with the result of Abuel-Naga et al. (2005), for soft Bangkok clay. At an initial pre-consolidation pressure of 300 kPa, they observed an increase in p_c of 105 kPa, following a thermal cycle of 22 → 90 → 22 °C. This is significantly higher than the increase of 9 kPa observed for KSS, which is small, but consistent, and based on a repeatable testing and data-processing methodology.

One possible explanation for the relatively small increase in p_c for KSS, is the lower plasticity of KSS (18.5 %) compared to soft Bangkok clay (60 %). The magnitude of thermally-induced

images/kss_results/kss_B_e_P_full.pdf

Figure 8.37: Normalised void ratio vs pressure for tests B1-3 - reloading only

images/kss_results/kss_B_e_P_pc.pdf

Figure 8.38: Normalised void ratio vs pressure for tests B1-3 - yield point

images/kss_results/kss9_YP-eps-converted-to.pdf

Figure 8.39: Calculation of yield point for test B1, showing reloading path only

images/kss_results/kss10_YP-eps-converted-to.pdf

Figure 8.40: Calculation of yield point for test B2, showing reloading path only

images/kss_results/kss11_YP-eps-converted-to.pdf

Figure 8.41: Calculation of yield point for test B3, showing reloading path only

contraction of normally-consolidated soil increases with increasing plasticity (Towhata et al., 1993; Di Donna and Laloui, 2015), which may affect the pre-consolidation pressure. It would be interesting to check this by repeating these tests on a higher-plasticity clay, such as London Clay.

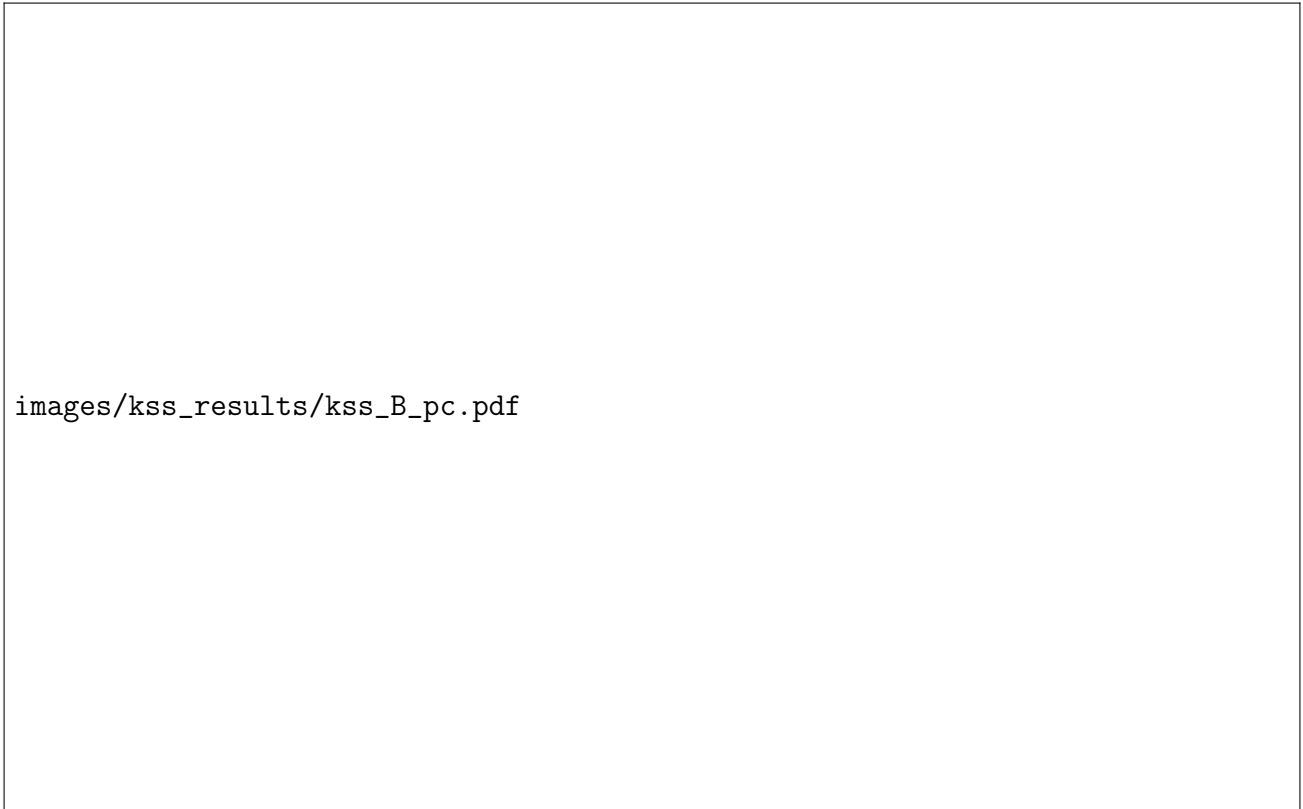


Figure 8.42: Yield point for tests B1, B2, B3 - showing assumed yield surface from test series C

Table 8.6: Test series B - maximum temperature of thermal cycle and yield point

Test	T_{max} [°C]	Yield point [kPa]
B3	22.5	319
B1	50	325
B2	70	328

With reference to Figure 8.33, the yield surface passes through two points. These are: (i) the point corresponding to T_{max} (T_1 or T_2) at the ambient temperature pre-consolidation pressure $p_{c,0}$, and (ii) the point corresponding to the pre-consolidation pressure upon ambient temperature reloading, following thermal over-consolidation ($p_{c,1}$ or $p_{c,2}$). Figure 8.43 shows the same data as in Figure 8.42, but this time the inferred yield surface based on the results of test series B only is shown (solid blue lines), in addition to the assumed yield surface based on test series C (dashed grey lines). The inferred yield surface is obtained by assuming a linear yield surface, which passes through the imposed position of the yield surface at elevated temperature, and the measured yield point upon reloading. For test B2, the inferred yield surface shape is different to the assumed yield surface shape, in which the reduction in yield stress with temperature is greater for the range 50 °C to 70 °C. The limited available data points makes it difficult to reach a firm conclusion on this issue. There could be an error in the measured pre-consolidation pressure for test C2, at 70 °C, shown in Figure 8.32. The yield surface may not expand with

heating in the way assumed by the IC Thermal model, by shifting towards higher pressures, without changing shape (moving right in the $p - T$ plane), as shown schematically in Figure 8.44. For example, heating may cause the yield surface to shift towards higher temperatures, without changing shape (moving up in the $p - T$ plane). Alternatively, the shape of the yield surface may change with temperature.

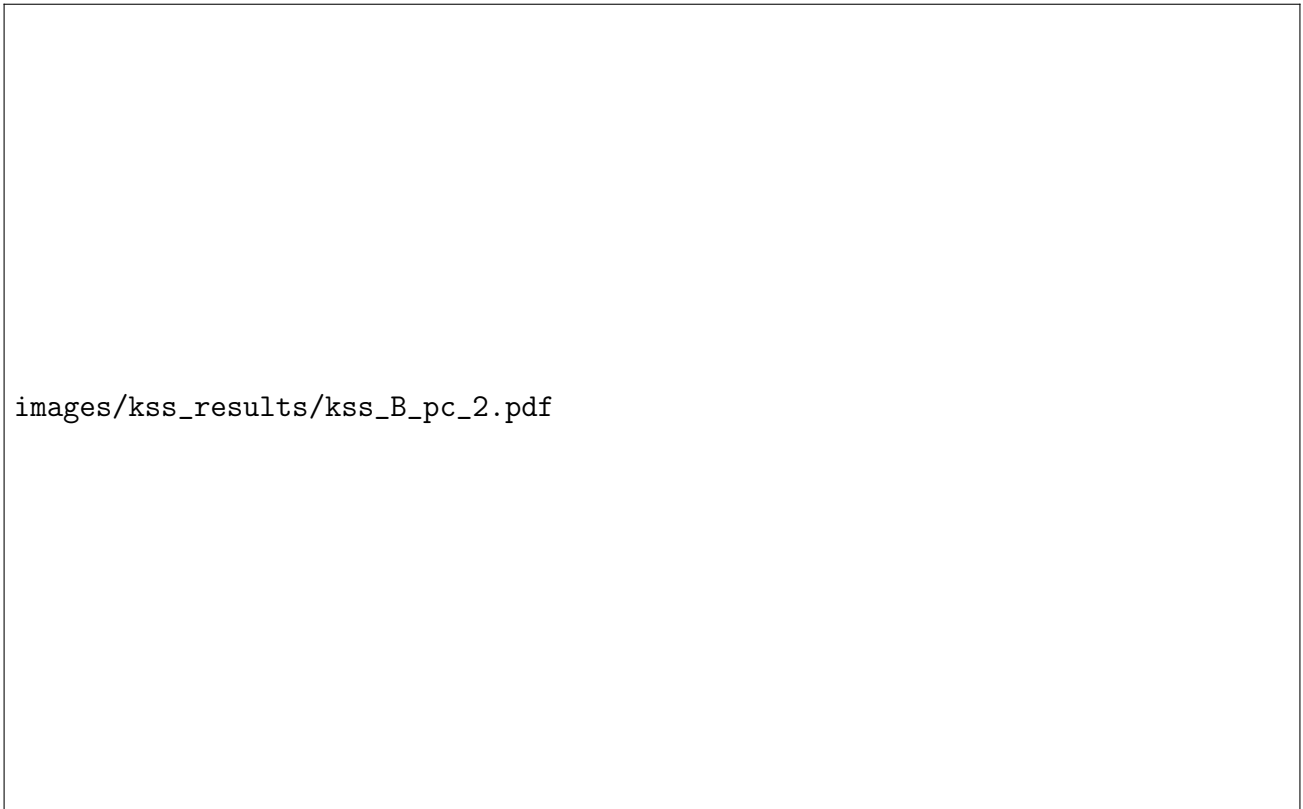


Figure 8.43: Yield point for tests B1, B2, B3 - showing inferred yield surface from test series B

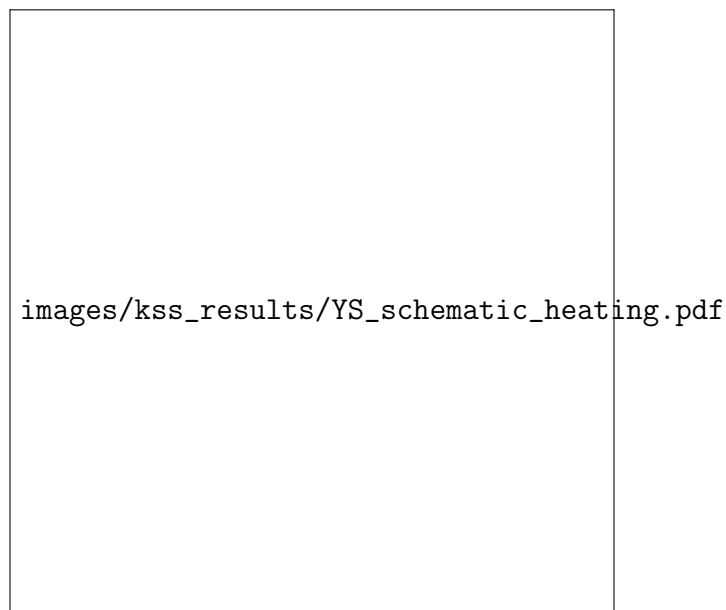


Figure 8.44: Effect of isobaric heating on the isotropic yield surface

8.5.3 Thermal volume change at different OCR and pressure values

The effect of OCR and pressure value on thermal volume change is discussed in relation to test series A, which comprises tests A1, A2, and A3. The test paths for these tests are given in Figure 8.1. In test A1, the thermal cycling was performed at 1500 kPa, under normally-consolidated conditions. In test A2, the thermal cycling was performed at 300 kPa, at an OCR of 5. In test A3, the thermal cycling was performed at 50 kPa, at an OCR of 30. This information is summarised in Table 8.7. Here, e_0 refers to the void ratio at the start of the thermal cycle.

Table 8.7: Test series A - pressure and OCR at which thermal cycles applied

Test	Pressure [kPa]	OCR [-]	e_0 [-]
A1	1500	1 (NC)	0.51
A2	300	5	0.53
A3	50	30	0.55

The IC Thermal constitutive model incorporates a primary isotropic yield surface which defines the yield point as a function of temperature, as shown in Figure 8.17. It is assumed that behaviour within the yield surface is elastic, but that once the yield surface is activated, the behaviour becomes elasto-plastic. The primary isotropic yield surface is shown in Figure 8.45 as the dashed line.



Figure 8.45: Effect of OCR on thermal volume change - example test paths in the isotropic $p - T$ plane

Three cases are considered: thermal cycling of mechanically normally-consolidated soil (as in test A1), thermal cycling of mechanically highly over-consolidated soil (as in tests A2 and A3), and thermal cycling of mechanically lightly over-consolidated soil. In the first case, the soil is consolidated from initial mean stress p_0 to p_1 at temperature T_0 . The yield surface passes through this point, as indicated by the dashed line. Upon heating from temperature T_0 to T_1 at mean stress p_1 , the yield surface expands, resulting in plastic contraction of the soil. Subsequent cooling and reheating causes elastic contraction and expansion respectively. For the highly

over-consolidated case, the soil is unloaded from p_1 to p_3 before heating. The stress state of the soil appears to be below (or within) the yield surface, so heating under isotropic loading conditions should cause elastic expansion. However, as discussed below, under one-dimensional (oedometric) conditions, the initial expansion is plastic. Subsequent cooling and reheating causes elastic contraction and expansion, as for the mechanically NC soil. The final case considered is the mechanically lightly over-consolidated soil, which is unloaded from p_1 to p_2 before heating. Below the yield surface, heating causes elastic expansion, but once the yield surface is reached, further heating causes plastic contraction. As in the two previous cases, subsequent cooling and reheating causes elastic contraction and expansion.

The response upon initial heating under oedometric conditions can be understood better by considering the yield surface in the $q - p$ plane, where q is the deviatoric stress, and p is the mean stress, defined in terms of vertical stress σ_v and horizontal stress σ_h :

$$q = \sigma_v - \sigma_h \quad (8.2)$$

$$p = \frac{\sigma_v + 2\sigma_h}{3} \quad (8.3)$$

The initial loading path is shown in Figure 8.46. The yield surface and critical state line (CSL) are also shown. Since this is an oedometer test, vertical stress increases more than horizontal stress, so q increases as well as p . At the end of the loading path, the stress state is on the yield surface, on the wet side of the CSL (sub-critical). If yielding occurs on the wet side of the CSL, it will result in plastic hardening behaviour, i.e. contraction. Initial heating causes plastic contraction. Subsequent cooling and reheating causes elastic contraction and elastic expansion respectively, since the stress state is below the yield surface.

The unloading path is shown in Figure 8.47. The vertical stress reduces until it is less than the horizontal stress (negative q). Eventually, at a low enough pressure, the soil reaches the Hvorslev surface. With further unloading, the yield surface contracts. This explains why it is important to perform the baseline test B3/C3 to obtain the pre-consolidation pressure against which to compare the results from other tests in series B and C. Contraction of the yield surface due to reaching the yield surface on unloading causes a reduction in pre-consolidation pressure, even without temperature change. This is the value against which results must be compared, otherwise the effect of temperature cannot be isolated. At the end of the unloading path, the stress state is on the yield surface, on the dry side of the CSL (super-critical). If yielding occurs on the dry side of the CSL, it will result in plastic softening behaviour, i.e. expansion. Initial heating causes plastic expansion. Subsequent cooling and reheating causes elastic contraction and elastic expansion respectively, since the stress state is below the yield surface.

The thermally-induced sub-incremental strain predicted by the IC Thermal model for tests A1-3 (test paths: Figure 8.1) is shown in Figure 8.48. In test A1 ($P = 1500$ kPa, OCR 1), initial heating causes plastic contraction. Subsequent cooling causes elastic contraction. There is a residual (permanent) contractive strain following the initial heating/cooling cycle. Further thermal cycling does not result in additional plastic strain, but heating and cooling causes elastic expansion and contraction.

In test A2 ($P = 300$ kPa, OCR 5), initial heating causes plastic expansion. Subsequent cooling causes elastic contraction. There is a residual (permanent) expansive strain following the initial heating/cooling cycle. As in test A1, further thermal cycling does not result in additional plastic strain, but heating and cooling causes elastic expansion and contraction.




Figure 8.46: Yield surface in the $q - p$ plane - NC loading



Figure 8.47: Yield surface in the $q - p$ plane - NC loading followed by unloading to OC

The behaviour for test A3 ($P = 50 \text{ kPa}$, OCR 30) is qualitatively similar to A2, except the expansive strain due to initial heating is greater for test A3. This is because at higher OCR values, the yield surface is engaged at a lower stress, and the gradient of the flow vector increases, resulting in greater plastic strain for a given change in stress (which in this case, is due to heating).



images/kss_results/kss_ICFEP_Str_comp.pdf

Figure 8.48: Behaviour predicted by IC Thermal model for tests A1-3

The variation in pressure and temperature against time for test A1 is given in Figure 8.49. First, the slurry is consolidated from 2.5 kPa to 1500 kPa at 22.5 °C. Then two thermal cycles are applied at 1500 kPa on the normally-consolidated soil. The first cycle (*cycle 1*) comprises heating from 22.5 °C to 70 °C and cooling from 70 °C to 5 °C. The second cycle (*cycle 2*) comprises heating from 5 °C to 70 °C, and cooling from 70 °C to 22.5 °C. Cooling from 22.5 °C to 5 °C was controlled using the chiller. All other thermal paths were controlled using the heaters, through TRIAX. Performing the second thermal cycle allowed the effect of multiple thermal cycles to be observed. The reason for truncating the second thermal cycle was the limited programme timescale. The variation in pressure and temperature against time for tests A2 and A3 is given in Figures 8.50 and 8.51 respectively. The total duration for each test was approximately 14 days.

The thermally-induced sub-incremental strain for tests A1-3 is shown in Figure 8.52. The increment start point is the start of the first heating stage. In test A1 (NC), cycle 1 heating causes contraction, which increases linearly with increasing temperature. Subsequent cooling causes further contraction, which increases linearly with reducing temperature, so that cycle 1 results in an overall, permanent contraction. This behaviour agrees with results from the literature, that heating NC soil causes contraction following completion of primary consolidation (Paaswell, 1967; Plum and Esrig, 1969; Towhata et al., 1993; Abuel-Naga et al., 2005; Ng et al., 2017; Sittidumrong et al., 2019), and that this contraction is not reversed upon cooling (Towhata et al., 1993; Abuel-Naga et al., 2005).

images/kss_results/kss_A1_P_T_time.pdf

Figure 8.49: Pressure and temperature vs time for test A1 - full test

images/kss_results/kss_A2_P_T_time.pdf

Figure 8.50: Pressure and temperature vs time for test A2 - full test

images/kss_results/kss_A3_P_T_time.pdf

Figure 8.51: Pressure and temperature vs time for test A3 - full test

images/kss_results/kss_A_comp_T_Str.pdf

Figure 8.52: Sub-incremental strain for thermal cycles in tests A1-3 (positive strain = contraction)

The results from the thermal cycle in tests B1 and B2, discussed in Section 8.5.4, confirm the cycle 1 behaviour for test A1. Cycle 2 heating causes expansion at low temperatures, which transitions into contraction at higher temperatures. The resultant strain due to the full cycle 2 heating path is negligible. Cycle 2 cooling causes contraction. The gradient of both cooling paths is the same. As with the previous cycle, cycle 2 causes an overall, permanent contraction. This additional irreversible contraction is lower for cycle 2, which suggests, in agreement with the literature, that for NC soil, most strain occurs during the first thermal cycle, and accumulation of strain reduces with each cycle (Di Donna and Laloui, 2015; Vega and McCartney, 2015; Ng et al., 2017; Sittidumrong et al., 2019).

In test A2 ($OCR = 5$), initial heating causes expansion, which increases linearly with increasing temperature. Subsequent cooling causes contraction. At the end of cycle 1, there is an overall expansion. Cycle 2 heating causes linear expansion. The expansion due to cycle 2 is less than for initial heating. Cycle 2 cooling causes linear contraction, which reverses the expansion due to second heating.

In test A3 ($OCR = 30$), initial heating causes linear expansion, of similar magnitude to test A2 initial heating. Subsequent cooling causes negligible further strain. The overall expansion at the end of cycle 1 is greater than in test A2. Cycle 2 heating causes linear expansion. As in test A2, the expansion due to cycle 2 heating is less than for initial heating. Cycle 2 cooling causes a slight contraction.

The results for test A2 and A3 generally agree with the literature. There is a consensus that initial heating of highly OC soil causes expansion (Towhata et al., 1993; Abuel-Naga et al., 2005; François et al., 2007; Di Donna and Laloui, 2015; Vega and McCartney, 2015; Favero et al., 2016). Most authors concluded that initial thermal expansion is irreversible (Vega and McCartney, 2015; Favero et al., 2016). Abuel-Naga et al. (2005) concluded that this initial thermal expansion is reversible, although as discussed in Section 2.4.2, their results appear to suggest otherwise.

These results can be compared to the behaviour predicted by the IC Thermal constitutive model in Figure 8.48, to assess the ability of the model to capture the observed soil behaviour.

First, considering test A1 (normally-consolidated), the model is able to simulate the plastic contraction due to initial heating, and elastic contraction due to subsequent cooling, as shown by the residual contractive displacement following this cycle. However, the model cannot replicate the further accumulation of plastic strain following the first thermal cycle seen in the measured data. Instead, it is assumed that further cycling results in elastic strains only.

Next, considering tests A2 and A3 (over-consolidated), the model is able to simulate the plastic expansion due to initial heating, and elastic contraction to subsequent cooling. As in test A1, the model cannot replicate the further accumulation of strain following the first thermal cycle seen in the measured data.

For the first heating path, the model shows higher expansive strain for test A3 (50 kPa, $OCR = 30$) than A2 (300 kPa, $OCR = 5$). However, the measured strain following initial heating is almost the same for both tests. In the model, the cooling response is the same for both tests. The measured cooling response is different. In test A2, cycle 1 cooling causes contractive strain, while in test A3, it causes negligible strain. In the model, the thermal response is independent of temperature history for thermal OCR values greater than one (i.e. following the first heating path). The measured response shows that the temperature history affects the thermal response, and that temperature cycling of thermally over-consolidated soil causes plastic strain to develop.

The individual strain components for test A1 are given in Figure 8.53. Here, *total* strain refers to total, thermally-induced, sub-incremental strain. *Thermal* strain refers to strain due to

thermal expansion of the soil solids, and is calculated from the thermal expansion coefficient given in Table 8.1. *Mechanical* strain is strain due to thermally-induced mechanical effects, and is calculated from the total and thermal strains. The definition and calculation of the individual strain components is presented in Section 4.6.1.

The thermal strain is expansive for temperatures above 22.5 °C (relative to the initial condition) and contractive for temperatures below this. The calculated mechanical strain is therefore more contractive than the total strain for temperatures above 22.5 °C, and less contractive for temperatures below this. For test A1, the total contractive strain due to cooling is slightly higher than predicted from purely thermal effects (in which case, the gradient of the cooling path would be the same as the gradient of the thermal strain). The mechanical strain is contractive throughout the test.



Figure 8.53: Components of thermally-induced strain for test A1 (positive strain = contraction)

The individual strain components for test A2 are given in Figure 8.54. The mechanical strain is expansive for initial heating, then expansive for subsequent cooling paths, and contractive for reheating paths. Following the first thermal cycle, the change in mechanical strain is small. This means that for cycle 2, most change in total strain can be attributed to purely thermal effects.

The individual strain components for test A3 are given in Figure 8.55. As in test A2, the mechanical strain is expansive for initial heating, then expansive for subsequent cooling paths, and contractive for reheating paths. During initial cooling, the expansive mechanical component is almost the same magnitude as the contractive thermal component, resulting in negligible change in total thermal strain.

The void ratio response for tests A1-3 is shown in Figure 8.56. The void ratio has been normalised by the void ratio at the start of the increment. In test A1, the void ratio reduces most during initial heating. Subsequent cooling results in a small reduction in void ratio. Cycle 2 heating

images/kss_results/kss_A2_T_Str_components.pdf

Figure 8.54: Components of thermally-induced strain for test A2 (positive strain = contraction)


images/kss_results/kss_A3_T_Str_components.pdf

Figure 8.55: Components of thermally-induced strain for test A3 (positive strain = contraction)

causes a further reduction in void ratio, which is smaller than for the first heating stage. Cycle 2 cooling causes a similar reduction in void ratio to cycle 1 cooling.

In test A2, initial heating causes an increase in void ratio. Subsequent cooling causes a further increase in void ratio. Cycle 2 heating causes a small reduction in void ratio, which is reversed during cycle 2 cooling.

In test A3, initial heating causes an increase in void ratio, of similar magnitude to test A2 initial heating. Subsequent cooling causes a further increase in void ratio. This increase due to cooling is several times greater than the increase due to initial heating. Cycle 2 heating causes a small reduction in void ratio, again of similar magnitude to test A2 cycle 2 heating. Cycle 2 cooling causes an increase in void ratio, which is greater than the reduction due to cycle 2 heating.



images/kss_results/kss_A_comp_T_e.pdf

Figure 8.56: Normalised void ratio for thermal cycles in tests A1-3

The measured and corrected displacements for test A3 are shown in Figure 8.57. The two corrections, vertical compliance, and confining ring (CR) correction are also plotted. Displacement, rather than strain, has been shown, since the corrections are applied to the displacement (or equivalently, the height) term, from which the strain is then calculated. Both corrections are important, and are of similar magnitude to the measured displacement. In fact, for the second thermal cycle, the magnitude of each correction is greater than the change in displacement, although they act in opposite directions, so that the total combined correction is small. As the number of cycles increases, the change in measured displacement reduces, but so (potentially) does the error in the vertical compliance, as the compliance becomes more repeatable and less hysteretic. Compliance effects are most important for measurement of thermal volume change. For measurement of the effects of temperature on soil properties, as in test series B and C, the effect of compliance is much less important (and less complex, since there is no need to apply the confining ring correction for isothermal loading stages). For example, a similar comparison is made between measured and corrected displacements for test C1 in Figure 8.26.

images/kss_results/kss_compliance_A3.pdf

Figure 8.57: Comparison of measured and corrected data for test A3

8.5.4 Effect of pressure level on thermal volume change


The results from test series A are useful for investigating the effect of multiple thermal cycles. There are clear differences in the responses, in terms of thermal volume change, to the same thermal path. However, these differences could be due to pressure level, or OCR, or a combination of both. To determine the effect of pressure level and OCR in isolation, the thermal paths from tests in series B and C can be compared with those from test series A.

The effect of pressure level on thermal volume change can be considered by comparing the thermal paths for tests A1, B1, and B2. In tests B1 and B2, this thermal cycle comprised heating from 22.5 °C to 50 °C (B1) or 70 °C (B2), cooling to 5 °C, and heating from 5 °C to 22.5 °C. This can be compared to the equivalent thermal path for test A1. In these tests, the thermal cycle was applied to normally-consolidated specimens, at different pressure values. Any difference in the thermal volume change can therefore be attributed to the pressure level. The test conditions are summarised in Table 8.8. Here, e_0 refers to the void ratio at the start of the thermal cycle.

Table 8.8: Test summary: effect of pressure level on thermal volume change for OCR = 1

Test	Thermal path [°C]	OCR [-]	Pressure [kPa]	e_0 [-]
A1	22.5 → 70 → 5 → 22.5	1	1500	0.51
B1	22.5 → 50 → 5 → 22.5	1	300	0.64
B2	22.5 → 70 → 5 → 22.5	1	300	0.63

The sub-incremental strain due to initial heating for tests A1, B1, and B2 is shown in Figure 8.58. The close agreement between the responses for tests B1 and B2 suggests that the results are reliable. In all cases, initial heating results in contractive strain. The strain is greater for test A1 than for B1 and B2. This suggests that pressure level does affect thermal volume change, and that for normally-consolidated KSS, thermal volume change due to initial heating increases with increasing pressure. Initial cooling results in further contractive strain for all three tests. The gradient of the cooling path appears to be independent of both pressure level and maximum cyclic temperature. Cycle 2 heating results in expansion for all three tests. However, this expansion is greater for test A1. This suggests that pressure level only affects the thermal volume change due to heating, while thermal volume change due to cooling is independent of pressure level, for normally-consolidated KSS.



images/kss_results/kss_comparison_P.pdf

Figure 8.58: Effect of pressure level on thermal strain for OCR 1 (positive strain = contraction)

The influence of initial void ratio should be noted at this point. The initial void ratio, at the start of heating, is lower for test series A, than test series B and C, as shown in Tables 8.8, 8.9, and 8.10. This is because the maximum consolidation pressure in test series A was 1500 kPa, whereas in test series B and C, it was 300 kPa. This consolidation results in a reduction in void ratio, which is only slightly reversed during unloading, as shown schematically in Figure 8.59. The maximum consolidation pressure has far greater influence on void ratio than the current pressure, for over-consolidated KSS.

For the three thermal paths carried out on NC soil (A1, B1 and B2), in which all specimens are consolidated from slurry, with approximately the same void ratio at 300 kPa (see Table 8.3), pressure level and void ratio are effectively interchangeable. If void ratio had a major effect on thermal volume change, then all tests in series A should be expected to have similar thermal behaviour, as should all tests in series B and C. This was not observed to be the case. The clear differences in the thermal response for tests A1-3 cannot be attributed to the change in void

ratio due to unloading, which is minor. Likewise, the difference in the thermal response for tests B1 and B2 (normally-consolidated) and tests C1 and C2 (over-consolidated), discussed in the next section, cannot be attributed to the marginally higher initial void ratio for tests C1 and C2. In both cases, OCR appears to be a far more important determinant of thermal response.



Figure 8.59: Schematic showing effect of initial loading and unloading on void ratio

8.5.5 Effect of over-consolidation ratio on thermal volume change

The effect of over-consolidation ratio (OCR) on thermal volume change can be considered by comparing the initial heating paths for tests at the same pressure level, but different OCR values. Any difference in the thermal volume change can therefore be attributed to the OCR.

Two sets of tests can be compared. In tests A2, B1, and B2, a thermal cycle was applied to specimens at the same pressure, 300 kPa, but different OCR values. The test conditions are summarised in Table 8.9. In tests A3, C1, and C2, specimens were heated at the same pressure, 50 kPa, but different OCR values. The test conditions are summarised in Table 8.10. In both tables, e_0 refers to the void ratio at the start of the thermal cycle.

The results for initial heating at 300 kPa, for tests A2, B1, and B2, are shown in Figure 8.60. The effect of OCR is stark. In tests B1 and B2, where the soil was normally-consolidated, initial heating causes contraction, whereas in test A2, at the same pressure level, with over-consolidated soil, initial heating causes expansion. The cooling paths for all three tests are contractive, but the gradient is steeper for the over-consolidated soil in test A2 (contraction amount is lower). Interestingly, the gradient of the initial heating path for test A2 is similar to the gradient of the cooling path for tests B1 and B2. Cycle 2 heating causes expansion for all three tests. The expansion amount for test A2 is greater than for tests B1 and B2, and is similar in magnitude to the expansion observed for cycle 2 heating in test A1, at 1500 kPa, shown in Figure 8.58. This similarity, between the initial cycle 2 heating response for test A1 ($P = 1500$ kPa, OCR 1) and test A2 ($P = 300$ kPa, OCR 5), suggests that similar soil behaviour may be observed either by increasing pressure level (loading), or increasing OCR (unloading). To clarify, this does not mean that they are equivalent, just that in some cases, they have similar effects, and that for example, it would be impossible to accurately infer the loading history of a soil based solely on its response to heating or cooling.

Table 8.9: Test summary: effect of OCR on thermal volume change for $P = 300$ kPa

Test	Thermal path [$^{\circ}\text{C}$]	Pressure [kPa]	OCR [-]	e_0 [-]
A2	22.5 \rightarrow 70 \rightarrow 5 \rightarrow 22.5	300	5	0.53
B1	22.5 \rightarrow 50 \rightarrow 5 \rightarrow 22.5	300	1	0.64
B2	22.5 \rightarrow 70 \rightarrow 5 \rightarrow 22.5	300	1	0.63

Table 8.10: Test summary: effect of OCR on thermal volume change for $P = 50$ kPa

Test	Thermal path [$^{\circ}\text{C}$]	Pressure [kPa]	OCR [-]	e_0 [-]
A3	22.5 \rightarrow 70	50	30	0.55
C1	22.5 \rightarrow 50	50	6	0.66
C2	22.5 \rightarrow 70	50	6	0.64

images/kss_results/kss_comparison_OCR_300.pdf

Figure 8.60: Effect of OCR on thermal strain for $P = 300$ kPa (positive strain = contraction)

The results for initial heating at 50 kPa, for tests A3, C1, and C2, are shown in Figure 8.61. This time, in contrast to the previous result, the effect of OCR is not significant. Heating causes a similar amount of expansion for all three tests, despite the difference in OCR. All of these soils can be considered highly over-consolidated.

images/kss_results/kss_comparison_OCR_50.pdf

Figure 8.61: Effect of OCR on thermal strain for $P = 50$ kPa (positive strain = contraction)

To summarise the results from the three comparisons:

- initial heating of normally-consolidated KSS causes contraction, which increases with pressure;
- initial heating of over-consolidated KSS causes expansion, which is independent of OCR, for OCR between 6 and 30 (between 5 and 30 if tests A2 and A3 are compared, as in Figure 8.52);
- initial cooling of KSS causes contraction, which is independent of pressure, but reduces with OCR;
- cycle 2 heating of KSS causes expansion, which increases with pressure for normally-consolidated soil, and is greater for over-consolidated soil than NC soil at the same pressure.

8.5.6 Compression characteristics

In the IC Thermal constitutive model, several assumptions are made about the effect of temperature on the normal consolidation line (NCL). The first is that the gradient of the normal consolidation lines (and swelling lines) are independent of temperature. The second is that an increase in temperature causes the NCL to shift to lower void ratios, so that for the same pressure level, the void ratio is lower at higher temperature. The final assumption is that the position of the NCL is uniquely determined by temperature, and does not depend on temperature history. These assumptions are discussed below using the data from test series B and C.

The effect of thermal history on the gradient of the normal consolidation line (NCL) at ambient temperature is considered using the data from test series B, shown in Figure 8.62. There is a small, possibly negligible, reduction in the compression index C_c (reduction in the gradient of the NCL) with increasing maximum cyclic temperature T_{max} .

images/kss_results/kss_B_NCL.pdf

Figure 8.62: Void ratio vs pressure for tests B1-3 - NCL

The effect of temperature on the gradient of the NCL is considered using the data from test series C, for temperatures of 22.5 °C, 50 °C and 70 °C, shown in Figure 8.63. The gradient of the NCL increases by a small amount with temperature. This result does not agree with the assumption made in the IC Thermal constitutive model, that the gradient of the NCL is independent of temperature.

The results for test series B and C are compared in Figure 8.64. The reduction in C_c with increasing T_{max} can be seen for test series B, in contrast to the increase in C_c with increasing T for test series C.

Note that when determining the gradient of the NCL, results must be plotted in terms of void ratio, not normalised void ratio. The schematic in Figure 8.65 shows why this is important.

images/kss_results/kss_C_NCL.pdf

Figure 8.63: Void ratio vs pressure for tests C1-3 - NCL

images/kss_results/kss_Cc.pdf

Figure 8.64: Compression index C_c for test series B and C

In Figure 8.65a the gradient of both lines is the same. However, in Figure 8.65b when normalised by their initial void ratios, the gradient of the dashed line, with lower initial void ratio, is greater than the solid line.



Figure 8.65: Schematic showing (a) void ratio and (b) normalised void ratio for two hypothetical normal consolidation lines

In both test series, e_0 reduces with temperature. In test series B, C_c reduces with temperature. The normalised responses, shown in Figure 8.37, have almost identical gradients, underestimating this reduction, since the higher cyclic temperature responses (lower e_0) become relatively steeper. In test series C, C_c increases with temperature. The normalised responses, shown in Figure 8.27, over-estimate this increase, since the higher temperature responses (lower e_0) become relatively steeper.

The effect of temperature on the position of the NCL is shown in Figure 8.66. The ambient temperature response for test C3 is shown in Figure 8.66a. A straight line has been fitted through the NCL for pressure from 25 kPa to 300 kPa, and extended to the higher pressure range. Compare this to the 70 °C reloading response for test C2 shown in Figure 8.66b. In this case, there is a greater reduction in void ratio at 300 kPa than for test C3. This result agrees with the assumption made in the IC Thermal constitutive model, that an increase in temperature causes the NCL to shift to lower void ratios.

The effect of temperature history (thermal over-consolidation) on the position of the NCL is shown in Figure 8.67. The response for test B3 is shown in Figure 8.67a, for the case where the soil has a thermal OCR of 1. A straight line has been fitted through the NCL for pressure from 25 kPa to 300 kPa, and extended to the higher pressure range. Compare this to the response for test B2 shown in Figure 8.67b, where the soil has experienced a thermal cycle and has a thermal OCR greater than 1. In this case, there is a greater reduction in void ratio at 300 kPa than for test B3.

This result disagrees with the assumption made in the IC Thermal constitutive model, that the position of the NCL is uniquely determined by temperature, and does not depend on temperature history. The thermal cycle in test B2 causes a reduction in void ratio, and since the subsequent unloading and reloading paths do not seem to be significantly affected by temperature history, the result is that the NCL for test B2 plots at a lower void ratio.

images/kss_results/KSS_C3_NCL.pdf

(a)

images/kss_results/KSS_C2_NCL.pdf

(b)

Figure 8.66: Effect of temperature on position of NCL (a) test C3 (b) test C2

images/kss_results/KSS_B3_NCL.pdf

(a)


images/kss_results/KSS_B2_NCL.pdf

(b)

Figure 8.67: Effect of temperature history on position of NCL (a) test B3 (b) test B2

The literature consensus is that current temperature has a negligible effect on the gradient of the NCL. Some researchers observed an increase in C_c with increasing temperature (Plum and Esrig, 1969). Others observed no significant effect on C_c (Gray, 1936; Finn, 1952; Eriksson, 1989; Tidfors and Sällfors, 1989; Towhata et al., 1993). Tidfors and Sällfors (1989) found that the position of NCL is uniquely determined by current temperature, whereas Plum and Esrig (1969) found that its position depends not just on the current temperature, but on the temperature history.

The effect of temperature on the coefficient of volume compressibility m_v is considered using the data from test series C. m_v quantifies the consolidation magnitude (how much the soil consolidates under a given load). The values for m_v are plotted for the reloading path at three different temperatures in Figure 8.68. m_v increases for pressure values from 100 kPa to 300 kPa, as the over-consolidated soil approaches the yield point. Above 300 kPa, m_v reduces with increasing pressure, as the normally-consolidated soil becomes stiffer. Based on the limited data, temperature does not appear to have a significant effect on m_v . At higher temperature, m_v is higher. The reduction in m_v between 300 kPa to 2400 kPa is greater at higher temperature, so that the difference in m_v with temperature becomes less significant at higher pressure.




images/kss_results/kss_mv_P.pdf

Figure 8.68: Coefficient of volume compressibility m_v for tests C1, C2, C3 (reloading path)

For the coefficient of volume compressibility, there is no clear literature consensus. Mon et al. (2013) found m_v to reduce with increasing temperature, for over-consolidated soil only. For normally-consolidated soil, temperature had no measurable effect. Di Donna and Laloui (2015) found no effect on m_v , for either over-consolidated or normally-consolidated soil. Favero et al. (2016) on the other hand found m_v to increase with increasing temperature.

8.5.7 Consolidation characteristics

The effect of temperature on the coefficient of consolidation c_v is considered using the data from test series C. c_v quantifies the consolidation rate (how quickly the soil consolidates under a given load). The values for c_v are plotted for the reloading path at three different temperatures in Figure 8.69. c_v reduces with increasing pressure. Based on the limited data, temperature does not appear to have a significant effect on c_v .




images/kss_results/kss_cv_P.pdf

Figure 8.69: Coefficient of consolidation c_v for tests C1, C2, C3 (reloading path)

This result differs from the literature consensus, which is that temperature has a clear and measurable effect on *rate* of primary consolidation. c_v increases with increasing temperature (Finn, 1952; McGinley, 1983; Towhata et al., 1993; Abuel-Naga et al., 2005; Mon et al., 2013; Di Donna and Laloui, 2015; Favero et al., 2016). The reason for this difference is possibly the method of load application. In the TC oedometer, at the end of an increment, the new, target load is not instantaneously applied. Instead, displacement is controlled, increased or decreased at a maximum rate set in TRIAX, until the target load is reached. Whilst the same control parameters are used for all tests, this method of load application affects the shape of the incremental pressure-displacement response, from which t_{50} , then c_v , is calculated. A potential improvement to the method of load application has been proposed in Chapter 9.

8.5.8 Coefficient of permeability

The effect of temperature on the coefficient of permeability k is considered using the data from test series C. k quantifies how easily a fluid with a particular dynamic viscosity flows through a soil. The values for k are plotted for the reloading path at three different temperatures in Figure 8.70. Temperature does not appear to have a significant effect on k .



images/kss_results/kss_k_P.pdf

Figure 8.70: Coefficient of permeability k for tests C1, C2, C3 (reloading path)

The intrinsic permeability, shown in Figure 8.71, appears to reduce with increasing temperature. Intrinsic permeability, unlike the coefficient of permeability, is an intrinsic property of the soil. The coefficient of permeability k is similar for all three tests. This means that the pore water was able to flow through at the same velocity. The dynamic viscosity of water μ_w reduces with temperature, in the range of temperatures considered. Dynamic viscosity is a measure of how easily the fluid shears. If the dynamic viscosity is lower, the fluid will flow more easily. So the water in test C2, at 70 °C should flow more easily, and quickly, than in test C3, at 22.5 °C, because it has lower dynamic viscosity. However, the result from Figure 8.70 shows that this is not the case. Something about the soil (either its void ratio, or structure/fabric) is causing the water to flow through more slowly than predicted based on its dynamic viscosity only. In other words, the intrinsic permeability is lower.

The result for k differs from the literature consensus, which suggests that the coefficient of permeability increases with increasing temperature (Towhata et al., 1993; Romero et al., 2001; Villar and Lloret, 2004; Abuel-Naga et al., 2005; Di Donna and Laloui, 2015). Moritz (1995) found that k reduces with increasing temperature, but they suggested that this result was erroneous. This difference is possibly because k was calculated using the previously-calculated coefficient of consolidation c_v . As discussed in Section 8.5.7, the values for c_v should be treated with suspicion due to the method of load application used.

images/kss_results/kss_Kint_P.pdf

Figure 8.71: Intrinsic permeability K_{int} for tests C1, C2, C3 (reloading path)

8.6 Summary

Three series of tests were carried out on an artificial clay, KSS, using the temperature-controlled oedometer. The aim of these tests was to evaluate the final methodology developed for tests on clay, and determine the capabilities and limitations of the current equipment set-up. Before each soil test, an individual calibration test was performed to measure the vertical thermal and mechanical compliance of the equipment for that particular test path.

In test series A, thermally-induced volume change was investigated, by performing thermal cycles at different OCR and pressure values. These results were combined with results from test series B and C to isolate the effects of OCR and pressure level. Both OCR and pressure level were found to affect volume change behaviour. Initial heating of NC KSS caused contraction, which increased with pressure. Initial heating of OC KSS caused expansion, which was independent of OCR, for the OCR values tested (5, 6 and 30). Initial cooling of OC and NC KSS caused contraction, which was independent of pressure, but reduced with OCR. For KSS at an OCR of 30, cooling caused negligible strain. A second heating path caused expansion, which increased with pressure level and OCR, although there was no significant difference between the expansion amount for highly over-consolidated KSS, at OCR values of 5 and 30.

In test series B, the effect of thermal over-consolidation on reloading behaviour was investigated. A thermal cycle was performed on normally-consolidated soil, which was then unloaded and reloaded beyond the initial pre-consolidation pressure to determine the effect of thermal OCR on pre-consolidation pressure and compression index C_c . Pre-consolidation pressure was found to increase with increasing thermal OCR, which fits with the current understanding of soil thermal behaviour. The gradient of the normal consolidation line (NCL), or compression index, was

found to reduce slightly with increasing thermal OCR.

In test series C, the effect of current temperature on reloading behaviour was investigated. An over-consolidated soil was heated to a target temperature, then reloaded beyond the initial, ambient-temperature pre-consolidation pressure. Pre-consolidation pressure was found to reduce with increasing temperature. This too fits with the current understanding of soil thermal behaviour. The gradient of the NCL was found to increase with increasing temperature.

These results were qualitatively compared with the assumptions used in the IC Thermal constitutive model. The model is able to predict the volumetric response during the first thermal cycle applied to the soil, for both normally-consolidated and highly over-consolidated soil, but cannot predict the accumulation of thermal strain due to repeated thermal cycling observed in test series A. The model assumes that the position of the normal consolidation line depends on temperature, but is independent of temperature history. In fact, both were found to affect the position of the NCL. An improved constitutive model should account for the following observed behaviours:

- Repeated thermal cycling results in the accumulation of permanent strain, which is contractive for normally-consolidated KSS, and expansive for over-consolidated KSS.
- The position of the NCL is affected both by temperature, *and* temperature history.
- The gradient of the NCL (compression index, C_c) increases with temperature, but reduces with maximum cyclic temperature.

Several additional tests are suggested in Chapter 9, to obtain more information on the shape of the yield surface, the effect of sub-ambient temperatures on mechanical properties, and to enable comparison with, and a better understanding of, the results already obtained.

Chapter 9

Conclusions

9.1 Introduction

The primary aim of the research was to develop a new piece of laboratory equipment, the temperature-controlled oedometer. In this chapter, the research objectives are discussed, and key results and conclusions are presented. Recommendations are given for potential improvements to the equipment, and future tests.

On a personal note, it is anticipated, or at least hoped, considering the real and present issues facing the planet, that this research continues in the spirit with which it began - to make things better.

9.2 Research objectives

In this section, the research objectives given in Section 1.2 are revisited, with a discussion as to what extent the objectives have been met. This includes a summary of the key research findings, and the resulting conclusions.

The primary research objectives were as follows:

1. Develop a new temperature-controlled (TC) oedometer for thermal testing
2. Calibrate the TC oedometer for thermal testing
3. Develop clear, comprehensive methodologies for calibration, testing, and data processing, for the TC oedometer
4. Validate these methodologies through tests on soil

A temperature-controlled oedometer has been developed, which can be used to perform thermal tests under oedometric conditions, up to a maximum vertical pressure of 2.6 MPa with the current set-up. Temperature can be controlled above and below ambient temperature, in the range 5 °C to 70 °C, by using a water bath to indirectly heat or cool the soil. This temperature range is appropriate for the proposed applications of the research: design of ground source heating/cooling systems, and design of geological disposal facilities for nuclear waste. Temperatures above ambient are controlled with three 150 W heaters, within the water bath. Temperatures below ambient are controlled by circulating water through a heat exchanger connected to a 1750 W chiller unit. Temperature is measured with three temperature sensors. Isotropic heating of the specimen is

ensured by circulating water through a hollow base-plate, directly below the specimen. This unique circulation design minimises the temperature gradient across the specimen, and is an improvement on previous designs. Displacement is measured using three linear variable displacement transducers (LVDTs), and load is measured using a load cell. The direct effect of temperature on instrumentation (LVDTs and load cell) has been avoided by isolating the instrumentation from the water bath. The LVDTs are mounted on an instrumentation plate, fixed to the loading ram, above the water bath lid. The load cell is positioned above the instrumentation plate. Extension pieces, which incorporate heat dissipators, are used to connect the LVDT cores to the top of the confining ring collar, within the water bath, from which point displacement is measured.

A series of calibration tests has been carried out, to develop the final calibration methodology. The effect of tilting of the loading ram has been measured, and then mitigated by using three LVDTs, equally spaced and equidistant from the centre of the specimen. This enables accurate measurement of displacement (and volume), even if tilting occurs, and enables any tilting effects to be quantified. The effect of friction between the top-cap o-ring, and the inner surface of the confining ring has been measured, and minimised by increasing the depth of the groove in the top-cap which holds the o-ring, and by applying grease to the o-ring and confining ring before testing. A combined thermal and mechanical calibration was developed, which could be used to calculate the vertical equipment compliance under any load and temperature combination within the tested ranges. However, this calibration was found to be inaccurate, so it was abandoned. The effect of filter papers and porous stones on the vertical equipment compliance was investigated through a series of tests. Filter papers were found to be highly-compressible, and to compress irreversibly during the first load application, making calibration difficult. A calibration methodology was developed which involved applying a loading sequence to the filter papers prior to the soil test, both to pre-load the filter papers, and to measure their response, from which the calibration was derived. Again, this calibration was found to be inaccurate. Further tests were performed without filter papers, which was found to simplify the calibration process, and result in a more accurate calibration. Based on the calibration tests, a strong case is presented for avoiding the use of filter papers in oedometer testing, and particularly in thermal oedometer testing.

A correction has been developed to account for the differential lateral thermal expansion of the stainless-steel confining ring and the soil, neither of which is measured, although the coefficient of thermal expansion of stainless-steel is well known. The theoretical cross-sectional area of the specimen under unconfined conditions is calculated (a hypothetical case), and compared to the cross-sectional area of the specimen based on the thermal expansion of the confining ring (the actual case). The correction is applied to the specimen height, by calculating what the change in height would be if the specimen volume remained constant, but the cross-sectional area was calculated for unconfined conditions, rather than the actual conditions. An additional correction is applied, which accounts for the Poisson's ratio of the soil. Unconfined conditions are considered, rather than true one-dimensional conditions, because this makes it possible to separate the mechanical and thermal strain components. Under unconfined conditions, assuming the rate of temperature change is low enough to prevent the development of excess pore-water pressure, there is theoretically no mechanical component of the total strain, and no change in void ratio. By comparing the corrected measured total strain to the theoretical unconfined case, the mechanical component of the total strain can be identified and quantified.

A similar method is used to calculate the void ratio at elevated temperature. The specimen cross-sectional area is taken as the theoretical cross-sectional area of the specimen under unconfined

conditions. The thermal expansion of the solid phase of the soil is calculated, based on the thermal expansion coefficient of the mineral solids. The void ratio is then calculated using the assumed volume of solids, and the measured total volume.

A final methodology has been developed for performing thermal tests using the TC oedometer. This methodology can be split into calibration, testing, and data-processing methods. The calibration methodology involves performing a unique compliance test for each soil test, which follows exactly the same test path, and test conditions, although the increment duration can be reduced, and load/unload and heat/cool rates can be increased, to reduce the compliance test duration. In the compliance test, filter papers are not used, only porous stones, with no additional dummy specimen. From this compliance test, separate calibrations are derived for thermal and mechanical stages. The testing methodology is presented step-by-step in Section 7.2, as in a technical standard. This includes how to set up, run, and finish a thermal test. Details are given on when, and how, to obtain all the necessary measurements. Finally, a data-processing methodology has been developed. Over the course of the research programme, it has become clear that data-processing methods offer just as much potential for subjective decision-making as testing methods. Therefore, in this thesis, effort has been made to develop a data-processing methodology which is (i) as far as possible, user-independent, and (ii) clearly and unambiguously explained. A full explanation is given of exactly how all calculated values are obtained from the measured values, particularly the derivation and application of the calibration. Details are given on the data-sampling method used, and the methodology for calculation of the yield point in reloading tests.

In this thesis, there is no clear division between equipment development, soil testing, and soil behaviour. Tests on bentonite clay (Chapter 5) and Leighton Buzzard sand (Chapter 6) were performed concurrently with the calibration tests covered in Chapter 4. The bentonite tests were important for the development of the final testing and data-processing methodology, particularly calculation of the yield point in reloading tests. The sand tests were important for the development of the final calibration methodology.

The last series of tests, on KSS clay, validated the final methodologies. Several aspects of soil behaviour were tested: thermal volume change (effect of over-consolidation ratio, effect of pressure level, effect of thermal cycling on OC and NC soil), effect of temperature, and temperature history, on pre-consolidation pressure, effect of temperature on compression characteristics (compression index, coefficient of volume compressibility), effect of temperature on coefficient of primary consolidation, and effect of temperature on coefficient of permeability. Both OCR and pressure level were found to affect volume change behaviour. Initial heating of NC KSS caused contraction, which increased with pressure level. Initial heating of OC KSS caused expansion, which was independent of OCR, for the OCR values tested (5, 6 and 30). Initial cooling of OC and NC KSS caused contraction, which was independent of pressure, but reduced with OCR. A second heating path caused expansion, which increased with pressure level and OCR. Pre-consolidation pressure was found to increase with increasing thermal OCR, which fits with the current understanding of soil thermal behaviour. The gradient of the normal consolidation line (NCL), or compression index, was found to reduce slightly with increasing thermal OCR. Pre-consolidation pressure was found to reduce with increasing temperature. This too fits with the current understanding of soil thermal behaviour. The gradient of the NCL was found to increase with increasing temperature.

The new temperature-controlled oedometer is now ready for further thermal testing with KSS, or other soils. Calibration of the equipment has been considered in depth. Clear, comprehensive methodologies have been developed, and validated, for all aspects of the testing process: calibration, soil testing, and data-processing, which are user-independent, as far as possible. The

innovative equipment design, together with these methodologies, enable high-quality data to be obtained, which is valuable for understanding the thermal behaviour of soils, and for calibrating thermo-hydro-mechanical constitutive models.

9.3 Recommendations

9.3.1 Equipment modifications

A number of potential equipment modifications are given below, to extend, and add to, the capabilities of the TC oedometer. These improvements include: increasing the loading capacity and temperature range, more closely approximating one-dimensional conditions during thermal tests, reducing friction effects, incorporating back pressure control, and suction control. Some of these can be achieved with minor changes to the current set-up, whereas others require more significant modifications and testing. To clarify, the TC oedometer is already fully operational, but these modifications may extend or improve the current capabilities of the equipment, or add new capabilities.

In the current configuration, with a 10 kN capacity load cell, and a 70 mm diameter specimen, the TC oedometer can apply vertical pressure up to 2.6 MPa. The model of load cell used, STALC-3 (Section 3.5.2), comes in capacities up to 100 kN, so capacity could be increased to 26 MPa if necessary. No other changes to the equipment set-up would be required. To apply higher vertical pressures than this, a new confining ring would be required, with the same outer diameter as the current confining ring (to fit the slight depression in the upper base-plate), but with an inner diameter of 50 mm. The inner diameter cannot be reduced further than this, because of the spacing of the base drainage holes. A new top-cap would also be required, to fit this new confining ring. With a 100 kN capacity load cell, and a 50 mm diameter specimen, the TC oedometer could apply vertical pressure up to 51 MPa. For even higher loads, more substantial modifications would be required.

The current temperature range is 5 °C to 70 °C. The lower limit is determined by the capacity of the chiller unit (Section 3.5.6), and to avoid the additional complication of freezing of the pore-water. The upper limit is determined by the softening of the PVC-U water bath and lid at temperatures above 70 °C. If higher temperature is required, the PVC-U could be replaced with a material less susceptible to thermal softening, such as PVC-C. This change would not affect the equipment calibration. With this change, the maximum temperature could be increased to at least 85 °C. If a higher heating rate is required, for example, to reduce test duration when performing a large number of thermal cycles on a free-draining soil such as sand, the number of heaters can be increased from the three 150 W capacity heaters currently installed, to a maximum of 11 (or 12, if the temperature transducer within the water bath is removed, and replaced with a heater). Higher capacity cartridge heaters, up to 300 W with similar dimensions to the current ones, can also be used. The total heating capacity could be increased to 3600 W (12 no. 300 W heaters), which is eight times the current capacity of 450 W (3 no. 150 W heaters).

The stainless-steel confining ring could be replaced with an Invar ring of the same dimensions. Stainless-steel and Invar confining rings were tested by Ng et al. (2017), and using a stainless-steel confining ring was found to result in higher measured contractive strain due to thermal cycling, compared to Invar. Invar has a much lower thermal expansion coefficient than stainless-steel, enabling thermal tests to be performed under (approximately) true one-dimensional conditions. If an Invar confining ring was used, an Invar top-cap should also be used. Otherwise, the

differential thermal expansion of the Invar confining ring and stainless-steel top-cap would cause an increase in friction between these components at higher temperatures, which would require further calibration. There would be no significant advantage to replacing any other stainless-steel components with Invar, even those affected by temperature change, for example the loading rod, and the LVDT extension pieces. Only the confining ring affects the shape of the specimen, and thermal expansion of the other components can be accounted for in the vertical thermal compliance. One potential issue would be the differential thermal expansion of the Invar confining ring, and the stainless-steel base-plate. The confining ring sits in a slight depression in the upper base-plate, which prevents lateral movement of the confining ring. The effect of this differential expansion would have to be considered, and possibly mitigated, for example by increasing the diameter of the depression in the upper base-plate, so that it does not compress the confining ring laterally during sub-ambient temperature cooling stages.

To reduce friction between the top-cap o-ring and the inner surface of the confining ring, this surface could be coated with Teflon (PTFE), which has an extremely low coefficient of friction. This method was used by Moritz (1995). After doing so, the friction tests discussed in Section 4.2 could be repeated, to quantify the improvement due to this change, in terms of reduction in friction.

It would be possible, with minor changes to the current equipment set-up, to apply back-pressure to the specimen. This could be done by connecting the upper specimen drainage (through the top-cap), and the lower specimen drainage (through the upper base-plate), via pressure transducers, to volume gauges with air/water interfaces, as shown schematically in Figure 9.1. The top-cap o-ring would isolate the specimen pore-water from the oedometer water bath at hydrostatic pressure. This would enable specimens to be saturated using back-pressure. It would enable permeability to be measured directly, by imposing a back-pressure differential across the specimen and measuring the resulting flow rate. Finally, it would also enable an alternative method of measuring specimen void ratio change, by measuring the water flow in or out of the specimen, although this water volume would have to be calibrated for temperature change.

Modifications to the equipment could be carried out to incorporate control of suction, as well as temperature. A suction-controlled oedometer has already been developed at Imperial College London, by Mantikos (2018). This oedometer shares the same geometry as the TC oedometer, so it would be possible to combine the capabilities of both oedometers by modifying the TC oedometer. As discussed above in relation to back-pressure control, the top-cap o-ring isolates the specimen from the oedometer water bath, so the relative humidity controlled air, used to control suction, could be isolated similarly. The temperature of the incoming air could be controlled by including several loops of heat-conducting stainless-steel tubing within the temperature-controlled water bath, which the air is forced to pass through before reaching the soil specimen. The relative humidity of the air is directly controlled, so does not need to be calibrated, but the temperature needs to be considered when converting the relative humidity into suction.

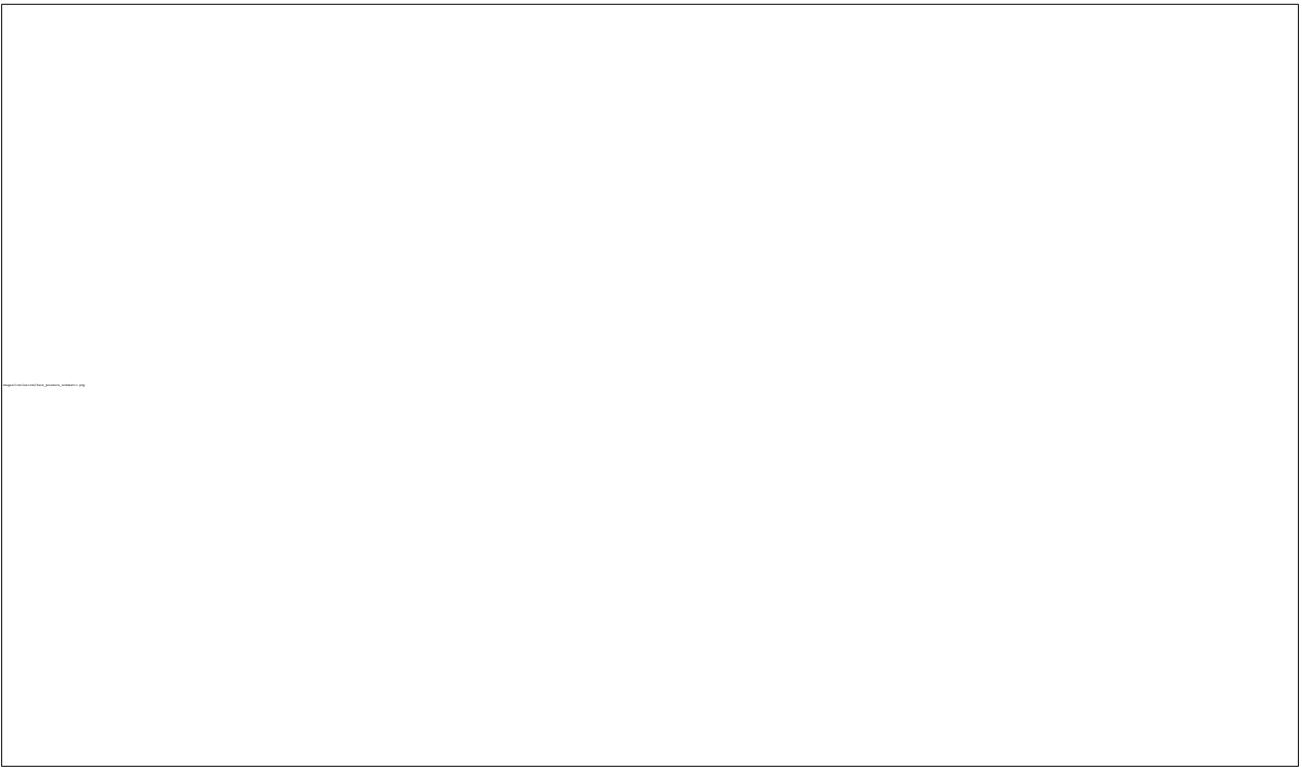


Figure 9.1: Schematic showing proposed back-pressure system: (1) top pressure transducer (2) top volume gauge (3) base pressure transducer (4) base volume gauge

9.3.2 Testing methodology

One of the issues identified from the KSS test results was the effect of non-instantaneous loading on the calculated coefficient of consolidation and coefficient of permeability, discussed in Sections 8.5.7 and 8.5.8. In the TC oedometer, displacement is controlled directly, and load indirectly. The maximum rate of displacement change is controlled in TRIAX through the *max change* value, as explained in Appendix K. If this rate is set too high, once the target load is reached, the control correction, to move the frame up or down, will cause the load to fluctuate above and below the target load, without stabilising. In effect, this will cause hundreds of load/unload cycles to be applied to the soil. However, if the rate of displacement change is set too low, it will take a long time for a new target load to be applied, affecting the incremental displacement response from which coefficient of consolidation is calculated.

Both issues can be avoided by splitting each loading increment into two stages in TRIAX. In the first stage, set the *max change* to a relatively high value. This will reduce the time taken to reach the target load. Set an alarm on the first stage, to move to the next stage once the target load is reached. In the second stage, set the *max change* to a relatively low value. This will prevent the load value from fluctuating either side of the target value, and allow it to stabilise. Two example TRIAX stages are shown below, for a target load of 1500 kPa. In Stage 1, the loading stage, the *max change* is 0.5 mm min^{-1} , whereas in stage 2, the hold stage, the *max change* is $0.005 \text{ mm min}^{-1}$.

[Stage 1]

Description="Load to 1500 kPa"

Device_loadframe=#TRUE#,"Pressure","1500",1500,.1,0,.5,0,"mm/min"

Alarm1=#TRUE#,"Pressure>1500","Continue","2","0:0:0"

[Stage 2]

Description="Hold at 1500 kPa"

Device_loadframe=#TRUE#,"Pressure","1500",1500,.1,0,.005,0,"mm/min"

As a recommendation from a laboratory researcher, to designers of geotechnical software, it would be extremely useful, when changing from the current stage to a different stage, to automatically record this transition in the output. For example in TRIAX, as discussed in Appendix K, alarms can be set, so that control automatically moves from the current stage, to a specified stage, once a certain condition is met. When analysing the output data, it is useful (sometimes essential) to know when the control stage was changed. This could be achieved by writing the stage number, and stage description, to the *Comments* column of the output file. As a recommendation to laboratory researchers using TRIAX, which does not currently have this capability, it often may be better to set these alarms to specific *timer* values, rather than using *wait* times, so that there is no ambiguity as to when stage changes occurred. If nothing else, this makes the analysis faster, and easier, which reduces the chance of making errors.

Another issue with the current version of TRIAX, is that the units for rates of change, defined by the *Increment* value, need to be set manually, and cannot be defined in the configuration settings file. In fact, the units are automatically set to the default units of the variable to be changed, and the *timer* units (minutes). To set rates in hours (for example, a heating rate of 2°C h^{-1}), the units have to be changed manually, via the TRIAX GUI (wizard). It would be better if the units for rates of change could be defined in the configuration settings file.

9.3.3 Further testing

A number of additional tests could be performed to supplement the tests on KSS discussed in Chapter 8. The aim of these additional tests would be to obtain more information about the shape of the yield surface, and the effect of thermal cycling at different OCR and pressure values.

In test series C, an additional test is proposed, with reloading at sub-ambient temperature. The proposed test path is shown in Figure 9.2. This would provide a further point on the yield surface, giving more information on the shape of the yield surface.

Test series A could be repeated with a maximum pressure of 300 kPa. In this case, it is recommended to use different over-consolidation ratios than used previously (OCR 5 for test A2, OCR 30 for test A3). For a pre-consolidation pressure of 300 kPa, at an OCR of 5, the pressure would be 60 kPa, which is acceptable, but for an OCR of 30, the pressure would be 10 kPa, at which point, frictional effects become significant. Pressure values less than 50 kPa should be avoided for thermal stages. Three tests are proposed, at OCR values of 1, 1.1 and 6. Proposed test paths are shown for these three tests, labelled A4-6, in Figure 9.3.

Test A4, at OCR 1, can be compared with tests A1 (same OCR: 1500 kPa, OCR 1), A2 (same pressure: 300 kPa, OCR 5), B1 and B2 (same pressure and OCR: both 300 kPa, OCR 1). Test A5, at OCR 1.1, is lightly over-consolidated, so may reach the yield surface during initial heating.

images/conclusions/loadpath_C_4.pdf

Figure 9.2: Proposed test path for additional test C4

images/conclusions/loadpath_A_4_6.pdf

Figure 9.3: Proposed test path for additional tests A4, A5, and A6

Test A6, at OCR 6, can be compared with tests A3 (same pressure: 50 kPa, OCR 30), C1 and C2 (same pressure and OCR: both 50 kPa, OCR 6).

The effect of thermal cycling was observed in test series A, over two thermal cycles. In future tests, it is recommended to apply additional cycles, time permitting.

Previous researchers (Towhata et al., 1993; Abuel-Naga et al., 2005) have observed that the magnitude of contraction of normally-consolidated soil due to initial heating increases with increasing plasticity. It would be interesting to test this by performing thermal tests on higher plasticity clays, such as London Clay, or bentonite, and comparing the results with those already obtained for KSS.

Appendix A

Calibration: load cell

In this appendix, the method for ambient-temperature calibration of the load cell is given.

The steps here are to calibrate a load cell using a Budenberg dead-weight calibrator, and specific values are given for the Budenberg calibrator at Imperial College London. A schematic of the system is given in Figure A.1.

Equipment required:

- Load cell
- Budenberg dead-weight calibrator

Choose the load increments:

Before starting the calibration, the load increments to be applied need to be chosen. The lowest value will be 108.53 N, which corresponds to applying no additional weights to the dead-weight platform. The highest value should be close to the limit of the load cell. At least five intermediate values should be tested. The effective loads, in N, can be calculated from the Budenberg table.

Account for the weight of the load cell:

The effective loads need to be reduced to account for the weight of the load cell itself. Measure the mass of the load cell, in kg, using an electronic balance, then convert this into weight, in N. Subtract this value from the effective load to get the true effective load, accounting for the weight of the load cell.

images/appendices/budenberg.jpg

Figure A.1: Schematic - Budenberg dead-weight calibrator

Install the load cell and set up for first value:

1. Put the load cell loosely into the Budenberg load frame (tight enough to hold in position, but without applying a load). Screw the large bolts tight either side of the load frame cross-bar.
2. Initial set-up:
 - Motor ON - main piston and dead-weight platform rotating
 - No weights on dead-weight platform
 - Screw press fully open (anticlockwise to open) minus a fraction
 - Primer pump about half open (anticlockwise to open)
 - Primer valve fully open (anticlockwise to open)
3. Screw in (i.e. close) primer pump (coarse adjustment) clockwise (increasing pressure) until:
 - the dead-weight platform rises into the blue (low) range;
 - or, the primer pump is fully screwed in.
4. Close the primer valve fully
5. Screw in (i.e. close) the screw press (fine adjustment) clockwise (increasing pressure) until the dead-weight platform rises into the blue range
6. Open both valves connecting to the loading column
 - This will cause the pressure to drop slightly
 - Screw in the screw press clockwise (increasing pressure) until the dead-weight platform rises into the blue range again.
 - The load can now be calibrated in TRIAX

Record the first value in TRIAX:

1. TRIAX: **Calibrate** → **New calibration**
 - Set **Variables** to the variable name, e.g. load
 - Set **Value** to 108.53 and **Units** to N
 - Press **Record** to record the value. Once the value has been recorded, it will show up in red.

Record subsequent values in TRIAX:

2. Close either one of the two valves connecting to the loading column
3. Apply net load increment:
 - (a) Add additional weights to the dead-weight platform (as per the load increments previously decided)
 - (b) Screw in (close) the screw press until the loading platform rises into blue range
 - (c) Open the valve connecting to the loading column (pressure will drop slightly)
 - (d) Screw in (close) the screw press again, until loading platform rises into blue range
4. Record the value in TRIAX using the same method as for the first value
5. After recording the final value, press **Stop**

Calculate and store the linear regression in TRIAX:

6. TRIAX: **Calibrate** → **Regression**
7. Select the variable, and press **Calculate**, then press **Save Regression**
8. Calibration data are stored in the folder “Calib”, with a file for each individual calibration, e.g. load.cal

View calibrated output in TRIAX:

9. TRIAX: **Monitor** → set **Convert** to ON. Load values should now be shown in N

Results:

The calibration data for the load cell is presented here.

In Table A.1 the calibration data for the load cell is presented. Fifteen load values were used, between 97 N and 4848 N. A load/unload path was calibrated, so that each value was repeated (except the maximum value).

With reference to the table, *Actual value* refers to the effective load applied to the load cell in N, calculated from the Budenberg table, accounting for the weight of the load cell (the known value). *Reading* refers to the voltage output from the load cell, in μV (the value to be calibrated). *Calculated value* refers to the load value calculated from the linear regression, in N, for the current reading. *Absolute error* is the difference, in N, between the actual value and the calculated value:

$$E_{abs} = |F_{actual} - F_{calculated}| \quad (\text{A.1})$$

where:

$$\begin{aligned} E_{abs} &= \text{absolute error [N]} \\ F_{actual} &= \text{known load [N]} \\ F_{calculated} &= \text{calculated load [N]} \end{aligned}$$

The regression for the load cell is shown in Figure A.2, with the regression equation given. The (absolute) error is plotted against actual value (known load) in Figure A.3. The maximum error is 2.21 N. There does not seem to be any relationship between absolute error and load value, nor does the error increase or decrease depending on the direction of loading.

One issue that is apparent is the lack of calibration data for load values below ≈ 100 N, which corresponds to pressures below ≈ 25 kPa for 70 mm diameter specimens. This is a limitation of the calibration method. However, it is not unreasonable to assume that the linear calibration holds for load values below the tested range. In any case, all thermal and reloading paths for the tests on KSS were carried out at a minimum pressure of 50 kPa, which is well within the calibrated range.

Table A.1: Calibration data for 10 kN load cell

Actual value [N]	Reading [μ V]	Calculated value [N]	Absolute error [N]
97.18	214.20	96.82	0.36
167.01	396.72	166.79	0.22
236.89	578.60	236.52	0.37
306.77	758.58	305.52	1.25
376.64	942.24	375.92	0.72
446.48	1124.89	445.95	0.53
516.36	1309.32	516.65	0.29
656.07	1669.89	654.88	1.19
795.87	2034.92	794.82	1.05
1075.34	2763.73	1074.22	1.12
1354.81	3495.69	1354.83	0.02
2053.50	5317.22	2053.14	0.36
2752.19	7142.66	2752.95	0.76
4149.58	10 784.98	4149.29	0.29
4848.27	12 606.34	4847.54	0.73
4149.58	10 785.61	4149.53	0.05
2752.19	7144.14	2753.52	1.33
2053.50	5319.09	2053.86	0.36
1354.81	3501.40	1357.02	2.21
1075.34	2763.09	1073.97	1.37
795.87	2039.36	796.52	0.65
656.07	1673.06	656.10	0.03
516.36	1308.04	516.16	0.20
446.48	1127.43	446.92	0.44
376.64	945.70	377.25	0.61
306.77	763.02	307.22	0.45
236.89	581.77	237.73	0.84
167.01	397.98	167.27	0.26
97.18	219.27	98.76	1.58

images/appendices/loadcell_calib.pdf

Figure A.2: Linear regression for load cell

images/appendices/loadcell_error.pdf

Figure A.3: Regression error for load cell

Appendix B

Calibration: LVDTs

In this appendix, the method for ambient-temperature calibration of the LVDTs is given.

The steps here are to calibrate an LVDT with 10 mm travel within the range -5 mm to 5 mm, such that increasing displacement corresponds to compression (LVDT core moving further into LVDT body).

First method, using micrometer:

Equipment required:

- LVDT body and core
- micrometer, with brass frame and housings for LVDT body and core
- modulator/demodulator
- small flat-blade screwdriver (≈ 2 mm tip)

Set the initial LVDT potential:

1. Connect the LVDT to TRIAX, via the modulator/demodulator
2. Show unconverted LVDT output, in mV, in TRIAX:
 - TRIAX: Monitor \rightarrow set **Convert** to OFF. Values should now be shown in mV
 - If values are not shown in mV (in which case, they are probably in μV), set to mV
 - TRIAX: Settings \rightarrow Channels \rightarrow set to the LVDT channel \rightarrow set **Type** to mV
3. Use the small screwdriver to turn the screw on the front of the modulator/demodulator, to set the initial potential to some value in the range ± 10 mV

Set up the micrometer:

The micrometer set up is shown in Figure B.1 and Figure B.2. The LVDT components and brass housing parts used in the micrometer set up are annotated in Figure B.3.

4. Screw the LVDT core into the brass housing
5. Use the brass spacer to hold the LVDT body in place, and tighten the screw from above until the LVDT cannot be easily moved by hand

6. Turn the micrometer thimble until the displacement reads ≈ 0 mV in TRIAX. Then turn the micrometer thimble so the micrometer value is set to the nearest 0.1 mm. To give an idea, fully inserting the core into the LVDT should give a value of around 6000 mV (6 V), so the total range is around ± 6 V.
7. Make a note of the value on the micrometer thimble. The screw value (whole mm) is not important, only the thimble value (fraction of mm).
8. Turn the micrometer thimble back, anticlockwise, (negative, decreasing values in TRIAX) five turns (5 mm) then a quarter turn extra (0.25 mm), to avoid the backlash effect. Then turn forwards (clockwise, positive in TRIAX) to the initial thimble value noted down previously. For example, if the initial thimble value was 0.6 mm, the current thimble value should also be 0.6 mm. Only turn forwards from this point.

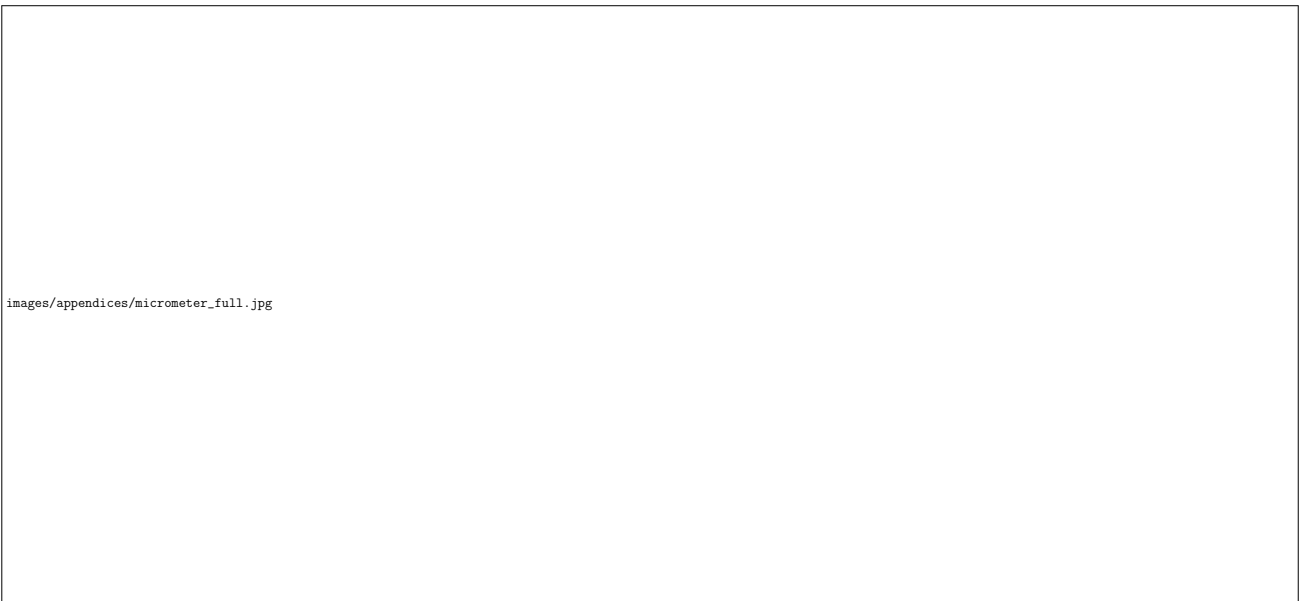


Figure B.1: Photograph of micrometer set up for LVDT calibration


Record the first value in TRIAX:

9. TRIAX: Calibrate \rightarrow New calibration

- (a) Set **Variables** to the variable name, e.g. displacement
- (b) Set **Value** to -5 and **Units** to mm
- (c) Press **Record** to record the value. Once the value has been recorded, it will show up in red.

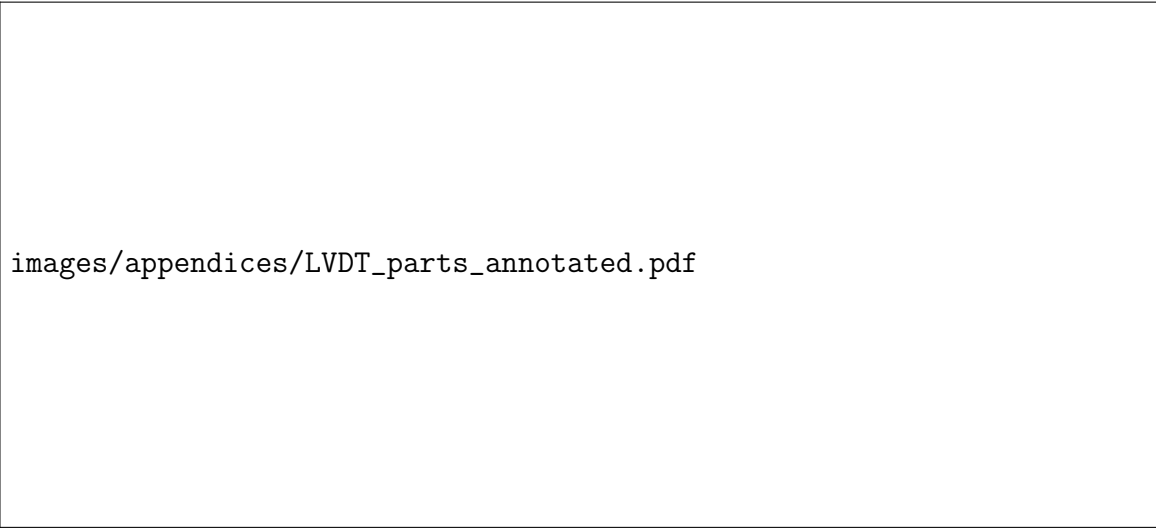
Record subsequent values in TRIAX:

10. Turn the micrometer thimble forward (clockwise, positive in TRIAX) by exactly 1 mm (setting the initial thimble value to an exact 0.1 mm fraction, as discussed above, makes this easier)
11. Press **Record** to record the value
12. Repeat for every mm value up to (and including) 5 mm
13. After recording the final value, press **Stop**



images/appendices/micrometer_detail.jpg

Figure B.2: Photograph of micrometer set up for LVDT calibration - detail



images/appendices/LVDT_parts_annotated.pdf

Figure B.3: Photograph of LVDT components and brass housings for micrometer calibration

Note: If the vernier is accidentally moved past the target value, do not just move it back to the target value, as this will introduce backlash error. Move it back a full quarter turn (0.25 mm), then forwards to the target value.

Calculate and store the linear regression in TRIAX:

14. TRIAX: **Calibrate** → **Regression**
15. Select the variable, and press **Calculate**, then **Save Regression**
16. Calibration data are stored in the folder “Calib”, with a file for each individual calibration, e.g. displacement.cal

View calibrated output in TRIAX:

17. TRIAX: **Monitor** → set **Convert** to ON. Displacement values should now be shown in mm

Alternative method, using digital calipers:

This alternative method is also accurate, and probably quicker than using a micrometer. It is also less error-prone because it does not require reading off a vernier scale.

Equipment required:

- LVDT body and core
- digital calipers with brass housings for LVDT body and core
- modulator/demodulator

Set the initial LVDT potential:

- Use the method above to set the initial LVDT potential to some value in the range ± 10 mV

Set up the calipers:

- Attach the brass parts to the calipers
- Fix the LVDT body and LVDT core to the brass housing parts (finger tight only)
- Adjust the calipers until displacement reads ≈ 0 mV on TRIAX
- Initialise the calipers to zero by pressing the zero button on the calipers
- Move the calipers out to approximately -5 mm, plus a little more (≈ 0.1 mm). Keep them in a vertical position.

Recording the calibration:

- Move the calipers back in to approximately -5 mm, and record the first value in TRIAX, using the method described above.
- Move the callipers in, at ≈ 1 mm intervals, recording each value in TRIAX, up to the final value of ≈ 5 mm. It is not necessary to move the calipers in by exact mm increments - instead, just record the caliper values, e.g. -4.91 mm, -3.85 mm and -2.98 mm etc.

Calculate and store the linear regression in TRIAX:

- Calculate and store the regression in the same way as in the previous method.

Results:

The calibration data for the three LVDTs used in the temperature-controlled oedometer are presented here.

In Table B.1, the calibration data for LVDT 1 is presented. With reference to the table, *Actual value* refers to the displacement measured by the micrometer, in mm (the known value). *Reading* refers to the voltage output from the LVDT, in mV (the value to be calibrated). *Calculated value* refers to the displacement value calculated from the linear regression, for the current reading, in mm. *Absolute error* is the difference, in mm, between the actual value and the calculated value:

$$E_{abs} = |D_{actual} - D_{calculated}| \quad (B.1)$$

where:

$$\begin{aligned} E_{abs} &= \text{absolute error [mm]} \\ D_{actual} &= \text{known displacement [mm]} \\ D_{calculated} &= \text{calculated displacement [mm]} \end{aligned}$$

The regression for LVDT 1 is shown in Figure B.4, with the regression equation given. The (absolute) error is plotted against actual value (known displacement) in Figure B.5. The maximum error for LVDT 1 is 0.015 mm.

The equivalent calibration data for LVDT 2 is given in Table B.2, and shown graphically in Figure B.6 and Figure B.7. The maximum error for LVDT 2 is 0.020 mm.

The equivalent calibration data for LVDT 3 is given in Table B.3, and shown graphically in Figure B.8 and Figure B.9. The maximum error for LVDT 3 is 0.009 mm.

Table B.1: Calibration data for LVDT 1

Actual value [mm]	Reading [mV]	Calculated value [mm]	Absolute error [mm]
-5	-3585.11	-4.985	0.015
-4	-2881.65	-4.001	0.001
-3	-2168.78	-3.003	0.003
-2	-1454.31	-2.004	0.004
-1	-740.29	-1.005	0.005
0	-25.33	-0.004	0.004
1	688.17	0.994	0.006
2	1402.92	1.995	0.005
3	2120.11	2.998	0.002
4	2841.09	4.007	0.007
5	3556.24	5.008	0.008

Table B.2: Calibration data for LVDT 2

Actual value [mm]	Reading [mV]	Calculated value [mm]	Absolute error [mm]
-5	-3703.22	-4.980	0.020
-4	-2976.07	-4.006	0.006
-3	-2231.40	-3.008	0.008
-2	-1483.18	-2.006	0.006
-1	-735.34	-1.005	0.005
0	13.05	-0.003	0.003
1	761.02	0.999	0.001
2	1505.90	1.997	0.003
3	2257.36	3.003	0.003
4	3007.55	4.008	0.008
5	3748.65	5.000	0.000

Table B.3: Calibration data for LVDT 3

Actual value [mm]	Reading [mV]	Calculated value [mm]	Absolute error [mm]
-5	-3864.81	-4.991	0.009
-4	-3100.67	-4.005	0.005
-3	-2320.96	-3.000	0.000
-2	-1545.48	-2.000	0.000
-1	-769.62	-0.999	0.001
0	3.50	-0.002	0.002
1	776.03	0.995	0.005
2	1549.70	1.993	0.007
3	2328.10	2.997	0.003
4	3110.73	4.006	0.006
5	3885.90	5.006	0.006

images/appendices/LVDT_1_calib.pdf

Figure B.4: Linear regression for LVDT 1

images/appendices/LVDT_1_error.pdf

Figure B.5: Regression error for LVDT 1

images/appendices/LVDT_2_calib.pdf

Figure B.6: Linear regression for LVDT 2

images/appendices/LVDT_2_error.pdf

Figure B.7: Regression error for LVDT 2

images/appendices/LVDT_3_calib.pdf

Figure B.8: Linear regression for LVDT 3

images/appendices/LVDT_3_error.pdf

Figure B.9: Regression error for LVDT 3

Appendix C

Calculation: perpendicular and total thermal expansion coefficients

Linear thermal expansion coefficients are sometimes given in the literature as a pair of linear coefficients, parallel and perpendicular to the layers of the soil structure. See for example, McKinstry (1965).

Montmorillonite is the primary constituent of Bentosund A100, the soil used in the bentonite tests described in Chapter 5. It has a basic three-layer structure, with an octahedral unit (gibbsite) between two tetrahedral units (silica). These basic structures are bonded together into a lattice by the van de Waals force, which is weak, and allows water to easily enter the lattice. This means that the lattice can absorb a lot of water, which causes swelling.

A schematic of a montmorillonite lattice is given in Figure C.1. The perpendicular (α_{\perp}) and parallel (α_{\parallel}) measurement directions are indicated.

The parallel and perpendicular linear coefficients can be converted into a single volumetric coefficient. Consider a solid, which when heated, undergoes strain in three directions, ϵ_1 , ϵ_2 and ϵ_3 , as shown schematically in Figure C.2. Again, the perpendicular (α_{\perp}) and parallel (α_{\parallel}) measurement directions are indicated.

The volumetric strain ϵ_v is the sum of the linear strains:

$$\epsilon_v = \epsilon_1 + \epsilon_2 + \epsilon_3 \quad (\text{C.1})$$

The thermal expansion coefficient is the thermally-induced strain for a given change in temperature. The linear thermal expansion coefficient, in direction n , is given by:

$$\alpha_{L,n} = \frac{\epsilon_n}{\Delta T} \quad (\text{C.2})$$

where:

- $\alpha_{L,n}$ = linear thermal expansion coefficient in direction n
- ϵ_n = linear strain in direction n
- ΔT = change in temperature



Figure C.1: Montmorillonite lattice, showing perpendicular and parallel measurement directions

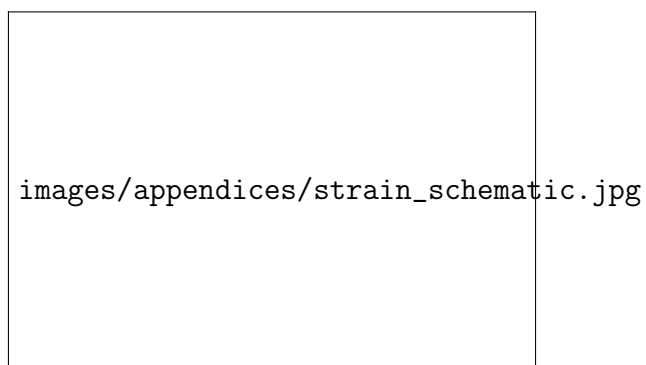


Figure C.2: Strain directions, with perpendicular and parallel measurement directions

This equation can be rearranged as:

$$\epsilon_n = \alpha_{L,n} \cdot \Delta T \quad (\text{C.3})$$

The volumetric thermal expansion coefficient is given by:

$$\alpha_v = \frac{\epsilon_v}{\Delta T} \quad (\text{C.4})$$

where:

α_v = volumetric thermal expansion coefficient

ϵ_v = volumetric strain

ΔT = change in temperature

Substituting Equation C.1 into Equation C.4:

$$\alpha_v = \frac{\epsilon_1 + \epsilon_2 + \epsilon_3}{\Delta T} \quad (\text{C.5})$$

Substituting Equation C.3 into Equation C.5:

$$\alpha_v = \frac{\alpha_{\parallel} \Delta T + \alpha_{\parallel} \Delta T + \alpha_{\perp} \Delta T}{\Delta T} \quad (\text{C.6})$$

which reduces to:

$$\alpha_v = 2\alpha_{\parallel} + \alpha_{\perp} \quad (\text{C.7})$$

Note that for isotropic minerals, where $\alpha_{\parallel} = \alpha_{\perp}$, this equation simplifies to:

$$\alpha_v = 3\alpha_L \quad (\text{C.8})$$

Appendix D

Calculation: linear and volumetric thermal expansion coefficients

Given the linear thermal expansion coefficient of a soil, it is possible to calculate the volumetric thermal expansion coefficient.

The linear thermal expansion coefficient α_L is defined as:

$$\alpha_L = \frac{\Delta l}{l_i} \cdot \frac{1}{\Delta T} \quad (\text{D.1})$$

where:

α_L = linear thermal expansion coefficient
 Δl = change in length
 l_i = initial length
 ΔT = change in temperature

which can be rearranged as:

$$\Delta l = l_i \alpha_L \Delta T \quad (\text{D.2})$$

The volumetric thermal expansion coefficient α_v is defined as:

$$\alpha_v = \frac{\Delta V}{V_i} \cdot \frac{1}{\Delta T} \quad (\text{D.3})$$

where:

α_v = volumetric thermal expansion coefficient
 ΔV = change in volume
 V_i = initial volume
 ΔT = change in temperature

Consider a rectangular cuboid with initial length l_i , width w_i and height h_i , at initial temperature T_i , as shown in Figure D.1.

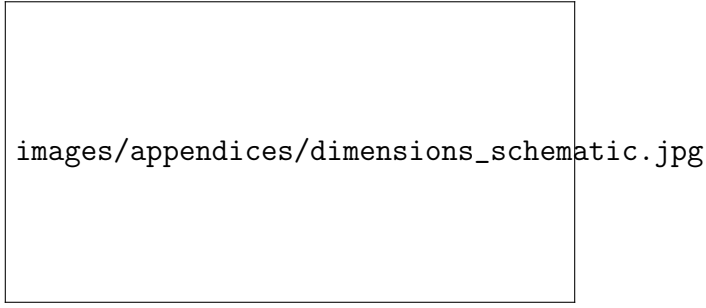


Figure D.1: Dimensions of rectangular cuboid at initial temperature T_i

The initial volume V_i of the cuboid, at initial temperature T_i , can be calculated as:

$$V_i = l_i w_i h_i \quad (\text{D.4})$$

The temperature is increased by ΔT from the initial temperature T_i , to the final temperature $T_i + \Delta T$. At temperature $T_i + \Delta T$, the volume is given by:

$$V_i + \Delta V = (l_i + \Delta L)(w_i + \Delta w)(h_i + \Delta h) \quad (\text{D.5})$$

where Δl , Δw and Δh are the change in length, width and height respectively.

Substituting Equation D.2 into Equation D.5:

$$V_i + \Delta V = (l_i + l_i \alpha_L \Delta T)(w_i + w_i \alpha_L \Delta T)(h_i + h_i \alpha_L \Delta T) \quad (\text{D.6})$$

$$= l_i(1 + \alpha_L \Delta T) \cdot w_i(1 + \alpha_L \Delta T) \cdot h_i(1 + \alpha_L \Delta T) \quad (\text{D.7})$$

$$= l_i w_i h_i (1 + \alpha_L \Delta T)^3 \quad (\text{D.8})$$

Substituting Equation D.4 into Equation D.8 and expanding the bracket:

$$V_i + \Delta V = V_i [1 + 3(\alpha_L \Delta T) + 3(\alpha_L \Delta T)^2 + (\alpha_L \Delta T)^3] \quad (\text{D.9})$$

Dividing both sides by V_i :

$$1 + \frac{\Delta V}{V_i} = 1 + 3(\alpha_L \Delta T) + 3(\alpha_L \Delta T)^2 + (\alpha_L \Delta T)^3 \quad (\text{D.10})$$

$$\frac{\Delta V}{V_i} = 3(\alpha_L \Delta T) + \underbrace{3(\alpha_L \Delta T)^2 + (\alpha_L \Delta T)^3}_{\alpha_L \ll 1 \text{ so neglect these terms}} \quad (\text{D.11})$$

This gives the volumetric strain $\Delta V/V_i$ as a function of the linear thermal expansion coefficient and the change in temperature:

$$\frac{\Delta V}{V_i} \approx 3(\alpha_L \Delta T) \quad (\text{D.12})$$

Rearranging gives:

$$\alpha_L \approx \frac{1}{3} \underbrace{\left(\frac{\Delta V}{V_i} \cdot \frac{1}{\Delta T} \right)}_{\alpha_v - \text{Equation D.3}} \quad (\text{D.13})$$

Linear thermal expansion coefficient α_L can be given in terms of the volumetric thermal expansion coefficient α_v :

$$\alpha_L \approx \frac{1}{3} \alpha_v \quad (\text{D.14})$$

Alternatively, α_v can be given in terms of α_L :

$$\alpha_v \approx 3\alpha_L \quad (\text{D.15})$$

Note that this is valid for soil with isotropic thermal properties only. For materials such as compacted clay, which may be strongly anisotropic, the linear thermal expansion coefficient will vary, depending on the orientation of the clay platelets. In this case, the linear thermal expansion coefficients parallel and perpendicular to the clay lattice structure can be considered, as discussed in Appendix C.

Appendix E

Definitions: compression parameters

In this appendix, some basic compression parameters are defined. These are: compression index, C_c and swelling index, C_s ; plastic compressibility, λ and elastic compressibility, κ ; coefficient of volume compressibility, m_v and oedometric modulus, E_{oed} . These are standard definitions, included here for completeness.

Compression index, C_c and swelling index, C_s

The compression index, C_c , is the slope of the one-dimensional normal compression line (1D NCL) and critical state line (CSL) in $e - \log_{10} \sigma'_v$ space, where e is the void ratio, and σ'_v is the effective vertical stress. The swelling index, C_s , is the slope of the swelling (unloading) line, in $e - \log_{10} \sigma'_v$ space. This is shown schematically in Figure E.1.

$$C_c = \frac{\Delta e}{\Delta \log_{10} \sigma'_v} \quad (\text{E.1})$$

Plastic compressibility, λ and Elastic compressibility, κ

The plastic compressibility, λ is the slope of the isotropic normal compression line (ISO NCL) in $v - \ln p'$ space, where v is the specific volume, and p' is the mean effective stress. The elastic compressibility, κ is the slope of the swelling (unloading) line in $v - \ln p'$ space. This is shown schematically in Figure E.2.

$$\lambda = \frac{\Delta v}{\Delta \ln p'} \quad (\text{E.2})$$

Coefficient of volume compressibility, m_v and oedometric modulus, E_{oed}

The coefficient of volume compressibility, m_v , sometimes known as modulus of volume change, is a measure of the soil compressibility, or compliance. It is defined as the compressive strain, ϵ_v per unit increase in effective vertical stress σ'_v . It is usually calculated for each loading increment, in which case it is the incremental strain divided by the incremental increase in effective vertical stress. This is shown schematically in Figure E.3.

$$m_v = \frac{\Delta \epsilon_v}{\Delta \sigma'_v} \quad (\text{E.3})$$

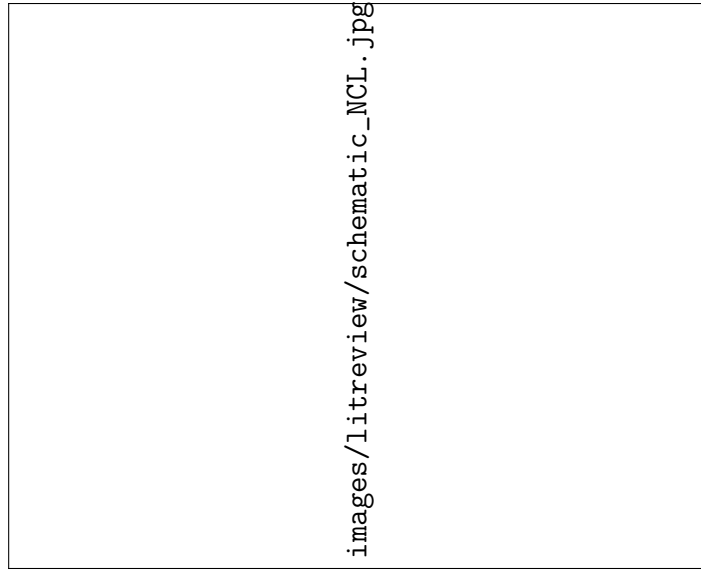


Figure E.1: Schematic - compression index, C_c and swelling index, C_s



Figure E.2: Schematic - plastic compressibility, λ and elastic compressibility, κ

Oedometric modulus, E_{oed}

The oedometric modulus, E_{oed} , or M_o , is a measure of the soil stiffness. It is the inverse, or reciprocal, of coefficient of volume compressibility, m_v . It is defined as the increase in effective vertical stress, per unit increase in compressive strain. As with m_v , it is usually calculated for each loading increment. This is shown schematically in Figure E.4.

$$E_{oed} = \frac{\Delta\sigma'_v}{\Delta\epsilon_v} \tag{E.4}$$

$$E_{oed} = \frac{1}{m_v} \tag{E.5}$$

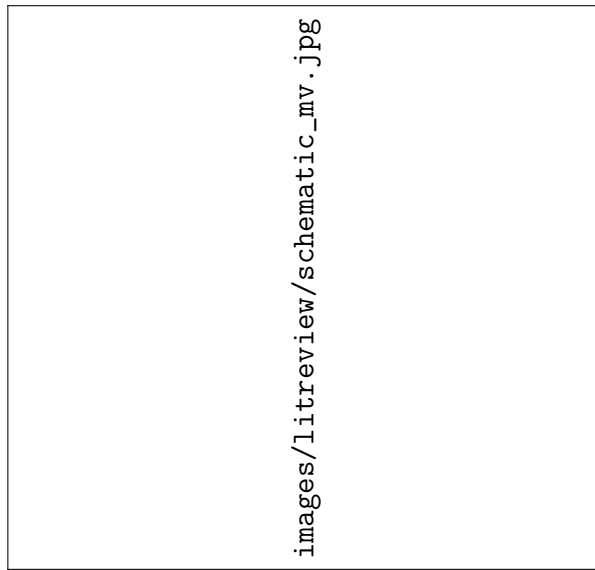


Figure E.3: Schematic - coefficient of volume compressibility, m_v

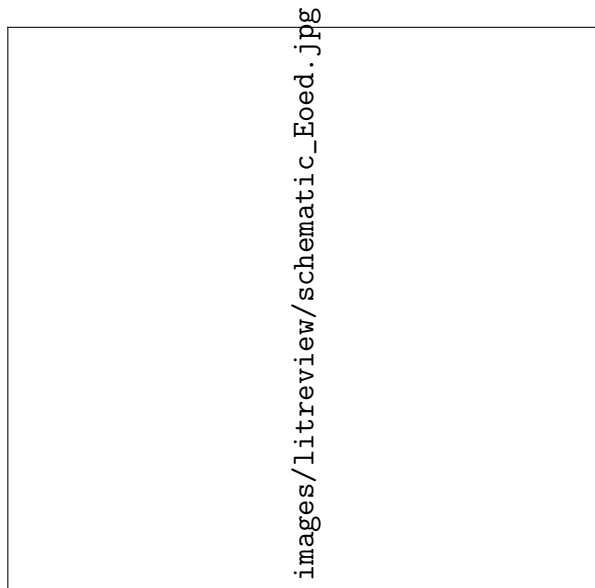


Figure E.4: Schematic - oedometric modulus, E_{oed}

Appendix F

Equipment dimensions

In this appendix, some measured equipment dimensions are given, to give an idea of the size of key components. However, these are not intended to represent reference values to be used in all future thermal testing with the temperature-controlled oedometer. It is recommended to re-measure the equipment dimensions before performing a new series of thermal tests (although not all these values are required, and it is not necessary to re-measure these before each individual test).

The confining ring (CR) and collar dimensions are given in Figure F.1. The LVDTs, associated components, and the top-cap dimensions are given in Figure F.2. The instrumentation plate dimensions are given in Figure F.3 (section) and Figure F.4 (plan).

All dimensions are in mm.

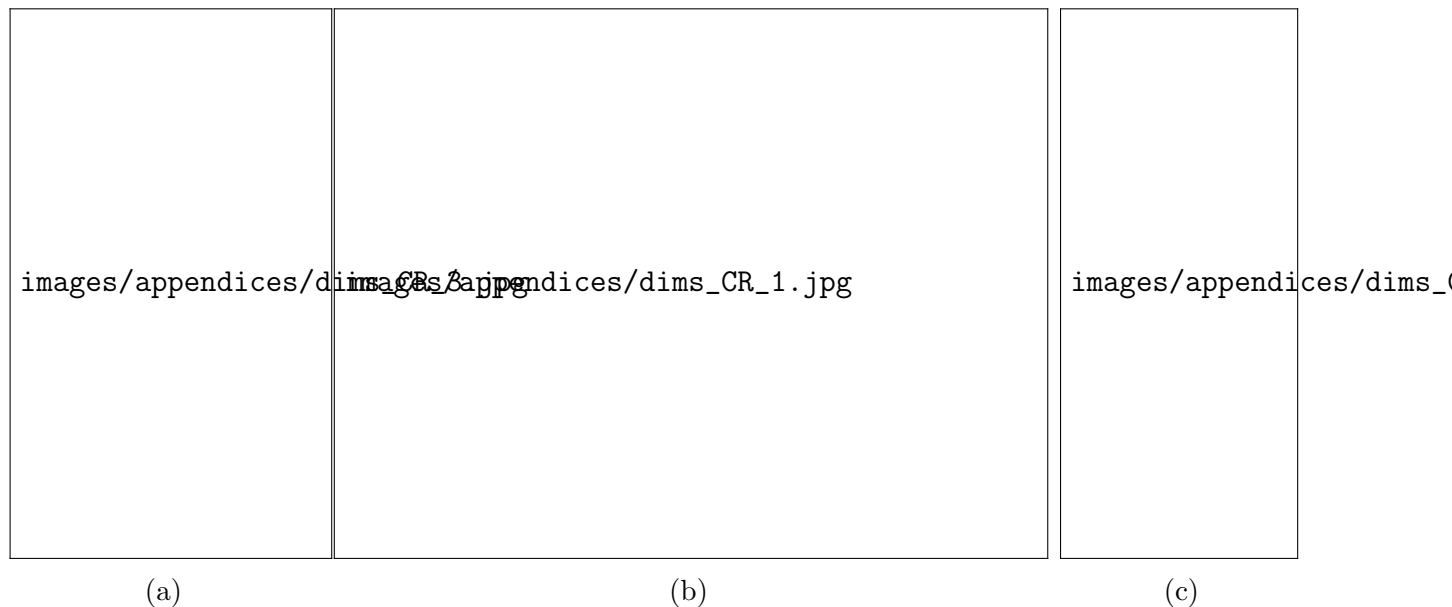


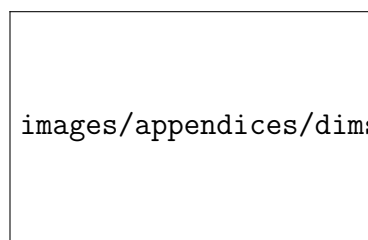
Figure F.1: Confining ring dimensions: (a) CR and collar assembly (b) CR and collar separate (c) holding-down bolt



(a)



(b)



(c)




(d)




(e)

Figure F.2: Equipment dimensions: (a) LVDT body (b) LVDT housing on instrumentation plate (c) heat dissipator (d) LVDT extension piece assembly (e) top-cap and o-ring



images/appendices/dims_IP_section.jpg

Figure F.3: Instrumentation plate dimensions - side view



images/appendices/dims_IP_plan.jpg

Figure F.4: Instrumentation plate dimensions - plan view

Appendix G

Calculation: specimen height using three displacement transducers

When calculating the displacement using three displacement transducers, positioned at 120° intervals, at equal distance from the centre of the specimen, the average (mean) displacement is used. This makes intuitive sense, but can also be proven mathematically. In this calculation, the validity of using the average displacement is shown.

The calculation method is as follows:

- Calculate the average of three vertical displacement values for three equally-spaced points in a plane.
- Calculate the equation of the plane that passes through all three vertical displacement values.
- Calculate the vertical coordinate at the mid-point of the plane (at $x = 0, y=0$).
- Show that this vertical coordinate is the same as the average.

Schematics of the problem are given in Figure G.1. A plan view is shown in Figure G.1a, and a three-dimensional sketch is shown in Figure G.1b. With reference to Figure G.1a, points P, Q, R are three equally-spaced points in the plane. The vertical displacement of points P, Q, R are z_1, z_2 and z_3 respectively.

The three-dimensional coordinates of points P, Q, R are given below, together with the average value:

$$P : (0, 1, z_1) \tag{G.1}$$

$$Q : \left(-\frac{\sqrt{3}}{2}, -\frac{1}{2}, z_2\right) \tag{G.2}$$

$$R : \left(\frac{\sqrt{3}}{2}, -\frac{1}{2}, z_3\right) \tag{G.3}$$

$$\text{Average} : \left(0, 0, \frac{z_1+z_2+z_3}{3}\right) \tag{G.4}$$

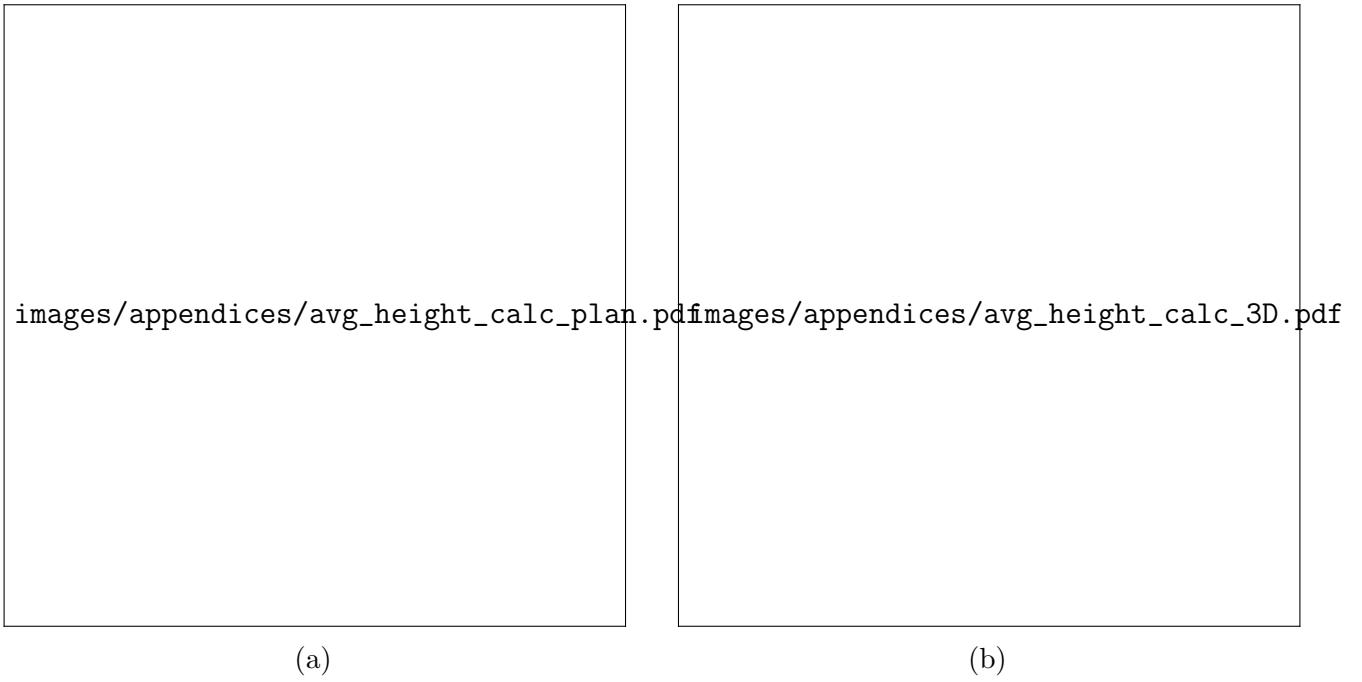


Figure G.1: Calculation of specimen height: (a) plan view (b) 3D sketch

The general equation of a plane is given by:

$$a(x - x_0) + b(y - y_0) + c(z - z_0) = 0 \quad (\text{G.5})$$

where:

(x_0, y_0, z_0) is a point in the plane
 $\langle a, b, c \rangle$ is a vector perpendicular to the plane

Calculate two vectors in the plane:

$$\overrightarrow{PQ} : \left\langle -\frac{\sqrt{3}}{2}, -\frac{3}{2}, (z_2 - z_1) \right\rangle \quad (\text{G.6})$$

$$\overrightarrow{PR} : \left\langle \frac{\sqrt{3}}{2}, -\frac{3}{2}, (z_3 - z_1) \right\rangle \quad (\text{G.7})$$

The cross product of the vectors \overrightarrow{PQ} and \overrightarrow{PR} gives a vector perpendicular to both, and normal to the plane containing them.

$$\overrightarrow{PQ} \times \overrightarrow{PR} = \begin{vmatrix} i & j & k \\ -\frac{\sqrt{3}}{2} & -\frac{3}{2} & (z_2 - z_1) \\ \frac{\sqrt{3}}{2} & -\frac{3}{2} & (z_3 - z_1) \end{vmatrix} \quad (\text{G.8})$$

$$= \begin{vmatrix} -\frac{3}{2} & (z_2 - z_1) \\ -\frac{3}{2} & (z_3 - z_1) \end{vmatrix} i - \begin{vmatrix} -\frac{\sqrt{3}}{2} & (z_2 - z_1) \\ \frac{\sqrt{3}}{2} & (z_3 - z_1) \end{vmatrix} j + \begin{vmatrix} -\frac{\sqrt{3}}{2} & -\frac{3}{2} \\ \frac{\sqrt{3}}{2} & -\frac{3}{2} \end{vmatrix} k \quad (\text{G.9})$$

$$= \left(-\frac{3}{2}(z_3 - z_1) + \frac{3}{2}(z_2 - z_1) \right) i + \left(\frac{\sqrt{3}}{2}(z_3 - z_1) + \frac{\sqrt{3}}{2}(z_2 - z_1) \right) j + \left(\frac{3\sqrt{3}}{4} + \frac{3\sqrt{3}}{4} \right) k \quad (\text{G.10})$$

$$= \left(-\frac{3}{2}z_3 + \frac{3}{2}z_1 \right) i + \left(\frac{\sqrt{3}}{2}z_3 + \frac{\sqrt{3}}{2}z_2 - \sqrt{3}z_1 \right) j + \left(\frac{3\sqrt{3}}{2} \right) k \quad (\text{G.11})$$

Substitute point P (or point Q or R), and the perpendicular vector, into the equation of plane, to get the equation of a plane which passes through the points P, Q, R .

Point P :

$$(x_0, y_0, z_0) = (0, 1, z_1) \quad (\text{G.12})$$

and perpendicular vector:

$$\langle a, b, c \rangle = \left\langle \left(-\frac{3}{2}z_3 + \frac{3}{2}z_1 \right), \left(\frac{\sqrt{3}}{2}z_3 + \frac{\sqrt{3}}{2}z_2 - \sqrt{3}z_1 \right), \left(\frac{3\sqrt{3}}{2} \right) \right\rangle \quad (\text{G.13})$$

Substitute both into Equation G.5 (equation of plane):

$$\left(-\frac{3}{2}z_3 + \frac{3}{2}z_1\right)(x - 0) + \left(\frac{\sqrt{3}}{2}z_3 + \frac{\sqrt{3}}{2}z_2 - \sqrt{3}z_1\right)(y - 1) + \left(\frac{3\sqrt{3}}{2}\right)(z - z_1) = 0 \quad (\text{G.14})$$

Now, find the value of z , by substituting $x = 0$ and $y = 0$ into the equation for the plane which passes through P, Q and R :

$$\left(-\frac{\sqrt{3}}{2}z_3 - \frac{\sqrt{3}}{2}z_2 + \sqrt{3}z_1\right) + \left(\frac{3\sqrt{3}}{2}\right)(z - z_1) = 0 \quad (\text{G.15})$$

Which can be rearranged to give:

$$z = \frac{z_1 + z_2 + z_3}{3} \quad (\text{G.16})$$

This is the same as the z coordinate found by taking the average of the z coordinate values of P, Q and R , as in Equation G.4. This shows that taking the average of the three displacement-gauge values gives the displacement at the centre of the specimen. This average displacement can be used to calculate an accurate specimen volume, irrespective of tilting effects.

The minimum number of displacement transducers required for accurate calculation of specimen volume is two. In this case, they would have to be positioned 180° from each other. In fact, any number of displacement transducers could be used, so long as they were equally spaced, and equidistant from the centre of the specimen. However, a minimum of three are required to understand tilting effects.

Appendix H

Calculation: deformation of dummy specimen

In a number of ambient-temperature compliance tests, discussed in Chapter 4, a brass dummy specimen is used, in place of the soil specimen. In the final calibration methodology, discussed in Chapter 7, no dummy specimen is used, only the upper and lower porous stones. In this appendix, the theoretical vertical mechanical deformation of the dummy specimen is calculated, and shown to be negligible compared to other components of the equipment compliance.

Vertical stress, as a function of the applied load and dummy specimen cross-sectional area, is given by:

$$\sigma = \frac{F}{A} \cdot 1000 \quad (\text{H.1})$$

where:

σ = stress [kPa]

F = applied load [N]

A = dummy cross-sectional area [mm²]

Vertical strain, as a function of the vertical stress and the Young's modulus of the dummy specimen, is given by:

$$\epsilon = \frac{\sigma}{E} \quad (\text{H.2})$$

where:

E = Young's modulus of brass [kPa]

σ = stress [kPa]

ϵ = strain [-]

Change in height of the dummy specimen, as a function of vertical strain and initial height, is given by:

$$\Delta H = \epsilon \cdot H_0 \quad (\text{H.3})$$

where:

ΔH = change in height of dummy [mm]

ϵ = strain [-]

H_0 = initial height of dummy [mm]

Using these equations, the theoretical change in height of the dummy specimen can be calculated for the compliance tests carried out.

Example calculation

This calculation is for one of the brass dummy specimens used for the calibration tests described in Chapter 4.

Properties of the dummy specimen:

Young's modulus of brass E (Granta Design Limited, 2009):

$$E = 100 \times 10^6 \text{ kPa}$$

Initial dimensions - initial diameter d_0 and initial height H_0 :

$$d_0 = 63.4 \text{ mm}$$

$$H_0 = 26.1 \text{ mm}$$

Note that the specimen cross-sectional area is assumed to remain constant.

The change in height is calculated for the maximum vertical load F based on the capacity of the load cell:

$$F = 10 \text{ kN}$$

The change in height ΔH , is calculated using Equations H.1, H.2, and H.3.

$$\Delta H = 0.83 \times 10^{-3} \text{ mm}$$

This is negligible compared to the equipment compliance, which is approximately two orders of magnitude higher. The theoretical deformation ΔH of three dummy samples used in the calibration tests in Chapter 4, of different initial dimensions, is given in Table H.1. In all cases, under the maximum load of 10 kN, the dummy specimen deformation is <0.001 mm.

Table H.1: Brass dummy specimen deformation

Dummy ID	Height [mm]	Diameter [mm]	ΔH under 10 kN load [mm]
1	26.1	63.4	0.83×10^{-3}
2	10.0	69.8	0.26×10^{-3}
3	15.3	50.8	0.75×10^{-3}

Appendix I

Calculation: void ratio at ambient temperature

Three methods can be used to calculate the void ratio at ambient temperature. These methods, the required measurements, calculations, and obtained values, are described in this appendix.

Method 1 provides the most information, but requires the final total mass m_f and the mass of solids m_s , so void ratio can only be calculated following completion of the test.

Method 2 allows void ratio to be calculated during the test, by assuming that the water content of the specimen trimmings is approximately equal to the initial water content of the specimen.

Method 3 requires the final water content w_f , so can only be calculated following completion of the test. The final degree of saturation S_f must be assumed.

Each method requires different measured values. However, the following values are required for *all* three methods.

G_s - specific gravity of solids [-]

ρ_w - density of water [g mm^{-3}]

H_0 - initial height [mm]

ΔH - change in height [mm] (which with H_0 gives height H)

The values that can be obtained by each method are different. However, all methods will calculate height of solids H_s and void ratio e . Method 1 gives the initial and final water content w and degree of saturation S , method 2 gives only the initial values and method 3 gives only the final values (and requires S_f to be assumed). This is summarised in Table I.1.

Table I.1: Obtained values from each void ratio calculation method

Obtained value	Method 1	Method 2	Method 3
e	✓	✓	✓
H_s	✓	✓	✓
w	w_0, w_f	w_0	w_f
S	S_0, S_f	S_0	S_f (assumed)

Method 1

Method 1 requires the final total mass m_f and mass of solids m_s . These can only be obtained at the end of the test.

Measurements

Before test:

H_0 - initial height [mm]

m_0 - initial total mass [g] (required to calculate w_0 and S_0)

During test:

ΔH - change in height [mm]

After test:

m_f - final total mass, before oven drying [g] (required to calculate w_f and S_f)

m_s - mass of solids, after oven drying [g]



Figure I.1: Calculation of void ratio - method 1

Method 1 - Equations

$$H_s = \frac{m_s}{A \cdot \rho_s} \quad (\text{M1.1})$$

$$e = \frac{H - H_s}{H_s} \quad (\text{M1.2})$$

$$w = \frac{m - m_s}{m_s} \quad (\text{M1.3})$$

$$S = \frac{wG_s}{e} \quad (\text{M1.4})$$

where:

A = specimen cross-sectional area [mm²]

e = void ratio [-]

H = total height [mm]

H_s = height of solids [mm]

m = total mass [g]

m_s = mass of solids [g]

S = degree of saturation [-]

w = water content [-]

ρ_s = density of solids [g mm⁻³]

Method 2

Method 2 uses values that can be measured at the start of the test: initial total mass m_0 and initial water content w_0 . In this case, w_0 is measured from trimmings, which is assumed to be similar to the water content of the installed specimen. This means that void ratio can be calculated during the test (unlike method 1 and method 3, in which it can only be calculated at the end of the test). It enables a useful comparison with the void ratio calculated with method 1, as discussed below.

Measurements

Before test:

H_0 - initial height [mm]

m_0 - initial total mass [g]

w_0 - initial water content [-] (from trimmings)

During test:

ΔH - change in height [mm]



images/appendices/VR_flow_calc_m2.pdf

Figure I.2: Calculation of void ratio - method 2

Method 2 - Equations

$$\rho_0 = \frac{m_0}{H_0 \cdot A} \quad (\text{M2.1})$$

$$\rho_{d,0} = \frac{\rho_0}{1 + w_0} \quad (\text{M2.2})$$

$$e_0 = \frac{\rho_s}{\rho_{d,0}} - 1 \quad (\text{M2.3})$$

$$S_0 = \frac{w_0 G_s}{e_0} \quad (\text{M2.4})$$

$$H_s = \frac{H_0}{1 + e_0} \quad (\text{M2.5})$$

$$e = \frac{H - H_s}{H_s} \quad (\text{M2.6})$$

where:

A = specimen cross-sectional area [mm²]

e = void ratio [-]

e_0 = initial void ratio [-]

G_s = specific gravity of solids [-]

H = total height [mm]

H_0 = initial total height [mm]

H_s = height of solids [mm]

m_0 = initial total mass [g]

S_0 = initial degree of saturation [-]

w_0 = initial water content [-] (from trimmings)

ρ_0 = initial total density [g mm⁻³]

$\rho_{d,0}$ = initial dry density [g mm⁻³]

ρ_s = density of solids [g mm⁻³]

Method 3

Method 3 requires the final water content w_f . The final degree of saturation has to be assumed. This assumption is discussed further in the comparison of methods below.

Measurements

Before test:

H_0 - initial height [mm]

During test:

ΔH - change in height [mm]

After test:

w_f - final water content [-]



Figure I.3: Calculation of void ratio - method 3

Method 3 - Equations

$$e_f = \frac{w_f G_s}{S_f} \quad (\text{M3.1})$$

$$e = \frac{H - H_s}{H_s} \quad (\text{M3.2})$$

$$m_s = H_s(A \cdot \rho_s) \quad (\text{M3.3})$$

where:

A = specimen cross-sectional area [mm²]

e = void ratio [-]

e_f = final void ratio [-]

G_s = specific gravity of solids [-]

H = total height [mm]

H_s = height of solids [mm]

m_s = mass of solids [g]

w_f = final water content [-]

S_f = final degree of saturation (assumed) [-]


ρ_s = density of solids [g mm⁻³]

Comparing methods

For method 3, a value for final degree of saturation S_f must be assumed. Degree of saturation S is defined as the ratio between volume of water V_w and volume of voids V_v . In other words, how much of the void space is filled with water.

$$S = \frac{V_w}{V_v} \quad (\text{I.1})$$

Typically, for fully-saturated soils, S_f is assumed to equal 1. However, some soils (for example, swelling clays such as bentonite), the presence of adsorbed water at a higher density than 1 g cm^{-3} results in calculated degrees of saturation greater than 1 (Villar and Lloret, 2004). If instead, the assumed value for final degree of saturation S_f used in method 3 is taken as the value calculated in method 1, then the two methods will give the same void ratio (so long as the same final total mass m is used). This is shown using flow diagrams in Figure I.4. Therefore the main value of method 3 is to provide a mathematical check on method 1.



images/appendices/VR_flow_calc_m1_3_comparison.pdf

Figure I.4: Calculation of void ratio - comparing method 1 and method 3

A more useful comparison can be made between the void ratio calculated using method 1 and method 2. Method 1 uses the final mass of solids m_s to calculate height of solids H_s (and e), whereas method 2 uses the initial total mass m_0 , initial water content w_0 , and initial height H_0 to calculate H_s (and e). A discrepancy between the void ratio calculated using method 1 and method 2 would suggest an error in one or more of the measured values.

Generally, method 2 is preferred. The initial water content (from trimmings) w_0 is a good estimate of the initial water content of the specimen. Method 3 requires the final degree of saturation S_f to be assumed, and gives identical values to method 1, if S_f from method 1 is used. Method 1 requires the final total mass m_f and the mass of solids m_s , which may be less accurate than the initial total mass m_0 due to soil losses during testing and during removal of the specimen from the confining ring.

The following are suggestions for useful checks to make:

- Compare w_0 and S_0 for method 1 and 2.
- Compare e or H_s for method 1,2 and 3 (differences between 1 and 2 suggest measurement error, while differences between 1 and 3 suggest mathematical error).
- Check S_f for method 1 is reasonable.

Calculating void ratio in more than one way provides a useful way of checking the calculation, and indicates the accuracy of measured values. It also provides alternate calculation routes if certain measurements are not obtained (for example, if the specimen is destroyed during extrusion from the confining ring, or lost).

- If m_0 is not measured, e can still be calculated from method 1 or method 3.
- If m_f is not measured, e can still be calculated using any method
- If m_s is not measured, e can still be calculated using method 2 or method 3.

The required measurements for each method are summarised in Table I.2. A measurement that is required for calculation of void ratio is indicated by a tick (✓). Some values are not required for calculation of void ratio, but are required for calculation of other values, and are indicated as such. Also, some values are calculated, but not measured, and are indicated as such. Values that are not required are indicated by a cross (✗).

Table I.2: Required measurements for each void ratio calculation method

Measured value	Method 1	Method 2	Method 3
H_0	✓	✓	✓
ΔH	✓	✓	✓
m_0	For w_0, S_0	✓	✗
m_f	For w_f, S_f	✗	✗
m_s	✓	✗	Calculated using w_f
w_0	Calculated using m_0	✓	✗
w_f	Calculated using m_f	✗	✓

In practice, the aim is always to obtain all measurements, because this provides the most reliable data, allows values to be compared and checked, and means that even if certain measurements are not obtained, it will still be possible to calculate the void ratio.

Appendix J

Methodology: tests on sand

In this appendix, the methodology followed for setting up the sand tests in Chapter 6 is explained. This is the methodology followed for sand tests 1 to 11, with filter papers above and below the specimen, and a porous stone below the specimen. For sand test 12, without filter papers, follow the steps below, with the following changes:

- In steps 5 and 12, do not install the filter papers.
- After levelling the surface in step 9, install the upper porous stone, and measure the depth to the surface using the method described in Section 7.2.
- To set the initial condition in step 13, follow the method described in Section 7.2.

Equipment required:

- small flat-blade screwdriver (≈ 2 mm tip)
- large flat-blade screwdriver (≈ 8 mm tip)
- 5 mm ball-end hex key screwdriver
- high-vacuum grease
- 150 mm steel rule
- small plastic cup
- small plastic funnel

1. Saturate the porous stone using the vacuum
2. Weigh a quantity of dry sand, enough for one test
3. Get the equipment and tools ready
4. If using grease, apply a thin layer of grease to the top-cap o-ring and the inner surface of the confining ring
5. Place the saturated porous stone, with a filter paper on upper surface, at the centre of the oedometer
6. Install the confining ring within the oedometer. Do not install the collar yet.
7. Half-fill the confining ring with reverse-osmosis filtered water

8. Pour the sand carefully into the confining ring
 - Fill the small plastic cup with sand
 - Hold the funnel with the tip just above the surface of the water
 - Gently tap/vibrate the sand from the plastic cup into the funnel
 - Some of the sand grains will float on the surface of the water - stir with a thin metal rod until these grains sink.
9. Set the required depth and level the surface of the sand using the levelling tool, as described below. Measure the depth to the top of the specimen using vernier calipers.
10. Weigh the remaining sand. This mass, together with the initial total mass of sand, is used to calculate the mass of the installed sand specimen.
11. Install the confining ring collar and bolt down with the six holding-down bolts using the 5 mm hex key
12. Screw the top-cap onto the loading arm. Then moisten a filter paper, and press it against the base of the top cap.
13. Set the initial condition. For full details, see below.
 - Using the manual controls on the load frame, raise the loading platform until the top-cap is just above the confining ring.
 - Initialise displacement transducer 4 (D4) level with base of top-cap
 - Using the manual controls on the load frame, raise the loading platform until D4 reading reaches the target value
14. Complete the set-up
 - Install LVDTs 1, 2 and 3
 - Fill the cell with water up to marked level (10L)
 - Plug in the heaters
 - Turn on circulator pump and cooling fan
 - Install outer lid pieces and loosen central lid piece
 - Set the initial position of the LVDTs
 - Use the large flat-head screwdriver to set the height of instrumentation plate.
 - Use the small flat-head screwdriver to set the individual LVDT positions.
15. Begin test in TRIAX
 - Begin Scanning
 - Begin Control

Levelling tool

To level the surface of the sand, a tool was developed, shown in Figure J.1. The tool comprises a rigid, PVC cross-bar, connected using a wing-nut and bolt to a plastic rectangle cut with a slot. The plastic rectangle can be moved up or down by loosening the wing-nut. The target depth to sand surface can be measured using a ruler or vernier calipers, and set by tightening the wing-bolt. The tool can then be brushed across the surface of the sand, with the cross-bar of the tool resting on the upper side of the confining ring.

The best method found is to pour the sand slowly, checking the level frequently. When the level is approaching the target height, level the sand surface using the tool. If there are areas of the surface that are not level with the bottom of the tool, add a small amount of sand, then level again. The process is finished when the surface of the sand is flat, and everywhere exactly level with the bottom of the tool. In this case, moving the tool should not noticeably redistribute the sand, but neither should there be any gap between the sand surface and the tool.



Figure J.1: Photograph of the levelling tool used for sand tests

Setting the initial condition

For sand tests 1 to 11, there was no porous stone above the specimen, only a filter paper. Without the upper porous stone in place, the method used to set the initial condition for clay tests, using one of the LVDTs mounted in a brass housing on the top-cap (Section 7.2), is no-longer valid.

An alternative method was developed, using displacement transducer 4 (DT 4). This transducer was used because it has a 50 mm travel. (Compare to the 10 mm travel for LVDTs 1, 2 and 3, which would need to be reset several times during this process). The procedure for setting the initial condition for sand tests 1 to 11 is shown in Figure J.2 below. This procedure can be used when there is no upper porous stone in place, otherwise the procedure given in Section 7.2 can be used.

First, initialise DT 4 in TRIAX (i.e. set to read zero) when level with the base of the top-cap. This can be done by pressing a steel ruler against the base of the top-cap, and initialising DT 4 against the ruler, as shown in Figure J.2a. When the top-cap is at the level of the top of the confining ring collar, DT 4 will read zero. Now raise the load frame until DT 4 reaches the target value. The target value is the distance from the top of the confining ring collar to the top of the specimen. The target value can be measured directly using vernier calipers, after installing the specimen, but before attaching the top-cap to the loading-ram. Alternatively, the distance from the top of the confining ring (without the collar) can be measured (d_0 in Figure J.2c), and added to the thickness of the confining ring lid (d_1 in Figure J.2c) to give the target value for DT 4.

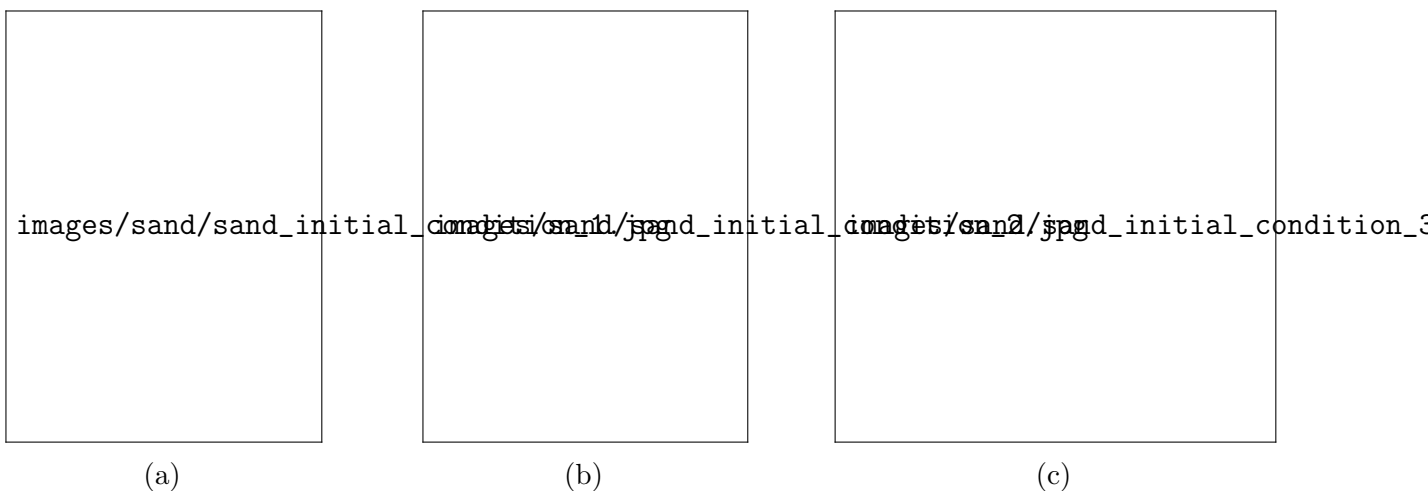


Figure J.2: Schematic showing set-up of initial condition for sand tests

Appendix K

Methodology: writing TRIAX stages in plain text

In this appendix, details of how to write TRIAX stages in plain text are given.

The plain text stages are stored in the configuration settings file, which is stored in the same folder as the TRIAX application, and is named “triax.ini”.

The configuration settings file is organised into sections. The section headings are enclosed within square brackets, as shown below.

```
[Main]
[Devices]
[Channels]
[Regressions]
[Variables]
[Stage 1]...[Stage 2]...etc
[Options]
[Monitor]
[Graph 1]...[Graph 2]...etc
[Scan]
[Control]
[Communications]
[Triaxial]
```

[Main] defines the TRIAX version, equipment ID, and main window size and position.

[Devices] lists the devices used, their number, name, type, settings, and whether the device is enabled or disabled.

[Channels] defines which the channel used by each device, and the units of the device output (either μV or mV).

[Regressions] defines the regressions (calibrations) for converting device output in V to meaningful units.

[Variables] defines the variables used in the program stages. These variables can be outputs from the instrumentation, such as load, user-input values such as specimen diameter, or calculated values such as pressure.

[Stage 1]...[Stage 2]...etc defines the program stages. Generally, this is the only part of the configurations setting file that needs to be modified. Details on how to write the program stages are given below.

[Options] defines some general options, including the data separator to be used for the output (comma or tab), and whether to turn comments on or off. Comments are extremely useful and important, so should be on. The refresh rate for TRIAX components (Monitor, Scan, Control, etc.) can be changed here, but this is easy to do via the TRIAX GUI (wizard).

[Monitor] defines the Monitor settings (not the PC monitor, but the Monitor window within TRIAX, which shows variable values in real time).

[Graph 1]...[Graph 2]...etc defines the graph settings. These settings do not affect the output data, only the appearance of the on-screen graphical output. They can be easily changed via the TRIAX GUI.

[Scan] defines the Scan settings, of which the most important are scan interval (how frequently data are written to the output file), and scan variables (which variable values are written to the output file).

[Control] defines the appearance of the Control window.

[Communications] defines the appearance of the Communications window.

[Triaxial] defines the built-in triaxial program, which was not used for oedometer testing.

Stages

The format used for each stage is the same, as shown in the example below. The stage number is given in the heading, within square brackets.

```
[Stage #]
Description
Device#=#TRUE/FALSE#,
    "Control Equation","Hold value" (as string), Hold value (as number),
    Tolerance, Increment, Max change, "Max change units"
Alarm#=#TRUE/FALSE#, "Control equation and condition",
    "Action", "Next stage", "Wait time"
```

In the first line the stage description is given. The stage details are not written to the output file (although this feature would be extremely useful), but this description makes checking the program much easier.

The next lines give the control details for each device. First, the device is defined as enabled or not for the current stage.

The control equation is the left hand side of an equation in terms of the variables defined in the variables section. To control the value of a single variable, this is just the variable name.

The hold value is the right hand side of the control equation.

The Tolerance defines the acceptable limits for the hold value, before TRIAX will attempt to change the state of the system to get closer to the hold value.

The Increment value is used to change the hold value at a defined rate (continuous, rather than incremental).

The max change defines the maximum rate that a variable can be changed to reach the hold value.

After the control details for each device, the alarm details are given. The control equation and condition define the condition that will trigger an action. This action is either to Stop, Continue to a certain stage, or Wait (hold current conditions for a certain amount of time before continuing).

For example, a stage from KSS test A2 (Stage 38) is shown below. Device6 refers to the load frame, while Device7 refers to the heaters. The value of Pressure is set to 1500 kPa, with a tolerance of ± 0.1 kPa and a maximum change of 0.005 kPa per control update. The value of Temperature_Cell is set to increase at a rate of $2\text{ }^{\circ}\text{C h}^{-1}$ from the current value, with a tolerance of $0.05\text{ }^{\circ}\text{C}$ and a maximum change of 1000 Steps per control update. The interval between control updates can be set in the [Options] section.

Setting the value of a variable to "Current" will override and automatically update the subsequent value (here $22.5\text{ }^{\circ}\text{C}$). Note that the units for rate of temperature change, defined by Increment, need to be set manually using the TRIAX GUI. This is a limitation of the software, which has been noted in the thesis conclusions.

```
[Stage 38]
Description="Heat to 70C at 1500 kPa"
Device6=#TRUE#,"Pressure","1500",1500,.1,0,.005,0,"mm/min"
Device7=#TRUE#,"Temperature_Cell","Current",22.5,.05,2,1000,2,"Steps"
Alarm1=#TRUE#,"Temperature_Cell>70","Continue","39","0:0:0"
```

Using this method, it was possible to write hundreds of stages, and reduce program errors to almost zero. For example, the complete KSS test series, including calibration tests, comprised over 170 stages, and was completed without a single program error.

For more details, consult the TRIAX user manual (Toll, 2002).

Bibliography

- Abuel-Naga, H.M., Bergado, D.T., and Bouazza, A. (2007). Thermally induced volume change and excess pore water pressure of soft Bangkok clay. *Engineering Geology*, 89(1), pp.144–154.
- Abuel-Naga, H.M., Bergado, D.T., Ramana, G.V., Grino, L., Rujivipat, P., and Thet, Y. (2006). Experimental evaluation of engineering behavior of soft Bangkok clay under elevated temperature. *Journal of Geotechnical and Geoenvironmental Engineering*, 132(7), pp.902–910.
- Abuel-Naga, H.M., Bergado, D.T., Soralump, S., and Rujivipat, P. (2005). Thermal consolidation of soft Bangkok clay. *Lowland Technology International*, 7(1), pp.13–21.
- ASTM International (2011). *D2435/D2435M - 11 Standard test methods for one-dimensional consolidation properties of soils using incremental loading*. West Conshohocken, Pennsylvania: ASTM.
- Baracos, A. (1976). Clogged filter discs. *Géotechnique*, 26(4), pp.634–636.
- Batchelor, G.K. (2000). *An introduction to fluid dynamics*. Cambridge: Cambridge University Press.
- British Standards Institution (1990). *BS 1377-5:1990 Methods of test for soils for civil engineering purposes. Part 5: compressibility, permeability and durability tests*. London: BSI.
- Campanella, R.G. and Mitchell, J.K. (1968). Influence of temperature variations on soil behavior. *Journal of the Soil Mechanics and Foundations Division: proceedings of the American Society of Civil Engineers*, 94(3), pp.709–734.
- Cengel, Y., Turner, R., and Cimbala, J. (2016). *Fundamentals of thermal-fluid sciences*. 5th ed. New York: McGraw-Hill.
- Clark, S.P., ed. (1966). *Handbook of physical constants*. Memoir 97. New York: Geological Society of America.
- Cui, Y.-J., Tang, A.-M., Qian, L.-X., Ye, W.-M., and Chen, B. (2011). Thermal-mechanical behavior of compacted GMZ bentonite. *Soils and Foundations*, 51(6), pp.1065–1074.
- Cunningham, M.R. (2000). *The mechanical behaviour of a reconstituted, unsaturated soil*. Thesis (PhD). Imperial College London.
- Di Donna, A. and Laloui, L. (2015). Response of soil subjected to thermal cyclic loading: experimental and constitutive study. *Engineering Geology*, 190, pp.65–76.

- Dixon, D., Gray, M.N., Lingnau, B., Graham, J., and Campbell, S.L. (1993). Thermal expansion testing to determine the influence of pore water structure on water flow through dense clays. *46th Canadian Geotechnical Conference*, Saskatoon, Canada, pp.177–183.
- Duffy, A. (2012). *Essential physics* [online]. Available from: https://www.webassign.net/question_assets/buelempphys1/chapter13/section13dash2.pdf [visited on June 2020].
- El Tawati, A. (2010). *Impact of the rate of heating on the thermal consolidation of compacted silt*. Thesis (MSc). University of Colorado.
- Engineering Toolbox (2003). *Coefficients of linear thermal expansion* [online]. Available from: https://www.engineeringtoolbox.com/linear-expansion-coefficients-d_95.html [visited on June 2020].
- Eriksson, L. (1989). Temperature effects on consolidation properties of sulphide clays. *International Conference on Soil Mechanics and Foundation Engineering*, Rio de Janeiro, Brazil, pp.2087–2090.
- Eshbach, O.W. and Tapley, B.D., eds. (1990). *Eshbach's handbook of engineering fundamentals*. 3rd ed. Hoboken, New Jersey: John Wiley and Sons.
- Favero, V., Ferrari, A., and Laloui, L. (2016). Thermo-mechanical volume change behaviour of Opalinus clay. *International Journal of Rock Mechanics and Mining Sciences*, 90, pp.15–25.
- Finn, F. (1952). The effect of temperature on the consolidation characteristics of remolded clay. *Symposium on Consolidation Testing of Soils*, New Jersey, USA, pp.65–71.
- Flügge, W., ed. (1962). *Handbook of engineering mechanics*. New York: McGraw-Hill.
- François, B. and Laloui, L. (2010). An oedometer for studying combined effects of temperature and suction on soils. *Geotechnical Testing Journal*, 33(2), pp.112–122.
- François, B., Salager, S., El Youssoufi, M.S., Ubals Picanyol, D., Laloui, L., and Saix, C. (2007). Compression tests on a sandy silt at different suction and temperature levels. *Geo-Denver: Computer Applications in Geotechnical Engineering*, Denver, USA, pp.1–10.
- Fredlund, D. (1969). Consolidometer test procedural factors affecting swell properties. *Proceedings of the Second International Conference on Expansive Clay Soils*, Texas, USA, pp.435–456.
- Gawecka, K.A. (2017). *Numerical analysis of geothermal piles*. Thesis (PhD). Imperial College London.
- Granta Design Limited (2009). *CES EduPack software* [computer program].
- Gray, H. (1936). Progress report on research on the consolidation of fine-grained soils. *1st International Conference on Soil Mechanics and Foundation Engineering*, Massachusetts, USA, pp.138–141.
- Gums, J. (2018). *Types of temperature sensors* [online]. Available from: <https://www.digikey.co.uk/en/blog/types-of-temperature-sensors> [visited on June 2020].
- Head, K.H. and Epps, R.J. (2011). *Manual of soil laboratory testing. Volume 2: permeability, shear strength and compressibility tests*. 3rd ed. Caithness: Whittles Publishing.

- Hodgman, C., Weast, R., and Selby, S., eds. (1958). *Handbook of chemistry and physics*. 40th ed. Cleveland, Ohio: Chemical Rubber Publishing.
- Hueckel, T. and Baldi, G. (1990). Thermoplasticity of saturated clays: experimental constitutive study. *Journal of Geotechnical and Geoenvironmental Engineering*, 116(12), pp.1778–1796.
- Hueckel, T. and Borsetto, M. (1990). Thermoplasticity of saturated soils and shales: constitutive equations. *Journal of Geotechnical and Geoenvironmental Engineering*, 116(12), pp.1765–1777.
- Jefferson, I. (1994). *Temperature effects on clay soils*. Thesis (PhD). Loughborough University.
- Kaye, G. and Laby, T. (1959). *Tables of physical and chemical constants*. 12th ed. Harlow: Longman.
- Laloui, L. and Di Donna, A., eds. (2013). *Energy geostructures*. Hoboken, New Jersey: ISTE & John Wiley and Sons.
- Mantikos, V. (2018). *Development of novel apparatus for establishing swelling and water retention characteristics of bentonite*. Thesis (PhD). Imperial College London.
- Marcial, D., Delage, P., and Cui, Y.-J. (2002). On the high stress compression of bentonites. *Canadian Geotechnical Journal*, 39(4), pp.812–820.
- Martínez Calonge, D. (2013). *Development of a new high temperature triaxial apparatus*. Thesis (MSc). Imperial College London.
- Martínez Calonge, D. (2017). *Experimental investigation of the thermo-mechanical behaviour and thermal properties of London clay*. Thesis (PhD). Imperial College London.
- McGinley, J.M. (1983). *The effects of temperature on the consolidation process of saturated fine-grained soils*. Thesis (PhD). University of Colorado.
- McKinstry, H.A. (1965). Thermal expansion of clay minerals. *American Mineralogist: Journal of Earth and Planetary Materials*, 50(1-2), pp.212–222.
- Menkiti, O.C. (1994). *Behaviour of clay and clayey-sand, with particular reference to principal stress rotation*. Thesis (PhD). Imperial College London.
- Mitchell, J.K. and Campanella, R.G. (1964). Creep studies on saturated clays. *Symposium on Laboratory Shear Testing of Soil*, Ottawa, Canada, pp.90–103.
- Mon, E.E., Hamamoto, S., Kawamoto, K., Komatsu, T., and Moldrup, P. (2013). Temperature effects on geotechnical properties of kaolin clay: simultaneous measurements of consolidation characteristics, shear stiffness, and permeability using a modified oedometer. *GSTF International Journal of Geological Sciences (JGS)*, 1(1), pp.1–10.
- Moritz, L. (1995). *Geotechnical properties of clay at elevated temperatures* (Report 47). Linköping: Swedish Geotechnical Institute.
- Naughton, P. and O’Kelly, B. (2003). The anisotropy of Leighton Buzzard sand under general stress conditions. *Proceedings of the Third International Symposium on Deformation Characteristics of Geomaterials*, Lyon, France, pp.285–291.

- Ng, C.W.W., Mu, Q., and Zhou, C. (2017). Effects of boundary conditions on cyclic thermal strains of clay and sand. *Géotechnique Letters*, 7(1), pp.73–78.
- Omega Engineering (2020). *Introduction to integrated circuit temperature sensors* [online]. Available from: <https://www.omega.co.uk/prodinfo/Integrated-Circuit-Sensors.html> [visited on June 2020].
- Paaswell, R.E. (1967). Temperature effects on clay soil consolidation. *Journal of the Soil Mechanics and Foundations Division*, 93(3), pp.9–22.
- Plum, R. and Esrig, M. (1969). Effects of temperature on some engineering properties of clay soils. *International Conference on Effects of Temperature and Heat on Engineering Behavior of Soils*, Washington, D.C., USA, pp.231–242.
- Potts, D.M. and Zdravković, L. (1999). *Finite element analysis in geotechnical engineering: theory*. London: Thomas Telford.
- Potts, D.M. and Zdravković, L. (2001). *Finite element analysis in geotechnical engineering: application*. London: Thomas Telford.
- REOTEMP Instruments (2011). *What is a thermocouple?* [Online]. Available from: <https://www.thermocoupleinfo.com/index.htm> [visited on June 2020].
- Romero, E. (1999). *Characterisation and thermo-hydro-mechanical behaviour of unsaturated Boom clay: an experimental study*. Thesis (PhD). Universitat Politècnica de Catalunya.
- Romero, E., Gens, A., and Lloret, A. (2001). Temperature effects on the hydraulic behaviour of an unsaturated clay. *Geotechnical and Geological Engineering*, 19(3-4), pp.311–332.
- Romero, E., Villar, M.V., and Lloret, A. (2005). Thermo-hydro-mechanical behaviour of two heavily overconsolidated clays. *Engineering Geology*, 81(3), pp.255–268.
- Rossato, G., Ninis, N., and Jardine, R. (1992). Properties of some kaolin-based model clay soils. *Geotechnical Testing Journal*, 15(2), pp.166–179.
- Salager, S., Francois, B., El Youssoufi, M., Laloui, L., and Saix, C. (2008). Experimental investigations of temperature and suction effects on compressibility and pre-consolidation pressure of a sandy silt. *Soils and Foundations*, 48(4), pp.453–466.
- Shariatmadari, N. and Saeidijam, S. (2011). The effect of elevated temperature on compressibility and swelling of bentonite-sand mixtures. *Electronic Journal of Geotechnical Engineering*, 16, pp.137–146.
- Shin Etsu Silicone (2019). *The unique properties of silicones* [online]. Available from: <https://www.shinetsusilicone-global.com/products/type/oil/detail/about/index2.shtml> [visited on June 2020].
- Simply Foam Products (2010). *EPF 30 closed cell polyethylene foam specification* [online]. Available from: <https://www.foam.co.uk/closed-cell-polyethylene-foam.php> [visited on June 2020].

- Sittidumrong, J., Jotisankasa, A., and Chantawarangul, K. (2019). Effect of thermal cycles on volumetric behavior of Bangkok sand. *Geomechanics for Energy and the Environment*, 20, p.100127.
- Skinner, B.P. (1966). Thermal expansion. *Handbook of Physical Constants*, pp.75–91.
- Smiths Metal Centres (2018). *PVC-u technical datasheet* [online]. Available from: <https://www.smithmetal.com/pdf/plastics/pvc-u.pdf> [visited on June 2020].
- Tang, A.-M., Cui, Y.-J., and Barnel, N. (2008). Thermo-mechanical behaviour of a compacted swelling clay. *Géotechnique*, 58(1), pp.45–54.
- Tidfors, M. and Sällfors, G. (1989). Temperature effect on preconsolidation pressure. *Geotechnical Testing Journal*, 12(1), pp.93–97.
- Toll, D. (1999). A data acquisition and control system for geotechnical testing. *Computing Developments in Civil and Structural Engineering*, Oxford, UK, pp.237–242.
- Toll, D. (2002). *TRIAX user manual, Version 4.2*. Durham: University of Durham.
- Towhata, I., Kuntiwattanakul, P., Seko, I., and Ohishi, K. (1993). Volume change of clays induced by heating as observed in consolidation tests. *Soils and Foundations*, 33(4), pp.170–183.
- Vega, A. and McCartney, J.S. (2015). Cyclic heating effects on thermal volume change of silt. *Environmental Geotechnics*, 2(5), pp.257–268.
- Verdugo, R. and Ishihara, K. (1996). The steady state of sandy soils. *Soils and Foundations*, 36(2), pp.81–91.
- Villar, M.V. and Lloret, A. (2004). Influence of temperature on the hydro-mechanical behaviour of a compacted bentonite. *Applied Clay Science*, 26(1-4), pp.337–350.
- Ye, W.-M., Zhang, Y.-W., Chen, B., Zheng, Z.-J., Chen, Y.-G., and Cui, Y.-J. (2012). Investigation on compression behaviour of highly compacted GMZ01 bentonite with suction and temperature control. *Nuclear Engineering and Design*, 252(1), pp.11–18.
- Ye, W.-M., Zhang, Y.-W., Chen, Y.-G., Chen, B., and Cui, Y.-J. (2013). Experimental investigation on the thermal volumetric behavior of highly compacted GMZ01 bentonite. *Applied Clay Science*, 83-84(1), pp.210–16.